DISSERTATION

Crystal Engineering of Oxidotellurates

ausgeführt zum Zwecke der Erlangung des akademischen Grades eines Doktors der technischen Wissenschaften unter der Leitung von

Matthias Weil

E164-05

Institut für Chemische Technologien und Analytik,

Forschungsbereich Strukturchemie

eingereicht an der Technischen Universität Wien

Fakultät für Technische Chemie

von

Felix Eder

01426661

Wien, am _____ _____

=

Abstract

Oxidotellurates are known to have a very rich and diverse crystal chemistry. This can be attributed to the different possible coordination polyhedra, which tellurium oxidocompounds can exhibit. Oxidotellurates(IV) usually have their Te atoms coordinated by three, four or five oxygen atoms in a one-sided coordination due to the stereoactivity of the non-bonding $5s^2$ electron pair of Te^{IV}. In oxidotellurates(VI), where no such lone pair is present, octahedral coordination is the predominant case.

New transition metal oxidotellurates(IV) are promising candidates in the search for new ferro-, pyro- and piezoelectrics, second harmonic generators, or, for selected metal cations, enticing magnetic properties. The low-symmetric and polar oxidotellurate(IV) group is a well-suited building block, as compounds exhibiting the previously mentioned properties, besides magnetics, need to be polar and therefore have to lack inversion symmetry.

While numerous ternary transition metal oxidotellurate phases have been discovered and characterized over the past decades, the area of quaternary or even more complicated compounds is much less explored. Therefore, the aim of this work was to modify transition metal oxidotellurates by incorporation of secondary ions, ideally ones with a considerably different crystal chemistry. In this thesis, three main paths were followed: the modification of oxidotellurates(IV) by foreign oxido anions, of oxidotellurates(IV) by alkali metal cations and of oxidotellurates(VI) by alkali metal cations.

For the incorporation of foreign anions into transition metal oxidotellurates(IV), the hydrothermal method proved to be the most reliable one. By this means, the anions nitrate ($Cd_5(TeO_3)_4(NO_3)_2$, $Cd_4Te_4O_{11}(NO_3)_2$ and $Pb_3Te_2O_6(NO_3)_2$), arsenate ($Zn_2(HTeO_3)(AsO_4)$), oxidotellurate(VI) ($Cu_2Te_4O_{12}(NH_3)(H_2O)_2$), phosphate ($Ni_3Te_2O_2(PO_4)_2(OH)_4$), hydroxide ($Mn_3(TeO_3)_2(OH)_2$, $Mn_{15}(TeO_3)_{14}(OH)_2$, $Co_2(TeO_3)(OH)_2$ and $Co_{15}(TeO_3)_{14}(OH)_2$), carbonate ($Rb_2Zn(TeO_3)(CO_3)(H_2O)$) and tungstate ($Cd_3(WO_4)(TeO_3)_2$ and $(NH_4)_2W_3O_9(TeO_3)$) were introduced to form novel oxidotellurate(IV) phases. For the channel structure of $Mn_3(TeO_3)_2(OH)_2$ and its isotypic literature phases $Co_3(TeO_3)_2(OH)_2$ and $Ni_3(TeO_3)_2(OH)_2$, it was shown that various other foreign anions (Cl^-, Br^-, NO_3^-, SO_4^{2-} and CO_3^{2-}) can partially substitute the hydroxide anions inside the channels.

In order to include alkali metal cations into transition metal oxidotellurates(IV), a modification of the hydrothermal method was found to be most successful. In the reactions between metal oxides, TeO_2 and alkali carbonates A_2CO_3, a reduction of the water content from several milliliters to only three droplets, corresponding to *ca*. 0.1 g, led to the discovery of numerous phases with new crystal structures. Eleven of the newfound phases ($Na_{1.79}Mg_{0.11}[Mg_2(TeO_3)_3](H_2O)_{3.86}$, $Na_2[Ni_2(TeO_3)_3](H_2O)_{2.5}$, $Na_2[Cu_2(TeO_3)_3](H_2O)_{1.5}$, $K_2[Co_2(TeO_3)_3](H_2O)_{2.5}$, $K_2[Ni_2(TeO_3)_3](H_2O)$, $K_2[Cu_2(TeO_3)_3](H_2O)_2$, $K_2[Zn_2(TeO_3)_3](H_2O)_2$, $Rb_{1.25}[Co_2(TeO_3)_3](H_2O)_{1.5}$, $Rb_{1.5}[Mn_2(TeO_3)_3](H_2O)_{1.25}$, $Rb_{1.24}[Mn_2(TeO_3)_3](H_2O)_2$ and $Cs[Mn_2(TeO_3)_3](H_2O)$) crystallize in the zemannite structure type, which consists of a hexagonal framework perforated by large channels, where the alkali metal cations and the crystal water molecules are situated.

Of the other phases with new crystal structures, $Li_2Cu_2Te_3O_9$ and $Li_2Cu_3Te_4O_{12}$ (A = Li), $Na_2Zn_2Te_4O_{11}$ and $Na_2Cu_3Te_4O_{12}$ (A = Na), $K_2Mn_2(TeO_3)_3$, $K_2Cd_2(TeO_3)_3$, $K_2Cu_3Te_4O_{12}$, $K_2Cu_3Te_6O_{16}$, $K_2Cu_2Te_4O_{11}(H_2O)_2$ and $K_4Sn_3Te_8O_{24}$ (A = K), $Rb_2Cu_3Te_6O_{16}$ and $Rb_2Zn(TeO_3)(CO_3)(H_2O)$ (A = Rb) and $Cs_2Cu_3Te_6O_{16}$ (A = Cs), many have modular structures formed by rods or layers. Several of these modular structures are heavily disordered, which can be noticed from the presence of diffuse scattering in the diffraction pattern and from disordered atomic positions. In order to explain the diffuse scattering, for several phases the OD theory was applied, and in some cases the diffuse scattering was simulated and qualitatively compared to the diffraction patterns.

Synthesis of alkali-modified oxidotellurates(VI) was, similarly to oxidotellurates(IV), most successful when reducing the water content for the hydrothermal set-up. Here, mixtures of metal oxides, H_6TeO_6 and *A*OH with a complete omission of additional water, were the most effective. Small amounts of water are formed during the reaction from H_6TeO_6 and the introduced hydroxide and function as a mineralizer. The majority of the newly discovered phases are potassium-modified oxidotellurate(VI) species with the Na-based $Na_3Te_2(FeO_4)_3$ and $Na_3FeTe_2O_9$, and $RbPb_3Te_2O_9(OH)$ as the only non-K-representatives. Most of the new phases in the K–Cu–Te^{VI}–O-system ($K_2Cu_2TeO_6$, $K_2Cu_2TeO_6(H_2O)$, $K_2Cu_2TeO_6(H_2O)_4$, $K_3Cu_2TeO_5(OH)(CO_3)(H_2O)$, *α*- and *β*-$KCuTeO_4(OH)$ and $K_4CuTe_4O_{14}(OH)_2$) have layered crystal structures, while the others consist of isolated [Cu–Te–O] units ($K_{10}Cu_2Te_3O_{16}$ and $K_5CuTe_2O_8(OH)_4(H_2O)_8$), [Cu–Te–O] chains ($K_3CuTeO_5(OH)(H_2O)$) or a tri-periodic [Cu–Te–O] framework ($K_6Cu_9Te_4O_{24}(H_2O)_2$). The other phases include Mn^{III} ($K_4Mn_2Te_3O_{12}(OH)_4$), Fe^{III} ($K_{12}Fe_6Te_4O_{27}(H_2O)_3$ and $K_3FeTe_2O_8(OH)_2(H_2O)$), Pb^{II} ($KPb_2TeO_5(OH)$, $K_2Pb_3TeO_7$ and $K_{14}Pb^{IV}Pb^{II}{}_9Te_7O_{36}(OH)_6(H_2O)_6$) or Bi^{III} ($K_6Bi_4Te_3O_{17}(CO_3)(H_2O)_3$) as their framework metal cations.

Besides these three main fields, the crystal structures of several ternary *M*–Te^{IV}–O-phases were determined as well. While the phases *α*-$MnTeO_3$ and $Mn_6Te_5O_{16}$ have been described previously in literature without solution of their crystal structures, the compounds *γ*-$MnTeO_3$, *β*-$CdTe_2O_5$ and $Cd_4Te_5O_{14}$ were synthesized and characterized for the first time.

While the main analysis methods of this work have been diffraction methods (powder and single-crystal X-ray diffraction), several complementary analytical techniques have been applied for selected phases as well. They include energy-dispersive X-ray spectroscopy conducted in a scanning electron microscope, infrared- and Raman-spectroscopy, thermogravimetry, differential scanning calorimetry and the determination of magnetic properties.

Zusammenfassung

Die Kristallchemie von Tellurit- und Telluratverbindungen ist sehr facettenreich, was vor allem auf die vielfältigen Koordinationspolyeder, die von Sauerstoff koordiniertes Tellur aufweisen kann, zurückzuführen ist. Die Tellurit-Anionen mit vierwertigem Tellur haben meist Koordinationszahlen von drei bis fünf. Die dabei entstehenden Koordinationspolyeder sind aufgrund des sterischen Einflusses des nichtbindenden $5s^2$ Elektronenpaars des Te^{IV} Atoms sehr einseitig und dadurch meist niedersymmetrisch. In Telluratverbindungen sind die Te^{VI} Atome hingegen oktaedrisch koordiniert.

Übergangsmetalltellurite sind als mögliche Ferro-, Pyro- oder Piezoelektrika oder Frequenzverdoppler Gegenstand der aktuellen Forschung. Die Tatsache, dass einige Telluritverbindungen solche Eigenschaften besitzen, lässt sich mit der Kristallchemie des Te^{IV} erklären. Um ein Ferroelektrikum, *etc*. sein zu können, muss die Kristallstruktur eines Stoffes polar sein und darf daher nicht inversionssymmetrisch sein. Die einseitigen, nicht zentrosymmetrischen Telluritgruppen stellen also gute Bausteine für solche Verbindungen dar.

Im Laufe der letzten Jahrzehnte sind etliche ternäre Übergangsmetalltelluritverbindungen hergestellt und charakterisiert worden. Der Bereich quaternärer Verbindungen oder gar noch komplizierterer Zusammensetzungen ist aber deutlich weniger weit erforscht. Ziel dieser Arbeit war es, dies zu tun, und Übergangsmetalltellurite und -tellurate durch Einbau von Sekundärionen zu modifizieren. Hierbei sollten sich diese Sekundärionen in ihrer Kristallchemie von den Übergangsmetallkationen und Telluritanionen deutlich unterscheiden, um die Kristallstruktur zugunsten von niedersymmetrischen Phasen ohne Inversionssymmetrie aufzubrechen. Die durchgeführten Experimente und erhaltenen Verbindungen bzw. deren Kristallstrukturen lassen sich dabei in drei Hauptbereiche der Modifikation unterteilen: Tellurite mit sauerstoffhaltigen Sekundäranionen, Tellurite mit zusätzlichen Alkalimetallkationen und Tellurate mit zusätzlichen Alkalimetallkationen.

Für den Einbau von Fremdanionen in Übergangsmetalltellurite waren Hydrothermalsynthesen unter alkalischen Bedingungen am erfolgreichsten. Hierbei konnten die Anionen Nitrat ($Cd_5(TeO_3)_4(NO_3)_2$, $Cd_4Te_4O_{11}(NO_3)_2$ und $Pb_3Te_2O_6(NO_3)_2$), Arsenat ($Zn_2(HTeO_3)(AsO_4)$), Tellurat ($Cu_2Te_4O_{12}(NH_3)(H_2O)_2$), Phosphat ($Ni_3Te_2O_2(PO_4)_2(OH)_4$), Hydroxid ($Mn_3(TeO_3)_2(OH)_2$, $Mn_{15}(TeO_3)_{14}(OH)_2$, $Co_2(TeO_3)(OH)_2$ und $Co_{15}(TeO_3)_{14}(OH)_2$), Carbonat ($Rb_2Zn(TeO_3)(CO_3)(H_2O)$) und Wolframat ($Cd_3(WO_4)(TeO_3)_2$ und $(NH_4)_2W_3O_9(TeO_3)$) zur Herstellung neuer Telluritverbindungen eingebaut werden. Für die Verbindungen mit Kanalstrukturen, hier $Mn_3(TeO_3)_2(OH)_2$ und die isotypen $Co_3(TeO_3)_2(OH)_2$ und $Ni_3(TeO_3)_2(OH)_2$, konnte weiters nachgewiesen werden, dass ein Teil der Hydroxidionen in den Kanälen der Kristallstruktur durch andere Anionen (Cl^-, Br^-, NO_3^-, SO_4^{2-} und CO_3^{2-}) ersetzt werden kann.

Zur Synthese von alkalimetallmodifizierten Übergangsmetalltelluriten stellte sich eine Modifikation der Hydrothermalmethode als am vielversprechendsten heraus. Zu den Eduktmischungen aus Metalloxid, TeO_2 und Alkalicarbonat A_2CO_3 wurden statt der üblichen wenigen Milliliter Wasser nur drei Tropfen, dies entspricht *ca*. 0.1 g, zugesetzt. Von den hierbei neu hergestellten Phasen kristallisieren gleich elf ($Na_{1.79}Mg_{0.11}[Mg_2(TeO_3)_3](H_2O)_n$, $Na_2[Ni_2(TeO_3)_3](H_2O)_{2.5}$, $Na_2[Cu_2(TeO_3)_3](H_2O)_{1.5}$, $K_2[Co_2(TeO_3)_3](H_2O)_{2.5}$, $K_2[Ni_2(TeO_3)_3](H_2O)$, $K_2[Cu_2(TeO_3)_3](H_2O)_2$, $K_2[Zn_2(TeO_3)_3](H_2O)_2$, $Rb_{1.25}[Co_2(TeO_3)_3](H_2O)_{1.5}$, $Rb_{1.5}[Mn_2(TeO_3)_3](H_2O)_{1.25}$, $Rb_{1.24}[Mn_2(TeO_3)_3](H_2O)_2$ und $Cs[Mn_2(TeO_3)_3](H_2O)$) im Zemannit-Strukturtyp. Dieser besteht aus einem hexagonalen Gerüst aus den Koordinationspolyedern der Übergangsmetalle und Telluratome und großen Kanälen, in denen sich die Alkalimetallkationen und Kristallwassermoleküle befinden.

Von den übrigen Verbindungen, $Li_2Cu_2Te_3O_9$ und $Li_2Cu_3Te_4O_{12}$ (A = Li), $Na_2Zn_2Te_4O_{11}$ und $Na_2Cu_3Te_4O_{12}$ (A = Na), $K_2Mn_2(TeO_3)_3$, $K_2Cd_2(TeO_3)_3$, $K_2Cu_3Te_4O_{12}$, $K_2Cu_3Te_6O_{16}$, $K_2Cu_2Te_4O_{11}(H_2O)_2$ und $K_4Sn_3Te_8O_{24}$ (A = K), $Rb_2Cu_3Te_6O_{16}$ und $Rb_2Zn(TeO_3)(CO_3)(H_2O)$ (A = Rb) und $Cs_2Cu_3Te_6O_{16}$ (A = Cs), besitzen etliche

modulare Strukturen aus Stäben oder Schichten, von denen wiederum einige starke Fehlordnung zeigen. Diese kann sowohl am Auftreten von diffuser Streuung als auch von teilbesetzten Atompositionen erkannt werden. Um die auftretenden Fehlordnungen zu modellieren, wurde in einigen Fällen die OD Theorie verwendet und manchmal zusätzlich die diffuse Streuung simuliert, um einen qualitativen Vergleich mit dem Beugungsbild zu erhalten.

Die Herstellung von neuen alkalimetallmodifizierten Metalltelluraten funktionierte ebenfalls mit einer massiven Reduktion des Wassergehalts am besten. Bei der bevorzugten Art von Ansatz wurden Metalloxid, H_6TeO_6 und *A*OH ohne jeglichen externen Wasserzusatz reagiert. Die geringen Wassermengen, die aus der Reaktion von Tellursäure und Hydroxid entstehen, fungieren hier nicht mehr als Lösungsmittel, sondern als Mineralisator.

Von den erhaltenen Verbindungen sind die meisten Kaliumverbindungen; daneben wurden noch die Phasen $Na_3Te_2(FeO_4)$, $Na_3FeTe_2O_9$ und $RbPb_3Te_2O_9(OH)$ erhalten. Unter den neu synthetisierten Kaliumkupfertelluraten haben die meisten Phasen ($K_2Cu_2TeO_6$, $K_2Cu_2TeO_6(H_2O)$, $K_2Cu_2TeO_6(H_2O)_4$, $K_3Cu_2TeO_5(OH)(CO_3)(H_2O)$, *α*- und *β*-$KCuTeO_4(OH)$ und $K_4CuTe_4O_{14}(OH)_2$) eine Schichtstruktur. Die übrigen bestehen aus isolierten [Cu−Te−O] Oligomeren ($K_{10}Cu_2Te_3O_{16}$ und $K_5CuTe_2O_8(OH)_4(H_2O)_8$), [Cu−Te−O] Ketten ($K_3CuTeO_5(OH)(H_2O)$) oder einem dreidimensionalen [Cu−Te−O] Gerüst ($K_6Cu_9Te_4O_{24}(H_2O)_2$). Die übrigen Kaliumtelluratphasen enthalten die Metalle Mangan(III) ($K_4Mn_2Te_3O_{12}(OH)_4$), Eisen(III) ($K_{12}Fe_6Te_4O_{27}(H_2O)_3$ und $K_3FeTe_2O_8(OH)_2(H_2O)$), Blei(II) ($KPb_2TeO_5(OH)$, $K_2Pb_3TeO_7$ und $K_{14}Pb^{IV}Pb^{II}_9Te_7O_{36}(OH)_6(H_2O)_6$) oder Bismut(III) ($K_6Bi_4Te_3O_{17}(CO_3)(H_2O)_3$).

Abseits dieser drei Hauptrichtungen wurden auch die Kristallstrukturen einiger ternärer Mangan- und Cadmiumtellurite bestimmt. *α*-$MnTeO_3$ und $Mn_6Te_5O_{16}$ waren bereits literaturbekannt, ihre Kristallstruktur jedoch noch nicht mit Einkristalldiffraktion ermittelt, während *γ*-$MnTeO_3$, *β*-$CdTe_2O_5$ und $Cd_4Te_5O_{14}$ bislang unbeschriebene Verbindungen darstellen.

Die hauptsächlich verwendete Analysenmethoden in dieser Arbeit waren Pulver- und Einkristallröntgendiffraktion. Daneben wurden bei ausgewählten Phasen komplementäre Analysenmethoden wie energiedispersive Röntgenspektometrie mittels eines Rasterelektronen-mikroskops, Infrarot- und Ramanspektroskopie, Thermogravimetrie, dynamische Differenzkalorimetrie und die Bestimmung magnetischer Eigenschaften eingesetzt.

Danksagung

Der größte Dank gebührt Matthias Weil für die Möglichkeit, diese Arbeit während der letzten vier Jahre in der Forschungsgruppe Strukturchemie durchführen zu können, seine Zuverlässigkeit, und seine Bereitschaft, jegliche Fragen und Anliegen von mir sofort zu beantworten und mir weiterzuhelfen. Durch Vergleich mit vielen Dissertanten in meinem Umfeld weiß ich, dass das alles keine Selbstverständlichkeit ist und wie glücklich ich mich mit seiner Betreuung schätzen kann. Ich habe außerdem die Möglichkeit, frei und uneingeschränkt zu forschen, sehr genossen.

Berthold Stöger hat mich in die Welt der (Einkristall-)Röntgendiffraktion eingeführt und mir bis zuletzt neue Aspekte der Kristallographie, einem Fachgebiet, das nach wie vor eine große Faszination auf mich ausübt, beigebracht. Dafür, für die stetige Hilfestellung bei meinen eigenen kristallographischen Problemen, seine Funktion als interner Gutachter dieser Arbeit und allgemein die gute Zusammenarbeit möchte ich mich herzlich bedanken.

Beim Röntgenzentrum der TU Wien und seiner Leiterin Klaudia Hradil möchte ich mich für die Bereitstellung der Pulver- und Einkristalldiffraktometer, sowie der Auswertungsinfrastruktur bedanken. Werner Artner sei hier einerseits für die ständige Wartung der Geräte, aber auch das Teilen seines Wissens über die Instandhaltung von Diffraktometern besonders gedankt. Bei der Forschungsgruppe Weinberger bedanke ich mich für die Verfügungstellung ihres IR-Spektrometers.

Bei Ronald Milteich will ich mich für die gute Zusammenarbeit im Zuge der Hochdruck-Ramanuntersuchungen von $K_2Cu_2TeO_6$ und der Strukturaufklärung eines seiner alten gemischvalenten Zemannitkristalle, sowie für seine Rolle als externen Gutachter und Prüfer bedanken.

Weiters möchte ich mich bei diversen ForschungspartnerInnen bedanken. In alphabetischer Reihenfolge sind dies Uwe Kolitsch für die EDX-Analysen am Rasterelektronenmikroskop, Eugen Libowitzky für die Raman-spektroskopischen Untersuchungen, Roland Mathieu und Prativa Pramanik für die magnetischen Untersuchungen, Sofija Milos für die Durchführung der Hochdruck-Ramanmessungen und Harishchandra Singh für die Hochtemperatur-Pulverdiffraktionsmessungen am Synchrotron.

Ich möchte mich bei den Praktikanten Ruben do Carmo, Georg Hatzl und Alexandre Marsollier, sowie Paul Sicher, der seine Bachelorarbeit bei uns verfasst hat, für ihren Anteil an der hier präsentierten Forschung herzlichst bedanken. Auf ihren Beitrag wird an gegebener Stelle nochmals hingewiesen.

Ich bedanke mich bei Angelika Graumann für ihre Hilfsbereitschaft und stetige organisatorische Arbeit im Hintergrund, sowie bei Mariana Pantazi und Melanie Anstiss für die angenehme Zusammenarbeit im Festkörperchemiepraktikum.

Außerdem will ich mich bei allen während der letzten vier Jahre aktiven oder aktiv gewesenen KollegInnen der anorganischen chemischen Technologie für das freundliche und angenehme soziale Umfeld bedanken. Ich habe nicht so viel Bier mit euch getrunken, wie ihr es verdient habt.

Besonders möchte ich mich bei meinen Eltern Gabi und Flo, und meinen Geschwistern Moritz und Marie für ihre Unterstützung in allen Lebenslagen und die Gewissheit, dass dies auch in Zukunft so ist, bedanken.

Die letzten vier Jahre waren für mich, trotz aller Irrungen der Covid-19-Pandemie, eine sehr schöne Zeit. Das liegt vor allem daran, dass ich im Herbst 2019 eine ganz besondere Frau kennen gelernt habe. Ich liebe dich, Alice, und ich will mir nicht vorstellen wie die vergangenen oder die kommenden Jahre ohne dich (gewesen) wären.

Table of contents

1 Introduction

1.1 Crystal chemistry of oxidotellurates

The element tellurium, located in the periodic table in the group of chalcogenides below oxygen, sulfur and selenium, appears quite rarely on earth. Its abundancy in the lithosphere of *ca*. 5 µg/kg (Missen et al., 2020) compares to that of gold or platinum. Hereby, the metalloid Te appears either as telluride Te^{2-} anion, mostly substituting sulfur in sulfide minerals or as an oxysalt of either Te^{IV} or Te^{VI}, which are called oxidotellurates. In literature, the names oxotellurates($Te^{IV/VI}$), tellurites (Te^{IV}) and (ortho)tellurates(Te^{VI}) can be found synonymously .

Oxidotellurates exhibit a multifarious crystal chemistry. The comprehensive review by Christy et al. from 2016 already lists more than 700 crystal structures of oxidotellurate phases, of which 55 were determined from minerals (there are more oxidotellurate minerals known, but their crystal structures have not been determined yet). These 703 structures can be split into one half containing Te^{IV} and the other half containing Te^{VI} each, with a slight surplus for the Te^{IV} compounds. Crystal structures containing Te in both valences are known as well but are much less common with the structures of only 35 mixed Te^{IV}/Te^{VI} compounds known as of a recent search in the Inorganic Crystal Structure Database (ICSD; Version 2022-1; Zagorac et al., 2019).

The structural richness of oxidotellurates in general can partially be attributed to the very different coordination behavior of Te in its two prevalent oxidation states, Te^{IV} and Te^{VI}. Te^{VI} is coordinated almost exclusively by six oxygen atoms in an octahedral shape, with only two examples each for fourfold (tetrahedral) and fivefold (trigonal bipyramidal) coordination. All of these phases, $Cs_2(TeO_4)$ (Weller et al., 1999), $Cs_2K_2(TeO_5)$ (Untenecker & Hoppe, 1986) and $Rb_6(TeO_5)(TeO_4)$ (Wisser & Hoppe, 1990) are characterized by the inclusion of a high amount of large counter cations, leading to a structural pressure for lower coordination numbers.

Te^{IV} exhibits a greater diversity of its coordination environments, which originates from the stereoactivity of the non-bonding $5s^2$ electron pair ψ of Te^{IV} (Galy et al., 1975). The large space consumption of this “lone pair” leads to the formation of rather one-sided coordination polyhedra (Figure 1) with 3, 4 and 5 being the most common coordination numbers (CNs) of Te^{IV}, but some rare cases of 2 and 6 have been reported as well. A $[TeO_3]$ unit typically has a trigonal-pyramidal shape with the lone pair sitting on the apex of the pyramid. $[TeO_4]$ groups have a bisphenoidal shape, which can be derived from a distorted trigonal bipyramidal coordination with ψ occupying one of the equatorial positions. The shape of the $[TeO_5\psi]$ polyhedron is that of a distorted octahedron with the non-bonding $5s^2$ electron pair occupying more space than the other ligands.

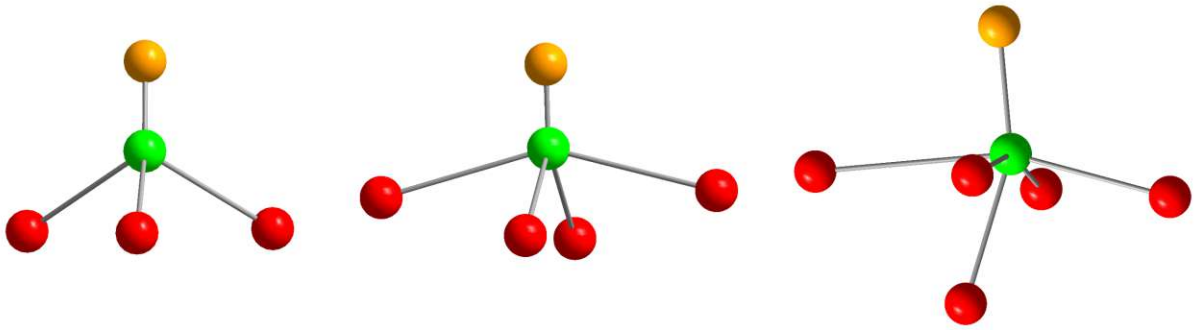

Figure 1. Examples for coordination polyhedra of oxidotellurates(IV) appearing in this work. Left: trigonal pyramid; middle: bisphenoid; right: tetragonal pyramid. Te atoms are drawn as green, O atoms as red, and the lone pairs ψ as orange spheres.

[TeO_x] groups, irrespective of Te^{IV} or Te^{VI}, have the ability to condense into larger structural units with the corresponding building blocks sharing corners, edges or planes (only Te^{VI}). These larger units can either be oligomeric or polymeric with periodicities of one (chains), two (layers) or three (frameworks). A categorization of all oxidotellurate structures known to date can be found in the extensive review by Christy et al. (2016).

The formation of crystal structures with reduced periodicity is a commonly observed phenomenon in oxidotellurate phases. For tetravalent Te, this can be attributed to the large amount of space consumption of the lone pairs ψ. Rod- or layer-structures with ψ being directed away from the building block, or channel structures with ψ oriented towards the center of the channels have frequently been observed for oxidotellurate(IV) phases. Examples for rod structures are $K_3GaTe_2O_8(OH)_2(H_2O)$ (Yu et al., 2004) or $A_2Te_2O_4(OH)_4$ (*A* = K, Rb) (Völkl et al., 2022).

β-TeO_2 (Beyer, 1967) and numerous oxidotellurates(IV) like $K_2Te_4O_9$ (Becker et al., 1997) and its more hydrated phases (Ok & Halasyamani, 2001), $(Te_3O_3)(AsO_4)_2$ (Weil, 2013), or $Ca_5Te_4O_{12}(NO_3)_2(H_2O)_2$ and $Ca_6Te_5O_{15}(NO_3)_2$ (Stöger & Weil, 2013) are layered structures. As the space between such layers is mostly occupied by the $5s^2$ lone pairs, the connection from one layer to the next can be rather weak. Therefore, it is not surprising that some layered oxidotellurate phases show disorder in their stacking, often observable by the presence of diffuse scattering in the diffraction patterns, like, *e.g.*, in $Ca_5Te_4O_{12}(NO_3)_2(H_2O)_2$ and $Ca_6Te_5O_{15}(NO_3)_2$ (Stöger & Weil, 2013).

Another possibility to account for the space requirements of the non-bonding $5s^2$ electron pairs, is the formation of channel structures with ψ being directed towards the channel-center. The mineral zemannite, $Mg_{0.5}[ZnFe(TeO_3)_3]\cdot 4.5H_2O$ (Miletich, 1995a; Cametti et al., 2017; Missen et al., 2019; Effenberger et al., 2023) and the family of zemannite-type structures, like $Na_2[Zn_2(TeO_3)_3](H_2O)_3$ and $Na_2[Co_2(TeO_3)_3](H_2O)_3$ (Miletich, 1995b) or $Ga_2(TeO_3)_3$ (Kong et al., 2010), or the $M_3(TeO_3)_2(OH)_2$ (*M* = Co, Ni; Perez et al., 1976; Poupon et al., 2019) structure type are representatives of Te^{IV}-based channel structures.

1.2 Possible applications

Another consequence of the stereoactivity of ψ is that the resulting one-sided [$Te^{IV}O_x$] coordination polyhedra lack inversion symmetry. This makes oxidotellurates(IV) promising candidates in the search for new ferro-, pyro- or piezoelectrics or second harmonic generators. In order to exhibit the aforementioned properties, a compound needs to be polar and therefore must not have inversion symmetry (Ok et al., 2006).

Ferroelectric properties have been investigated for several examples of oxidotellurate(IV) phases, *e.g.,* for $CaTeO_3$ (Rai et al., 2002), $SrTeO_3$ (Yamada & Iwazaki, 1973), $(NH_4)_2Te_2WO_8$ (Kim et al., 2007) or, most recently, thin flakes of Bi_2TeO_5 (Han et al., 2022). The pyroelectricity of certain oxidotellurates(IV) has been revealed, in example, for $Na_2Te_3Mo_3O_{16}$ (Chi et al., 2006), $(NH_4)_2Te_2WO_8$ (Kim et al., 2007) or $AgTlTeO_3$ (Linda et al., 2010), while piezoelectric effects were discussed for, *e.g.,* $LiNbTeO_5$ (Chen et al., 2021) or Bi_2TeO_5 (Antonenko et al., 1999).

In the field of second harmonic generators (SHG), the combination of oxidotellurates(IV) with d^0 metals proves to be very promising. Especially the field of oxidotellurate(IV) molybdates and tungstates has seen a surge over the past years. A comprehensive review on this area was recently published by Guo et al. (2022), while Kong & Mao (2020) summarized the state of oxidotellurate(IV)- and oxidoselenate(IV)-based SHG materials. Some examples for Te^{IV}-based SHGs are the tungstates $(NH_4)_2Te_2WO_8$ (Kim et al., 2007), *β*-$BaTeW_2O_9$ (Zhang et al., 2013), $Cs_2TeW_3O_{12}$ (Goodey et al., 2003) and $Na_2TeW_2O_9$ (Goodey et al., 2002), the molybdates $Na_2Te_3Mo_3O_{16}$ (Chi et al., 2006), $Cs_2TeMo_3O_{12}$

(Zhang et al., 2011), $MgMoTeO_6$ (Zhang et al., 2012) or $CdTeMoO_6$ (Zhao et al., 2013) as well as the niobates $InNbTe_2O_8$ (Kim et al., 2014) and $LiNbTeO_5$ (Chen et al., 2021).

Many of the phases mentioned above have incorporated alkali or alkaline earth metals as counter-cations. This can be attributed to the rather easy accessibility and higher reactivity of their salts during synthesis. In particular, alkali metal salts are easily dissolved during hydrothermal synthesis and have a comparably low melting point if the compound is synthesized by solid-state synthesis or from the melt.

1.3 Aim of this work

The search for new oxidotellurate phases and the characterization of such, as illustrated by the past section, is a popular and current field of research, given by the high number of recent publications. While the search for new ferro-, pyro- or piezoelectric compounds as well as SHG materials has focused on the inclusion of early d^0 transition metals together with oxidotellurates(IV) and alkali metal counter-cations, starting from late transition metals, like Mn^{II}, Fe^{III}, Co^{II}, Ni^{II} or Cu^{II}, instead provides the possibility for exciting magnetic properties as well.

Research on the crystal chemistry of oxidotellurates(IV) has a long tradition at TU Wien. Some earlier foci in the structural chemistry research group have been alkaline earth oxidotellurate phases (Stöger, 2010) as well as lead(II) oxidotellurate(IV) compounds (Artner, 2010). The most recent direction of research has been the modification of transition metal oxidotellurate(IV) structures by the incorporation of secondary oxido-anions. By introducing anions lacking inversion symmetry, like the coordination polyhedra of Te^{IV}, themselves, one can hope for a more frequent formation of polar structures and possibly some of the previously mentioned optoelectrical properties. Possible building blocks are the tetrahedral SO_4^{2-}, SeO_4^{2-}, PO_4^{3-}, AsO_4^{3-} or SiO_4^{4-} groups, the trigonal planar NO_3^- or CO_3^{2-} anions, or simply OH^- ions, which might lower the symmetry of the crystal structure towards non-centrosymmetry as well. The predominantly used anions in previous investigations over the past years were sulfate ($Cd_3(SO_4)(Te_3O_8)(H_2O)$, $Cd_4(SO_4)(Te_3O_8)$, $Cd_5(SO_4)_2(TeO_3)_2(OH)_2$ (Weil & Shirkhanlou, 2017a), $Pb_2(SO_4)_2(TeO_3)$ (Weil & Shirkhanlou, 2017b), $Zn_4(SO_4)(TeO_3)_3$, $Mg_2(SO_4)(TeO_3)(H_2O)$, $Mg_3(SO_4)(TeO_3)(OH)_2(H_2O)_2$ (Weil & Shirkhanlou, 2017c)), selenate ($Ca_3(SeO_4)(TeO_3)_2$, $Ca_3(SeO_4)(Te_3O_8)$, $Cd_3(SeO_4)(Te_3O_8)$, $Sr_3(SeO_4)(TeO_3)_2(H_2O)_2$ (Weil & Shirkhanlou, 2017a), $Pb_3(SeO_4)(TeO_3)_2$, $Pb_7O_4(SeO_4)_2(TeO_3)$, $Pb_5(SeO_4)_2(TeO_4)(CO_3)$ (Weil & Shirkhanlou, 2017b), $Zn_2(SeO_4)(TeO_3)$ (Weil & Shirkhanlou, 2017c)) and nitrate ($Ca_5Te_4O_{12}(NO_3)_2(H_2O)_2$, $Ca_6Te_5O_{15}(NO_3)_2$ (Stöger & Weil, 2013), $[Pb_2Cu_2(Te_4O_{11})](NO_3)_2$ (Weil et al., 2019)) anions.

For the current thesis, the goal was to explore new ways of modifying transition metal oxidotellurate frameworks by several approaches. The first one was to build on the most recent investigations and to expand the repertoire of non-centrosymmetric anions, which can be incorporated into transition metal oxidotellurate(IV) phases beyond sulfate and selenate groups. Hereby, the anions PO_4^{3-}, AsO_4^{3-}, NO_3^- and CO_3^{2-} figured to be the most promising candidates.

Another path to be explored was the modification of transition metal oxidotellurates(IV) by secondary cations with completely different ionic radii than the ones of the existing (transition) metal. Hereby, alkali metal cations were the obvious choice, due to their large size and easy introduction into the synthesis. While the incorporation of alkali metal cations into oxidotellurate phases to form quaternary *A*–*M*–Te-oxides is frequently realized for early d^0 transition metals in the research for new SHG materials (Guo et al., 2022), for late transition metals *M*, there are only few examples.

An ICSD query (Version 2022-1; Zagorac et al., 2019) for ternary *A*–*M*–Te^{IV}–O-compounds (*A* = alkali metal, *M* = transition metal) resulted in 34 entries. 30 of these have a d^0 transition metal as *M* (seven W^{VI}, six V^V, five Y^{III}, five Nb^V, four Mo^{VI} and two Ta^V) and only four structures include later transition

metal cations. These four are the mixed-valent oxidotellurate(IV/VI) $Ag_{0.4}Na_{1.6}Te_5O_{14}$ (Loeksmanto et al., 1980), $NaFe(TeO_3)_2$ (Weil & Stöger, 2008) and two entries for the mineral zemannite with a composition of $Na_2Zn_2(TeO_3)_3$ (Matzat, 1967). The latter formula, however, is incorrect, as already in the corresponding publication, the sum formula is written as $\{(Zn,Fe)_2[TeO_3]_3\}Na_xH_{2-x}(H_2O)_y$ including a partial Fe occupancy and crystal water molecules. Furthermore, the Na^+ cations were re-assigned to be Mg^{2+} cations in a subsequent study (Miletich, 1995a). If hydrogen is allowed in the search as well as a fifth element, this includes hydrated phases as well. Then, the synthetic zemannite-type phases $Na_2[Zn_2(TeO_3)_3](H_2O)_3$ and $Na_2[Co_2(TeO_3)_3](H_2O)_3$ (Miletich, 1995b) are the only additional non-d^0 metal hits. Therefore, it was attempted to fill this void on the structural landscape.

1.4 Categorization of oxidotellurates

1.4.1 Structural architecture

Christy et al. (2016) categorized the the crystal structures of available oxidotellurate compounds by their coordination and condensation behavior. For this purpose, they chose a bond length threshold of *ca.* 2.45 Å to determine the connectivity and shape of the formed units. This categorization will be used as well for the crystal structures of the newly found oxidotellurate phases presented in this work. They introduced a 'Q notation' for tetravalent Te similar to that for silicate species. Each Te^{IV} atom is assigned with a Q^{abcz} descriptor, where *a* corresponds to the number of bound oxygen atoms not shared with other $[TeO_x]$ units, *b* to the amount of connected oxygen atoms shared with one other $[TeO_x]$ unit and *c* the number of oxygen atoms shared with two neighboring $[TeO_x]$ units; *z* describes the number of edges shared with neighboring $[TeO_x]$ units. This notation will be used in the present work as well.

Additionally, they defined a second notation to describe the oligo-/polymerization state of oxidotellurate units. The symbols Δ (TeO_3), ◊ (TeO_4), ⌂ (TeO_5) and ◯ (TeO_6) are connected by − (corner-sharing) or = (edge-sharing). Units forming cycles are written within brackets, chains are represented with parentheses.

As it is visible from Figure 1, the shapes of various $[TeO_x]$ groups are substantially influenced by the non-bonding $5s^2$ lone pair ψ of the Te^{IV} atoms. In order to locate and visualize the stereochemical impact of ψ, Hamani & Masson (2019) developed the *LPLoc* program in connection with their extensive study on steric effects of the lone pairs of Te^{IV} amongst other *p*-block element cations (Hamani et al., 2020). Given the atomic coordinates and Wyckoff positions in a CIF-file, the program calculates the location of lone pairs ψ of selected elements, as well as their distance from the nucleus, and their radii. The localization of the lone pairs was performed for other lone-pair atoms like Pb^{II} and Bi^{III} as well.

1.4.2 Geometry index

The transition metal atoms in this work appear with three main coordination numbers: 4, 5 and 6. As their coordination polyhedra do not always correspond to ideal, high-symmetric shapes, the form of these $[MO_n]$ (n = 4−6) units can be described using corresponding geometrical parameters. For n = 4, the geometry index τ_4 (Yang et al., 2007) is defined as

$$\tau_4 = \frac{360° - \alpha - \beta}{360° - (2 * \theta_{tetr})} \quad (1)$$

with α and β being the two largest O—*M*—O-angles and ϑ_{tetr} the O—*M*—O-angle in a tetrahedron (109.47°). τ_4 adopts a value of 0 for a regular square-planar coordination, and a value of 1 for a regular tetrahedron. The definition of τ_4 is flawed, as, given a sum (α + β), the relative sizes of α and β to each other are irrelevant, leading to similar τ_4 values for different forms. Furthermore, τ_4 = 0 does only correspond to a planar coordination, which can differ vastly from that of a square by different bond lengths and variable angles between its two diagonals.

For a coordination number of 5, the two most prominent regular coordination possibilities are a square pyramid and a trigonal bipyramid. In order to recognize similarities to one of these, the τ_5 geometry index (Addison et al., 1984) is employed. τ_5 is calculated as

$$\tau_5 = \frac{\alpha - \beta}{60°} \tag{2}$$

with α and β again being the two largest O—*M*—O-angles ($\alpha \geq \beta$). For a square pyramid, α and β are both 180° and $\tau_5 = 0$, while for a trigonal bipyramid $\alpha = 180°$, $\beta = 120°$ and $\tau_5 = 1$.

1.4.3 Octahedral distortion

The shape of most [MO_6] polyhedra originates from that of an octahedron. However, deviations from ideal octahedral symmetry can commonly be observed in transition metal oxidotellurates. The distortion of [MO_6] octahedra is either imposed by the surrounding framework or is caused by the electronic configuration of the *M* cation itself in the form of so-called Jahn–Teller-effects (JT-effects). The presence and strength of JT-effects depends on the number of *d*-electrons of *M*. Examples for strong JT-effects are the d^4 and d^9 cations Mn^{III} and Cu^{II} (Lufaso & Woodward, 2004). The degree of octahedral distortion can be described with several different parameters. The *OctaDist* software by Ketkaew et al. (2021) calculates the following values:

The arithmetic mean of interatomic (*M*—O) distances d_{mean} (Å)

$$d_{mean} = \frac{\sum_{i=1}^{6} d_i}{6} \tag{3}$$

The distance distortion ζ (Å)

$$\zeta = \sum_{i=1}^{6} |d_i - d_{mean}| \tag{4}$$

The tilting distortion Δ

$$\Delta = \frac{1}{6} \sum_{i=1}^{6} \left(\frac{d_i - d_{mean}}{d_{mean}} \right)^2 \tag{5}$$

The angle distortion Σ (°) is based on the O—*M*—O-angles of neighboring oxygen atoms φ_i

$$\Sigma = \sum_{i=1}^{12} |\varphi_i - 90| \tag{6}$$

The torsional distortion ϑ (°) is based on O—*M*—O-angles ϑ_i, which are measured off projections of two opposite planes by their (pseudo-)threefold rotation onto the central plane containing the *M* atom.

$$\vartheta = \sum_{i=1}^{24} |\theta_i - 90| \tag{7}$$

1.4.4 Bond valence

The bond valence method (Brown, 2002) is a useful tool for analyzing the validity of a structure model and individual crystal-chemical features from crystallographic data. Based on the interatomic distances obtained from the refinement, a theoretical charge of an atomic site is calculated. In this regard, information about the oxidation state or hints to mixed occupancies of different species at the same crystallographic site can be gathered. The bond valence v_i of a contact of neighboring atoms is calculated by

$$v_i = e^{\frac{r_0 - r_i}{b}} \tag{8}$$

with r_i being the interatomic distance between the two atoms and r_0 and *b* being empirically derived parameters. The parameters determined by Brese & O'Keeffe (1991) are commonly used and will be

applied in this work as well. They assume a general value of 0.37 Å for *b*, and the values for r_0 are usually between 1 and 2.5 Å. For the Te^{IV}—O and the Te^{VI}—O bond pairs, the revised parameters by Mills & Christy (2013) were employed instead. These different parameter sets use a different value of *b* than the general 0.37 Å from Brese & O'Keeffe, and require the consideration of all oxygen contacts within a distance of 3.5 Å. They generally lead to better agreements with the ideal charges of 4 and 6 for oxidotellurate(IV and VI) compounds.

For Te^{VI}—O, both different sets of parameters usually lead to bond valence sums (BVS) below the expected value of 6, with the set by Mills and Christy yielding values that are *ca*. 0.1 v.u. higher than that of Brese and O'Keeffe. Concerning Te^{IV}—O, the parameters by Brese and O'Keeffe work well, if additional oxygen contacts beyond the first coordination sphere are few and at remote distances. The more additional oxygen contacts are present, especially in the distance range of 2.6−2.9 Å, the more necessary it is to rely on the revised parameters.

1.4.5 Comparison of crystal structures

In several cases, crystal structures isotypic with either known literature phases or other new structures discovered in this work were found. In order to verify their similarity and to quantify the closeness of their relationship, the *compstru* software available at the Bilbao Crystallographic Server (de la Flor et al., 2016) was used. Based on atomic coordinates, unit-cell dimensions and Wyckoff positions, which can be provided from a CIF-file, several parameters are determined:

- The degree of lattice distortion *S* describes the closeness of the relationship between the lattice parameters of the two structures, which is calculated by the spontaneous strain (for details see: Catti, 1985).
- The displacements between paired atoms d_i are calculated by comparing the atomic coordinates of both structures and determined relative to the unit-cell dimensions of the first structure. They are indicated together with their average value $d_{av.}$. The pair of atoms with the largest differences $d_{max.}$ often offers a hint at the source of structural differences between the two crystal structures.
- The measure of similarity Δ was introduced as "structural descriptor" by Bergerhoff et al. (1999) and is the most complete parameter of the three. It is dependent of both the differences of the unit-cell parameters and the atomic positions (the latter are weighted based on the respective multiplicity of the crystallographic sites).

1.4.6 OD theory

As already mentioned in section 1.1, the large stereochemical influence of the $5s^2$ lone pair ψ of Te^{IV} frequently leads to the formation of modular structures, especially layered structures, which are prone to exhibiting stacking disorder. In several cases, the disordered stacking can be rationalized by application of the OD theory (Dornberger-Schiff & Grell-Niemann, 1961).

Hereby, the crystal structure is decomposed into an arrangement of modules, usually layers, which do not have to follow the crystal-chemically most sensible boundaries. In order to be described as an OD-structure, the following conditions (known as "vicinity conditions") have to be fulfilled:

- The crystal structure consists of a finite number of layer types.
- Neighboring layers share a common (2D)-translational lattice.
- Equivalent sides of equivalent layers form contacts to the neighboring layer in such a way that the resulting pairs of layers are geometrically equivalent.

In OD theory, the symmetry operations that map a module(= layer) onto itself or an adjacent module are called partial operations (POs), as they do not have to apply for the whole crystal structure. The

POs are categorized by two systems. λ-POs map a layer onto itself, while σ-POs map a layer onto a different one. Additionally, POs are divided into ρ-POs, which invert the stacking direction, and τ-POs, which do not. If a layer has at least one $\lambda\rho$-PO, it is an apolar layer, otherwise it is polar. Based on the number of layer types, their polarity and the availability of ρ-POs, each OD-system can be assigned to a certain OD category. All layer types present in the structure, their respective (idealized) symmetry and one possible translational relation between adjacent layer types are summarized in the OD groupoid family symbol (Dornberger-Schiff & Grell, 1982a).

NFZ-relationship

The third vicinity condition introduces ambiguity into the formed stacking of layers, as at each layer contact, multiple options can be realized, as long as they are geometrically equivalent. In order to quantify these possibilities, the NFZ-relationship, $Z = N/F = [\mathcal{G}_n : \mathcal{G}_n \cap \mathcal{G}_{n+1}]$, is analyzed. $\mathcal{G}_n$ is the group of $\lambda\tau$-POs, the partial operations of the layer n that map the layer onto itself and that do not invert the stacking direction. The $\mathcal{G}_n \cap \mathcal{G}_{n+1}$ operations apply to the adjacent $n + 1$ layer as well. Z corresponds to the index of $\mathcal{G}_n \cap \mathcal{G}_{n+1}$ in $\mathcal{G}_n$ ($Z = [\mathcal{G}_n : \mathcal{G}_n \cap \mathcal{G}_{n+1}]$) and defines the number of possibilities the layer $n + 1$ can be placed on the layer n.

If the layer pair is polar and there is at least one $\sigma\rho$-PO, which maps one layer onto the other one, but there is no $\sigma\rho$-PO, which is a symmetry element of the pair, the condition changes to $Z = 2N/F$.

MDO polytypes

If $Z > 1$ for at least one type of layer contact, several equivalent ways to place the adjacent layer onto the previous one are possible. Consequently, infinitely many polytypes for an OD-crystal are theoretically possible that are also energetically equivalent, provided that interactions over one layer width are neglegible. However, in reality, OD-crystals often have a preferred stacking type, which is in most cases a very simple one. This can be explained by weak interactions over the distance of more than one layer contact or, in most cases, by small desymmetrizations (Ďurovič, 1979) of the layers from the OD groupoid symmetry, which in some cases is only idealized anyway.

The simplest polytypes are called “maximum degree of order” (short: MDO) polytypes and cannot be decomposed into fragments of a simpler polytype (Dornberger-Schiff, 1982; Dornberger-Schiff & Grell, 1982b). In most cases, this means that while adjacent layer pairs are symmetrically equivalent, there are several geometrically different layer triples possible. Each MDO polytype exclusively consists of only one of these triple-types. It has to be noted that there are also more complicated OD-structures, where the distinction between respective MDO polytypes has to be made from larger n-tuples than triples (where $n = 3$).

In order to analyze the stacking of a disordered OD structure, from the individual layers one can derive all possible MDO polytypes, determine their unit-cell and space group, and subsequently compare it to the diffraction pattern. The preferred stacking can often be determined based on the positions of the maxima on the streaks of diffuse scattering, if available. Additionally, the intensity distribution of diffuse streaks can be simulated by programs like *DIFFAX* (Treacy et al., 1991) or *DISCUS* (Proffen & Neder, 1997) and compared with the actual diffraction data.

1.5 General remarks

In order to specify the oxidation state of atoms in crystal structures, several formulations are possible, *e.g.*, Te^{IV}, Te^{4+}, Te(IV), tellurium(IV), … . In this work, the crystal structures are generally divided into the strongly bound framework, consisting of oxidotellurate groups and the coordination polyhedra of transition metal atoms (and those of Pb^{II}, Sn^{IV} and Bi^{III}), and the weaker connected alkali metal cations

and crystal water molecules. Framework constituents will be denominated as “atoms” and their oxidation number will be given as a superscript with roman letters, *e.g.,* Te^{IV}, Cu^{II}. The extra-framework species, mostly alkali-metals, will be described as cations and their charge will be given in the superscript, *e.g.,* K^+, Rb^+. If the name of an element is spelled out, the oxidation number, if given, will be written in parentheses, *e.g.,* copper(II) oxidotellurates(IV).

A similar method is also applied for the graphical representations of the crystal structures, which were generated with *DIAMOND* (Brandenburg et al., 2016) if no additional information is given. Bonds and coordination polyhedra are shown for the framework constituents, while alkali metal cations and crystal water molecules are depicted as being isolated. The general color scheme is: Te (green), O (red), H (white), alkali metal (yellow), transition metal (blue) and lone pair (orange). For most graphical crystal structure representations, all atoms are drawn as spheres with radii fixed to a value of 0.25 Å, the H atoms are drawn with a smaller radius of 0.135 Å. In the cases, where displacement ellipsoids are shown, they can be recognized from the black lines spanning the ellipsoid and represent the 90% probability level. Deviations from these default settings will be specified individually.

For each refined crystal structure, numerical data are compiled in the appendix (8.2, Tables 68−82).

1.6 List of abbreviations and symbols

A	Alkali metal
ADP	Anisotropic displacement parameter
BASF	Batch scale factor
BE	Backscattered electrons
BVS	Bond valence sum
CCD	Charge coupled device
CN	Coordination number
EDS	Element dispersive spectroscopy (also: EDX)
ICSD	Inorganic crystal structure database
IR	Infrared
JT	Jahn–Teller
M	(transition) Metal
MDO	Maximum degree of order
OD	Order-disorder
p.f.u.	Per formula unit
PO	Partial operation
PXRD	Powder X-ray diffraction
SEM	Scanning electron microscope
SHG	Second harmonic generator/generation
s.o.f.	Site occupation factor
s.u.	Standard uncertainty
v.u.	Valence unit
Unit-cell	
a, *b*, *c*	Unit-cell axes
a*, **b***, **c***	Reciprocal unit-cell axes
α, *β*, *γ*	Unit-cell angles
h, *k*, *l*	Reciprocal space coordinates
V	Unit-cell volume
x, *y*, *z*	Direct space coordinates
Z	Number of formula units per unit-cell
Crystal Chemistry	
ψ	Non-bonding electron lone pair
τ_4, τ_5	Geometry index
Δ	[TeO_3] group
◊	[TeO_4] group
⏢	[TeO_5] group
◯	[TeO_6] group
Compstru	
S	Degree of lattice distortion
$d_{av.}$	Average distance between paired atoms
$d_{max.}$	Maximum distance between paired atoms
Δ	Measure of similarity
Octahedral distortion	
d_{mean}	Arithmetic mean of *M*—O distances
ζ	Distance distortion
Δ	Tilting distortion
Σ	Angle distortion
ϑ	Torsional distortion

1.7 Already published parts of this thesis

The experimental part of this work was carried out from September 2019 to December 2022 at TU Wien, Institute for Chemical Technology and Analytics, Department of Structural Chemistry.

Some parts of this thesis have already been published in peer-reviewed journals. The corresponding phases and their crystal structures will be briefly discussed; for a more detailed discussion the reader is referred to the original articles. This concerns the following phases and crystal structures:

$Ni_3Te_2O_2(PO_4)_2(OH)_4$

> Eder, F. & Weil, M. (2020a). $Ni_3Te_2O_2(PO_4)_2(OH)_4$, an open-framework structure isotypic with $Co_3Te_2O_2(PO_4)_2(OH)_4$. *Acta Cryst*. E**76**, 625–628.

***β*-$CdTe_2O_5$**

> Eder, F. & Weil, M. (2020b). The crystal structure of a new $CdTe_2O_5$ polymorph, isotypic with ε-$CaTe_2O_5$. *Acta Cryst.* E**76**, 831–834.

$Zn_2(HTeO_3)(AsO_4)$

> Eder, F. & Weil, M. (2021). Crystal structure of $Zn_2(HTeO_3)(AsO_4)$. *Acta Cryst*. E**77**, 555–558.

$Li_2Cu_2Te_3O_9$, $Li_2Cu_3Te_4O_{12}$, $Rb_2Cu_3Te_6O_{16}$ and $Cs_2Cu_3Te_6O_{16}$

> Eder, F. & Weil, M. (2022a). The alkali metal copper(II) oxidotellurates(IV) $Li_2Cu_2Te_3O_9$, $Li_2Cu_3Te_4O_{12}$, $Rb_2Cu_3Te_6O_{16}$ and $Cs_2Cu_3Te_6O_{16}$ – four new structure types. *Z. Anorg. Allg. Chem*. **648**, 23: e202200089.

$Rb_2Zn(TeO_3)(CO_3)(H_2O)$ and $Na_2Zn_2Te_4O_{11}$

> Eder, F., Stöger, B. & Weil, M. (2022a). Order-disorder (OD) structures of $Rb_2Zn(TeO_3)(CO_3)\cdot H_2O$ and $Na_2Zn_2Te_4O_{11}$. *Z. Kristallogr. – Cryst. Mater.* **237**, 8–9, 329–341.

***α*-$MnTeO_3$, *γ*-$MnTeO_3$, $Mn_6Te_5O_{16}$, $Mn_3(TeO_3)_2(OH)_2$ and $Mn_{15}(TeO_3)_{14}(OH)_2$**

> Eder, F. & Weil, M. (2022b). Phase formation studies and crystal structure refinements in the $Mn^{II}/Te^{IV}/O/(H)$ system. *Z. Anorg. Allg. Chem*. **648**, 24.
>
> and for $Mn_3(TeO_3)_2(OH)_2$, additionally: Eder, F., Weil, M., Missen, O. P., Kolitsch, U. & Libowitzky, E. (2022b). The Family of $M^{II}_3(Te^{IV}O_3)_2(OH)_2$ (*M* = Mg, Mn, Co, Ni) Compounds—Prone to Inclusion of Foreign Components into Large Hexagonal Channels. *Crystals* **12**, 1380.

$Co_2(TeO_3)(OH)_2$ and $Co_{15}(TeO_3)_{14}(OH)_2$

> Eder, F., Weil, M., Pramanik, P. & Mathieu, R. (2023a). The Cobalt(II) Oxidotellurate(IV) Hydroxides $Co_2(TeO_3)(OH)_2$ and $Co_{15}(TeO_3)_{14}(OH)_2$. *Crystals* **13**, 176.

$Na_2[Ni_2(TeO_3)_3](H_2O)_{2.5}$, $K_2[Ni_2(TeO_3)_3](H_2O)$, $K_2[Zn_2(TeO_3)_3](H_2O)_2$, $Rb_{1.25}[Co_2(TeO_3)_3](H_2O)_{1.5}$, $Rb_{1.24}[Mn_2(TeO_3)_3](H_2O)_2$, $K_2[Cu_2(TeO_3)_3](H_2O)_2$, $K_2[Co_2(TeO_3)_3](H_2O)_{2.5}$, $Na_2[Cu_2(TeO_3)_3](H_2O)_{1.5}$, $Rb_{1.5}[Mn_2(TeO_3)_3](H_2O)_{1.25}$ and $Cs[Mn_2(TeO_3)_3](H_2O)$

> Eder, F., Marsollier, A. & Weil, M. (2023b). Structural studies on synthetic $A_{2-x}[M_2(TeO_3)_3]\cdot nH_2O$ phases (*A* = Na, K, Rb, Cs; *M* = Mn, Co, Ni, Cu, Zn) with zemannite-type structures. *Mineral. Petrol.* https://doi.org/10.1007/s00710-023-00814-5.

$Na_3Te_2(FeO_4)_3$

Eder, F. & Weil, M. (2023). Garnet-type $Na_3Te_2(FeO_4)_3$. *Acta Cryst*. E**79**, 328−330.

2 Experimental

2.1 Synthesis

Several synthetic approaches towards new transition metal oxidotellurate phases were employed. While the hydrothermal method was the preferred path in previous investigations in similar systems and pertained its status in the actual research, experiments under similar conditions in a microwave furnace and an autoclave furnace, as well as solid-state reactions were conducted. The hydrothermal method was used as the main initial synthesis technique in order to systematically hunt for new phases, while the other methods were employed on selected, promising systems, subsequently and/or ancillary. A complete list of all performed hydrothermal experiments and solid-state reactions can be found in the appendix (8.1, Tables 66 and 67).

2.1.1 Hydrothermal synthesis

The hydrothermal method has been a reliable tool in obtaining new (inorganic) solids for decades. While the term hydrothermal actually refers to water above its critical point (374 °C), it is generally used for reactions using water as a solvent or reaction medium at temperatures significantly above 100 °C and under increased (autogenous) pressure. The higher the temperature, the better the dissolution ability of water most frequently is. The need for these elevated temperatures and pressures is caused by the fact that transition metal oxidotellurates generally show a very low solubility in water at ambient conditions. Therefore, crystal growth at milder conditions usually does not yield products suitable for single-crystal diffraction experiments.

Figure 2. A set of steel autoclave and Teflon inlays used for hydrothermal experiments.

In this thesis, hydrothermal experiments were carried out at a temperature of 210 °C and with a reaction time of approximately one week. The reaction containers were small Teflon vessels with an inner volume of *ca*. 3−4 ml. The educts, generally a total of 0.5−1 g, were weighed using a Mettler Toledo AB 184-A3 scale and manually mixed using a spatula in these vessels. Afterwards, water was added until the reaction chamber was filled to *ca*. 2/3 of its volume, and the mixture was manually stirred again. Then, the Teflon containers were placed into steel autoclaves (Figure 2) and put in a pre-heated Heratherm OGH60 (Thermo Fischer) drying furnace. Cooling down after the reaction within *ca*. 3 hours was achieved by taking the autoclaves out of the furnace without any additional temperature-controlling measures. In order to obtain a good solubility of Te^{IV}, it is necessary to adjust the pH-value in the reaction to an alkaline environment. This was facilitated by addition of either alkali metal hydroxides, such as NaOH or KOH, ammonia (NH_3) solution or by an excess of alkali metal carbonates A_2CO_3.

Modifications of the hydrothermal method

Over the course of this work, several variations of the hydrothermal setup were established. The most important one is characterized by a drastic reduction of the employed water content. Only three droplets of water instead of a few milliliters were added for systems without “hidden” water sources in their starting materials. If the educts had the ability to emit water when heated, *e.g.,* telluric acid (H_6TeO_6) with KOH, or hydrated metal salts, usually no additional water was added at all.

If KOH was introduced as the base of such water-deprived reactions, this leads to the formation of a highly alkaline KOH-H_2O flux. This approach is nothing new to solid-state chemistry and is known as a "hydroflux reaction" (Chance et al., 2013; Bugaris et al., 2013). Typically, a hydrothermal setup with a KOH-H_2O mixture of molar ratios close to 1:1 is employed for hydroflux reactions. In this work, experiments in a hydrothermal setup introducing alkali metal hydroxides and only small amounts of water will therefore be referred to as "hydroflux-like" conditions.

For numerous experiments synthesizing novel ternary *A*–*M*–Te^{IV}–O-compounds, a weaker form of this hydroflux reaction was performed. Instead of *A*OH, the A_2CO_3 carbonates were used as the base and alkali source, and typically three droplets of demineralized water (*ca.* 0.1 g) were added. This changes the type of reaction from a hydrothermal reaction to a solid-state reaction with water functioning as a mineralizer instead as a solvent. These setups will be referred to "mild hydroflux" conditions in this work.

Another modification of the hydrothermal method was tested, although it was not as successful as the (mild) hydroflux variants. In an attempt to perform a solid-state reaction with water functioning as a mineralizer but still obtaining completely dry final products, several experiments were prepared like a normal hydrothermal setup, but then placed the Teflon container inside the drying furnace without the steel autoclave, but just with the Teflon lid on top of it. These "open hydrothermal" syntheses resulted in dry reaction products, as the introduced water readily evaporated during the reaction. However, single-crystalline material was obtained only occasionally by this method.

Problems of hydrothermal reactions

While hydrothermal reactions are easy to perform and frequently lead to new products, the method has its limitations. The only homogenization of the reactants happens before the reaction, as, for the given set-up, no stirring is possible while the autoclave is in the furnace. This often leads to inhomogeneities in the reaction chamber and, consequently, to the frequent formation of phase mixtures as reaction products. While this is unproblematic in the hunt for unknown phases, the hydrothermal method in not very suitable for obtaining phase-pure products in a reliabe and reproducable way. Furthermore, the reproducibility of the method is limited by the large number of parameters that can influence the reaction: (local) concentrations, temperature, filling degree, reaction time, cooling rate, pH-value, contaminations of the Teflon container from previous reactions, *etc.*. Hence, optimizing a hydrothermal reaction to a potential phase-pure product can be a tedious task.

2.1.2 Experiments under mild hydrothermal conditions with stirring for better homogeneity

In attempts to obtain phase-pure products of phases found in hydrothermal experiments with the set-up described in 2.1.1., syntheses with continuous stirring of the reaction mixture at similar temperatures were conducted. Two different reactors were used (Figure 3).

The CEM Mars6 240/50 is a microwave-heated furnace. *Ca*. 0.5 g of educts were filled into a Teflon vessel with an inner volume of 100 ml, which was then filled to *ca*. 1/3 of the volume with water. After the reaction chamber was closed, it was heated to maximum temperature (usually 200 °C) within 25 minutes and kept at this temperature for 2 hours. Cooling to room temperature was achieved within one hour. During the whole process, the reaction was magnetically stirred. The results of all experiments conducted in the microwave furnace are collated in Table 65.

For reactions on an even larger scale, a Berghof BW700 autoclave with mechanical stirring was used. The inner volume of the Teflon reaction chamber was 700 ml, about 300 ml of water were used for the reactions. Heating was applied by direct contact of the Teflon inlay with the surrounding furnace, stirring was applied mechanically. The temperature program started with a 1 °C/min ramp to 200 °C,

which was held for 30 minutes in order to keep the furnace from overheating. After this time, the final temperature of 210 °C was reached by a slow ramp of 1 °C/3 min and subsequently held for 24 hours. The reaction container was then left to cool to room temperature, which typically took about six hours. The results of the reactions in this setup can be found in Table 49 in section 5.1.2.

Figure 3. Left: CEM Mars6 240/50 microwave-heated furnace. Right: Berghof BW700 autoclave.

2.1.3 Solid-state reactions

Solid-state reactions were conducted in a variety of setups (Figure 4). Prior to the reaction, the educts were ground and mixed with a mortar and, in some cases, pressed with a manual P/O/Weber PW10 press in order to obtain compact pellets. The main crucible materials were either platinum or silica glass (half-)ampoules. Additionally, a series of solid-state reactions at temperatures below 600 °C was conducted in small aluminum crucibles usually used for DSC analyses. Reactions under ambient atmosphere were conducted in Nabertherm N11 (S19 Controller), Nabertherm LH4 04/16, Nabertherm L3-11-B170 (B170 Controller) and Thermo Scientific K144 furnaces. For syntheses under inert (Ar) atmosphere, a FROK 500/100/1300 reduction furnace was used.

Figure 4. Left: Manual P/O/Weber PW10 press; middle: Nabertherm N11 furnace; right: FROK 500/100/1300 reduction furnace.

Some experiments were conducted under vacuum inside of glass ampoules, which were consequently heated in one the previous furnaces. A summary of all conducted solid-state experiments can be found in the appendix (8.1, Table 66).

2.2 Analysis

2.2.1 Powder X-ray diffraction (PXRD)

PXRD measurements were conducted on every synthesized sample as an initial analytical method. The measurements were executed on a PANalytical X'Pert Pro type PW 3040/60 equipped with an X'Celerator detector using Cu-$K_{\alpha1,2}$ radiation. Measurements were done in Bragg-Brentano θ-2θ mode in a 5−80° 2θ range and a measurement time of 12 minutes. In some cases, similar measurements were performed on a PANalytical Empyrean diffractometer.

Phase analysis and Rietveld refinements were done using the *Highscore Plus* suite (Degen et al., 2014). Simulated PXRD patterns based on the refined structures are drawn in red, while the actual measurement is depicted in black.

For temperature-dependent PXRD measurements, an Anton Paar HTK 1200 N high-temperature chamber was mounted on a PANalytical X'Pert MPDIII instrument. Diffraction experiments at temperatures of up to 900 °C were conducted under either ambient atmosphere or pure N_2.

2.2.2 Single-crystal X-ray diffraction

Two types of single-crystal diffraction instruments and corresponding evaluation software were used in this work. Most measurements were conducted on a Bruker Kappa APEX-II diffractometer (Figure 5) with graphite-monochromatized Mo-K_α radiation and a CCD area detector. Single crystals were pre-selected under a polarizing microscope and then mounted on Kapton micro-loops with perfluorinated oil (Fomblin).

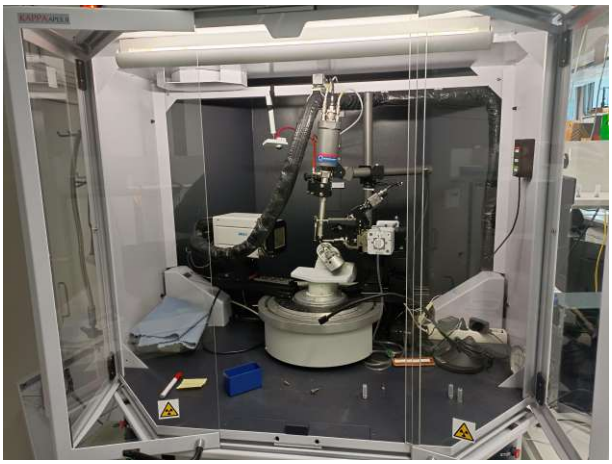

Figure 5. Bruker Kappa APEX-II single-crystal X-ray diffractometer.

Measurement temperatures were either −173 °C or room temperature with the cooling unit turned off (20−25 °C). Instrument software (*APEX-4*, *SAINT* (Bruker, 2021a, b)) was used for unit-cell determination, calculation of measurement strategies and integration; absorption correction by the multi-scan approach was done with *SADABS* (Krause et al., 2015).

Since the beginning of 2022, a Stoe STADIVARI diffractometer (Figure 6) equipped with two Anton Paar Primus 50 microsources (Mo-K_α and Cu-K_α) and a Dectris EIGER®2 R 1M CdTe detector was used as well. The *X-AREA* software (Stoe, 2021) was employed for unit-cell determination, calculation of measurement strategies and integration, while absorption correction (multi-scan) was done with *LANA* (Koziskova et al., 2016).

Structure solution and refinement were performed with *SHELXT* (Sheldrick, 2015a) and *SHELXL* (Sheldrick, 2015b). In some cases, in particular when dealing with disordered systems or an incommensurately modulated structure, *JANA-2020* (Petříček et al., 2014) was used. In numerous cases, several features of the crystallographic software-suite of *PLATON* (Spek, 2003) were employed. Atom labels and coordinates were assigned in accordance with isotypic literature phases, otherwise using *STRUCTURE TIDY* (Gelato & Parthé, 1987).

Figure 6. Stoe STADIVARI single-crystal X-ray diffractometer.

2.2.3 Thermogravimetry (TG)

For thermogravimetric investigations, a Netzsch TG209 F3 Tarsus system was employed. The measurements were performed under an inert atmosphere facilitated by an Ar flow of 20 ml/min and with a heating rate of 10 °C/min. The samples were weighed into an alumina crucible, which was subsequently closed by a pierced lid. A correction measurement of the empty crucible was recorded and afterwards subtracted from the measurement.

2.2.4 Differential Scanning Calorimetry (DSC)

DSC measurements were conducted on a Netzsch DSC 200 F3 Maia system under inert atmosphere with an Ar flow of 20 ml/min. The samples were weighed into small aluminum crucibles (m ≈ 40 mg), which were afterwards cold-welded with pierced aluminum lids. The heating rate was chosen at 10 °C/min like for TG measurements.

2.2.5 Fourier Transformed Infrared (FTIR) Spectroscopy

For collection of infrared spectra, a Spectrum Two FT-IR Spectrometer (UATR Two; Perkin Elmer) was used. IR-measurements were carried out in an interval of 4000–400 cm^{-1} and were recorded as an average of four single measurements. The background was determined before the measurement against air and subsequently subtracted. For fitting the band positions of both IR- and Raman spectra, the *fityk* software (Wojdyr, 2010) was employed. The areas of interest were isolated from the spectrum, the background was determined and subtracted, and the bands were refined as Lorentz-peaks using the Levenberg–Marquardt-algorithm.

2.2.6 Raman Spectroscopy

Raman Spectra were obtained with a confocal micro-Raman spectrometer Renishaw RM1000 equipped with a 17 mW HeNe laser (λ = 632.8 nm) for excitation, an ultra-steep edge filter set facilitating measurements as close as > 40 cm^{-1} to the Rayleigh line, a Leica DLML microscope with a 50×/0.75 objective, a 1200 lines/mm grating in a 300 mm monochromator and a thermo-electrically cooled CCD detector. The Raman shift of the instrument was calibrated by the Rayleigh line and the 520.5 cm^{-1} line of a Si standard, the resolution of the system was 3–4 cm^{-1}. The spectral range was 4000–20 cm^{-1}. Instrumental set-up and control were supervised with the Grams32 software. Peak-

fitting, background handling and determination of band positions was performed with *fityk* (Wojdyr, 2010).

2.2.7 Energy-Dispersive X-ray Spectrometry (EDS)

Crystals of specific samples were mechanically separated, and carbon coated. The analysis was performed with a JEOL JSM-6610LV scanning electron microscope (SEM) equipped with a high-sensitivity and high-resolution energy-dispersive Bruker e-FlashHR+ X-ray spectrometer operated by the Bruker Esprit 2.0 software. The spectra were collected over 60 s with an accelerating voltage of 15 kV. No calibration with external standards was conducted. Given the experience of the operator, the usual relative deviations from the actual values are in the range of 2−10%. As these analyses have a semi-quantitative character, no s.u.s are presented for the individual data points. In some cases, when no plane surface perpendicular to the beam direction was available, this resulted in a higher variance of the determined atomic contents due to shading effects.

3 Modification of transition metal oxidotellurates(IV) with foreign oxido anions

The incorporation of secondary oxido anions into transition metal oxidotellurates opens up a plethora of possibilities for novel phases and their crystal structures. Anions employed so far on preceding investigations were the tetrahedral SO_4^{2-} and SeO_4^{2-} anions. As already several novel structures including these ions were published by the research group in the past years, it was chosen to experiment with various other anions than these two.

3.1 Nitrates

3.1.1 Hydrothermal experiments

Transition metal nitrate salts are readily soluble in water, which makes them good starting materials for hydrothermal experiments. However, the good solubility of the nitrate group also has the drawback that it might readily stay in solution, while the reaction products crystallize. Three series of hydrothermal experiments, consisting of eight samples each, were performed in the nitrate system (H1−H24). For each series, the nitrate salts of eight different transition metals were employed: Co^{II}, Cu^{II}, Fe^{III}, Zn^{II}, Cr^{III}, Ni^{II}, Cd^{II} and Pb^{II}. The other reactants were TeO_2 and either KOH (H1−H8), $HNO_{3\ 65\%(wt),\ aq.}$ (9−16) or $NH_{3\ 25\%(wt),\ aq.}$ (H17−H24) (Table 67).

Experiments H1−H8 resulted in a surprisingly large number of Te^{VI}-compounds as (side) products: $CoTeO_4$ (Isasi, 2001), Cu_3TeO_6 (Hostachy & Coing-Boyat, 1968), Fe_2TeO_6 and Cr_2TeO_6 (Kunnmann et al., 1968). As these were the first hydrothermal experiments conducted at all, this could hint at possible initial oxidative contaminations, possibly due to incompletely removed aqua regia from a prior cleaning step for some of the used Teflon vessels. During the third series (H17−H24; NH_3 as a base), only one oxidotellurate(VI), Cu_3TeO_6, was identified. Besides various known tetra- or hexavalent oxidotellurates, samples H7 (Cd) and H8 (Pb) contained unknown phases. The crystal structures of $Cd_5(TeO_3)_4(NO_3)_2$ (3.1.3) and $Pb_3Te_2O_6(NO_3)_2$ (3.1.5) are presented in the following sections.

Performing the synthesis under highly acidic (H9−H16) instead of moderately alkaline conditions did not lead to encouraging results. The solubility of TeO_2 is much lower in an acidic environment compared to an alkaline environment. Additionally, most employed metal cations readily stayed in solution during synthesis. Therefore, for six of the eight samples, only α-TeO_2 (Stehlik & Balak, 1948) was obtained as a solid reaction product. The only identifiable oxidotellurate products were Fe_2TeO_6 (H11; Kunnmann et al., 1968) and a Cr−Te-oxide phase (H13; see 3.1.2).

The series H17−H24 using $NH_{3\ aq.}$ as a base did not lead to the discovery of any new phase. The only unclear sample is H24, where besides the starting materials PbO and α-TeO_2 a third phase was present. The non-assigned reflections in the PXRD pattern do not match any known Pb−Te−O-phase but correspond well to a tetragonal unit-cell with $a \approx 4$ Å and $c \approx 15$ Å. Oxygen-containing literature phases with such unit-cells crystallize in the γ-$Bi_4V_2O_{11}$-type (Vannier et al., 2003), known as "BIMEVOX"-phases (bismuth metal vanadium oxide). Another structure type with a similar unit-cell corresponds to the phases $BiPbO_2(NO_3)$ (Ziegler et al., 2004) and $LaPbO_2(NO_3)$ (Dill et al., 2006). The most reasonable assumption about the composition of the unknown phase relates to a mixed lead oxide nitrate phase with possible compositions of $MPbO_2(NO_3)$ or even $(Pb^{II},Pb^{IV})_2O_2(NO_3)$. No single crystals of this phase could be found for crystal structure determination. Based on the crystal structure of the reference phase of $BiPbO_2(NO_3)$ (a = 3.972 Å, c = 14.826 Å; Ziegler et al., 2004), the lattice parameters of the unknown phase were refined to a = 3.97191(7) Å and c = 15.0135(3) Å by the Rietveld method (Figure 7).

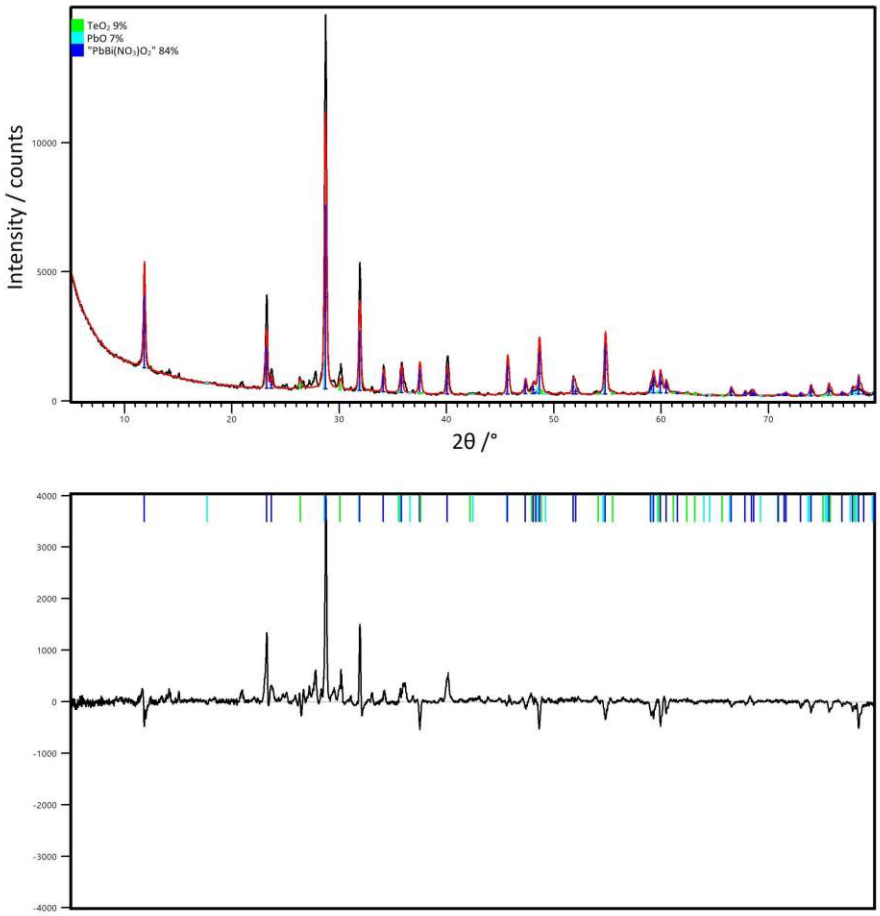

Figure 7. Rietveld refinement performed for experiment H24.

3.1.2 $Cr_{1-x}Te_xO_2$

H13 (Cr^{III}) yielded a dark brown powder with a PXRD pattern (Figure 8) perfectly corresponding to rutile-TiO_2 (refined lattice parameters a = 4.6044(2) Å, c = 2.9798(2) Å). CrO_2 has a rutile-type structure as well, but with a significantly smaller lattice parameter (a = 4.419 Å, c = 2.915 Å; Dho et al., 2010) than the measured phase. As the reflections of the rutile-type phase were rather broad, it was tempered in a platinum crucible at 920 °C for 10 h under ambient atmosphere in the hope of obtaining material of better crystallinity. Afterwards, the sample was found to be a mixture of 60% Cr_2O_3 and 40% Cr_2TeO_6. Based on this, it is assumed that the original rutile-type phase was a chromium(IV) oxide incorporating some Te, leading to the increased lattice parameter. It is unlikely that Te^{IV} is substituted on the octahedral Cr-positions. Instead, Te^{VI} will be included, paired with a partial reduction of Cr^{IV} to Cr^{III}. By increasing the Te^{VI} content to one third of the Cr atoms, one reaches the decomposition product Cr_2TeO_6, which has a trirutile structure itself (Kunnmann et al., 1968). The lattice parameters of the obtained Cr_2TeO_6 (a = 4.54101(3) Å, c = 8.99553(12) Å; Figure 8) are only slightly below the literature values of a = 4.546(2) Å and c = 9.0140(3) Å. In total, the unknown Cr−Te−O-phase from experiment H13 is best described with the composition $Cr_{1-x}Te_xO_2$, or more accurately, $Cr^{III}_{2x}Cr^{IV}_{1-3x}Te^{VI}_xO_2$ ($x < 1/3$).

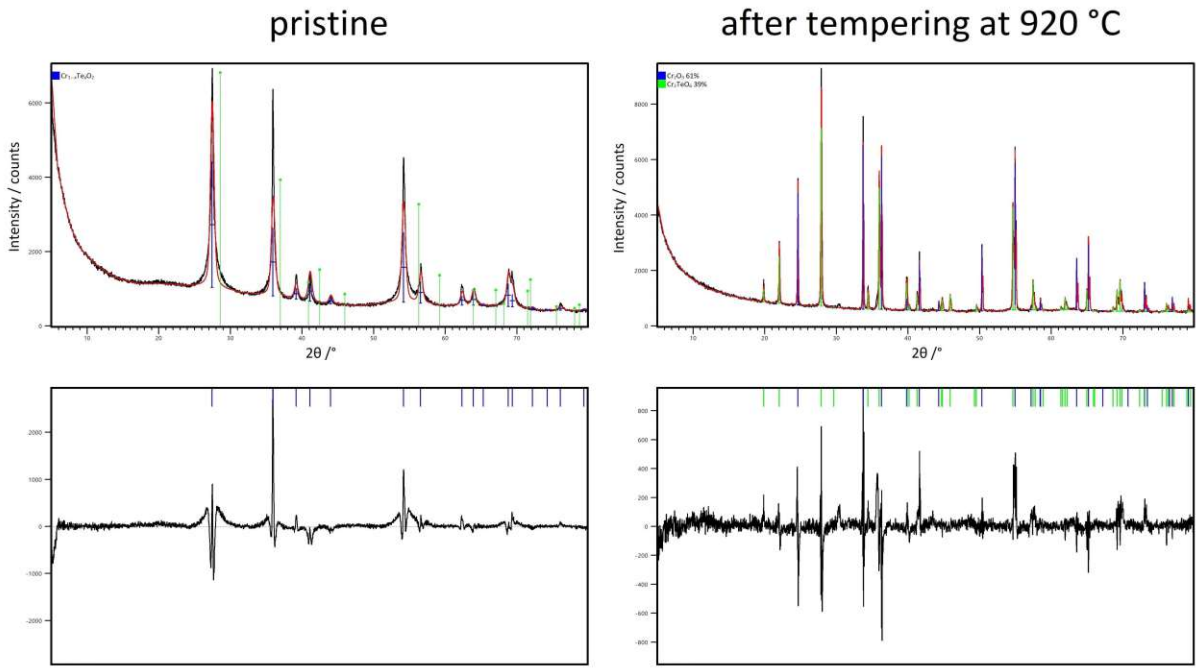

Figure 8. Rietveld refinement of the products from experiment H13 before and after sintering at 920 °C. On the upper left, the reflections of CrO_2 are marked in green as a reference.

3.1.3 $Cd_5(TeO_3)_4(NO_3)_2$

Synthesis

Initially, $Cd_5(TeO_3)_4(NO_3)_2$ was obtained in a hydrothermal reaction from $Cd(NO_3)_2(H_2O)_6$, TeO_2 and KOH (molar ratios 2:1:2; H7). Hydrothermal experiments H237−H244 and H249−H252 aimed at the repeated synthesis of $Cd_5(TeO_3)_4(NO_3)_2$, but started from different ratios of $Cd(NO_3)_2(H_2O)_4$, KOH and either K_2TeO_3 or TeO_2 and were performed under normal hydrothermal conditions or without any additional water. $Cd_5(TeO_3)_4(NO_3)_2$ was obtained in seven of the twelve batches, including hydrothermal and hydroflux-like setups. Additionally, a second cadmium oxidotellurate(IV) nitrate phase with the composition of $Cd_4Te_4O_{11}(NO_3)_2$ (3.1.4) was discovered in three of the samples (H238, H243, H249). From experiment H238, single crystals of yet another new phase, $Cd_4Te_5O_{14}$ (5.2.2), were isolated as well. The PXRD patterns of products from experiments H240, H242 and H244 all share the same unidentified phase exhibiting rather broad reflections. No phase with a similar powder pattern was found in the database and no material suitable for single-crystal diffraction was obtained.

The lattice parameters of monoclinic $Cd_5(TeO_3)_4(NO_3)_2$ were refined from all those PXRD measurements, where the phase could be identified. In all cases, $Cd_5(TeO_3)_4(NO_3)_2$ exhibited a preferred orientation of the (*n*00) planes, which is not surprising because the crystal structure has a build-up from (100) layers. The reaction conditions of the hydrothermal setup (no/little/normal amount of water) have no significant influence on the metrics of the unit-cell of $Cd_5(TeO_3)_4(NO_3)_2$ (Table 1).

Table 1. Refined lattice parameters of various $Cd_5(TeO_3)_4(NO_3)_2$ batches.

Batch	Water	*a* / Å	*b* / Å	*c* / Å	*β* /°	*V* / Å³
H7	yes	9.96697(7)	5.61834(7)	16.6693(2)	102.4713(2)	911.42
H237	yes	9.96301(9)	5.62053(8)	16.6375(3)	102.6250(2)	909.13
H238	yes	9.9609(4)	5.6067(4)	16.6260(11)	102.6529(10)	905.98
H239	no	9.9666(2)	5.61550(13)	16.6321(4)	102.6025(4)	908.43
H243	no	9.96590(13)	5.61715(11)	16.6387(3)	102.6444(3)	908.84
H249	yes	9.93974(9)	5.62872(11)	16.6377(3)	102.5328(2)	908.67
H251	little	9.9574(3)	5.6170(2)	16.6436(7)	102.5642(6)	908.59
PXRD average		9.960(9)	5.618(7)	16.641(14)	102.558(7)	908.7(16)
H7 single-crystal	yes	9.9442(4)	5.6173(2)	16.6136(7)	102.7370(10)	905.19(6)

Single crystals of $Cd_5(TeO_3)_4(NO_3)_2$ are colorless and have the form of an elongated plate. Single-crystal diffraction experiments were performed on a Bruker Apex-II single-crystal diffractometer at room temperature and −173 °C and did not reveal any differences in the crystal structures.

Crystal structure

The asymmetric unit of $Cd_5(TeO_3)_4(NO_3)_2$ contains two Te, three Cd, one N and nine O atoms. With the exception of Cd3 (site symmetry $\bar{1}$; 2 *a*), all atoms are located at sites corresponding to general 4 *e* Wyckoff positions of space group $P2_1/c$. Both Te sites are coordinated by three oxygen atoms in a trigonal-pyramidal shape (coordinates of ψ: *x* = 0.3787, *y* = 0.4979, *z* = 0.0221 for ψ_{Te_1} and *x* = 0.6617, *y* = 0.3689, *z* = 0.2780 for ψ_{Te_2}). The [TeO_3] units are isolated from each other with a connectivity of Q^{3000}. The BVS of the Te^{IV} atoms are well-defined with values of 3.91 (Te1) and 4.06 (Te2) v.u..

The Cd^{II} atoms exhibit coordination numbers of [5+2] for Cd1, [5+1] for Cd2, and 6 for Cd3. The inner coordination sphere consists of oxygen atoms at distances of 2.179(3)−2.389(5) Å (Table 2), while the more distant contacts appear at distances of 2.524(3)−2.658(2) Å. Including these farther oxygen atoms into the BVS calculation, the values of the Cd^{II} atoms amount to 1.92 (Cd1), 2.02 (Cd2) and 2.09 (Cd3) v.u.. The [$CdO_{6/7}$] units are connected by corner- and edge-sharing and thereby form layers

parallel to (100) (Figure 9). The [TeO_3] groups are part of these layers as well and their lone pairs are directed away from the layer.

The space between the layers is, besides by the non-bonding $5s^2$ pairs of the Te^{IV} atoms, occupied by the nitrate groups, consisting of the atoms located at the N1, O6, O7 and O8 sites (Figure 10). The NO_3^- anions are bound to the layers by sharing an edge with the [$Cd2O_6$] unit. Hereby, the O7 contact (2.389(5) Å) is closer to the Cd^{II} atom, while O8 (2.587(5) Å) is more distant. The third oxygen atom of the nitrate anion, O6, is not in the coordination sphere of any Cd^{II} atom and has a slightly smaller N—O bond length of 1.234(5) Å compared to the other two (1.242(6) and 1.245(6) Å).

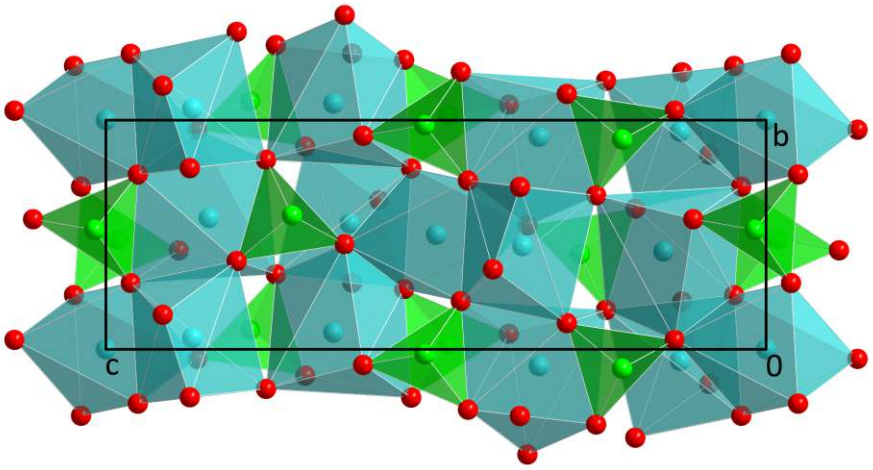

Figure 9. The crystal structure of $Cd_5(TeO_3)_4(NO_3)_2$ viewed along [$\bar{1}00$]. Cd^{II} atoms are drawn turquoise.

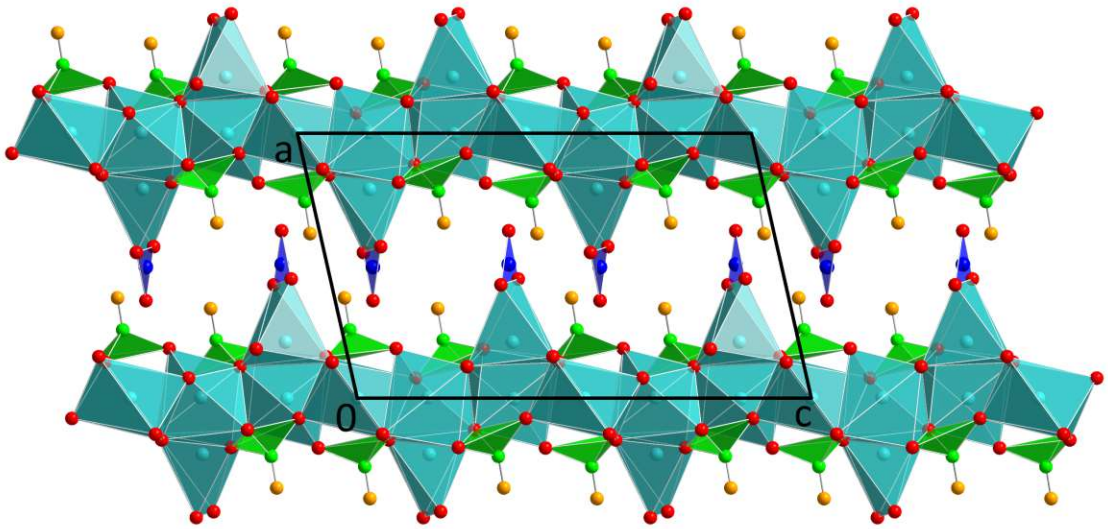

Figure 10. The crystal structure of $Cd_5(TeO_3)_4(NO_3)_2$ viewed along [$0\bar{1}0$]. Color codes refer to Figure 9, N atoms are drawn dark blue.

Relationship between $Cd_5(TeO_3)_4(NO_3)_2$ and $Ca_5(TeO_3)_4(NO_3)_2(H_2O)_2$

While there are no phases isotypic with $Cd_5(TeO_3)_4(NO_3)_2$ known so far, the crystal structure of $Ca_5(TeO_3)_4(NO_3)_2(H_2O)_2$ (space group *Cc*, *Z* = 4; Stöger & Weil, 2013) has similarities with that of $Cd_5(TeO_3)_4(NO_3)_2$. $Ca_5(TeO_3)_4(NO_3)_2(H_2O)_2$ consists of [Ca−Te−O] layers that are built in the same way as the [Cd−Te−O] layers in $Cd_5(TeO_3)_4(NO_3)_2$. This is reflected in the similar lattice parameters *b* and *c*

for both phases. The slightly higher values of b = 5.7289(7) Å and c = 17.007(2) Å for $Ca_5(TeO_3)_4(NO_3)_2(H_2O)_2$ compared to b = 5.6173(2) Å and c = 16.6136(7) Å in $Cd_5(TeO_3)_4(NO_3)_2$ are caused by the larger ionic radii (Shannon, 1976) of Ca^{II} (1.00 Å for CN 6, 1.06 Å for CN 7) compared to Cd^{II} (0.93 Å for CN 6, 1.03 Å for CN 7).

The main differences between the two structures originate from the space between the layers. In $Ca_5(TeO_3)_4(NO_3)_2(H_2O)_2$, the two crystal water molecules are closely bound to one of the Ca^{II} atoms with bond lengths of 2.390(9) and 2.39(2) Å. The nitrate groups, however, are not connected that well to the framework. One nitrate group shares one corner with a Ca—O distance of 2.462(11) Å, while the other NO_3^- anion is completely isolated from the layers. The more loosely bound NO_3^- groups can be seen as the main reason, why $Ca_5(TeO_3)_4(NO_3)_2(H_2O)_2$ exhibits diffuse scattering caused by stacking disorder and can be described using OD theory (Dornberger-Schiff & Grell-Niemann, 1961). On the contrary, no signs of diffuse scattering are discernable in the diffraction pattern of $Cd_5(TeO_3)_4(NO_3)_2$.

Table 2. Selected interatomic distances in the crystal structure of $Cd_5(TeO_3)_4(NO_3)_2$.

	d / Å		*d* / Å
Te1—O5	1.847(3)	Cd2—O9^{iii}	2.256(3)
Te1—O3^{i}	1.875(3)	Cd2—O2	2.261(3)
Te1—O9^{ii}	1.886(3)	Cd2—O3	2.296(3)
Te2—O1^{iii}	1.858(3)	Cd2—O7	2.389(5)
Te2—O4^{iii}	1.869(3)	Cd2—O8^{iii}	2.587(5)
Te2—O2^{iv}	1.886(3)	Cd3—O1	2.269(3)
Cd1—O5	2.281(3)	Cd3—O1^{viii}	2.269(3)
Cd1—O2	2.292(3)	Cd3—O3^{i}	2.289(3)
Cd1—O1	2.326(3)	Cd3—O3^{vii}	2.289(3)
Cd1—O9^{v}	2.361(3)	Cd3—O9^{ix}	2.326(3)
Cd1—O4^{vi}	2.380(3)	Cd3—O9^{v}	2.326(3)
Cd1—O2^{vii}	2.524(3)	N1—O6	1.234(5)
Cd1—O3^{vi}	2.658(2)	N1—O7^{iv}	1.242(6)
Cd2—O4	2.179(3)	N1—O8	1.245(6)

Symmetry codes: (i) x, 1/2−y, −1/2+z; (ii) 1−x, 1−y, −z; (iii) 1−x, 1/2+y, 1/2−z; (iv) 1−x, −1/2+y, 1/2−z; (v) −1+x, y, z; (vi) −x, 1/2+y, 1/2−z; (vii) −x, −1/2+y, 1/2−z; (viii) −x, −y, −z; (ix) 1−x, −y, −z.

3.1.4 $Cd_4Te_4O_{11}(NO_3)_2$

In experiment H238 (hydrothermal, $Cd(NO_3)_2(H_2O)_4$ and K_2TeO_3 in molar ratios of 2:1), crystals of a second novel cadmium oxidotellurate(IV) nitrate phase were obtained. Crystals of $Cd_4Te_4O_{11}(NO_3)_2$ are colorless and have a plank-like shape. Structure solution and refinement were complicated by twinning effects. About a dozen crystals of this phase were investigated by short matrix scans and four different crystals were measured over an extended period of time (16+ hours) on both diffractometers. All of them exhibited the same twinning behavior, which could not be noticed from the appearance of the crystals under the microscope. Analysis of the twinning behavior was based on data from the Stoe STADIVARI instrument (Figure 11), while the final refinement, ignoring half of the twin domains, was done on a data set from the Bruker Apex-II diffractometer.

Twinning of $Cd_4Te_4O_{11}(NO_3)_2$

The unit-cell of $Cd_4Te_4O_{11}(NO_3)_2$ is triclinic with a = 9.4304(15) Å, b = 9.4301(15) Å, c = 9.6096(16) Å, α = 92.142(6)°, β = 108.293(6)°, γ = 109.514(5)°, V = 755.1(2) Å^3. The metrics of the unit-cell with identical a and b values already hint at a susceptibility for twinning. Based on indexing and reconstructed reciprocal space images, a total of four twin domains were identified. While in the *hkn* planes ($n \in \mathbb{Z}$; accounts for the whole section) no twinning is discernable, the *nkl* and *hnl* planes (Figure 11) reveal the complicated twinning behavior.

Based on domain 1, to which the depicted precession images refer, the other three twin domains can be obtained by a 180° rotation along **c*** (domain 2), a 180° rotation along [110] (domain 3) and a 180° rotation along [$\bar{1}$10] (domain 4). The latter two transformations can be interpreted as an exchange of **a** and **b**, which does not influence the length of the two axes (they are the same), but exchanges α and β relative to the initial setting. The two pairs of domains connected by the 180° rotation along **c*** (1 and 2, 3 and 4) are more closely related and have similar relative intensities.

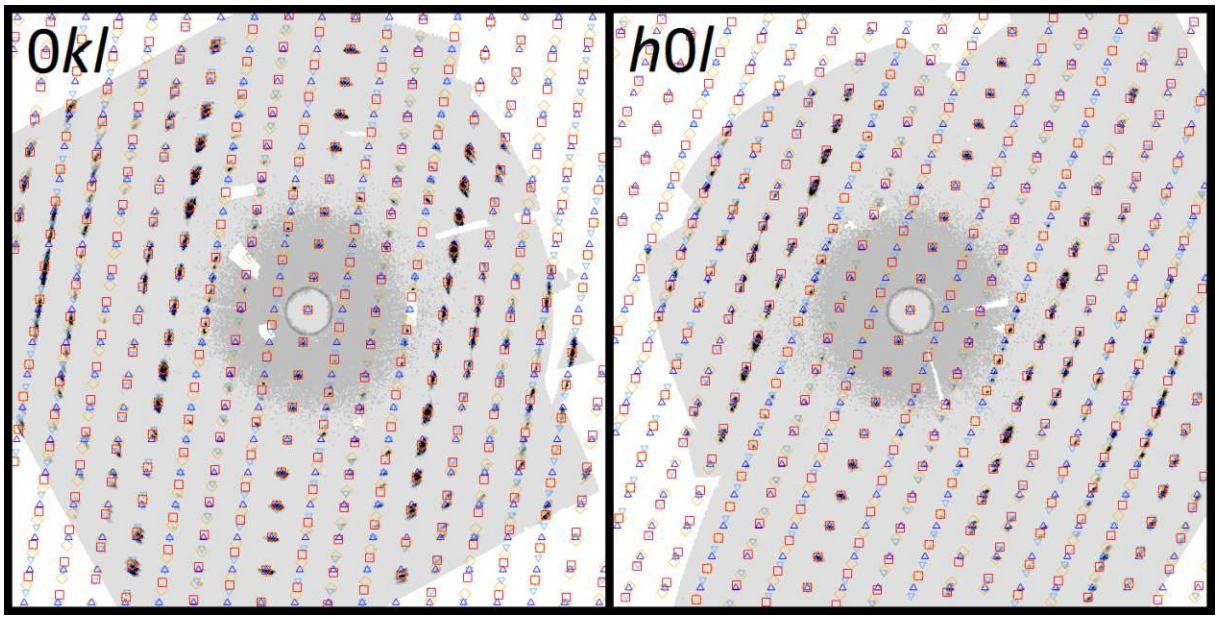

Figure 11. Reconstructed reciprocal lattice planes of $Cd_4Te_4O_{11}(NO_3)_2$. The **c*** direction, which is parallel for all domains, is drawn vertically with slight tilt to the right. Expected reflection positions are marked with dark blue triangles (domain 1), light blue inverted triangles (domain 2), red squares (domain 3) and orange rotated squares (domain 4).

In the 0*kl* plane (Figure 11, left), reflections of all four domains coincide on the *k* = 0 rod. When increasing *k* in integer steps, the reflections of the four domains split up in the **c*** direction. At *k* = 3*n*, reflections of domains 1 and 2 overlap again, while those of domains 3 and 4 do so at the *k* = 4*n* rods. In the *h*0*l* plane (Figure 11, right), this behavior is inverted: reflections of domains 1 and 2 overlap at *h* = 4*n* and those of domains 3 and 4 at *h* = 3*n*. The fact that reflections of domains 1 and 2 overlap at the *k* = 3*n*, but at *h* = 4*n*, with a transformation matrix between the two domains of

$$\begin{pmatrix} \bar{1} & 0 & 3/4 \\ 0 & \bar{1} & 1/3 \\ 0 & 0 & 1 \end{pmatrix},$$

can be explained by the different inclinations of **c** from **a** and **b** indicated by the significantly different sizes of the angles *α* and *β*. The rotation along **c*** influences the **a*** axis much more, because *β* is much larger than *α*. In domains 3 and 4, the roles of *α* and *β* are switched and therefore the overlap conditions are exchanged relative to domains 1 and 2.

Although the four twin domains could be determined and resolved in indexing and reciprocal space reconstructions, it was not possible to obtain a valid quantitative solution and refinement of the crystal structure on basis of the fourfold twin. Great overlaps of the reflections inhibited the generation of clean intensity data. Structure refinement based on the fourfold twin data resulted in very high reliability factors (*R*1 of 20−25%), despite most atoms being reasonably placed. Hereby, the ratios of the four twin domains refined to values of 0.453(8):0.341(8):0.103(5):0.103(5) for domains 1−4, respectively.

The best structure model was obtained from a measurement of a different crystal, which was integrated as a twofold twin of domains symmetrically connected by a 180° rotation along **c***, ignoring the other two domains, which, again, exhibited weaker intensities. The relative ratios of the two twin domains refined to values of 0.551:0.449(2) based on a *hkl*5-type file. While most atoms of the structure follow $P\bar{1}$ symmetry, half of the NO_3^- anions do not fit the inversion symmetry. As the ultimate refinement was performed in space group *P*1, many atoms exhibited negative ADPs − an issue not present in the $P\bar{1}$ model. Because of this, all atoms were refined only with isotropic displacement parameters in *P*1. Atomic coordinates and interatomic distances exhibit high uncertainties and the bond lengths, especially of the nitrate anions, vary by a large margin.

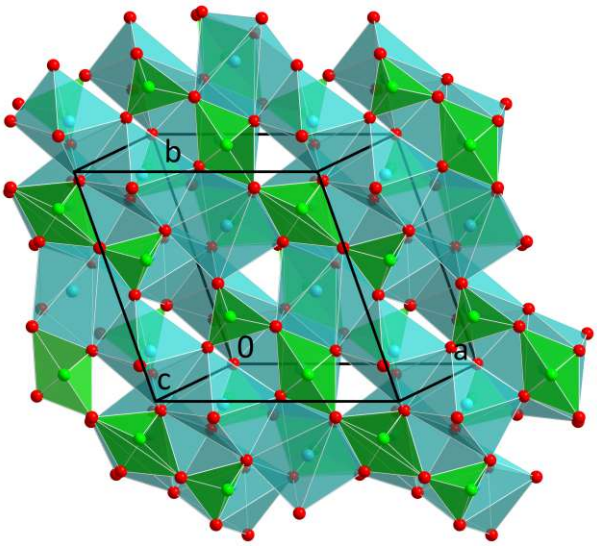

Figure 12. $^{2}_{\infty}[Cd_4Te_4O_{11}]$ layer in the crystal structure of $Cd_4Te_4O_{11}(NO_3)_2$ viewed along **c***. Color codes and atomic radii refer to Figure 9.

Crystal structure

The asymmetric unit in *P*1 contains eight Te, eight Cd, 34 O and four N atoms. Oxygen atoms O1−O22 form the coordination polyhedra of the Cd^{II} and Te^{IV} atoms, while O23−O34 are part on the NO_3^- anions. The Te^{IV} atoms have two different coordination numbers with four atoms each having a CN of 3 (Te2, Te5, Te7, Te8) and 4 (Te1, Te3, Te4, Te6). The [$TeO_{3/4}$] polyhedra are connected to neighboring

units by corner-sharing, forming finite (Δ–◊–◊–Δ) [Te_4O_{11}] units aligned in the [$\bar{1}10$] direction with connectivities of Q^{2100} for the CN3, and Q^{2200} for the CN4 Te^{IV} atoms. As expected from the overall quality of the dataset, the BVS of the Te^{IV} atoms are not very well-defined and amount to values (in v.u.) of 3.98, 4.14, 3.99, 4.12, 4.00, 4.21, 3.82 and 4.47 for Te1–Te8, respectively.

The Cd^{II} atoms exhibit coordination numbers of 6 (Cd6), 7 (rest) or 8 (Cd5). Hereby, one of the oxygen contacts of Cd1, Cd5, Cd6, Cd7 and Cd8 belongs to NO_3^- anions. The BVS of the Cd^{II} atoms were calculated to values of (in v.u.) of 1.89, 2.12, 1.77, 1.97, 1.84, 2.03, 2.00 and 1.98 v.u. for the respective Cd1–Cd8 sites. The [CdO_{6-8}] polyhedra are connected to each other, forming layers parallel to (001). The Te^{IV} atoms are located on the boundaries of the $^2_\infty$[$Cd_4Te_4O_{11}$] layers (Figure 12) with their non-bonding $5s^2$ pairs pointing into the interspace.

The four nitrate groups have very irregular bond lengths and are the most affected by the reduced data quality due to the ignored additional twin domains. The N1 and N4 nitrate groups could be located rather easily in the refinement, while those of N2 and N3 posed more difficulties. This can be explained by the fact that the N1- and N4-NO_3^- anions are connected to a layer-Cd^{II} atom with distances of 2.47(5) and 2.51(6) Å, while the other two have a weaker layer contact of 2.66(7) and 2.68(6) Å to the closest Cd^{II} atom (larger than the bond length threshold of 2.65 Å in Table 3). The $N4O_3^-$ anion works as a weak bridging unit between adjacent $^2_\infty$[$Cd_4Te_4O_{11}$] layers as it has, besides a 2.51(6) Å Cd—O distance, a second, weaker Cd—O contact of 2.67(4) Å to the opposite layer (Figure 13).

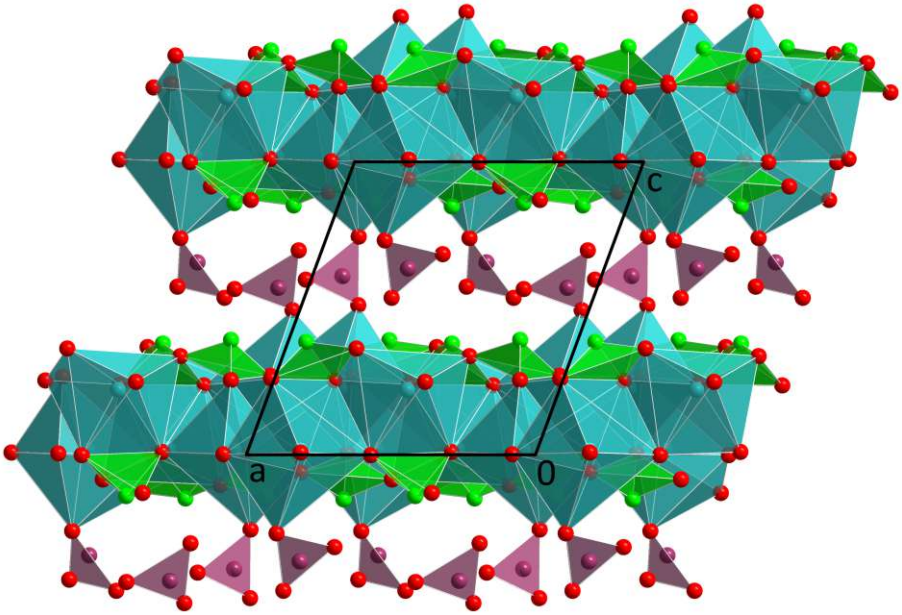

Figure 13. The crystal structure of $Cd_4Te_4O_{11}(NO_3)_2$ viewed along [$0\bar{1}0$]. Atom styles and color codes refer to Figure 9, N atoms are drawn in purple.

Table 3. Selected interatomic distances in the crystal structure of $Cd_4Te_4O_{11}(NO_3)_2$.

	d / Å		*d* / Å
Te1—O10	1.87 (6)	Cd3—O10^{vii}	2.42 (6)
Te1—O5^{i}	1.93 (4)	Cd3—O15^{ix}	2.49 (4)
Te1—O9	2.01 (4)	Cd3—O1^{ix}	2.64 (4)
Te1—O4	2.12 (5)	Cd4—O11	2.31 (4)
Te2—O3	1.83 (3)	Cd4—O13	2.32 (4)
Te2—O6	1.84 (4)	Cd4—O8	2.35 (6)
Te2—O11	1.89 (4)	Cd4—O19	2.35 (4)
Te3—O8^{i}	1.82 (6)	Cd4—O16^{vii}	2.42 (6)
Te3—O16	1.94 (6)	Cd4—O15	2.43 (4)
Te3—O9	2.00 (4)	Cd4—O21	2.44 (4)
Te3—O12	2.32 (4)	Cd5—O10^{vii}	2.31 (6)
Te4—O7^{ii}	1.85 (4)	Cd5—O17	2.33 (5)
Te4—O15	1.91 (4)	Cd5—O9^{vii}	2.40 (4)
Te4—O14^{ii}	1.96 (5)	Cd5—O22	2.40 (3)
Te4—O11	2.28 (4)	Cd5—O16^{vii}	2.45 (6)
Te5—O12	1.86 (4)	Cd5—O18	2.48 (4)
Te5—O17^{iii}	1.88 (5)	Cd6—O17^{ii}	2.17 (5)
Te5—O20	1.90 (3)	Cd6—O3^{v}	2.25 (3)
Te6—O18	1.77 (4)	Cd6—O15	2.27 (4)
Te6—O13	1.92 (4)	Cd6—O21	2.28 (4)
Te6—O14	2.04 (5)	Cd6—O18^{ii}	2.35 (4)
Te6—O19	2.20 (4)	Cd7—O20^{vii}	2.14 (3)
Te7—O1^{iv}	1.86 (4)	Cd7—O16^{vii}	2.23 (6)
Te7—O4^{v}	1.89 (5)	Cd7—O22	2.30 (3)
Te7—O22^{i}	1.94 (3)	Cd7—O5^{v}	2.40 (3)
Te8—O2^{v}	1.77 (5)	Cd7—O2^{v}	2.49 (4)
Te8—O21	1.84 (4)	Cd8—O7^{v}	2.24 (4)
Te8—O19	1.88 (4)	Cd8—O22	2.26 (3)
Cd1—O1	2.19 (4)	Cd8—O3^{x}	2.32 (4)
Cd1—O20^{vi}	2.32 (3)	Cd8—O2^{v}	2.35 (5)
Cd1—O8	2.36 (6)	Cd8—O18	2.45 (4)
Cd1—O6	2.37 (4)	Cd8—O24^{v}	2.47 (5)
Cd1—O5	2.40 (4)	Cd8—O1^{x}	2.62 (4)
Cd1—O34^{vi}	2.51 (6)	N1—O24	1.03 (6)
Cd2—O5	2.22 (4)	N1—O25^{ix}	1.49 (9)
Cd2—O14	2.26 (5)	N1—O26^{ix}	1.39 (5)
Cd2—O6	2.28 (4)	N2—O27	1.43 (12)
Cd2—O13	2.29 (4)	N2—O28	1.28 (9)
Cd2—O2	2.41 (5)	N2—O29	1.15 (10)
Cd2—O7	2.53 (4)	N3—O30	1.22 (7)
Cd2—O10^{vii}	2.61 (6)	N3—O31	1.09 (5)
Cd3—O12^{viii}	2.33 (4)	N3—O32	1.42 (7)
Cd3—O4^{vii}	2.34 (5)	N4—O23^{v}	1.46 (6)
Cd3—O7	2.37 (4)	N4—O33	1.08 (5)
Cd3—O8^{ix}	2.40 (6)	N4—O34	1.32 (6)

Symmetry codes: (i) *x*, *y*, 1+*z*; (ii) *x*, −1+*y*, *z*; (iii) *x*, −1+*y*, 1+*z*; (iv) 1+*x*, 1+*y*, 1+*z*; (v) 1+*x*, *y*, *z*; (vi) −1+*x*, *y*, −1+*z*; (vii) *x*, *y*, −1+*z*; (viii) *x*, 1+*y*, −1+*z*; (ix) *x*, 1+*y*, *z*; (x) 1+*x*, 1+*y*, *z*.

3.1.5 $Pb_3Te_2O_6(NO_3)_2$

Synthesis

During hydrothermal experiment H8 ($Pb(NO_3)_2$, TeO_2 and KOH in molar ratios of 2:1:2), colorless needles of $Pb_3Te_2O_6(NO_3)_2$ were obtained. Experiments M7–M12 tried to resynthesize $Pb_3Te_2O_6(NO_3)_2$ in the CEM Mars6 240/50 microwave furnace. For M9 and M10, very small amounts of the target phase were obtained. Samples M11 and M12 possibly contained not only α-$PbTeO_3$ (Mariolacos, 1969), but also its γ-polymorph (Weil et al., 2018), which had incorrectly been assumed as $PbTeO_3(H_2O)_{1/3}$ (Berchenko & Belyaev, 1967) and $PbTeO_3(H_2O)_{2/3}$ (Tananaev & Novoselova, 1967).

Diffraction measurements

While investigated crystals looked clean and untwinned under polarized light, their respective diffraction patterns all exhibit a very high mosaicity. This was observed for several crystals measured on both diffractometers (Figure 14). The unit-cell was determined to be monoclinic *C*-centered, with a = 18.683(5) Å, b = 5.6720(16) Å, c = 11.907(4) Å, β = 111.712(5)°, V = 1172.3(6) Å^3. In reciprocal space reconstructions, smearing of the reflections by small-angle rotation along the **b*** axis was visible. While it was tried to consider these features with increased box sizes during integration, the resulting data sets were of subordinate quality.

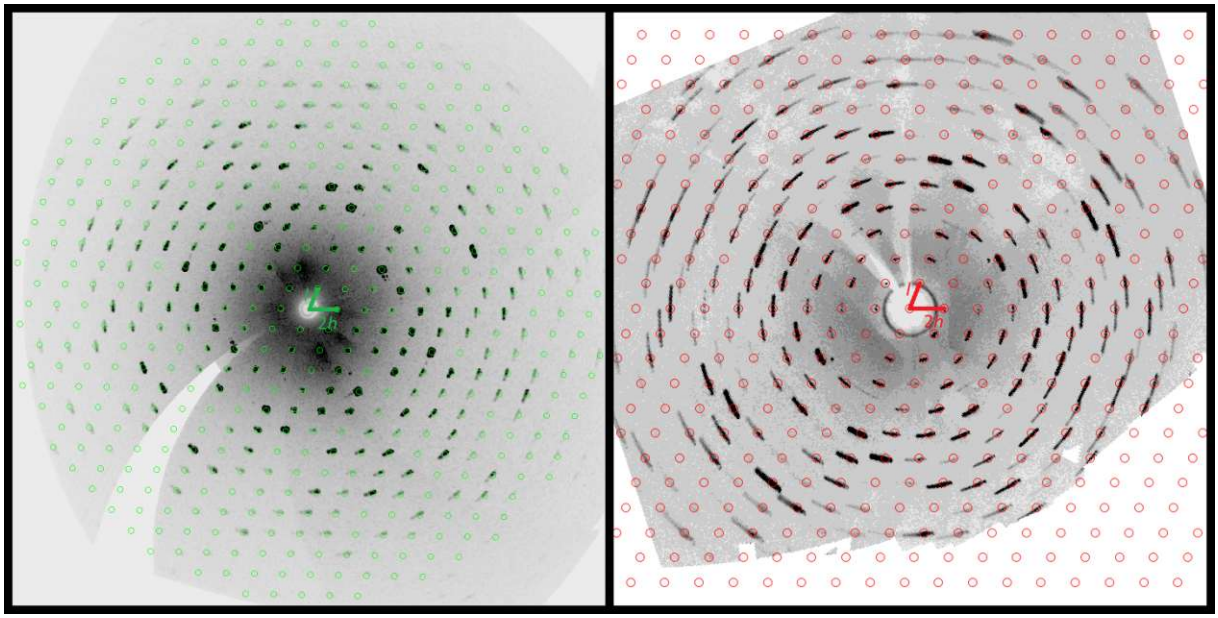

Figure 14. Reconstructed reciprocal *h*0*l* plane of $Pb_3Te_2O_6(NO_3)_2$ from two different crystals and measurements (left on Bruker APEX-II, right on STOE STADIVARI).

Crystal structure

The crystal structure of $Pb_3Te_2O_6(NO_3)_2$ is formed by $^2_\infty[Pb_3Te_2O_6]$ layers extending parallel to $(20\bar{1})$ and NO_3^- anions in the interspace (Figure 15). The choice of the most appropriate space group for the refinement is not straightforward because some parts of the structure exhibit a higher local symmetry. The $^2_\infty[Pb_3Te_2O_6]$ layers have *C*2/*m* symmetry, while one half of the NO_3^- anions follows the *Cm* space group. The remaining NO_3^- anions do not even agree with the $m_{(010)}$ plane and would need a further symmetry reduction. However, attempts for refinement in the triclinic space group *P*1 (with a halved unit-cell volume) were not successful, as not even the $^2_\infty[Pb_3Te_2O_6]$ layers were properly defined. The "best" model was obtained, when the structure was refined under consideration of twinning (twin

operation $2_{[010]}$, relative ratios refined to 0.50:0.50(6)) in space group *Cm*, despite noticing from the behavior of the N3 and N4 nitrate groups that the actual space group has a lower symmetry.

In the final *Cm* model, the asymmetric unit contains six Pb (site symmetry *m*, 2 *a*), four Te (*m*, 2 *a*), sixteen O (O2, O7, ON1b, ON2a, ON3a, ON4a: *m*, 2 *a*; rest: 1, 4 *b*) and four N atoms (*m*, 2 *a*; N4: 4 *b*). The $^{2}_{\infty}[Pb_3Te_2O_6]$ layers consist of the Pb, Te and O1−O7 sites. The Te^{IV} atoms are coordinated by three (Te1, Te3) or four (Te2, Te4) oxygen atoms. The $[TeO_3]$ units are isolated from each other, while the $[TeO_4]$ groups form $[Te_2O_6]$ dimers by edge-sharing. From this, the sum formula can be subdivided into $Pb_6(TeO_3)_2(Te_2O_6)(NO_3)_4$. The Pb^{II} atoms have three to six close oxygen contacts and, like the Te^{IV} atoms, exhibit one-sided coordination polyhedra caused by the stereochemical activity of their non-bonding lone pairs, which are directed away from the layers.

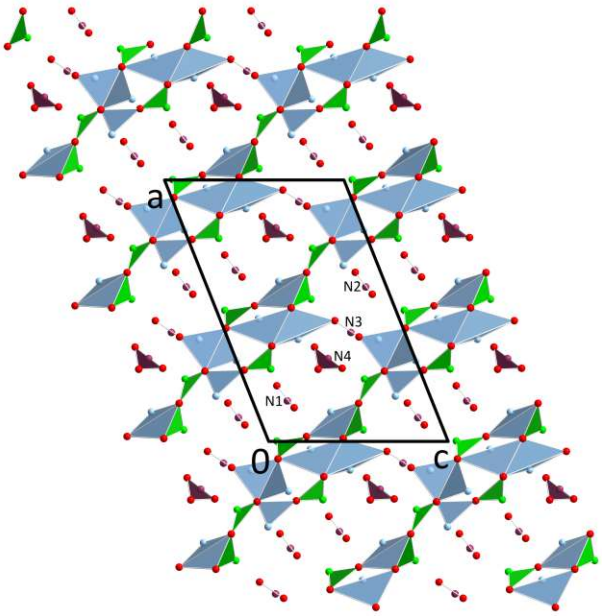

Figure 15. The crystal structure of $Pb_3(TeO_3)_2(NO_3)_2$ in a projection along $0\bar{1}0$. Pb atoms are drawn light blue and N atoms are drawn purple.

The layer interspace is occupied by these $5s^2$ and $6s^2$ electron lone pairs ψ and the NO_3^- anions. Atomic positions belonging to nitrate anions were labelled based on the central N atom, *e.g.,* N1, ON1a and ON1b form one NO_3^- group. While the N1 and N2 nitrate groups could be modelled from difference-Fourier maps without complications, the other two anions do not follow *Cm* symmetry: the N4 nitrate could be observed as a superposition of two orientations, symmetrically connected by the $m_{(010)}$ plane. Except for the ON4a position, which is situated on the mirror plane, all constituents of the N4 nitrate anion were refined with s.o.f.s of 1/2. For the N3 nitrate anion, a similar behavior is assumed, as the locations of the N3 and N4 anions exhibit a similar pattern of difference density peaks. However, a refinement with a disorder model like for N4 was not stable in this case. Instead, the N3 nitrate anion had to be forced into a symmetric position using strong constraints.

SEM-EDS

EDS measurements of the crystals confirm the Pb:Te ratio of 3:2 and the presence of only Pb, Te, N and O in the structure. The crystals have a needle-like shape and show a tendency to grow together as bunches (Figure 16), which is in accordance with the problematic scattering behavior of the crystals. The O and N contents (Table 4) have a ratio of *ca.* 7:1, which is in decent agreement with the proposed formula of $Pb_3Te_2O_6(NO_3)_2$. No speculations on the crystal water content can be made from EDS measurements, as potential crystal water molecules would most likely evaporate in the

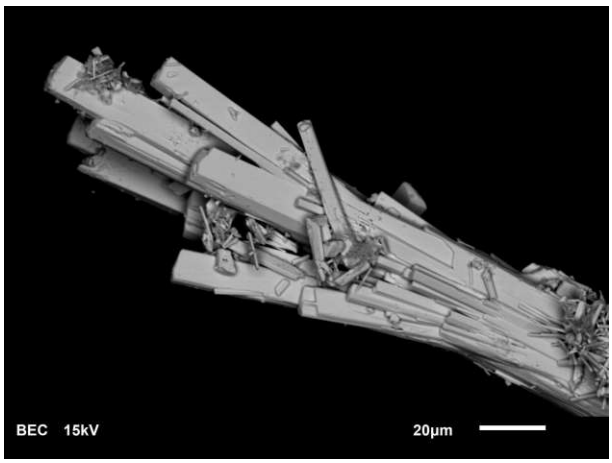

Figure 16. SEM-BE image of crystals of $Pb_3Te_2O_6(NO_3)_2$.

vacuum of the instrument. However, the absence of visible cracks in the crystals indicates a rather low water content, if any. In the refined crystal structure model of $Pb_3Te_2O_6(NO_3)_2$, no significant voids hinting at water molecules of crystallization are present.

Table 4. SEM-EDS data of crystals of $Pb_3Te_2O_6(NO_3)_2$.

Data point	Pb /%	Te /%	O /%	N /%
1	20.5	14.2	57	8.1
2	20.2	14.7	57	8.0

3.2 Tungstates

As already discussed in the introduction, oxidotellurate(IV)-tungstate phases are a very popular field in the search for new SHGs (Guo et al., 2022). While the present literature focuses on alkali or alkaline earth metals or d^{10} transition metals like Cd^{II} or Ag^{I}, for the present investigation, mostly transition metals with an incomplete *d* shell (Cu^{II}, Fe^{III}, Cr^{III}, Ni^{II}, and Mn^{II}) or with additional *s* electrons (Pb^{II}) were chosen, next to Zn^{II} and Cd^{II}.

3.2.1 Hydrothermal experiments

The first hydrothermal series (H25–32) introduced metal oxides, TeO_2 and WO_3 in water without any additional acid or base. Four of the eight experiments did not show any reaction yielding just the educt oxides (Table 67). For Mn^{II}, Cd^{II} and Pb^{II}, the corresponding tungstate was formed, while for Zn^{II} both $ZnWO_4$ (Filipenko et al., 1968) and $ZnTeO_3$ (Hanke, 1967) were obtained. Samples H27 (Zn^{II}) and H32 (Mn^{II}) contained further unassignable reflections, and neither measurable single crystals nor a literature phase with a similar PXRD pattern could be found.

To increase the reactivity of TeO_2, additional base was added for further hydrothermal tungstate reactions. At first, the influence of KOH and NH_3 was tested on a reaction between NiO, TeO_2 and WO_3 (H33, H34). While for the KOH-experiment (H33) only NiO was obtained as a solid product, H34 (NH_3) yielded more different phases. Besides NiO and α-TeO_2 (Stehlik & Balak, 1948), a phase with hexagonal metrics, isotypic with $Rb_2W_3O_9(TeO_3)$ (Goodey et al., 2003) with a = 7.28824(5) Å and c = 12.15272(10) Å was observed.

As the ammonia-based experiment H34 was more promising than H33, samples H39–H46 included the same reactants as H25–32 with $NH_{3\,aq.}$ in higher concentrations. The increased alkalinity led to a higher reactivity of the starting materials. However, in most cases either a metal oxidotellurate or tungstate, but no combined phases, with the exception of sample H44 (Cd^{II}; 3.2.3), had formed. The hexagonal phase observed in H34 was identified in several batches as well (see 3.2.4).

3.2.2 Solid-state reactions

Because several of the recently discovered oxidotellurate(IV) tungstate compounds were synthesized by solid-state reactions, this synthetic route was explored for potential transition metal oxidotellurate(IV) tungstate phases in experiments S1–S8, S11, S52 and S54. Reactions were performed under ambient atmosphere in a platinum (S1–S8, S11) or aluminum (S52, S54) crucible (Table 66).

S1 and S2 started from nickel(II)- and cobalt(II) salts, TeO_2 and WO_3 (*M*:Te:W = 1:1:1) and yielded Ni/$CoWO_4$ (Keeling, 1957; Weitzel, 1976) and α-TeO_2 (Stehlik & Balak, 1948) as reaction products after tempering at 760 °C. Nickel/cobalt tungstate forms preferably over potential oxidotellurate phases or hypothetical mixed phases. Adding an excess of nickel to the reaction (S3) led to the formation of NiO and separate oxidotellurate and tungstate phases (Ni_3TeO_6 (Newnham & Meagher, 1967) and $NiWO_4$). Performing reaction S1 (Ni^{II}) at a lower temperature of 600 °C (S5), again yielded only $NiWO_4$ and α-TeO_2. If additional WO_3 was added to that reaction (S6), WO_3 was found as an additional product.

Because nickel and cobalt prefer to form tungstate over oxidotellurate phases at the chosen temperatures, it was tried to modify the reaction by using nickel/cobalt oxidotellurates(IV) and WO_3 as starting materials (S4, S7, S8). In the PXRD patterns of the three experiments, only α-TeO_2, nickel oxidotellurates and MWO_4 (*M* = Co, Ni) were found. It should be noted that nickel/cobalt oxidotellurate(VI) molybdate phases with compositions of $Ni_3Mo_2TeO_{12}$ (Słkoczyński & Śliwa, 1978) and $Co_4Mo_3TeO_{16}$ (Kozłowski & Słkoczyński, 1976) have been reported with the same unit-cell as MWO_4 or $MMoO_4$ (*M* = Co, Ni). This indicates that a potential partial incorporation of Te^{VI} into the crystal

structure of cobalt or nickel tungstates could remain comparatively unnoticed by powder diffraction. No single crystals of $Ni_3Mo_2TeO_{12}$ (Słkoczyński & Śliwa, 1978) and $Co_4Mo_3TeO_{16}$ (Kozłowski & Słkoczyński, 1976) have been investigated yet and for samples S1–S8, no material suitable for single-crystal diffraction experiments was found either.

Solid state reaction S11, based on $ZrO(NO_3)_2(H_2O)_6$, TeO_2 and WO_3 yielded $ZrTe_3O_8$ (Meunier & Galy, 1971) and WO_3. Two solid-state reactions employing MnO/CdO, WO_3 and TeO_2 were performed in small, sealed aluminum crucibles (S48, S49). However, mixed oxidotellurate tungstate phases were not obtained.

3.2.3 $Cd_3(WO_4)(TeO_3)_2$

In experiment H44, reflections perfectly matching the phase $Cd_3(MoO_4)(TeO_3)_2$ (Feng et al., 2016) were observed besides $CdWO_4$ (Chichagov et al., 1966). $Cd_3(MoO_4)(TeO_3)_2$ is a SHG material with a non-linear coefficient similar to KDP (KH_2PO_4). Given the presence of W instead of Mo during synthesis and the very similar (crystal-)chemistry of the two metals, it can be assumed that the tungstate-isotype $Cd_3(WO_4)(TeO_3)_2$ was formed instead. The lattice parameters of the phase were refined based on the PXRD measurement and the structural model of $Cd_3(MoO_4)(TeO_3)_2$ (space group $P2_1$), and are a = 8.4775(8) Å, b = 5.4650(3) Å, c = 10.7186(11) Å, β = 107.766(2)° (Figure 17) compared to a = 8.5162 Å, b = 5.4850 Å, c = 10.9160 Å, β = 108.185° for $Cd_3(MoO_4)(TeO_3)_2$. Unfortunately, suitable single crystals to confirm the assumed crystal structure were not available.

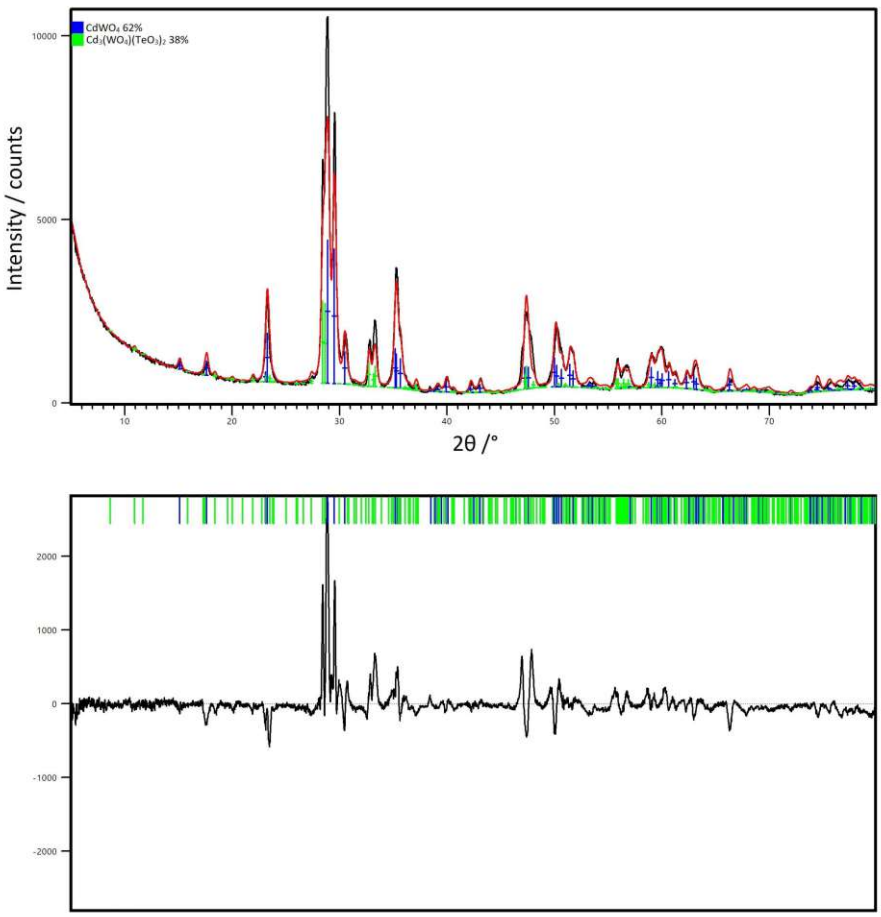

Figure 17. Rietveld refinement of sample H44 containing the assumed phase $Cd_3(WO_4)(TeO_3)_2$.

3.2.4 $(NH_4)_2W_3O_9(TeO_3)$

Samples H40 (Fe^{III}), H42 (Cr^{III}), H43 (Ni^{II}), H45 (Pb^{II}) and H46 (Mn^{II}) all share the same hexagonal phase already observed in H34. Given its frequent formation from ammonia-based experiments and the fact that several compounds, which exhibit a hexagonal unit-cell with similar metrics ($(NH_4)_2Mo_3O_9(SeO_3)$) (Harrison et al., 1994), $(NH_4)_2Mo_3O_9(TeO_3)$ (Balraj & Vidyasagan, 1998), $Rb_2W_3O_9(TeO_3)$ (Goodey et al., 2003), $Cs_2W_3O_9(TeO_3)$ (Zhao et al., 2015) and $Cs_2Mo_3O_9(TeO_3)$ (Zhang et al., 2011)), have the same formula type $A_2B_3O_9(XO_3)$, an assumed composition of $(NH_4)_2W_3O_9(TeO_3)$ is apparent. A PXRD pattern of phase-pure $(NH_4)_2W_3O_9(TeO_3)$ was obtained from a hydrothermal experiment based on TeO_2, WO_3 and $NH_{3\,aq.}$ in molar rations of 1:3:12 (H90). Its lattice parameters were refined to a = 7.28453(1) Å and c = 12.15153(2) Å (Figure 18) based on the structural model of $Rb_2W_3O_9(TeO_3)$ (Goodey et al., 2003; a = 7.2980(2) Å, c = 12.0640(2) Å). Replacing the Rb atoms of the literature phase by N atoms in the refined model led to a significantly better agreement of the simulated profile with the observed intensities.

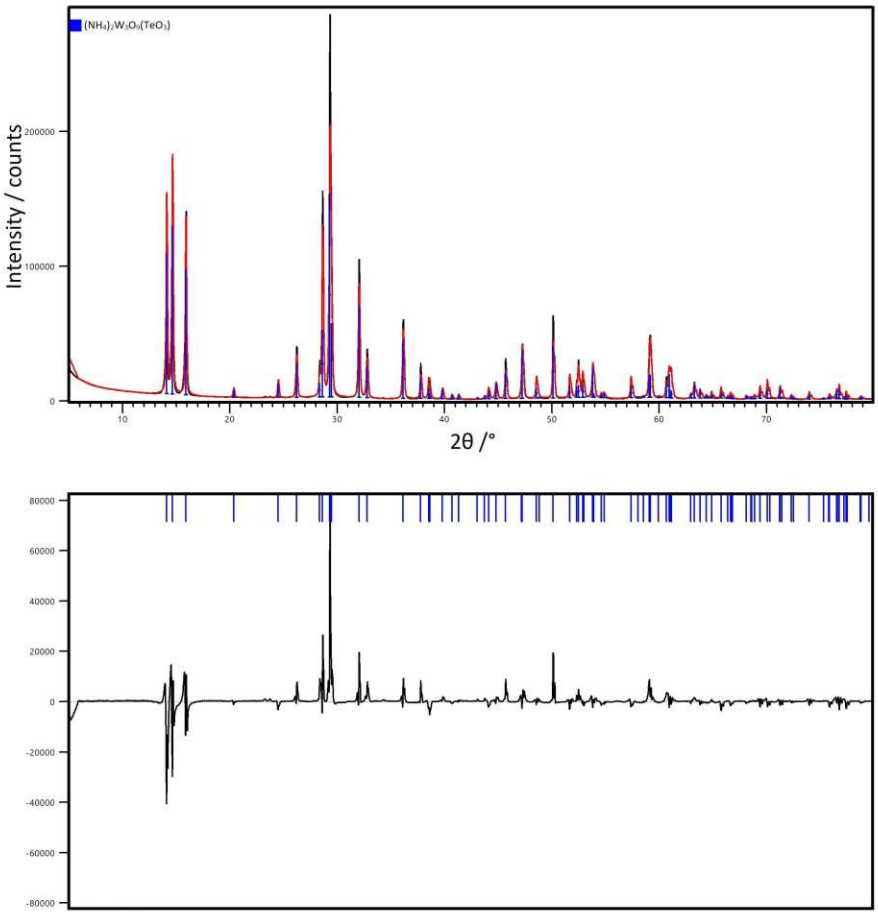

Figure 18. Rietveld refinement of the assumed phase $(NH_4)_2W_3O_9(TeO_3)$ in experiment H90.

3.3 Arsenates

3.3.1 Starting from As^{III}

First experiments on the inclusion of arsenates were performed under hydrothermal conditions employing Ni^{II}, Te^{IV} and As^{III} (H35−H38). The use of As_2O_3 as a source of arsenic led to an internal redox-reaction with TeO_2, yielding As^{V} salts and Te in elemental form visible as grey needles. The unwanted redox reaction was minimized in the experiments lacking an external base (KOH or NH_3). In sample H36 (NiO, As_2O_3, TeO_2, NH_3), a novel alkaline nickel ammonium arsenate with the composition $(NH_4)Ni_3(HAsO_4)(AsO_4)(OH)_2$ was identified and its crystal structure determined by single-crystal X-ray diffraction (6.5). After one unsuccessful attempt (H89), the new phase was resynthesized from nickel nitrate, arsenic(V) oxide and ammonia (H91) as the main product. A solid-state reaction between $Ni(NO_3)_2(H_2O)_6$, TeO_2 and As_2O_3 (molar ratios 2:1:3) at 400 °C (S12) only yielded α-TeO_2 and NiO as identifiable reaction products.

3.3.2 Starting from As^{V}

Systematic experiments on potential transition metal oxidotellurate(IV) arsenate(V) phases were conducted based on metal (Co^{II}, Cu^{II}, Fe^{III}, Zn^{II}, Cr^{III}, Ni^{II}, Cd^{II} and Pb^{II}) nitrates, TeO_2, H_3AsO_4 and KOH (H121−H128). Various arsenate(V) and oxidotellurate(IV) compounds were identified in the PXRD patterns, but no oxidotellurate(IV) arsenate was observed (Table 67). From H127, (Cd^{II}) single crystals of $Cd_5(TeO_3)_4(NO_3)_2$ (3.1.3) were isolated. The diffraction patterns of H126 (Ni^{II}) and H127 (Cd^{II}) both contained numerous unassignable reflections. A plausible explanation can not be given, and suitable single-crystalline material was not found.

The second hydrothermal series of experiments exchanged the employed KOH to $NH_{3\,aq.}$ (H131−H138). The product of sample H133 (Fe^{III}) was yellowish green and exhibited a powder pattern, in which no known phase could be identified (3.3.3). In H136 (Ni^{II}), unassignable reflections, the most intense at $2\theta = 12.66°$ (d = 6.984 Å) were observed. Most of them can be related to the PXRD pattern of a phase with composition $Na_3Fe_2(PO_4)_3$ (*hR*, a = 13.39(1) Å, c = 17.91(2) Å; Belokoneva et al., 2002). This points to a so far unknown ammonium nickel arsenate compound, other than $(NH_4)Ni_3(HAsO_4)(AsO_4)(OH)_2$ (6.5) . In experiment H134, single crystals of a new phase with the composition $Zn_2(HTeO_3)(AsO_4)$ were found (3.3.4).

3.3.3 An unidentified NH_4–Fe–As–O-phase

The most prominent features of the PXRD pattern are two intense reflections at 10.86 and 21.59° 2θ (*d* = 8.139, 4.112 Å). Under the microscope, a mixture of thin colorless translucent plates, cloudy light yellow thicker plates and opaque yellow blocks could be distinguished. Neither of the observed species showed any reflections when investigated on the single-crystal diffractometer. It is assumed that the thicker blocks consist of a multitude of plates grown together. The best fit for this phase relates to the powder diffraction pattern of pharmacosiderite ($Fe_4K(AsO_4)_3(OH)_4(H_2O)_7$; Zemann, 1948), but with a significantly larger lattice parameter of *a* = 8.3366(2) Å instead of 7.93 Å (Figure 20).

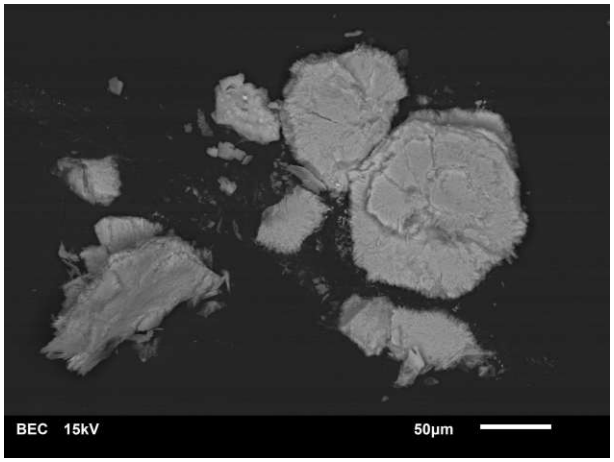

Figure 19. BE-SEM picture of crystals of the unidentified NH_4–Fe–As–O-phase.

Crystals of the unknown phase were investigated using SEM-EDS (Figure 19). The plates, which before had clean hexagonal shapes, showed significant signs of dehydration in the vacuum of the instrument and cracked especially at the crystal edges. This caused some variance in the obtained values, because of the rough surface for analysis. The EDS data (Table 5) support the hypothesis of a Te-free, hydrated iron(III) ammonium arsenate(V) phase, which easily loses crystal water at ambient conditions. It is assumed that potentially available single crystals have lost too much water before they could be examined on the diffractometer. Subsequent re-synthesis of this compound (H423, H424) resulted in the same phase, however together with zemannite-type $Fe_2(TeO_3)_3$ (4.1.6.4). Expectedly, the reflections of the unknown NH_4–Fe–As–O-phase disappear after tempering the sample at 210 °C for two days.

Table 5. SEM-EDS measurements on crystals of the NH_4–Fe–As–O-phase.

Data point	Fe /%	As /%	Te /%	N /%	O /%
1	17.9	17.0	0.8	9.1	55
2	13.2	12.7	0.4	10.0	63
3	16.0	12.7	0.5	9.8	58
4	12.6	12.1	0.5	9.8	65
Average	15(2)	14(2)	0.55(2)	9.7(4)	60(4)

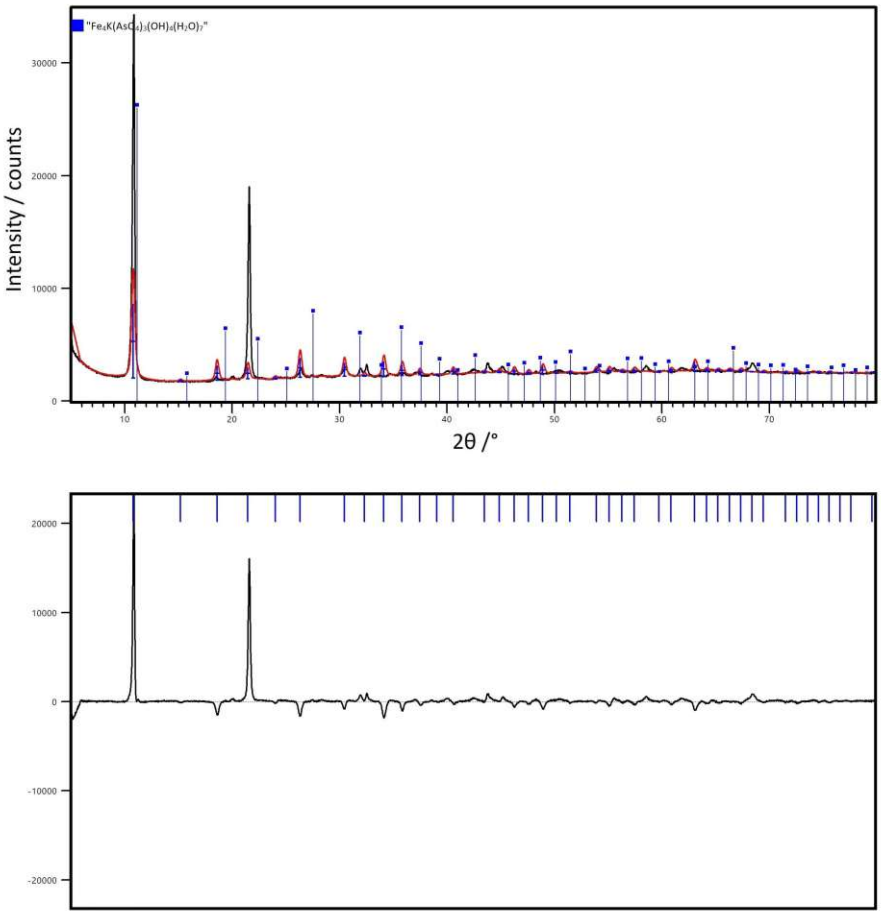

Figure 20. Rietveld refinement of experiment H133 with $Fe_4K(AsO_4)_3(OH)_4(H_2O)_7$ (Zemann, 1948) as the reference phase. Reflection positions of $Fe_4K(AsO_4)_3(OH)_4(H_2O)_7$ are marked with blue squares.

3.3.4 $Zn_2(HTeO_3)(AsO_4)$

Colorless block-shaped single crystals of $Zn_2(HTeO_3)(AsO_4)$ were obtained from a hydrothermal reaction based on $Zn(NO_3)_2(H_2O)_6$, TeO_2, H_3AsO_4 and $NH_{3\ aq.}$ in molar ratios of 2:1:2:6. The crystal structure of $Zn_2(HTeO_3)(AsO_4)$ is monoclinic (*Cm*, a = 6.9040(12) Å, b = 7.7212(13) Å, c = 5.7260(10) Å, β = 101.195(5)°, V = 299.43(9) Å^3), and the asymmetric unit contains one Te, one As, one Zn, five O and one H atom.

The Te1 site is coordinated by three oxygen atoms and a hydroxide group at distances between 1.880(2) and 2.131(4) Å in a bisphenoidal shape. The resulting $[TeO_3(OH)]$ units are isolated from each other. The As^V atoms are coordinated tetrahedrally by four oxygen atoms (distances 1.673−1.716(3) Å) forming $[AsO_4]^{3-}$ anions isolated from each other. The Zn^{II} atoms are coordinated by four oxygen atoms and the hydroxide group in a trigonal bipyramidal shape. The hydroxide group has a significantly longer distance of 2.3259(18) Å from the Zn^{II} atom than the other four oxygen contacts (1.979(3)−2.0486(16) Å).

The $[ZnO_4(OH)]$ polyhedra are connected to four neighboring units by corner-sharing to form $^1_\infty[Zn_2O_{6/2}(OH)_{2/2}O_{2/1}]$ layers parallel to (001). These layers build the backbone of the crystal structure of $Zn_2(HTeO_3)(AsO_4)$. The $[TeO_3(OH)]$ units are connected to one side of the Zn−O-layers, while the $[AsO_4]$ tetrahedra are positioned on the other side and share one corner with a $[TeO_3(OH)]$ group from the adjacent layer (Figure 21).

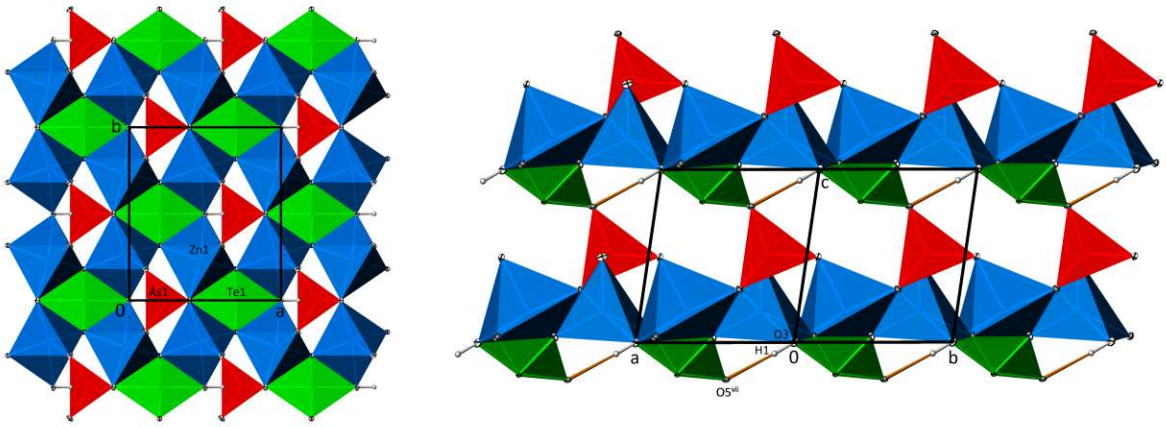

Figure 21. The crystal structure of $Zn_2(HTeO_3)(AsO_4)$ viewed along $[00\bar{1}]$ (left) and $[\bar{1}\bar{1}0]$ (right). O atoms are drawn white and H atoms grey. Hydrogen bonds are drawn as orange lines. Structure representations were generated with ATOMS (Dowty, 2006).

Despite the much smaller pK_b value of the $[AsO_4]^{3-}$ anion compared to the $[TeO_3]^{2-}$ anion (2.40 vs. 6.30 at room temperature; Weast & Astle, 1982), the hydroxide group is surprisingly not part of the arsenate(V) anion but of the oxidotellurate(IV) group. The OH group forms a very weak hydrogen bond with an O—H···O distance of 3.213(5) Å.

For a more elaborate discussion of the crystal structure of $Zn_2(HTeO_3)(AsO_4)$, see:

Eder, F. & Weil, M. (2021). Crystal structure of $Zn_2(HTeO_3)(AsO_4)$. *Acta Cryst*. E**77**, 555−558.

3.4 Oxidotellurates(VI)

Tellurium is able to coexist in both stable oxidation states of +IV and +VI in oxidotellurates, for which more than 30 mixed IV/VI oxidotellurate phases are known up to now. Mixed-valent compounds are promising candidates in the search for controlled valency semiconductors or catalytic applications (Day, 1981; Murase et al., 2017). Therefore, the incorporation of oxidotellurate(VI) anions into oxidotellurates(IV) was explored.

3.4.1 Hydrothermal experiments

3.4.1.1 $Ni^{II}/Te^{IV}/Te^{VI}$ – search for $Ni_4Te_2O_9$

The first experiments aiming at mixed-valent oxidotellurate phases (H47−H49) were performed based on NiO, TeO_2 and H_6TeO_6 (molar ratios 4:1:1), trying to resynthesize $Ni_4Te_2O_9$, which had been obtained as a side product of a chemical transport reaction (Veyer, T. & Weil, M.; unpublished results). PXRD measurement of the product of H47 (additional KOH) revealed, besides NiO and $KTeO_3(OH)$ (Lindqvist, 1972), broad reflections, which could not be assigned. The two most intense reflections were at 12.51 and 25.22° 2θ (7.07 and 3.53 Å), which hints at a layered structure with a layer-layer-distance of *ca.* 7.07 Å. For the NH_3-equivalent experiment H48, more unassigned reflections remained. Next to α-TeO_2 and NiO, reflections corresponding to a face-centered cubic phase with $a \approx 10.06$ Å could be assigned. Literature phases with a similar PXRD pattern are KOs_2O_6 (Yamaura et al., 2006) and $(NH_4)CrTeO_{6.5}(H_2O)$ (García-Martín et al., 1988).

Repeating experiments H47 and H48 with nickel nitrate instead of nickel oxide and increased base concentrations led to different phases. Increasing the KOH concentration relative to H48 led to the formation of $NiTeO_4$ (H85; Isasi, 2001), and after further increase, a mixture of "$Ni_3(TeO_3)_2(OH)_2$" (Perez et al., 1976) and KNO_3 was identified. Additional reflections in the PXRD measurement were very broad (H86). Raising the NH_3 concentration relative to H47 led to similar results: $NiTeO_4$ for H87, and the same unassigned broad reflections as in H87 also in H88. These broad reflections match with a rhombohedral cell with $a \approx 3.06$ Å and $c \approx 13.97$ Å in the hexagonal setting.

The $Ni(NO_3)_2(H_2O)_6/TeO_2/H_6TeO_6$ system was explored further with a different $Ni^{II}/Te^{IV}/Te^{VI}$ stoichiometry (2:1:2; H73−H76). Without any base, only α-TeO_2 and $NiTeO_4$ were observed. Additional NH_3 led to the same unexplained cubic phase as in H48. Experiments H74 (more KOH) and H76 (less KOH) again yielded very broad unassigned reflections, besides KNO_3 and $KTeO_3(OH)$.

For further hydrothermal reactions in this system, water was not added at all (H114−120). Nickel(II) was employed either as an oxide or nitrate and reacted with TeO_2, H_6TeO_6 and, in some cases, KOH. No interesting phase was observed in the seven reactions, the most noteworthy reaction product was the mixed-valent oxidotellurate phase $Te_2O_4(OH)_2$ (Lindqvist & Moret, 1973) (Table 67).

3.4.1.2 $M/Te^{IV}/Te^{VI}/NH_3$

The first systematic series (H50−H57) was conducted with metal (Mn^{II}, Cu^{II}, Fe^{III}, Zn^{II}, Cr^{III}, Ni^{II}, Cd^{II} and Pb^{II}) oxides, TeO_2, H_6TeO_6 and NH_3 (molar ratios 2:1:2:12) as starting materials. Two phases of interest were observed for several samples. For all samples except H56 (Cd^{II}), the mixed-valent oxidotellurate(IV/VI) $NH_4Te_2O_5(OH)$ (Philippot et al., 1979) was identified. The other multiple received phase was that with the face-centered cubic ($a \approx 10.06$ Å) structure discussed in paragraph 3.4.1.1. Given its frequent appearance (H50−H55; Mn^{II}, Cu^{II}, Fe^{III}, Zn^{II}, Cr^{III} and Ni^{II}), it seems likely that no transition metal, but most probably ammonium cations are part of the structure. Based on the possibly isotypic $(NH_4)CrTeO_{6.5}(H_2O)$ (García-Martín et al., 1988), a composition of $(NH_4)Te_2^{VI}O_{6.5}(H_2O)$ appears to be reasonable.

Next to the two majority phases, two batches included more unassigned reflections. In experiment H51 (Cu^{II}), a novel mixed-valent copper oxidotellurate(IV/VI) with the composition $Cu_2Te_4O_{12}(NH_3)(H_2O)_2$ could be identified (3.4.3). For H56 (Cd^{II}), an unknown phase was observed; the reflection pattern could not be related to possible isotypic structures. The reflections of this phase were rather broad, and no single crystals could be found under the microscope.

Similar experiments with $Te^{IV}/Te^{VI}/NH_3$ were conducted, starting from metal nitrates instead of oxides (H106−H113). Several batches yielded products of interest: H107 (Cu^{II}) contained at least one unknown phase besides Cu_3TeO_6 (Hostachy & Coing-Boyat, 1968), and in H112 (Cd^{II}) a new polymorph of $CdTe_2O_5$, denominated as *β*-$CdTe_2O_5$ (5.2.1), was discovered.

3.4.1.3 M/Te^{IV}/Te^{VI}/KOH

The second systematic series (H66−H73) replaced NH_3 with KOH as the base. Here, the formation of oxidotellurate(VI) phases was clearly favored over tetravalent Te-compounds (Table 67). Only H66 (Cu^{II}) exhibited a PXRD pattern with most of the reflections unassigned.

Experiments H66−H69 were repeated with a longer reaction time of *ca.* 3 weeks. (H100−H103). When opening the autoclave afterwards, it was observed that no liquid had remained in all four containers. Presumably, it had been forgotten to add water to the reaction before putting it into the furnace. Only a little amount of H_2O originated from the employed H_6TeO_6 and KOH during the reaction. Surprisingly, in two of the four samples, single crystals of unknown phases were discovered, and their crystal structures determined. Details on the observed phases $K_2Cu_2TeO_6$ (4.2.2.6.4), $K_3CuTeO_5(OH)(H_2O)$ (4.2.2.6.3) and $K_{12}Fe_6Te_4O_{27}(H_2O)_3$ (4.2.2.3.1) and further syntheses in these systems can be found in chapter 4 (cationic modification of transition metal oxidotellurates). The serendipitous synthesis of these three phases was later mimicked in numerous hydroflux-like and mild hydroflux reactions.

3.4.1.4 Experiments targeting at $A_2Te^{IV}Te^{VI}O_4(OH)_4$ (A = K, Rb)

During attempts to resynthesize $K_4Sn_3Te_8O_{24}$, which is characterized by a disordered layered crystal structure (4.1.3.6), the isotypic phases $K_2Te^{IV}Te^{VI}O_4(OH)_4$ and $Rb_2Te^{IV}Te^{VI}O_4(OH)_4$ were obtained instead (Völkl et al., 2022). Their crystal structure consists of $^1_\infty[Te^{IV}Te^{VI}O_4(OH)_4]$ rods formed by alternating $[Te^{IV}O_4]$ and $[Te^{VI}O_2(OH)_4]$ units connected by corner-sharing and the K^+/Rb^+ cations located in between. Each $[Te^{IV}O_4]$ unit is located on one of three possible locations connected by a threefold rotation along the rod-axis. The distribution of the Te^{IV} atoms within a rod and within the plane perpendicular to the rod direction is disordered. The latter follows the same rules as a bipartite partitioning of a honeycomb net or a lozenge tiling. This heavily disordered system leads to rather unique diffraction patterns dominated by diffuse scattering.

In subsequent studies, it was attempted to increase the yield of $A_2Te^{IV}Te^{VI}O_4(OH)_4$ (*A* = K, Rb) and optimize the formation conditions in hydrothermal experiments H384−H400. The most successful experimental setup turned out to be a mixture of TeO_2, H_6TeO_6 and A_2CO_3 with molar ratios of 1:1:4 in a usual hydrothermal reaction (H386 for Rb and H395 for K). In H386, single crystals of the new phase $RbTeO_3(OH)$ (6.3) were obtained as well. While $KTeO_3(OH)$ (Lindqvist, 1972) was a common but unwanted reaction product in numerous hydrothermal experiments performed during this thesis, its Rb-homologue has not been described yet. The corresponding Cs-compound $CsTeO_3(OH)$ was discovered as well (Völkl et al.; unpublished results).

3.4.2 Solid-state reactions

It was tried to prepare mixed-valent oxidotellurates by solid-state reactions as well (S50−S57). For this purpose, the oxides of Co^{II}, Cu^{II}, Fe^{III}, Zn^{II}, Cr^{III}, Ni^{II}, Cd^{II} and Mn^{II} were mixed with TeO_2 and TeO_3 in small aluminum crucibles, which were subsequently sealed and heated to 600 °C. For all reactions except S51 (Cu^{II}), the PXRD patterns of the reaction products could be explained by literature

oxidotellurate(IV or VI) phases and starting materials (Table 66). The Cu^{II}-based sample included Cu_3TeO_6 and at least one unknown phase, of which no material suitable for single-crystal diffraction experiments could be isolated.

3.4.3 $Cu_2Te_4O_{12}(NH_3)(H_2O)_2$

Synthesis

$Cu_2Te_4O_{12}(NH_3)(H_2O)_2$ was obtained from a hydrothermal reaction starting form CuO, TeO_2, H_6TeO_6 and $NH_{3\,aq.}$ in molar ratios of 2:1:2:12 (H51). It was tried to resynthesize novel $Cu_2Te_4O_{12}(NH_3)(H_2O)_2$ from $Cu(NO_3)_2(H_2O)_{2.5}$, TeO_2, H_6TeO_6 (molar ratios 1:1:1) and varying additions of bases using the magnetically stirred microwave heated reactor (M1−M6). In experiments M1−M3, apparently too little amounts of base (NH_3) were added to properly dissolve the reactant TeO_2. Only TeO_2 starting material, which was a mixture of its *α*- and *γ*-polymorph (Stehlik & Balak, 1948; Champarnaud-Mesjard et al., 2000), was found as solid residue after the reaction. For experiments M4 and M5 with higher alkaline environments, the main drawback of the method became evident: even though an unknown phase was obtained, the broad reflections in the PXRD pattern (Figure 22) indicated that reaction products obtained unser these conditions usually appear as very fine powders. Consequently, structure determination by single-crystal X-ray diffraction was not possible for these samples.

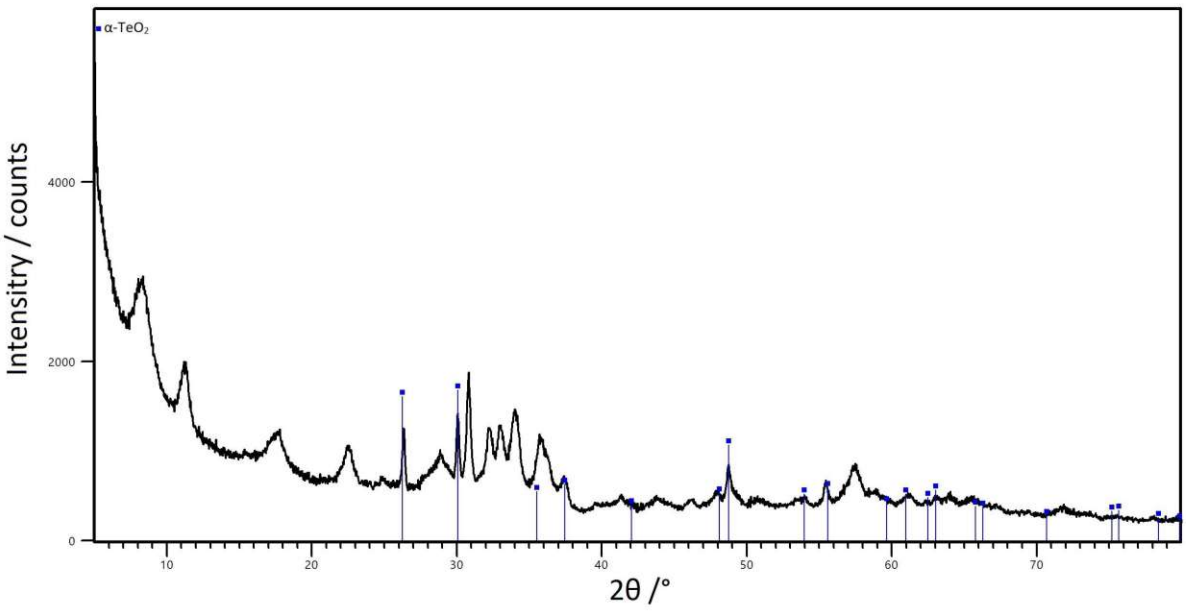

Figure 22. PXRD pattern of the products from experiment M4.

Single crystals of $Cu_2Te^{IV}_2Te^{VI}_2O_{12}(NH_3)(H_2O)_2$ have a light-green color and the shape of broad needles/pointed bars. They usually grow in clusters and had to be separated manually from each other for the single-crystal X-ray study. The investigated crystal was not single-crystalline but contained small fractions of a second twin domain. The main and secondary domain are symmetrically connected by a 180° rotation along **a**. Integration and absorption correction were performed under consideration of both domains, and refinement was based on a hklf5-type intensity file. The BASFs of the two twin domains refined to values of 0.984:0.016(4).

Crystal structure

The asymmetric unit of the triclinic unit-cell (*P*1, *a* = 6.7775(2) Å, *b* = 6.9042(2) Å, *c* = 7.1158(2) Å, *α* = 78.0813(8)°, *β* = 75.7477(9)°, *γ* = 78.5470(8)°, *V* = 311.91(2) Å^3) contains 28 atoms, four Te, two Cu, fourteen O and one N and seven hydrogen atoms.

$Cu_2Te^{IV}_2Te^{VI}_2O_{12}(NH_3)(H_2O)_2$ is a mixed-valent oxidotellurate phase with half of the Te atoms appearing in the oxidation states +IV and +VI each. According to the Robin–Day classification, it belongs to class I (Robin & Day, 1968). The tetravalent Te atoms, located at the Te1 and Te4 sites, appear with a coordination number of 5, which is rather rare for oxidotellurates(IV). However, this is not surprising, as mixed-valent oxidotellurates have some preference for higher coordination numbers at the Te^{IV} atoms (Loeksmanto et al., 1980). The $[TeO_5]$ units have a square-pyramidal shape (Figure 23), verified by the geometry index τ_5, which adopts values close to 0 of 0.030 for $[Te1O_5]$ and 0.052 for $[Te2O_5]$. The coordinates of the non-bonding $5s^2$ electron pairs are *x* = 0.0777, *y* = 0.0530, *z* = 0.5188 for ψ_{Te_1} and *x* = 0.6727, *y* = 0.6774, *z* = 0.7269 for ψ_{Te_4}. The $[Te^{IV}O_5]$ units are isolated from each other but share four of their five corners with the coordination polyhedra of the Te^{VI} atoms.

The hexavalent Te atoms at the Te2 and Te3 sites are coordinated by six oxygen atoms in an octahedral shape. Two neighboring $[TeO_6]$ units form $[Te_2O_{10}]$ dimers by edge-sharing. Together with the $[TeO_5]$ pyramids, they form $^2_\infty[Te^{IV}_2Te^{VI}_2O_{20/2}O_{2/1}]$ layers oriented parallel to (001) (Figure 24). Such $Te^{IV}Te^{VI}X_6$ layers with the Te atoms forming double-triangles and 4-rings have also been described for another mixed-valent oxidotellurate(IV/VI) phase, namely $Ag_2Te^{IV}Te^{VI}O_6$ (Weil, 2007). Using the nomenclature of Christy et al. (2016), the connectivities of the Te^{IV} atoms are Q^{1400}, and Q^{0510} for the Te^{VI} atoms. The BVS of the Te atoms amount to 3.89 (Te1), 5.85 (Te2), 6.00 (Te3) and 4.02 (Te4) v.u..

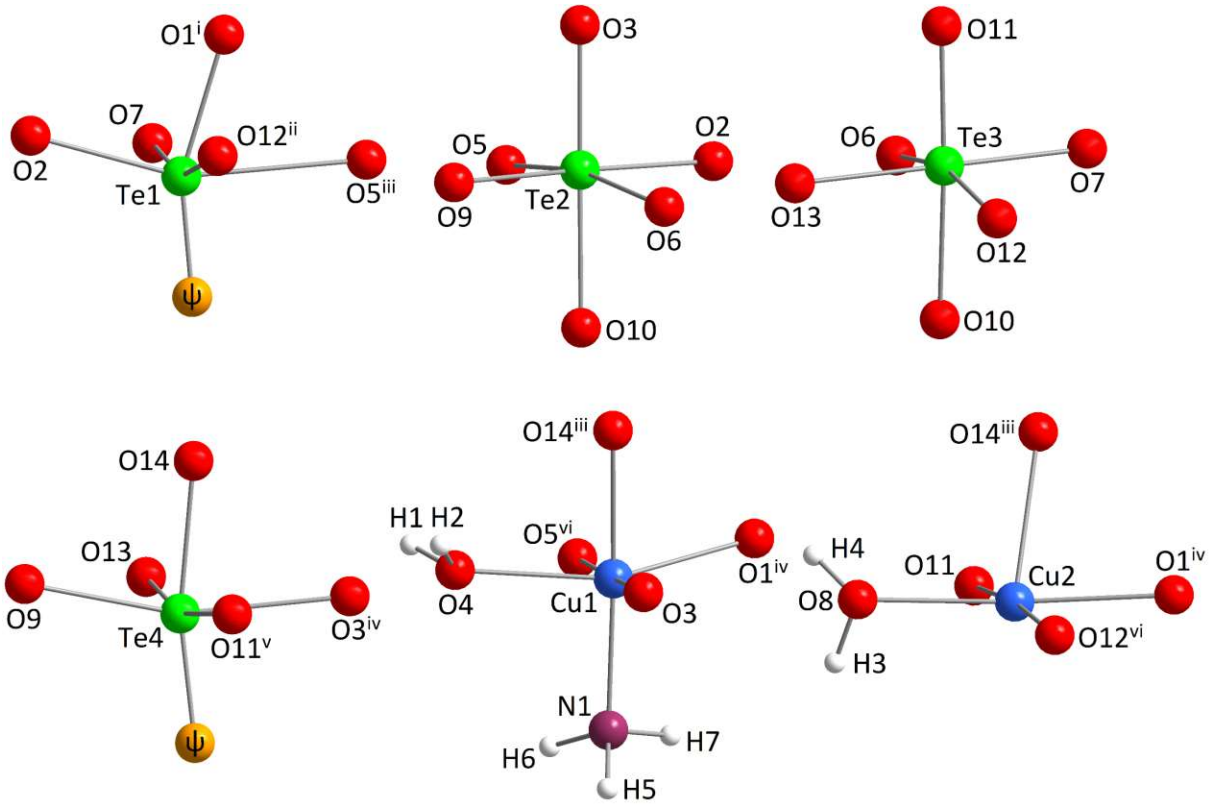

Figure 23. Atomic environments of the Te and Cu atoms in the crystal structure of $Cu_2Te^{IV}_2Te^{VI}_2O_{12}(NH_3)(H_2O)_2$.

The $^{2}_{\infty}[Te_4O_{12}]$ layers are interconnected by the coordination polyhedra of the two Cu^{II} atoms, which have CNs of 5 (Cu2) and 6 (Cu1). While four of the oxygen contacts of each Cu position are shared with the Te–O-layers and exhibit a saturated BVS slightly above 2.00 v.u., the other three oxygen sites just have one Cu^{II} atom at a distance slightly below 2 Å as their only notable contact (Table 6). At first, it was assumed that all three of these positions are occupied by water molecules. However, one of the three sites exhibited a significantly larger displacement parameter and when the s.o.f. was refined freely, resulted in a value of 0.65(3). Given the large amount of NH_3 present in the synthesis, an N atom was placed at the respective position instead, which led to a displacement parameter similar to the other oxygen atoms. The hydrogen atoms belonging to the assumed NH_3 and H_2O molecules (N1, O4, O8) were discernible from difference-Fourier maps, and reasonable positions concerning hydrogen bonds were derived. The bond lengths of the O—H and N—H contacts had to be restrained using the DFIX command.

The $[Cu1O_4(NH_3)(H_2O)]$ polyhedron has the shape of a distorted octahedron, while the $[Cu2O_4(H_2O)]$ unit has a square-pyramidal shape (τ_5 = 0.040), missing one ligand for (pseudo-)octahedral coordination. If a sixth contact (being a H_2O or even a NH_3 molecule) would be located at a distance of 2.0–2.5 Å from Cu2, completing the octahedral coordination, this would result in a rather close distance of less than 2.5 Å to the N1 atom of the NH_3 molecule ligating the Cu1 atom. Hence, steric restrictions hinder both Cu^{II} atoms to achieve sixfold coordination. If not for this steric requirement, the crystal structure of $Cu_2Te^{IV}_2Te^{VI}_2O_{12}(NH_3)(H_2O)_2$ would have inversion symmetry, as all sites except for the H_2O/NH_3 molecules follow the (pseudo-) space group $P\bar{1}$.

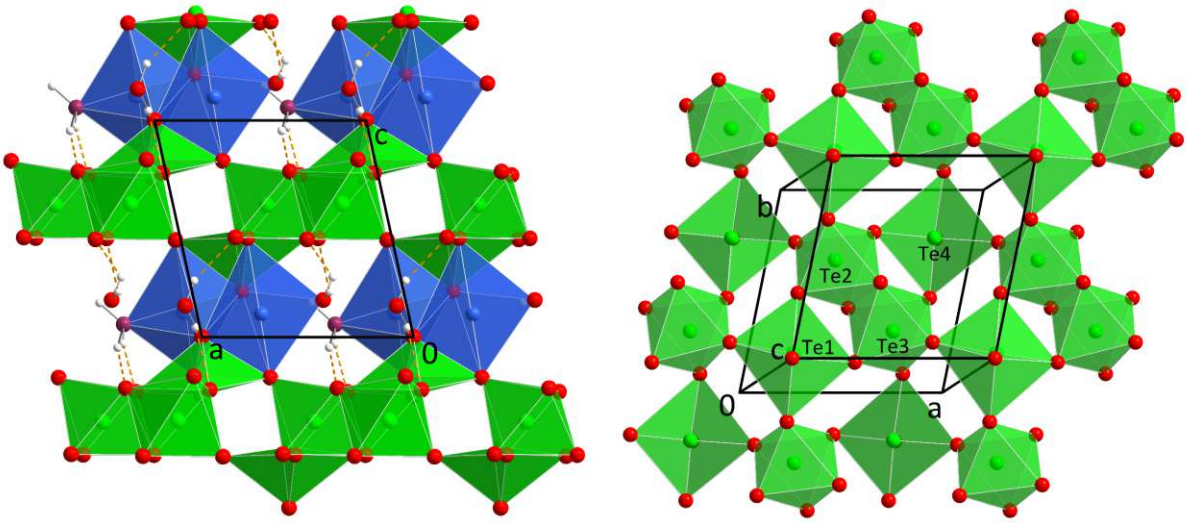

Figure 24. The crystal structure of $Cu_2Te^{IV}_2Te^{VI}_2O_{12}(NH_3)(H_2O)_2$ in a projection along $[0\bar{1}0]$ (left) and showing a (001) plane at $z \approx 0.6$ (right).

Table 6. Selected interatomic distances in the crystal structure of $Cu_2Te^{IV}_2Te^{VI}_2O_{12}(NH_3)(H_2O)_2$.

	d / Å		*d* / Å
Te1—O1^{i}	1.850(8)	Te4—O14	1.915(8)
Te1—O2	2.030(13)	Te4—O13	2.025(10)
Te1—O7	2.066(8)	Te4—O9	2.038(8)
Te1—O12^{ii}	2.235(7)	Te4—O3^{iv}	2.167(7)
Te1—O5^{iii}	2.370(7)	Te4—O11^{v}	2.269(7)
Te2—O3	1.837(7)	Cu1—N1	1.919(15)
Te2—O2	1.923(14)	Cu1—O14^{ii}	1.943(8)
Te2—O9	1.954(8)	Cu1—O4	2.011(7)
Te2—O5	1.968(7)	Cu1—O1^{v}	2.055(9)
Te2—O10	1.973(14)	Cu1—O5^{vi}	2.058(8)
Te2—O6	1.973(11)	Cu1—O3	2.295(7)
Te3—O11	1.787(7)	Cu2—O8	1.999(12)
Te3—O7	1.896(8)	Cu2—O1^{iv}	2.000(9)
Te3—O13	1.942(11)	Cu2—O12^{vi}	2.021(8)
Te3—O12	1.955(7)	Cu2—O14^{iii}	2.205(9)
Te3—O6	1.979(12)	Cu2—O11	2.435(8)
Te3—O10	1.989(13)		
O4—H1*	0.91(14)	O4—H1···O2	2.899(17)
O4—H2*	0.87(9)	O4—H2···O13^{ii}	2.663(11)
O8—H3*	0.90(9)	O8—H3···O6	2.908(19)
O8—H4*	0.90(11)	O8—H4···O9^{iii}	2.869(13)
N1—H5*	1.02(13)	N1—H5···O9	3.001(19)
N1—H6*	1.01(12)	N1—H6···O10	2.85(2)
N1—H7*	1.02(9)	N1—H7···O7^{vii}	2.999(14)

* Value constrained to 0.89 Å (O—H) or 1.01 Å (N—H) with DFIX command.

Symmetry codes: (i) *x*, *y*, 1+*z*; (ii) −1+*x*, *y*, *z*; (iii) *x*, −1+*y*, *z*; (iv) 1+*x*, *y*, *z*; (v) *x*, 1+*y*, *z*; (vi) *x*, *y*, −1+*z*; (vii) *x*, 1+*y*, −1+*z*.

3.5 Phosphates

3.5.1 Hydrothermal experiments

First experiments were conducted with $NiCO_3(Ni(OH)_2)_2(H_2O)_4$, TeO_2 and H_3PO_4 in molar ratios of 1:3:3 (H62−64). Without the addition of any base (H62), the novel phase $Ni_3Te_2O_2(PO_4)_2(OH)_4$ (3.5.2), was obtained besides α-TeO_2 (Stehlik & Balak, 1948). With additional NH_3 (H63), some unassignable reflections were observed in the PXRD measurement, next to those of $Ni(OH)_2$.

Systematic studies of metal cations Mn^{II}, Cu^{II}, Fe^{III}, Zn^{II}, Cr^{III}, Ni^{II}, Cd^{II} and Pb^{II} were conducted with the respective metal carbonates or nitrates, TeO_2, H_3PO_4 and two different alkalinity levels using NH_3 as the base. The more acidic series H77−H84 yielded various metal phosphate phases, as well as the educt TeO_2 for most of the batches. Sample H82 (Ni^{II}) mainly consisted of $Ni_3Te_2O_2(PO_4)_2(OH)_4$ (3.5.2) with only a minor percentage of α-TeO_2 as a by-product. In H83 (Cd^{II}), a novel triplite-type cadmium phosphate phase with a composition of $Cd_2(PO_4)(OH)$ (6.6.1) was found besides α-TeO_2. When it was tried to resynthesize $Cd_2(PO_4)(OH)$ from $Cd(NO_3)_2(H_2O)_6$, H_3PO_4 and KOH (H130), a different novel alkaline cadmium phosphate, $Cd_5(PO_4)_2(OH)_4$ (6.6.2), was obtained instead.

The second series, including higher concentrations of NH_3 (H92−H99), did not yield any noteworthy phases, just as the third series, starting from metal oxides, TeO_2 and K_3PO_4 (H288−H293) (Table 67).

3.5.2 The crystal structure of $Ni_3Te_2O_2(PO_4)_2(OH)_4$

$Ni_3Te_2O_2(PO_4)_2(OH)_4$ occurred as light-green block-shaped crystals and was obtained in the highest yield, besides side-product α-TeO_2, from a hydrothermal reaction between $NiCO_3(Ni(OH)_2)_2(H_2O)_4$, TeO_2 and H_3PO_4 in molar ratios of 2:4:5 (H82). It crystallizes isotypically with the Co-compound $Co_3Te_2O_2(PO_4)_2(OH)_4$ (Zimmermann et al., 2011) in the monoclinic space group *C*2/*m* (*a* = 19.241(7) Å, *b* = 5.943(2) Å, *c* = 4.7808(18) Å, *β* = 104.094(8)°, *V* = 530.3(3) Å^3).

Five oxygen atoms, two of which belong to a hydroxide group, coordinate the Te^{IV} atoms. The resulting $[TeO_3(OH)_2]$ units have a square-pyramidal shape, with the closest oxygen contact forming the apex of the pyramid. The non-bonding $5s^2$ electron pair ψ of the Te^{IV} atoms corresponds to the opposite apex of the $[\psi TeO_5]$ octahedron. The PO_4^{3-} anion has a regular tetrahedral shape with bond lengths in a range of 1.534(3)−1.5449(18) Å.

The two independent Ni^{II} atoms are both coordinated by six oxygen atoms in an octahedral shape. The $[Ni1O_6]$ octahedra form $^1_\infty[Ni1O_{4/2}O_{2/1}]$ chains by edge-sharing, which propagate in the [010] direction. Four of the six oxygen positions bound to the Ni2 site are occupied by hydroxide groups. The $[Ni2O_2(OH)_4]$ units are isolated from other Ni−O-polyhedra. The hydroxide groups form medium-strong (*d* O—H···O = 2.813(3) Å) hydrogen bonds towards the oxygen atoms of neighboring $[Ni2O_2(OH)_4]$ units (Figure 25).

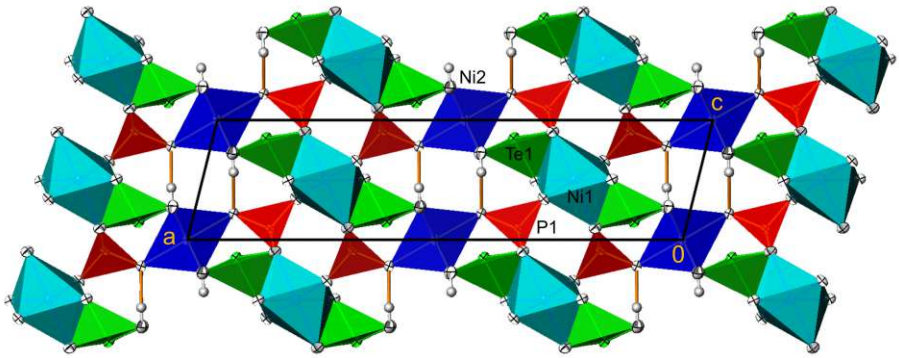

Figure 25. The crystal structure of $Ni_3Te_2O_2(PO_4)_2(OH)_4$ viewed along $[0\bar{1}0]$. Te atoms are drawn green, Ni atoms dark and light blue, P atoms red, O atoms white and H atoms grey. Hydrogen bonds are drawn orange. Structure representation was generated with ATOMS (Dowty, 2006).

For more information on the crystal structure of $Ni_3Te_2O_2(PO_4)_2(OH)_4$, see:

Eder, F. & Weil, M. (2020a). $Ni_3Te_2O_2(PO_4)_2(OH)_4$, an open-framework structure isotypic with $Co_3Te_2O_2(PO_4)_2(OH)_4$. *Acta Cryst*. E**76**, 625−628.

3.6 Borates

3.6.1 Hydrothermal experiments

An exploratory series of hydrothermal experiments (H147–H154) based on eight combinations of copper(II) oxide or nitrate, TeO_2 or H_6TeO_6, with or without KOH was conducted. For all combinations except for $CuO/H_6TeO_6/H_3BO_3/KOH$ (2:1:1:6; H153), the reaction products could be identified as literature phases from the PXRD patterns. In the washed residue of H153, only CuO as a minor side product could be identified (Figure 26). Unfortunately, no single-crystalline material to determine the structure of the major phase was available.

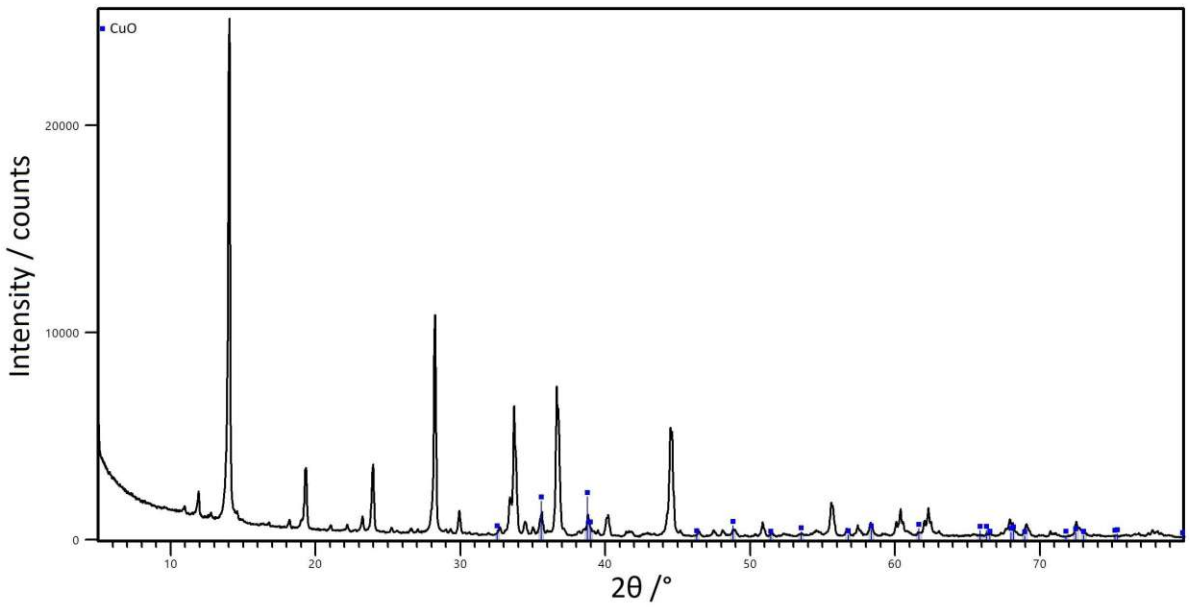

Figure 26. PXRD pattern of hydrothermal experiment H153.

3.6.2 Solid-state reactions

A solid-state reaction of Fe_2O_3, H_3BO_3 and H_6TeO_6 at 800 °C (S18) yielded Fe_2TeO_6 (Kunnmann et al., 1968) as the only crystalline product. Solid-state reactions based on the oxides of Mn^{II}, Cu^{II}, Fe^{III}, Zn^{II}, Cr^{III}, Ni^{II}, Cd^{II} and Pb^{II}, TeO_2 (S58–S65) or TeO_3 (S66–S73) and B_2O_3 were conducted in small, sealed aluminum crucibles. In the Te^{IV}-based experiments (S58–S65), no combined borate-oxidotellurate compound could be identified, although the powder diffraction patterns of samples S60 (Fe^{III}) and S63 (Ni^{II}) contained numerous non-assignable reflections. Material suitable for single-crystal diffraction experiments was not present.

Starting with hexavalent Te in form of TeO_3 did not lead to any oxidotellurate(VI) phases, but only oxidotellurates(IV). All introduced metal species were present in their original oxidation state in the reaction products. Apparently, TeO_3 does not react under these conditions while maintaining its oxidation state and releases oxygen under formation of TeO_2. The PXRD patterns of S66–S73 could all be explained by literature phases (Table 66).

3.7 Hydroxides

Incorporation of hydroxide anions into the crystal structure of oxidotellurates was not forced systematically. However, since the majority of the hydrothermal syntheses in this work were performed under partially strong alkaline conditions, basic oxidotellurate phases were a common by-product. Novel oxidotellurate phases modified by both an alkali metal cation and hydroxide groups will be presented in section 4. Additionally, four new transition metal oxidotellurate(IV) hydroxides, all with a composition of $M_x(TeO_3)_{x-1}(OH)_2$ (x = 2, 3, 15) were found.

3.7.1 $Mn_{15}(TeO_3)_{14}(OH)_2$

$Mn_{15}(TeO_3)_{14}(OH)_2$ was initially discovered in the products of hydrothermal experiment H253 (MnO, TeO_2 and K_2CO_3 in molar ratios of 2:3:10) besides starting material MnO. It crystallizes as large, colorless crystals with a nearly isotropic, block-like shape. Experiments H277−H279, H294 and H295 were aimed at the re-synthesis of $Mn_{15}(TeO_3)_{14}(OH)_2$. The highest yield in synthesizing $Mn_{15}(TeO_3)_{14}(OH)_2$ with only minor traces of Mn_3O_4 present could be achieved from a 6:5 mixture of $MnCO_3$ and K_2TeO_3 (H294). Repeating the reaction with Na_2TeO_3 instead of the potassium compound (H295), yielded $Mn_6Te_5O_{16}$ (5.1.6) as a significant by-product.

$Mn_{15}(TeO_3)_{14}(OH)_2$ crystallizes in space group $R\bar{3}$ (a = 10.027(3) Å, c = 27.977(7) Å, V = 3505(2) Å^3) and is isotypic with $Co_{15}(TeO_3)_{14}F_2$ (Lü et al., 2020). Its asymmetric unit contains three Te, three Mn, eight O and one H atom. The Te^{IV} atoms are all coordinated by three oxygen atoms and form trigonal [TeO_3] pyramids, which are isolated from each other. The Mn^{II} atoms are coordinated by five (Mn2) or six (Mn1, Mn3) oxygen atoms, resulting in a distorted square-pyramidal shape (τ_5 = 0.384) for the [$Mn2O_5$] unit and distorted octahedral environments for [$Mn1O_6$] and [$Mn3O_5(OH)$]. By edge-sharing, the coordination polyhedra of Mn2 and Mn3 form [$Mn_4O_{12}(OH)_4$] units, which are connected by corner-sharing with the [$Mn1O_6$] groups, leading to a tri-periodic Mn−O-framework (Figure 27). The hydroxide group is connected to three Mn3 atoms and both O and H are located at positions with 3. site symmetry. No acceptor atom for hydrogen-bonding could be assigned, although it cannot be ruled out that the OH group is actually tilted away from the threefold axis towards possible acceptor oxygen atoms.

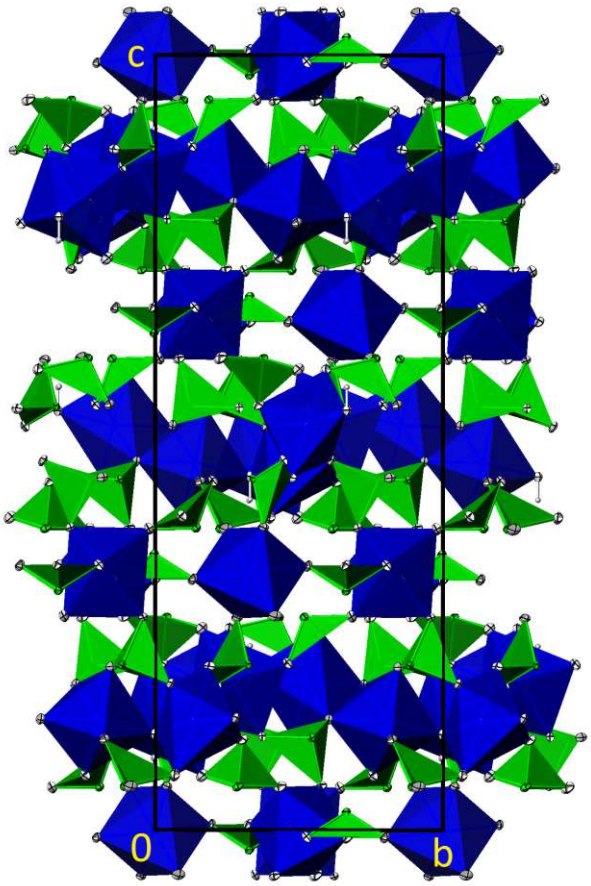

Figure 27. The crystal structure of $Mn_{15}(TeO_3)_{14}(OH)_2$ viewed along [$\bar{1}$00]. Structure representation was generated with ATOMS (Dowty, 2006).

3.7.2 "$Mn_3(TeO_3)_2(OH)_2$"

Single crystals of "$Mn_3(TeO_3)_2(OH)_2$" were initially discovered from experiment H215 ($MnSO_4(H_2O)$, TeO_2, K_2CO_3 and KOH in molar ratios of 1:1:2:4), although the phase has already been revealed by PXRD measurements of the products from other batches (Table 7). Single-crystal diffraction experiments were performed on crystals from experiments H181, H379, H380, H381 and H383 as well.

The crystal structure of "$Mn_3(TeO_3)_2(OH)_2$" (*P*6_3*mc*, *a* = 13.410(4) Å, *c* = 5.1393(17) Å, *V* = 800.3(6) Å^3) is isotypic to the corresponding Co- and Ni-compounds (Perez et al., 1976), and comprises trigonal-pyramidal [TeO_3] and octahedral [$MnO_4(OH)_2$] units. While the [TeO_3] units are isolated from each other, the [$MnO_4(OH)_2$] groups are sharing edges and corners to form a tri-periodic framework. Together with the Te^{IV} atoms, this framework has an overall composition of $[Mn_3Te_2O_6(OH)_{1.5}]^{0.5+}$ and forms large, hexagonal channels extending parallel to [001] (Figure 28). The Te^{IV} lone pairs are directed towards the center of the channels, where the remaining 0.5 OH^- anions p.f.u. are situated.

This remaining hydroxide anion, corresponding to the O5 site in Figure 28, exhibits a significantly enlarged displacement parameter. Furthermore, weak residual electronic density peaks are visible inside the channels besides the central O5 position at distances of *ca*. 1–1.2 Å from the channel center. If only hydroxide anions were present inside the channels, they would form a linear chain with rather close OH···OH distances of 2.567 Å. These difficulties were resolved when it was found that foreign anions could also be incorporated into the channel under partial substitution of the OH^- anions (3.7.3).

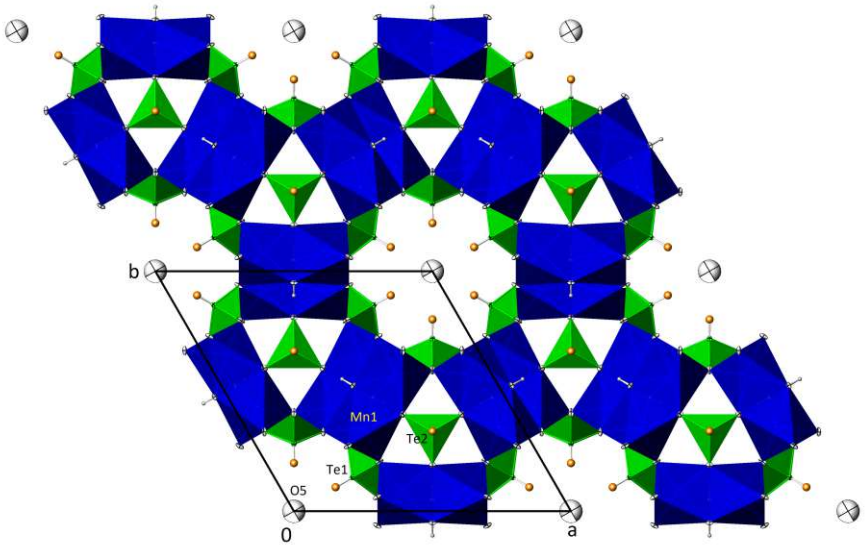

Figure 28. The crystal structure of $Mn_3(TeO_3)_2(OH)_2$ viewed along [00$\bar{1}$]. Oxygen atoms are drawn in white instead of red. Structure representation was generated with ATOMS (Dowty, 2006).

More detailed information on the crystal structures of $Mn_{15}(TeO_3)_{14}(OH)_2$ and "$Mn_3(TeO_3)_2(OH)_2$" can be found in:

Eder, F. & Weil, M. (2022b). Phase formation studies and crystal structure refinements in the $Mn^{II}/Te^{IV}/O/(H)$ system. *Z. Anorg. Allg. Chem*. **648**, 24.

3.7.3 Foreign anion inclusions into "$M_3(TeO_3)_2(OH)_2$" (*M* = Co, Ni, Mn, Mg) phases

The potential incorporation of anions other than OH^- into the channels of "$M_3(TeO_3)_2(OH)_2$" (*M* = Co, Ni, Mn, Mg) phases was systematically investigated with numerous hydrothermal experiments (H214–H220 (Mn only) and H355–H387). Most experiments were conducted for "$Mn_3(TeO_3)_2(OH)_2$", while some attention was paid to "$Co_3(TeO_3)_2(OH)_2$" and "$Ni_3(TeO_3)_2(OH)_2$" in order to compare them with the literature phases (Perez et al., 1976). Additionally, few experiments were performed for "$Mg_3(TeO_3)_2(OH)_2$" as well, as the given phase had been obtained as an unexpected product in a hydrothermal reaction several years ago.

For the respective batches, *M* salts with various counter-anions (SO_4^{2-}, NO_3^-, CO_3^{2-}, Cl^-, Br^-, $C_2O_4^{2-}$, CH_3COO^-, O^{2-}) were introduced with TeO_2 together with a base *B* (KOH, K_2CO_3 or NaOH) in different *M*:TeO_2:*B* ratios. Experimental details on the performed experiments can be found in Table 67. Lattice parameters, as obtained from Rietveld refinements of PXRD measurements, of all "$M_3(TeO_3)_2(OH)_2$" phases obtained in these experiments are collated in Table 7.

3.7.3.1 "$Ni_3(TeO_3)_2(OH)_2$"

For the obtained "$Ni_3(TeO_3)_2(OH)_2$" phases, the lattice parameters have the same size or are smaller than the ones reported by Perez et al. (1976). The counter-anion seems to have a smaller influence on the obtained lattice-parameters than the employed pH-conditions. The resulting reaction products were very fine needles, too small for single-crystal diffraction experiments.

In SEM-EDS measurements of products from experiments H357 (SO_4^{2-}) and H358 (NO_3^-), small needle-shaped crystals of "$Ni_3(TeO_3)_2(OH)_2$" could be identified based on the Ni:Te ratio of 3:2. For these crystals, an S content of 1.1(2)% on average (based on 4 data points) was detected for sample H357, while no S was found for those originating from H358.

3.7.3.2 "$Mg_3(TeO_3)_2(OH)_2$"

A significant difference between the unit-cell volumes of experiments H359 and H365 (SO_4^{2-} and KOH), and that of experiment H376 (NO_3^- and K_2CO_3) is visible. The first two are in close correspondence with the older single-crystalline sample, which was synthesized from a 1:1:1:1 ratio of NiO, $Fe(NO_3)_3(H_2O)_9$, $Mg(OH)_2$ and TeO_2 under hydrothermal conditions (Eder et al., 2022b). Like for "$Ni_3(TeO_3)_2(OH)_2$", the synthesis from a carbonate solution resulted in smaller lattice parameters than the reactions in a hydroxidic environment.

3.7.3.3 "$Mn_3(TeO_3)_2(OH)_2$"

The variable influence of foreign anions being present during synthesis could be tracked by various analytical methods. The unit-cell volumes of most "$Mn_3(TeO_3)_2(OH)_2$" samples are very similar, only the sulfate-containing samples exhibit increased lattice parameters. However, this enlargement of the unit-cell metrics is only pronounced, if no other non-hydroxide anions (mostly in the form of CO_3^{2-} ions) are present in the solution.

Using SEM-EDS, point analyses on "$Mn_3(TeO_3)_2(OH)_2$" crystals (identified by the correct Mn:Te ratio and their characteristic form of elongated hexagonal prisms) allowed to trace the presence of several of the foreign anions. For sulfate-based sample H379, an S content of 1.5(3)% (based on three data points) was determined, while for the sulfate- and carbonate-based H215 no S-signal could be detected. The halogenide anions Cl^- and Br^- in experiments H380 and H381 could clearly be confirmed with mass contents of 2.78(11)% (four data points) and 3.1(2)% (five data points), respectively.

With the help of Raman-spectroscopy, the hypothetical presence of CO_3^{2-} anions inside the channels of sample H383 is supported by the presence of additional bands at 1080 and 1040 cm^{-1}, which are not present for the Cl^- and Br^- based phases from H380 and H381.

Table 7. Refined lattice parameters of various "$M_3(TeO_3)_2(OH)_2$" phases. Literature phases are written in blue.

Batch	*M*	Anion	Base	*a* / Å	*c* / Å	V / Å³
H17	Co	NO_3^-	NH_3	13.0724(13)	5.0607(6)	748.9
H121	Co	NO_3^-, AsO_4^{3-}	KOH	13.0197(3)	5.06199(15)	743.1
H355	Co	SO_4^{2-}	KOH	13.1146(7)	5.0475(3)	751.8
H356	Co	NO_3^-	KOH	13.1126(7)	5.0452(3)	751.3
H371	Co	CO_3^{2-}	KOH	13.003(2)	5.0334(8)	737.0
H418	Co	CO_3^{2-}	KOH	12.998(2)	5.0355(9)	736.8
H419	Co	CO_3^{2-}	KOH	13.0178(3)	5.0329(2)	738.6
H430	Co	CO_3^{2-}	Na_2CO_3	13.0475(8)	5.0397(4)	743.0
Perez et al. (1976)	Co			13.034(6)	5.016(3)	738.0
Poupon et al. (2019)	Co	NO_3^-	NaOH	13.164(1)	5.0321(6)	755.2
H6	Ni	NO_3^-	KOH	12.99253(11)	4.98076(5)	728.1
H22	Ni	NO_3^-	NH_3	12.9827(2)	4.97438(10)	726.1
H82	Ni	CO_3^{2-}/OH^-	H_3PO_4	12.9930(3)	4.97639(15)	727.6
H120	Ni	NO_3^-	KOH	12.9888(3)	4.97333(15)	726.6
H357	Ni	SO_4^{2-}	KOH	12.9419(3)	4.95898(12)	719.3
H358	Ni	NO_3^-	KOH	12.9250(4)	4.9521(2)	716.4
H367	Ni	CH_3COO^-	KOH	12.9200(2)	4.95694(8)	716.6
H373	Ni	SO_4^{2-}	K_2CO_3	12.8384(6)	4.9829(3)	711.3
H374	Ni	NO_3^-	K_2CO_3	12.8250(5)	4.9759(2)	708.8
Perez et al. (1976)	Ni			12.993(6)	4.958(3)	724.9
H59	Mn	CO_3^{2-}	KOH	13.4282(5)	5.1693(2)	807.2
H61	Mn	CO_3^{2-}	KOH/K_2CO_3	13.42463(14)	5.16762(6)	806.5
H180	Mn	CO_3^{2-}	KOH	13.4319(8)	5.1727(3)	808.2
H181	Mn	CO_3^{2-}	KOH	13.42725(16)	5.16573(7)	806.6
H183	Mn	CO_3^{2-}	KOH/K_2CO_3	13.4320(5)	5.1658(2)	807.1
H214	Mn	CO_3^{2-}	KOH/K_2CO_3	13.4262(2)	5.16696(10)	806.6
H215	Mn	SO_4^{2-}	KOH/K_2CO_3	13.4273(3)	5.16877(10)	807.0
H216	Mn	CH_3COO^-	KOH/K_2CO_3	13.4318(3)	5.16633(11)	807.2
H218	Mn	SO_4^{2-}	KOH	13.4780(2)	5.16843(12)	813.1
H219	Mn	CH_3COO^-	KOH	13.4402(4)	5.16507(13)	808.0
H253	Mn	O^{2-}	K_2CO_3	13.4109(6)	5.1635(3)	804.2
H361	Mn	SO_4^{2-}	KOH/K_2CO_3	13.4155(6)	5.1737(3)	806.4
H362	Mn	Cl^-	KOH/K_2CO_3	13.4272(5)	5.1654(2)	806.5
H377	Mn	CO_3^{2-}	KOH	13.4222(10)	5.1621(5)	805.4
H378	Mn	CH_3COO^-	NaOH	13.4344(7)	5.1762(3)	809.1
H379	Mn	SO_4^{2-}	NaOH	13.4903(4)	5.1673(2)	814.4
H380	Mn	Cl^-	NaOH	13.4206(2)	5.17517(8)	807.2
H381	Mn	Br^-	NaOH	13.4383(2)	5.17202(8)	808.9
H383	Mn	CO_3^{2-}	NaOH	13.4171(3)	5.16516(11)	805.3
H359	Mg	SO_4^{2-}	KOH	13.0838(5)	5.0450(3)	747.9
H365	Mg	SO_4^{2-}	KOH	13.0763(5)	5.0542(2)	748.4
H376	Mg	NO_3^-	K_2CO_3	12.9424(11)	5.0544(6)	733.2

In single-crystal diffraction experiments of "$Mn_3(TeO_3)_2(OH)_2$" crystals originating from experiments H181, H215, H379, H380, H381 and H383, pronounced differences inside the channels were visible in the refinements. For the Cl^- and Br^- based samples H380 and H381, the partial substitution of OH^- by halogenide anions was visible from a significant increase in (residual) electronic density at the channel center. For single crystals from the sulfate-based reaction H379, the SO_4^{2-} anions could be localized inside the hexagonal channels. They show occupational disorder with the OH^- anions and are furthermore disordered by the threefold rotation axis in the center of the channels (Figure 29).

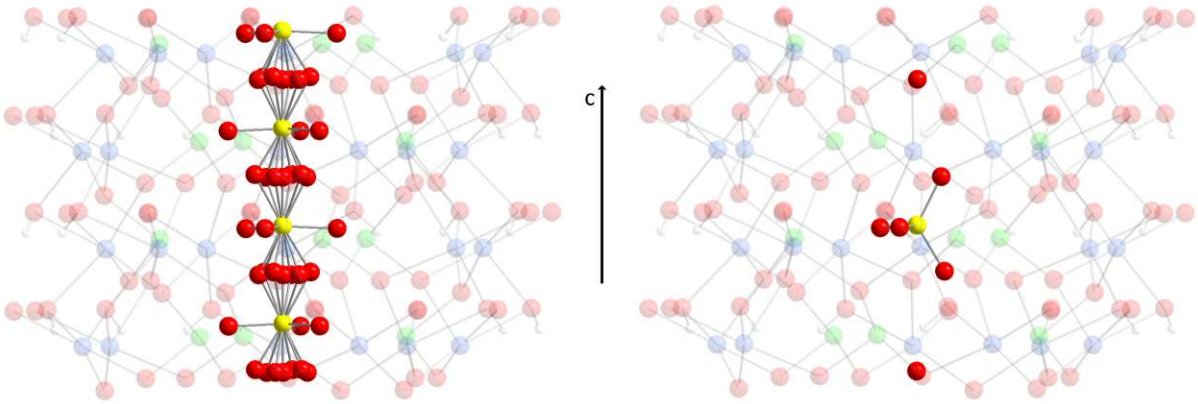

Figure 29. The crystal structure of "$Mn_3(TeO_3)_2(OH)_2$" containing additional SO_4^{2-} in the channels (H381). Framework constituents are drawn transparent. All possible atomic positions inside the channels are drawn on the left, while on the right, one possible distribution of channel contents is shown. Sulfur atoms are drawn as yellow spheres.

3.7.3.4 "$Co_3(TeO_3)_2(OH)_2$"

The crystal structures of previously reported $Co_3(TeO_3)_2(OH)_2$ (Perez et al., 1976) and the hydrated $Co_3(TeO_3)_2(OH)_2(H_2O)_{0.43}$ (Poupon et al., 2019) differ by the size of their unit-cell, in particular with respect to *a*. The increase in lattice parameters is caused by the presence of additional crystal water in the large channels, which run through the crystal structure along [001]. The lattice parameters of "$Co_3(TeO_3)_2(OH)_2$" phases obtained from experiments in this work show a variance of values between those of the two literature phases. The increase of the size of the unit-cells from H355 (based on $CoSO_4(H_2O)_7$) and H356 (based on $Co(NO_3)_2(H_2O)_6$) does not originate from additional crystal water in the channels, as the lattice parameters do not change significantly after tempering the samples at 210 °C for one week (Figure 30). During the investigation of $Co_3(TeO_3)_2(OH)_2(H_2O)_{0.43}$ (Poupon et al., 2019), the crystal water had been completely released at *ca*. 170 °C.

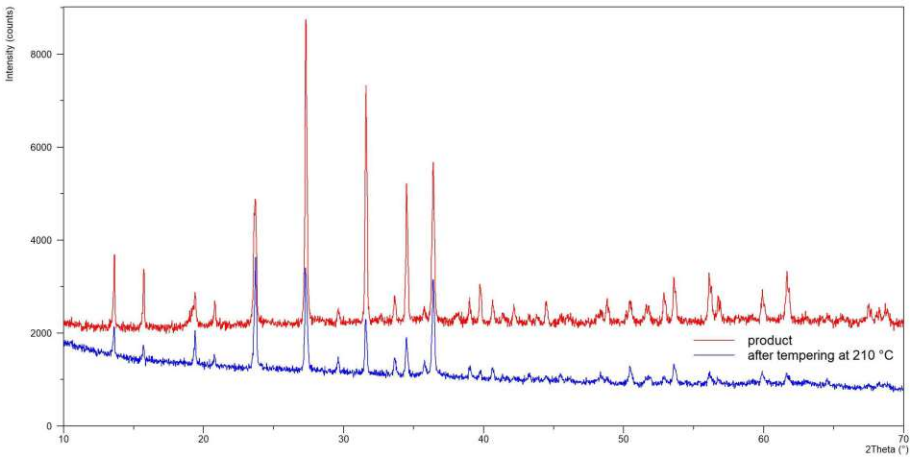

Figure 30. PXRD pattern of "$Co_3(TeO_3)_2(OH)_2$" from experiment H355 before (red) and after (blue) tempering at 210 °C for one week.

Crystals from both batches H355 and H356 were large enough to be investigated by single-crystal X-ray diffraction and Raman spectroscopy, besides SEM-EDS. EDS data revealed 0.9(2)% S on "$Co_3(TeO_3)_2(OH)_2$"-needles from H355 but no S for those from H356. The Raman spectra of the samples strongly differ in the region between 900 and 1100 cm^{-1} (Figure 31). For H355, a band at 971 cm^{-1} was

observed, which is in good agreement with the S—O stretching vibration of a sulfate anion, like in Na_2SO_4 (981 cm^{-1}; Weidlein et al., 1981). The crystals from H356 instead showed a sharp band with a Raman shift of 1044 cm^{-1}. This fits the N—O stretching vibration in various alkali-metal nitrates (ANO_3) of 1050 cm^{-1} (Weidlein et al., 1981). From single-crystal diffraction measurements, the presence of sulfate or nitrate anions was deduced from residual electronic density peaks in the difference-Fourier maps.

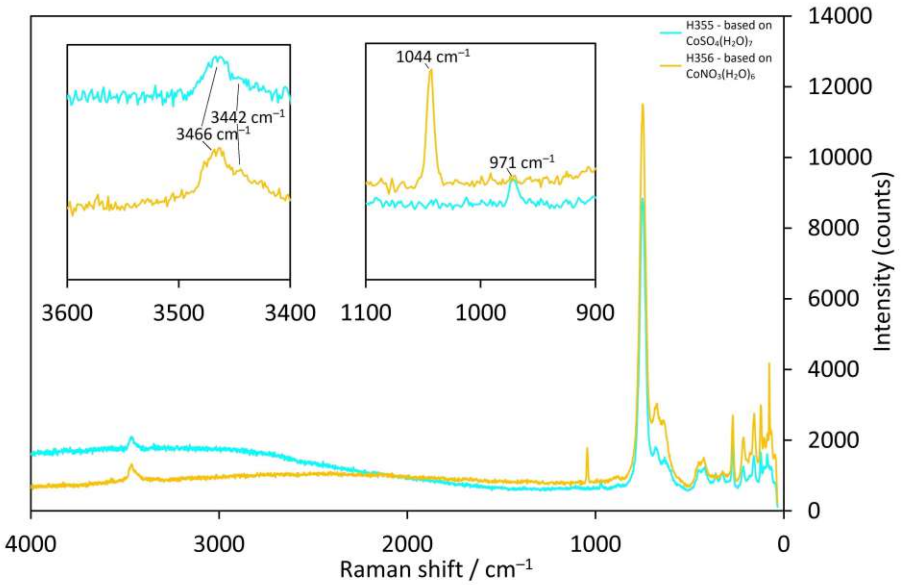

Figure 31. Comparison of the Raman-spectra of "$Co_3(TeO_3)_2(OH)_2$" samples originating from hydrothermal experiments H355 and H356.

A more detailed discussion on the foreign anion inclusion into "$M_3(TeO_3)_2(OH)_2$" phases can be found in:

Eder, F., Weil, M., Missen, O. P., Kolitsch, U. & Libowitzky, E. (2022b). The Family of $M^{II}_3(Te^{IV}O_3)_2(OH)_2$ (*M* = Mg, Mn, Co, Ni) Compounds—Prone to Inclusion of Foreign Components into Large Hexagonal Channels. *Crystals* **12**, 1380.

3.7.4 $Co_{15}(TeO_3)_{14}(OH)_2$

From hydrothermal experiments targeted at "$Co_3(TeO_3)_2(OH)_2$" phases (3.7.3.4), two different new basic cobalt(II) oxidotellurates(IV), $Co_2(TeO_3)(OH)_2$ (3.7.5) and $Co_{15}(TeO_3)_{14}(OH)_2$ were obtained. $Co_{15}(TeO_3)_{14}(OH)_2$ is isotypic with $Mn_{15}(TeO_3)_{14}(OH)_2$ (3.7.1) and $Co_{15}(TeO_3)_{14}F_2$ (Lü et al., 2020). It was obtained as a by-product in experiments H366 ($Co(C_2O_4)(H_2O)_2$:TeO_2:KOH = 3:2:9) and H371 ($CoCO_3$:TeO_2:KOH = 3:2:4). Just like $Mn_{15}(TeO_3)_{14}(OH)_2$, $Co_{15}(TeO_3)_{14}(OH)_2$ forms large cuboid crystals, which have an intense dark-blue color. As it is isotypic with $Mn_{15}(TeO_3)_{14}(OH)_2$ (3.7.1), the crystal structure of $Co_{15}(TeO_3)_{14}(OH)_2$ ($R\bar{3}$, a = 11.6453(2) Å, c = 27.3540(5) Å, V = 3212.57(12) Å^3) is not described again.

Small amounts of phase-pure $Co_{15}(TeO_3)_{14}(OH)_2$ were isolated by hand-picking the crystals, resulting in *ca*. 40 mg of product, for which several analyses were performed. From thermal analysis measurements (30–580 °C), $Co_{15}(TeO_3)_{14}(OH)_2$ does not exhibit any mass loss (TG) or phase transitions (DSC). Also, the IR-spectra of $Co_{15}(TeO_3)_{14}(OH)_2$ before and after thermal analysis look identical with one weak band at 3425 cm^{-1} corresponding to the stretching vibration of the hydroxide group (Figure 32). Magnetic measurements revealed some magnetic frustration, which was also observed in the isotypic $Co_{15}(TeO_3)_{14}F_2$ (Lü et al., 2020).

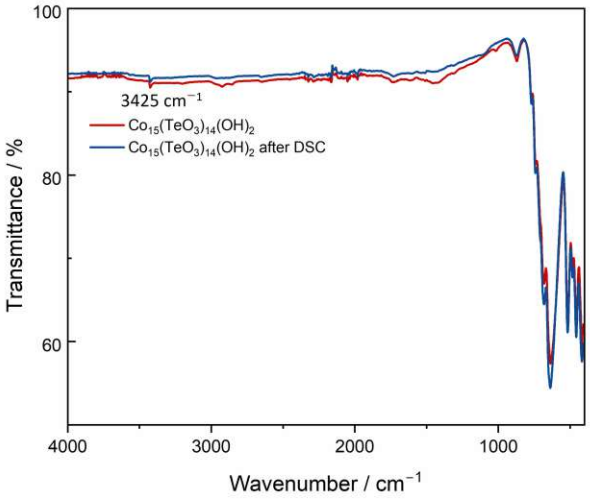

Figure 32. IR-spectra of $Co_{15}(TeO_3)_{14}(OH)_2$ before and after heating to 580 °C for DSC-measurement.

3.7.5 $Co_2(TeO_3)(OH)_2$

Synthesis

Phase-pure $Co_2(TeO_3)(OH)_2$ resulted from hydrothermal experiment H363 ($CoCO_3$, TeO_2 and KOH in ratios of 3:2:9), as revealed by PXRD. In order to produce sufficiently enough phase-pure material of both $Co_2(TeO_3)(OH)_2$ and $Co_{15}(TeO_3)_{14}(OH)_2$ for physical measurements, systematic experiments starting from $CoCO_3$, TeO_2 (ratios 3:2) and rising concentrations of KOH (H417–H422) were conducted. Without added KOH (H417), only $Co_2Te_3O_8$ (Feger et al., 1999) and the educts TeO_2 and $CoCO_3$ were found. Increasing the alkalinity of the solution led at first to the simultaneous appearance of "$Co_3(TeO_3)_2(OH)_2$" and $Co_{15}(TeO_3)_{14}(OH)_2$ (neither phase was generated as phase-pure) (H418–H419). At higher base concentrations, the more alkaline phase $Co_2(TeO_3)(OH)_2$ was the majority product besides $Co_{15}(TeO_3)_{14}(OH)_2$ (H420) and was obtained almost as a phase-pure product besides traces of $Co(OH)_2$ (Natta & Reina, 1926) in H421. At even higher concentrations of KOH, $Co(OH)_2$ was the main product. For phase-pure $Co_2(TeO_3)(OH)_2$, sample H421 was leached with diluted H_2SO_4 for an hour in order to dissolve the minor side product $Co(OH)_2$. Single crystals of $Co_2(TeO_3)(OH)_2$ appear in form of pink needles, which tend to grow in bunches and need to be separated before single-crystal X-ray diffraction measurements.

Crystal structure

$Co_2(TeO_3)(OH)_2$ crystallizes in the triclinic space group $P\bar{1}$ (a = 5.8898(5) Å, b = 5.9508(5) Å, c = 6.8168(5) Å, α = 101.539(2)°, β = 100.036(2)°, γ = 104.347(2)°, V = 220.40(3) Å^3) and its asymmetric unit comprises one Te, two Co, five O and two H atoms. The Te^{IV} atoms are coordinated by three oxygen atoms, forming isolated trigonal [TeO_3] pyramids. The Co sites exhibit coordination numbers of [5+1] (Co1) and 6 (Co2). The [$Co1O_2(OH)_4$] and [$Co2O_4(OH)_2$] polyhedra are connected to each other by edge-

and corner-sharing and form layers extending parallel to (001). These layers are interconnected by the [TeO_3] units. The two hydroxide groups exhibit a very different hydrogen-bonding behavior. The OH1 group does not have any suitable acceptor atom within an O···O radius of 3.5 Å, while OH2 forms a medium-strong hydrogen bond with a O—H···O distance of 2.730(2) Å.

Properties

The differences of the two OH groups in hydrogen-bonding are clearly visible in the IR-spectrum (Figure 33) and can be correlated by Libowitzky's (1999) empirical relation between stretching frequency and O—H···O distance. The sharp band at 3570 cm^{-1} belongs to the isolated OH group. Based on Libowitzky's formula, a maximum O—H···O distance of 3.5 Å corresponds to a frequency of 3592 cm^{-1}, which is similar to the observed band position. The broader band at 3202 cm^{-1} originates from the hydroxide group partaking in hydrogen-bonding. Applying Libowitzky's relation, a frequency of 3202 cm^{-1} belongs to an O—H···O distance of 2.705 Å, which is in good agreement with the value obtained from the refinement (2.730(2) Å).

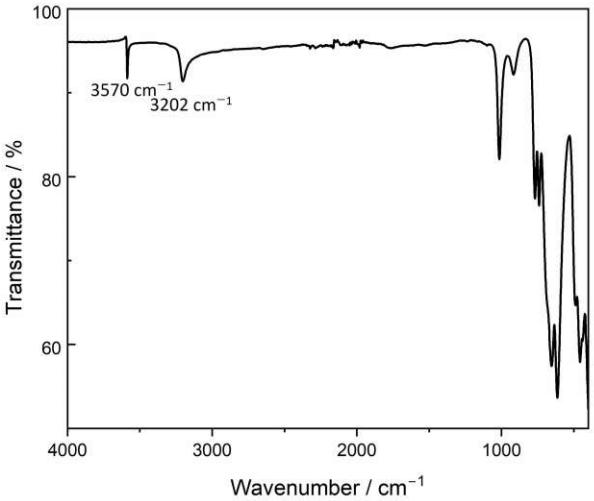

Figure 33. IR-spectrum of $Co_2(TeO_3)(OH)_2$.

$Co_2(TeO_3)(OH)_2$ does not share the thermal stability of $Co_{15}(TeO_3)_{14}(OH)_2$ and decomposes at temperatures above 450 °C accompanied with a mass loss of 5.6% as determined by TG measurement. This corresponds to the loss of one H_2O molecule per $Co_2(TeO_3)(OH)_2$ (theoretical value 5.5%). The thermal decomposition products after heating to 580 °C were identified as $Co_6Te_5O_{16}$ (Trömel & Scheller, 1976) and CoO (Natta & Reina, 1926) in mass fractions of *ca*. 3:1 by PXRD. This leads to an assumed reaction of:

$$5\ Co_2(TeO_3)(OH)_2 \rightarrow 1\ Co_6Te_5O_{16} + 4\ CoO + 5H_2O\uparrow$$

Magnetic measurements of $Co_2(TeO_3)(OH)_2$ indicate an antiferromagnetic transition from a paramagnetic phase at a temperature of −203 °C.

For more information on $Co_{15}(TeO_3)_{14}(OH)_2$ and $Co_2(TeO_3)(OH)_2$, see:

Eder, F., Weil, M., Pramanik, P. & Mathieu, R. (2023a). The Cobalt(II) Oxidotellurate(IV) Hydroxides $Co_2(TeO_3)(OH)_2$ and $Co_{15}(TeO_3)_{14}(OH)_2$. *Crystals* **13**, 176.

3.8 Chromates

While sulfate and selenate anions have been incorporated into metal oxidotellurate(IV) phases on numerous occasions, examples of the chromate anion CrO_4^{2-} are less frequent, despite the similar chemical behavior of chromate and sulfate anions. $Pb_2(CrO_4)(TeO_3)$ (Weil, 2017) is the sole example of a chromate-oxidotellurate phase. Three exploratory solid-state reactions (S45−S47) with PbO, CuO and CdO, respectively, and TeO_2 and CrO_3 were performed at 600 °C. For the Pb^{II}-based experiment S45, the literature phase $Pb_2(CrO_4)(TeO_3)$ was resynthesized. Otherwise, no new phases could be obtained.

4 Modification of transition metal oxidotellurates with foreign cations

4.1 Oxidotellurates(IV)

4.1.1 Lithium

4.1.1.1 Hydrothermal experiments

Two experimental series in a hydrothermal setup based on 2:3:10 mixtures of MO_x (M = Mn^{II}, Cu^{II}, Fe^{III}, Zn^{II}, Cr^{III}, Ni^{II}, Cd^{II}, Pb^{II}), TeO_2 and Li_2CO_3 were conducted. Experiments H302−H309 were performed as mild hydroflux reactions. Different to the other alkali metal carbonates, Li_2CO_3 has a much lower solubility in water. Therefore, it is not surprising that unreacted Li_2CO_3 was determined in almost every sample even after leaching the reaction products with water (Table 67). Another frequently observed side product was β-$Li_2Te_2O_5$ (Cachau-Herreillat et al., 1981). The only transition metal oxidotellurate(IV) phase incorporating lithium as secondary cation observed was $Li_3FeTe_4O_{11}$ (Lü et al., 2017) in batch H304. The Cu^{II}-based sample H303 exhibits several unassigned reflections with high intensities in its PXRD pattern. However, single crystals for structure determination were not present.

The hydrothermal experiments including the usual amount of water, H326−H333, yielded more phases of significance than the mild-hydroflux reactions. This is possibly caused by the low solubility of Li_2CO_3, which requires a high amount of water in order to achieve an incorporation of Li^+ cations into the oxidotellurate structures. In sample H327 (Cu^{II}), single crystals corresponding to two novel lithium copper(II) oxidotellurates(IV) with compositions of $Li_2Cu_2Te_3O_9$ (4.1.1.2) and $Li_2Cu_3Te_4O_{12}$ (4.1.1.3), could be isolated. Additionally, the Ni^{II}- and Cd^{II}-based samples H331 and H332 both exhibit at least one unknown phase in their respective PXRD patterns. Attempts to resynthesize $Li_2Cu_2Te_3O_9$ and $Li_2Cu_3Te_4O_{12}$ from stoichiometric mixtures (H401−H403) failed and only yielded $CuTe_2O_5$ (Hanke et al., 1973) and the starting materials CuO, α-TeO_2 and Li_2CO_3.

4.1.1.2 $Li_2Cu_2Te_3O_9$

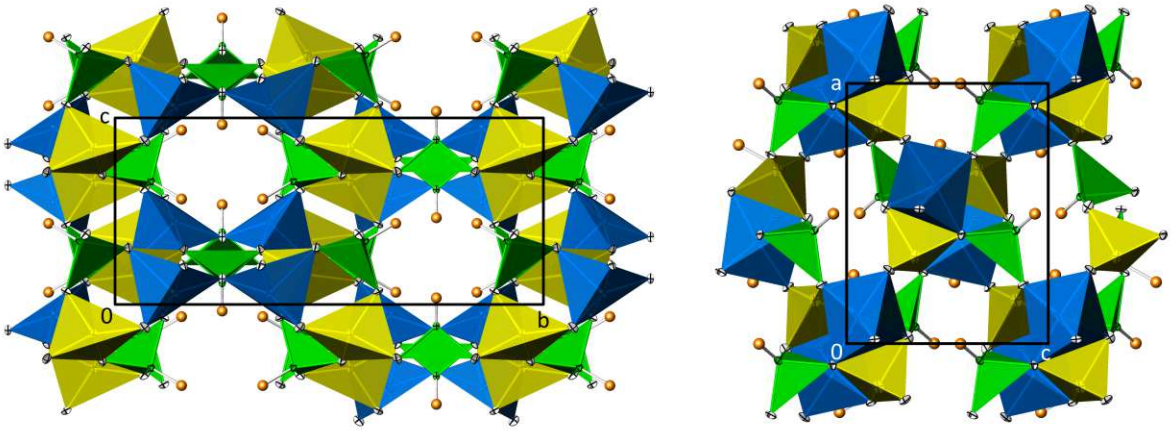

Figure 34. The crystal structure of $Li_2Cu_2Te_3O_9$ viewed along [$\bar{1}$00] (left) and [0$\bar{1}$0] (right). Non-bonding lone pairs ψ and [LiO_4] polyhedra are included in the representations. Oxygen atoms are drawn in white. Structure representations were generated with ATOMS (Dowty, 2006).

$Li_2Cu_2Te_3O_9$ forms intense green, block-shaped crystals and exhibits orthorhombic symmetry (*Pnma*, a = 8.81620(10) Å, b = 15.7707(3) Å, c = 6.84820(10) Å, V = 952.16(3) Å^3). Its asymmetric unit contains two Te, one Cu, one Li and five O atoms with one Te and one O position having *.m.* site symmetry. The Te sites and their adjacent oxygen atoms form [TeO_3] pyramids isolated from each other. The Cu^{II} atom exhibits a CN of [4+1] with oxygen distances of 1.8911(18)−1.9940(12) Å and 2.507(2) Å for the inner

and outer coordination sphere, respectively. The more distant O contact is located at the apex of the distorted square-pyramidal coordination polyhedron (τ_5 = 0.363), and two neighboring [CuO_5] pyramids form a [Cu_2O_9] dimer by sharing this apical O atom. Li^+ is coordinated by four oxygen atoms (d = 1.962(5)–1.999(5) Å) in a distorted tetrahedral shape (τ_4 = 0.679). A fifth, more distant oxygen contact (d = 2.745(6) Å) would connect the [LiO_{4+1}] coordination polyhedra to form zig-zag chains extending in the [100] direction. The crystal structure of $Li_2Cu_2Te_3O_9$ is perforated by large channels, into which the lone-pairs of the Te atoms are pointing (Figure 34).

4.1.1.3 $Li_2Cu_3Te_4O_{12}$

$Li_2Cu_3Te_4O_{12}$ was obtained as a minority phase besides $Li_2Cu_2Te_3O_9$ in hydrothermal experiment H327. Single crystals of $Li_2Cu_3Te_4O_{12}$ have a more anisotropic, shard-like appearance compared to the blocks of $Li_2Cu_2Te_3O_9$. The crystal structure of $Li_2Cu_3Te_4O_{12}$ is monoclinic ($P2_1/c$, a = 8.7726(12) Å, b = 7.4892(9) Å, c = 9.8846(12) Å, β = 114.926(3)°, V = 588.92(13) Å^3) and comprises two Te, two Cu, one Li and six O sites in its asymmetric unit.

The Cu1 site exhibits a coordination number of [4+1] with the inner O contacts at distances of 1.918(3)–1.966(3) Å and the more distant O atom at 2.469(2) Å. The Cu2 position is the only one with increased site symmetry ($\bar{1}$) and is coordinated by four oxygen atoms in a square-planar shape. The [$Cu1O_5$] pyramids (τ_5 = 0.091) form [$Cu1_2O_8$] dimers be edge-sharing, which subsequently are connected to each other by corner-sharing with a [$Cu2O_4$] square, leading to the formation of $^1_\infty$[$Cu_3O_{8/2}O_{6/1}$] chains extending in the [100] direction. These chains are cross-linked by [Li_2O_6] dimers, consisting of edge-sharing [LiO_4] tetrahedra (τ_4 = 0.855), in the [010] direction. The resulting $^2_\infty$[$Li_2Cu_3O_{20/2}O_{2/1}$] (001) layers are interconnected by trigonal-pyramidal [TeO_3] units to form the crystal structure (Figure 35).

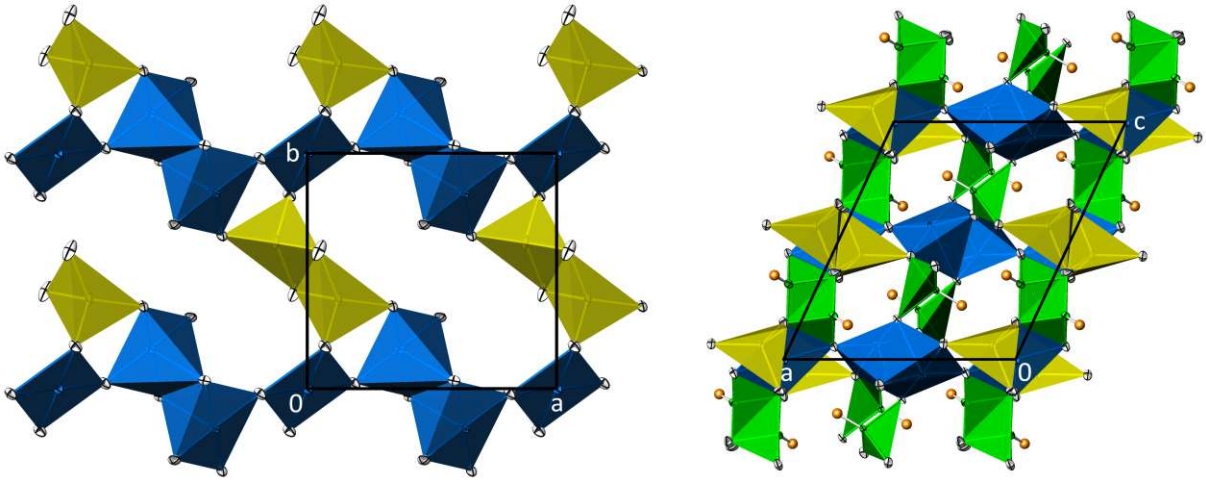

Figure 35. The crystal structure of $Li_2Cu_3Te_4O_{12}$. Left: (001) plane at $z \approx 0$; right: projection along [$0\bar{1}0$]. Color codes refer to Figure 34. Structure representations were generated with ATOMS (Dowty, 2006).

For more detailed information on the crystal structures of $Li_2Cu_2Te_3O_9$ and $Li_2Cu_3Te_4O_{12}$, see:

Eder, F. & Weil, M. (2022a). The alkali metal copper(II) oxidotellurates(IV) $Li_2Cu_2Te_3O_9$, $Li_2Cu_3Te_4O_{12}$, $Rb_2Cu_3Te_6O_{16}$ and $Cs_2Cu_3Te_6O_{16}$ – four new structure types. *Z. Anorg. Allg. Chem*. **648**, 23: e202200089.

4.1.2 Sodium

4.1.2.1 Hydrothermal experiments

Mild hydroflux reactions starting from 2:3:10 mixtures of MO_x (M = Mn^{II}, Cu^{II}, Fe^{III}, Zn^{II}, Cr^{III}, Ni^{II}, Cd^{II}, Pb^{II}), TeO_2 and Na_2CO_3 (H261−H268) resulted in three new phases: $Na_2Cu_3Te_4O_{12}$ (H262) has a crystal structure similar to $K_2Cu_3Te_4O_{12}$, which was obtained under the same conditions with K_2CO_3 instead (H230). Due to their apparent similarity, the crystal structure of $Na_2Cu_3Te_4O_{12}$ is discussed together with its K-analogue (4.1.3.3). $Na_2Zn_2Te_4O_{11}$ (H264, 4.1.2.2) was obtained as a side product besides the zinc oxidotellurates(IV) $ZnTeO_3$ (Hanke, 1967) and $Zn_2Te_3O_8$ (Hanke, 1966) as majority phases. $Na_2Zn_2Te_4O_{11}$ exhibits diffuse scattering due to stacking disorder. $Na_2[Ni_2(TeO_3)](H_2O)$ (H266) adopts the zemannite structure type and is discussed together with the other zemannite-type phases at the end of this section (4.1.6).

Sodium carbonate based hydrothermal experiments H280−H287 yielded only for H281 (Cu^{II}) new phases: Single crystals of $Na_2Cu_3Te_4O_{12}$, which was already observed in the PXRD pattern of H262 (Cu^{II}, three water droplets), were isolated from this batch, besides those of zemannite-type $Na_2[Cu_2(TeO_3)_3](H_2O)_{1.5}$. The latter phase, again, is discussed in the zemannite-section 4.1.6, just as the Na−Mg-zemannite phase obtained from a mild hydroflux reaction between MgO, TeO_2 and Na_2CO_3 (molar ratios 2:3:10; H464; 4.1.6.3).

4.1.2.2 $Na_2Zn_2Te_4O_{11}$

Single crystals of $Na_2Zn_2Te_4O_{11}$ have the form of colorless blocks and were obtained from a hydrothermal reaction starting from ZnO, TeO_2 and Na_2CO_3 in molar ratios of 2:3:10. Based on a preliminary data collection, a small tetragonal unit-cell ($P\bar{4}2c$, a = 7.6474(3) Å, c = 9.3892(4) Å) was determined. However, the structural model contained several oxygen atoms disordered equally over two sites hinting either at a too high space group symmetry or at the presence of a potential superstructure. A longer measurement time of a larger crystal subsequently revealed superstructure reflections, together with diffuse scattering.

Crystal structure

Half of the Te^{IV} atoms exhibit CNs of 3 and 4, respectively, and the resulting [TeO_3] and [TeO_4] polyhedra form linear [Te_4O_{11}] units (Δ−◊−◊−Δ) by corner-sharing. Considering longer Te—O contacts of 2.734(5) and 2.808(5) Å, these finite groups form $^1_\infty$[Te_8O_{22}] chains, which are depicted in the left half of Figure 36. The crystal structure of $Na_2Zn_2Te_4O_{11}$ is distinctively layered (stacking direction **c**). Each layer is formed by a tiling of parallel [Te_4O_{11}] groups. The Zn^{II} atoms and Na^+ cations are located inbetween neighboring layers and are coordinated by four and seven O atoms, respectively.

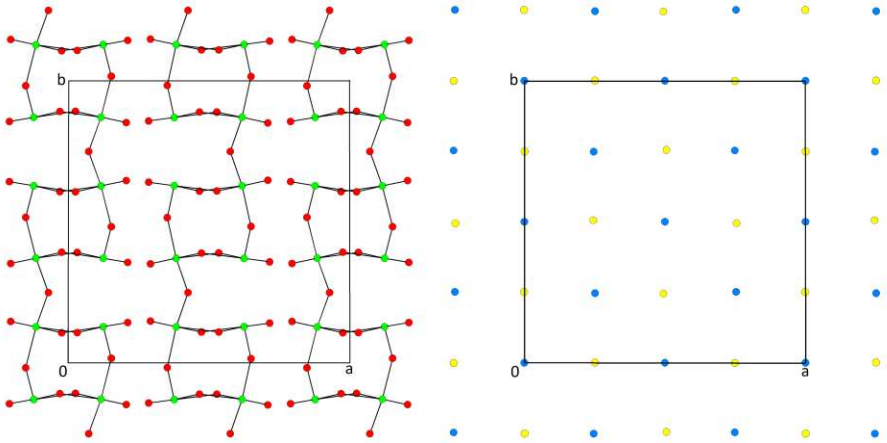

Figure 36. Layers in the crystal structure of $Na_2Zn_2Te_4O_{11}$. Left: Te–O-layer at $z \approx 1/8$; right: Na–Zn-layer at $z \approx 0$. Structure representations were generated with ATOMS (Dowty, 2006).

Adjacent Te–O-layers have the orientation of their $[Te_4O_{11}]$ units rotated by 90°. Furthermore, there are two arrangement possibilities for each Te–O-layer, which differ by a translation of half the length of a $[Te_4O_{11}]$ group. This leads to an ambiguity in the stacking, which can be described by the OD theory (Dornberger-Schiff & Grell-Niemann, 1961). The observed diffraction pattern can be explained by one of the two MDO polytypes (Dornberger-Schiff, 1982; Dornberger-Schiff & Grell, 1982b). The preferred MDO_2 stacking (Figure 37) corresponds to a unit-cell of a = 15.2949(3) Å, c = 18.7783(7) Å, V = 4392.9(2) Å^3 in space group $I\bar{4}2d$.

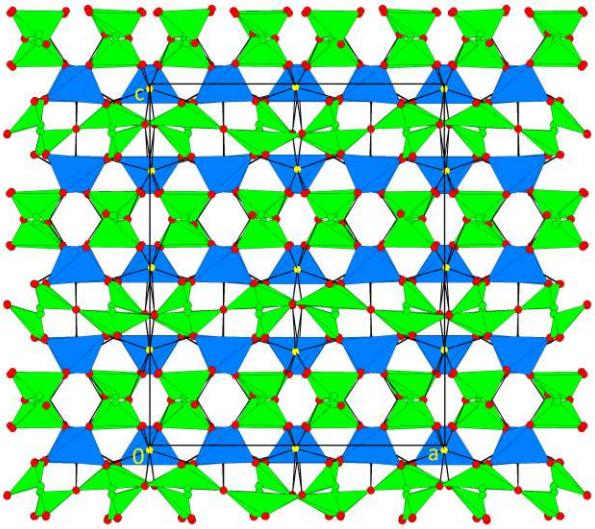

Figure 37. The preferred stacking of the crystal structure of $Na_2Zn_2Te_4O_{11}$ viewed along $[0\bar{1}0]$. Structure representation was generated with ATOMS (Dowty, 2006).

For additional information and a detailed OD-analysis of the crystal structure of $Na_2Zn_2Te_4O_{11}$, see:

Eder, F., Stöger, B. & Weil, M. (2022a). Order-disorder (OD) structures of $Rb_2Zn(TeO_3)(CO_3)\cdot H_2O$ and $Na_2Zn_2Te_4O_{11}$. *Z. Kristallogr. – Cryst. Mater.* **237**, 8–9, 329–341.

4.1.3 Potassium

4.1.3.1 Hydrothermal experiments

For mild hydroflux experiments H229−H236, metal oxides (Mn^{II}, Cu^{II}, Fe^{III}, Zn^{II}, Cr^{III}, Ni^{II}, Cd^{II} and Pb^{II}), TeO_2 and K_2CO_3 in molar ratios of 2:3:10 were employed with three droplets of demineralized water. In the reaction products of these eight batches (Table 67), four new phases were discovered, and even more unidentified phases were revealed by the PXRD patterns, however without the presence of suitable single crystals for structure determination.

The similar phases $K_2Mn_2(TeO_3)_3$ (H229) and $K_2Cd_2(TeO_3)_3$ (H235) were obtained as main products in their respective batches, and both exhibit a layered crystal structure determined under consideration of twinning (4.1.3.2). $K_2Cu_3Te_4O_{12}$ (H230) exhibits a characteristic diffraction pattern with cross-shaped diffuse streaks (4.1.3.3). $K_3FeTe_2O_8(OH)_2(H_2O)$ (4.2.2.3.2) could not be identified in the PXRD pattern of the bulk sample, from which the corresponding single crystals were isolated (H231). This is not surprising, as $K_3FeTe_2O_8(OH)_2(H_2O)$ is an oxidotellurate(VI) and was obtained as a minority phase only due to potential contaminations with H_6TeO_6 from previous hydrothermal experiments in the same Teflon container.

The series H229−H236 was repeated under normal hydrothermal conditions with the usual filling degree of *ca*. 2/3 (H253−H260). While the formation of various metal oxidotellurate(IV) phases occurred in most samples, incorporation of potassium into the crystal structure was only observed for a minority phase in H254 (Cu^{II}): The novel zemannite-type $K_2[Cu_2(TeO_3)_3](H_2O)_2$ was obtained besides CuO and $K_2Te_4O_9(H_2O)_{3.2}$ (Ok & Halasyamani, 2001). In general, layered $K_2Te_4O_9(H_2O)_x$ phases with unknown water contents were assumed to be present in the products, as revealed by similar PXRD patterns of H253−H260 relative to $K_2Te_4O_9(H_2O)_{3.2}$ but with different reflection positions, especially those corresponding to lattice planes parallel to the layers of the structure. Batch H253 yielded a new alkaline manganese(II) oxidotellurate(IV) with composition $Mn_{15}(TeO_3)_{14}(OH)_2$ (3.7.1) besides MnO, $Mn_6Te_5O_{16}$ (5.1.6) and the alkaline manganese(II) oxidotellurate(IV) "$Mn_3(TeO_3)_2(OH)_2$" (3.7.2).

For experiments H269−H276, a different set of metal oxides (*M* = Ag^{I}, Ca^{II}, Mg^{II}, Sn^{II}, Sr^{II}, Hg^{II} and Bi^{III}, hydroxide for Ba^{II}) were introduced into a mild hydroflux reaction together with TeO_2 and K_2CO_3. Ag^{I} (H269) participated in an internal redox reaction with Te^{IV} resulting in elemental Ag and Te^{VI} ($KTeO_3(OH)$; Lindqvist, 1972). In H270 (Ba^{II}), single crystals of a new $K_2Te_4O_9(H_2O)_3$ phase (6.1) were discovered. This phase was also present in H273 (Sn^{II}) and H274 (Sr^{II}). In the PXRD pattern of H272 (Mg^{II}), reflections of a zemannite-type phase with a = 9.40303(11) Å and c = 7.69556(9) Å were observed besides those of MgO and $MgCO_3$ (4.1.6.3). In H273 (Sn^{II}), at least parts of Sn^{II} were oxidized to Sn^{IV}, which then formed the novel layered crystal structure of $K_4Sn_3Te_8O_{24}$ exhibiting stacking disorder and diffuse scattering (4.1.3.6). In the PXRD pattern of H276 (Bi^{III}) unassignable reflections were observed besides those of Bi_2TeO_5 (Mercurio et al., 1983). Although single crystals of the new oxidotellurate(VI) phase $K_6Bi_4Te_3O_{17}(CO_3)(H_2O)_3$ (4.2.2.8) were isolated and a subsequent structure determination performed, this phase does not explain the main reflections of the PXRD pattern.

4.1.3.2 $K_2Mn_2(TeO_3)_3$ and $K_2Cd_2(TeO_3)_3$

The two phases $K_2Mn_2(TeO_3)_3$ and $K_2Cd_2(TeO_3)_3$ have many features in common: Both were obtained from mild hydroflux experiments starting from *M*O, TeO_2 and K_2CO_3 in molar ratios of 2:3:10 with only three droplets of water added to the reaction mixture. Single crystals of the two phases have a plate-like form with the Mn-crystals being much thicker than the Cd-crystals. Both crystal species are colorless, although $K_2Mn_2(TeO_3)_3$ crystals have a yellowish tinge. The crystal structures of $K_2Mn_2(TeO_3)_3$ and $K_2Cd_2(TeO_3)_3$ are isotypic with each other, and both phases exhibit the same kind of twinning behavior, which can be understood by applying OD theory (Dornberger-Schiff & Grell-Niemann, 1961). Therefore, the two phases are presented together in one section.

Initial measurements of $K_2M_2(TeO_3)_3$ (*M* = Mn, Cd) crystals indicated an orthorhombic *C*-centered unit-cell with $a \approx 8$ Å, $b \approx 12.2$ Å and $c \approx 11.3$ Å (pink lines in Figure 38). Closer inspection of reconstructed reciprocal space planes revealed weak superstructure reflections, which could be explained by superposition of two monoclinic cells. After integration under consideration of twinning and refinement based on *hkl*5-type files, one of the three Te sites (Te3) exhibited positional disorder with the alternative Te position being located on the other side of the three coordinating oxygen atoms. The relative occupancies of the disordered Te sites were refined to 0.835:0.165(4) for $K_2Mn_2(TeO_3)_3$ and 0.920:0.080(8) for $K_2Cd_2(TeO_3)_3$. The presence of these "shadow atoms", as well as that of weak one-dimensional diffuse scattering (especially for the Cd-compound) hinted at stacking disorder in the crystal structures of $K_2M_2(TeO_3)_3$ (*M* = Mn, Cd). For one of the two K sites (K2), the presence of "shadow atoms" was noticed as well. Since the s.o.f.s of K2 and its "shadow atom" refined to similar values than that for Te3, both atoms were refined with the same parameter.

In order to better describe the stacking disorder, the setting of the monoclinic cell (yellow lines in Figure 38) in space group $P2_1/n$ was changed to a setting with the layers now being spanned by **b** and **c**. Transformation by the matrix

$$\begin{pmatrix} 1 & 0 & 0 \\ 0 & 1 & 0 \\ \bar{1} & 0 & 1 \end{pmatrix}$$

resulted in the setting $P2_1/c$. The relative twin fractions were refined to 0.759:0.241(7) for the Cd-compound and 0.474:0.526(8) for its Mn-analog.

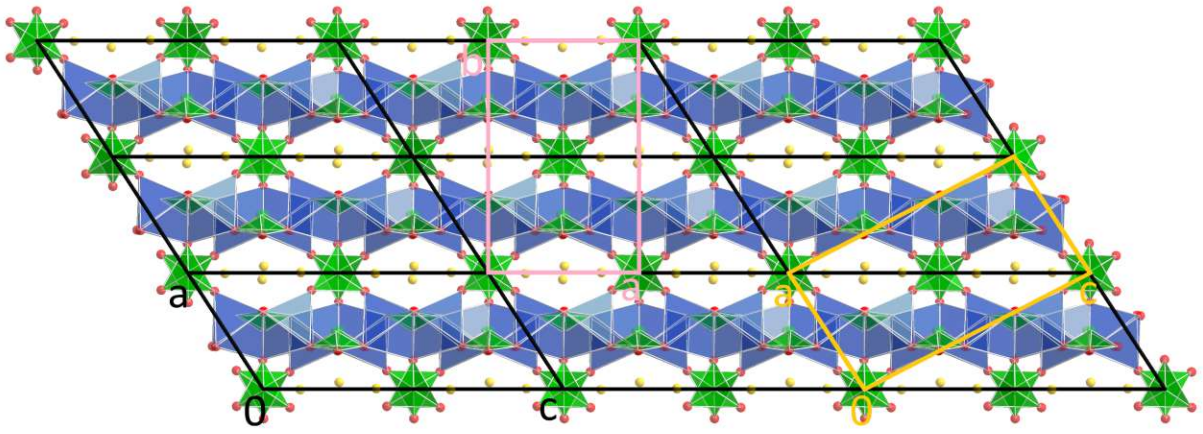

Figure 38. Relations between the final unit-cell ($P2_1/c$) of $K_2M_2(TeO_3)_3$ (*M* = Mn, Cd) (drawn black), the incorrect orthorhombic *C*-centered pseudo-cell (pink), and the initial monoclinic setting ($P2_1/n$, yellow).

Crystal chemistry

The crystal structure of $K_2M_2(TeO_3)_3$ (M = Mn, Cd) can be decomposed into two kinds of layers, A^1 and A^2, extending parallel to (100) (Figure 39). A^1 is formed by the M^{II} atoms, the Te1 and Te2 sites and their coordinating oxygen atoms, while A^2 consists of the Te3 atom, its coordinating oxygen atoms and the K^+ cations (Figure 40). The O7, O8 and O9 sites belong to the coordination spheres of both Te3 and the M^{II} atoms and are therefore located at the interface of two adjacent layers.

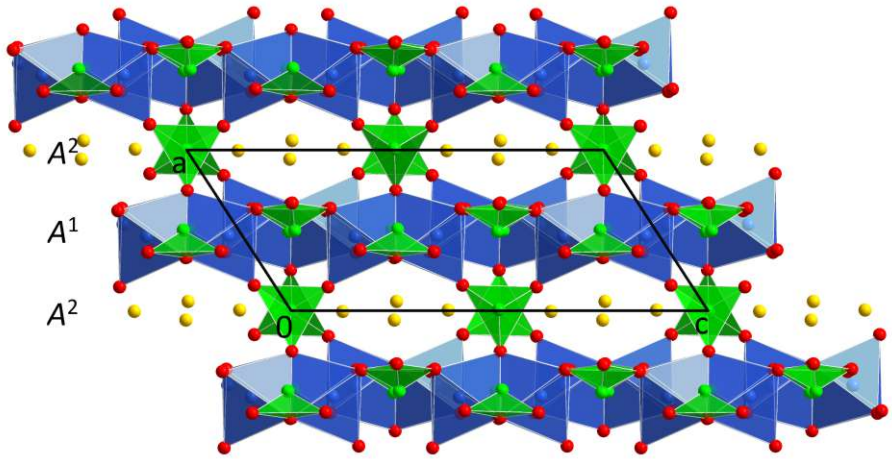

Figure 39. The crystal structure of $K_2M_2(TeO_3)_3$ (M = Mn, Cd) viewed along $[0\bar{1}0]$. The names of the two kinds of layers for the OD-description are given to the left.

All three Te^{IV} atoms are coordinated by three oxygen atoms, forming trigonal-pyramidal $[TeO_3]$ units, which are isolated from each other. The two M^{II} atoms are surrounded by six oxygen atoms, each forming a distorted octahedron. The distortion of the $[MO_6]$ groups is primarily caused by the formation of $[M_2O_9]$ dimers through plane-sharing. These $[M_2O_9]$ units are connected to each other by sharing corners with $[TeO_3]$ groups. The connection withing the A^1 layer is facilitated by the coordination spheres of Te1 and Te2, while the $[Te3O_3]$ units of the A^2 layer type are responsible for linking the A^1 layers along the stacking direction. The K^+ cations have coordination numbers of 8 (K1) and 6 (K2) and fill the remaining space of the A^2 layers. Further details (BVS vallues; coordinates of the ψ lone pairs) of the $K_2M_2(TeO_3)_3$ (M = Mn, Cd) phases are collated in Table 8.

Table 8. BVS and coordinates of ψ in $K_2Mn_2(TeO_3)_3$ and $K_2Cd_2(TeO_3)_3$.

BVS / v.u.	$K_2Mn_2(TeO_3)_3$	$K_2Cd_2(TeO_3)_3$
Te1	3.98	4.18
Te2	3.79	3.73
Te3	3.99	3.94
Mn/Cd1	1.83	2.02
Mn/Cd2	1.98	1.99
K1	1.19	1.13
K2	0.92	0.97
Coordinates of ψ		
$x(\psi_{Te_1})$	0.6954	0.6844
$y(\psi_{Te_1})$	0.9853	0.9872
$z(\psi_{Te_1})$	0.4157	0.4099
$x(\psi_{Te_2})$	0.6680	0.6668
$y(\psi_{Te_2})$	0.5100	0.5105
$z(\psi_{Te_2})$	0.4230	0.4287
$x(\psi_{Te_3})$	1.0035	1.0049
$y(\psi_{Te_3})$	0.6009	0.6033
$z(\psi_{Te_3})$	0.5030	0.5040

OD description

Both layer types A^1 and A^2 follow orthorhombic metrics and are spanned by **b** and **c**. The axis normal to the plane, $\mathbf{a_0}$ is defined as [10¼] relative to the monoclinic unit-cell. Determining the (idealized) symmetries of the A^1 and A^2 layer types proved to be challenging because the degree of idealization initially was not clear. The uncertainty concerned the O8 site, which is marked in Figure 40.

In a first approach, it was decided that the deviations of its *y* coordinate (0.7791(11) for Mn, 0.7718(17) for Cd), from the ideal values of 1/4 or 3/4 were too high. Consequently, the A^2 layer has a higher symmetry (*P*(*n*)*cm*) compared to the A^1 layer. The resulting OD groupoid family symbol (Dornberger-Schiff & Grell, 1982a) reads as

A^1	A^2
P(1)2_1/*c*1	*P*(*n*)*cm*
[*r*,*s*]	

or

A^1	A^2
P(1)2_1/*c*1	*P*(*n*)*cm*
[0, 1/8]	

when adding the correct values for *r* and *s*. The corresponding NFZ-relationship can be derived as followed: $\mathcal{G}_n$ = *P*(1)*c*1 for the A^1 layer and $\mathcal{G}_n$ = *P*(2)*cm* for the A^2 layer. Because *r* = 0, the *c* glide planes of both layer types overlap (they are always located at *y* = 1/4, 3/4) and $\mathcal{G}_n \cap \mathcal{G}_{n+1}$ is always *P*(1)*c*1. The number of stacking possibilities at a specific contact, $N = F/Z = [\mathcal{G}_n : \mathcal{G}_n \cap \mathcal{G}_{n+1}]$, is [*P*(1)*c*1 : *P*(1)*c*1]= 2/2 = 1 for the $A^1_n \rightarrow A^2_{n+1}$ contacts, while for the $A^2_n \rightarrow A^1_{n+1}$ contacts, it is [*P*2*cm* : *P*(1)*c*1] = 4/2 = 2. This would mean that, given a specific A^1 layer, there is only one possibility to place the following A^2 layer, but given an A^2 layer, there are two ways to place the next A^1 layer. This does not agree with the fact that "shadow atoms" were exclusively observed for atoms belonging to the A^2 layer type (Te3, K2).

In a second approach, an alternative model, in which the A^1 layer type is higher- and not lower-symmetric compared to the A^2 layer, was established. Thereby it was necessary to consider the O8 atoms as if they were positioned at *y* = 1/4 or 3/4. This idealization significantly increases the layer symmetry of the A^1 layers to *P*(*n*)*mm* with **c'** = **c**/2 (Figure 40). In this case, the OD groupoid family symbol (Dornberger-Schiff & Grell, 1982a) changes to

A^1	A^2
*P(n)mm**	*P*(*n*)*cm*
[*r*,*s*]	
* **c'** = **c**/2	

A description of the A^1 layer type using the same metrics as the A^2 layer type by application of a non-standard *X*-centering was considered, but was discarded because it would not have been possible to properly describe the *n* glide plane within the doubled unit-cell. The values for *r* and *s* do not change as long as the length of **c** remains the same.

A^1	A^2
*P(n)mm**	*P*(*n*)*cm*
[0, 1/8]	
* **c'** = **c**/2	

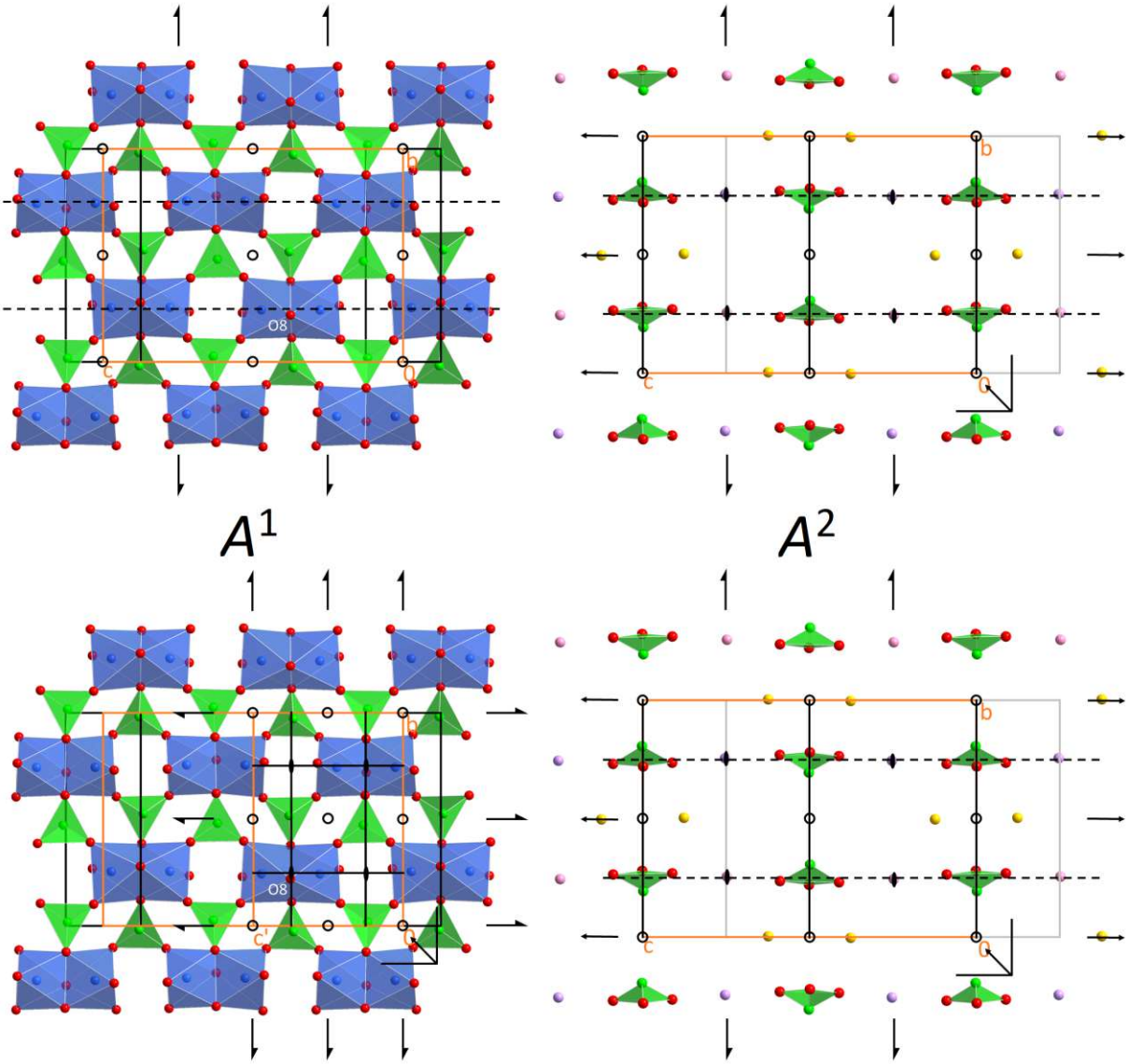

Figure 40. The A^1 (left) and A^2 (right) layer types in $K_2M_2(TeO_3)_3$ (M = Mn, Cd) viewed normal to the (100) layer plane. The initial model considering the displacement of the O8 site is presented on the top, the final, more idealized model is drawn at the bottom. On the right, K^+ cations located in the layer plane are drawn yellow, while those slightly above and below are drawn pink and purple. (Pseudo-)symmetry operations are given with their respective graphical symbols (Hahn & Arroyo, 2016).

NFZ relationship

Relative to the first approach, the group of operations of a specific layer that do not invert the stacking direction, $\mathcal{G}_n$, changes to $P(2)mm$ (**c'** = **c**/2) for the A^1 layers and remains $P(2)cm$ for the A^2 layers. The increased translational symmetry of A^1 compared to A^2 leads to the presence of twice as many 2_{100} axes and m_{001} planes for the A^1 layer type with half of them coinciding with those of the A^2 layer type. Concerning the (010) symmetry operations, the m_{010} planes in the A^1 layers (**c'** = **c**/2) include the c_{010} glide planes of the A^2 layers. Therefore, for both layer contacts, $\mathcal{G}_n \cap \mathcal{G}_{n+1}$ is $P(2)cm$. Out of this, $N = F/Z = [\mathcal{G}_n : \mathcal{G}_n \cap \mathcal{G}_{n+1}]$ is determined to $[P(2)mm\ (\mathbf{c'} = \mathbf{c}/2) : P(2)cm] = 8/4 = 2$ for the $A^1_n \rightarrow A^2_{n+1}$ contacts and $[P2cm : P2cm] = 4/4 = 1$ for the $A^2_n \rightarrow A^1_{n+1}$ contacts. Now, there are two possibilities to place an A^2 layer onto an A^1 layer (denoted as A^{2+} and A^{2-}), while the placement of an A^1 layer on an A^2 layer is unambiguous.

MDO polytypes

Given the symmetrically equivalent pairs of layers, A^1A^{2+} and A^1A^{2-}, there are two different triples of layers possible: $A^{2+}A^1A^{2+}$ and $A^{2+}A^1A^{2-}$. They are the building blocks of the two possible MDO polytypes (Dornberger-Schiff, 1982; Dornberger-Schiff & Grell, 1982b):

- MDO_1: …$A^1A^{2+}A^1A^{2+}$…; $P2_1/c$, **a** = $\mathbf{a_0}$−0.25**c**
- MDO_2: …$A^1A^{2+}A^1A^{2-}$…; *Pnca* , **a** = $2\mathbf{a_0}$

The investigated single crystals of both $K_2Mn_2(TeO_3)_3$ and $K_2Cd_2(TeO_3)_3$ exhibited reflections corresponding to the stacking of the MDO_1 polytype. The systematic twinning of the examined crystals originates from the two possible MDO_1 domains with stackings of …$A^1A^{2+}A^1A^{2+}$… and …$A^1A^{2-}A^1A^{2-}$… . The overlap of the twin domains is clearly visible in the reciprocal *hnl* (*n* odd) planes (Figure 41).

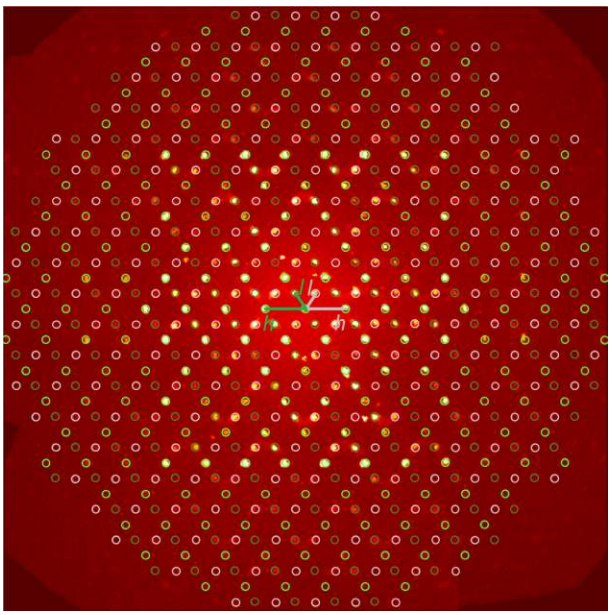

Figure 41. Reconstructed *h*3*l* plane of $K_2Mn_2(TeO_3)_3$. Reflections of the two twin domains are marked in dark green and grey, overlapping reflections are marked in light green.

Comparison of crystal structures

As already noted, the crystal structures of $K_2Mn_2(TeO_3)_3$ and $K_2Cd_2(TeO_3)_3$ are isotypic with each other and exhibit the same twinning behavior. Their close structural relationship becomes apparent when comparing the crystal structures using *compstru*. The degree of lattice distortion *S* is 0.0086, the arithmetic mean of the distances of paired atoms $d_{av.}$ is 0.1010 Å and the measure of similarity Δ is 0.102. The distances between the paired atoms are 0.0723 Å (Te1), 0.0630 Å (Te2), 0.0614 Å (Te3), 0.2148 Å (Te3B), 0.0529 Å (Mn/Cd1), 0.0522 Å (Mn2/Cd2), 0.0450 Å (K1), 0.0660 Å (K2), 0.3029 Å (K2B; the largest value), 0.1436 Å (O1), 0.0754 Å (O2), 0.1062 Å (O3), 0.0437 Å (O4), 0.1336 Å (O5), 0.0939 Å (O6), 0.1280 Å (O7), 0.0525 Å (O8) and 0.1102 Å (O9). The Te3B and K2B sites, which exhibit only minor occupation and have significantly larger uncertainties of their respective atomic coordinates, show the largest difference. This possibly originates from the fact, that these positions are poorly defined compared to the other atoms. The differences in unit-cell dimensions between $K_2Mn_2(TeO_3)_3$ and $K_2Cd_2(TeO_3)_3$ (Table 9) can be attributed to the different ionic radii (Shannon, 1976) of Mn^{II} and Cd^{II} of 0.83 and 0.95 Å, respectively.

Table 9. Comparison of structure data and interatomic distances in the crystal structures of $K_2Mn_2(TeO_3)_3$ and $K_2Cd_2(TeO_3)_3$.

	$K_2Mn_2(TeO_3)_3$	$K_2Cd_2(TeO_3)_3$
a / Å	7.2599(11)	7.3433(13)
b / Å	11.197(2)	11.380(2)
c / Å	15.762(2)	16.041(3)
β /°	122.989(2)	123.062(4)
V/ Å^3	1074.7(3)	1123.4(4)
Interatomic distances / Å		
Te1—O1	1.849(15)	1.826(18)
Te1—O3	1.866(18)	1.828(19)
Te1—O2^{i}	1.887(11)	1.873(15)
Te2—O6	1.879(19)	1.869(18)
Te2—O4	1.885(11)	1.887(15)
Te2—O5	1.892(15)	1.922(18)
Te3—O9	1.83(2)	1.847(17)
Te3—O8^{ii}	1.851(11)	1.865(11)
Te3—O7	1.857(18)	1.833(19)
*M*1—O3	2.127(16)	2.214(18)
*M*1—O6	2.189(17)	2.259(18)
*M*1—O9	2.21(2)	2.253(17)
*M*1—O8	2.276(17)	2.370(16)
*M*1—O4^{iii}	2.293(15)	2.378(18)
*M*1—O2^{iii}	2.325(14)	2.417(18)
*M*2—O7	2.12(2)	2.253(18)
*M*2—O5	2.124(17)	2.251(19)
*M*2—O1	2.133(16)	2.278(18)
*M*2—O2^{iv}	2.240(15)	2.350(17)
*M*2—O4^{iv}	2.285(16)	2.399(18)
*M*2—O8^{v}	2.346(14)	2.369(17)
K1—O2^{vi}	2.783(12)	2.774(16)
K1—O3	2.82(2)	2.804(19)
K1—O4^{vi}	2.820(12)	2.835(16)
K1—O7^{vii}	2.84(2)	2.92(2)
K1—O6	2.85(2)	2.916(19)
K1—O5	2.851(17)	2.85(2)
K1—O9^{viii}	2.87(2)	2.869(19)
K1—O1	2.893(16)	2.91(2)
K2—O3^{ix}	2.584(19)	2.674(19)
K2—O5	2.73(2)	2.64(2)
K2—O7^{x}	2.83(2)	2.79(2)
K2—O9^{viii}	2.84(2)	2.744(19)
K2—O2^{vi}	3.133(17)	3.144(19)
K2—O4	3.169(17)	3.204(19)

Symmetry codes: (i) *x*, 1+*y*, *z*; (ii) 1+*x*, *y*, *z*; (iii) 1−*x*, 1−*y*, 1−*z*; (iv) 1−*x*, 1/2+*y*, 1/2−*z*; (v) *x*, 3/2−*y*, −1/2+*z*; (vi) −*x*, 1/2+*y*, 1/2−*z*; (vii) −1+*x*, *y*, *z*; (viii) −1+*x*, 3/2−*y*, −1/2+*z*; (ix) −*x*, −1/2+*y*, 1/2−*z*; (x) 1−*x*, −1/2+*y*, 1/2−*z*.

4.1.3.3 $K_2Cu_3Te_4O_{12}$ and $Na_2Cu_3Te_4O_{12}$

$K_2Cu_3Te_4O_{12}$ and $Na_2Cu_3Te_4O_{12}$ have the same formula type and have many aspects in common. They both can be obtained from CuO, TeO_2 and K_2CO_3/Na_2CO_3 in molar ratios of 2:3:10 in either a typical hydrothermal reaction or in a mild hydroflux reaction. Their crystals have an intense dark green, rather opaque color and the shape of elongated quadratic prisms. Their average structures (Figure 42) are isotypic with each other and both compounds exhibit characteristic cross-shaped diffuse scattering. However, the orientation of the diffuse scattering relative to the average structure is different, hinting at different rules for the preferred arrangement of the disordered systems.

4.1.3.3.1 Average structure

The average structure of $A_2Cu_3Te_4O_{12}$ (*A* = Na, K) is obtained by completely ignoring the diffuse scattering and only integrating the sharp Bragg-reflections. To this effect, a small tetragonal unit-cell (Table 10) results. In space group *P*4/*ncc*, the asymmetric unit comprises only five atomic sites. Of these five, two pairs (Te1 and *A*1, and O1 and O2) are disordered in close vicinity to the other position of the respective pair. Only the Cu1 site is fully occupied. With respect to the average structure, it is difficult to accurately describe the exact coordination environments of the respective atoms. A few main details can be derived: The Cu^{II} atoms are coordinated by four oxygen atoms in perfect or slightly distorted square-planar shape. The Te^{IV} atoms have either a CN of 3 or 4. Together with their coordination polyhedra, the Te^{IV} and *A* atoms form chains oriented parallel to [001]. These chains are connected by the [CuO_4] squares.

When comparing the two family structures with *compstru*, the distances between paired atoms are 0.0779 Å (Te1), 0.0201 Å (Cu1), 0.2629 Å (*A*1), 0.0595 Å (O1) and 0.1498 Å (O2). The greatest difference between the two average structures concerns the location of the *A*1 position. In $K_2Cu_3Te_4O_{12}$, it is positioned farther away from the Te^{IV} atoms than in the Na-analog. An obvious reason for this behavior is the larger ionic radius of K^+ compared to Na^+.

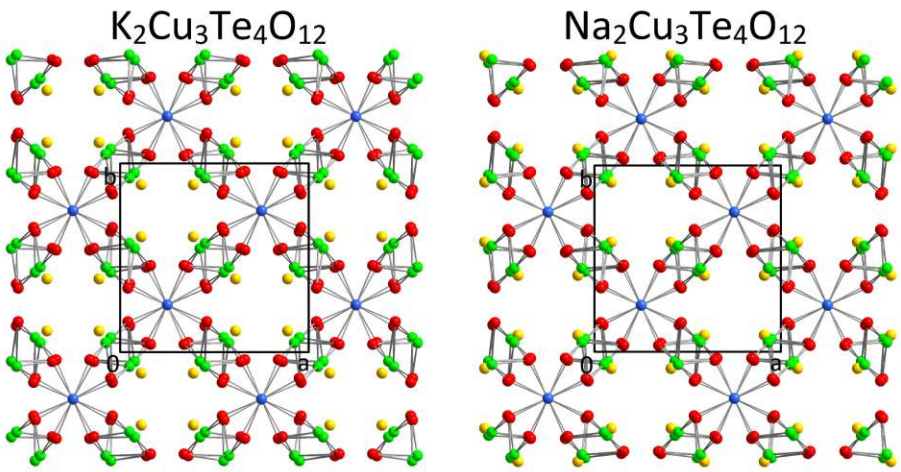

Figure 42. The average structures of $K_2Cu_3Te_4O_{12}$ and $Na_2Cu_3Te_4O_{12}$ viewed along [00$\bar{1}$].

Table 10. Details on the average structures of $K_2Cu_3Te_4O_{12}$ and $Na_2Cu_3Te_4O_{12}$.

		$K_2Cu_3Te_4O_{12}$	$Na_2Cu_3Te_4O_{12}$
Space group		*P4/ncc*	*P4/ncc*
a / Å		8.426(9)	8.2980(17)
c / Å		6.403(6)	6.1633(12)
V / Å³		454.6(8)	424.39(15)
Site (site symmetry; multiplicity & Wyckoff letter; s.o.f.) and coordinates			
Te1 (1; 16 *g*; 1/3)	*x*	0.57638(13)	0.5682(2)
	y	0.45073(13)	0.4489(2)
	z	0.2732(3)	0.2789(3)
Cu1 (4..; 4 *c*; 1)	*x*	1/4	1/4
	y	1/4	1/4
	z	0.42466(14)	0.42140(11)
*A*1 (..2; 8 *f*; 1/3)	*x*	0.6119(4)	0.5895(9)
	y	0.3881(4)	0.4105(9)
	z	1/4	1/4
O1 (1; 16 *g*; 2/3)	*x*	0.3611(4)	0.3558(6)
	y	0.4495(5)	0.4542(6)
	z	0.3764(7)	0.3779(6)
O2 (1; 16 *g*; 1/3)	*x*	0.3389(10)	0.3434(13)
	y	0.4591(10)	0.4655(13)
	z	0.4795(15)	0.4576(14)

4.1.3.3.2 Cross-shaped diffuse scattering and structure of $[A_2Te_4O_{12}]$ rods

The diffraction patterns of both $A_2Cu_3Te_4O_{12}$ phases exhibit diffuse streaks in the *hkn* = *m* ± 1/3 (*m* ∈ ℤ) planes. As the diffuse scattering is present exactly in these planes, but not at other values of *l* (see Figure 43), this indicates that the structure has strict translational symmetry in the [001] direction with $\mathbf{c} = 3\mathbf{c}_{ave}$. This can be explained by the ordering of the *A* and Te^{IV} atoms along **c**, which therefore has a translational period of $3\mathbf{c}_{ave}$ or six *A*/Te atoms.

Several sequences of *A* and Te^{IV} atoms are theoretically possible (…—Te—Te—Te—Te—*A*—*A*—…, …—Te—*A*—Te—*A*—Te—Te—… or …—Te—Te—*A*—Te—Te—*A*—…). Based on bond valence considerations for the adjacent oxygen atoms, the order …—Te—Te—*A*—Te—Te—*A*—… is the most appropriate. Given this sequence, there are three possibilities for the atomic arrangement within the rod, with the two adjacent Te^{IV} atoms having a Te···Te distance of either 3.284(4), 3.534(4) or 3.819(4) Å (values based on the average structure of $K_2Cu_3Te_4O_{12}$). Here, the most probable model was chosen on basis of the relative intensities of the diffuse scattering in the various *hkn* planes. As it can be seen in Figure 43, the diffuse scattering significantly varies in its intensity in different reciprocal *hkn* planes, *e.g.,* it is very intense in the *hk*4/3 plane and very weak in *hk*5/3. Based on simulations of disordered stackings with the programs *DIFFAX* (Treacy et al., 1991) and *DISCUS* (Proffen & Neder, 1997), only the arrangement with the largest distance between the Te^{IV} atoms appropriately describes the observed intensity distribution. The relative intensities of the diffuse scattering depending on *l* showed the

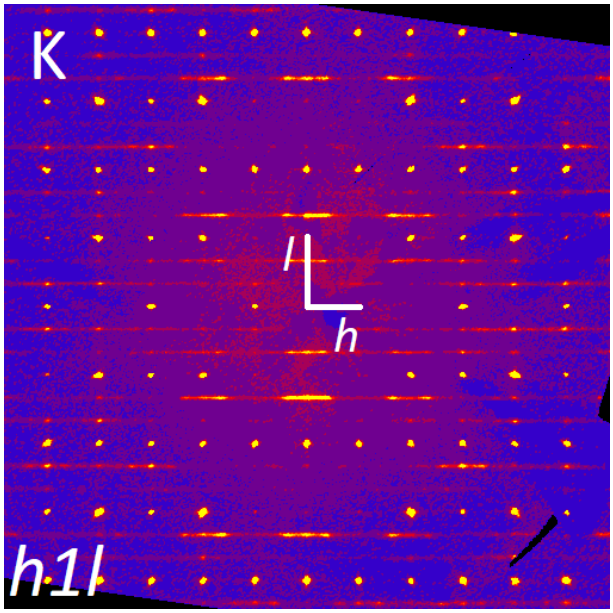

Figure 43. Reconstructed *h*1*l* plane of $K_2Cu_3Te_4O_{12}$. Reciprocal lattice vectors refer to the average structure.

same behavior for $K_2Cu_3Te_4O_{12}$ and $Na_2Cu_3Te_4O_{12}$ and the same rod-model (Figure 44) can be applied for both structures.

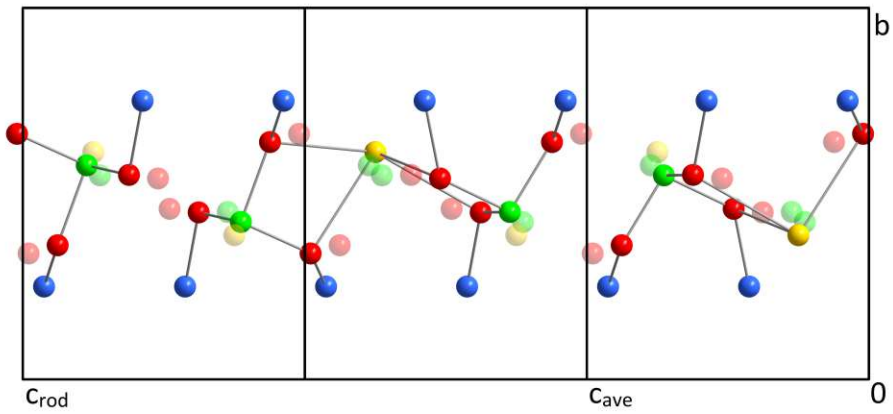

Figure 44. An [$A_2Te_4O_{12}$] rod, based on the refinement data of $K_2Cu_3Te_4O_{12}$. Atoms of the average structure not realized are drawn as transparent spheres.

While the fact that diffuse scattering only appears in the reciprocal $l = n \pm 1/3$ ($n \in \mathbb{Z}$) planes is explained by the triplication of **c** due to ordering within the [*A*−Te−O] rods, the diffuse scattering itself is caused by disorder of the arrangements of the rods relative to their neighbors. The diffuse scattering appears almost exclusively on one-dimensional streaks propagating in perpendicular directions, forming a characteristic cross-shaped pattern. What is surprising, is that the direction of the streaks is different for the K-and Na-phase. In $K_2Cu_3Te_4O_{12}$, they are oriented parallel to <100> of the average structure, while in $Na_2Cu_3Te_4O_{12}$, they are propagating in the <110> directions (Figure 45). It was tried to understand the (dis-)order conditions in both structures by developing models and simulating the diffuse scattering with *DIFFAX* and some approaches in *DISCUS*. Hereby, the analysis of $K_2Cu_3Te_4O_{12}$ proved to be more promising than of its Na-analog.

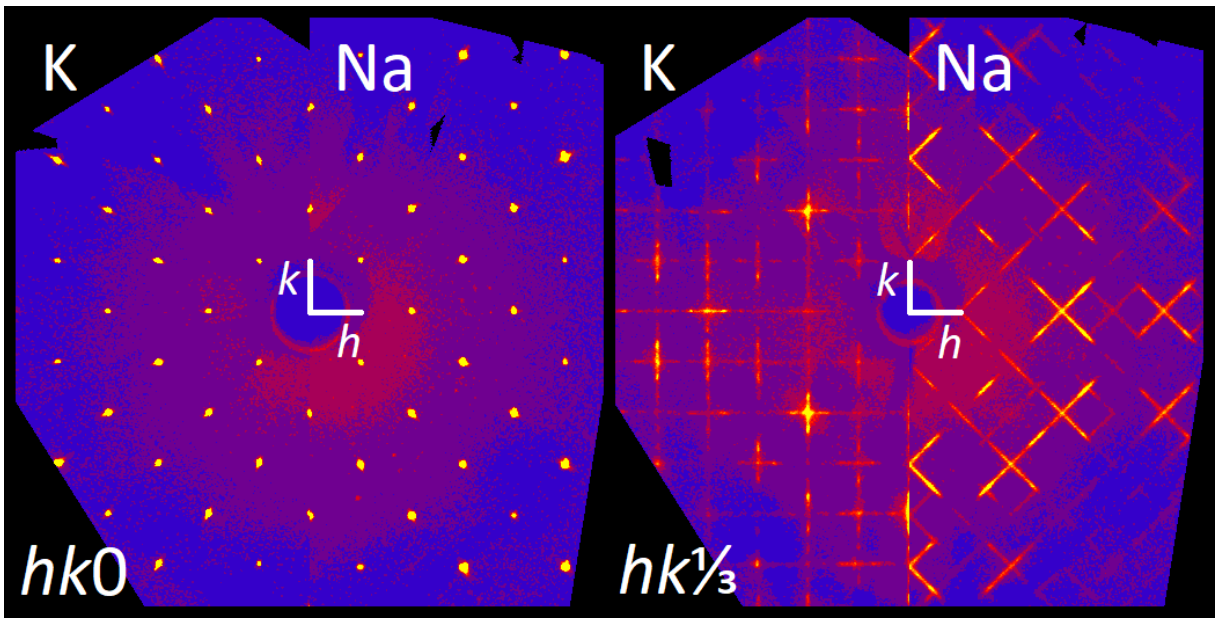

Figure 45. Reconstructed reciprocal *hk*0 (left) and *hk*1/3 (right) planes of $A_2Cu_3Te_4O_{12}$. Reciprocal lattice vectors refer to the average structure. Indidual half-images are scaled to the same length of reciprocal lattice vectors for a better comparability of the two phases.

4.1.3.3.3 $K_2Cu_3Te_4O_{12}$

The general shape of the diffuse scattering provides several hints on the disorder-behavior. The presence of one-dimensional streaks indicates a one-periodic disorder within the crystal structure, *viz*. a disordered stacking of layers. In this case, the cross-shaped diffraction pattern is a result of twinning by a 90° rotation along **c***. Streaks oriented in the **a*** direction only appear at integer *k* (relative to the average structure) values. This means that the assumed disordered layers have a translational symmetry of $\mathbf{b}_{ave}$ normal to the stacking direction. The same consideration can be made for the streaks propagating parallel to **b***. The streaks have varying intensities along their propagating direction, revealing an intensity distribution with maxima at approximately one and two thirds between integer *h* (or *k*) values.

Arrangement of $[K_2Te_4O_{12}]$ rods

While each $[K_2Te_4O_{12}]$ rod is fully ordered in the **c** direction, their disordered arrangement relative to each other is regarded as the origin of the observed diffuse streaks. In order to understand the interactions between the rods, the average structure of $K_2Cu_3Te_4O_{12}$ is depicted again, but with the K and Te^{IV} atoms drawn in different colors depending on their location along **c** (Figure 46). The most influential contacts of one rod are not the neighboring rods in the <100> directions but two neighboring rods either along ±[110] or ±[1$\bar{1}$0]. At such a diagonal rod-contact, a realization of the K position on both rods at the same *z* value would result in a rather close K···K contact of 3.291(5) Å (see black line in Figure 46). Such a short K···K distance is not impossible and is realized, for example, in various K–Cu^{II}–Te^{VI}–O-phases (4.2.2.6). However, other than in these layered potassium copper oxidotellurate structures, the two K^+ cations in $K_2Cu_3Te_4O_{12}$ do not share any oxygen contact (they generally exhibit a rather one-sided coordination environment), and their positive charges are therefore less shielded from each other. For this reason, the K···K contact was deemed unfavored compared to the other two possible K···Te contacts (Figure 48).

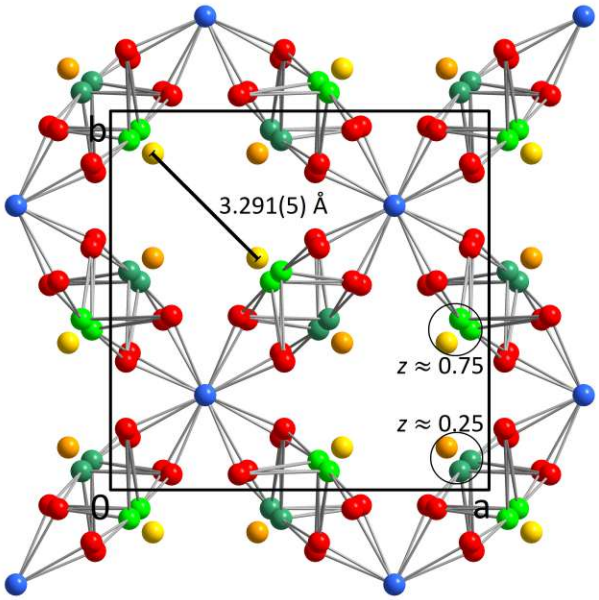

Figure 46. The average structure of $K_2Cu_3Te_4O_{12}$ viewed along [00$\bar{1}$]. K and Te^{IV} atoms at different *z* coordinates are colored either light green and yellow, or dark green and orange.

Concerning the four contacts to neighboring rods in the <100> directions, no such deduction can be made. The small positional differences between the two possible oxygen positions influence the shape of the $[CuO_4]$ unit to a more or less distorted square. However, no reasonable conditions for this type of neighbors could be worked out from a crystal-chemical point of view. While there should be some ordering rules in the direction of the **a** or **b** translational symmetry, one would expect them to not apply in the same fashion in the direction relative to the disorder. However, given the tetragonal symmetry of the average structure, all four <100> contacts are symmetrically equivalent. Generally, given one rod, the "ordered and disordered direction" of its neighboring contacts must be assigned arbitrarily, as the atomic positions do not offer signs for an unambiguous modelling.

Simulations of the diffuse scattering with *DIFFAX*

As it can be seen in Figure 46, the most important contacts for determining the arrangement of the $[K_2Te_4O_{12}]$ rods are only between one half of the rods, while the contacts to the other half seem to be of less importance. Therefore, it was at first tried to simulate only the diffuse scattering originating from one half of the $[K_2Te_4O_{12}]$ rods, all oriented in the same direction (Figure 47). For simulations with *DIFFAX*, the unit-cell at first had to be transformed, as *DIFFAX* only accepts **c** as the stacking direction for modelling the disorder. The unit-cell of the average structure (Table 10) was therefore transformed by the matrix

$$\begin{pmatrix} 0 & 1 & 0 \\ 0 & 0 & 3 \\ 1 & 0 & 0 \end{pmatrix}.$$

This results in a unit-cell setting with a = 8.426(9) Å (the short translational symmetry of the layers), b = 19.209(18) Å (the direction the rods are extending in) and c = 8.426(9) Å (the stacking direction with disorder) were obtained. This setting is used throughout when modelling the disorder with *DIFFAX*.

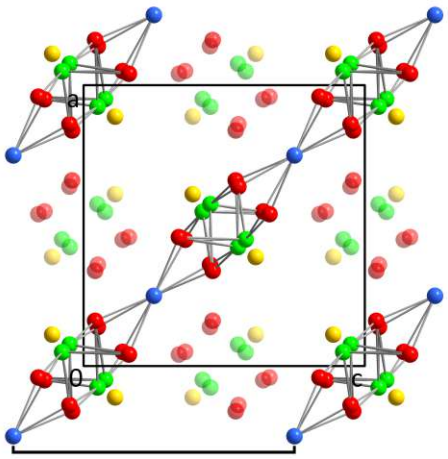

Figure 47. One half-set of rods used for simulations of diffuse scattering with *DIFFAX*. The ignored atoms are drawn transparent.

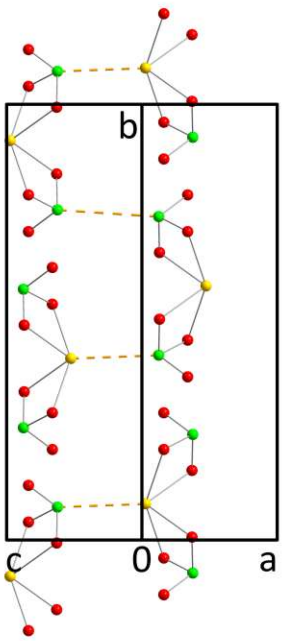

Figure 48. An example of an allowed rod-contact in $K_2Cu_3Te_4O_{12}$.

Each $[K_2Te_4O_{12}]$ rod has three arrangement possibilities, which are connected by a translation of ±**b**/3 (or $\mathbf{c}_{ave}$); the three possible rod positions will be denoted as "*A*, *B* and *C*". Relative to *A*, *B* is translated by +**b**/3, and *C* by −**b**/3. Because the disorder is modelled for only one "half-structure" of $K_2Cu_3Te_4O_{12}$, the $[K_2Te_4O_{12}]$ rods drawn as transparent in Figure 47 were left out from the simulation.

Each layer type used in the simulation consists of two $[K_2Te_4O_{12}]$ rods, located at $z \approx 0$ and $z \approx 0.5$ (black bracket at the bottom of Figure 47) The rods at $z \approx 0.5$ are translated relative to those at $z \approx 0$, by **a**/2**,** **c**/2, and either **b**/6, − **b**/6 or **b**/2. The latter +**b**/2 option is not realized, as it would result in the already discussed close K···K contacts of 3.291(5) Å. This leaves two possibilities for the neighboring layer, and the resulting layer pairs are described as A^+ or A^-, depending on the translation vector in **b** direction. One possible rod-contact is shown in Figure 48.

The A^+ and A^- layer pairs are geometrically equivalent. Considering the arrangement of a third layer, there are two types of layer triples possible, with the third layer being translated by just **c** from the first one or by **c** ± **b**/3 (only one option of +/− is allowed depending on the location of the intermediate layer). For example, based on an A^+ layer, the two possible triples are $A^+A^?$ or $A^+B^?$, while an $A^+C^?$ triple would result in the unfavorable K···K contact from the second to the third layer. A complete list of the possible layer contacts is presented in Table 11.

This situation of symmetrically equivalent pairs and different types of triples consisting of translationally equivalent layers corresponds to that of an OD-structure (Dornberger-Schiff & Grell-Niemann, 1961). Given the speculative nature of layer definition (rods, which exhibit for an unknown reason translational symmetry in one direction but disorder in the perpendicular direction), a detailed

OD-analysis is not provided at this point. However, it is possible to define the stacking of the two possible MDO polytypes:

- MDO_1: …A^+A^+…; **c'** = **c** (= **a**/**b**$_{ave}$)
- MDO_2: …$A^+B^+C^+$…; **c'** = 3**c** (= 3**a**/**b**$_{ave}$)

Table 11. Summary of the possible layer types and their contact possibilities.

	Relative **b** translation (A = 0)		Possible contacts	
Layer pair	First layer	Second layer	MDO_1	MDO_2
A^+	0	+ 1/6	*A*	*B*
A^-	0	− 1/6	*A*	*C*
B^+	+ 1/3	+ 1/2	*B*	*C*
B^-	+ 1/3	+ 1/6	*B*	*A*
C^+	− 1/3	− 1/6	*C*	*A*
C^-	− 1/3	+ 1/2	*C*	*B*

In order to perform simulations in *DIFFAX*, the transition probabilities between the specific layer types need to be defined: The probability of an MDO_2 triple is given as p, while that for MDO_1 is $q = 1 - p$. This results in the probabilities given in Table 12. As two layer pairs result in a total of four layers and therefore two triples, two probabilities are multiplied in each case.

Table 12. Layer transition probabilities for *DIFFAX* based on an OD-model.

	Next layer	1	2	3	4	5	6
Layer	Layer type	A^+	A^-	B^+	B^-	C^+	C^-
1	A^+	$(1-p)^2$	$p(1-p)$	p^2	$p(1-p)$	0	0
2	A^-	$p(1-p)$	$(1-p)^2$	0	0	$p(1-p)$	p^2
3	B^+	0	0	$(1-p)^2$	$p(1-p)$	p^2	$p(1-p)$
4	B^-	$p(1-p)$	p^2	$p(1-p)$	$(1-p)^2$	0	0
5	C^+	p^2	$p(1-p)$	0	0	$(1-p)^2$	$p(1-p)$
6	C^-	0	0	$p(1-p)$	p^2	$p(1-p)$	$(1-p)^2$

Given the features of the diffuse streaks (maxima at approximately one and two thirds between integer l values), it can be deducted that MDO_2 triples are preferred over MDO_1 triples. A preference of the MDO_1 stacking would only result in maxima at integer l values, while the MDO_2 stacking explains the observed intensities at non-integer l (Figure 49).

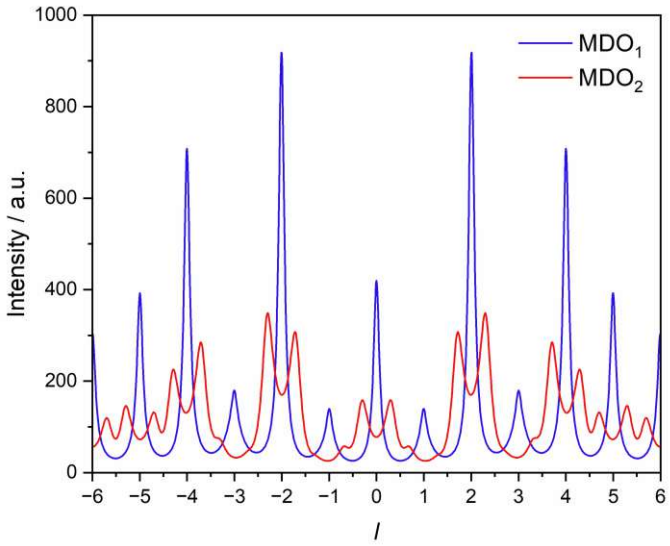

Figure 49. *DIFFAX* simulation of diffuse intensities on the 11l rod for p = 0.3 (MDO_1 preferred; blue) and p = 0.7 (MDO_2 preferred; red).

By variation of the values of *p*, a value of 0.7 was found to lead to good agreements with the observed diffuse scattering (Figure 50). This corresponds to the transition probabilities given in Table 13.

Table 13. Layer transition probabilities of the final simulation in *DIFFAX*.

	Next layer	1	2	3	4	5	6
Layer	Layer type	A^+	A^-	B^+	B^-	C^+	C^-
1	A^+	0.09	0.21	0.49	0.21	0	0
2	A^-	0.21	0.09	0	0	0.21	0.49
3	B^+	0	0	0.09	0.21	0.49	0.21
4	B^-	0.21	0.49	0.21	0.09	0	0
5	C^+	0.49	0.21	0	0	0.09	0.21
6	C^-	0	0	0.21	0.49	0.21	0.09

It should be noted that, in order to obtain a satisfactory shape of the intensity profile, the simulated I(*l*) values had to be added to the I(−*l*) values. Thereby, the intensity profile of the other half of $[K_2Te_4O_{12}]$ rods, which were not included in the model, is eventually added. The two halves of rods are symmetrically related by a twofold rotation along an axis parallel to the stacking direction affected by disorder (**c**). Consequently, it is not surprising that their intensity distributions can be obtained from each other by inverting the *l*-axis of the simulation. In the planes of the sharp reflections representing the average structure, the *DIFFAX* simulations were unrealistic because half of the atoms present in the structure were then ignored. Nevertheless, it is noteworthy that a good approximation of the observed diffuse scattering can be obtained by taking into account the interactions between only one half of the $[K_2Te_4O_{12}]$ rods (Figure 50).

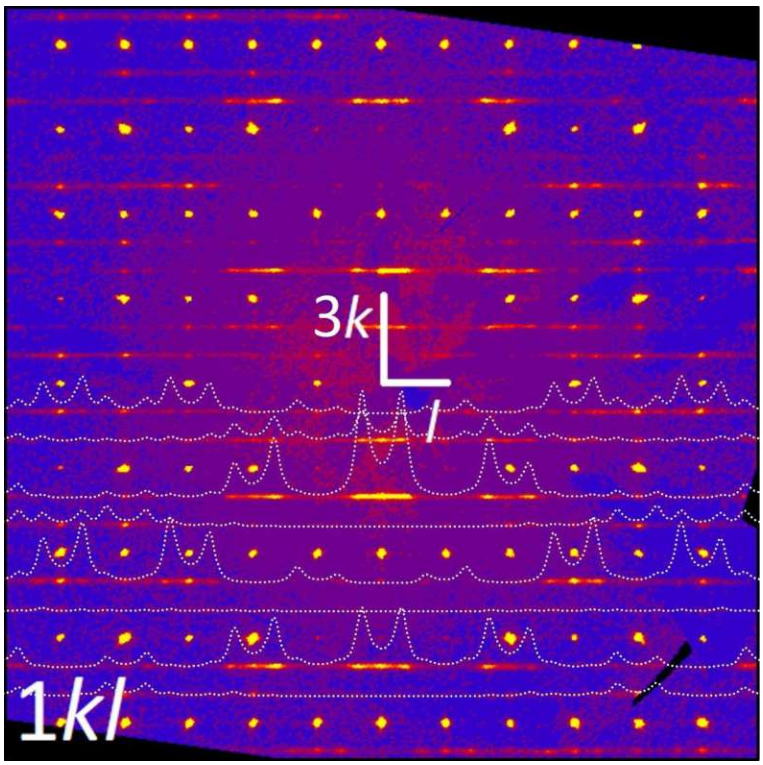

Figure 50. Reconstructed *1kl* plane of $K_2Cu_3Te_4O_{12}$. Dotted lines in the lower half correspond to intensity profiles simulated with *DIFFAX*. Peaks on diffuse rods at integer *h* values originate from streaks perpendicular to the drawn plane and are therefore not part of the simulation. Reciprocal lattice parameters refer to the unit-cell transformed for *DIFFAX*.

Simulated crystal structure considering the preferred stacking arrangement

After the preferred stacking was identified from *DIFFAX* simulations, it was tried to describe a hypothetical unit-cell under consideration of the preferred stacking. Given the satisfactory modelling of the diffuse scattering by interactions between only one half of the available $[K_2Te_4O_{12}]$ rods, different "ordered and stacking directions" for the two halves of $[K_2Te_4O_{12}]$ rods in one unit-cell (Figure 51) were considered for the hypothetical structure model.

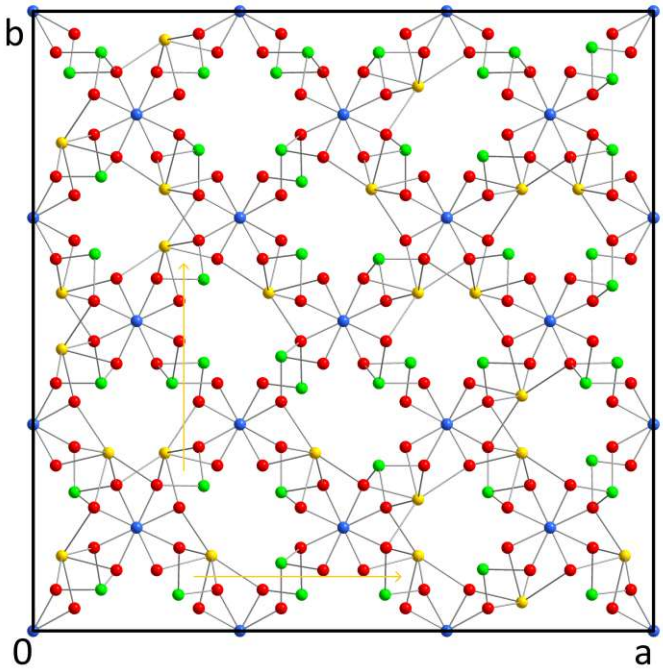

Figure 51. The super-cell used for simulations of the diffraction pattern in *JANA-2020* viewed along $[00\bar{1}]$. Only the region $0.06 < z < 0.46$ is drawn. "Ordered" direction of the two subgroups of $[K_2Te_4O_{12}]$ rods drawn in yellow.

For this purpose, an enlarged unit-cell with $\mathbf{a} = 3\mathbf{a}_{ave}$, $\mathbf{b} = 3\mathbf{b}_{ave}$ and $\mathbf{c} = 3\mathbf{c}_{ave}$ was constructed. Half of the $[K_2Te_4O_{12}]$ rods were positioned with a translational period of $\mathbf{a} = \mathbf{a}_{ave}$, $\mathbf{b} = 3\mathbf{b}_{ave}$ (corresponding to the disordered stacking direction) and the other half vice-versa with $\mathbf{a} = 3\mathbf{a}_{ave}$ and $\mathbf{b} = \mathbf{b}_{ave}$. Based on this super-cell, which follows $P\bar{1}$ space group symmetry, a single-crystal diffraction pattern was simulated with *JANA-2020* (Petříček et al., 2014). After including eight-fold twinning (fourfold rotation along **c** and the <100> and <110> mirror planes as twin operations) in order to account for the arbitrarily chosen directions of the preferred stacking and to be in accordance with the *P*4/*ncc* space group symmetry of the family structure, the simulated patterns show close agreement with the actual intensity data (Figure 52).

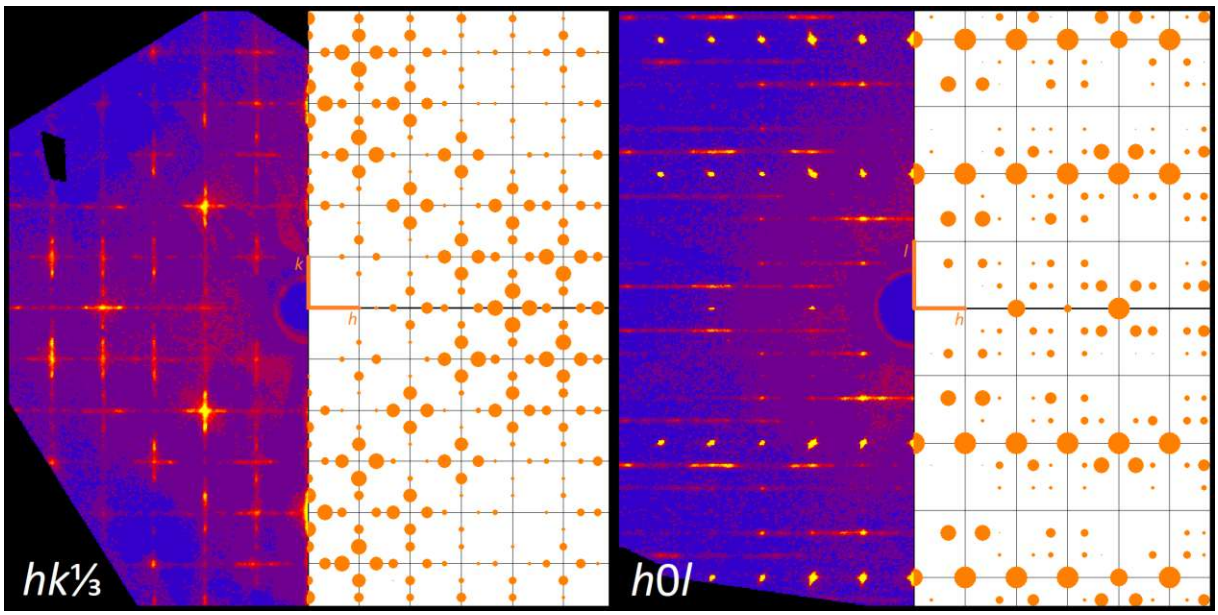

Figure 52. Reconstructed reciprocal lattice planes of $K_2Cu_3Te_4O_{12}$ compared with a simulation of the diffraction pattern in JANA-2020 of the $\mathbf{a} = 3\mathbf{a}_{ave}$, $\mathbf{b} = 3\mathbf{b}_{ave}$ and $\mathbf{c} = 3\mathbf{c}_{ave}$ super-cell corresponding to the preferred stacking.

Simulation attempts with *DISCUS*

In contrast to the strictly one-periodic approach of *DIFFAX*, simulation attempts introducing two-periodic disorder using the *DISCUS* suite (Proffen & Neder, 1997) were conducted.

In a preparatory step, the fractional coordinates of the three possible arrangements of a $[K_2Te_4O_{12}]$ rod on the four different positions (see numbers 1–4 in Figure 53) within a unit-cell of **a** = $\mathbf{a}_{ave}$, **b** = $\mathbf{b}_{ave}$ and **c** =3$\mathbf{c}_{ave}$ were prepared and saved as twelve .stru files. Then, based on this unit-cell, a large, two-periodic super-cell with dimensions of 81×81×1 unit-cells was created and filled with dummy Al atoms at *x*|*y* coordinates of 0|0, 0|1/2, 1/2|1/2 and 1/2|0. The choice of dummy atoms has no chemical meaning, the elements were assigned to represent the first letters of the alphabet. The chosen coordinates correspond to the locations of the $[K_2Te_4O_{12}]$ rods on positions 1, 2, 3 and 4. Using the *replace* command, one third of the Al atoms was randomly exchanged by dummy B atoms and afterwards, half of the remaining Al by dummy C atoms. Thereby, a random distribution of the three types of dummy atoms within the super-cell was warranted. Actually, Al, B and C represent the three different heights in **c** direction where the K^+ cations can be located within the rod (0 and +**c**/2, +**c**/6 and −**c**/3 or **c**/3 and −**c**/6).

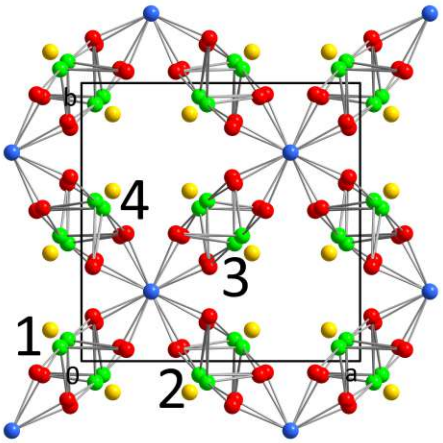

Figure 53. Description of the four different rod/ dummy atom positions used during DISCUS simulations.

Based on this random assignment of Al, B and C dummy atoms, the three atom types were now sorted using Monte−Carlo simulations. Hereby, several “ordering conditions” were applied by assigning certain types of neighbor-contacts corresponding “energy values”, which led to positive or negative correlations. The introduced conditions were:

- A strong negative correlation for same type of dummy atoms at next-neighbor contacts corresponding to the diagonal contact depicted in Figure 47, to inhibit the unfavored K···K contacts.
- A weak negative correlation for same type of dummy atoms at second-next neighbors in the same direction as above. This introduces the discovered preference of MDO_2 triples over MDO_1 triples.
- A medium-strong positive correlation for third-next neighbors in the same direction, which further supports the preference of MDO_2 triples over MDO_1 triples.
- Strong positive correlation for atoms of the same type as neighbors in the direction of the assumed translational symmetry. During initial tests, this condition was violated by the simulation very frequently. Therefore, this condition was expanded to the adjacent five unit-cells, after which the translational symmetry was followed much more consistently.

The now “ordered” dummy atoms were then replaced by more types of dummy atoms, one for each of the three rod possibilities on each of the four atomic positions in the unit-cell, resulting in a total of twelve different dummy atoms (named Al, As, At, Au, B, Ba, Be Bi, C, Ca, Co and Cs). Subsequently, each of the twelve dummy atom types had finally to be replaced by one of the twelve corresponding .stru rod-files, which turned out to be rather inapt and time-consuming:

A copy of the 81×81 plane of twelve dummy atom types was read into the program, and all but one of the atom types was deleted. This one-dummy-atom file was then used to define the places where the rods of the corresponding type were to be inserted into the structure (using the *domain* function and

the fitting .stru file). These steps were repeated for all twelve dummy atom types until an 81×81 layer of the disordered rod structure was completed.

Thereafter, using the *stack* command, an 81-layer stacking was generated. While this option is usually used to generate stackings under consideration of disorder, here it was applied to increase the periodicity of the model to be tri-periodic and to ensure that the strict translational symmetry along **c** was not violated.

Based on the generated stacking, the diffraction intensities were calculated by Fourier-transformation. Like the simulation in *JANA-2020*, the obtained diffraction pattern had to be added to the one that was obtained from a simulation based on the other possible translational symmetry. After adding the other diffraction patterns, corresponding to hypothetical twin domains, a suitable simulation was obtained. The representation of the reciprocal *hk*1/3 plane (Figure 54) is in accordance with the experimental diffraction pattern (Figure 45) or the simulation from *JANA-2020* (Figure 52).

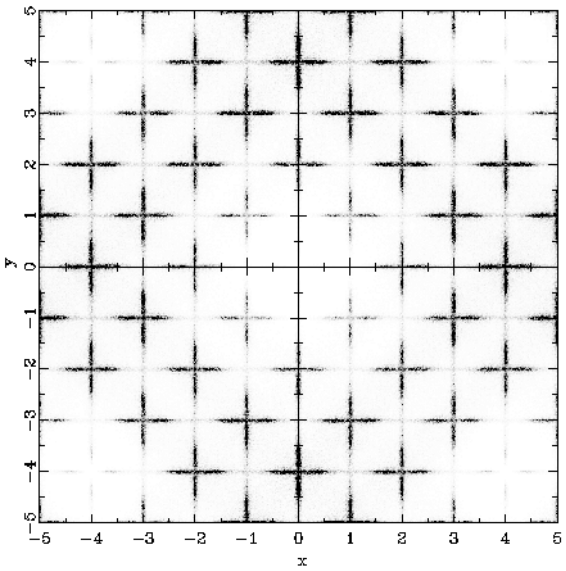

Figure 54. Simulated *hk*1/3 (referring to the average structure) diffraction pattern based on the presented model in *DISCUS*.

Problems with the presented simulations

While it is satisfying to be able to simulate the diffuse scattering of the diffraction pattern in various ways, the simulations in *JANA-2020* and *DISCUS* did not provide any additional insight into the arrangement of rods in the crystal structure of $K_2Cu_3Te_4O_{12}$. Although it is possible to describe the neighboring conditions for one half of the crystal structure, the interaction between the two "substructures of $[K_2Te_4O_{12}]$ rods" remains unclear. Two interpretations of this behavior seem plausible:

a) Both halves of the $[K_2Te_4O_{12}]$ rods have the same "ordered and disordered direction" within a domain. The cross-shaped diffraction pattern is a result of twinning induced by the fourfold rotation axis. In this case, there should be some distinct neighboring conditions between rods of different orientations directly next to each other in the [100] or [010] direction (whatever corresponds to the ordered direction). However, no such condition could be derived.

b) The disorder of half of the $[K_2Te_4O_{12}]$ rods is relatively independent from the other half. Within one domain, the "ordered and disordered direction" of the two groups of rods can be both the same or not, or might even change within a domain. As already mentioned previously, in this case some correlations

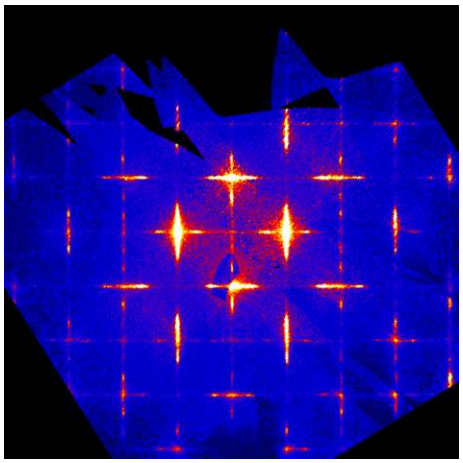

Figure 55. Reciprocal *hk*4/3 plane of $K_2Cu_3Te_4O_{12}$. The broadening of the streaks is clearly visible at the four intersections close to the center.

between all of the rods can exist, although the exact guiding principles remain unclear. Stronger correlations between the two "substructures of $[K_2Te_4O_{12}]$ rods" would result in a more complicated two-periodic disorder problem. A significant "widening" of the diffuse streaks in the higher intensity *hkn* planes (Figure 55) hints that this might indeed be the case.

The simulations in *JANA-2020* and *DISCUS* were performed under assumption of interpretation b) (independent groups of rods with translational symmetry in different directions). The simulated diffraction patterns fittingly match the experimental data. However, the simulations appear to be overparametrizied since they could only be generated under consideration of high-order twinning, which most likely "averages" over many aspects of the structure. Likewise, a structure model assuming that both "halves of $[K_2Te_4O_{12}]$ rods" share the same direction of translational symmetry and disorder, can satisfactorily match the experimental diffraction patterns as well, when high-order twinning is considered. Therefore, a deeper insight in the probable arrangement conditions of the $[K_2Te_4O_{12}]$ rods cannot be given at this stage.

4.1.3.3.4 $Na_2Cu_3Te_4O_{12}$

While for $K_2Cu_3Te_4O_{12}$, reasonable conditions for the arrangement of neighboring rods could be developed and proven with simulations in good accordance with the experimentally observed diffuse scattering, $Na_2Cu_3Te_4O_{12}$ turned out to be even more problematic. The diffuse streaks propagate parallel to <110> relative to the unit-cell of the average structure and, at first glance, have a distance of (h + k) or (h – k) from each other. Closer investigation revealed additional weak streaks half-way between the more intense ones. The diffuse rods are less structured than in $K_2Cu_3Te_4O_{12}$, but some minima and maxima are still discernable. No inferences about the potential size of the unit-cell under consideration of a preferred stacking can be drawn from the intensity profiles of the streaks, like it was possible for $K_2Cu_3Te_4O_{12}$.

Simulation experiments with *DIFFAX*

For attempts to model the diffuse scattering, it is favorable to change the setting of the unit-cell in a way that the diffuse streaks are parallel to a reciprocal cell axis. This was achieved with the following transformation matrix

$$\begin{pmatrix} 1 & 1 & 0 \\ \bar{1} & 1 & 0 \\ 0 & 0 & 3 \end{pmatrix}.$$

For simulations with *DIFFAX*, the axes were rotated to have **c** as the stacking direction. The resulting unit-cell is depicted in Figure 56. Other than in $K_2Cu_3Te_4O_{12}$, the choice of the stacking direction (**c**) and the direction of translational symmetry (**a**) is not arbitrary anymore. If, as for the K-compound, the diffuse scattering is simulated for one half of equally oriented [$Na_2Te_4O_{12}$] rods, the choice of the disorder direction heavily influences the obtained simulated intensities.

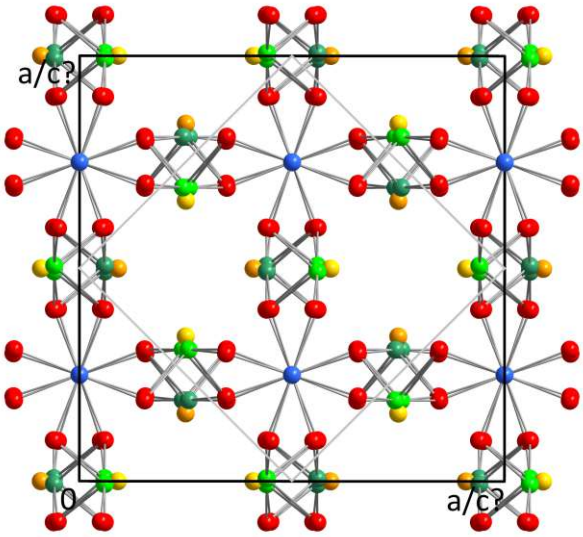

Figure 56. Unit-cell setting used for simulations of diffuse scattering of $Na_2Cu_3Te_4O_{12}$. Na and Te atoms at different *y* coordinates are colored either light green and yellow, or dark green and orange. The unit-cell of the average structure is drawn in grey.

Another point to consider pertains the ordered direction of translational symmetry (**a**), where only the second-next neighbor of the same [$Na_2Te_4O_{12}$] rod substructure is symmetrically connected by the unit-cell metrics. The relation of the arrangement of directly neighboring rods in the direction of translational symmetry (**a**) must be derived by an educated guess from the simulations. What complicates matters even more when compared to $K_2Cu_3Te_4O_{12}$, is that the main ordering condition for adjacent rods in the K-compound (the unfavourable K···K contacts of 3.291(5) Å) does not necessarily have to be fullfilled here as well. The Na sites are located much closer to the Te sites and a Na···Na pair from opposite rods has a much more reasonable distance of 3.744(8) Å. If all three types of hypothetical layer contacts are allowed, this further complicates the stacking description and, consequently, the OD theory is also not applicable because not all rod/layer pairs are geometrically equivalent anymore.

Nevertheless, some general conclusions can be drawn about the crystal structure of $Na_2Cu_3Te_4O_{12}$ based on the performed simulation attempts and the experimental diffraction patterns. In this regard, only horizontal streaks in Figure 57 are considered, with **a** being the direction of translational

symmetry, **b** (= 3$\mathbf{c}_{ave}$) the rod direction and **c** the direction of the disorder (green reciprocal lattice vectors):

- The intense diffuse streaks only appear at *h* odd in the *k* odd planes (Figure 57a) and at *h* even in the *k* even planes (Figure 57b, c), while streaks at *h* + *k* = odd are very weak. This behavior was not observed for $K_2Cu_3Te_4O_{12}$ and indicates a pseudo-*C* centering. This is caused by the fact that in the ordered **a** direction next to a [$Na_2Te_4O_{12}$] rod, the neighbouring rod is translated by **b**/2 (or ±**b**/6), and only the second-next rod is oriented the same way again. It is unclear, how this pseudo-*C* centering can be taken as a hint at the relationship between neighbouring rods in the ordered **a** direction.
- In the *k* = odd planes, the *l* = 0 streaks (which would be weak anyway) are completely missing, indicating the presence of a *b* glide reflection in the stacking direction **c**.
- As already mentioned for $K_2Cu_3Te_4O_{12}$, especially in the intense *k* = 4 plane (Figure 57c), deviations from the superposition of one-periodic streaks and the presence of two-periodic diffuse scattering can be observed. This indicates that a model, which only takes into account the disordered stacking of layers, is not accurate.
- In the higher *k* planes of the average structure, for reflections ($k = 3n$, $n \in \mathbb{Z}$) starting at the *h*6*l* plane (Figure 57d), weak signs of diffuse streaks are visible as well. This further indicates the deviation of the actual crystal structure from the idealized assumption of disordered layers, which are symmetrically equivalent.
- When simulating the diffuse scattering originating from one half of the [$Na_2Te_4O_{12}$] rods, choosing the direction, in which the lone pairs of the Te^{IV} atoms are directed and in which a Na···Na contact of 3.744(8) Å can exist, as stacking direction led to more appropriate results for the disorder model.
- It is likely that, other than in $K_2Cu_3Te_4O_{12}$, all [$Na_2Te_4O_{12}$] rods must be included into modeling to obtain a meaningful description of the experimental diffraction pattern. However, extensive simulation experiments have not yet led to a suitable modeling of the stacking disorder. Given the large amount of possible layer types and transition probabilities, it is possible that the correct combination has not been found so far.

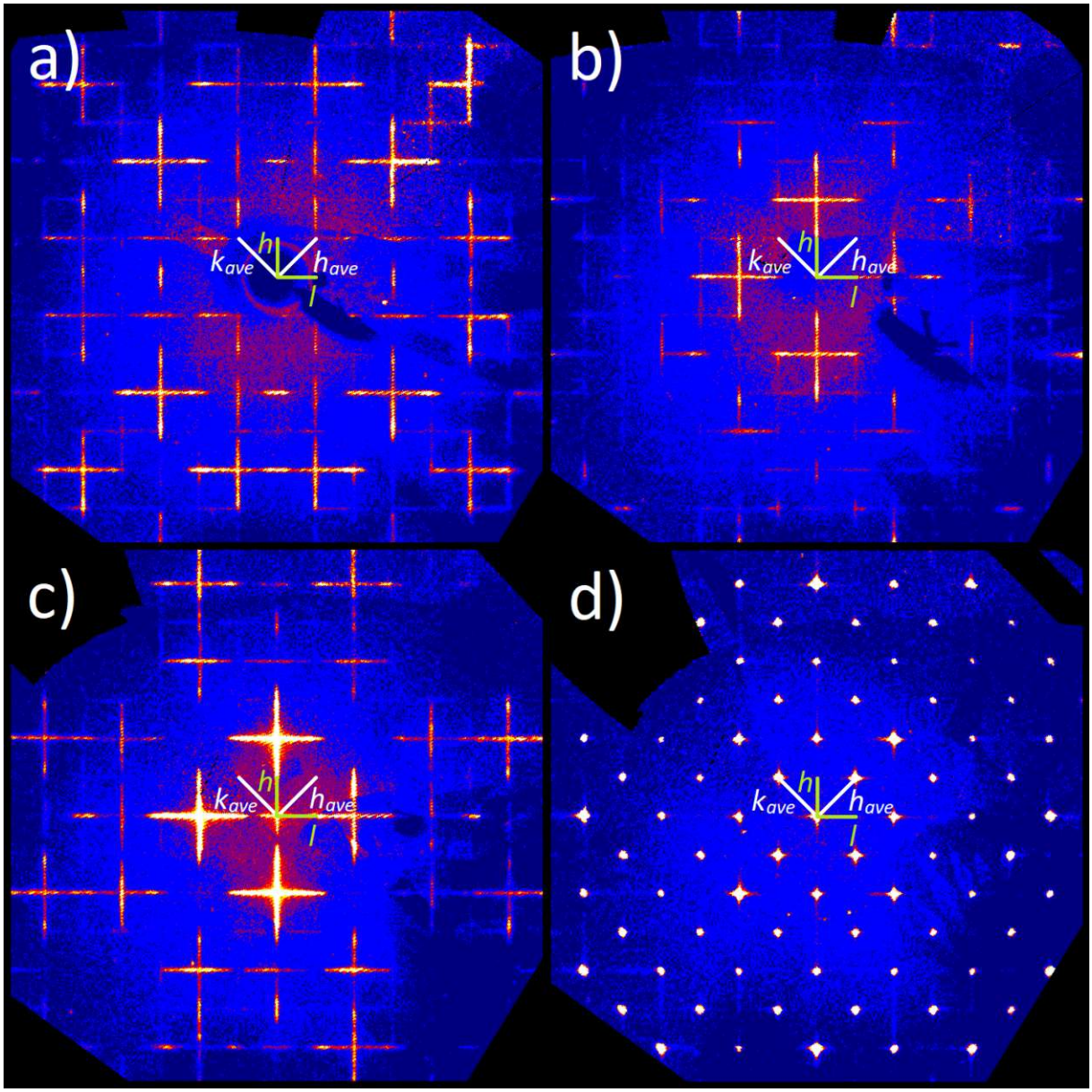

Figure 57. Reconstructed reciprocal lattice planes of $Na_2Cu_3Te_4O_{12}$ drawn relative to the unit-cell of Figure 56. Relative to the average structure (Table 10): a) *hk*1/3, b) *hk*2/3, c) *hk*4/3, d) *hk*2; relative to the *DIFFAX* model (Figure 56): a) *h*1*l*, b) *h*2*l*, c) *h*4*l*, d) *h*6*l*.

4.1.3.4 $A_2Cu_3Te_6O_{16}$ (A = K, Rb, Cs)

After the crystal structures of $Rb_2Cu_3Te_6O_{16}$ and $Cs_2Cu_3Te_6O_{16}$ have been published (Eder & Weil, 2022a), their K-analog was determined as well. The crystal structure of $K_2Cu_3Te_6O_{16}$ is isotypic with that of $Rb_2Cu_3Te_6O_{16}$ and isopointal to that of $Cs_2Cu_3Te_6O_{16}$. During re-evaluation of the data sets, it was noticed that the published unit-cell data of $Rb_2Cu_3Te_6O_{16}$ is inaccurate, and the re-determined values are discussed here.

Synthesis

Single crystals of $K_2Cu_3Te_6O_{16}$ have a dark green color and a block-like form. $K_2Cu_3Te_6O_{16}$ and $K_2Cu_2Te_4O_{11}(H_2O)_2$ (4.1.3.5) have both been obtained serendipitously as by-products from a hydrothermal reaction (H314) of $MnCl_2(H_2O)_4$, MnO_2, $CuCl_2(H_2O)_2$, TeO_2 and K_2CO_3 in molar ratios of 1.1:2:7:16. Initial goal of the experiment was a re-synthesis of a mixed $K[(Cu^{II}, Mn^{II}, Mn^{III})_2(TeO_3)_3]\cdot(H_2O)_2$ zemannite-type phase (Miletich, 1993; Eder et al., 2023c).

$Rb_2Cu_3Te_6O_{16}$ can be obtained from mixtures of CuO, TeO_2 and Rb_2CO_3 (molar ratios 2:3:6) under hydrothermal conditions (H319), or from a mild hydroflux reaction (H311). It forms intense green, block-shaped single crystals. $Rb_2Cu_3Te_6O_{16}$ was resynthesized under mild hydroflux conditions from stoichiometric ratios of CuO, TeO_2 and Rb_2CO_3 (H405) or a stoichiometric ratio of CuO and TeO_2 with an excess of Rb_2CO_3 (H404). In both types of batches, the leached product was single-phase $Rb_2Cu_3Te_6O_{16}$, as revealed by PXRD, albeit, in the case of H404 with a small impurity of CuO.

Like $Rb_2Cu_3Te_6O_{16}$, $Cs_2Cu_3Te_6O_{16}$ was obtained from a 2:3:6 mixture of CuO, TeO_2 and Cs_2CO_3 under mild hydroflux conditions (H335). Adding a water amount typical for hydrothermal experiments (H343) was not successful, and re-synthesis of $Cs_2Cu_3Te_6O_{16}$ based on stoichiometric ratios of CuO, TeO_2 and Cs_2CO_3 did not yield the desired phase (H406, H407). However, a hydrothermal experiment based on a 1:3:6 mixture of $CuCO_3\cdot Cu(OH)_2$, TeO_2 and Cs_2CO_3 (H351) yielded $Cs_2Cu_3Te_6O_{16}$ as the main phase.

Crystal structure

The asymmetric unit of all three phases contains three Te, two Cu, one *A* and eight O sites, with all atoms except for Cu2 (site symmetry $\bar{1}$, 2 *a*) being located at general 4 *e* positions.

The Te^{IV} atoms are connected to four (Te1) or three (Te2, Te3) oxygen atoms, resulting in a bisphenoidal shape for the [Te1O_4] unit and a trigonal-pyramidal shape for the [Te2,3O_3] groups. The coordination polyhedra of Te1 and Te2 are connected by corner-sharing, which results in [010] zig-zag-chains propagating parallel to [010] (Figure 58). Following the nomenclatures by Christy et al., (2016), these chains are denoted as Te_4X_{10} single chains (…−Δ−◊−Δ−◊−…), and the connectivities of the Te^{IV} atoms are described as Q^{2200} for Te1, Q^{1200} for Te2 and Q^{3000} for the isolated Te3. The $^1_\infty[Te_4O_{8/2}O_{6/1}]$ chains are interconnected by the square-planar coordination polyhedra of the Cu2 atoms in the [001] direction (Figure 59).

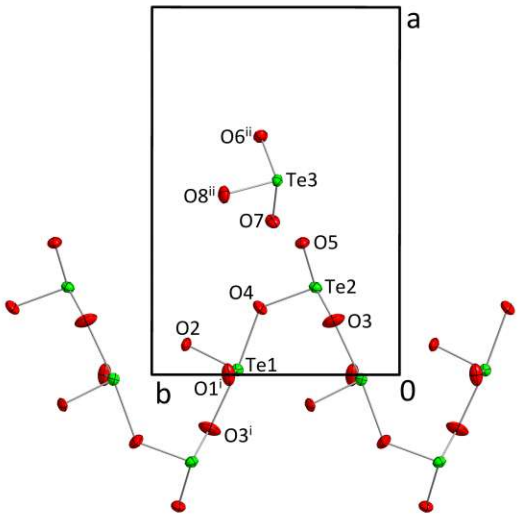

Figure 58. $^1_\infty[Te_4O_{10}]$ chains and [TeO_3] unit in the crystal structure of $K_2Cu_3Te_6O_{16}$. Symmetry codes refer to Table 15.

The differences between the isotypic K- and Rb-compounds compared to $Cs_2Cu_3Te_6O_{16}$ originate from the coordination sphere of the Cu1 site and the position of the Te3 atom and its adjacent oxygen atoms. While in the first two structures, Cu1 exhibits a fourfold coordination, close to a square-planar polyhedron, in $Cs_2Cu_3Te_6O_{16}$, a fifth oxygen contact at a distance of 2.590(4) Å changes the CN to [4+1] (Table 15). Through this fifth oxygen atom, the Cu1 atoms form $[Cu_2O_8]$ dimers in $Cs_2Cu_3Te_6O_{16}$, while they are present as isolated $[CuO_4]$ units in $K_2Cu_3Te_6O_{16}$ and $Rb_2Cu_3Te_6O_{16}$. The resulting differences are clearly visible in the (100) planes at $x \approx 0.5$, while those at $x \approx 0$ look virtually the same (Figure 60).

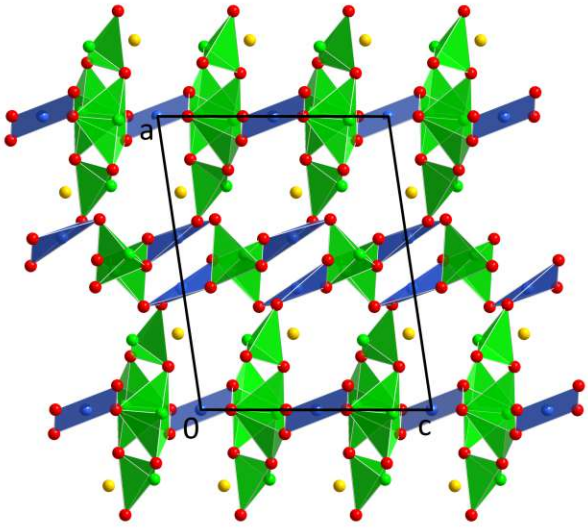

Figure 59. The crystal structure of $K_2Cu_3Te_6O_{16}$ viewed along $[0\bar{1}0]$.

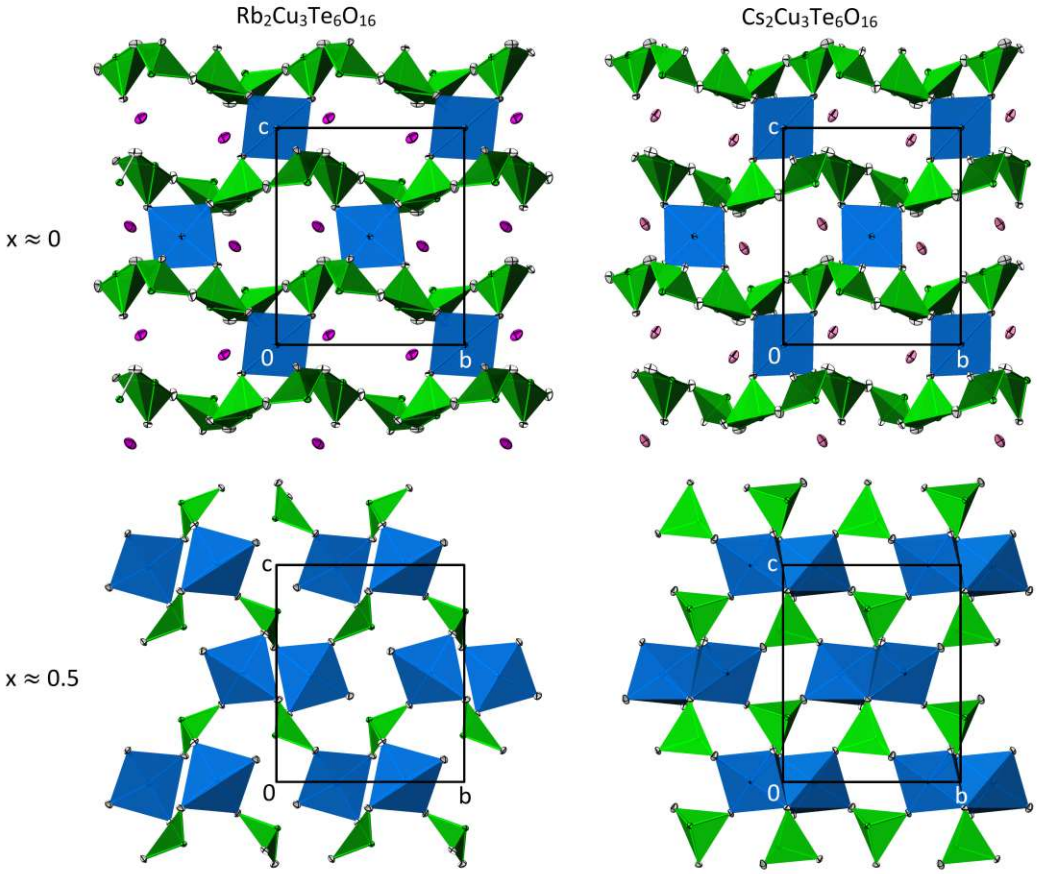

Figure 60. Comparison of (100) layers at different heights of *x* in the crystal structures of isopointal $Rb_2Cu_3Te_6O_{16}$ and $Cs_2Cu_3Te_6O_{16}$. Oxygen atoms are drawn in white, *A* atoms in pink. Structure representations were generated with ATOMS (Dowty, 2006).

The crystal structure of $K_2Cu_3Te_6O_{16}$ was quantitatively compared with both $Rb_2Cu_3Te_6O_{16}$ and $Cs_2Cu_3Te_6O_{16}$ using *compstru* (Table 14). The lattice parameters *a* and *c* and the unit-cell Volume *V* become larger with the increase of the ionic radii of the included alkali cation K^+–Rb^+–Cs^+. Interestingly,

the length of the *b*-axis of $Cs_2Cu_3Te_6O_{16}$ is smaller than that of both $K_2Cu_3Te_6O_{16}$ and $Rb_2Cu_3Te_6O_{16}$. This could be attributed to the closer contacts between the Cu1 atoms, which form $[Cu_2O_8]$ dimers in the Cs-compound but are isolated from each other in the K- and Rb- analogs, and the concomitant re-arrangement of the [Te3O$_3$] groups (Figure 60).

Comparing $K_2Cu_3Te_6O_{16}$ and $Rb_2Cu_3Te_6O_{16}$, the largest of the relatively small differences in atomic positions concern atoms of the $^1_\infty[Te_4O_{10}]$ chains. In comparison with isopointal $Cs_2Cu_3Te_6O_{16}$, the $^1_\infty[Te_4O_{10}]$ chains are the most preserved part of the crystal structure. The largest differences now belong to the Cu1 and Te3 atoms and their coordination polyhedra, most significantly the O7 position.

Table 14. Comparison of $K_2Cu_3Te_6O_{16}$ with isotypic $Rb_2Cu_3Te_6O_{16}$ and isopointal $Cs_2Cu_3Te_6O_{16}$.

	$K_2Cu_3Te_6O_{16}$	$Rb_2Cu_3Te_6O_{16}$	$Cs_2Cu_3Te_6O_{16}$
a / Å	11.9120(14)	12.264(6)	12.7754(7)
b / Å	7.9433(10)	8.055(4)	7.7715(4)
c / Å	9.2787(11)	9.405(6)	9.5782(5)
β / Å	98.456(3)	98.64(2)	97.696(2)
V / Å^3	868.4(2)	918.5(9)	942.40(9)
Coordinates of ψ			
ψ_{Te_1} (*x*, *y*, *z*)	−0.0210, 0.5098, 0.1155	−0.0234, 0.5015, 0.1119	−0.0390, 0.4838, 0.0994
ψ_{Te_2} (*x*, *y*, *z*)	0.2615, 0.2881, 0.1388	0.2595, 0.2838, 0.1425	0.2483, 0.2167, 0.1553
ψ_{Te_3} (*x*, *y*, *z*)	0.5772, 0.3806, 0.3872	0.5691, 0.4024, 0.3943	0.4165, 0.5892, 0.1524
BVS / v.u.			
Te1	4.04	4.05	4.03
Te2	3.94	3.94	3.95
Te3	3.98	4.02	3.98
Cu1	1.99	1.96	2.03
Cu2	1.96	2.00	2.04
*A*1	0.85	0.98	0.97
Quantitative comparison (*compstru*) of $K_2Cu_3Te_6O_{16}$ with the other two structures			
S / Å		0.0065	0.0257
d (Te1) / Å		0.0829	0.2653
d (Te2) / Å		0.0436	0.2103
d (Te3) / Å		0.0254	0.8588
d (Cu1) / Å		0.0099	1.1186
d (Cu2) / Å		0	0
d (*A*1) / Å		0.0818	0.0932
d (O1) / Å		0.0715	0.2134
d (O2) / Å		0.1060	0.3124
d (O3) / Å		0.1247	0.1586
d (O4) / Å		0.1252	0.5589
d (O5) / Å		0.0512	0.6293
d (O6) / Å		0.0687	0.7829
d (O7) / Å		0.0250	2.8043
d (O8) / Å		0.0177	0.6809
$d_{av.}$ / Å		0.0617	0.6435
$d_{max.}$ / Å		0.1252	2.8043
Δ		0.144	0.373

Table 15. Selected interatomic distances / Å in the crystal structures of $A_2Cu_3Te_6O_{16}$ (*A* = K, Rb, Cs). For three oxygen contacts of $Cs_2Cu_3Te_6O_{16}$, a different symmetry code applies.

d / Å	$K_2Cu_3Te_6O_{16}$	$Rb_2Cu_3Te_6O_{16}$	$Cs_2Cu_3Te_6O_{16}$
Te1—O2	1.859(2)	1.855(2)	1.855(4)
Te1—O1^{i}	1.863(3)	1.860(2)	1.858(3)
Te1—O3^{i}	2.099(3)	2.079(2)	2.170(4)
Te1—O4	2.135(3)	2.159(2)	2.093(4)
Te2—O3	1.886(3)	1.891(2)	1.873(4)
Te2—O5	1.888(3)	1.885(2)	1.857(3)
Te2—O4	1.896(3)	1.889(2)	1.888(4)
Te3—O7	1.886(2)	1.881(2)	1.867(3)
Te3—O8^{ii}	1.898(3)	1.891(2)	1.900(3) (O8)
Te3—O6^{ii}	1.920(3)	1.907(2)	1.897(3)
Cu1—O8^{iii}	1.905(3)	1.913(2)	1.922(3)
Cu1—O6	1.930(3)	1.937(2)	1.974(3)
Cu1—O7^{iii}	1.943(2)	1.945(2)	1.961(3) (O7^{x})
Cu1—O5	1.975(3)	1.981(2)	1.926(3)
Cu1—O7			2.590(4)
Cu2—O2^{iv}	1.940(2)	1.947(2)	1.931(3)
Cu2—O2^{v}	1.940(2)	1.947(2)	1.931(3)
Cu2—O1	1.944(3)	1.926(2)	1.927(4)
Cu2—O1^{vi}	1.944(3)	1.926(2)	1.927(4)
*A*1—O4^{vii}	2.733(3)	2.829(3)	3.263(4)
*A*1—O7^{viii}	2.802(3)	2.855(2)	3.322(3) (O7^{xi})
*A*1—O6^{ii}	2.828(3)	2.963(2)	3.207(3)
*A*1—O8	3.061(3)	3.178(2)	3.255(4)
*A*1—O4^{viii}	3.134(3)	3.185(3)	3.205(4)
*A*1—O1^{ix}	3.152(3)	3.226(3)	3.380(4)
*A*1—O2^{viii}	3.237(3)	3.240(2)	3.303(4)
*A*1—O2^{vii}	3.271(3)	3.363(2)	3.565(4)
*A*1—O5^{vii}	3.375(3)	3.379(2)	2.966(3)

Symmetry codes: (i) −*x*, 1/2+*y*, 1/2−*z*; (ii) 1−*x*, 1/2+*y*, 1/2−*z*; (iii) *x*, 1/2−*y*, 1/2+*z*; (iv) −*x*, 1−*y*, −*z*; (v) *x*, −1+*y*, *z*; (vi) −*x*, −*y*, −*z*; (vii) 1−*x*, −1/2+*y*, 1/2−*z*; (viii) 1−*x*, 1−*y*, −*z*; (ix) 1+*x*, *y*, *z*; (x) 1−*x*, 1−*y*, 1−*z*; (xi) *x*, 1/2−*y*, −1/2+*z*.

For a more detailed discussion of the crystal structures of $Rb_2Cu_3Te_6O_{16}$ and $Cs_2Cu_3Te_6O_{16}$, see:

Eder, F. & Weil, M. (2022a). The alkali metal copper(II) oxidotellurates(IV) $Li_2Cu_2Te_3O_9$, $Li_2Cu_3Te_4O_{12}$, $Rb_2Cu_3Te_6O_{16}$ and $Cs_2Cu_3Te_6O_{16}$ – four new structure types. *Z. Anorg. Allg. Chem*. **648**, 23: e202200089.

4.1.3.5 $K_2Cu_2Te_4O_{11}(H_2O)_2$

Single crystals of $K_2Cu_2Te_4O_{11}(H_2O)_2$ have the form of thin plates and a light blue-green color. Based on the PXRD pattern of H413, lattice parameters of $K_2Cu_2Te_4O_{11}(H_2O)_2$ were refined to a = 7.3990(4) Å, b = 9.8619(5) Å, c = 19.7445(3) Å, β = 96.9677(8)°, and a preferred orientation of the (00(2n)) planes was modeled.

Crystal structure

A single-crystal X-ray diffraction measurement at −173 °C yielded a unit-cell of slightly smaller size ($P2_1/c$, a = 7.3688(14) Å, b = 9.8118(19) Å, c = 19.675(4) Å, β = 96.821(6)°, V = 1412.5(5) Å^3). All atoms of the asymmetric unit, four Te, two Cu, two K and thirteen O, are located on sites corresponding to general 4 *e* positions. Hydrogen atoms could not be located.

The four Te^{IV} atoms are coordinated by three oxygen atoms each, leading to the common trigonal-pyramidal [TeO_3] units. Each lone pair ψ (coordinates: x = 0.1146, y = 0.8087, z = 0.0542 for ψ_{Te_1}; x = 0.3237, y = 0.4505, z = 0.1120 for ψ_{Te_2}; x = 0.0719, y = 0.6213, z = 0.2940 for ψ_{Te_3}; x = 0.4624, y = 0.2907, z = 0.0610 for ψ_{Te_4}) is directed away from the apex of the pyramid. The coordination polyhedra of Te2 and Te3 share one corner with each other, forming a [Te_2O_5] dimer, while the [$Te1O_3$] and [$Te4O_3$] pyramids are isolated from each other. The connectivities of the Te^{IV} atoms can be denoted as Q^{3000} for Te1 and Te4, and Q^{2100} for Te2 and Te3. The BVS of the Te^{IV} atoms were calculated to 3.92 (Te1), 3.87 (Te2), 3.88 (Te3) and 4.00 (Te4) v.u..

The copper atoms Cu1 and Cu2 exhibit a very similar [4+1] bonding environment of four oxygen atoms with distances of 1.927(6)–1.974(7) Å and a fifth contact at distances of 2.456(6) and 2.468(6) Å, respectively (Table 16). Considering the close contacts only, the corresponding [CuO_4] units both have a nearly square-planar shape, which is underlined by their geometry indices τ_4 of 0.204 (Cu1) and 0.108 (Cu2) being close to the value of 0 for a square. The [CuO_4] units are isolated from each other. However, if the fifth, more distant oxygen contact is considered, two [CuO_5] units form [Cu_2O_8] dimers by edge-sharing. The [CuO_5] polyhedra have a square-pyramidal shape, which is also visible from their geometry index τ_5. (0.185 for Cu1 and 0.120 for Cu2). The values of the BVS of the copper atoms are 1.99 (Cu1) and 2.02 (Cu2) v.u. involving the fifth oxygen contact, but are only 1.87 (Cu1) and 1.90 (Cu2) v.u. for a fourfold coordination. Therefore, a CN of 5 for the Cu^{II} atoms is used for the following structure descriptions.

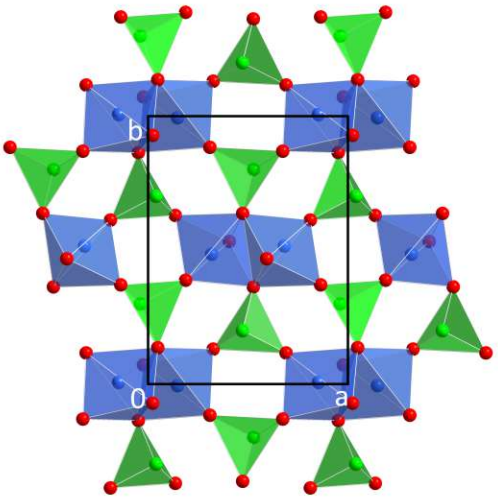

Figure 61. $^2_\infty$[$Cu_2Te_2O_8$] layer in the crystal structure of $K_2Cu_2Te_4O_{11}(H_2O)_2$.

The crystal structure of $K_2Cu_2Te_4O_{11}(H_2O)_2$ consists of $^2_\infty$[$Cu_2Te_2O_{6/3}O_{8/2}O_{2/1}$] layers extending parallel to (001), which are formed alternatingly by the [Cu_2O_8] dimers and isolated [$Te1O_3$] and [$Te4O_3$] units (Figure 61). These [$Cu_2Te_2O_8$] layers have the same structural set-up as those in the crystal structure of $Cs_2Cu_3Te_6O_{16}$, but not those in $K_2Cu_3Te_6O_{16}$ and $Rb_2Cu_3Te_6O_{16}$ (Eder & Weil, 2022a; 4.1.3.4). The difference in the crystal structures of $K_2Cu_2Te_4O_{11}(H_2O)_2$ and $Cs_2Cu_3Te_6O_{16}$ mainly originates from the different links between the layers. While in $Cs_2Cu_3Te_6O_{16}$, the connecting units can be described as infinite $^1_\infty$[$Te_4O_{8/2}O_{6/1}$] chains, which are connected by a square-planar [CuO_4] group, the layers in $K_2Cu_2Te_4O_{11}(H_2O)_2$ are cross-linked by [Te_2O_5] dimers. The interlayer space, which is not occupied by [Te_2O_5] units or their lone pairs, is filled with the K^+ cations and water molecules (Figure 62).

The crystal water molecules OW1 and OW2 were identified as such by the low BVS of 0.26 (OW1) and 0.53 (OW2) v.u.. Acceptors for potential hydrogen bonds with the water molecules were identified by a slight under-bonding in their BVS and their proximity to the water molecules. For OW1, O1 (2.809(9) Å, 1.75 v.u.) and O4 (2.778(10) Å, 1.78 v.u.) are possible acceptor atoms, for OW2, O1 (2.758(10) Å, 1.75 v.u.) and O11 (2.706(10) Å, 1.68 v.u.). All other oxygen positions exhibit BVS values slightly above 2.00 v.u.. The angles between the O atoms of the water molecules and the two potential acceptors of the hydrogen bonds are 106.9(3)° for O1—OW1—O4 and 107.5(3)° for O1—OW2—O11 and are thereby very close to the H—O—H-angle of water (104.5°).

The K^+ cations are coordinated by six (K1) and eight (K2) oxygen atoms with distances below 3.15 Å and have BVS of 1.07 and 1.18 v.u., respectively. The K^+ cations and H_2O molecules inhabit channels, which are oriented parallel to [100] (Figure 62).

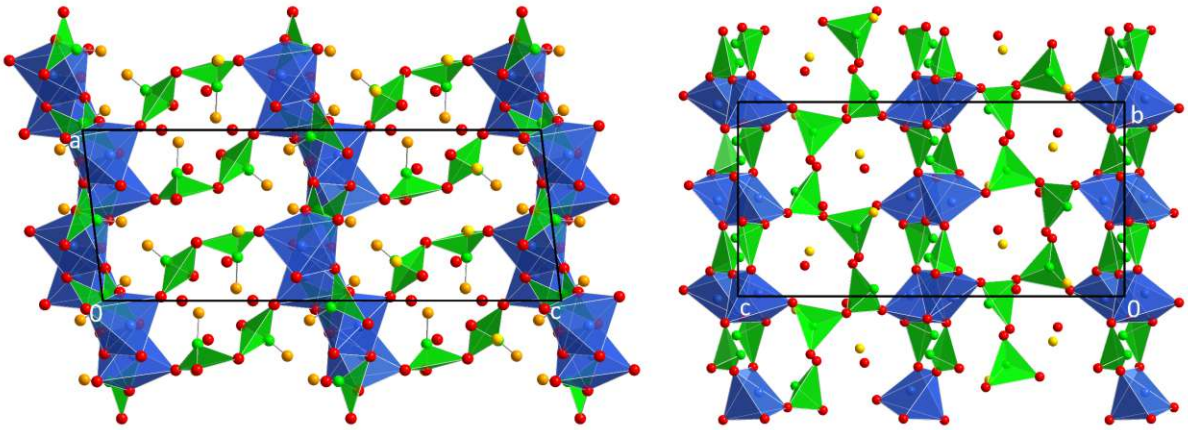

Figure 62. The crystal structure of $K_2Cu_2Te_4O_{11}(H_2O)_2$ viewed along [0$\bar{1}$0] including the Te^{IV} lone pairs (left) and viewed along [$\bar{1}$00] (right).

Table 16. Selected interatomic distances in the crystal structure of $K_2Cu_2Te_4O_{11}(H_2O)_2$.

	d / Å		*d* / Å
Te1—O3^{i}	1.875(6)	Cu2—O6^{v}	1.956(6)
Te1—O5^{ii}	1.881(6)	Cu2—O1^{viii}	1.961(6)
Te1—O2^{ii}	1.887(6)	Cu2—O2^{viii}	1.974(7)
Te2—O4	1.836(7)	Cu2—O2^{v}	2.468(6)
Te2—O1	1.894(6)	K1—OW2	2.592(7)
Te2—O8	1.954(6)	K1—O5	2.693(7)
Te3—O11^{iii}	1.821(7)	K1—O10	2.751(7)
Te3—O10^{iii}	1.857(6)	K1—OW1^{ix}	2.849(8)
Te3—O8	1.968(6)	K1—O4	2.885(7)
Te4—O7^{iv}	1.861(7)	K1—O3^{ix}	2.982(7)
Te4—O9^{iv}	1.863(6)	K2—OW2	2.686(7)
Te4—O6^{v}	1.873(6)	K2—O8^{x}	2.719(7)
Cu1—O9	1.950(7)	K2—O10^{iii}	2.731(7)
Cu1—O3	1.956(6)	K2—O7	2.781(7)
Cu1—O5^{vi}	1.969(6)	K2—O4	2.820(7)
Cu1—O10^{iii}	1.970(6)	K2—O11	3.019(7)
Cu1—O9^{vii}	2.456(6)	K2—OW1	3.123(8)
Cu2—O7^{iii}	1.927(6)	K2—O9	3.138(7)

Symmetry codes: (i) *x*, 3/2−*y*, −1/2+*z*; (ii) −*x*, 1−*y*, −*z*; (iii) 1−*x*, 1/2+*y*, 1/2−*z*; (iv) *x*, 1/2−*y*, −1/2+*z*; (v) 1−*x*, 1−*y*, −*z*; (vi) *x*, 1/2−*y*, 1/2+*z*; (vii) 1−*x*, 1−*y*, 1−*z*; (viii) 1+*x*, *y*, *z*; (ix) −*x*, −1/2+*y*, 1/2−*z*; (x) 1−*x*, −1/2+*y*, 1/2−*z*.

4.1.3.6 $K_4Sn_3Te_8O_{24}$

Crystals of $K_4Sn_3Te_8O_{24}$ were grown from a mild hydroflux reaction of SnO, TeO_2 and K_2CO_3 (molar ratios 2:3:10; H273). At least a part of the introduced Sn^{II} was oxidized to Sn^{IV}, although no reduced products hinting at the oxidation agent were identified by microscopy or PXRD. Single crystals of $K_4Sn_3Te_8O_{24}$ have the form of colorless, hexagonal plates with a diameter of *ca*. 200 µm. When cut with a surgical knife, some plates dissipate into thinner platelets, which glide to the sides. Several crystals from sample H273 have been investigated in single-crystal diffraction experiments, resulting in a variety of diffraction patterns for different crystals. What all crystals and determined crystal structures have in common, is the composition of $K_4Sn_3Te_8O_{24}$, and the same types of structural building blocks. In addition, their respective diffraction patterns are dominated by one-dimensional diffuse scattering.

Initially, two measurements (here denoted as I) and II)) of relatively large hexagonal crystals were performed on the Bruker Apex-II diffractometer. For measurements on the STOE STADIVARI instrument, a smaller crystal size was necessary due to the smaller beam diameter of the Mo-microfocus tube. Measuring fractions cut out of the large hexagonal crystals resulted in very diffuse reflections, which were often split into two or three sub-reflections. It appears possible that when cutting the crystal, parts of the lattice planes were slightly shifted or tilted by the applied stress with the knife, resulting in very poor peak profiles. From even smaller uncut crystals, for one, the unit-cell according to II) was confirmed, while for several other small crystals, a third, different unit-cell (III)) was determined. All resulting crystal structure models are of substandard quality, because the integrated intensities were strongly affected by the diffuse scattering. However, for I) and II), an ordering of layers and the preferred stacking thereof can be deducted. The unit-cell data of the three observed polytypes are collated in Table 17.

Table 17. Determined unit-cells for $K_4Sn_3Te_8O_{24}$ phases.

	I)	II)	III)
Crystal system	trigonal	monoclinic	monoclinic
Bravais type	*P*	*C*	*C*
a / Å	11.256(2)	19.536(12)	17.025(2)
b / Å		11.278(7)	11.2260(11)
c / Å	17.816(3)	12.477(7)	6.9092(9)
β /°		107.002(8)	102.538(11)
V / Å³	1954.9(6)	2629(3)	1289.0(3)
Z	3	4	2
V/*Z* / Å³	651.5	657.3	644.5

4.1.3.6.1 General features of the crystal structure of $K_4Sn_3Te_8O_{24}$ polytypes

The crystal structure of $K_4Sn_3Te_8O_{24}$ can be derived from $^2_\infty[Sn_3Te_8O_{24}]$ layers, which are interconnected only by intermediate K^+ cations. The rather weak interlayer interactions facilitate the observed stacking disorder. The $^2_\infty[Sn_3Te_8O_{36/2}O_{6/1}]$ layers include $[TeO_3]$ units, which are isolated from each other but linked by $[SnO_6]$ octahedra through corner-sharing. If all oxygen atoms would be corner-sharing two coordination polyhedra, this would result in a charge-balanced formula of $^2_\infty[Sn_4Te_8O_{24}]$ for the layers. Instead, every fourth potential Sn position is empty, resulting in six oxygen atoms being connected only to a Te^{IV}, but no Sn^{IV} atom.

The individual layers have idealized $p\bar{3}m$ symmetry ($a = b \approx 11.26$ Å, $\gamma = 120°$). For description of the different observed polytypes of $K_4Sn_3Te_8O_{24}$, the individual layers can be divided into hexagonal tiles using a honeycomb net (Figure 63). The positions of the Sn, Te and K atoms can be ascribed relative to one of the hexagons. The hexagon covering is divided into three classes of hexagonal tiles, which are denominated with letters *A*, *B* and *C*. The Sn^{IV} atoms of a specific layer and its void are located exclusively on either the *A*, *B* or *C* hexagons. The other two types of tiles are occupied by the Te^{IV} atoms.

Half of the Te^{IV} atoms have their lone pairs directed above the plane, the other half below the plane. Next to the void, the six adjacent Te^{IV} atoms are alternatingly pointing up and down, while next to a $[SnO_6]$ unit, three Te^{IV} atoms next to each other point upwards and the other three downwards.

The K^+ cations between two layers are also exclusively located on exactly one type of hexagonal tile, which is not the same as that of the Sn^{IV} atoms for the contacting layer. Since the two layers of K^+ cations above and below a $^2_\infty[Sn_3Te_8O_{24}]$ layer are not positioned on the same type of hexagonal tiles, they occupy the two types of tiles, which are also co-occupied by the Te^{IV} atoms of the layer. Hereby, the K^+ cations are preferably positioned on the opposite direction of the Te^{IV} atom and its lone pair relative to the $[TeO_3]$ group. This is realized in a straightforward way for the six Te^{IV} atoms next to the void, as neighboring Te^{IV} atoms are directed towards the opposite direction. For the other two Te^{IV} atoms, this requirement cannot be fulfilled, leading to a displacement of the K^+ cations away from the Te^{IV} atom. Thereby, the distribution of the K^+ cations is distorted, as emphasized in Figure 65.

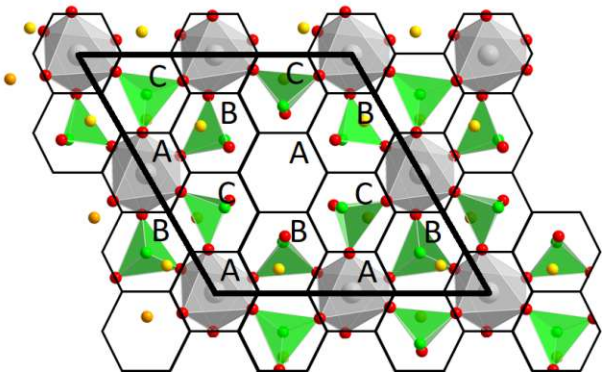

Figure 63. A $^2_\infty[Sn_3Te_8O_{24}]$ layer in the crystal structure of $K_4Sn_3Te_8O_{24}$. Sn atoms are drawn grey. The honeycomb net forming three types of hexagonal tiles (A, B and C) is used for describing the different stackings.

Placing the next $^2_\infty[Sn_3Te_8O_{24}]$ layer onto a K^+ layer follows simple rules: The Sn^{IV} atoms are preferably placed on a different hexagonal tile than in the previous layer. Because Sn^{IV} atoms and neighboring K^+ cations do not occupy the same type of tile, only one option remains for the following layer. While the placement of the adjacent layer concerning the overall positions of Sn^{IV} and Te^{IV} on their respective hexagonal tiles seems to be rather simple, the placement of the void within the $^2_\infty[Sn_3Te_8O_{24}]$ layer is more complex. The position of the void is influenced by the distribution of the K^+ cations in the adjacent layer. As it can be seen in Figure 65, the K^+ cations next to the void are all displaced away from it. The void of the next layer can ideally be placed in such a manner that the K^+ cations of the given layer have the largest possible distance from it. However, this condition is assumed to be violated in some cases and to be the origin of the observed stacking disorder.

4.1.3.6.2 I) Trigonal $K_4Sn_3Te_8O_{24}$

The determined unit-cell ($P3_2$; a = 11.2563(16) Å, c = 17.816(3) Å, V = 1954.9(6) Å^3) follows the metrics of a single $^2_\infty[Sn_3Te_8O_{24}]$ layer in the **a** and **b** directions, and the length of **c** corresponds to a stacking of three layers (Figure 64). The asymmetric unit contains eight Te, three Sn, four K and 24 O sites, all belonging to general 3 *a* positions. The stacking disorder and the unaccounted diffuse scattering resulted in the presence of high remaining electronic density peaks in difference-Fourier maps. They correspond to the positions of the heavy atoms of the other layer types and are also known as "shadow atoms". In addition, the loss of electronic density from the "main positions" of Te^{IV} and Sn^{IV} causes several of corresponding atoms to exhibit negative ADPs when refined with full occupancy. If the Te^{IV} and Sn^{IV} atoms are refined with isotropic displacement parameters, most oxygen atoms exhibit negative U_{eq} values.

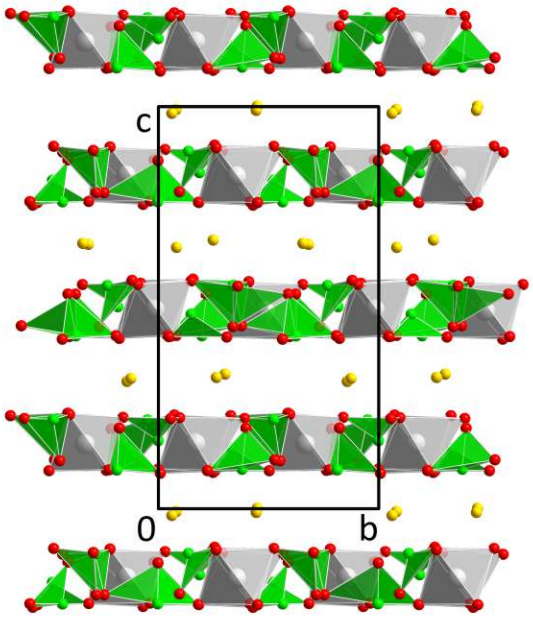

Figure 64. The crystal structure of trigonal $K_4Sn_3Te_8O_{24}$ viewed along [$\bar{1}$00].

The distorted distribution of the K^+ cations (rhomboids of different sizes in Figure 65) causes the void in the $^2_\infty[Sn_3Te_8O_{24}]$ layer to stay in the same region of the layer, alternating between three adjacent hexagonal tiles. Hereby, the void is always in the center of one of the two equilateral triangles forming the large rhombus in the distribution of K^+ cations. This can be recognized in the left half of Figure 65, where the respective layer is located between the potassium cations given in yellow and purple color.

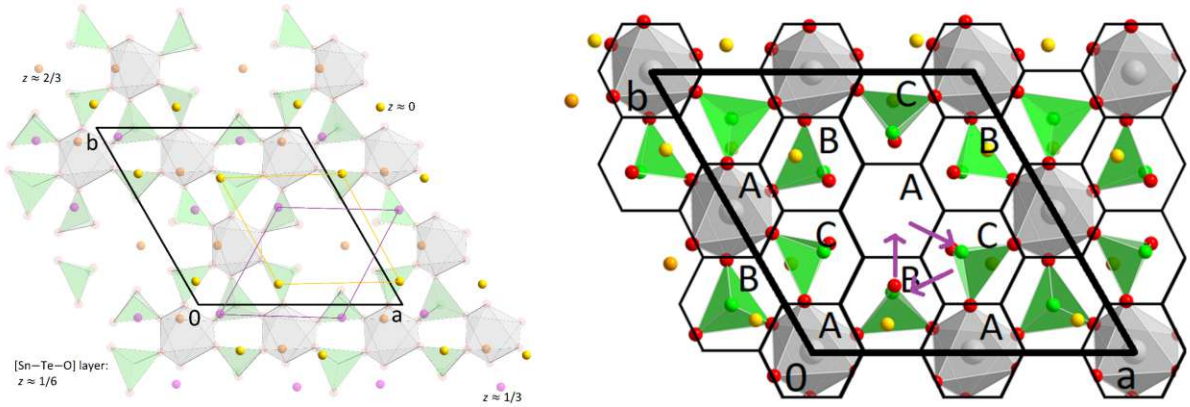

Figure 65. Illustrations on the stacking within the trigonal $K_4Sn_3Te_8O_{24}$ polytype, as viewed along [00$\bar{1}$]. Left: Distribution of K^+ cations above (purple) and below (yellow) a given $^2_\infty[Sn_3Te_8O_{24}]$ layer. Right: Evolution of the location of the hole in the $^2_\infty[Sn_3Te_8O_{24}]$ layer when moving along the stacking direction.

Closer inspection of the reconstructed reciprocal space images (Figure 66) revealed an even larger *c*-axis, assumably a stacking of six layers. However, no feasible integration procedure and structure solution could be accomplished on the basis of this stacking.

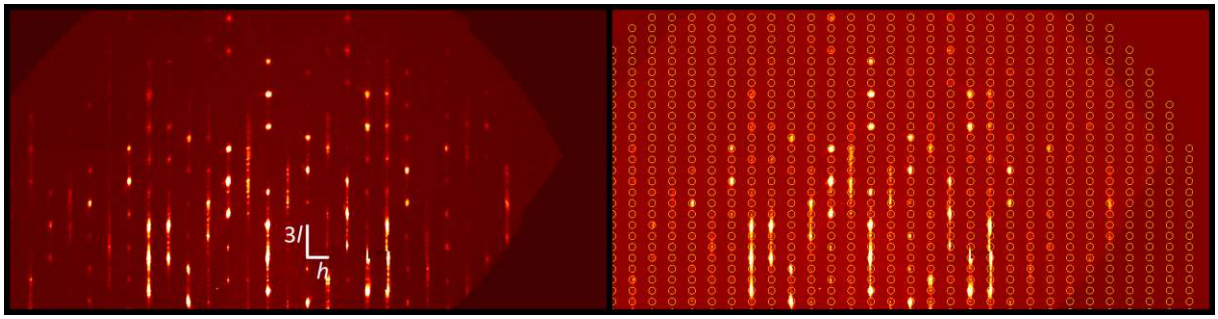

Figure 66. Reconstructed reciprocal *h*4*l* plane of trigonal $K_4Sn_3Te_8O_{24}$. On the right part, possible reflection positions relative to the trigonal unit-cell I) are marked.

4.1.3.6.3 II) Monoclinic $K_4Sn_3Te_8O_{24}$

This polytype was observed for several crystals and includes only two layers in the unit-cell (*C*2/c, *a* = 19.536(12) Å, *b* = 11.278(7) Å, *c* = 12.477(7) Å, *β* = 107.002(8)°, *V* = 2629(3) Å^3). Relative to the trigonal cell, $\mathbf{a}_{mon} = \mathbf{2a}_{tri} + \mathbf{b}_{tri}$, and **c** is no longer perpendicular to the layers, from which the structure is built. The asymmetric unit contains 20 atoms, four Te, two Sn, two K and twelve O. The Sn2 atom is located at a position with site symmetry 2 (4 *e*), while all other atoms correspond to general 8 *f* positions. The integrated intensity data and the concomitant refinement is, as in I), strongly influenced by diffuse scattering. Several strong peaks of residual electronic density corresponding to "shadow atoms" are also part of the model. As some of these "shadow atoms" are in close vicinity to oxygen positions, the coordinates of the respective oxygen atoms had to be fixed in the refinement.

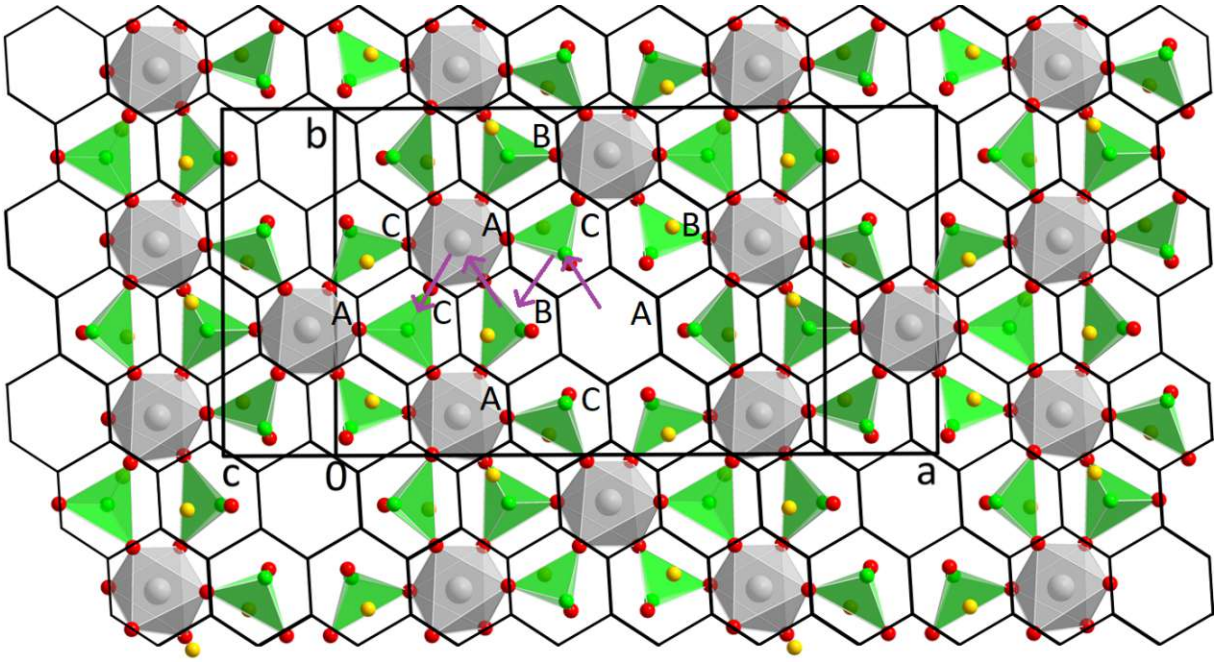

Figure 67. A (001) projection of a $^2_\infty[Sn_3Te_8O_{24}]$ layer in the monoclinic polytype of $K_4Sn_3Te_8O_{24}$. Purple arrows indicated the propagation of the hole within the $^2_\infty[Sn_3Te_8O_{24}]$ layer when progressing in the stacking direction.

The stacking of the layers follows, in principle, the same rules as previously discussed. The Sn^{IV} atoms in adjacent layers alternate their position from either A, B or C tiles, the Te^{IV} atoms within a layer are located on the other two types of hexagonal tiles. However, the distribution of the K^+ cations shows a slightly different pattern, owing to a different placement of the K^+ cations located on the same side of the layer relative to a neighboring Te^{IV} atom. This influences the placement of the void in the layer

when progressing through the stacking. Instead of a constant alteration between the same three hexagonal tiles, the location of the void follows a zigzag like path when viewed perpendicular to the layer plane. The inclination of **c** follows the path of the void from one layer to the second next (Figure 67).

Like for the trigonal polytype, the precession images exhibited additional reflections along **c*** (Figure 68). This feature was observed for different crystals on both diffractometers. The additional reflections are located in the middle between two expected reflections and hint at a duplication of the *c*-axis. However, as for the stacking in the trigonal structure of I), a suitable (and thus more complicated) model could not be obtained.

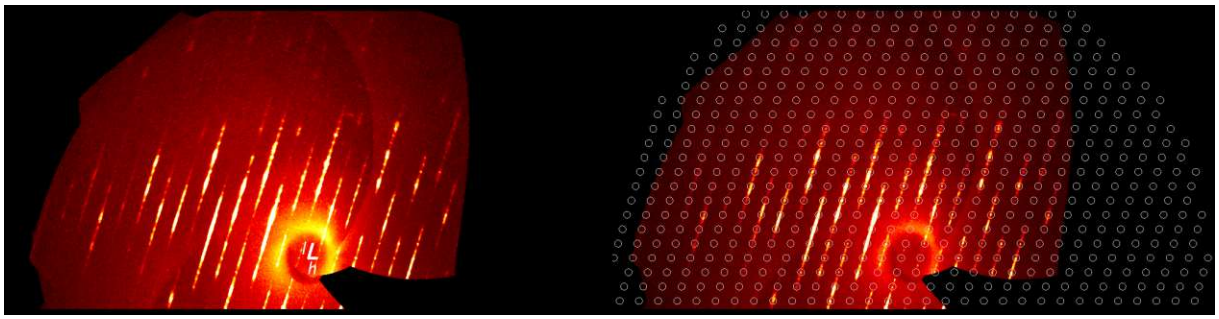

Figure 68. Reconstructed reciprocal *h*1*l* plane of monoclinic $K_4Sn_3Te_8O_{24}$. On the right part, possible reflection positions relative to the monoclinic unit-cell II) are marked.

4.1.3.6.4 III) A different monoclinic polytype

The unit-cell of III) given in Table 17 was determined from several crystals investigated with the STOE Stadivari diffractometer. Given the difficulties of the handling of datasets with (extreme) diffuse scattering by the instrument software, no structural model of even limited quality could be obtained. From preliminary crystal structure solution attempts, a layered structure is recognizable, and it can be assumed that the composition is $K_4Sn_3Te_8O_{24}$ as well. The *b*-axis has the same length as in structures I) and II), while the *a*- and *c*-axes connect atoms belonging to the next and second-next layers, respectively.

4.1.4 Rubidium

4.1.4.1 Hydrothermal experiments

The series of batches H310−H317 includes mild hydroflux reactions starting from metal oxides (Mn^{II}, Cu^{II}, Fe^{III}, Zn^{II}, Cr^{III}, Ni^{II}, Cd^{II} and Pb^{II}), TeO_2 and Rb_2CO_3 in molar ratios of 2:3:6 and three droplets of water. Several products exhibited unassignable reflections in their PXRD patterns, some of which could by explained by new phases structurally determined afterwards.

While the PXRD pattern of H310 (Mn^{II}) can be completely explained by the phases $MnCO_3$, $Mn_2Te_3O_8$ (Cooper & Hawthorne, 1996) and $Mn_{15}(TeO_3)_{14}(OH)_2$ (3.7.1), additionally, single crystals belonging to a zemannite-type phase with a composition of $Rb_{1.5}[Mn_2(TeO_3)_3](H_2O)_{1.25}$ (4.1.6.2) were obtained. The leached residue of experiment H311 (Cu^{II}) consisted of the new oxidotellurate(IV) phase $Rb_2Cu_3Te_6O_{16}$ (4.1.3.4) in almost phase-pure form besides minor traces of CuO as determined by PXRD. The Fe^{III}-based experiment H312 contained a variety of iron oxide and hydroxide phases but still a multitude of reflections remained unassigned. Experiment H313 (Zn^{II}) yielded a mixture of $Rb_4(HCO_3)_2(CO_3)(H_2O)$ (Cirpus & Adam, 1995) and the new phase $Rb_2Zn(TeO_3)(CO_3)(H_2O)$ (4.1.4.2). The PXRD pattern of H315 (Ni^{II}) exhibits unassignable reflections at lower diffraction angles. The three most intense reflections are located at 11.13, 22.40 and 32.54° 2θ, corresponding to *d*-values of 7.94, 3.97 and 2.75 Å. Given the fact that the first two reflections are the first two observed reflections at all, and their *d*-values are twice of one another, this can hint to a phase exhibiting preferred orientation, possibly a layered crystal structure.

The second series, based on the same reactants but with a water filling degree of *ca*. 2/3, (H318−H325) did not yield any new phases. $Rb_2Cu_3Te_6O_{16}$ was obtained again in the Cu^{II}-based experiment H319, but with a significantly higher amount of starting material CuO as a product. The main phase in the diffraction patterns of H322 (Cr^{III}) and H323 (Ni^{II}) resembles that of $Rb_2Te_4O_9(H_2O)_2$ (Chen et al., 2018), whereby the observed differences might hint at a different hydration state.

4.1.4.2 $Rb_2Zn(TeO_3)(CO_3)(H_2O)$

Colorless plates of $Rb_2Zn(TeO_3)(CO_3)(H_2O)$ were obtained from ZnO, TeO_2 and Rb_2CO_3 (2:3:6) and small amounts of water and were isolated directly from the reaction products. Neither $Rb_2Zn(TeO_3)(CO_3)(H_2O)$, nor the other products $Rb_4(HCO_3)_2(CO_3)(H_2O)$ (Cirpus & Adam, 1995) or $Rb_2(CO_3)(H_2O)_{1.5}$ (Cirpus et al., 2001) are stable after leaching the reaction products in water. The PXRD pattern of the washed product consisted of only a few broad reflections not belonging to either phase.

The crystal structure of $Rb_2Zn(TeO_3)(CO_3)(H_2O)$ is layered and exhibits stacking disorder, detectable from one-dimensional diffuse streaks in the diffraction pattern. This behavior can be explained by OD theory (Dornberger-Schiff & Grell Niemann, 1961), and the crystal structure consists of two types of apolar layers.

The first layer type (A^1) is formed by trigonal-pyramidal [TeO_3] groups, [ZnO_4] tetrahedra and atoms of one of the two Rb^+ cations (Rb1). The coordination polyhedra of Te^{IV} and Zn^{II} together form $^2_\infty[ZnTeO_{6/2}O_{1/1}]$ layers extending parallel to (100). Two of these [$ZnTeO_4$] layers are connected by a layer of $Rb1^+$ cations and together form this first layer type.

The other layers (A^2) consist of the CO_3^{2-} anions, the H_2O molecules and the $Rb2^+$ cations. Layer A^2 comprises two layers of carbonate anions and water molecules of crystallization connected to a central layer of $Rb2^+$ cations. Discernable from the refinement, the A^2 layers also exhibit "shadow atoms" corresponding to an alternate stacking possibility.

The A^1 layer type has a higher translational symmetry, manifested by an *A*-centering relative to the primitive A^2 layers. This leads to a symmetrical ambiguity when stacking A^2 layers onto A^1 layers and consequently to the observed stacking disorder. Based on an OD-analysis, the MDO polytypes were determined (Dornberger-Schiff, 1982; Dornberger-Schiff & Grell, 1982b), and the MDO_2 polytype (Figure 69) was found to be in agreement with the observed diffraction pattern. It consists of two A^1 and A^2 layers each and has monoclinic symmetry (*I*2/*c*, a = 29.5915(12) Å, b = 5.8670(3) Å, c = 10.3140(5) Å, β = 104.736(2)°, V = 1731.75(14) Å^3).

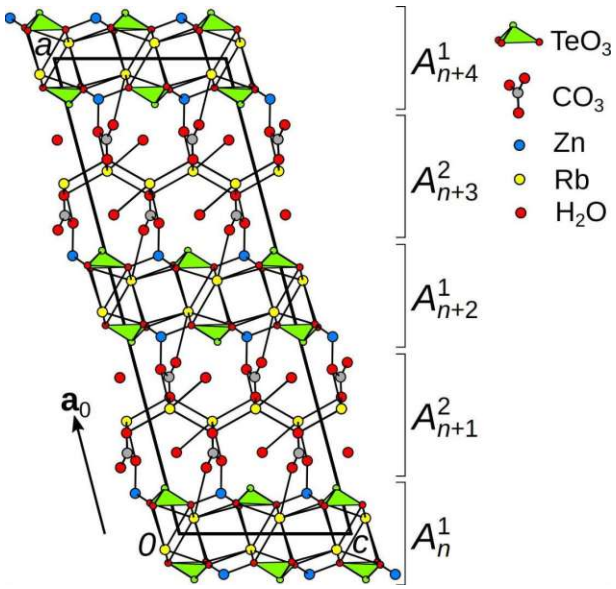

Figure 69. The preferred stacking in the crystal structure of $Rb_2Zn(TeO_3)(CO_3)(H_2O)$. Structure representation was generated with ATOMS (Dowty, 2006).

For a more detailed discussion of the crystal structure and a detailed OD-analysis, see:

Eder, F., Stöger, B. & Weil, M. (2022a). Order-disorder (OD) structures of $Rb_2Zn(TeO_3)(CO_3)\cdot H_2O$ and $Na_2Zn_2Te_4O_{11}$. *Z. Kristallogr. – Cryst. Mater.* **237**, 8–9, 329–341.

4.1.5 Cesium

4.1.5.1 Hydrothermal experiments

Like for the Rb-based samples, mild hydroflux experiments of metal oxides (Mn^{II}, Cu^{II}, Fe^{III}, Zn^{II}, Cr^{III}, Ni^{II}, Cd^{II} and Pb^{II}), TeO_2 and Cs_2CO_3 in molar ratios of 2:3:6 (H334−H341) resulted in a higher number of non-literature phases than the more hydrated setup (H342−H349). The PXRD pattern of H334 (Mn^{II}) can be explained by a mixture of MnO, $Mn_2Te_3O_8$ (Cooper & Hawthorne, 1996) and the new zemannite-type phase $Cs[Mn_2(TeO_3)_3](H_2O)$ (4.1.6.2). The leached product of H335 (Cu^{II}) is phase-pure $Cs_2Cu_3Te_6O_{16}$ (4.1.3.4), another novel oxidotellurate(IV), as revealed by PXRD. The Fe^{III}-based batch H336 yielded an unknown phase besides Fe_2O_3 with a PXRD pattern resembling that of a compound with a body-centered cubic (a ≈ 13.7−13.8 Å) unit-cell like that of $Cs_2CdSi_5O_{12}$ (Bell et al., 1994) or $CsGaSi_2O_6$ (Bell & Stone, 2021). This could indicate a possible composition of $CsFeTe_2O_6$ for the unidentified side-product. In the Ni^{II}-based sample H339, an additional phase besides NiO and $Cs_2Te_4O_9$ (Loopstra & Goubitz, 1986) was observed. However, neither in H336 or H339, suitable single crystals for structure determination were obtained.

From the second series of batches (H342−H349), new compounds were not obtained. Samples H344 (Fe^{III}, similar to H336) and H346 (Ni^{II}, possibly a layered nickel oxide intercalated with Cs^+ cations and crystal water molecules) exhibited unidentified phases in their PXRD patterns. Likewise, suitable single crystals for structure determinations were not available.

For the metals Mn^{II}, Cu^{II}, Co^{II}, Ni^{II} and Cd^{II}, hydrothermal experiments were conducted based on the metal carbonate instead of the oxide (H350−H354). No novel oxidotellurate(IV) phases were found in the reaction products except for the re-synthesis of $Cs_2Cu_3Te_6O_{16}$ from sample H350 (Cu^{II}).

4.1.6 Zemannite-type structures

The structure type of novel *A*–*M*–Te^{IV}–O-phases adapted in most cases was the zemannite structure type with a dozen new crystal structures determined. Its name originates from the mineral zemannite, which was named in honor of the Austrian mineralogist and crystallographer Josef Zemann (1923–2022). Originally, its composition was assumed as $Na_xH_{2-x}[(Zn^{II},Fe^{III})_2(TeO_3)_3](H_2O)_y$ (Matzat, 1967) and later revised to $Mg_{0.5}[Zn^{II}Fe^{III}(TeO_3)_3](H_2O)_{4.5}$ (Miletich, 1995a).

Most of the novel zemannite-type phases were obtained during the exploratory combination of various transition metal oxides, TeO_2 and alkali metal carbonates under hydrothermal conditions with variable water contents. Additional experiments targeted at zemannite-type phases were performed during the internship of Alexandre Marsollier (H428–H469). Six different transition metal cations (Ni^{II}, Cu^{II}, Co^{II}, Mn^{II}, Zn^{II} and Cd^{II}) were introduced in form of their respective oxides into hydrothermal or mild hydroflux reactions with TeO_2 and A_2CO_3 (*A* = Na, K, Rb, Cs). Some of the performed experiments were reruns of previous syntheses with the goal to obtain crystals of better quality for single-crystal diffraction experiments.

Zemannite-type phases were identified in numerous products. A summary of all refined lattice parameters (PXRD data) of zemannite-type phases is given in Table 18.

Table 18. Summary of all obtained zemannite-type phases, as revealed from PXRD measurements.

Batch	*A*	*M*	Water	*a* / Å	*c* / Å	*V* / Å^3
H254	K	Cu	yes	9.3581(4)	7.6622(4)	581.1
H266	Na	Ni	3 dr.	9.1774(2)	7.6361(2)	557.0
H272	K	Mg	3 dr.	9.39953(12)	7.68685(9)	588.2
H281	Na	Cu	yes	9.2628(15)	7.6250(15)	566.6
H334	Mn	Cs	3 dr.	18.7945(7)	7.8285(3)	2394.8
H357	K	Ni	yes	9.321(2)	7.656(2)	576.0
H358	K	Ni	yes	9.3246(7)	7.5967(6)	572.0
H367	K	Ni	yes	9.2720(15)	7.6127(13)	566.8
H408	K	Cu, Mn	yes	9.36689(10)	7.68422(10)	583.9
H409	K	Cu, Mn	open	9.3979(4)	7.7194(4)	590.4
H410	K	Cu, Mn	3 dr.	9.40379(15)	7.72918(11)	591.9
H411	K	Cu, Mn	yes	9.4011(2)	7.6970(2)	589.1
H412	K	Cu, Mn	3 dr.	9.4262(2)	7.77062(15)	598.0
H413	K	Cu, Mn	yes	9.38159(9)	7.68688(9)	585.9
H423		Fe	yes	9.2277(4)	7.5880(4)	559.6
H424		Fe	yes	9.1889(11)	7.5759(8)	554.0
H425		Fe	yes	9.2199(8)	7.5849(6)	558.4
H426		Fe	yes	9.1960(8)	7.5832(6)	555.4
H427		Fe	yes	9.1955(6)	7.5807(5)	555.1
H428	Na	Ni	yes	9.2387(2)	7.6460(2)	565.2
H429	Na	Cu	yes	9.3545(5)	7.6841(5)	582.3
H430	Na	Co	yes	9.37293(15)	7.72322(15)	588.4
H446	K	Ni	3 dr.	9.3380(13)	7.6497(14)	577.7
H447	K	Cu	3 dr.	9.4009(2)	7.6814(2)	587.9
H448*	K	Co	3 dr.	9.42895(15)	7.74750(15)	596.5
H450	K	Zn	3 dr.	9.4584(3)	7.7022(2)	596.7
H455	Rb	Mn	3 dr.	9.5577(7)	7.8733(7)	622.9
H461	Cs	Mn	3 dr.	18.773(6)	7.753(2)	2366.3
H464	Na	Mg	3 dr.	9.3235(2)	7.7335(2)	582.2

* Splitting of reflections relative to the hexagonal zemannite structure observed

4.1.6.1 The zemannite structure type

Zemannite-type structures with general formula $A_x[M_2(XO_3)_3](H_2O)_n$ are characterized by a framework (usually negatively charged) and channels with their constituents. The framework is made up of trigonal-pyramidal [XO_3] units (X = Se, Te; all obtained phases in this thesis are oxidotellurates) and [M_2O_9] dimers formed by plane-sharing [MO_6] (M = di- or trivalent transition metal) octahedra, which results in a considerable distortion from ideal octahedral symmetry for individual [MO_6] units. The $[M_2(TeO_3)_3]^{y-}$ framework is negatively charged with $0 \leq y \leq 2$, depending on the relative amounts of di- and trivalent M atoms. Large, hexagonal channels, in which the A^{z+} (A = Na^+, K^+, Rb^+, Cs^+, Mg^{2+}, Ba^{2+}) cations and water molecules can be situated, perforate this framework. Depending on their charge, the A^{z+} cations are located either in the channel center (Mg^{2+}, Ba^{2+}) or located at distances of up to 2 Å away from it (Na^+, K^+, Rb^+, Cs^+) (Figure 70).

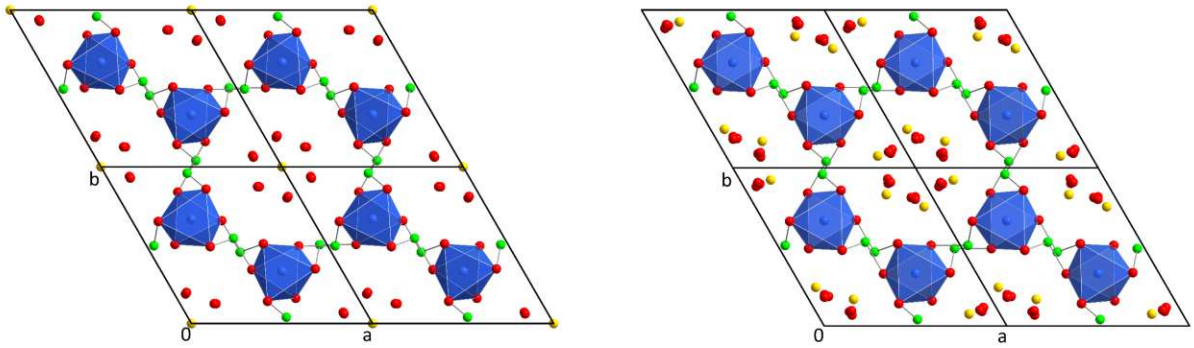

Figure 70. Examples of zemannite-type structures with divalent (left) and monovalent (right) cations (both yellow) inside their channels.

Most zemannite-type structures follow hexagonal unit-cell metrics with $a \approx 9.3$ Å and $c \approx 7.7$ Å, which will be referred to as the zemannite *parental* structure. Most zemannite-type literature phases with metrics corresponding to the parental structure were refined in space group $P6_3/m$. However, for the zemannite mineral phase itself, recent re-investigations indicated a symmetry reduction to $P6_3$ (Cametti et al., 2017, Missen et al., 2019) or even to $P3$ (Effenberger et al., 2023). Several of the new synthetic zemannite-type phases discovered in the scope of the present thesis exhibit superstructures based on this parental structure (Eder et al., 2023b).

4.1.6.2 Overview of discovered zemannite-type structures

All novel zemannite-type phases, for which structure refinements by single-crystal diffraction were possible, are collated in Table 19. Most of these zemannite-type structures have been published recently (Eder et al., 2023b) and only the most important information is summarized here. The so far unpublished Na–Mg- and K–Mg-zemannite-type phases (4.1.6.3), and the crystal structure of $Fe_2(TeO_3)_3$ (4.1.6.4) are discussed in more detail.

The crystal structures of **$Na_2[Ni_2(TeO_3)_3](H_2O)_{2.5}$**, **$K_2[Ni_2(TeO_3)_3](H_2O)$** and **$K_2[Zn_2(TeO_3)_3](H_2O)_2$** follow the zemannite parental structure. For the two Ni-based phases, only very small, thin light green needle-shaped crystals were obtained, which resulted in low-intensity data sets. It is, in theory, possible that these two compounds exhibit superstructures as well, if it were possible to grow larger crystals. On the contrary, $K_2[Zn_2(TeO_3)_3](H_2O)_2$ grew in form of larger colorless block-shaped single crystals and the formation of a superstructure can unambiguously be ruled out for this phase.

Single crystals of **$Na_2[Cu_2(TeO_3)_3](H_2O)_{1.5}$** lose water under the dry stream of nitrogen on the diffractometer when measured at ambient conditions, identifiable through a reduction of the unit-cell volume during the measurement. The crystals exhibited weak superstructure reflections indicating a

rhombohedral superstructure. They were twinned by reticular merohedry, also known as "obverse-reverse twinning".

$K_2[Cu_2(TeO_3)_3](H_2O)_2$ exhibits a dehydration behavior similar to that of $Na_2[Cu_2(TeO_3)_3](H_2O)_{1.5}$. The crystals are also twinned, here in form of threefold twins, and the crystal structure is a twofold superstructure. However, these features apply only for partly dehydrated crystals. When crystals of $K_2[Cu_2(TeO_3)_3](H_2O)_2$ were measured at − 173 °C, no superstructure reflections were observed.

$K_2[Co_2(TeO_3)_3](H_2O)_{2.5}$ has a twofold superstructure closely related to that of $K_2[Cu_2(TeO_3)_3](H_2O)_2$. Additional to the twofold superstructure normal to the channel direction, an incommensurate modulation, accompanied with diffuse scattering in the reciprocal channel direction was observed. The modulation vector was determined as **q** = 0.3886(5)**c*** and the superspace group to be $P112_1/m(00\gamma)s0$. Refinements under consideration of the incommensurate modulation did not converge, and some of the atomic positions corresponding to the channel contents were unstable at their respective sites. It is assumed that the incommensurate modulation, as well as the superstructure formation in $K_2[Co_2(TeO_3)_3](H_2O)_{2.5}$, $Na_2[Cu_2(TeO_3)_3](H_2O)_{1.5}$ and $K_2[Cu_2(TeO_3)_3](H_2O)_2$ are influenced or even caused by the actual water contents inside the channels and their possible changes.

Table 19. Crystal structure data of zemannite-type phases investigated by single-crystal X-ray diffraction.

Formula	Space group	*a* / Å	*b* / Å	*c* / Å	*β* /°	*V* / Å³	Superstructure
$Fe_2(TeO_3)_3$	$P6_3/m$	9.24060(10)		7.5924(2)		561.45(2)	–
$Na_{2-2x}Mg_x[Mg_2(TeO_3)_3](H_2O)_n$	$P6_3/m$	9.3146(3)		7.7232(2)		580.30(4)	–
$Na_2[Cu_2(TeO_3)_3](H_2O)_{1.5}$	$P6_3/m$	9.2833(6)		7.6607(6)		571.75(9)	–
	$R3$	16.0879(10)		22.9668(18)		5147.9(8)	threefold
$Na_2[Ni_2(TeO_3)_3](H_2O)_{2.5}$	$P6_3/m$	9.1982(17)		7.6163(17)		558.1(2)	–
$K_2[Co_2(TeO_3)_3](H_2O)_{2.5}$	$P6_3/m$	9.3954(6)		7.6964(6)		588.37(6)	–
	$P2_1/m$	9.3924(5)	7.7157(5)	16.2726(8)	90.310(4)	1179.24(11)	twofold*
$K_2[Cu_2(TeO_3)_3](H_2O)_2$	$P6_3/m$	9.3410(5)		7.6463(4)		577.79(7)	–
	$P2_1/m$	9.2889(7)	7.6256(4)	16.0832(11)	90.032(6)	1139.23(13)	twofold
$K_2[Ni_2(TeO_3)_3](H_2O)$	$P6_3/m$	9.262(3)		7.605(3)		564.9(4)	–
$K_2[Zn_2(TeO_3)_3](H_2O)_2$	$P6_3/m$	9.4222(4)		7.6498(3)		588.15(6)	–
$Rb_{1.25}[Co_2(TeO_3)_3](H_2O)_{1.5}$	$P\bar{6}$	9.4114(4)		7.6720(4)		588.50(6)	–
$Rb_{1.24}[Mn_2(TeO_3)_3](H_2O)_2$	$P6_3/m$	9.5424(7)		7.8205(8)		616.71(11)	–; presumably monoclinic
$Rb_{1.5}[Mn_2(TeO_3)_3](H_2O)_{1.25}$	$P6_3$	18.7942(8)		7.8749(4)		2408.9(2)	fourfold
$Cs[Mn_2(TeO_3)_3](H_2O)$	$P6_3$	18.7337(9)		7.7724(5)		2362.3(3)	fourfold

* Plus, incommensurate modulation in channel direction

In the diffraction pattern of **$Rb_{1.25}[Co_2(TeO_3)_3](H_2O)_{1.5}$**, clear violations of the absences corresponding to the 6_3 screw axis were observed. The channel contents also do not show the distribution typical for the $P6_3/m$ parental structure. However, the obtained model is incomplete, as it was not possible to allocate two Rb^+ cations p.f.u. in the channels. The Co^{II} atoms exhibit BVS values slightly below 2.00 v.u., which indicates that an inclusion of cobalt in form of trivalent cations can be excluded. However, this raises questions about the charge-balance of the compound based on the derived formula.

From two separate mild hydroflux experiments introducing the same educts (MnO, TeO_2 and Rb_2CO_3) in the same ratios (2:3:6), two different Rb–Mn-zemannite phases were obtained. **$Rb_{1.5}[Mn_2(TeO_3)_3](H_2O)_{1.25}$** (batch H318) forms large, thick, dark brown pillars. The crystal structure adapts to the space requirement of the large Rb^+ cations by a deformation of 3/4 of the channels and leads to the formation of a fourfold superstructure. Additionally, part of the introduced Mn^{II} was oxidized to Mn^{III}. This is a commonly observed side reaction when Te^{IV} and Mn^{II} compounds react under hydrothermal conditions, as indicated by the presence of Mn_3O_4 and Te as minor products. In the

formed crystals, the partial oxidation correlates with increased BVS values of the Mn positions (2.29 v.u. on average) and explains the reduced Rb content in the structure.

$Rb_{1.24}[Mn_2(TeO_3)_3](H_2O)_2$ (batch H455) crystallizes as thin, brown needles, which do not scatter to very high diffraction angles. In the diffraction patterns, a weak splitting of the reflections into three sub-reflections was observed. This would fit to a symmetry reduction to a monoclinic unit-cell, paired with threefold twinning. However, it was not possible to separate these three twin domains during integration, and the final model with hexagonal symmetry must be considered as suboptimal.

$Cs[Mn_2(TeO_3)_3](H_2O)$ has a fourfold superstructure similar to that of $Rb_{1.5}[Mn_2(TeO_3)_3](H_2O)_{1.25}$. The even more pronounced oxidation of parts of the Mn atoms is evident from the high BVS values of the Mn sites (2.58 v.u. on average). The Cs^+ cations exhibit positional disorder over two or more positions in close ± *z* vicinity, which complicated modeling and refinement.

A more detailed discussion of crystal structures of synthetic zemannite-type phases can be found in:

Eder, F., Marsollier, A. & Weil, M. (2023b). Structural studies on synthetic $A_{2-x}[M_2(TeO_3)_3]\cdot nH_2O$ phases (*A* = Na, K, Rb, Cs; *M* = Mn, Co, Ni, Cu, Zn) with zemannite-type structures. *Mineral. Petrol.* https://doi.org/10.1007/s00710-023-00814-5.

4.1.6.3 *New $[Mg_2(TeO_3)_3]$-based zemannite-type phases*

In hydrothermal experiments H272 (K) and H464 (Na), zemannite-type phases were identified in the PXRD patterns, despite no transition metal cations being present in the solution. Instead, Mg^{II}, which has up to now only been present as a channel-constituent in Te-based zemannite-type phases like the mineral zemannite itself (Miletich, 1995a), solely forms the $[M_2(TeO_3)_3]$ framework together with the oxidotellurate(IV) anions. For Se-based zemannite-type phases, a Mg-containing framework is known for $Ba[Mg_2(SeO_3)_3](H_2O)_3$ (Johnston & Harrison, 2011).

4.1.6.3.1 Na–Mg–zemannite

In the product of batch H464, small colorless needles, large enough for structure determination by single-crystal X-ray diffraction were present. The diffraction pattern exhibited only reflections corresponding to the zemannite parental structure with a = 9.3720(10) Å, c = 7.729(2) Å, and no signs of superstructure reflections were found. The crystal structure of the Na–Mg-zemannite is remarkable in the sense that Mg^{II} is present not only in the framework but also inside the channels, partially substituting the Na^+ cations. The overall composition can be given as $Na_{2-2x}Mg_x[Mg_2(TeO_3)_3](H_2O)_n$.

SEM-EDS data support the refined structure model. The EDS-data points, recorded on small hexagonal prismatic crystals (Figure 71), exhibited some variance but always showed a relative excess of Mg compared to Na (Table 20). In the crystal structure, a superposition of Mg^{2+} and Na^+ cations with their respective coordination environments by water molecules was considered for modeling.

Table 20. SEM-EDS data on crystals of Na–Mg-zemannite.

Data point	Na /%	Mg /%	Te /%	O /%
1	9.4	15.6	21.4	54
2	11.1	15.3	19.7	54
3	13	15.7	22.4	49
Average	11(2)	15.5(2)	21(1)	52(3)

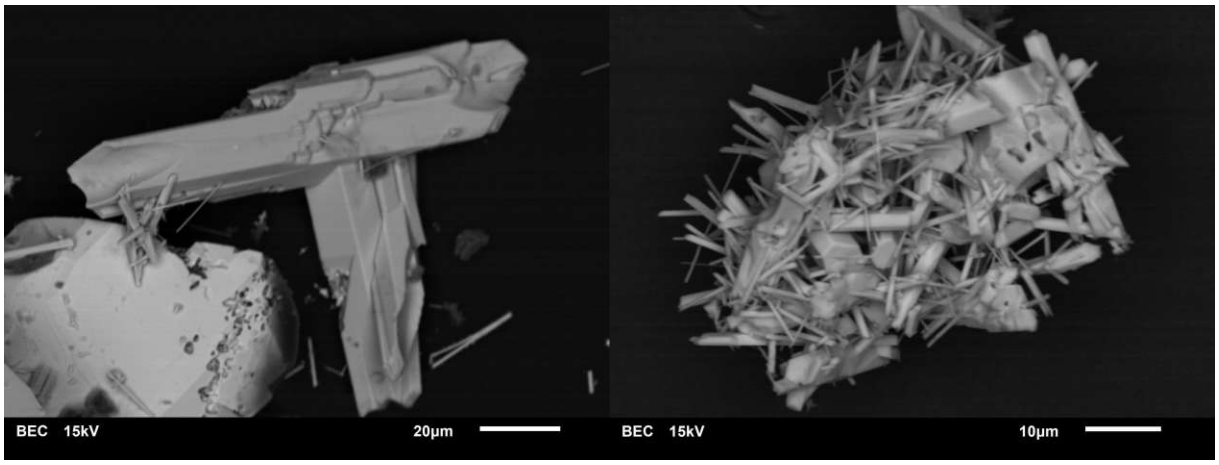

Figure 71. BE-SEM images of crystals of the Na–Mg-zemannite phase.

Crystal structure

The asymmetric unit contains the fully occupied framework sites Te1 (*m*.., 6 *h*), Mg1 (3.., 4 *f*), O1 (*m*.., 6 *h*) and O2 (general position, 12 *i*), and the disordered channel constituent sites Mg2 ($\bar{3}$.., 2 *b*)), Na1 (12 *i*), O3 (*m*.., 6 *h*) and O4–O6 (12 *i*). Atom labels and coordinates were assigned in accordance with the crystal structures of the first synthetic zemannite-type phases $Na_2[Zn_2(TeO_3)](H_2O)_3$ and $Na_2[Co_2(TeO_3)](H_2O)_3$ (Miletich, 1995b).

The $[Mg_2(TeO_3)_3]$ framework consists of trigonal-pyramidal $[TeO_3]$ units and $[Mg_2O_9]$ dimers (Figure 72). The $[TeO_3]$ groups are isolated from each other (connectivity Q^{3000}), and the Te^{IV} atoms have a BVS of 4.01 v.u.. The $[MgO_6]$ octahedra have an average bond length of 2.095 Å, a distance distortion ζ of 0.293 Å, a tilting distortion Δ of 0.00054, an angle distortion Σ of 52.23° and a torsional distortion ϑ of 99.60°. These values are very similar to those of other synthetic zemannite-type phases adapting the $P6_3/m$ parental structure (Eder et al., 2023b). The BVS of the Mg1 site amounts to 2.04 v.u..

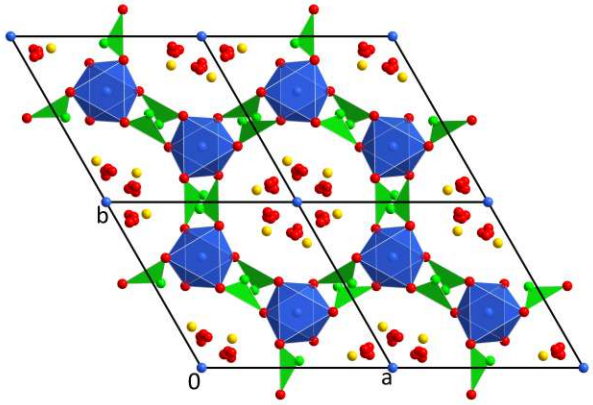

Figure 72. The crystal structure of $Na_{2-2x}Mg_x[Mg_2(TeO_3)_3](H_2O)_n$ viewed along $[00\bar{1}]$. Mg^{II} atoms are drawn as blue spheres.

The situation inside the hexagonal channels is less clear. The majority of the channel interspace is occupied with Na^+ cations and water molecules, which correspond to the Na1, O3, O4 and O5 sites. Their respective s.o.f.s are limited to a maximum value of 1/3 or 1/6 due to symmetry limitations, otherwise this would result in unrealistically close interatomic distances to their own symmetry-equivalent atoms.

Besides these positions, which are very similar to the channel constituents of $Na_2[Zn_2(TeO_3)](H_2O)_3$ and $Na_2[Co_2(TeO_3)](H_2O)_3$ (Miletich, 1995b), significant residual electron density was observed from difference-Fourier maps at the center of the channel. This position (Mg2) corresponds to that of the Mg^{2+} cations in various zemannite-type mineral phases, most notably zemannite $Mg_{0.5}[Zn^{II}Fe^{III}(TeO_3)](H_2O)_n$ (Miletich, 1995a) itself. The water molecules located at the O6 site coordinate the Mg2 site in an octahedral shape. In the refinement, the occupancies of the Na1, O3, O4, O5 and Mg2 and O6 positions were linked by a shared parameter, so that either a pair of Na^+ cations on opposite sides of the channel with their surrounding water molecules, or a $[Mg(H_2O)_6]^{2+}$ unit at the center of the channel is realized (Figure 73). Thus, a 0.5Na:Mg ratio of 0.893:0.107(8) was obtained, leading to a composition of $Na_{1.79}Mg_{0.11}[Mg_2(TeO_3)_3](H_2O)_{3.86}$. This is in decent accordance with the EDS-measurements, from which a composition of $Na_{1.57}Mg_{0.21}[Mg_2(TeO_3)_3](H_2O)_n$ was derived.

Modeling of the disordered water molecules proved to be challenging. While the s.o.f.s of most channel-O sites were successfully refined with the same parameter as the Na:Mg ratio, the O3 site exhibited a negative displacement parameter, indicating a higher occupancy. Free refinement of its s.o.f. resulted in a value higher than symmetrically allowed (due to O3···O3 contacts of only 2.3 Å). A strong dependence of the coordinates of the O6 site on the s.o.f. and displacement parameter of O3 complicated matters. For the final model, the s.o.f. of O3 was refined freely to a value of 0.476(16), accepting the

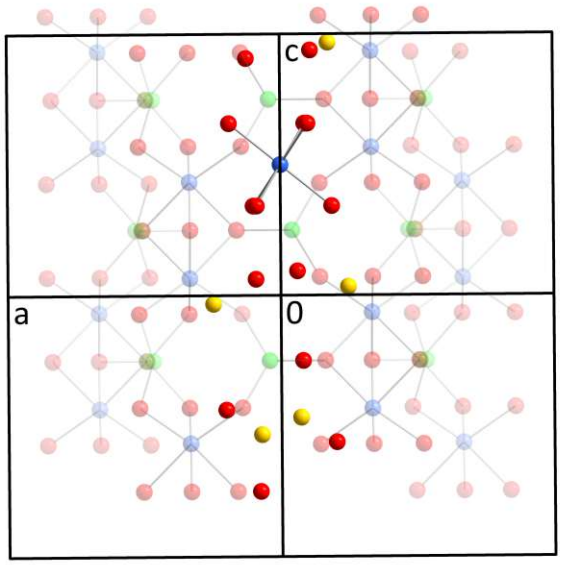

Figure 73. One possible distribution of channel contents inside the channels of the Na–Mg-zemannite phase. Framework atoms are drawn transparent.

short O3···O3 distances, resulting in a crystal water content of 3.86 molecules p.f.u..

It should be noted that, in general, a crystal structure model for zemannite-type phases with hexagonal symmetry is not fully appropriate to correctly describe the heavily disordered channel contents, and even more so with a superposition of two different channel-cations and their respective coordination by water molecules. The weakness of a model, which is based on few distinct atomic positions, can clearly be recognized in the Na−Mg-zemannite. In the actual crystal, the O atoms of the water molecules assumably move away from their average sites, depending on the realization of the Na−Mg-disorder and the positional disorder of the Na^+ cations in their vicinity.

4.1.6.3.2 K−Mg-zemannite

In the K-based experiment H272, suitable single crystals for structure determination were not present. From PXRD data, a hexagonal unit-cell of a zemannite-type phase was evident. Its lattice parameters were refined by the Rietveld method (Table 18; Figure 74). SEM-EDS analysis confirmed the powder to indeed contain the elements K, Mg, Te and O (Table 21). The determined ratios show a Te content, which is, relative to Mg and K, too high for a phase-pure zemannite-type phase.

Table 21. SEM-EDS data of K−Mg-zemannite.

Data point	K /%	Mg /%	Te /%	O /%
1	5.9	11.7	23.6	59
2	5.7	14.3	25.1	54
3	4.9	16.5	27	51
Average	5.5(5)	14(2)	25(2)	55(4)

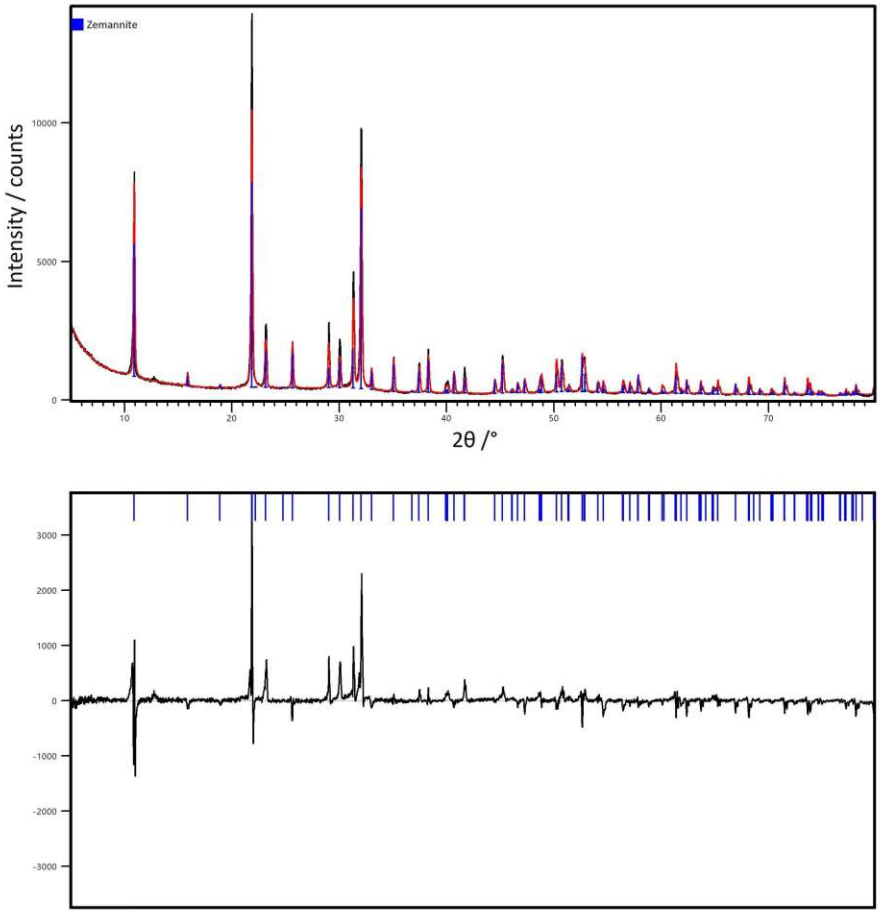

Figure 74. PXRD pattern of the K−Mg-zemannite-type phase from experiment H272.

Based on the structure model of $Na_{1.79}Mg_{0.11}[Mg_2(TeO_3)_3](H_2O)_{3.86}$, it was tried to determine the K:Mg ratio inside the channels by Rietveld-refinement. The occupancy of the K1 (Na1) and Mg2 sites was freely refined and resulted in values of 0.236 for K(Na)1 and 0.310 for Mg2 (the standard uncertainties displayed by the software were unrealistically small and therefore are not indicated). This would correspond to a composition of $K_{1.41}Mg_{0.31}[Mg_2(TeO_3)_3](H_2O)_n$. The refined content is certainly associated with high uncertainty and must be considered as preliminary. Nevertheless, from the obtained model and the EDS data it can be assumed that the K−Mg-zemannite-type phase also consists of a $[Mg_2(TeO_3)_3]$ framework with additional Mg^{2+} present in the hexagonal channels, just like for the Na−Mg-zemannite phase.

4.1.6.4 $Fe_2(TeO_3)_3$

Yellow needle-shaped single crystals of $Fe_2(TeO_3)_3$ were obtained from hydrothermal experiments H423 and H424 during the internship of Georg Hatzl. Initial goal was the growth of single crystals of the NH_4−Fe−As−O-phase described in 3.3.3. The target phase was obtained, again without suitable single crystals for structure determination, but with $Fe_2(TeO_3)_3$ as a new side product. The investigated single crystals originated from batch H423.

Crystal structure

$Fe_2(TeO_3)_3$ crystallizes in the zemannite parental structure in space group $P6_3/m$, and its atom labels and coordinates were assigned corresponding to those of $Na_2M_2(TeO_3)_3(H_2O)_3$ (M = Zn, Co; Miletich, 1995b). The asymmetric unit contains two Te (one main and one disordered site; site symmetry *m*.., 6 *h*), one Fe (3.., 4 *f*) and two O (O1: *m*.., 6 *h*; O2: 1, 12 *i*) atoms.

The Te1 atom exhibits the usual trigonal-pyramidal coordination by three oxygen atoms. However, other than in most zemannite-type phases, Te1 exhibits positional disorder and was refined with two positions (relative ratios 0.9125:0.0875(13) for Te1 and Te1b). The two possible Te positions share the same oxygen contacts and are mirrored by the plane spanned by the three adjoined oxygen atoms (Figure 75). A similar behavior, although not as pronounced, was observed in the crystal structure of $Rb_{1.24}[Mn_2(TeO_3)_3](H_2O)_2$ (4.1.6.2) as well. The BVS values of the two Te sites amount to 4.04 (Te1) and 3.72 (Te1b) v.u.. The rather low value for Te1b might be correlated with the fact that no further oxygen contacts besides the three closest are available. The presence of minor amounts of water molecules in the channels might compensate for this (see below).

As expected for a zemannite-type structure, the Fe^{III} atoms are octahedrally coordinated by six oxygen atoms and form $[Fe_2O_9]$ dimers by plane-sharing. The BVS of 2.90 v.u. confirms the presence of trivalent iron in the structure, leading to an uncharged $^3_\infty[Fe_2Te_3O_9]$ framework. The charge-balanced framework eliminates the necessity of the inclusion of cations inside the hexagonal [001] channels. The octahedral distortion parameters of the Fe^{III} atoms (distance distortion ζ = 0.420 Å, tilting distortion Δ = 0.00118, angle distortion Σ = 72.98° and torsional distortion ϑ = 155.62°) are surprisingly high for a phase crystallizing in the $P6_3/m$ parental structure. Higher values were only obtained for various superstructure phases (Eder et al., 2023b).

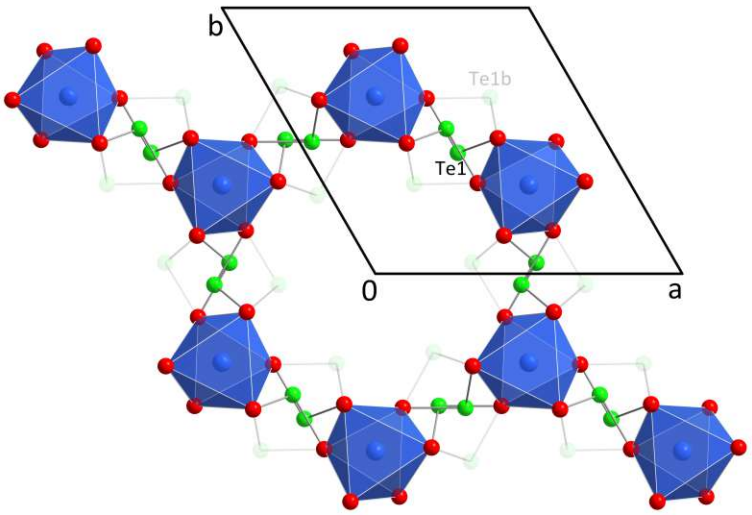

Figure 75. The crystal structure of $Fe_2(TeO_3)_3$ viewed along [00$\bar{1}$].

Other than in most zemannite-type phases, the channels in $Fe_2Te_3O_9$ are assumed to be (almost) empty. The two highest remaining difference electronic density peaks are situated at close distances of 0.594 (Q1; 3.13 e·Å^{-3}) and 1.169 (Q2; 2.26 e·Å^{-3}) Å from the Te1 position. Additionally, there are other difference-electronic peaks of smaller density close to the center of the channels. However, oxygen atoms could not be stably refined at one of the inner-channel sites. If water molecules are present in the channels, the most probable position for a water O site corresponds to the Q2 peak (paired with a realization of the Te1B site) with three oxygen contacts at distances of 2.628 (2×) and 2.751 Å.

All in all, the presence of small amounts of water inside the channels seems plausible. The unit-cell of $Fe_2(TeO_3)_3$, refined from PXRD data of H423 (a = 9.2277(4) Å, c = 7.5880(4) Å, V = 559.6 Å^3), slightly decreases after drying the sample at 210 °C for two days ((a = 9.2004(2) Å, c = 7.6001(2) Å, V = 557.1 Å^3). Based on an older sample from a previous internship (Genoud & Weil; unpublished results), it is known that $Fe_2(TeO_3)_3$-phases synthesized under similar conditions can indeed incorporate crystal water molecules in their channels. If the crystal water content is high enough, this leads to the formation of a fourfold superstructure, similar to those of $Rb_{1.5}[Mn_2(TeO_3)_3]\cdot 1.25H_2O$ and $Cs[Mn_2(TeO_3)_3]\cdot H_2O$ (Eder et al., 2023b).

$Fe_2Te_3O_9$ (without possibly incorporated water molecules in the channels) is isotypic with $Ga_2Te_3O_9$ (Kong et al., 2010) and $Sc_2Se_3O_9$ (Wontcheu & Schleid, 2003). A quantitative crystal structure comparison between $Fe_2Te_3O_9$ and the isotypes was performed with *compstru* (Table 22). The structures of $Fe_2Te_3O_9$ and $Ga_2Te_3O_9$ show a high similarity, which is not surprising given the very similar ionic radii (Shannon, 1976) of Fe^{III} (high-spin, CN6: 0.645 Å) and Ga^{III} (CN6: 0.62 Å). The comparison with $Sc_2Se_3O_9$ revealed a much lower similarity, most probably caused by the much shorter Se—O bond lengths and the greater ionic radius of Sc^{III} (0.745 Å for CN6) compared to Fe^{III} and Ga^{III}. Irrespective of the M^{III} atom, the [MO_6] octahedra exhibit a [3+3] distortion, which is caused by the [M_2O_9] dimer formation by plane-sharing. In the [M_2O_9] dimer, the bridging oxygen atoms have a significantly longer M—O bond compared to the terminal O atoms (Table 22).

Table 22. Comparison of $Fe_2(TeO_3)_3$ with isotypic compounds $Ga_2(TeO_3)_3$ (Kong et al., 2010) and $Sc_2(SeO_3)_3$ (Wontcheu & Schleid, 2003).

	$Fe_2Te_3O_9$	$Ga_2Te_3O_9$	$Sc_2Se_3O_9$
a / Å	9.24060(10)	9.2291(18)	8.1428(5)
c / Å	7.5924(2)	7.488(2)	7.6456(4)
V / Å³	561.45(2)	552.4(3)	439.03(6)
Selected interatomic distances / Å			
*X*1—O2^{i}	1.871(3)	1.887(11)	1.663(3)
*X*1—O2^{ii}	1.871(3)	1.887(11)	1.663(3)
*X*1—O1^{iii}	1.886(4)	1.896(10)	1.698(5)
*X*1B—O2^{ii}	1.856(5)		
*X*1B—O2^{i}	1.856(5)		
*X*1B—O1^{iii}	1.911(7)		
*M*1—O2^{iv}	1.965(3)	1.966(11)	2.019(3)
*M*1—O2^{v}	1.965(3)	1.966(11)	2.019(3)
*M*1—O2^{vi}	1.965(3)	1.966(11)	2.019(3)
*M*1—O1	2.105(3)	2.065(12)	2.198(4)
*M*1—O1^{vii}	2.105(3)	2.065(12)	2.198(4)
*M*1—O1^{iii}	2.105(3)	2.065(12)	2.198(4)
compstru			
S		0.0047	0.0679
d(*M*1) / Å		0.0263	0.1323
d(*X*1) / Å		0.0162	1.7709
d(O1) / Å		0.0285	1.3006
d(O2) / Å		0.0325	1.4571
$d_{max.}$ / Å		0.0325	1.7709
$d_{av.}$ / Å		0.0273	1.3015
Δ		0.017	0.374

Symmetry codes: (i) 1−*x*+*y*, 1−*x*, 1/2−*z*; (ii) 1−*x*+*y*, 1−*x*, *z*; (iii) 1−*y*, 1+*x*−*y*, *z*; (iv) *y*, 1−*x*+*y*, −*z*; (v) 1−*x*, 1−*y*, −*z*; (vi) *x*−*y*, *x*, −*z*; (vii) −*x*+*y*, 1−*x*, *z*.

4.2 Oxidotellurates(VI)

4.2.1 Sodium

4.2.1.1 Hydrothermal experiments

Hydroflux-like experiments starting from the oxides of Mn^{II}, Cu^{II}, Fe^{III}, Zn^{II}, Cr^{III}, Ni^{II}, Cd^{II} and Pb^{II}, TeO_2, H_6TeO_6 and NaOH (molar ratios 2:1:2:15, no additional water) were conducted during the internship of Ruben do Carmo (H155−H162). In several of the experiments, the incorporation of Na^+ cations into transition metal oxidotellurates(VI) was successful: For H156 (Cu^{II}), the sodium copper oxidotellurate(VI) Na_4CuTeO_6 (He et al., 2018) was identified, and the same type of formula was found with Na_4ZnTeO_6 (Nalbandyan & Evstigneeva, 2007) in H158 (Zn^{II}). Aiming at a phase isostructural with $K_{12}Fe_6Te_4O_{27}(H_2O)_3$ (4.2.2.3.1), the Fe^{III}-based batch H157 was performed both with and without added water. While the dry version of the experiment yielded Fe_2O_3 as the only product phase as revealed by the PXRD pattern, for the classic hydrothermal setup single based on iron nitrate instead of iron oxide crystals of two different sodium iron oxidotellurates(VI) were obtained (H157b, Figure 76). $Na_3Te_2(FeO_4)_3$ (4.2.1.2) crystallizes in a body-centered cubic garnet-type structure and was described previously by Plakthii et al. (1977) on basis of powder data. The other phase, $Na_3FeTe_2O_9$ or $Na_2Fe_{2/3}Te_{4/3}O_6$ (4.2.1.3) is isotypic with Na_2TiTeO_6 (Woodward et al., 1999; $R\bar{3}$, a = 5.2201 Å, c = 15.8375 Å). In batch H159 (Cr^{III}), a multitude of unassignable reflections was observed in the PXRD pattern of the leached product besides Cr_2O_3. Some of them might correspond to a phase similar to the Na_2TiTeO_6-like structure of H157: they match those of Li_2GeTeO_6 (Woodward et al., 1999; $R3$, a = 5.0079 Å, c = 14.3422 Å).

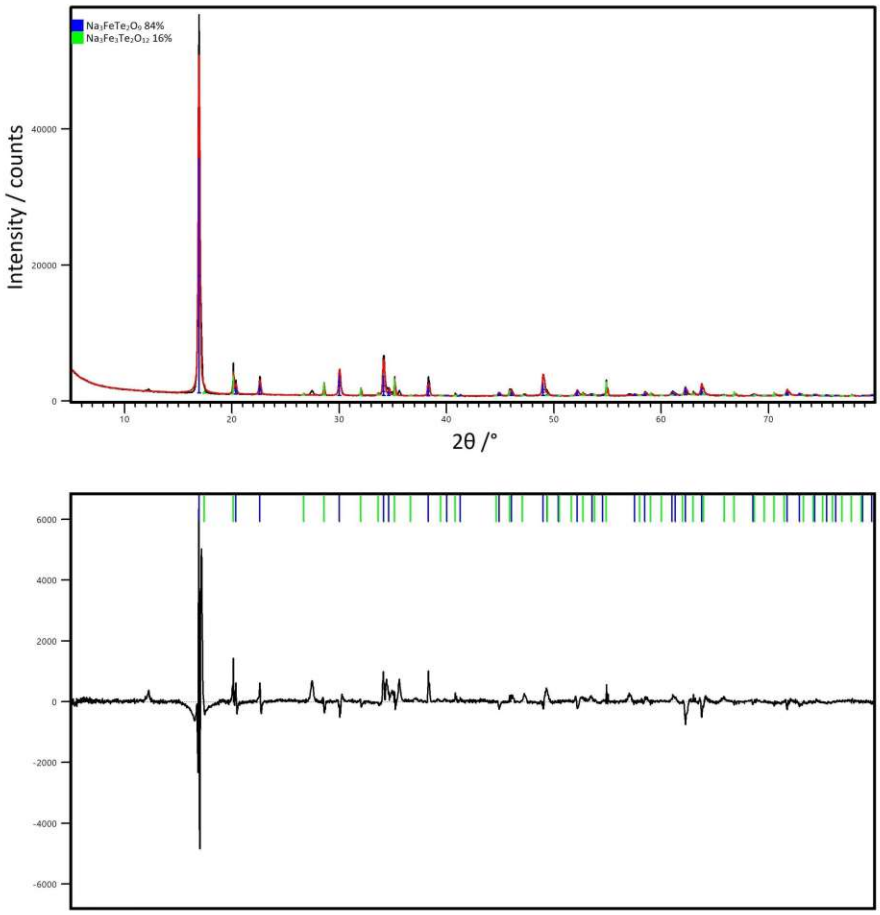

Figure 76. Rietveld refinement of experiment H157b yielding a mixture of the novel phases $Na_3FeTe_2O_9$ and $Na_3Te_2(FeO_4)_3$.

4.2.1.2 $Na_3Te_2(FeO_4)_3$

Single crystals of $Na_3Te_2(FeO_4)_3$ have the form of amber-colored cubes and were obtained from a hydrothermal reaction of $Fe(NO_3)_3(H_2O)_9$, TeO_2, H_6TeO_6 and NaOH in molar ratios of 2:1:2:15. The garnet-type crystal structure (Figure 77) is built-up by octahedral [TeO_6], tetrahedral [FeO_4], and [NaO_8] polyhedra. Te^{VI}-containing garnet-type structures have already been reported for $Na_3Te_2((Fe_{0.5}Al_{0.5})O_4)_3$ (Wedel & Sugiyama, 1999) and $Na_3Te_2(GeO_4)_3$ (Frau et al., 2008).

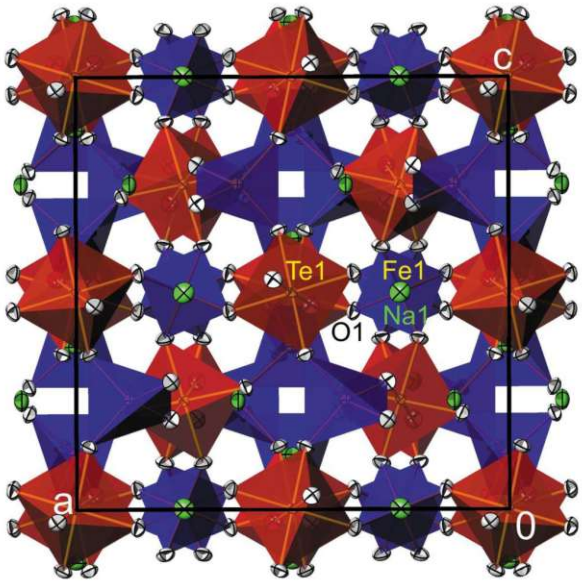

Figure 77. The crystal structure of $Na_3Te_2(FeO_4)_3$ viewed along [$0\bar{1}0$]. Te atoms are drawn red, Fe atoms blue, Na atoms green and O atoms white. Structure representation was generated with ATOMS (Dowty, 2006).

For more information on the crystal structure of $Na_3Te_2(FeO_4)_3$, see:

Eder, F. & Weil, M. (2023). Garnet-type $Na_3Te_2(FeO_4)_3$. *Acta Cryst*. E**79**, 328–330.

4.2.1.3 $Na_3FeTe_2O_9$

Single crystals of $Na_3FeTe_2O_9$ have the form of very small, colorless plates. The diffraction pattern of all investigated $Na_3FeTe_2O_9$ crystals revealed systematic twinning of at least two domains with rhombohedral symmetry. The characteristic shape of the diffraction pattern in the *nkl* and *hnl* ($n \in \mathbb{Z}$) planes corresponds to that of "obverse-reverse" twinning (Figure 78). During the integrating and scaling process, a pseudo-Laue class of $\bar{3}.m$ was suggested by X-Area (Stoe, 2021) with similar R_{int} values compared to the Laue class corresponding to the actual structure ($\bar{3}$). From this pseudo-symmetry imposed by the twinning, one possible twin law ($m_{(010)}$) with a transformation matrix of

$$\begin{pmatrix} 1 & 0 & 0 \\ \bar{1} & \bar{1} & 0 \\ 0 & 0 & 1 \end{pmatrix}$$

was derived. For the final structure model in $R\bar{3}$ (a = 5.2598(8) Å, c = 15.778(3) Å, V = 378.03(14) Å^3), the intensity data were integrated on basis of a hexagonal primitive unit-cell of same dimensions to include the reflections of both twin domains. By applying the twin law given above, the ratios of the respective domains refined to values of 0.540:0.460(2).

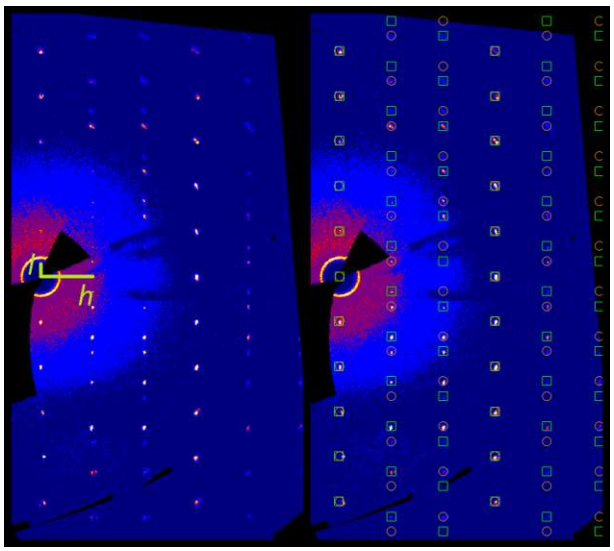

Figure 78. Reconstructed reciprocal *h*0*l* plane of $Na_3FeTe_2O_9$. On the right, reflections belonging to the two twin domains marked with green squares and orange circles.

Crystal structure

The asymmetric unit of $Na_3FeTe_2O_9$ comprises only three sites, one mixed (Fe,Te) (3., 6 *c*), one Na (3., 6 *c*) and one O (1, 18 *f*) position. The (Fe^{III},Te^{VI}) site is coordinated octahedrally by six oxygen atoms at distances of 1.951(3)–1.993(3) Å. The relative ratios of Fe^{III} and Te^{VI} refined to values close to the values required for a charge-balanced formula (1/3:2/3) and were subsequently fixed at these values. Atomic coordinates and ADPs of the Te1 and Fe1 positions were constrained to the same values using EADP and EXYZ commands in SHELXL. Attempts to resolve the disorder of the Fe^{III} and Te^{VI} atoms on the mixed site in lower-symmetric space groups were not successful.

The [(Fe,Te)O_6] octahedra share edges with three neighboring units, thus forming $^2_\infty$[(Fe,Te)$_2O_{12/2}$] layers oriented parallel to (001). Their structure resembles that of the layers in the crystal structure of MoS_2 (Dickinson & Pauling, 1923; Bell & Hefert, 1957), with every third *M* atom from the layer missing, resulting in a honeycomb shape (Figure 79). The location of the void in the layers alternates between the three possible positions when moving along the stacking direction **c**, and one unit-cell of $Na_3FeTe_2O_9$ comprises three layers – one of each possible arrangement.

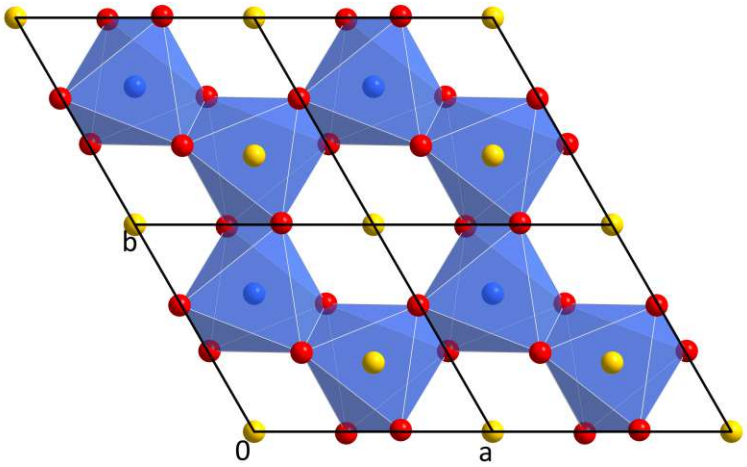

Figure 79. One $[(Fe,Te)_2O_6]$ layer in the crystal structure of $Na_3FeTe_2O_9$ including adjacent Na^+ cations.

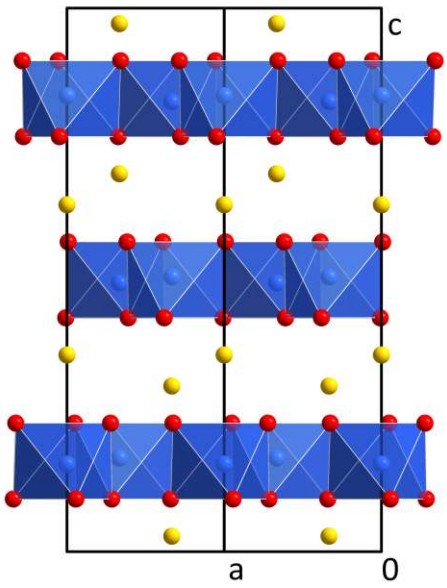

Figure 80. The crystal structure of $Na_3FeTe_2O_9$ viewed along $[0\bar{1}0]$.

The Na^+ cations are situated between these layers and exhibit a CN of [3+3]. The Na^+ cations located above and below the voids in the [Fe−Te−O] layers are displaced from the middle between two adjacent layers (Figure 80).

The crystal structure of $Na_3FeTe_2O_9$ (or $Na_2Fe_{2/3}Te_{4/3}O_6$) is isotypic with Na_2TiTeO_6 (Woodward et al., 1999). Their crystal structures were quantitatively compared using *compstru*. The comparison (S = 0.0038, $d_{av.}$ = 0.0235 Å, Δ = 0.015) reveals a very close structural relationship between the isotypic phases. The Na1 site exhibits a significantly larger difference (0.0442 Å) between the two structures than the other two sites (*M*/Te1: 0.0167 Å and O1: 0.0189 Å).

The larger cell-volume of $Na_3FeTe_2O_9$ (Table 23) can be explained by the longer *M*/Te1—O1 bond lengths in $Na_3FeTe_2O_9$ compared to Na_2TiTeO_6 , which is attributed to the larger ionic radius of Fe^{III} (high-spin, CN6: 0.645 Å) relative to Ti^{IV} (CN6: 0.605 Å; Shannon, 1976). Both ionic radii are comparable to that of Te^{VI} (CN6: 0.56 Å), which explains why a mixed oxide with occupational disorder had formed for both phases.

Table 23. Comparison of the crystal structures of $Na_3FeTe_2O_9$ and Na_2TiTeO_6 (Woodward et al., 1999).

	$Na_3FeTe_2O_9$	Na_2TiTeO_6
a / Å	5.2598(8)	5.2201(2)
c / Å	15.778(3)	15.8375(6)
V / Å³	378.03(14)	373.74(2)
Selected interatomic distances / Å		
M/Te1—O1 (3×)	1.951(3)	1.942(5)
M/Te1—O1 (3×)	1.993(3)	1.966(6)
Na1—O1 (3×)	2.297(3)	2.326(2)
Na1—O1 (3×)	2.545(4)	2.510(3)

4.2.2 Potassium

4.2.2.1 Hydrothermal experiments

Inspired by the serendipitous synthesis of $K_2Cu_2TeO_6$ (4.2.2.6.4), $K_3CuTeO_5(OH)(H_2O)$ (4.2.2.6.3) and $K_{12}Fe_6Te_4O_{27}(H_2O)_3$ (4.2.2.3.1) resulting from batches H100 and H101, several hydroflux-like experiments were performed based on metal oxides, telluric acid and KOH without addition of external water. The focus of follow-up investigations was the (ideally phase-pure) re-synthesis of $K_2Cu_2TeO_6$ and $K_{12}Fe_6Te_4O_{27}(H_2O)_3$, and the extension of this synthesis route to other elements.

The first experimental series repeated the setup of H100−H103 of metal oxide, TeO_2, H_6TeO_6 and KOH in molar ratios of 2:1:2:15 without additional water with the metals Mn^{II}, Cu^{II}, Fe^{III}, Zn^{II}, Cr^{III}, Ni^{II}, Cd^{II} and Pb^{II} (H139−H146). Aimed at the reproduction of H100, (Cu^{II}, H140), only $K_2Cu_2TeO_6$, but no $K_3CuTeO_5(OH)(H_2O)$ was identified. The repetition of H101, (Fe^{III}, H141), yielded (after leaching) again $K_{12}Fe_6Te_4O_{27}(H_2O)_3$ with small amounts of Fe_2O_3 as a by-product. The PXRD patterns of the leached products of H142 (Zn^{II}) and H145 (Cd^{II}) could not be explained by literature phases. However, suitable single crystals for crystal structure determination were not obtained. According to its PXRD pattern, the leached sample of H146 (Pb^{II}) was phase-pure $KPb_2TeO_5(OH)$ (4.2.2.7.2), another new phase. Significant preferred orientation of the crystallites in the (00*n*) direction was determined.

Later re-synthesis attempts of potassium-modified oxidotellurates(VI) were based on metal oxides, H_6TeO_6 and the weaker base K_2CO_3 (H221−H228). The predominant products were $KTeO_3(OH)$ (Lindqvist, 1972), which seems to be favored at the given lower pH conditions, and the educt metal oxides. In H221 (Mn^{II}), some of the introduced Mn^{II} was oxidized during the reaction leading to the formation of the new phase $K_4Mn^{III}_2Te_3O_{12}(OH)_4$ (4.2.2.2). Significant unassigned reflections were observed in the PXRD patterns of H222 (Cu^{II}) and H224 (Zn^{II}). In the Zn^{II}-based sample, single crystals of the new carbonate $K_6[Zn(CO_3)_4]$ (6.7) were isolated and their crystal structure determined. Since some reflections still remained unassigned, (an)other unknown phase(s) must be present in the product of H224.

4.2.2.2 $K_4Mn_2Te_3O_{12}(OH)_4$

A mild hydroflux reaction of MnO, H_6TeO_6 and K_2CO_3 (ratios 2:3:10) yielded $K_4Mn_2Te_3O_{12}(OH)_4$ as a side product, besides MnO and $KTeO_3(OH)$ (Lindqvist, 1972) as the main phase. $K_4Mn_2Te_3O_{12}(OH)_4$ is a Mn^{III} compound, meaning that parts of the introduced Mn^{II} were oxidized under the given conditions. Single crystals of $K_4Mn_2Te_3O_{12}(OH)_4$ are dark orange platelets, which tend to grow together to larger clumps.

Crystal structure

Of the 15 atoms (two Te, one Mn, two K, eight O and two H) in the asymmetric unit all but Te2 (2 *a*; $\bar{1}$) are located at sites corresponding to general Wyckoff positions (4 *e*).

The two Te^{VI} atoms are coordinated octahedrally by six oxygen atoms with distances between 1.845(4) and 1.979(4) Å (Table 24). Two [Te1O_5(OH)] groups, symmetrically linked by the inversion center, on which the Te2 site is situated, are connected to each [Te2$O_4(OH)_2$] octahedron by corner-sharing, leading to the formation of linear [$Te_3O_{12}(OH)_4$] units (Figure 81). Such finite Te_3X_{16} groups have so far not been described for the structural architecture of oxidotellurates (Christy et al., 2016). This novel structural element for oxidotellurates(VI) can be denoted as (◯ – ◯ – ◯). In the crystal structure of $K_4Mn_2Te_3O_{12}(OH)_4$, the [$Te_3O_{12}(OH)_4$] groups are oriented in the [201] direction. The BVS of the Te^{VI} sites were calculated to be 5.94 (Te1) and 5.87 (Te2) v.u..

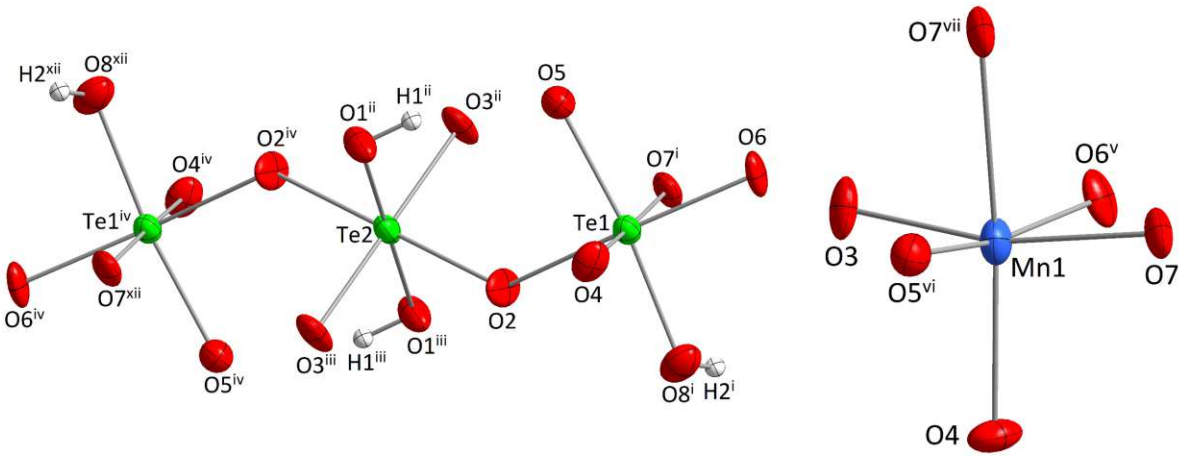

Figure 81. The novel [$Te_3O_{12}(OH)_4$] unit and the coordination sphere of Mn1 in the crystal structure of $K_4Mn_2Te_3O_{12}(OH)_4$. Symmetry codes refer to Table 24. (xii) −1+*x*, 1/2−*y*, −1/2+*z*.

The Mn1 site is connected to six oxygen atoms in a [4+1+1] coordination resulting in an uniaxially distorted octahedron. The four closest oxygen contacts are located in the equatorial plane with almost the same distances (1.935(4)−1.942(4) Å). The other two oxygen atoms have bond lengths of 2.132(4) and 2.373(4) Å. This large distortion is caused by Jahn−Teller effects, which are known to be very distinctive for the d^4 cation Mn^{III} (Lufaso &Woodward, 2004). The BVS of the Mn1 position amounts to 3.02 v.u. and clearly confirms the oxidation of employed Mn^{II} during the reaction. Two adjacent [MnO_6] octahedra are connected to each other by edge-sharing. Each [$Te_3O_{12}(OH)_4$] unit is connected to two [Mn_2O_{10}] dimers by sharing two edges and a corner, and to two different [Mn_2O_{10}] groups by sharing only one corner. Together, they form a rather loose framework, which is perforated by channels, where the K^+ cations are situated. The largest channels extend parallel to [100], [010] and [0$\bar{1}$1] (Figure 82).

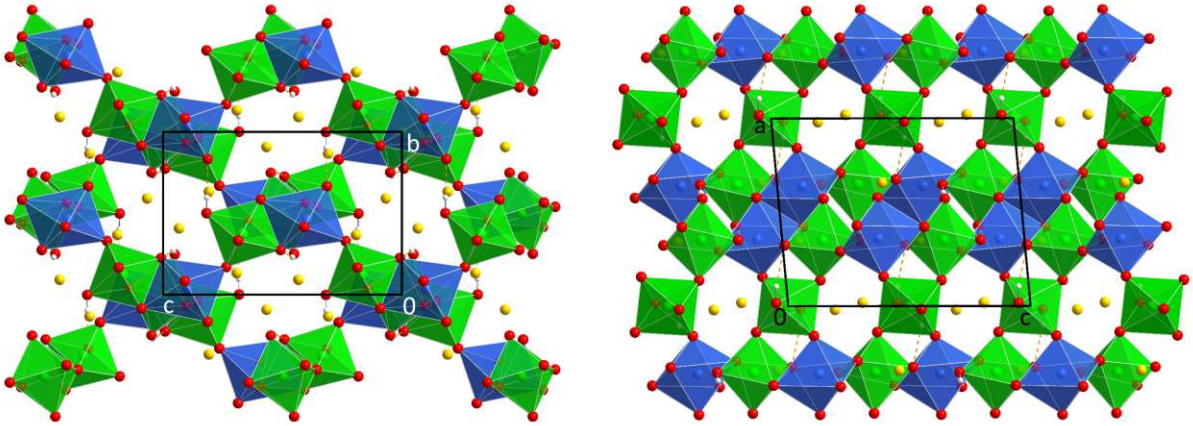

Figure 82. The crystal structure of $K_4Mn_2Te_3O_{12}(OH)_4$ viewed along [$\bar{1}$00] (left) and [0$\bar{1}$0] (right).

The two K sites are coordinated by eight and six oxygen atoms, respectively, with distances below 3.2 Å. Two K2 sites are located at a rather small distance of 3.541(3) Å from each other. The K1 sites do not form such close pairs, the smallest K1—K1 distance being 4.037(2) Å. The values of the BVS for the K^+ cations amount to 1.15 (K1) and 0.97 (K2) v.u.. Both hydrogen sites were located from difference-Fourier maps and were refined without any distance constraints. The resulting O—H bond lengths are comparably small with values of 0.78(7) Å for O1—H1 and 0.82(11) for O8—H2. Both hydrogen atoms are part of hydroxide groups and partake in hydrogen-bonding. Their corresponding donor-acceptor distances are 2.715(6) and 2.623(4) Å for H1 and H2, resulting in hydrogen bonds of medium strength (Table 24).

Table 24. Selected interatomic distances in the crystal structure of $K_4Mn_2Te_3O_{12}(OH)_4$.

	d / Å		*d* / Å
Te1—O4	1.845(4)	K1—O2^{viii}	2.580(4)
Te1—O6	1.931(4)	K1—O4^{ix}	2.733(4)
Te1—O7^{i}	1.932(4)	K1—O3	2.765(4)
Te1—O5	1.938(4)	K1—O1^{x}	2.897(5)
Te1—O8^{i}	1.949(4)	K1—O2^{ix}	2.927(5)
Te1—O2	1.974(4)	K1—O1^{ix}	3.039(5)
Te2—O3^{ii}	1.887(4)	K1—O8^{v}	3.076(5)
Te2—O3^{iii}	1.887(4)	K1—O3^{ix}	3.129(4)
Te2—O2^{iv}	1.937(4)	K1—O1^{viii}	3.348(5)
Te2—O2	1.937(4)	K2—O7^{v}	2.574(4)
Te2—O1^{ii}	1.979(4)	K2—O4	2.817(4)
Te2—O1^{iii}	1.979(4)	K2—O6^{v}	2.871(4)
Mn1—O7	1.935(4)	K2—O5	2.876(4)
Mn1—O6^{v}	1.939(4)	K2—O8^{xi}	2.894(5)
Mn1—O3	1.939(4)	K2—O8	2.940(5)
Mn1—O5^{vi}	1.942(4)	K2—O1^{ix}	3.359(4)
Mn1—O4	2.132(4)	K2—O5^{xi}	3.397(4)
Mn1—O7^{vii}	2.373(4)		
O1—H1	0.78(7)	O1—H1···O5^{vi}	2.715(6)
O8—H2	0.82(11)	O8—H2···O6	2.623(4)

Symmetry codes: (i) 1−*x*, −1/2+*y*, 1/2−*z*; (ii) *x*, 1/2−*y*, −1/2+*z*; (iii) −*x*, −1/2+*y*, 1/2−*z*; (iv) −*x*, −*y*, −*z*; (v) 1−*x*, 1/2+*y*, 1/2−*z*; (vi) *x*, 1/2−*y*, 1/2+*z*; (vii) 1−*x*, 1−*y*, 1−*z*; (viii) *x*, 1+*y*, *z*; (ix) −*x*, 1/2+*y*, 1/2−*z*; (x) −*x*, 1−*y*, 1−*z*; (xi) 1−*x*, 1−*y*, −*z*.

4.2.2.3 Potassium iron oxidotellurates(VI)

4.2.2.3.1 $K_{12}Fe_6Te_4O_{27}(H_2O)_3$

Synthesis

Single crystals of $K_{12}Fe_6Te_4O_{27}(H_2O)_3$ were obtained in experiment H101 from a hydroflux-like reaction between Fe_2O_3, TeO_2, H_6TeO_6 and KOH (molar ratios 2:1:2:15) and have a cuboid shape and an intense dark yellow color. After the serendipitous initial synthesis, it was attempted to obtain phase-pure $K_{12}Fe_6Te_4O_{27}(H_2O)_3$ in numerous follow-up experiments. Because the unreacted educt Fe_2O_3, which was present in all products, could not be removed easily with chemical methods, different synthesis conditions were varied in the hope to obtain a single-phase product. Experiments H170–173 all started from mixtures of Fe_2O_3, H_6TeO_6 and KOH in either hydroflux-like conditions or open hydrothermal experiments. $K_{12}Fe_6Te_4O_{27}(H_2O)_3$ was always obtained as the main phase, but for each batch with noticeable amounts of Fe_2O_3 as a side product. Adding a few extra droplets of water to the dry hydrothermal experiment of H170 (Fe_2O_3, H_6TeO_6, KOH; 3:4:15; H297) inhibited the formation of $K_{12}Fe_6Te_4O_{27}(H_2O)_3$ and only Fe_2O_3 was identified.

Several attempts to obtain $K_{12}Fe_6Te_4O_{27}(H_2O)_3$ were made via solid-state reactions as well. Experiment S9 ($Fe(NO_3)_3(H_2O)_9$, K_2TeO_3; 1:1, in excess of KNO_3) was performed at rather low temperatures (360 °C). The leached reaction product consisted of Fe_2TeO_6 (Kunnmann et al., 1968) exhibiting very broad reflections in the powder diffraction pattern. However, successful re-synthesis of $K_{12}Fe_6Te_4O_{27}(H_2O)_3$ could be accomplished in solid-state reaction S14 ($Fe(NO_3)_3(H_2O)_9$, H_6TeO_6 and KOH in ratios 3:2:15 at 500 °C). Some additional reflections, which could not be assigned, were observed besides the target phase. Starting from iron(III) oxide instead of iron nitrate and introducing less KOH at 600°C (S15) only yielded Fe_2O_3 and an unidentified minor phase.

Crystal structure

The crystal structure of $K_{12}Fe_6Te_4O_{27}(H_2O)_3$ (Figure 83) is cubic and non-centrosymmetric ($I\bar{4}3d$, a = 14.7307(12) Å, V = 3196.5(8) Å^3). The asymmetric unit contains one Te (site symmetry .3., 16 *c*), one Fe (2.., 24 *d*), one K (1, 48 *e*) and four O atoms (O3: $\bar{4}$.., 12 *a*; others: 1, 48 *e*).

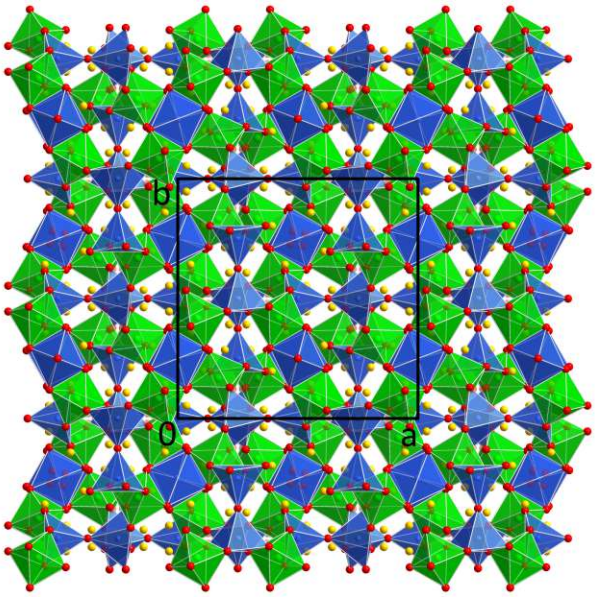

Figure 83. The crystal structure of $K_{12}Fe_6Te_4O_{27}(H_2O)_3$ viewed along [00$\bar{1}$].

The Te^{VI} atoms are coordinated by six oxygen atoms in an almost perfect octahedral shape. The [TeO_6] units are isolated from each other, and the Te^{VI} atoms have a BVS of 5.85 v.u.. The Fe^{III} atoms are connected to five oxygen atoms, forming a distorted square pyramid (τ_5 = 0.313). The apical O3 atom is located at a much closer distance of 1.8514(6) Å than the other four oxygen atoms (1.984(2)–2.034(2) Å). Two [FeO_5] pyramids share their apical oxygen atom, forming [Fe_2O_9] dimers. By sharing edges with the [TeO_6] octahedra, they form a tri-periodic framework (Figure 83), perforated by small channels oriented along <111> (Figure 84).

The remaining space in the loose [Fe–Te–O] framework is occupied by the K^+ cations and crystal water molecules associated with the O4 site. The O4 position lies very close to a fourfold rotation axis and

can therefore only be one quarter occupied. The s.o.f. of the O4 site refines to a value of 0.243(7) and was subsequently fixed to the symmetrically allowed maximum value of 0.25.

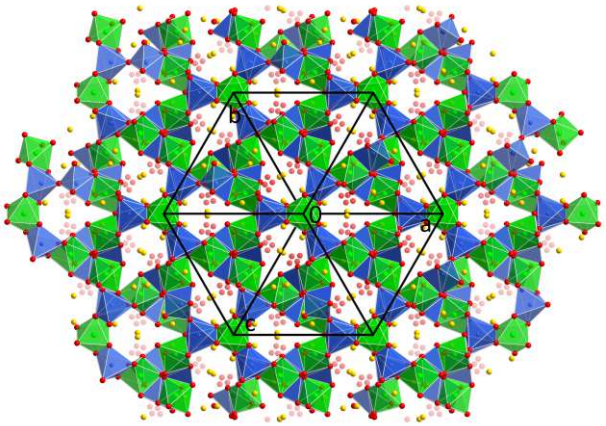

Figure 84. The crystal structure of $K_{12}Fe_6Te_4O_{27}(H_2O)_3$ viewed along $[\bar{1}\bar{1}\bar{1}]$.

The $K_{12+6x}Fe_6Te_{4-x}O_{27}$ phase

At the time when $K_{12}Fe_6Te_4O_{27}(H_2O)_3$ was investigated, a very similar phase with composition $K_{12+6x}Fe_6Te_{4-x}O_{27}$ (*x* was determined to 0.222(4), resulting in a gross formula of $K_{13.33(2)}Fe_6Te_{3.778(4)}O_{27}$) has been reported by Albrecht et al. (2021) and was synthesized in a KOH-hydroflux reaction between $Fe(NO_3)_3(H_2O)_9$, TeO_2 and H_2O_2. The $K_{12}Fe_6Te_4O_{27}(H_2O)_3$ phase obtained during the present thesis was obtained under hydroflux-like conditions as well, but Te^{VI} was introduced directly as H_6TeO_6 and Fe^{III} was added as an oxide instead of the nitrate.

While the unit-cells and coordinates of the atomic sites of the two phases are almost identical (Table 26), Albrecht et al. (2021) reported a different distribution of the atoms over the crystallographic sites. They found an under-occupation of the Te1 site with an s.o.f. of only 0.9439(10). The missing positive charges are compensated by additional K^+ cations, which are positioned at the O4 positions, instead of water molecules as in our model.

Based on our diffraction data, the occupancy of the Te1 site refines without constraints to a value of 0.3324(9) (1/3 corresponds to an s.o.f. of 1). The O4 position has two K1 contacts with distances of 2.693(15) and 2.879(15) Å. If a K^+ cation would sit on this site, the resulting K—K distances are unrealistically short. In the final model of Albrecht et al. (2021), the KA—KB distance is 2.704(9) Å.

In order to confirm the composition assumed by the refinement, SEM-EDS measurements were performed on several crystals of $K_{12}Fe_6Te_4O_{27}(H_2O)_3$ (Figure 85, Table 25). Although the determined atomic compositions show a large variance, a reduced Te- and an increased K content relative to the sum formula are not indicated. Relative to the Fe content, which can be regarded to be accurately determined with six atoms p.f.u., the EDS-data on average corresponds to a K:Fe:Te ratio of 11.11:6:4.09.

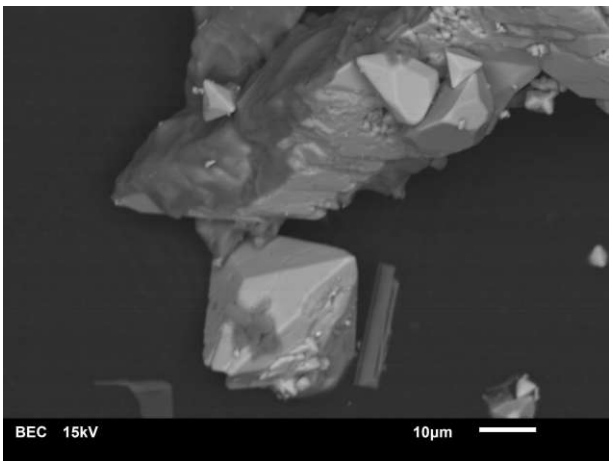

Figure 85. BE-SEM picture of crystals of $K_{12}Fe_6Te_4O_{27}(H_2O)_3$.

Table 25. SEM-EDS data on crystals of $K_{12}Fe_6Te_4O_{27}(H_2O)_3$.

Data point	K /%	Fe /%	Te /%	O /%
1	18.7	13	9.1	59
2	23.9	13.1	8.4	55
3	24.8	11.9	8.4	55
4	30.8	15.9	10.7	43
Average	25(3)	13.5(7)	9.2(4)	53(2)

Table 26. Comparison of the crystal structure models of $K_{12}Fe_6Te_4O_{27}(H_2O)_3$ and $K_{13.33(2)}Fe_6Te_{3.778(4)}O_{27}$ (Albrecht et al., 2021).

$K_{12}Fe_6Te_4O_{27}(H_2O)_3$		$K_{13.33(2)}Fe_6Te_{3.778(4)}O_{27}$	
a / Å	14.7307(12)	14.7440(10)	
V / Å^3	3196.5(8)	3205.1(7)	
Space group	$I\bar{4}3d$	$I\bar{4}3d$	
Selected interatomic distances / Å			
Te1—O2^{i}	1.931(2)	Te—O2	1.9335(12)
Te1—O2^{ii}	1.931(2)	Te—O2^{i}	1.9335(12)
Te1—O2	1.931(2)	Te—O2^{ii}	1.9335(12)
Te1—O1^{i}	1.9385(19)	Te—O1	1.9370(12)
Te1—O1^{ii}	1.9385(19)	Te—O1^{i}	1.9370(12)
Te1—O1	1.9385(19)	Te—O1^{ii}	1.9370(12)
Fe1—O3	1.8514(6)	Fe—O3	1.8512(3)
Fe1—O1	1.984(2)	Fe—O1	1.9834(12)
Fe1—O1^{iii}	1.984(2)	Fe—O1^{iii}	1.9835(12)
Fe1—O2^{iii}	2.034(2)	Fe—O2	2.0331(13)
Fe1—O2	2.034(2)	Fe—O2^{iii}	2.0331(13)
K1—O1^{iv}	2.667(2)	KA—O1^{iv}	2.6715(13)
K1—O4^{v}	2.693(13)	KA—KB^{v}	2.704(9)
K1—O1	2.766(2)	KA—O1	2.7663(14)
K1—O2^{vi}	2.767(2)	KA—O2^{vi}	2.7587(15)
K1—O2^{vii}	2.815(2)	KA—O2^{vii}	2.8262(14)
K1—O4^{ii}	2.879(16)	KA—KB^{ii}	2.904(10)
K1—O1^{ii}	2.886(2)	KA—O1^{ii}	2.8972(13)
K1—O3^{iv}	2.9521(8)	KA—O3^{iv}	2.9527(5)
K1—O2^{iii}	3.080(2)	KA—O2^{iii}	3.0798(15)
K1—O4^{iv}	3.187(17)	KA—KB^{iv}	3.207(9)
K1—O4^{viii}	3.273(13)	KA—KB^{viii}	3.260(8)

Symmetry codes: (i) *y*, *z*, *x*; (ii) *z*, *x*, *y*; (iii) *x*, 1−*y*, 1/2−*z*; (iv) *z*, 1−*x*, 1/2−*y*; (v) 1/4−*z*, 3/4−*y*, −1/4+*x*; (vi) −1/4+*y*, −1/4+*x*, −1/4+*z*; (vii) −1/4+*z*, −1/4+*y*, −1/4+*x*; (viii) 1/4−*z*, 1/4+*y*, 3/4−*x*.

4.2.2.3.2 $K_3FeTe_2O_8(OH)_2(H_2O)$

Single crystals of $K_3FeTe_2O_8(OH)_2(H_2O)$ were obtained as small colorless plates from experiment H230 (Fe_2O_3, TeO_2 and K_2CO_3 in the ratios 2:3:10 with three extra droplets of water). The formation of an oxidotellurate(VI) from a Te^{IV}-based experiment might be due to contaminations of the reaction vessel, as several Te^{VI}-based experimental series were performed in the Teflon inlay prior to the conduction of experiment H230.

The crystals all exhibited twinning under presence of several domains. For the investigated crystal, a two-domain integration was performed. The relative twin fractions were refined to be 0.792(2):0.208(2) from the *hkl*5-type intensity data. Although the refinement converged with rather high reliability factors ($R1$ = 7.55%), all atoms could be refined with ADPs. Hydrogen atoms could not be located. Atom labels and coordinates were chosen in correspondence with isotypic $K_3GaTe_2O_8(OH)_2(H_2O)$ (Yu et al., 2004).

Crystal structure

The asymmetric unit of the triclinic unit-cell ($P\bar{1}$; a = 7.435(6) Å, b = 7.496(6) Å, c = 11.533(9) Å, α = 83.980(10)°, β = 74.582(9)°, γ = 62.229(9)°, V = 548.2(7) Å^3) contains two Te, one Fe, three K and eleven O sites, all located at general 2 *i* positions.

The Te^{VI} atoms are all surrounded octahedrally by six oxygen atoms with distances between 1.870(12) Å and 2.013(12) Å (Table 27). Two $[Te1O_5(OH)]$ or $[Te2O_5(OH)]$ octahedra form $[Te_2O_8(OH)_2]$ pairs by edge-sharing, the shared oxygen atoms are located at slightly longer distances than the other four. The BVS of the Te atoms are 5.96 (Te1) and 5.87 (Te2) v.u..

The Fe^{III} atom (BVS 3.08 v.u.) exhibits a tetrahedral coordination by four oxygen atoms. The shape of the $[FeO_4]$ units is rather regular with a τ_4 parameter of 0.954. The $[FeO_4]$ tetrahedra are isolated from each other but share two edges with adjacent $[Te_2O_8(OH)_2]$ dimers, thus forming infinite $^1_\infty[Fe_2Te_4O_{24/2}O_{4/1}(OH)_{4/1}]$ chains, which are propagating along [001] (Figure 86).

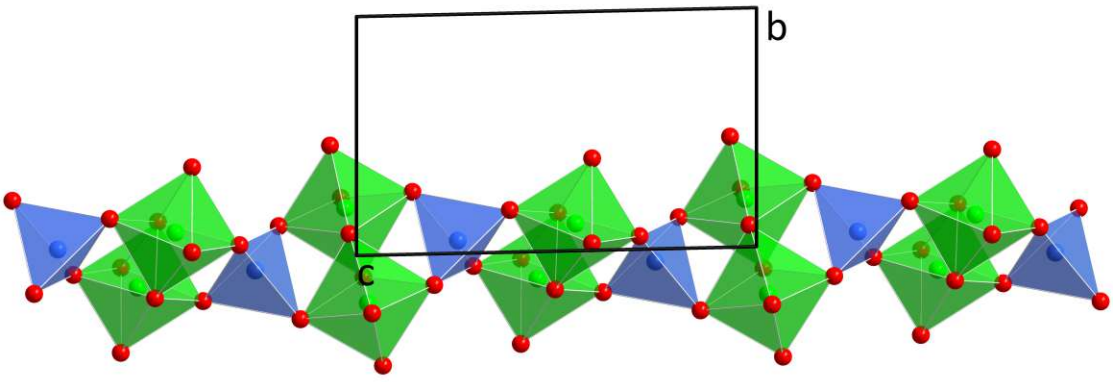

Figure 86. $^1_\infty[Fe_2Te_4O_{16}(OH)_4]$ chain in the crystal structure of $K_3FeTe_2O_8(OH)_2(H_2O)$ propagating along [001].

Information about the location of hydrogen atoms and resulting potential hydrogen bonds can be drawn from the values of BVS and interatomic distances between oxygen atoms. Oxygen atoms shared between Fe^{III} and Te^{VI} or between two Te^{VI} atoms (O1, O3, O4, O6, O7 and O9) have BVS values close to 2.00 v.u. (2.05, 2.01, 2.33, 2.05, 2.20 and 2.05 v.u., respectively) and thus are not additionally bonded to an H atom. On the other hand, the four terminal atoms only connected to one Te^{VI} atom

(O2, O5, O8, O10), have lower BVS of 1.48, 1.57, 1.73 and 1.62 v.u., and the O11 site, which has only K^+ cations in its vicinity, exhibits a BVS of just 0.48 v.u.. Due to this fact, it can be assumed that the O atom of a water molecule is located at the O11 position and forms hydrogen bonds towards O2 and O5, which are situated at distances of 2.83(2) and 2.76(2) Å, respectively. The O2 and O5 sites each have another very close distance towards one symmetry-equivalent site (2.51(2) and 2.53(2) Å), indicating a second hydrogen bond between each symmetry-related pair. The corresponding H atoms either are part of a symmetrical hydrogen-bond (then sitiuated at the inversion center) or an unsymmetrical hydrogen bond (then situated closer to one of the O atoms, but with half-occupation). The remaining hydrogen atom is positioned between O8 and O10, which have an interatomic distance of 2.58(2) Å. All hydrogen bonds are between terminal oxygen atoms of $^1_\infty[Fe_2Te_4O_{24/2}O_{4/1}(OH)_{4/1}]$ chains and play an important role in the crystal packing (Figure 87).

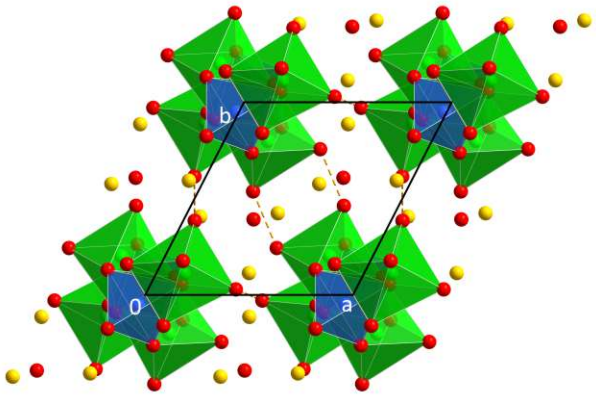

Figure 87. The crystal structure of $K_3FeTe_2O_8(OH)_2(H_2O)$ viewed along $[00\bar{1}]$. Donor- and acceptor O atoms of assumed close hydrogen bonds between the $^1_\infty[Fe_2Te_4O_{16}(OH)_4]$ chains are connected by orange dashed lines.

$K_3FeTe_2O_8(OH)_2(H_2O)$ is isotypic with the corresponding Ga-compound $K_3GaTe_2O_8(OH)_2(H_2O)$ (Yu et al., 2004), for which the H atoms could likewise not be located. The two crystal structures were quantitatively compared using *compstru*. The close similarity between the two structures is underlined by a small degree of lattice distortion *S* of 0.0038, a measure of similarity Δ of 0.016 and an arithmetic mean of the distances between paired atoms $d_{av.}$ of 0.0264 Å. The distances between paired atoms are 0.0102 Å (Te1), 0.0121 Å (Te2), 0.0192 Å (Ga/Fe1), 0.0097 Å (K1), 0.0231 Å (K2), 0.0057 Å (K3), 0.0157 Å (O1), 0.0268 Å (O2), 0.0420 Å (O3), 0.0421 Å (O4), 0.0116 Å (O5), 0.0326 Å (O6), 0.0462 Å (O7), 0.0236 Å (O8), the largest value of 0.0583 Å (O9), 0.0234 Å (O10) and 0.0465 Å (O11).

The largest differences (> 0.04 Å) are noted for the four oxygen atoms connected to the Fe/Ga1 position, and the crystal water molecule corresponding to the O11 site. The ionic radii (Shannon, 1976) of Fe^{III} (0.49 Å) and Ga^{III} (0.47) in fourfold coordination are very similar but the slightly larger size of the Fe^{III} cation causes the differences in the atomic coordinates of the adjacent atoms. In the unit-cell dimensions, the difference is noticeable especially for the *c*-axis. While the size of the $[Fe/GaO_4]$ tetrahedra can influence the length of the $^1_\infty[Fe_2Te_4O_{24/2}O_{4/1}(OH)_{4/1}]$ chains, their width and distance to each other (corresponding to **a** and **b**) is dominated by the $[Te_2O_8(OH)_2]$ dimers and their hydrogen bonds, which do not change between the two structures.

Table 27. Comparison of the crystal structures of $K_3FeTe_2O_8(OH)_2(H_2O)$ and $K_3GaTe_2O_8(OH)_2(H_2O)$ (Yu et al., 2004).

	$K_3FeTe_2O_8(OH)_2(H_2O)$	$K_3GaTe_2O_8(OH)_2(H_2O)$
a / Å	7.435(6)	7.4369(9)
b / Å	7.496(6)	7.4903(9)
c / Å	11.533(9)	11.4128(15)
α /°	83.980(10)	84.071(2)
β /°	74.582(9)	75.065(2)
γ /°	62.229(9)	62.227(2)
V / Å^3	548.1(7)	543.40(12)
Selected interatomic distances / Å		
Te1—O5	1.887(12)	1.887(8)
Te1—O2	1.896(11)	1.889(8)
Te1—O4^{i}	1.897(11)	1.919(9)
Te1—O3^{ii}	1.922(11)	1.920(9)
Te1—O1^{iii}	1.970(12)	1.991(9)
Te1—O1	1.988(11)	1.985(8)
Te2—O8	1.870(12)	1.886(9)
Te2—O10	1.892(11)	1.896(10)
Te2—O7^{iv}	1.912(11)	1.917(7)
Te2—O9^{i}	1.923(11)	1.916(8)
Te2—O6	2.009(11)	2.001(9)
Te2—O6^{v}	2.013(12)	2.012(9)
Fe/Ga1—O3	1.809(12)	1.819(9)
Fe/Ga1—O9	1.859(11)	1.853(7)
Fe/Ga1—O4	1.880(11)	1.843(11)
Fe/Ga1—O7	1.882(12)	1.843(7)
K1—O4^{i}	2.709(12)	2.712(8)
K1—O8^{iv}	2.837(13)	2.827(9)
K1—O8	2.896(13)	2.888(11)
K1—O2	2.899(12)	2.854(8)
K1—O6^{vi}	2.926(13)	2.915(9)
K1—O7	2.952(12)	2.988(12)
K1—O11^{ii}	2.962(18)	2.901(11)
K1—O10^{vii}	3.023(12)	3.017(9)
K2—O4^{i}	2.789(12)	2.758(9)
K2—O10^{v}	2.831(12)	2.828(11)
K2—O5	2.832(13)	2.803(9)
K2—O9^{viii}	2.835(13)	2.858(11)
K2—O8^{iv}	2.928(13)	2.933(8)
K2—O6^{v}	2.940(13)	2.956(11)
K2—O10^{ix}	2.946(13)	2.916(9)
K2—O11^{x}	3.103(17)	3.105(9)
K3—O11	2.682(16)	2.669(15)
K3—O7^{xi}	2.741(12)	2.749(7)
K3—O5^{xi}	2.880(13)	2.879(12)
K3—O2^{xi}	3.009(14)	3.021(11)
K3—O11^{xi}	3.150(19)	3.146(12)
K3—O1^{ii}	3.200(12)	3.191(8)

Symmetry codes: (i) −1+*x*, *y*, *z*; (ii) 1−*x*, −*y*, 1−*z*; (iii) −*x*, −*y*, 1−*z*; (iv) 1−*x*, −*y*, −*z*; (v) −*x*, −*y*, −*z*; (vi) 1+*x*, *y*, *z*; (vii) 1−*x*, −1−*y*, −*z*; (viii) −1+*x*, 1+*y*, *z*; (ix) *x*, 1+*y*, *z*; (x) −*x*, 1−*y*, 1−*z*; (xi) 1−*x*, 1−*y*, 1−*z*.

4.2.2.4 Cobalt oxidotellurates(VI)

The attempt to synthesize potassium cobalt oxidotellurate phases from $CoCO_3$, TeO_2 and H_6TeO_6 (molar ratios 2:1:1) in an excess of KNO_3 (S16) at high temperatures led to a mixture of KCo_2O_4 (Jansen & Hoppe, 1974) and a layered phase with a similar crystal structure and an enlarged unit-cell. After SEM-EDS analysis and single-crystal diffraction studies, this phase turned out to be a layered $K–Co^{III}–Pt^{IV}$-oxide (6.4) instead of a desired potassium cobalt oxidotellurate. Exchanging KNO_3 with KCl in the reaction (S17) led to Co_3TeO_6 (Becker et al., 2006) as the sole residue after leaching the reaction product with water.

4.2.2.5 Nickel oxidotellurates(VI)

Solid state reaction S10 ($Ni(NO_3)_2(H_2O)_6$ and K_2TeO_3 with molar ratios of 1:1 in excess of KNO_3) yielded a mixture of NiO, $NiTeO_4$ and a face-centered cubic phase with $a \approx 10.07$ Å. A similar PXRD pattern corresponding to an unidentified cubic phase was observed several times from hydrothermal experiments H50–H55 (3.4.1.2), for which the composition of the cubic phase was assumed as "$NH_4Te_2O_{6.5}(H_2O)$". For batch S10, "$KTe_2O_{6.5}(H_2O)$" is an educated guess.

S20, starting from a 1:3:1.2:1.2 mixture of $NiCO_3(Ni(OH)_2)_2(H_2O)_4$, TeO_2, KNO_3 and K_2CO_3, resulted in an unknown phase, as revealed by PXRD. The reflections do not match any known literature phase and can be vaguely assigned to a phase with a crystal structure related to that of $K_2Cu_2TeO_6$ (4.2.2.6.4). It seems possible that a layered $K–Ni^{II}–Te^{VI}–O$-phase was obtained in this case, however with a different symmetry than $K_2Cu_2TeO_6$. The most intense reflections corresponding to lattice planes parallel to the layers, from which the structure is built, are very similar, while the other reflections show less agreement.

4.2.2.6 Copper oxidotellurates(VI)

Based on the serendipitous synthesis of $K_2Cu_2TeO_6$ and $K_3CuTeO_5(OH)(H_2O)$ from experiment H100, it was tried to resynthesize the two phases. Hereby the main focus was placed on $K_2Cu_2TeO_6$, because washing the reactions products with water leads to a disappearance of $K_3CuTeO_5(OH)(H_2O)$. By performing hydrothermal experiments with or without the inclusion of water in the K–Cu^{II}–Te^{VI}–O-system, a multitude of novel potassium copper oxidotellurate(VI) phases was subsequently obtained. Experiments performed during the bachelor thesis of Paul Sicher (2020) played a major role in this regard, and the most important batches from this work are included with the labels H174–H177, H203–H210, S74 and S75. In total, the bachelor thesis resulted in the discovery of seven new phases, for which the crystal structures could be determined: $K_2Cu_2TeO_6(H_2O)_4$, two polymorphs of $KCuTeO_4(OH)$, $K_4CuTe_4O_{14}(OH)_2$, $K_6Cu_9Te_4O_{24}(H_2O)_2$, $K_{10}Cu_2Te_3O_{16}$ and $K_5CuTe_2O_8(OH)_4(H_2O)_8$. In total, eleven phases in the K–Cu–Te^{VI}–O–(H)-system were found and their crystal structures analyzed (Table 28). A search in the ICSD (Version 2022-1; Zagorac et al., 2019) revealed that only one crystal structure in this system, namely that of $K_2CuTeO_4(OH)_2(H_2O)$ (Effenberger & Tillmanns, 1993), has been reported previous to the present work.

The inclusion of large K^+ cations into copper oxidotellurates(VI) frequently leads to a reduction of the periodicity of the [Cu–Te^{VI}–O] building units. The higher the K content relative to the amounts of Cu and Te in the structure, the lower the periodicity (Table 29). All possible periodicities, *i.e.*, from isolated (zero-periodic) [Cu–Te^{VI}–O] units over rods (mono-periodic) and layers (di-periodic) to a framework (tri-periodic), are observed. The various crystal structures are sorted and presented with regard to the adapted periodicity (Table 29). In this respect, it can be stated that a layered structural set-up is the most frequently observed one.

Table 28. Unit-cell data of all novel K–Cu–Te^{VI}–O–(H) phases determined by single-crystal X-ray diffraction.

Composition	Space group	*Z*	*a* / Å	*b* / Å	*c* / Å	*α* /°	*β* /°	*γ* /°	*V* / Å^3
$K_{10}Cu_2Te_3O_{16}$	*C*2/*c*	4	6.2482(10)	11.4304(18)	30.127(5)		90.992(3)		2151.3(6)
$K_5CuTe_2O_8(OH)_4(H_2O)_8$	*Pna*2$_1$	4	11.2034(17)	8.5341(14)	21.302(4)				2036.7(6)
$K_3CuTeO_5(OH)(H_2O)$	*P*2$_1$/*c*	4	6.4669(7)	12.2103(13)	10.1932(11)		101.481(3)		788.78(15)
$K_2Cu_2TeO_6$	*P*2$_1$/*c*	2	6.4096(3)	9.2386(4)	5.2840(2)		104.7060(10)		302.65(2)
$K_2Cu_2TeO_6(H_2O)$	*Cmcm*	4	8.7405(4)	5.8193(3)	12.7318(6)				649.11(5)
$K_2Cu_2TeO_6(H_2O)_4$	*P*2$_1$/*c*	4	9.810(11)	9.400(10)	10.654(12)		106.949(19)		939.8(18)
$K_3Cu_2TeO_5(OH)(CO_3)(H_2O)$	*P*2$_1$/*c*	4	10.3104(17)	9.2675(16)	10.5852(18)		93.024(6)		1008.1(3)
α-$KCuTeO_4(OH)$*	$P\bar{1}$	4	8.7693(7)	11.4715(9)	5.4687(4)	90.494(2)	80.9620(10)	124.3240(10)	446.53(6)
β-$KCuTeO_4((OH))$	*P*2$_1$/*c*	4	7.3945(3)	11.6097(5)	5.4024(3)		105.2580(10)		447.44(4)
$K_4CuTe_4O_{14}(OH)_2$	*C*2/*m*	2	13.4741(11)	7.2275(6)	7.6060(6)		101.837(3)		724.95(10)
$K_6Cu_9Te_4O_{24}(H_2O)_2$	*Pmn*2$_1$	2	12.6695(13)	10.5976(11)	9.2512(11)				1242.1(2)

* Non-standard setting chosen for similarity to monoclinic *β*-polymorph

Table 29. Crystal-chemical details of various K–Cu–Te^{VI}–O-phases.

Composition	K:(Cu+Te) ratio	Type	[Te–O] units	[Cu–O] units	[Cu–Te–O] units	CN (Cu)	BVS (Te) / v.u.	BVS (Cu) / v.u.
$K_{10}Cu_2Te_3O_{16}$	2	cluster	$[TeO_5]$, $[TeO_6]$	$[CuO_4]$	$[Cu_2Te_3O_{16/2}O_{8/1}]$	4	5.27, 5.68	1.97
$K_5CuTe_2O_8(OH)_4(H_2O)_8$	$1.\bar{6}$	cluster	$[TeO_6]$	$[CuO_4]$	$[CuTe_2O_{8/2}O_{4/1}(OH)_{4/1}]$	4	5.93, 5.82	2.99
$K_3CuTeO_5(OH)(H_2O)$	1.5	rod	$[TeO_6]$	$[CuO_4]$	$^{1}_{\infty}[Cu_2Te_2O_{16/2}O_{2/1}(OH)_{2/1}]$	4	5.79	1.98
$K_3Cu_2TeO_5(OH)(CO_3)(H_2O)$	1	layer	$[TeO_5(OH)]$	$^{2}_{\infty}[Cu_2O_{10/2}(OH)_{2/2}]$	$^{2}_{\infty}[Cu_2TeO_{15/3}(OH)_{3/3}]$	[4+1+1], [4+2]	5.86	1.90, 2.02
$K_4CuTe_4O_{14}(OH)_2$	0.8	layer	$^{1}_{\infty}[Te_4O_{16/2}O_{6/1}(OH)_{2/1}]$	$[CuO_4]$	$^{2}_{\infty}[CuTe_4O_{24/2}O_{2/1}(OH)_{2/1}]$	4	5.88	1.94
$K_2Cu_2TeO_6$	$0.\bar{6}$	layer	$[TeO_6]$	$^{2}_{\infty}[Cu_2O_{12/2}]$	$^{2}_{\infty}[Cu_2TeO_{18/3}]$	[4+2]	5.8	1.91
$K_2Cu_2TeO_6(H_2O)$	$0.\bar{6}$	layer	$[TeO_6]$	$^{2}_{\infty}[Cu_2O_{12/2}]$	$^{2}_{\infty}[Cu_2TeO_{18/3}]$	[4+2]	5.8	1.86
$K_2Cu_2TeO_6(H_2O)_4$	$0.\bar{6}$	layer	$[TeO_6]$	$^{2}_{\infty}[Cu_2O_{10/2}O_{1/1}]$	$^{2}_{\infty}[Cu_2TeO_{15/3}O_{2/2}]$	[4+1], [4+2]	5.81	1.79, 1.89
α-$KCuTeO_4(OH)$	0.5	layer	$[Te_2O_8(OH)_2]$	$^{2}_{\infty}[Cu_2O_{4/2}O_{4/1}]$	$^{2}_{\infty}[Cu_2Te_2O_{6/3}O_{12/2}(OH)_{2/1}]$	4	5.85, 5.87	1.88, 1.86
β-$KCuTeO_4(OH)$	0.5	layer	$[Te_2O_8(OH)_2]$	$^{2}_{\infty}[Cu_2O_{8/2}O_{4/1}]$	$^{2}_{\infty}[Cu_2Te_2O_{18/3}O_{4/2}(OH)_{2/1}]$	[4+2]	5.84	1.96
$K_6Cu_9Te_4O_{24}(H_2O)_2$	0.46	framework	$[TeO_6]$	$^{3}_{\infty}[Cu_9O_{48/2}(H_2O)_{1/1}]$	$^{3}_{\infty}[Cu_9Te_4O_{72/2}(H_2O)_{1/1}]$	[4+2], [4+1], [4+1], 6, [4+1]	5.87, 5.81	1.96, 1.86, 1.93, 1.91, 1.91

Potassium copper oxidotellurates(VI) with isolated [Cu−Te−O] units

Both phases, $K_{10}Cu_2Te_3O_{16}$ and $K_5CuTe_2O_8(OH)_4(H_2O)_8$, resulted from solid-state reactions performed at 400 °C under ambient atmosphere. The starting materials were CuO, H_6TeO_6 and KOH in molar ratios of 1:1:8 (S74, $K_{10}Cu_2Te_3O_{16}$) or 2:3:10 (S75, $K_5CuTe_2O_8(OH)_4(H_2O)_8$). The block-shaped crystals of $K_{10}Cu_2Te_3O_{16}$ have a blue color and seem to slowly decompose at ambient conditions after being cut into smaller pieces. Single crystals of $K_5CuTe_2O_8(OH)_4(H_2O)_8$ (preliminary composition) occurred under unclear conditions. The product of the solid-state reaction was an olive green solid, for which single crystals initially could not be found. However, after storing parts of the sample overnight in perfluorinated oil (Fomblin), which is used for mounting samples for diffraction measurements, the next day, thin orange needles of $K_5CuTe_2O_8(OH)_4(H_2O)_8$ had formed.

4.2.2.6.1 $K_{10}Cu_2Te_3O_{16}$

The asymmetric unit comprises 17 atoms (two Te, one Cu, six K and eight O), of which three (Te2, K5 and K6) are located at a higher symmetric position (site symmetry 2, 4 *e*), while all other atoms sit at general 8 *f* positions. The Te^{VI} atoms exhibit two different coordination numbers. While Te2, as common for Te^{VI}, is coordinated octahedrally by six oxygen atoms, Te1 has the rare coordination number of 5. As of 2016 (Christy et al.), only two other oxidotellurate(VI) compounds with Te^{VI} being five-coordinated are known: $Cs_2K_2TeO_5$ (Untenecker & Hoppe, 1986) and $Rb_6(TeO_5)(TeO_4)$ (Wisser & Hoppe, 1990). Like $K_{10}Cu_2Te_3O_{16}$, both literature phases contain a high amount of large alkali metal cations. The steric influence and the amount of alkali metal cations plays a significant role in the reduction of the coordination number of the Te^{VI} atoms (Sicher, 2020). The $[TeO_5]$ polyhedron has a distorted trigonal-pyramidal shape with a geometry index τ_5 of 0.716.

The $[TeO_{5/6}]$ units are isolated from each other but linked through $[CuO_4]$ units by edge-sharing to form $[Cu_2Te_3O_{16/2}O_{8/1}]$ groups, the building blocks of the structure. The Cu1 site is coordinated by four oxygen atoms in a distorted square-planar shape (τ_4 = 0.262). The resulting $[Cu_2Te_3O_{16}]$ unit has a bent shape and is oriented in the $[\bar{1}01]$ direction (Figure 88). The space between the $[Cu_2Te_3O_{16}]$ units is occupied by the K^+ cations (Figure 89), which exhibit rather low coordination numbers of 6 or 5 (K2). It can be assumed that the high K content, which forced the Te1 atoms into fivefold coordination, leads to the K^+ cations being surrounded by few, close oxygen contacts as well.

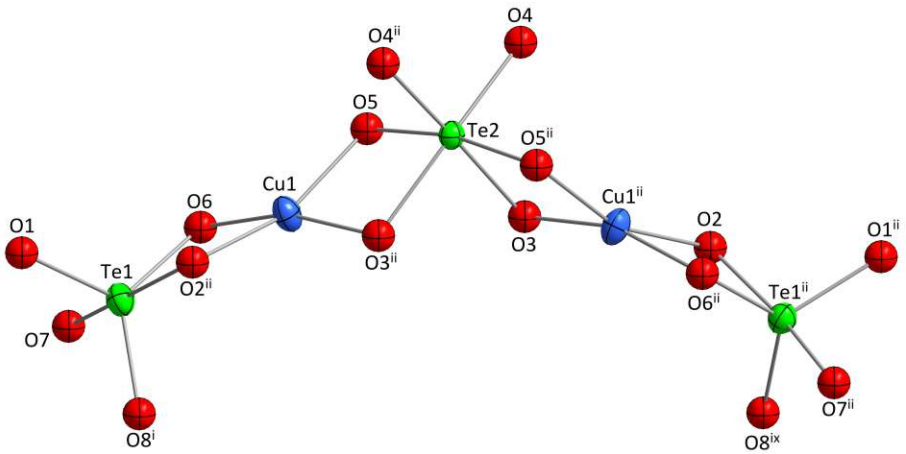

Figure 88. $[Cu_2Te_3O_{16}]$ unit in the crystal structure of $K_{10}Cu_2Te_3O_{16}$. Symmetry codes refer to Table 30.

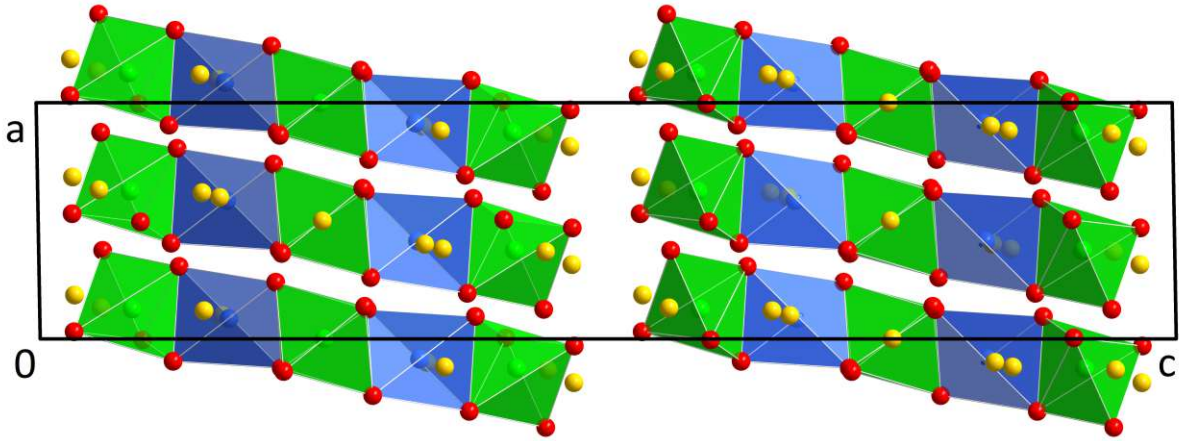

Figure 89. The crystal structure of $K_{10}Cu_2Te_3O_{16}$ viewed along $[0\bar{1}0]$.

Table 30. Selected interatomic distances in the crystal structure of $K_{10}Cu_2Te_3O_{16}$.

	d / Å		*d* / Å
Te1—O8^{i}	1.8520(12)	K2—O1^{vi}	2.8250(12)
Te1—O1	1.8541(11)	K3—O2	2.7218(12)
Te1—O7	1.8802(11)	K3—O4^{vii}	2.7397(11)
Te1—O6	1.9231(11)	K3—O6^{viii}	2.8070(13)
Te1—O2^{ii}	1.9543(10)	K3—O8^{ix}	2.9626(14)
Te2—O4	1.8920(10)	K3—O5^{ix}	2.9779(11)
Te2—O4^{ii}	1.8921(10)	K3—O7^{viii}	3.0566(14)
Te2—O5^{ii}	1.9837(9)	K4—O8^{viii}	2.6367(13)
Te2—O5	1.9837(9)	K4—O3	2.6527(11)
Te2—O3^{ii}	1.9856(10)	K4—O4	2.6860(11)
Te2—O3	1.9857(10)	K4—O5^{viii}	2.6920(10)
Cu1—O3^{ii}	1.9120(10)	K4—O6^{viii}	2.7125(11)
Cu1—O2^{ii}	1.9390(11)	K4—O2	2.9274(11)
Cu1—O5	1.9501(10)	K5—O4^{i}	2.6068(10)
Cu1—O6	1.9668(11)	K5—O4^{ix}	2.6068(10)
K1—O2^{iii}	2.6803(12)	K5—O3	2.7262(11)
K1—O8^{iv}	2.7177(13)	K5—O3^{ii}	2.7262(11)
K1—O1^{v}	2.7531(13)	K5—O5^{i}	2.9384(11)
K1—O1^{ii}	2.7617(12)	K5—O5^{ix}	2.9384(11)
K1—O7^{iv}	2.9339(15)	K6—O4	2.7056(11)
K1—O6^{iv}	3.0519(12)	K6—O4^{ii}	2.7056(11)
K2—O7^{v}	2.6005(12)	K6—O3^{x}	2.7164(10)
K2—O8	2.6810(13)	K6—O3^{xi}	2.7164(10)
K2—O7^{vi}	2.6811(13)	K6—O5^{x}	2.7898(11)
K2—O1	2.7857(14)	K6—O5^{xi}	2.7898(11)

Symmetry codes: (i) −1/2+*x*, −1/2+*y*, *z*; (ii) −*x*, *y*, 1/2−*z*; (iii) 1/2−*x*, 1/2−*y*, 1−*z*; (iv) −1/2+*x*, 1/2−*y*, 1/2+*z*; (v) 1/2+*x*, 1/2−*y*, 1/2+*z*; (vi) 1/2−*x*, 1/2−*y*, −*z*; (vii) 1/2+*x*, −1/2+*y*, *z*; (viii) 1−*x*, *y*, 1/2−*z*; (ix) 1/2−*x*, −1/2+*y*, 1/2−*z*; (x) 1/2−*x*, 1/2+*y*, 1/2−*z*; (xi) −1/2+*x*, 1/2+*y*, *z*.

4.2.2.6.2 $K_5CuTe_2O_8(OH)_4(H_2O)_8$

All atoms in the asymmetric unit, *viz*. two Te, one Cu, five K and 20 O, are located at general 4 *a* positions. No hydrogen atoms could be localized from difference-Fourier maps. In general, the dataset used for refinement was rather poor, as expected from the weak diffraction. The two Te^{VI} sites are octahedrally coordinated by six oxygen atoms with two of them belonging to hydroxide groups. The $[TeO_4(OH)_2]$ octahedra are isolated from each other but share an edge with an adjacent square-planar (τ_4 = 0.050) $[CuO_4]$ group. This arrangement leads to the formation of $[Te_2CuO_{8/2}O_{4/1}(OH)_{4/1}]$ units (Figure 90), which are oriented either in the [101] or $[\bar{1}01]$ directions (Figure 91).

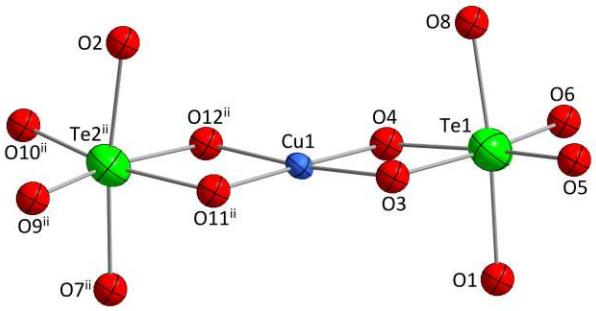

Figure 90. $[CuTe_2O_8(OH)_4]$ unit in the crystal structure of $K_5CuTe_2O_8(OH)_4(H_2O)_8$. Symmetry codes refer to Table 32.

The Cu1 site is coordinated by four oxygen atoms at unusually short distances of 1.821(18)–1.845(17) Å (Table 32) for Cu^{II}. The BVS of Cu1 amounts to 2.64 v.u. when applying the parameters for Cu^{II}—O contacts. Calculating the BVS for Cu^{III}—O bonds instead, a more fitting value of 2.99 v.u. is obtained, which matches very well the assumed oxidation number of +III for Cu.

Similar literature phases

While trivalent copper is far less common than Cu^{II}, there are a few examples of copper(III) oxidotellurate phases known. A search in the ICSD-2022.1 (Zagorac et al., 2019) for Cu^{III}–Te^{VI}–O-structures yielded the three very similar phases of $Na_{4.36}H_{0.64}(Cu[TeO_4(OH)_2]_2)(H_2O)_{16}$ (Levason et al., 1988), $Na_4H(Cu[TeO_4(OH)_2]_2)(H_2O)_{17}$ (Wu et al., 1992) and $Na_5(Cu[TeO_4(OH)_2]_2)(H_2O)_{16}$ (Al Ansari et al., 2007) as only hits. These literature crystal structures all consist of $[CuTe_2O_8(OH)_4]^{5-}$ units, just like $K_5CuTe_2O_8(OH)_4(H_2O)_8$, which would support the assumed presence of Cu^{III} in the structure. All three literature phases include the Cu^{III} atom in square-planar coordination with average Cu—O bond lengths of 1.836(4), 1.837(9) and 1.840(8) Å, respectively. The average Cu—O distance in $K_5CuTe_2O_8(OH)_4(H_2O)_8$ is 1.832(10) Å, the slightly lower value can be attributed to the measurement temperature of −173 °C compared to room temperature for the literature phases. Al Ansari et al. (2007) reported that crystals of $Na_5(Cu[TeO_4(OH)_2]_2)(H_2O)_{16}$ have a brownish orange color, which is comparable to that of the thin needles observed for $K_5CuTe_2O_8(OH)_4(H_2O)_8$. Levason et al. (1988) reported the same color and shape for crystals of $Na_{4.36}H_{0.64}(Cu[TeO_4(OH)_2]_2)(H_2O)_{16}$. Both literature phases were obtained by the oxidation of Cu^{II} in alkaline oxidotellurate(VI) solutions with the strong oxidizing agent $S_2O_8^{2-}$.

Possible interpretations of the nature of *M*1

Given the +III oxidation state of Cu and the conditions of crystallization (see above) without any known addition of a strong oxidizing agent, the possibility of other metals at the Cu1 site due to contaminations of the crucible was considered. The square-planar coordination of the *M*1 site makes Ni^{II} as a d^8-metal a possible alternative, but the BVS of Ni^{II} of 2.47 v.u. does not support this hypothesis. Based on the yellow-orange color of the crystal needles, Fe^{III} or Mn^{III} are reasonable alternatives. However, when the s.o.f. of the Cu1 site is freely refined, a value of 0.976(12) is obtained, while refining this site with a Fe or Mn atom instead resulted in values of 1.142(14) or 1.204(15), respectively. Furthermore, the BVS of the *M*1 site amounts to 3.28 v.u. based on the parameters for Fe^{III}—O contacts, and 3.29 v.u. for Mn^{III}—O. Considering Mn^{II} on the site leads to an even worse agreement with a BVS of 3.57 v.u..

Another considered option was an under-occupation of the K sites, similar to what was reported for the Na positions in $Na_{4.36}H_{0.64}(Cu[TeO_4(OH)_2]_2)(H_2O)_{16}$ (Levason et al., 1988). However, when freely refining the s.o.f.s of the five K positions, values of 0.94(2), 1.03(3), 0.99(2), 1.02(2) and 1.04(3) v.u. were obtained for the K1−K5 sites, which averages to 1.00(4) v.u. and thus supports a full occupation solely by K^+ cations.

Cu^{III} fits the crystallographic data the best of all transition metals. However, a potential mixed-occupation of different metal species on the *M*1 site might be able to emulate a similar agreement with respect to electronic density and BVS values of this site. For example, a mixture of different valences of Mn (Mn^{II} and Mn^{III}) at one site was observed for various Mn-based zemannite-type phases (4.1.6.2), and a mixed-occupancy by Mn^{II}, Mn^{III} and Cu^{II} was revealed for the synthetic zemannite-type phase $K[(Cu^{II},Mn^{II},Mn^{III})_2(TeO_3)_3](H_2O)_2$ (Eder et al., 2023c). A potential mixed occupation by different elements at the *M*1 site needs to be validated by SEM-EDS measurements, an option that was foregone due to limited amounts of material, which was additionally contaminated by the fluorinated oil, under which the crystals were stored. For the current structure model, Cu^{III} was retained. However, more follow-up investigations are needed to confirm the true nature of the metal species located at the *M*1 site. Hence, the composition of $K_5CuTe_2O_8(OH)_4(H_2O)_8$ has to be considered as preliminary.

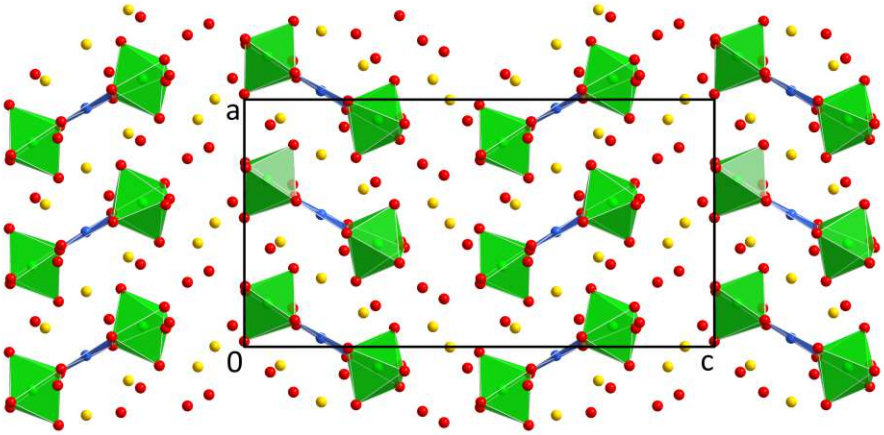

Figure 91. The crystal structure of $K_5CuTe_2O_8(OH)_4(H_2O)_8$ in a projection along [0$\bar{1}$0].

Assignment of different oxygen species

While hydrogen atoms could not be located from the diffraction data, indirect information about their positions can be drawn from BVS values and interatomic distances between the O sites (Table 31). In the crystal structure of $K_5CuTe_2O_8(OH)_4(H_2O)_8$, the O3, O4, O11 and O12 sites correspond to bridging oxygen atoms between the Cu^{III} and Te^{VI} atoms, whereas O1, O2, O5−O8, O11 and O12 correspond to terminal oxygen atoms connected to one Te^{VI} atom, and the O13−O20 sites do not have any contacts to the Cu^{III} or Te^{VI} atoms. Of the terminal O sites, the O5, O6, O9 and O10 atoms ligate with significantly shorter bonds to the Te^{VI} atom than the other four (O1, O2, O7 and O8) atoms, to which the hydroxide groups are assumed to belong (Table 32). The latter O atoms possibly augment the coordination of the central metal species as part of the second coordination sphere at Cu^{III}—O distances < 3.5 Å), while O5, O6, O9 and O10 are positioned outside this threshold. In neither of the similar Na-based reference phases, the H atoms could likewise not be located.

Table 31. Assignments of the O sites in $K_5CuTe_2O_8(OH)_4(H_2O)_8$.

Site		BVS / v.u.		Site		BVS / v.u.	
O1	terminal	1.15	OH	O11	bridging	2.07	O
O2	terminal	0.99	OH	O12	bridging	1.60	O
O3	bridging	1.64	O	O13	isolated	0.31	H_2O
O4	bridging	2.02	O	O14	isolated	0.55	H_2O
O5	terminal	1.51	O	O15	isolated	0.32	H_2O
O6	terminal	1.17	O	O16	isolated	0.51	H_2O
O7	terminal	0.94	OH	O17	isolated	0.20	H_2O
O8	terminal	1.02	OH	O18	isolated	0.24	H_2O
O9	terminal	1.24	O	O19	isolated	0.32	H_2O
O10	terminal	1.32	O	O20	isolated	0.30	H_2O

Table 32. Selected interatomic distances in the crystal structure of $K_5CuTe_2O_8(OH)_4(H_2O)_8$.

	d / Å		*d* / Å
Te1—O5	1.834(19)	K2—O17	2.87(2)
Te1—O6	1.858(18)	K2—O18	2.90(2)
Te1—O4	1.956(18)	K2—O10^{ii}	2.93(2)
Te1—O3	1.969(19)	K2—O5^{v}	3.14(2)
Te1—O8	1.990(18)	K2—O20^{ii}	3.15(3)
Te1—O1	2.003(19)	K3—O11	2.68(2)
Te2—O10	1.85(2)	K3—O4	2.690(19)
Te2—O9	1.875(19)	K3—O14^{vi}	2.70(3)
Te2—O11	1.960(19)	K3—O19^{vi}	2.73(3)
Te2—O12	1.974(16)	K3—O16	2.77(2)
Te2—O7	1.984(19)	K3—O15^{vi}	2.86(2)
Te2—O2^{i}	2.008(17)	K3—O8	3.21(2)
Cu1—O11^{ii}	1.821(18)	K4—O14^{i}	2.77(3)
Cu1—O3	1.828(18)	K4—O1^{iii}	2.820(19)
Cu1—O4	1.835(19)	K4—O9	2.926(19)
Cu1—O12^{ii}	1.845(17)	K4—O2^{i}	2.93(2)
K1—O14	2.83(2)	K4—O5^{iii}	3.00(2)
K1—O20^{ii}	2.83(2)	K4—O20	3.05(2)
K1—O8^{iii}	2.85(2)	K4—O13^{vi}	3.13(2)
K1—O4^{iv}	2.866(18)	K4—O17^{i}	3.14(2)
K1—O5^{iii}	2.98(2)	K5—O11	2.79(2)
K1—O15	3.02(3)	K5—O16^{vii}	2.805(19)
K1—O19^{ii}	3.09(2)	K5—O18^{vii}	2.91(2)
K1—O19	3.26(2)	K5—O7^{i}	2.965(19)
K2—O1^{iv}	2.72(2)	K5—O13^{vi}	2.99(2)
K2—O16	2.79(3)	K5—O2^{i}	3.03(2)
K2—O13^{v}	2.84(2)	K5—O15^{viii}	3.03(3)

Symmetry codes: (i) 1/2+*x*, 1/2-*y*, *z*; (ii) −1/2+*x*, 1/2−*y*, *z*; (iii) 1/2−*x*, 1/2+*y*, 1/2+*z*; (iv) −*x*, 1−*y*, 1/2+*z*; (v) −*x*, 1−*y*, −1/2+*z*; (vi) 1/2−*x*, 1/2+*y*, −1/2+*z*; (vii) 1/2+*x*, 3/2−*y*, *z*; (viii) 1−*x*, 1−*y*, −1/2+*z*.

Potassium copper oxidotellurates(VI) with [Cu–Te–O] chains

4.2.2.6.3 $K_3CuTeO_5(OH)(H_2O)$

$K_3CuTeO_5(OH)(H_2O)$ was obtained from a hydroflux-like reaction (H100) of CuO, TeO_2, H_6TeO_6 and KOH (molar ratios 2:1:2:15) and dissolves when the sample is leached with water after the reaction. Dark-blue crystals of $K_3CuTeO_5(OH)(H_2O)$ scattered very well, and H atoms could be localized without difficulties.

Crystal structure

The asymmetric unit contains one Te, one Cu, three K, seven O and three H sites, all located at general 4 *e* positions. The Te1 site is coordinated by five oxygen atoms and a hydroxide group in an octahedral shape. The $[TeO_5(OH)]$ units are connected to each other by sharing edges with distorted square-planar $[CuO_4]$ groups (τ_4 = 0.202). Other than in the previously discussed $K_5CuTe_2O_8(OH)_4(H_2O)_8$, each $[TeO_5(OH)]$ octahedron shares two (instead of one) of its edges with $[CuO_4]$ units, thus leading to the formation of infinite $^1_\infty[Cu_2Te_2O_{16/2}O_{2/1}(OH)_{2/1}]$ chains instead of finite $[CuTe_2O_8(OH)_4]$ groups. These $[CuTeO_5(OH)]$ rods have a weak zig-zag shape and extend parallel to [001] (Figure 92).

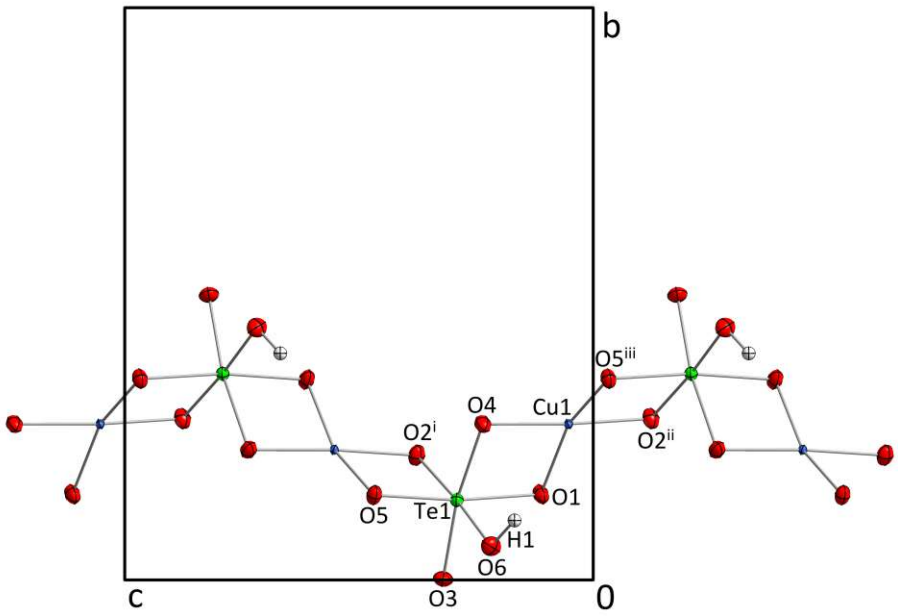

Figure 92. $^1_\infty[Cu_2Te_2O_{10}(OH)_2]$ chains in the crystal structure of $K_3CuTeO_5(OH)(H_2O)$. Symmetry codes refer to Table 33.

The space between the chains is filled by three K^+ cations and one water molecule p.f.u.. The K sites have variable coordination numbers of 9 (K1), 6 (K2) and 7 (K3) and are coordinated by the oxygen atoms of the $[CuTeO_5(OH)]$ chains and the crystal water molecule associated with the O7 position. The BVS of the K^+ cations were calculated to 1.02 (K1), 1.21 (K2) and 1.22 (K3) v.u.. The water molecule (O7) is a donor for medium-strong hydrogen bonds towards O1 and O5 atoms in different chains, and an acceptor for the weaker hydrogen bond formed by the hydroxide group located at the O6 site. The hydrogen bonds of O7 connect the $[CuTeO_5(OH)]$ rods along [100] (Figure 93). O6 is, besides O3, one of two terminal Te—O positions. O3 compensates its low bond valence within the chain by four close K-contacts at distances of 2.6750(7)–2.7163(7) Å (Table 33). The hydroxide group at the O6 position only has two of these K-contacts.

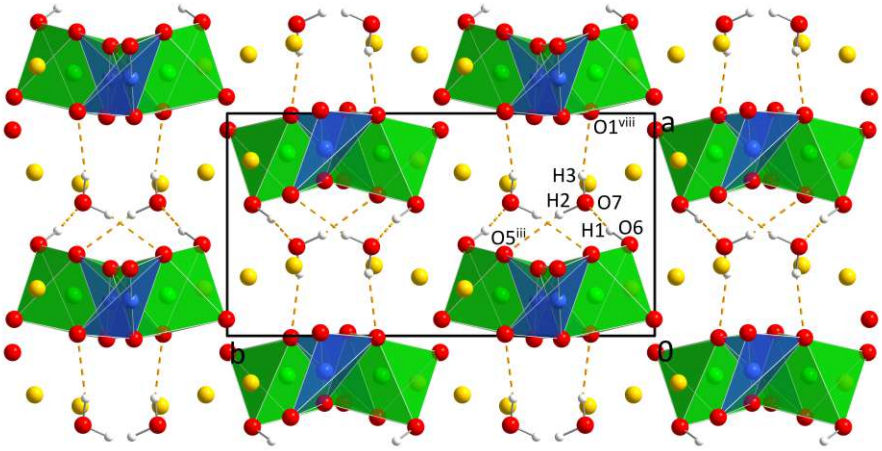

Figure 93. The crystal structure of $K_3CuTeO_5(OH)(H_2O)$ viewed along $[00\bar{1}]$.

Table 33. Selected interatomic distances in the crystal structure of $K_3CuTeO_5(OH)(H_2O)$.

	d / Å		*d* / Å
Te1—O3	1.8621(7)	K1—O2^{i}	3.1215(7)
Te1—O2^{i}	1.9239(7)	K1—O6^{vi}	3.2421(7)
Te1—O4	1.9339(7)	K1—O6^{v}	3.2515(8)
Te1—O1	1.9461(6)	K2—O3^{iii}	2.6750(7)
Te1—O5	1.9567(6)	K2—O6^{vi}	2.7012(7)
Te1—O6	2.0370(7)	K2—O3^{iv}	2.7163(7)
Cu1—O4	1.9108(6)	K2—O2	2.7371(7)
Cu1—O2^{ii}	1.9157(6)	K2—O5^{iii}	2.7648(7)
Cu1—O1	1.9475(7)	K2—O5^{vi}	2.7681(7)
Cu1—O5^{iii}	1.9862(7)	K3—O4	2.5958(7)
K1—O3^{iv}	2.6933(7)	K3—O2^{vii}	2.6088(7)
K1—O4	2.8175(7)	K3—O3^{vi}	2.6751(7)
K1—O1^{iv}	2.8666(7)	K3—O6^{vi}	2.7274(8)
K1—O7^{v}	2.8847(8)	K3—O7^{v}	2.9194(8)
K1—O7^{vi}	2.9671(8)	K3—O7	3.1873(8)
K1—O1^{v}	2.9889(7)	K3—O5^{iii}	3.2033(7)
O6—H1	0.90(2)	O6—H1···O7	2.8393(11)
O7—H2	0.82(2)	O7—H2···O5^{iii}	2.7521(10)
O7—H3	0.78(2)	O7—H3···O1^{viii}	2.6276(10)

Symmetry codes: (i) $-x, -1/2+y, 1/2-z$; (ii) $-x, 1-y, -z$; (iii) $x, 1/2-y, -1/2+z$; (iv) $-x, 1/2+y, 1/2-z$; (v) $x, 1/2-y, 1/2+z$; (vi) $1-x, 1/2+y, 1/2-z$; (vii) $1-x, -1/2+y, 1/2-z$; (viii) $1+x, y, z$.

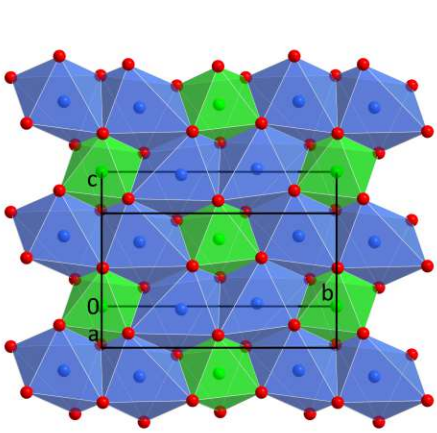

a) $K_2Cu_2TeO_6$ (d = 6.120 Å)

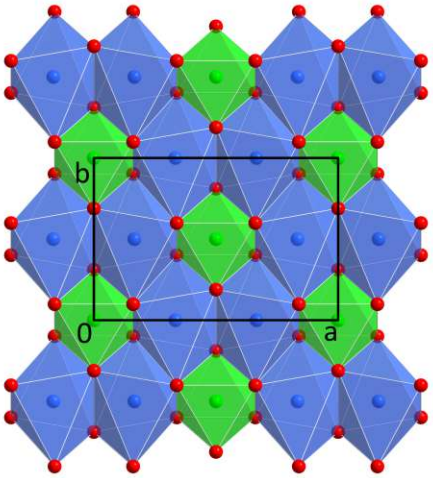

b) $K_2CuTeO_6(H_2O)$ (d = 6.366 Å)

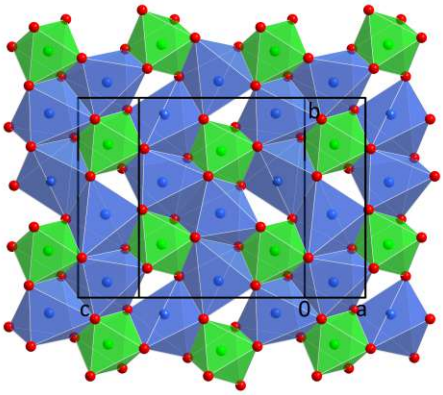

c) $K_2CuTeO_6(H_2O)_4$ (d = 9.384 Å)

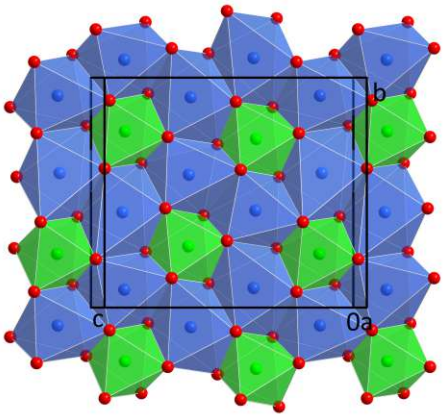

d) $K_3Cu_2TeO_5(OH)(CO_3)(H_2O)$ (d = 10.296 Å)

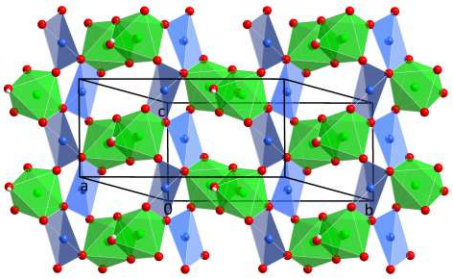

e) α-$KCuTeO_4(OH)$ (d = 7.118 Å)

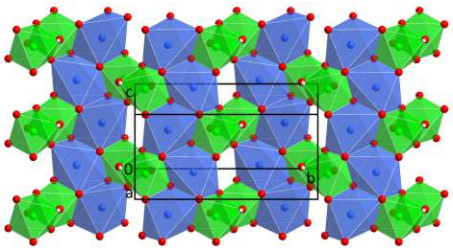

f) β-$KCuTeO_4(OH)$ (d = 7.134 Å)

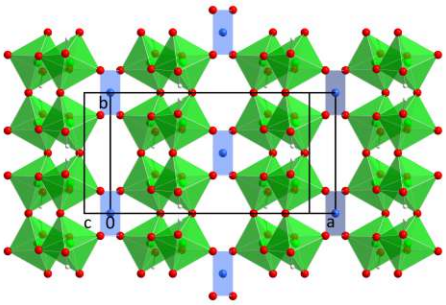

g) $K_4CuTe_4O_{14}(OH)_2$ (d = 7.444 Å)

Figure 94. [Cu–Te–O] layers in the crystal structures of all layered K–Cu–Te^{VI}–O-phases projected along the normal of the layer plane. The interlayer distance d is indicated in this direction as well.

4.2.2.6.4 $K_2Cu_2TeO_6$

Synthesis

$K_2Cu_2TeO_6$ was initially synthesized from a hydroflux-like reaction (H100) of CuO, TeO_2, H_6TeO_6 and KOH (molar ratios 2:1:2:15), but different to $K_3CuTeO_5(OH)(H_2O)$ is also stable after the leaching process with water. In the PXRD pattern of the washed reaction product, CuO and assumably higher hydrated phases of $K_2Cu_2TeO_6$ were identified. Hydroflux experiments H414−H416 were targeted at the phase-pure synthesis of $K_2Cu_2TeO_6$. The best yields were obtained for molar ratios of 2:1:10 of CuO, H_6TeO_6 and KOH (H416).

$K_2Cu_2TeO_6$ was resynthesized from a solid-state reaction based on $Cu(NO_3)_2(H_2O)_{2.5}$, H_6TeO_6 and KOH (2:1:8) at 500 °C (S13). Another successful, but also not phase-pure synthesis of $K_2Cu_2TeO_6$ (S19) was based on a mixture of $CuCO_3Cu(OH)_2$, H_6TeO_6, KNO_3 and K_2CO_3 (molar ratios 1:2:0.8:0.8), which was tempered at 800 °C.

Five hydrothermal experiments targeting at $K_2Cu_2TeO_6$ were performed in the magnetically stirred microwave furnace (M13−M17). The first four experiments (M13−M16) started from $Cu(NO_3)_2(H_2O)_{2.5}$, H_6TeO_6 and increasing amounts of KOH. For M13−M15, Cu_3TeO_6 (Hostachy & Coing-Boyat, 1968) was the main reaction product, while for the batch with the highest alkalinity (M16), $K_6Cu_9Te_4O_{24}(H_2O)_2$ (4.2.2.6.10) was obtained. Starting from CuO instead of $Cu(NO_3)_2(H_2O)_{2.5}$ (M17), only the starting material CuO was identified as the solid residue. No signs of $K_2Cu_2TeO_6$ were found in any of these experiments.

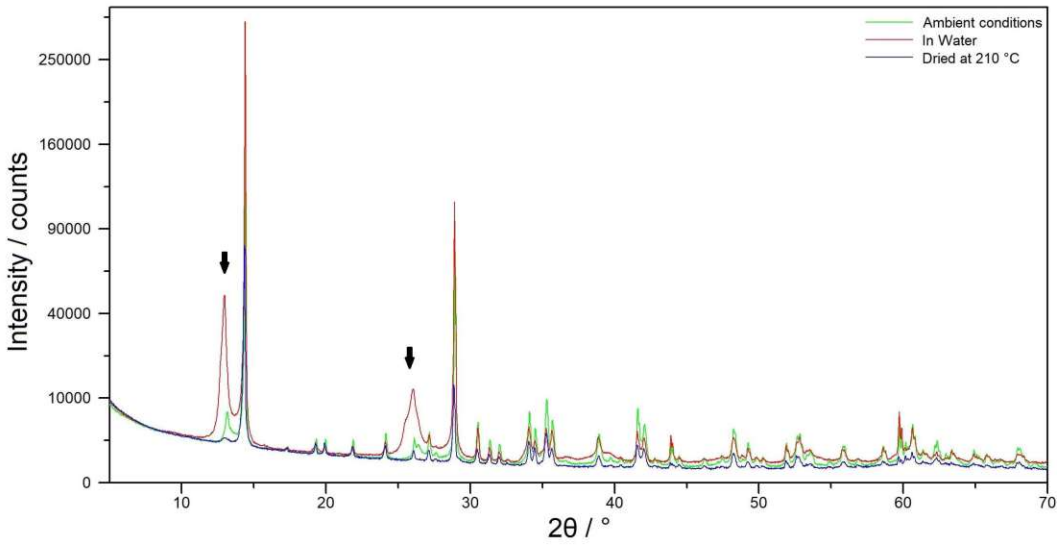

Figure 95. PXRD patterns of $K_2Cu_2TeO_6$ stored for several months under ambient conditions (green), stored in water for a few days (red), or dried at 210 °C (blue). Selected reflections of hydration products are marked with black arrows.

Single crystals of $K_2Cu_2TeO_6$ have an emerald-green color and the form of thick plates. The plate-like habit has an impact on PXRD measurements, where a strong (100) texture was consistently observed. Crystals of $K_2Cu_2TeO_6$ slowly weather when stored at ambient conditions, which is caused by the incorporation of water between the layers. This process can be tracked by PXRD, where additional broad reflections appear at lower diffraction angles next to the intense (*n*00) reflections, as the inclusion of water increases the distance *d* between the layers (Figure 95). The included water can be driven out of the crystal structure by heating up the sample; hereby a temperature of 210 °C is sufficient.

Crystal structure

In the crystal structure of $K_2Cu_2TeO_6$, the asymmetric unit contains one Te (site symmetry $\bar{1}$, 2 *a*), one Cu, one K and three O (all 4 *e*) atoms. The Te1 site exhibits, aided by its $\bar{1}$ site symmetry, an almost perfect octahedral coordination by six oxygen atoms; the [TeO_6] octahedra are isolated from each other. The Cu1 position exhibits a [4+2] coordination by four oxygen atoms at distances of 1.975(2)−2.064(2) Å (τ_4 = 0.104) and two remote oxygen atoms at 2.468(2) and 2.501(2) Å (Table 34). This shape is frequently observed for strong Jahn−Teller induced distortions (Lufaso & Woodward, 2004). The BVS of Cu^{II} for the fourfold coordination amounts to only 1.69 v.u., while it is 1.91 v.u. considering all six neighbors. The [CuO_6] polyhedra are connected to each other by sharing edges with three adjacent units, thus forming $^2_\infty$[$Cu_2O_{12/2}$] layers oriented parallel to (100). The Cu^{II} atoms of such a layer form a slightly distorted honeycomb net. The hexagonal voids in the net are occupied by the Te^{VI} atoms, resulting in $^2_\infty$[$Cu_2TeO_{18/3}$] layers. The space between the layers is occupied by the K^+ cations, which have a CN of 7 and a BVS of 1.23 v.u. (Figure 96).

The structure of the $[Cu_2TeO_6]^{2-}$ layers can be derived from those in the crystal structure of MoS_2 (Dickinson & Pauling, 1923; Bell & Hefert, 1957), with one-third of the Cu^{II} atoms substituted by Te^{VI} atoms to form a honeycomb-like pattern (Figure 94a). Such a set-up is rather common in phases with $A_2M_2TeO_6$ (*A* = alkali metal, *M* = transition metal) composition. The layers in $K_2Cu_2TeO_6$ show a high degree of distortion, whereas for other $A_2M_2TeO_6$ structures they can have (pseudo-)hexagonal symmetry ($Li_2Cu_2TeO_6$ (*C*2/*m*, Kumar et al., 2013), $Na_2Cu_2TeO_6$ (*C*2/*m*, Xu et al., 2005), $Li_2Ni_2TeO_6$ (*Cmca*, Grundish et al., 2019; *Fddd*, Kumar et al., 2013), $Na_2Co_2TeO_6$ ($P6_322$, Bera et al., 2017), and $Na_2Ni_2TeO_6$ ($P6_3/mcm$, Kurbakov et al., 2020)). In general, the Cu^{II}-containing phases exhibit a lower symmetry than the Co^{II}- and Ni^{II}-compounds, which is attributed to the distorted [CuO_6] coordination polyhedra caused by the strong Jahn−Teller effect, which consequently lower the symmetry. It should be noted that in most reported high-symmetric $A_2M_2TeO_6$ structures, the A^+ cations between the layers are positionally disordered.

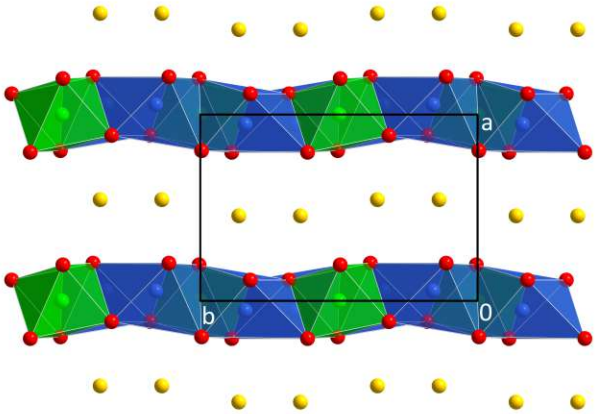

Figure 96. The crystal structure of $K_2Cu_2TeO_6$ viewed along [00$\bar{1}$].

Table 34. Selected interatomic distances in the crystal structure of $K_2Cu_2TeO_6$.

	d / Å		*d* / Å
Te1—O2	1.9232(19)	Cu1—O3	2.468(2)
Te1—O2^{i}	1.9232(19)	Cu1—O2^{vi}	2.501(2)
Te1—O1^{ii}	1.9476(18)	K1—O2^{vii}	2.614(2)
Te1—O1^{iii}	1.9476(18)	K1—O1^{viii}	2.632(2)
Te1—O3^{ii}	1.949(2)	K1—O2	2.658(2)
Te1—O3^{iii}	1.949(2)	K1—O3^{ii}	2.700(2)
Cu1—O2	1.975(2)	K1—O1^{ix}	2.950(2)
Cu1—O1^{iv}	1.981(2)	K1—O3^{viii}	3.044(2)
Cu1—O3^{v}	1.984(2)	K1—O3	3.267(2)
Cu1—O1^{iii}	2.064(2)		

Symmetry codes: (i) −*x*, −*y*, −*z*; (ii) *x*, 1/2−*y*, −1/2+*z*; (iii) −*x*, −1/2+*y*, 1/2−*z*; (iv) −*x*, 1−*y*, 1−*z*; (v) *x*, 1/2−*y*, 1/2+*z*; (vi) −*x*, −*y*, 1−*z*; (viii) 1−*x*, −*y*, 1−*z*; (ix) 1−*x*, −1/2+*y*, 1/2−*z*; (x) 1−*x*, 1−*y*, 1−*z*.

Additional studies on $K_2Cu_2TeO_6$

As noted in the previous section, several $A_2M_2TeO_6$ phases exhibit orthorhombic or hexagonal crystal structures, while the symmetry of $K_2Cu_2TeO_6$ is monoclinic. Hence, the existence of $A_2M_2TeO_6$ phases with higher symmetry makes $K_2Cu_2TeO_6$ a possible candidate for a structural phase transition. Therefore, the behavior of $K_2Cu_2TeO_6$ with increasing temperature and pressure was investigated.

High-temperature powder diffraction

Temperature-dependent PXRD measurements on $K_2Cu_2TeO_6$ were performed at the at the Brockhouse High Energy Wiggler Beamline, Canadian Light Source (CLS), Canada. The starting material, $K_2Cu_2TeO_6$ had been pre-dried at 210 °C for more than one week to ensure that no water was incorporated between the [Cu−Te−O] layers, was ground to a fine powder and was filled into a glass capillary, which was subsequently sealed. The PXRD measurements were performed in a 2−30° 2θ range with an X-ray wavelength of 0.408 Å. After a starting measurement at 25 °C, 17 measurements were executed in a range of 100−900 °C with increments of 50 °C.

During heating from 25 to 700 °C, no significant changes could be observed in the diffraction pattern. $K_2Cu_2TeO_6$ is present as the main phase, although small traces of CuO are assumed to be present as well. Unfortunately, the most pronounced reflections of CuO overlap with ones from $K_2Cu_2TeO_6$, making a qualitative identification difficult (Figure 97). The lattice parameters of $K_2Cu_2TeO_6$ increase linearly with temperature, albeit with significantly different individual values. The linear coefficient of thermal expansion (CTE) α was calculated using the lattice parameters at 25 °C as reference value l_0 (Figure 98). The thermal expansion is significantly larger in the stacking direction **a** than within the layer plane (**b**, **c**). The apparent weaker K—O bonds present along the stacking direction compared to the stronger Cu—O and Te—O bonds within a [Cu−Te−O] layer presumably are resposible for this behavior.

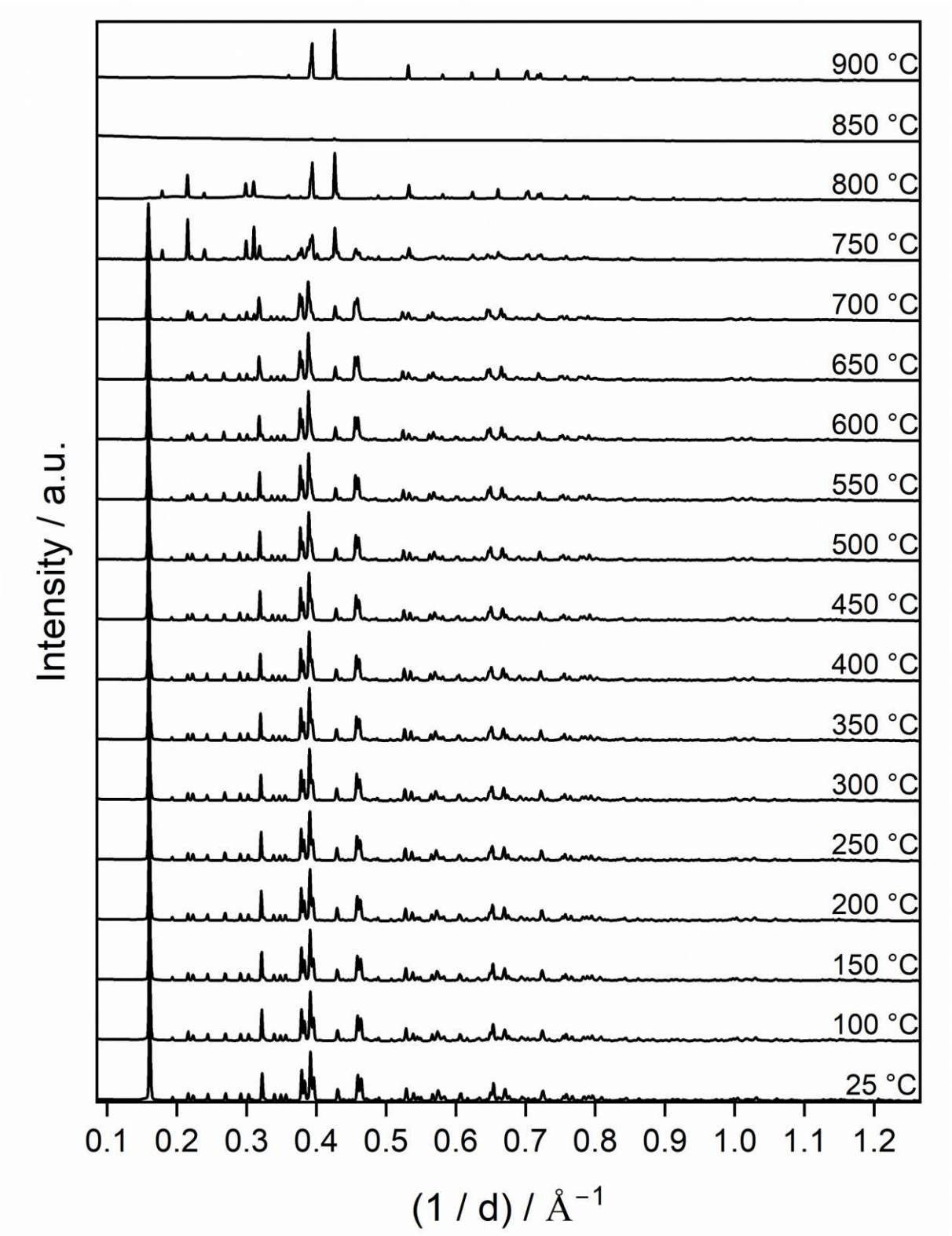

Figure 97. Temperature-dependent PXRD measurements of $K_2Cu_2TeO_6$.

The diffraction pattern drastically changes at 750 °C. The monoclinic $K_2Cu_2TeO_6$ phase is not present anymore, instead reflections preliminary assigned to two unknown phases (denoted as A and B), were observed. The A phase shows reflections at positions formerly corresponding to $K_2Cu_2TeO_6$, including the most intense (100) reflection. This could indicate either a structurally related decomposition product of $K_2Cu_2TeO_6$ or a potential phase transition of monoclinic $K_2Cu_2TeO_6$ to a high-temperature modification. However, attempts to fit the reflections (750 °C measurement) to crystal structures of several higher-symmetric $A_2M_2TeO_6$ phases with adjusted lattice parameters failed. The B phase has a different pattern with its strongest reflections appearing at 2θ|*d* values of 4.19°|5.59 Å, 5.04°|4.65 Å, 5.60°|4.18 Å, 7.00°|3.35 Å and 7.27°|3.22 Å.

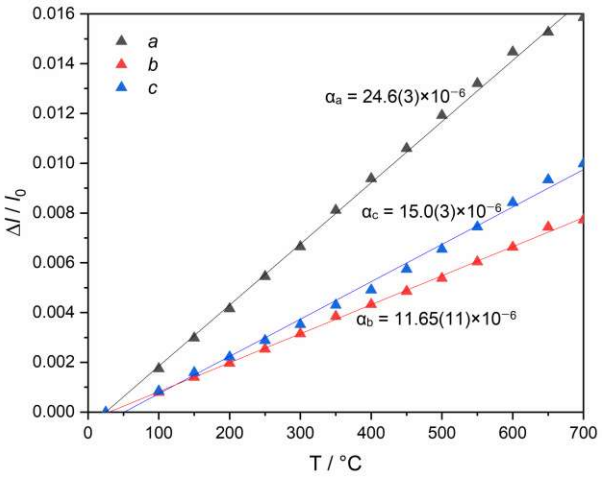

Figure 98. Relative change of lattice parameters of $K_2Cu_2TeO_6$ with increasing temperature.

At 800 °C, the A phase is no longer visible, possibly supporting the hypothesis of an intermediate decomposition product of $K_2Cu_2TeO_6$. Only CuO and the B phase are present. The background shows two broad low-intensity signals, which might indicate an amorphous phase or small amounts of a liquid phase. The measurement at 850 °C completely differs from the others, as that reflections appear only at much weaker intensities and the background intensity is about twice as large. CuO is the predominant phase then, albeit with much weaker reflections than in the measurements at both 800 °C and 900 °C. This strange behavior might correlate with the dominance of a liquid phase at 850 °C. Interestingly, the measurement at 900 °C again features intensities comparable to all measurements except for 850 °C and contains CuO as the only crystalline product. Similar to the 800 °C measurement, varying background intensities indicate the presence of an amorphous/liquid phase.

High-pressure Raman spectroscopy

Previously to the measurements, a $K_2Cu_2TeO_6$ single crystal was stored at temperatures of 210 °C to ensure the absence of water. The crystal was then loaded into a diamond anvil-cell with Ar as the pressure medium. During the measurements, the pressure inside the cell was monitored by Raman spectra of a reference crystal (ruby) placed inside the cell. After loading of the cell, a pressure of 8.19 GPa was adjusted. The pressure then was increased to 10.15 GPa in four steps and afterwards released in steps of *ca.* 1 GPa. A Raman-spectrum was recorded with a Horiba Jobin Yvon Labram HR spectrometer at each pressure point (Figure 99).

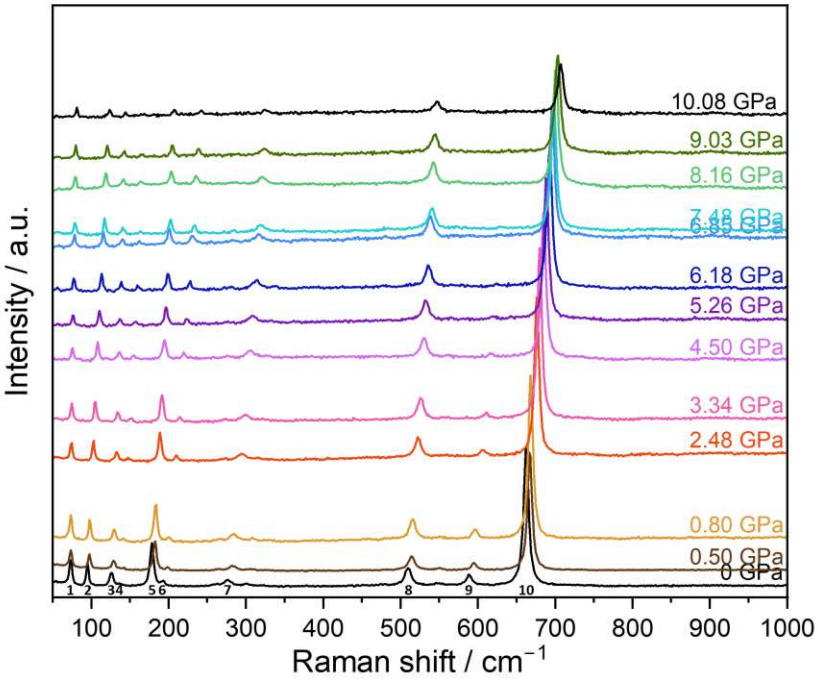

Figure 99. Raman spectra of the decompression series of $K_2Cu_2TeO_6$ from 10.08 GPa to ambient pressure. The vertical shift of the respective measurements was chosen proportionally to the pressure differences.

Although increasing the pressure resulted in the expected blue-shift of the vibration bands, a few irregularities were observed.

- The band at around 600 cm^{-1} (9) appeared only after reducing the pressure to *ca.* 5–7 GPa. Very weak bands starting with Raman-shifts of 261 cm^{-1} and 300 cm^{-1} at ambient pressure (not labelled) show a similar behavior.
- When plotting the Raman shifts of the respective bands against the applied pressure, a slight change of the slope could be observed in the same 5–7 GPa region (Figure 100).
- Unrelated to this, the data point at ambient pressure does not match the remaining data sets.

These features hint at a potential second-order phase transition of $K_2Cu_2TeO_6$ in the pressure range of 5–7 GPa. For future follow-up experiments, single-crystal X-ray diffraction studies at *ca*. 10 GPa are necessary to get a deeper picture of this behavior.

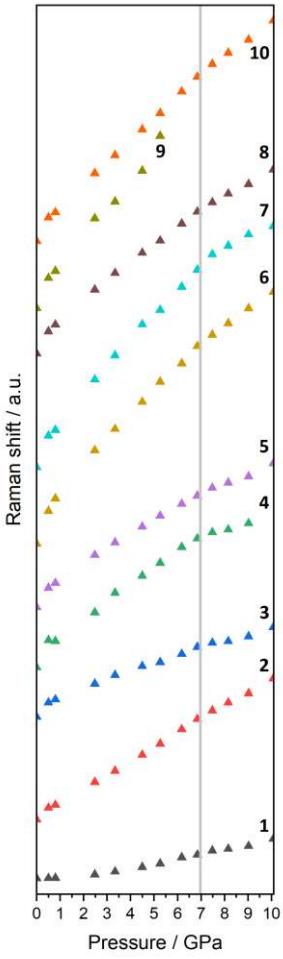

Figure 100. Shift of selected bands of $K_2Cu_2TeO_6$.

4.2.2.6.5 $K_2Cu_2TeO_6(H_2O)$

$K_2Cu_2TeO_6(H_2O)$ was obtained from CuO, H_6TeO_6 and KOH (molar ratios 2:1:5) in a hydroflux-like reaction (H104). The simulated powder diffraction pattern of $K_2Cu_2TeO_6(H_2O)$ does not match the PXRD patterns of weathered $K_2Cu_2TeO_6$ exposed to humidity for a longer amount of time (Figure 95), which assumably features a more disordered structure caused by the unsystematic inclusion of water. Single crystals of $K_2Cu_2TeO_6(H_2O)$ have the shape of thick plates and a grass-green color.

Crystal structure

The asymmetric unit contains seven atoms, with most of them being located at positions with increased site symmetry. The sites with their symmetries, multiplicity and Wyckoff letters are Te1 (2/*m*.., 4 *a*), Cu1 (2.., 8 *e*), K1 (..*m*, 8 *g*), O1 (1, 16 *h*), O2 (*m*.., 8 *f*) O3 (*m*2*m*, 4 *c*) and H1 (*m*.., 8 *f*).

The constitution of the $^{2}_{\infty}[Cu_2TeO_{18/3}]$ layers is very similar to those of $K_2Cu_2TeO_6$ (Figure 94a, b), except for the layers being oriented parallel to (001) instead of (100) due to the different unit-cell setting. The $[Cu1O_6]$ polyhedra in $K_2Cu_2TeO_6(H_2O)$ are even more distorted than in the anhydrous phase. The two remote oxygen atoms located in *trans*-positions are 2.6134(11) Å away from Cu1 (Table 35). Nevertheless, they were attributed to the coordination sphere of Cu1, as their exclusion would result in a low BVS of 1.70 v.u. instead of 1.86 v.u..

Discernable from the given site symmetries, the hydrogen atoms adjacent to the crystal water O3 sites are connected by m_{001} symmetry. They form weak hydrogen bonds towards O2 positions (Figure 101). As there are two O2 atoms available at the exact same distance for each H atom, it can be assumed that the H atoms are actually tilted towards one of the two possible acceptors and that the H1 position is only an average position between the two possible arrangements. This could also explain the too small H1—O3—H1-angle of 93(4)°.

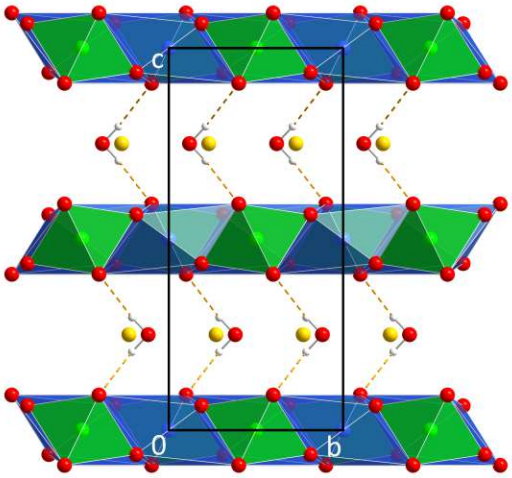

Figure 101. The crystal structure of $K_2Cu_2TeO_6(H_2O)$ viewed along [$\bar{1}$00]. The "doubled" hydrogen-bonds are not visible, as the two possible O2 sites are symmetrically connected by the m_{100} site symmetry of the H1 and O3 positions.

Table 35. Selected interatomic distances in the crystal structure of $K_2Cu_2TeO_6(H_2O)$.

	d / Å		*d* / Å
Te1—O1	1.9190(11)	Cu1—O1^{viii}	2.6134(11)
Te1—O1^{i}	1.9190(11)	Cu1—O1	2.6134(11)
Te1—O1^{ii}	1.9190(11)	K1—O1^{iv}	2.6631(12)
Te1—O1^{iii}	1.9190(11)	K1—O1	2.6631(12)
Te1—O2^{iv}	1.9858(14)	K1—O3^{x}	2.743(2)
Te1—O2^{v}	1.9858(14)	K1—O1^{xi}	2.7799(12)
Cu1—O2^{vi}	1.9933(10)	K1—O1^{xii}	2.7799(12)
Cu1—O2^{vii}	1.9933(10)	K1—O2^{xiii}	2.8739(13)
Cu1—O1^{iii}	2.0001(11)	K1—O2^{vi}	2.8739(13)
Cu1—O1	2.0002(11)	K1—O3	2.8989(8)
O3—H1	0.79(4)	O3—H1···O1/O1^{ii}	2.9572(17)
O3—H1^{xiv}	0.79(4)	O3—H1···O1^{iv}/O1^{xiv}	2.9572(17)

Symmetry codes: (i) −*x*, −*y*, −*z*; (ii) −*x*, *y*, *z*; (iii) *x*, −*y*, −*z*; (iv) *x*, *y*, 1/2−*z*; (v) −*x*, −*y*, −1/2+*z*; (vi) 1/2−*x*, 1/2−*y*, −1/2+*z*; (vii) 1/2+*x*, −1/2+*y*, 1/2−*z*; (viii) 1/2−*x*, 1/2−*y*, −*z*; (ix) 1/2−*x*, −1/2+*y*, *z*; (x) 1/2+*x*, −1/2+*y*, *z*; (xi) 1/2−*x*, 1/2+*y*, 1/2−*z*; (xii) 1/2−*x*, 1/2+*y*, *z*; (xiii) 1/2−*x*, 1/2−*y*, 1−*z*; (xiv) −*x*, *y*, 1/2−*z*.

4.2.2.6.6 $K_2Cu_2TeO_6(H_2O)_4$

$K_2Cu_2TeO_6(H_2O)_4$ was discovered in the residue of hydroflux-like experiment H176 (CuO, H_6TeO_6 and KOH in molar ratios of 1:1:8) after leaching the sample with water. The green plate-shaped single crystals of $K_2Cu_2TeO_6(H_2O)_4$ showed weaker diffraction intensities than those of $K_2Cu_2TeO_6$ and $K_2Cu_2TeO_6(H_2O)$. Moreover, twinning of the crystals indicated by splitting of reflections as well as one-dimensional diffuse scattering in the reciprocal stacking direction was observed for $K_2Cu_2TeO_6(H_2O)_4$. Consequently, the results of the subsequent refinement were of rather low quality. The majority of the observed reflections can be assigned to two monoclinic twin domains (a = 9.810(11) Å, b = 9.400(10) Å, c = 10.654(12) Å, β = 106.949(19)°, V = 939.8(18) Å^3). Their unit-cells are related by a twofold rotation along the c-axis. Integration of the intensities under consideration of two domains (hkl5-type file) and subsequent refinement revealed a twin ratio of 0.543:0.457(4). Additional reflections were clearly visible along certain rods in reciprocal space, which indicated the presence of further domains. However, consideration of two additional domains resulted in unreasonable models.

Crystal structure

Hydrogen atoms could not be localized. The asymmetric unit contains one Te, two Cu, two K and ten O atoms, all located at general 4 *e* positions. Oxygen labels O7−O10 were assigned to the crystal water molecules. Generally, the $^2_\infty[Cu_2TeO_6]$ layers have the same honeycomb-like structure as those in $K_2Cu_2TeO_6$ and $K_2Cu_2TeO_6(H_2O)$ (Figure 94a−c). However, the Te^{VI} and Cu^{II} atoms forming the layers exhibit more distorted coordination environments than in the less-hydrated phases.

The Te1 atoms are coordinated by six oxygen atoms with distances between 1.889(11) and 1.980(11) Å, which is a larger interval than in $K_2Cu_2TeO_6$ and $K_2Cu_2TeO_6(H_2O)$. A bigger difference to the less-hydrated phases is observed for the coordination sphere of the Cu1 position. The four close oxygen contacts with bond lengths of 1.965(11)−2.008(11) Å form a $[CuO_4]$ square (τ_4 = 0.114), like in the other $K_2Cu_2TeO_6$ phases. The fifth and sixth oxygen atoms are located much farther away at distances of 2.626(11) and 2.933(12) Å (Table 36). While the first value is comparable to the longest Cu—O distances in $K_2Cu_2TeO_6(H_2O)$ (2.6134(11) Å), the larger contact is too far away to be part of the first coordination sphere of Cu1. The resulting $[Cu1O_5]$ unit has a square-pyramidal shape (τ_5 = 0.072). Cu2 exhibits a [4+2] coordination with interatomic distances similar to the Cu site in $K_2Cu_2TeO_6$.

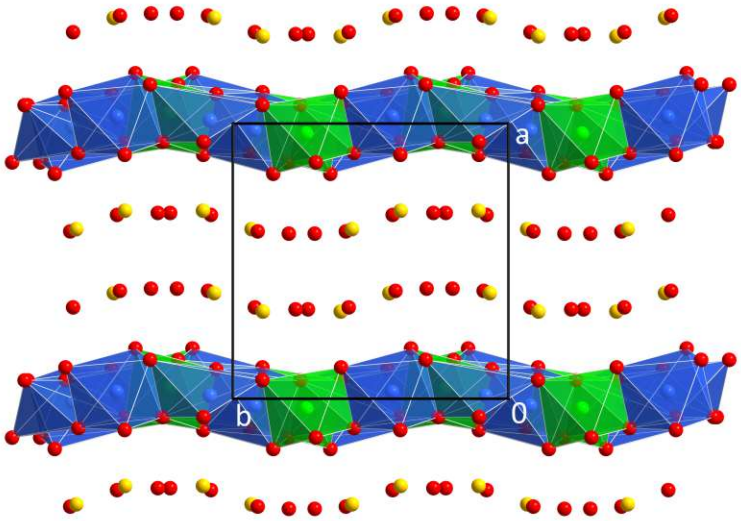

Figure 102. The crystal structure of $K_2Cu_2TeO_6(H_2O)_4$ viewed along [00$\bar{1}$].

Based on coordination environments of [Te1O_6], [Cu1O_5] and [Cu2O_6], the [$CuO_{5,6}$] polyhedra are connected to two neighboring [$CuO_{5,6}$] units by edge-sharing and one more by corner-sharing, leading to the formation of $^2_\infty$[$Cu_2O_{10/2}O_{1/1}$] layers extending parallel to (100). With the inclusion of the Te^{VI} atoms, the layers can be denominated as $^2_\infty$[$Cu_2TeO_{15/3}O_{2/2}$]. They have a slightly undulated shape when viewed along [00$\bar{1}$].

The crystal structure of $K_2Cu_2TeO_6(H_2O)_4$ exhibits a significantly longer distance between two adjacent [Cu−Te−O] layers (9.384 Å) than $K_2Cu_2TeO_6$ (6.1996 Å) or $K_2Cu_2TeO_6(H_2O)$ (6.3659 Å). This difference results from the significantly larger amount of water molecules leading to the formation of a K^+–H_2O-double-layer rather than a single-layer in the less-hydrated phases. The arrangement of K^+ cations and water molecules follows the weak undulation of the $^2_\infty$[Cu_2TeO_6] layers (Figure 102).

The appearance of complicated twinning and diffuse scattering most likely is associated with the larger number of atoms between the $^2_\infty$[Cu_2TeO_6] layers. The presence of two (instead of one) layers of K^+ cations and water molecules decreases the interlayer interactions and therefore the ordering along the stacking direction. A description of the crystal structure applying OD theory has been considered, but the grade of simplification for an appropriate higher pseudo-symmetry of one of the two layer types would have been too high.

Table 36. Selected interatomic distances in the crystal structure of $K_2Cu_2TeO_6(H_2O)_4$.

	d / Å		*d* / Å
Te1—O5	1.889(11)	K1—O9	2.769(18)
Te1—O6	1.899(12)	K1—O10^{vi}	2.856(19)
Te1—O4^{i}	1.941(11)	K1—O9^{vii}	3.032(17)
Te1—O1^{i}	1.965(11)	K1—O8	3.06(2)
Te1—O2^{i}	1.965(11)	K1—O4^{ii}	3.203(12)
Te1—O3	1.980(11)	K1—O7	3.216(19)
Cu1—O3	1.965(11)	K1—O7^{vii}	3.28(2)
Cu1—O2^{ii}	1.995(11)	K1—O3	3.313(12)
Cu1—O2^{iii}	2.004(10)	K1—O8^{viii}	3.33(2)
Cu1—O1^{i}	2.008(11)	K2—O2^{vi}	2.728(12)
Cu1—O5^{iv}	2.626(11)	K2—O3^{ix}	2.740(12)
Cu1—O6^{i}	2.933(12)	K2—O1^{vi}	2.905(12)
Cu2—O5^{iv}	1.977(11)	K2—O7^{x}	2.928(19)
Cu2—O1^{i}	1.984(10)	K2—O7	2.938(19)
Cu2—O4	2.011(11)	K2—O9	2.963(17)
Cu2—O3^{v}	2.029(11)	K2—O10	2.963(19)
Cu2—O6	2.493(14)	K2—O10^{viii}	3.010(18)
Cu2—O4^{iii}	2.527(13)	K2—O8^{ix}	3.05(2)
K1—O5	2.624(13)	K2—O8^{viii}	3.13(2)

Symmetry codes: (i) −*x*, −1/2+*y*, 1/2−*z*; (ii) *x*, −1+*y*, *z*; (iii) −*x*, 1−*y*, 1−*z*; (iv) *x*, 1/2−*y*, 1/2+*z*; (v) −*x*, 1/2+*y*, 1/2−*z*; (vi) 1−*x*, −1/2+*y*, 1/2−*z*; (vii) 1−*x*, −*y*, −*z*; (viii) *x*, 1/2−*y*, −1/2+*z*; (ix) 1−*x*, 1/2+*y*, 1/2−*z*; (x) 1−*x*, 1−*y*, −*z*.

4.2.2.6.7 $K_3Cu_2TeO_5(OH)(CO_3)(H_2O)$

Single crystals of $K_3Cu_2TeO_5(OH)(CO_3)(H_2O)$ were grown in a hydrothermal reaction of a 2:3:10:10 mixture of CuO, H_6TeO_6, KOH and $KHCO_3$, and have the form of light green plates. The investigated crystal was not single-crystalline but included small fractions (refined ratio 0.912:0.088(4)) of a second domain. The two domains are symmetrically connected by a twofold rotation along **c**. Integration was based on the presence of two twin domains (hkl5-type data). The subsequent refinement converged with considerably higher reliability factors. For the final structural model, only the major domain was eventually used for integration, ignoring the contributions of the small secondary domain.

Crystal structure

The crystal structure of $K_3Cu_2TeO_5(OH)(CO_3)(H_2O)$ is built similarly to the previously presented $K_2Cu_2TeO_6(H_2O)_x$ (x = 0, 1, 4) phases. Here, [Cu−Te−O] layers alternate with layers of K^+ cations, CO_3^{2-} anions and water molecules. The asymmetric unit contains seventeen atoms: one Te, two Cu, three K, ten O and one C, all located at general 4 *e* positions. The hydrogen atoms could not be localized from difference-Fourier maps.

The $^2_\infty[Cu_2TeO_5(OH)]$ layers are formed by rather regular $[TeO_5(OH)]$ octahedra and Jahn−Teller distorted $[CuO_5(OH)]$ polyedra by edge-sharing. The O6 site, which is occupied by the oxygen atom of an OH group (BVS 1.12 v.u.) is displaced from its ideal “higher-symmetric” position. This leads to a discrepancy in the outer coordination spheres of the two Cu sites. Both Cu positions have, besides their four close oxygen contacts, one oxygen atom at a distance of 2.46 Å. The other contact, the O6 site, has a distance of 2.672(6) Å to the Cu1 site, but only 2.382(6) Å to Cu2, resulting in the different coordination spheres and BVS values for the two Cu positions. The OH group at the O6 position forms a hydrogen bond towards O8, which is part of the CO_3^{2-} anion and is situated at an O···O distance of 2.628(9) Å (Table 37).

The $^2_\infty[Cu_2TeO_{15/3}(OH)_{3/3}]$ layers extend parallel to (100) and have a distance of 10.2960 Å from each other. The interspace is filled with a double-layer of K^+ cations (K1−3) and water molecules (O7), and the CO_3^{2-} anions (C1, O8−10) in between (Figure 103). The crystal water molecule was clearly identified on the O7 position by its low BVS of 0.42 v.u., and forms hydrogen bonds towards the O10 (2.615(10) Å) and O2 (2.852(9) Å) atoms. The carbonate anion has a very regular shape with C—O bond lengths of 1.276(10)−1.289(10) Å. The K^+ cations exhibit CNs of 7 (K2) or 8 (K1, K3) and have BVS of 1.16 (K1), 0.99 (K2) and 1.15 (K3) v.u..

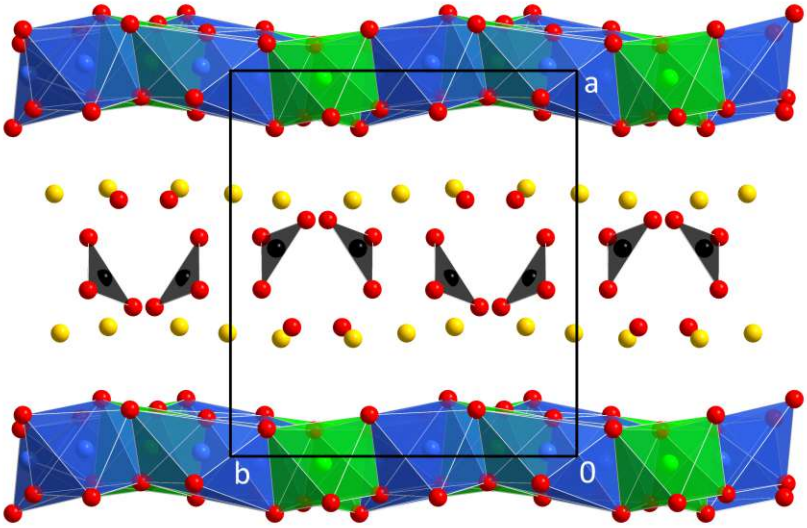

Figure 103. The crystal structure of $K_3Cu_2TeO_5(OH)(CO_3)(H_2O)$ viewed along $[00\bar{1}]$. C atoms are drawn in black.

Table 37. Selected interatomic distances in the crystal structure of $K_3Cu_2TeO_5(OH)(CO_3)(H_2O)$.

	d / Å		*d* / Å
Te1—O5^{i}	1.886(5)	K1—O8	2.815(7)
Te1—O4^{ii}	1.906(6)	K1—O3	2.871(6)
Te1—O2^{ii}	1.941(5)	K1—O5^{i}	2.889(6)
Te1—O1^{ii}	1.955(5)	K1—O7^{iii}	3.134(7)
Te1—O6	1.959(5)	K2—O5	2.714(6)
Te1—O3	1.961(5)	K2—O10^{vi}	2.718(7)
Cu1—O3	1.955(5)	K2—O9	2.748(7)
Cu1—O2^{iii}	2.000(5)	K2—O8^{vii}	2.823(8)
Cu1—O2^{iv}	2.008(6)	K2—O8	2.920(7)
Cu1—O1^{ii}	2.014(5)	K2—O7^{vii}	3.183(8)
Cu1—O5	2.460(6)	K2—O3	3.214(6)
Cu1—O6^{ii}	2.672(6)	K3—O9^{vi}	2.659(7)
Cu2—O1^{ii}	1.948(5)	K3—O7^{vi}	2.703(7)
Cu2—O4	1.971(5)	K3—O1^{vi}	2.704(6)
Cu2—O5	1.983(6)	K3—O10	2.795(8)
Cu2—O3^{v}	2.044(5)	K3—O4^{vi}	2.804(6)
Cu2—O6	2.382(6)	K3—O6^{vi}	3.076(6)
Cu2—O4^{iv}	2.458(6)	K3—O7^{viii}	3.096(7)
K1—O4^{i}	2.769(6)	C1—O8	1.278(11)
K1—O9^{vi}	2.798(7)	C1—O9	1.276(10)
K1—O10^{vi}	2.799(8)	C1—O10	1.289(10)
K1—O9^{i}	2.809(7)		

Symmetry codes: (i) *x*, 1/2−*y*, −1/2+*z*; (ii) −*x*, −1/2+*y*, 1/2−*z*; (iii) *x*, −1+*y*, *z*; (iv) −*x*, 1−*y*, 1−*z*; (v) −*x*, 1/2+*y*, 1/2−*z*; (vi) 1−*x*, −1/2+*y*, 1/2−*z*; (vii) *x*, 1/2−*y*, 1/2+*z*; (viii) 1−*x*, 1−*y*, −*z*.

4.2.2.6.8 *α*- and *β*-$KCuTeO_4(OH)$

The phase $KCuTeO_4(OH)$ was obtained in two different crystalline forms from several hydrothermal experiments. The two polymorphs, a triclinic and a monoclinic form, were labelled as *α*- and *β*-$KCuTeO_4(OH)$, respectively, based on their unit-cell volumes. The triclinic, denser polymorph was assigned as the *α*-phase, as it is assumed to be the thermodynamically more stable form based on the Ostwald-Vollmer rule. Interestingly, *α*-$KCuTeO_4(OH)$ was only obtained in standard hydrothermal experiments with a water filling degree of *ca*. 2/3 (H204, H208, H210, H211, H212), while *β*-$KCuTeO_4(OH)$ grew only in hydroflux-like experiments without additional water (H203, H209). This nourishes the hypothesis that *β*-$KCuTeO_4(OH)$ is the energetically less-favored form and was obtained only in experiments with a reduced mobility and/or diffusion rates of ions during synthesis.

The unit-cells of *α*- and *β*-$KCuTeO_4(OH)$ have a similar cell-volume. The setting of the unit-cell of triclinic *α*-$KCuTeO_4(OH)$ was adapted in order to describe the layered structure more conveniently and for better comparison with the unit-cell of monoclinic *β*-$KCuTeO_4(OH)$. This required a non-conventional unit-cell setting for the *α*-polymorph. Its atom labels were chosen in a way that Te1 and its coordination polyhedron (O1−O5) was as similar to the monoclinic form as possible, and that pairs of oxygen atoms with similar environment are labelled as O*n* and O(*n* + 5) (Table 38). For *β*-$KCuTeO_4(OH)$, atom labels and coordinates are based on *STRUCTURE TIDY*.

Crystal structures

For *α*-$KCuTeO_4(OH)$, the asymmetric unit contains two Te, two Cu, two K, ten O and two H atoms, all corresponding to general 2 *i* positions, and half as many (one Te, one Cu, one K, five O and one H; all at 4 *e*) for the *β*-polymorph. The Te^{VI} atoms are coordinated octahedrally by six oxygen positions, with one of them corresponding to the hydroxide group. The $[TeO_5(OH)]$ octahedra share one edge with a neighboring unit, thus forming $[Te_2O_8(OH)_2]$ dimers, which are further connected by the coordination polyhedra of the Cu^{II} atoms. The resulting $^2_\infty[Cu_2Te_2O_8(OH)_2]$ layers extend parallel to (100).

While the coordination chemistry of the Te^{VI} atoms is the same in the two polymorphs, the differences are clearly visible in the coordination spheres of the Cu^{II} atoms. In *α*-$KCuTeO_4(OH)$, the CN of the Cu^{II} atoms is best described with a value of 4. The square-planar (τ_4 = 0.119 (Cu1) and 0.114 (Cu2)) $[CuO_4]$ units are formed by four oxygen atoms with distances of 1.915(3)−2.029(2) Å and no further oxygen atoms within 2.7 Å. In *β*-$KCuTeO_4(OH)$, the Cu1 site has, besides the four close atoms, two additional oxygen neighbors at distances of 2.4138(11) and 2.5344(10) Å. The shape of the $[Cu1O_6]$ polyhedron (Figure 104, left) is that of an axially distorted octahedron, which is rather common for Cu^{II} atoms affected by the Jahn−Teller effect (Lufaso & Woodward, 2004). The two remote O atoms are counted as part of the coordination sphere of Cu1, as otherwise the BVS would amount to 1.73 v.u. only, instead of 1.96 v.u.. For the two Cu^{II} atoms of *α*-$KCuTeO_4(OH)$, acceptable BVS of 1.88 (Cu1) and 1.86 (Cu2) v.u. were calculated based on fourfold coordination.

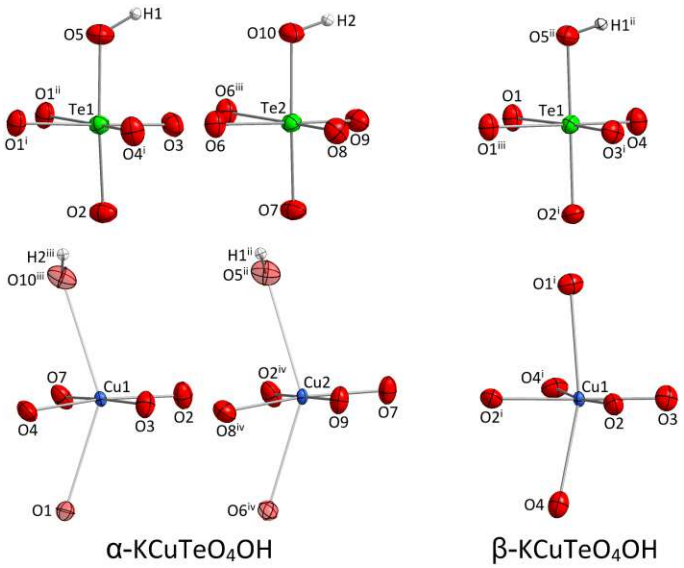

Figure 104. Atomic environments of the Te^{VI} and Cu^{II} atoms in the crystal structures of α- and β-$KCuTeO_4OH$. Oxygen contacts with Cu—O distances larger than 2.7 Å are drawn transparent.

The resulting layers, $^{2}_{\infty}[Cu_2Te_2O_{6/3}O_{12/2}(OH)_{2/1}]$ for α-$KCuTeO_4(OH)$ and $^{2}_{\infty}[Cu_2Te_2O_{18/3}O_{4/2}(OH)_{2/1}]$ for β-$KCuTeO_4(OH)$, have a different structure (Figure 105). In both cases, the layers are corrugated, whereby the positions of the Te^{VI} and Cu^{II} atoms vary between two different *x* coordinates (this corresponds to the location in the stacking direction). In the α-polymorph, adjacent Cu^{II} atoms, which share a corner of their $[CuO_4]$ group, are located at different *x* coordinates, while in the β-form, they are positioned at the same *x*. The structural differences between the two types of layers are visible in Figure 94 and, more clearly in Figure 105. Since a possible $\beta \rightarrow \alpha$ phase transition would require a more or less complete structural reconstruction, it is assumed to be irreversible.

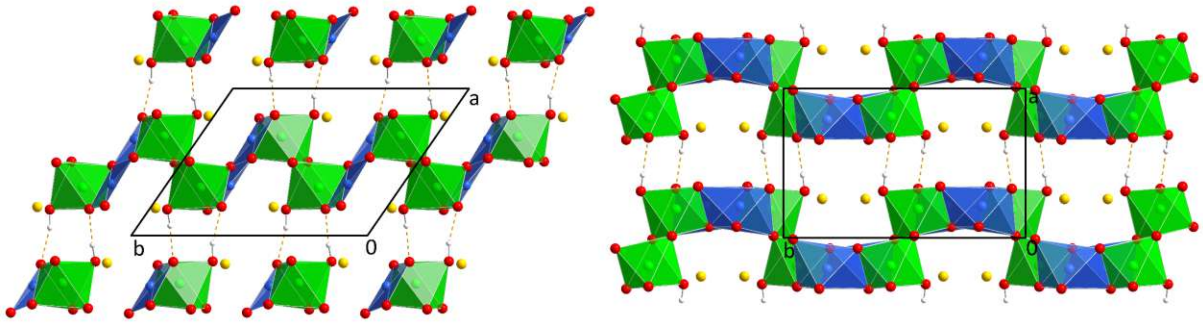

Figure 105. The crystal structures of α- (left) and β- (right) $KCuTeO_4(OH)$ viewed along $[00\bar{1}]$.

Table 38. Selected interatomic distances in the crystal structures of α- and β-$KCuTeO_4(OH)$.

α-$KCuTeO_4(OH)$		β-$KCuTeO_4(OH)$	
	d / Å		d / Å
Te1—O4^{i}	1.864(3)	Te1—O4	1.8804(11)
Te1—O3	1.899(2)	Te1—O3^{i}	1.8919(10)
Te1—O2	1.944(3)	Te1—O2^{i}	1.9416(10)
Te1—O5	1.956(3)	Te1—O5^{ii}	1.9454(11)
Te1—O1^{i}	1.958(2)	Te1—O1	1.9725(10)
Te1—O1^{ii}	2.001(3)	Te1—O1^{iii}	1.9910(11)
Te2—O8	1.872(3)		
Te2—O9	1.887(2)		
Te2—O7	1.939(2)		
Te2—O10	1.949(3)		
Te2—O6	1.960(2)		
Te2—O6^{iii}	2.000(3)		
Cu1—O7	1.915(3)	Cu1—O3	1.9245(11)
Cu1—O3	1.927(3)	Cu1—O2^{i}	1.9695(10)
Cu1—O4	1.972(2)	Cu1—O4^{i}	1.9994(10)
Cu1—O2	2.029(2)	Cu1—O2	2.0843(10)
Cu1—O1	2.701(3)	Cu1—O4	2.4136(11)
Cu1—O10^{iii}	2.938(3)	Cu1—O1^{i}	2.5344(10)
Cu2—O9	1.920(3)		
Cu2—O2^{iv}	1.925(3)		
Cu2—O8^{iv}	1.989(3)		
Cu2—O7	2.023(2)		
Cu2—O6^{iv}	2.730(3)		
Cu2—O5^{ii}	2.978(3)		
K1—O5^{iv}	2.639(3)	K1—O3	2.6888(11)
K1—O8^{ii}	2.698(3)	K1—O5^{iv}	2.6900(12)
K1—O3	2.720(3)	K1—O4^{v}	2.8401(12)
K1—O9^{v}	2.780(3)	K1—O2^{vi}	2.8581(12)
K1—O1^{ii}	2.838(3)	K1—O1^{vii}	2.8759(11)
K1—O5	2.968(3)	K1—O5^{v}	2.9510(12)
K1—O7^{ii}	3.048(3)	K1—O5^{viii}	3.0198(12)
K1—O2^{ii}	3.077(3)	K1—O2^{vii}	3.1341(11)
K1—O1	3.142(3)	K1—O1^{i}	3.2860(12)
K2—O10^{iv}	2.663(3)		
K2—O4^{vi}	2.686(3)		
K2—O9	2.714(3)		
K2—O4^{vii}	2.790(3)		
K2—O6^{iii}	2.842(3)		
K2—O10	2.926(3)		
K2—O2^{iii}	3.083(3)		
K2—O6^{iv}	3.202(3)		
K2—O7^{vi}	3.217(3)		
O5—H1	0.89(5)	O5—H1	0.78(4)
O5—H1···O8^{v}	2.732(4)	O5—H1···O3	2.5953(16)
O10—H2	0.83(5)		
O10—H2···O3^{vii}	2.609(4)		
Symmetry codes: (i) x, y, $-1+z$; (ii) $1-x$, $1-y$, $1-z$; (iii) $1-x$, $-y$, $1-z$; (iv) x, y, $1+z$; (v) $-1+x$, y, z; (vi) $1-x$, $-y$, $2-z$; (vii) $1+x$, y, z.		Symmetry codes: (i) x, $1/2-y$, $-1/2+z$; (ii) $1-x$, $-1/2+y$, $1/2-z$; (iii) $-x$, $-y$, $-z$; (iv) $1-x$, $1-y$, $-z$; (v) $1-x$, $1/2+y$, $1/2-z$; (vi) $-x$, $1-y$, $-z$; (vii) $-x$, $1/2+y$, $1/2-z$; (viii) $1-x$, $1-y$, $1-z$.	

4.2.2.6.9 $K_4CuTe_4O_{14}(OH)_2$

Single crystals of $K_4CuTe_4O_{14}(OH)_2$ were available only as small, green plates. Because they had a rather low diffraction intensity, integration could be performed only up to *d*-values of 0.75 Å, as hardly any reflections were visible at higher diffraction angles. The asymmetric unit (site symmetries, multiplicity and Wyckoff letter in parentheses) contains one Te (8 *j*), one Cu (2/*m*, 2 *a*), two K (*m*, 4 *i*), five O (O1–3: 8 *j*, O4, O5: *m*, 4 *i*) and one H (8 *j*) atom. The H atom has a small distance of 0.81 Å towards its own symmetry equivalent and is disordered with an s.o.f. of 1/2. The two close H atoms are symmetrically connected by the m_{010} plane, indicating a potential symmetry reduction to *C*2 caused by ordering of the hydrogen atoms. However, structure solution and refinement attempts in space group *C*2 did not result in a more accurate model. Therefore, the refinement in *C*2/*m* was retained as the final model. It is unclear, whether either the distribution of the H atoms is disordered, or the measured intensities were too weak to reveal an actual ordering.

Crystal structure

The Te1 atoms have six oxygen contacts with distances of 1.852(4)–1.987(4) Å (Table 39), forming $[TeO_{5.5}(OH)_{0.5}]$ octahedra, which share one edge with a second unit. These $[Te_2O_9(OH)]$ groups are linked to two neighboring dimers by corner-sharing into $^1_\infty[Te_4O_{16/2}O_{6/1}(OH)_{2/1}]$ double chains extending parallel [010] (Figure 106). Such *zweier* (Liebau, 1985) double chains are a new structural element for oxidotellurates(VI), as the only Te_4X_{16} chains in the compilation of Christy et al. (2016) are helical *vierer* single chains in the crystal structure of Li_2TeO_4 (Daniel et al., 1977).

The $^1_\infty[Te_4O_{14}(OH)_2]$ chains are interconnected by the $[CuO_4]$ groups, which, determined by the 2/*m* site symmetry of Cu1, have an almost square-planar shape (O—Cu—O-angles of 92.63(15)° and 87.37(15)°). The two types of polyhedra form $^2_\infty[CuTe_4O_{24/2}O_{2/1}(OH)_{2/1}]$ layers extending parallel to (001) (Figures 94, 107).

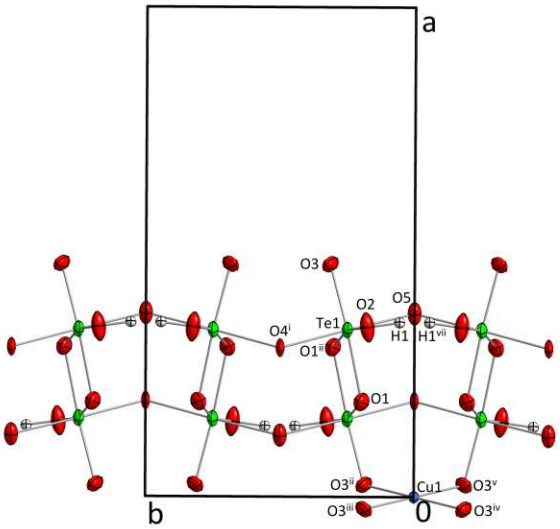

Figure 106. $^1_\infty[Te_4O_{14}(OH)_2]$ chains propagating in the [010] direction in the crystal structure of $K_4CuTe_4O_{14}(OH)_2$ viewed along $[00\bar{1}]$.

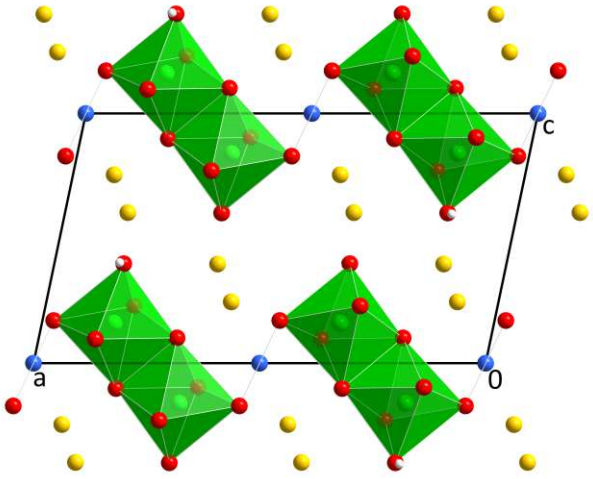

Figure 107. The crystal structure of $K_4CuTe_4O_{14}(OH)_2$ viewed along $[0\bar{1}0]$.

The O2 site is solely connected to one Te^{VI} atom. Two adjacent O2 atoms, symmetrically connected by the m_{010} plane, have a short distance of 2.543(5) Å to each other, indicating the presence of a strong O—H···O hydrogen bond between them. The H1 atom is disordered between two positions and its exact location cannot be discerned from the recorded data set. The superposition between two possible states is not only visible in the s.o.f. of 1/2 for H1, but as well from the elongated displacement ellipsoids of the O2 atoms, as seen in Figure 106. Because the strong O2—H1···O2 hydrogen bond is formed between neighboring $[Te_2O_9(OH)]$

dimers of the same $^{1}_{\infty}[Te_4O_{14}(OH)_2]$ chain (making it an intrachain contact), the actual position of a specific H atom on one of the two possible H1 sites seems to have little impact on the remaining structure.

The K^+ cations fill the space between the zig-zag shaped $^{2}_{\infty}[CuTe_4O_{14}(OH)_2]$ layers and have a coordination sphere of nine oxygen atoms at comparably similar distances of 2.789(6)−3.073(5) Å for K1 and 2.748(4)−2.953(4) Å for K2. The BVS of K1 and K2 amount to rather high values of 1.21 and 1.28 v.u., respectively.

Table 39. Selected interatomic distances in the crystal structure of $K_4CuTe_4O_{14}(OH)_2$.

	d / Å		*d* / Å
Te1—O3	1.852(4)	K1—O3^{iii}	2.841(4)
Te1—O2	1.876(4)	K1—O1^{vii}	2.886(4)
Te1—O5	1.952(2)	K1—O1	2.886(4)
Te1—O4^{i}	1.969(2)	K1—O2^{vii}	3.073(5)
Te1—O1	1.973(4)	K1—O2	3.073(5)
Te1—O1^{ii}	1.987(4)	K2—O5^{viii}	2.732(5)
Cu1—O3^{iii}	1.946(4)	K2—O3^{vii}	2.748(4)
Cu1—O3^{iv}	1.946(4)	K2—O3	2.748(4)
Cu1—O3^{ii}	1.946(4)	K2—O4^{ix}	2.898(6)
Cu1—O3^{v}	1.946(4)	K2—O5	2.904(6)
K1—O4	2.789(6)	K2—O1^{x}	2.929(4)
K1—O2^{i}	2.796(4)	K2—O1^{xi}	2.929(4)
K1—O2^{vi}	2.796(4)	K2—O2^{xii}	2.953(4)
K1—O3^{v}	2.841(4)	K2—O2^{ix}	2.953(4)
O2—H1	0.88(3)*	O2—H1···O2^{vii}	2.543(5)

* Value constrained to 0.89 Å with DFIX command.

Symmetry codes: (i) 1/2−*x*, 1/2−*y*, 1−*z*; (ii) 1/2−*x*, 1/2−*y*, −*z*; (iii) −1/2+*x*, 1/2−*y*, *z*; (iv) 1/2−*x*, −1/2+*y*, −*z*; (v) −1/2+*x*, −1/2+*y*, *z*; (vi) 1/2−*x*, −1/2+*y*, 1−*z*; (vii) *x*, −*y*, *z*; (viii) 1−*x*, −*y*, −*z*; (ix) 1−*x*, −*y*, 1−*z*; (x) 1/2+*x*, 1/2−*y*, *z*; (xi) 1/2+*x*, −1/2+*y*, *z*; (xii) 1−*x*, *y*, 1−*z*.

4.2.2.6.10 $K_6Cu_9Te_4O_{24}(H_2O)_2$

Structure solution and refinement of $K_6Cu_9Te_4O_{24}(H_2O)_2$ was challenging, as all investigated green plate-shaped crystals were twinned. The crystal finally measured consisted of two domains, which were connected by a 60° rotation along the *a*-axis of the orthorhombic unit-cell (*a* = 12.6695(13) Å, *b* = 10.5976(11) Å, *c* = 9.2512(11) Å, *V* = 1242.1(2) Å^3) (Figure 108). The crystal structure of $K_6Cu_9Te_4O_{24}(H_2O)_2$ was consequently solved and refined against a *hkl*5-type file. Hereby, the twin ratios refined to 0.731:0.269(4). The combination of twin domains resulted in pseudo-hexagonal metrics with *a* = 21.195(2) Å, *c* = 12.6695(13) Å at initial solution attempts. The connection to (pseudo-) hexagonality is also visible in the *c*/*b* ratio of the orthorhombic cell (0.8730), which is close to $\sqrt{3}/2$ (0.8660).

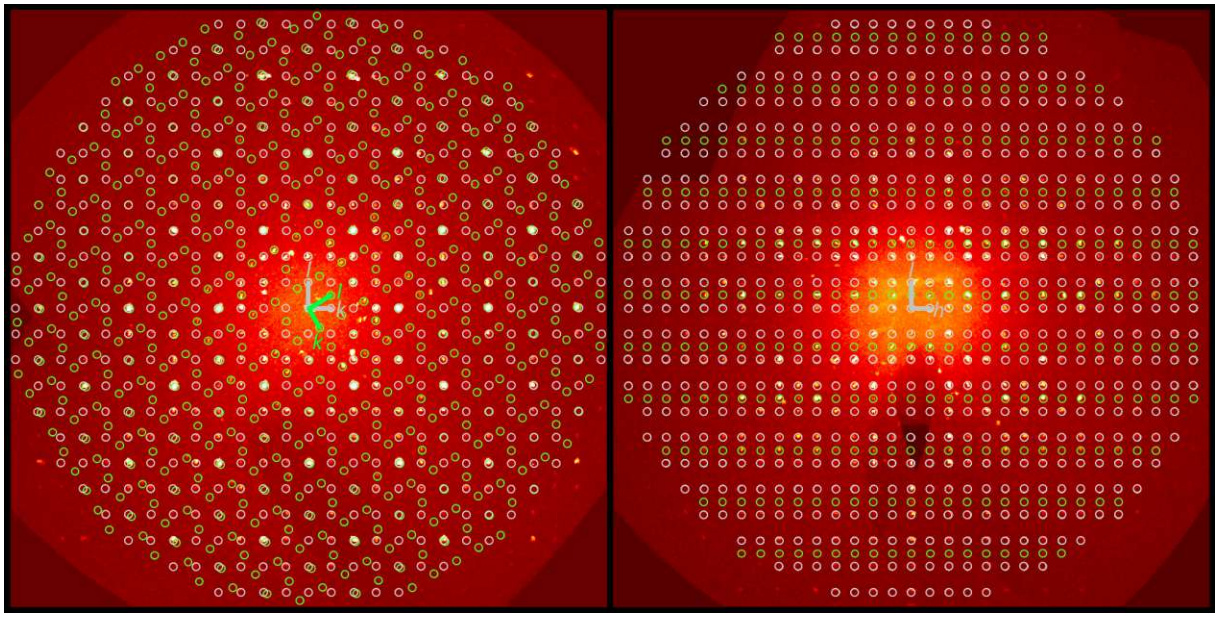

Figure 108. Reconstructed reciprocal 4*kl* (left) and *h*1*l* (right) planes of $K_6Cu_9Te_4O_{24}(H_2O)_2$. Reflections of the two twin domains are indicated by grey and green circles.

Crystal structure

The asymmetric unit of $K_6Cu_9Te_4O_{24}(H_2O)_2$ comprises 27 atoms, two Te, five Cu, six K and fourteen O; the hydrogen atoms of the assumed water molecules could not be localized. The Cu5, O13, O14 and all K sites exhibit *m*.. site symmetry (2 *a*), while the rest of the atoms is located at general 4 *b* positions.

The Te^{VI} atoms exhibit the usual CN of 6 and form $[TeO_6]$ octahedra, which are isolated from each other. The Cu^{II} sites show a variability in their coordination numbers. Cu1 and Cu4 have six oxygen contacts within less than 2.5 Å, forming Jahn−Teller distorted polyhedra, as commonly observed for Cu^{II}. Cu2 and Cu3 exhibit a [4+1] coordination with four oxygen atoms within distances of 1.948(12)−2.014(10) Å and the fifth atom at 2.461(10) and 2.485(10) Å, respectively (Table 40). The $[CuO_5]$ units have a square-pyramidal shape (τ_5 = 0.030 for Cu2 and 0.093 for Cu3), which could be extended to a strongly distorted octahedron by a sixth oxygen atom at a distance of 2.782(10) and 2.753(11) Å for Cu2 and Cu3, respectively. For BVS calculations, these oxygen atoms were considered as too far for being relevant. Cu5 as well has a coordination number of [4+1], which consists of four closely bound oxygen atoms and a water molecule (O14) at a distance of 2.38(2) Å (Figure 109).

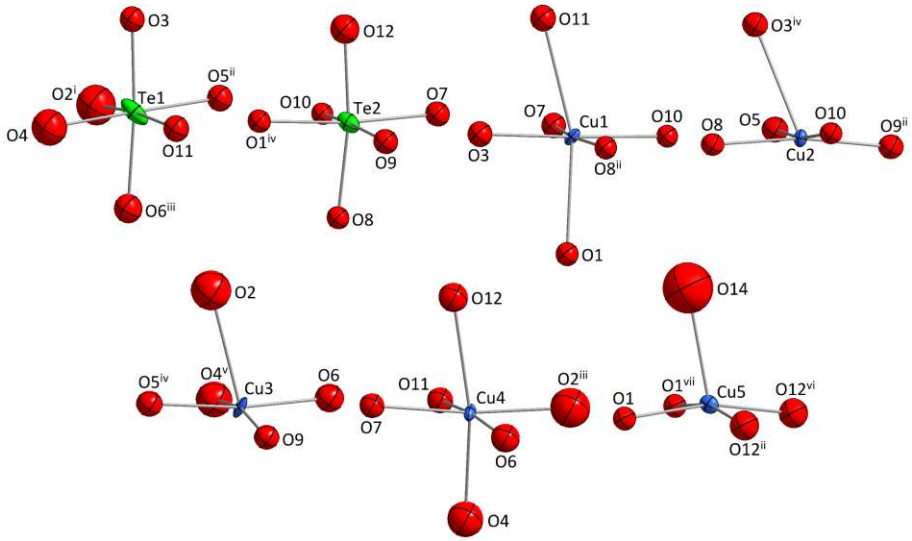

Figure 109. Environments of the Te^{VI} and Cu^{II} atoms in the crystal structure of $K_6Cu_9Te_4O_{24}(H_2O)_2$.

While the coordination polyhedra of the Cu^{II} and Te^{VI} atoms form a $^3_\infty[Cu_9Te_4O_{72/2}H_2O_{1/1}]$ framework extending in all three dimensions, the crystal structure of $K_6Cu_9Te_4O_{24}(H_2O)_2$ can also be derived from a layered arrangement. All atoms located at general 4 *b* positions (Te1, Te2, Cu1–4, O1–12) form idealized MoS_2-type (Dickinson & Pauling, 1923; Bell & Hefert, 1957) $[Cu_2TeO_6]$ layers, just like in the various $K_2Cu_2TeO_6(H_2O)_n$ phases (Figure 94), here extending parallel to (100) (Figure 110). In theory, the hexagonal symmetry of the layers is broken by the Cu5 atoms, which are, like the K^+ cations and water molecules, located in the interlayer space where they link the layers in the stacking direction (**a**). The two oxygen atoms within each layer connected to Cu5, O1 and O12, are displaced from their "ideal symmetric" position and slightly point away from the layer plane. The dislocation of these two oxygen sites leads to the reduced coordination numbers of Cu2 and Cu3, as the Cu2—O1 and Cu3—O12 distances are, as a result, larger than 2.75 Å. To emphasize the layered structure and the structural relationship with the $K_2Cu_2TeO_6(H_2O)_n$ phases, the sum formula of $K_6Cu_9Te_4O_{24}(H_2O)_2$ can also be written as $K_{1.5}Cu_{0.25}[Cu_2TeO_6](H_2O)_{0.5}$.

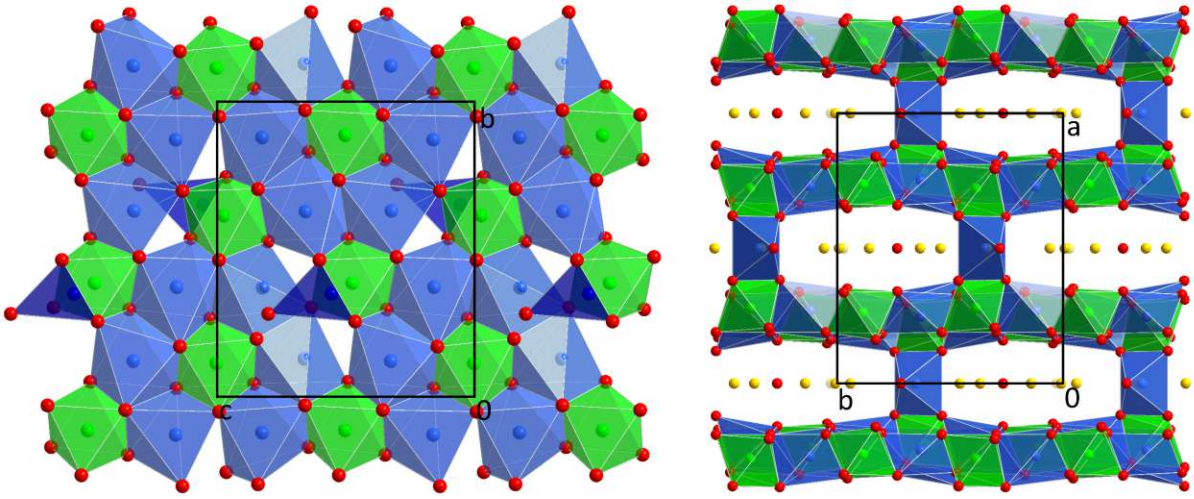

Figure 110. The crystal structure of $K_6Cu_9Te_4O_{24}(H_2O)_2$ viewed along $[\bar{1}00]$ (left; copper atoms linking the respective layers are drawn in dark blue) and along $[00\bar{1}]$ (right).

The interlayer contents are all located at x = 0, 1/2 in alignment with their m.. site symmetries. The two O atoms (O13 and O14) of the crystal water molecules can be identified as such due to their low BVS values of 0.50 (O13) and 0.31 (O14) v.u.. Both sites have two reasonable acceptors for hydrogen-bonding in their vicinity. For O13, two O9 atoms have a distance of 2.721(13) Å, while O14 has two close O5 contacts at 2.545(13) Å. One of the six K sites, K6 exhibits occupational disorder (0.788:0.212(9)) with a second site, labelled K6b. The artificial K6···K6b distance amounts to 0.919(19) Å.

Table 40. Selected interatomic distances in the crystal structure of $K_6Cu_9Te_4O_{24}(H_2O)_2$.

	d / Å		*d* / Å
Te1—O2^{i}	1.902(13)	K1—O11^{viii}	2.783(11)
Te1—O3	1.905(9)	K1—O11^{v}	2.783(11)
Te1—O11	1.928(10)	K1—O6^{vii}	2.836(11)
Te1—O4	1.944(13)	K1—O6	2.836(11)
Te1—O5^{ii}	1.949(11)	K1—O13	2.84(2)
Te1—O6^{iii}	1.975(9)	K2—O13	2.73(2)
Te2—O12	1.914(9)	K2—O4	2.737(14)
Te2—O1^{iv}	1.923(10)	K2—O4^{vii}	2.737(14)
Te2—O7	1.929(10)	K2—O7^{vii}	2.928(11)
Te2—O9	1.948(11)	K2—O7	2.928(11)
Te2—O10	1.953(10)	K2—O6	3.116(13)
Te2—O8	1.968(8)	K2—O6^{vii}	3.116(13)
Cu1—O3	1.953(10)	K3—O3^{ix}	2.563(10)
Cu1—O8^{ii}	1.996(11)	K3—O3^{x}	2.563(10)
Cu1—O7	1.999(11)	K3—O10^{iv}	2.897(10)
Cu1—O10	2.044(11)	K3—O10^{xi}	2.897(10)
Cu1—O1	2.391(10)	K3—O1^{ix}	2.998(11)
Cu1—O11	2.461(10)	K3—O1^{x}	2.998(11)
Cu2—O10	1.966(10)	K3—O13	3.32(2)
Cu2—O9^{ii}	1.970(11)	K4—O1^{vii}	2.760(11)
Cu2—O8	1.996(12)	K4—O1	2.760(11)
Cu2—O5	2.014(10)	K4—O14	2.79(2)
Cu2—O3^{iv}	2.485(10)	K4—O13	2.93(2)
Cu2—O1	2.782(10)	K4—O8^{vii}	2.94(1)
Cu3—O4^{v}	1.948(12)	K4—O8	2.941(10)
Cu3—O6	1.971(13)	K4—O7^{vii}	2.945(11)
Cu3—O9	1.975(11)	K4—O7	2.945(10)
Cu3—O5^{iv}	1.999(12)	K5—O11^{iv}	2.707(11)
Cu3—O2	2.451(13)	K5—O11^{xi}	2.707(11)
Cu3—O12	2.753(11)	K5—O10^{xi}	2.899(11)
Cu4—O11	1.957(11)	K5—O10^{iv}	2.899(11)
Cu4—O6	1.994(13)	K5—O8	3.180(11)
Cu4—O2^{iii}	2.057(12)	K5—O8^{vii}	3.180(11)
Cu4—O7	2.119(10)	K5—O12^{iv}	3.253(13)
Cu4—O4	2.270(13)	K5—O12^{xi}	3.253(13)
Cu4—O12	2.396(10)	K5—O14	3.42(2)
Cu5—O12^{ii}	1.974(10)	K6—K6B^{xii}	0.919(19)
Cu5—O12^{vi}	1.974(10)	K6—O12^{vi}	2.595(10)
Cu5—O1^{vii}	1.993(10)	K6—O12^{ii}	2.595(10)
Cu5—O1	1.993(10)	K6—O2^{xiii}	2.624(13)
Cu5—O14	2.38(2)	K6—O2^{xiv}	2.624(13)
K1—O2	2.730(14)	K6—O4^{xii}	2.633(13)
K1—O2^{vii}	2.730(14)	K6—O4^{xv}	2.633(13)

Symmetry codes: (i) x, y, −1+z; (ii) 1/2−x, 1−y, −1/2+z; (iii) 1/2−x, −y, −1/2+z; (iv) 1/2−x, 1−y, 1/2+z; (v) 1/2−x, −y, 1/2+z; (vi) −1/2+x, 1−y, −1/2+z; (vii) −x, y, z; (viii) −1/2+x, −y, 1/2+z; (ix) x, y, 1+z; (x) −x, y, 1+z; (xi) −1/2+x, 1−y, 1/2+z; (xii) x, 1+y, z; (xiii) −x, 1+y, −1+z; (xiv) x, 1+y, −1+z; (xv) −x, 1+y, z.

4.2.2.7 Lead oxidotellurates(VI)

4.2.2.7.1 Hydrothermal experiments

After the discovery of $KPb_2TeO_5(OH)$ (4.2.2.7.2) from the hydroflux-like experiment H146, a follow-up study on the hydrothermal formation conditions of this phase was conducted (H190–H202). Most batches consisted of PbO, H_6TeO_6 and KOH as educts in different molar ratios.

H190 and H191 employed the educts in the same molar ratios as in H146 (PbO, TeO_2, H_6TeO_6, KOH; 2:1:2:15). However, experiment H191 used the sixfold amount of all educts, leading to a Teflon container almost completely filled with solid before the reaction. While the exact replication of H146 (H190) again yielded $KPb_2TeO_5(OH)$, phase-pure based on the PXRD pattern, in the over-loaded sample H191, no $KPb_2TeO_5(OH)$ could be identified at all. Instead, $KPb_2(CO_3)_2(OH)$ (Brooker et al., 1983), a different novel potassium lead oxidotellurate(VI) phase with a composition of $K_2Pb_3TeO_7$ (4.2.2.7.3), and significant amounts of amorphous products were revealed by the PXRD pattern. $K_2Pb_3TeO_7$ was obtained in phase-pure form (PXRD) from H192 (PbO, H_6TeO_6, KOH; 1:1:8), and crystals for single-crystal diffraction experiments were taken from this batch. Several other experiments (H194, H195, H197, H198, H200) all yielded $K_2Pb_3TeO_7$ as the majority phase, with $KPb_2(CO_3)_2(OH)$ as the main by-product and, in some cases, traces of Pb_3O_4 (Bystroem & Westgren, 1943) and starting material PbO.

From batch H193 (PbO, H_6TeO_6, KOH; 1:1:4), yet another new potassium lead oxidotellurate(VI) phase with the complex composition of $K_{14}Pb^{IV}Pb^{II}_9Te_7O_{36}(OH)_6(H_2O)_6$ was obtained (4.2.2.7.4). Although lead was introduced as PbO, this mixed-valent phase was obtained reliably under the given synthesis conditions, as confirmed by several re-syntheses.

4.2.2.7.2 $KPb_2TeO_5(OH)$

$KPb_2TeO_5(OH)$ was obtained from a hydroflux-like reaction starting from PbO, TeO_2, H_6TeO_6 and KOH in the molar ratios 2:1:2:15. The PXRD pattern of the leached reaction product contained only reflections of $KPb_2TeO_5(OH)$ (Figure 111). Single crystals of $KPb_2TeO_5(OH)$ are small colorless plates with a trigonal form. The unit-cell of $KPb_2TeO_5(OH)$ was refined both on basis of PXRD data of H146 and H190 and from single-crystal data. The powder measurements reveal a significant (002) texture. The refined lattice parameters are collated in Table 41 and are in good agreement with the single-crystal data, considering the different measurement temperatures.

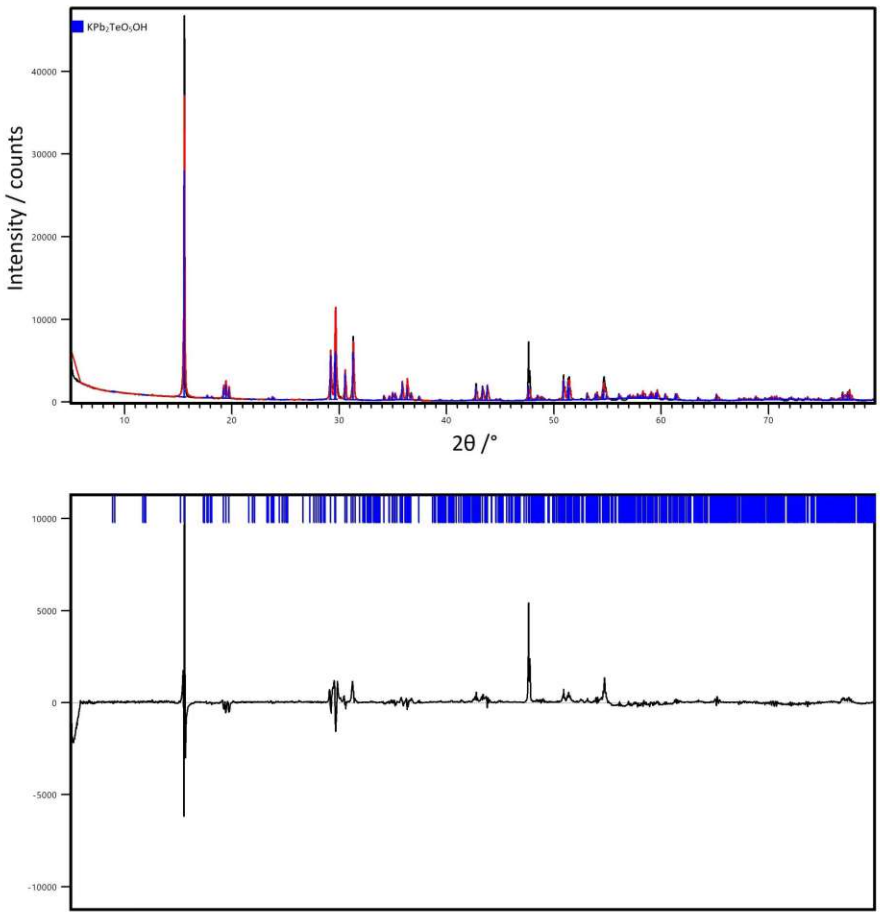

Figure 111. Rietveld refinement of experiment H146 containing only $KPb_2TeO_5(OH)$.

Table 41. Refined lattice parameters of various $KPb_2TeO_5(OH)$ samples.

Batch		*T* / °C	*a* / Å	*b* / Å	*c* / Å	*β* /°	V / Å^3
H146	single-crystal	−173	11.7017(4)	19.6111(6)	11.4303(3)	90.960(2)	2622.69(14)
H146	PXRD	22	11.74097(12)	19.6991(2)	11.47202(8)	90.9808(2)	2652.9
H190	PXRD	22	11.73802(9)	19.6912(2)	11.46963(7)	90.97549(14)	2650.9

Preliminary data indicated a monoclinic unit-cell (*C*2/*c*, *a* = 5.8510(2) Å, *b* = 9.8057(3) Å, *c* = 11.4303(3) Å, *β* = 90.966(3)°, *V* = 655.70(4) Å^3; left half of Figure 112). The asymmetric unit of this cell contains one Pb (8 *f*), one Te (4 *b*, site symmetry $\bar{1}$), one K (4 *e*, site symmetry 2) and three O positions (8 *f*). Each of the three oxygen sites is split into two crystallographic positions, as two octahedral coordination spheres of Te1, which are slightly tilted relative to each other, are superposed in the model. A closer look at the diffraction pattern revealed very weak superstructure reflections in the *hkn* ($n \in \mathbb{Z}$) planes half-way between the reflections of the initial structure (Figure 112).

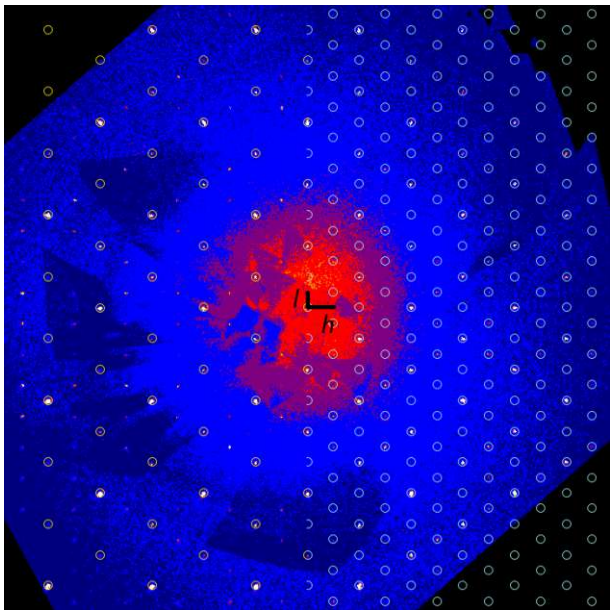

Figure 112. Reconstructed reciprocal *h*2*l* plane of KPb_2TeO_5OH. Reciprocal lattice vectors refer to the final unit-cell. Reflections belonging to the preliminary smaller cell are marked in yellow on the left half.

The additional weak reflections can be explained by a fourfold monoclinic *C*-centered superstructure with $\mathbf{a} = 2\mathbf{a}_{average}$ and $\mathbf{b} = 2\mathbf{b}_{average}$. While Wilson-plots and E-statistics hinted at a centrosymmetric structure, the only space group, in which the disorder of all [TeO_6] octahedra was successfully resolved, was *Cc*. The centrosymmetry suggested by the software was imposed by inversion twinning with twin ratios of 0.539:0.461(9). Atoms labels and coordinates in *Cc* were assigned using *STRUCTURE TIDY*, except for the labels of the oxygen atoms, which were chosen that Te1 is coordinated by O1−O6, Te2 by O7−O12 *etc*..

The asymmetric unit of the final structural model (*Cc*, *a* = 11.7017(4) Å, *b* = 19.6111(6) Å, *c* = 11.4303(3) Å, *β* = 90.960(2)°, *V* = 2622.69(14) Å^3) contains eight Pb, four Te, four K, four H and 24 oxygen atoms, all located at general 4 *a* positions. The Te^{VI} atoms are all coordinated octahedrally by six oxygen atoms with bond lengths in a range of 1.831(11)−2.041(11) Å (Table 43). The BVS of the Te^{VI} atoms are 5.81 (Te1), 5.84 (Te2), 5.87 (Te3) and 5.87 (Te4) v.u..

The Pb^{II} atoms exhibit a [3+3] coordination by six oxygen atoms. The three closer oxygen atoms have distances of 2.227(10)−2.449(11) Å, while the outer coordination sphere consists of oxygen atoms with Pb—O bond lengths of 2.617(10)−3.023(13) Å. In Figure 113 and 114, only the inner coordination sphere is depicted. The shape of the [PbO_3], as well as the [PbO_6] units is strongly influenced by the 6*s*^{2} lone pair of the Pb^{II} atoms. The coordinates of the lone pairs of the Pb^{II} atoms were determined and are listed in Table 42.

Based on the [3+3] coordination, the BVS of the Pb^{II} atoms are 1.88 (Pb1), 1.98 (Pb), 1.99 (Pb3), 2.00 (Pb4), 2.00 (Pb5), 1.91 (Pb6), 1.93 (Pb7) and 2.03 (Pb8) v.u.. The [PbO_3] units are connected to each other by corner-sharing, forming linear $^1_\infty[Pb_2O_{4/2}O_{2/1}]$ chains, which are crosslinked by the [TeO_5(OH)] octahedra, forming $^2_\infty[Pb_2TeO_{6/3}O_{4/2}O_{1/1}(OH)_{1/1}]$ layers parallel to (001). The Pb−O-chains are oriented alternatingly in the [110] and [$\bar{1}$10] directions in adjacent layers (Figure 113).

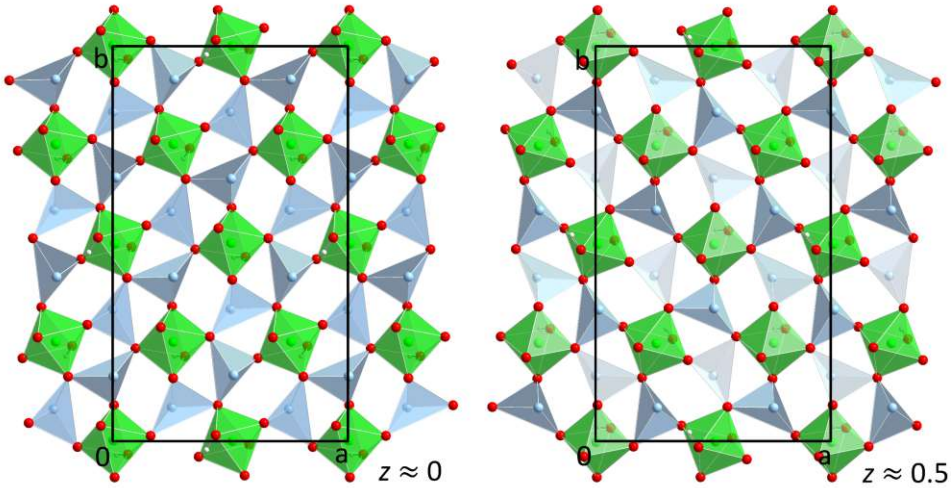

Figure 113. $^{2}_{\infty}$[$Pb_2TeO_5(OH)$] layers in the crystal structure of $KPb_2TeO_5(OH)$ at different *z* coordinates.

Table 42. Geometric details of the $6s^2$ lone pairs of the Pb^{II} atoms in the crystal structure of $KPb_2TeO_5(OH)$.

	x	*y*	*z*	*d* (ψ—Pb) / Å
Pb1	0.9856	0.3433	−0.0447	0.5639
Pb2	−0.0185	0.1627	0.4587	0.5790
Pb3	0.0230	0.1691	0.2374	0.6329
Pb4	0.2368	0.5952	−0.0481	0.6334
Pb5	0.2293	0.0847	−0.0416	0.6089
Pb6	0.2771	0.4190	0.2289	0.5515
Pb7	0.2790	0.0942	0.7357	0.6180
Pb8	0.5299	0.1579	0.2323	0.6187

The hydroxide groups could be located from the BVS values of the oxygen atoms. While sixteen oxygen atoms exhibited BVS of 2.00−2.18 v.u., the four O atoms of hydroxide groups and the acceptors of the exerted hydrogen bonds were identified by their respective under-valence. For the O4—H···O6 and O11—H···O9 bonds, the roles in hydrogen-bonding could clearly be assigned by their BVS of 1.21 v.u. (O4) and 1.13 v.u. (O11) for the hydroxide groups, and 1.70 (O6) v.u. and 1.63 v.u. (O9) as acceptor oxygen atoms. The other four under-valent O positions have comparable BVS values of 1.45 (O14), 1.46 (O16), 1.49 (O23) and 1.41 (O24) v.u., and their respective roles were assigned from available difference electron density peaks. After omission of several faulty reflections, the hydrogen atoms could be localized and their O—H distances were constrained to a value of 0.87 Å. The final hydrogen bonds are: O4—H···O6, O11—H···O9, O14—H···O24 and O23—H···O16.

The hydrogen atoms are directed away from the $^{2}_{\infty}$[$Pb_2TeO_{6/3}O_{4/2}O_{1/1}(OH)_{1/1}$] layers and form hydrogen bonds with oxygen atoms of the neighboring layers (Figure 114). The remaining interspace is occupied by the lone pairs of the Pb^{II} atoms and by the K^+ cations. All K^+ cations are coordinated by six oxygen atoms in a distorted trigonal-prismatic shape, with three oxygen atoms each belonging to the layer above and below. All K—O bond lengths are in a rather narrow range of 2.630(11)−2.877(12) Å, and the potassium atoms all exhibit slightly enlarged BVS of 1.11 (K1), 1.14 (K2), 1.18 (K3) and 1.20 (K4) v.u..

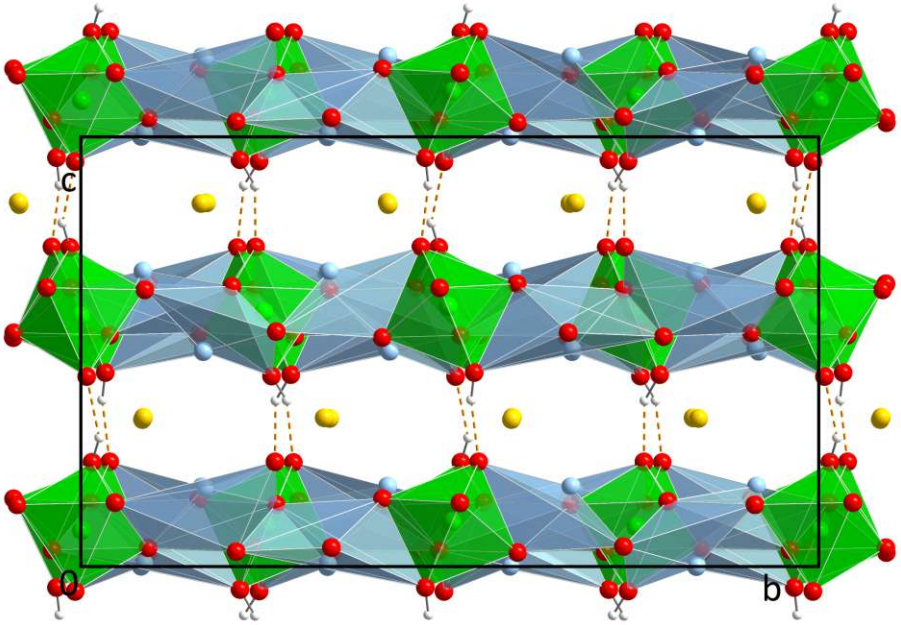

Figure 114. The crystal structure of $KPb_2TeO_5(OH)$ viewed along $[\bar{1}00]$. Hydrogen bonds drawn as orange dashed lines.

Table 43. Selected interatomic distances in the crystal structure of $KPb_2TeO_5(OH)$.

	d / Å		*d* / Å
Pb1—O19^{i}	2.298(9)	Te1—O6^{v}	1.861(9)
Pb1—O15	2.308(10)	Te1—O3	1.919(10)
Pb1—O7	2.36(1)	Te1—O2^{vi}	1.93(1)
Pb1—O9^{ii}	2.724(10)	Te1—O1	1.935(10)
Pb1—O20^{ii}	2.991(9)	Te1—O5^{v}	1.959(10)
Pb1—O1^{iii}	3.025(11)	Te1—O4^{vi}	2.030(9)
Pb2—O2	2.276(9)	Te2—O9^{ii}	1.836(9)
Pb2—O21	2.334(10)	Te2—O10^{i}	1.920(11)
Pb2—O18^{iv}	2.347(9)	Te2—O7	1.933(9)
Pb2—O4	2.776(10)	Te2—O8	1.936(10)
Pb2—O20	2.801(10)	Te2—O12^{x}	1.971(10)
Pb2—O17^{iv}	2.938(9)	Te2—O11^{x}	2.040(9)
Pb3—O1	2.259(10)	Te3—O17	1.893(10)
Pb3—O22^{v}	2.299(9)	Te3—O18	1.914(10)
Pb3—O15	2.397(9)	Te3—O14^{ii}	1.93(1)
Pb3—O6^{v}	2.617(10)	Te3—O13	1.936(11)
Pb3—O19^{i}	2.898(10)	Te3—O16	1.951(9)
Pb3—O13	2.995(11)	Te3—O15	1.97(1)
Pb4—O8	2.227(9)	Te4—O19	1.891(10)
Pb4—O5	2.26(1)	Te4—O23	1.906(10)
Pb4—O22	2.396(10)	Te4—O22^{xi}	1.928(10)
Pb4—O9^{ii}	2.723(11)	Te4—O21	1.933(10)
Pb4—O20^{ii}	2.991(10)	Te4—O20	1.952(10)
Pb4—O1^{iii}	3.025(11)	Te4—O24^{iv}	1.976(11)
Pb5—O13	2.24(1)	K1—O20	2.679(11)
Pb5—O12	2.319(10)	K1—O19^{i}	2.696(11)
Pb5—O3	2.40(1)	K1—O12^{iv}	2.767(10)
Pb5—O14^{ii}	2.725(11)	K1—O16	2.788(10)
Pb5—O10^{vi}	2.807(10)	K1—O14^{v}	2.822(11)
Pb5—O1	2.899(11)	K1—O7	2.826(10)
Pb6—O17	2.253(10)	K2—O13	2.642(11)
Pb6—O7	2.334(10)	K2—O10	2.669(12)
Pb6—O5	2.452(9)	K2—O4	2.738(10)
Pb6—O16	2.658(10)	K2—O21	2.783(10)
Pb6—O8	2.910(10)	K2—O11	2.812(9)
Pb6—O2^{vii}	2.969(9)	K2—O3	2.877(12)
Pb7—O10	2.289(10)	K3—O17^{xi}	2.643(10)
Pb7—O3^{viii}	2.291(11)	K3—O8	2.664(11)
Pb7—O21	2.333(10)	K3—O6	2.683(10)
Pb7—O19	2.854(10)	K3—O9	2.798(10)
Pb7—O11^{viii}	2.908(9)	K3—O5^{xi}	2.816(11)
Pb7—O2	2.977(9)	K3—O22	2.845(10)
Pb8—O20^{vii}	2.258(9)	K4—O1^{xii}	2.630(11)
Pb8—O18	2.283(9)	K4—O2^{vii}	2.656(10)
Pb8—O12	2.312(11)	K4—O24	2.722(11)
Pb8—O24	2.789(11)	K4—O23	2.757(11)
Pb8—O8^{ix}	2.851(10)	K4—O15^{xii}	2.819(11)
Pb8—O13	3.017(10)	K4—O18	2.837(11)

Symmetry codes: (i) −1/2+*x*, 1/2−*y*, −1/2+*z*; (ii) *x*, 1−*y*, −1/2+*z*; (iii) 1/2+*x*, 1/2+*y*, *z*; (iv) −1/2+*x*, 1/2−*y*, 1/2+*z*; (v) −1/2+*x*, −1/2+*y*, *z*; (vi) *x*, −*y*, −1/2+*z*; (vii) 1/2+*x*, 1/2−*y*, −1/2+*z*; (viii) *x*, −*y*, 1/2+*z*; (ix) 1/2+*x*, −1/2+*y*, *z*; (x) −1/2+*x*, 1/2+*y*, *z*; (xi) *x*, 1−*y*, 1/2+*z*; (xii) 1/2+*x*, 1/2−*y*, 1/2+*z*.

4.2.2.7.3 $K_2Pb_3TeO_7$

$K_2Pb_3TeO_7$ was obtained from several hydroflux-like experiments employing PbO, H_6TeO_6 and KOH in different molar ratios without adding any water. The highest yields after leaching with water, as determined by PXRD, were delivered by H192 (PbO:H_6TeO_6:KOH 1:1:8; Figure 115). The lattice parameters of the unit-cell were refined from each measurement and are collated in Table 44. The colorless single crystals of $K_2Pb_3TeO_7$ have a block-like shape and scattered very well, which also led to the necessity of including an extinction correction in the refinement.

Table 44. Refined lattice parameters of various $K_2Pb_3TeO_7$ samples.

Batch	*a* / Å	*c* / Å	*V* / Å³
H191	6.8492(3)	11.0387(6)	448.46
H192	6.84724(3)	11.03582(6)	448.09
H194	6.84891(3)	11.03711(5)	448.36
H195	6.84849(4)	11.03669(6)	448.29
H197	6.84913(7)	11.03736(12)	448.40
H198	6.84949(3)	11.03421(6)	448.32
H200	6.84889(4)	11.03639(6)	448.33
PXRD average	6.8488(7)	11.0366(14)	448.32
H192 single-crystal	6.85330(10)	11.04340(10)	449.193(14)

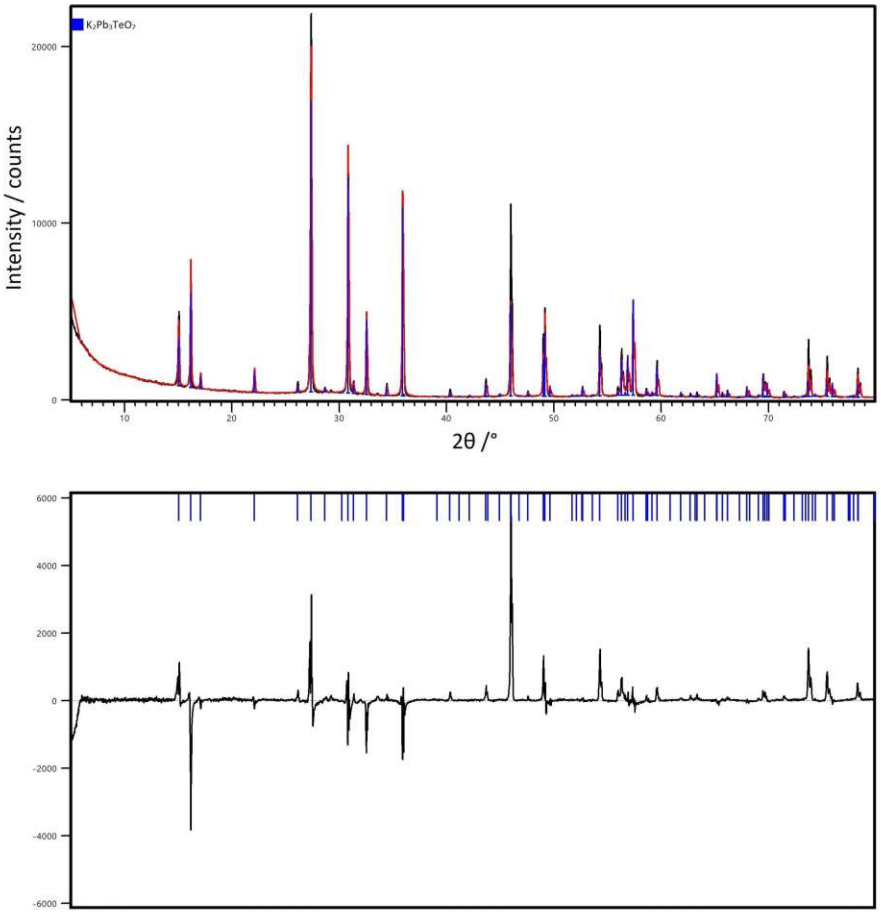

Figure 115. Rietveld refinement of the product of experiment H192 containing only $K_2Pb_3TeO_7$.

Crystal structure

The asymmetric unit of $K_2Pb_3TeO_7$ ($P6_3/m$; a = 6.85330(10) Å, c = 11.04340(10) Å, V = 449.193(14) Å^3) contains five atoms, all located at a different Wyckoff position with different site symmetry: Pb1 (6 *h*; *m*..), Te1 (2 *b*; $\bar{3}$..), K1 (4 *f*; 3..), O1 (12 *i*; 1) and O2 (2 *d*; $\bar{6}$..).

The Te1 position is coordinated octahedrally by six oxygen atoms at a distance of 1.9411(15) Å. The [TeO_6] octahedra are isolated from each other and the Te^{VI} atom exhibits a BVS of 5.79 v.u.. Pb1 is coordinated by three short-bonded oxygen atoms (2.20855(11)−2.2629(16) Å) and two additional atoms at distances of 2.914 (2) Å (Table 45). Under consideration of this [3+2] coordination, the BVS of Pb1 is 1.98 v.u., while it would be only 1.69 v.u. for a [PbO_3] unit. The oxygen atoms of the Pb^{II} atom are positioned in a very one-sided way due to the large space consumption of the 6s^2 lone pair, which is located at x = 0.3139, y = 0.4216, z = 1/4 (d(Pb—ψ) = 0.8040 Å). Three [PbO_3] pyramids share one corner (the O2 site), forming a [Pb_3O_7] trimer. If the two more distant Pb—O contacts are taken into consideration as well, the [PbO_5] units form $^2_\infty$[$Pb_3O_{3/3}O_{12/2}$] layers oriented parallel to (001) (Figure 116). Together with the [TeO_6] octahedra, the Pb−O-units consolidate a tri-periodic framework, which is broken up by the lone pairs ψ of the Pb^{II} atoms and the K^+ cations. The latter are coordinated by seven oxygen atoms and have a BVS of 0.85 v.u..

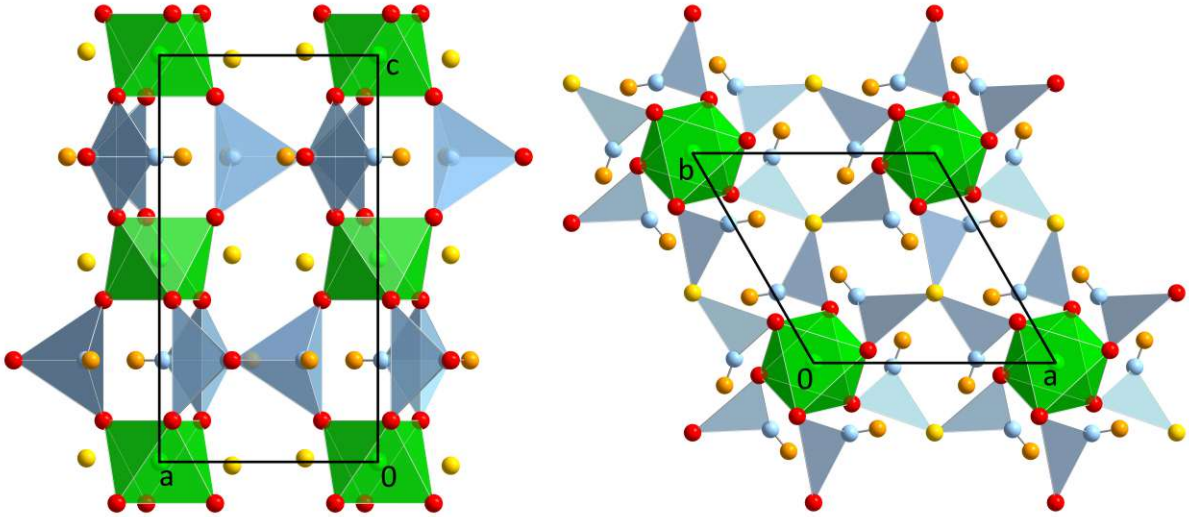

Figure 116. The crystal structure of $K_2Pb_3TeO_7$ viewed along [0$\bar{1}$0] (left) and [00$\bar{1}$] (right), including 6s^2 lone pairs of Pb^{II}.

Table 45. Selected interatomic distances in the crystal structure of $K_2Pb_3TeO_7$.

	d / Å		*d* / Å
Pb1—O2	2.2085(1)	Te1—O1^{vii}	1.9412(15)
Pb1—O1^{i}	2.2629(16)	Te1—O1^{ii}	1.9412(15)
Pb1—O1	2.2629(16)	K1—O1^{viii}	2.7716(17)
Pb1—O1^{ii}	2.914(2)	K1—O1^{ix}	2.7716(17)
Pb1—O1^{iii}	2.914(2)	K1—O1^{v}	2.7716(17)
Te1—O1^{iv}	1.9411(15)	K1—O2^{ix}	2.8608(8)
Te1—O1	1.9411(15)	K1—O1^{x}	3.1689(17)
Te1—O1^{v}	1.9411(15)	K1—O1^{ii}	3.1689(17)
Te1—O1^{vi}	1.9411(15)	K1—O1^{xi}	3.1689(17)

Symmetry codes: (i) *x*, *y*, 1/2*z*; (ii) −*y*, *x*−*y*, *z*; (iii) −*y*, *x*−*y*, 1/2−*z*; (iv) −*x*, −*y*, −*z*; (v) *x*−*y*, *x*, −*z*; (vi) −*x*+*y*, −*x*, *z*; (vii) *y*, −*x*+*y*, −*z*; (viii) *y*, 1−*x*+*y*, −*z*; (ix) 1−*x*, 1−*y*, −*z*; (x) 1−*x*+*y*, 1−*x*, *z*; (xi) *x*, 1+*y*, *z*.

4.2.2.7.4 $K_{14}Pb^{IV}Pb^{II}_{9}Te_7O_{36}(OH)_6(H_2O)_6$

$K_{14}Pb^{IV}Pb^{II}_{9}Te_7O_{36}(OH)_6(H_2O)_6$ was obtained from PbO, H_6TeO_6 and KOH in molar ratios of 1:1:4 under hydroflux-like conditions (H193). The phase has a bright green color and single crystals of $K_{14}Pb^{IV}Pb^{II}_{9}Te_7O_{36}(OH)_6(H_2O)_6$ have the form of thin colorless hexagonal plates. After being exposed to ambient conditions over a longer amount of time, these plates tend to weather.

Crystal structure

In the single-crystal X-ray diffraction experiment, all observed reflections can be indexed in a hexagonal (space group $P\bar{6}2m$) unit-cell with a = 10.2304(2) Å, c = 14.6263(3) Å, V = 1325.72(6) Å^3. The asymmetric unit of $K_{14}Pb^{IV}Pb^{II}_{9}Te_7O_{36}(OH)_6(H_2O)_6$ contains three Pb, two Te, five K and six O sites, most of them sit at higher-symmetric positions. Pb3 exhibits site symmetry $\bar{6}2m$ (1 *a*), K5 3.*m* (2 *e*), Te2, K3 and K4 *m*2*m* (3 *f* for Te2 and 3 *g* for K3 and K4), Te1 and K2 3.. (4 *h*), Pb1, Pb2, K1, O4, O5 and O6 ..*m* (6 *i*), O3 *m*.. (6 *j*), and O1 and O2 are situated at general 12 *l* positions.

Both Te^{VI} atoms are coordinated by six oxygen atoms in a rather regular octahedral shape, which is partially caused by the higher symmetry of the Te sites. The $[Te1O_{4.5}(OH)_{1.5}]$ and $[Te2O_6]$ octahedra are isolated from each other. The BVS of the Te^{VI} atoms amount to 5.90 v.u. for Te1 and 5.75 v.u. for Te2.

The Pb atoms appear in two different oxidation states with Pb3, corresponding to one Pb atom p.f.u., being in the tetravalent state, while the other nine Pb atoms in $K_{14}Pb_{10}Te_7O_{36}(OH)_6(H_2O)_6$ are all present as Pb^{II}. Accidental internal redox reactions, here oxidizing Pb^{II} to Pb^{IV}, are commonly observed for reactions performed under hydrothermal conditions. In this case, the side-reaction took place reliably, as $K_{14}Pb_{10}Te_7O_{36}(OH)_6(H_2O)_6$ could successfully be resynthesized. Furthermore, Pb_3O_4 ($Pb^{II}_2Pb^{IV}O_4$; Bystroem & Westgren, 1943) was obtained as a side-product in several hydroflux-like experiments employing PbO, H_6TeO_6 and KOH (H195−197, H199). The BVS of Pb3 (4.04 v.u.) confirms the oxidation state of +IV, revealing that minor parts of the employed PbO were indeed oxidized. The Pb3 atom is connected to six oxygen atoms at a distance of 2.188(7) Å in a trigonal-prismatic shape, imposed by the $\bar{6}2m$ site symmetry (Figure 117).

The other two Pb sites are coordinated by three shortly bound oxygen atoms and by two (for Pb1) or four (for Pb2) remote oxygen atoms at distances > 2.8 Å. When taking the second coordination sphere into account, the BVS of the Pb^{II} atoms are 1.89 (Pb1) and 1.86 (Pb2) v.u.. The trigonal-pyramidal shape of the $[PbO_3]$ units is caused by the steric influence of their $6s^2$ lone pair ψ located at x = 0.7000, y = 0, z = 0.2696 for ψ_{Pb_1} and x = 0.2970, y = 0, z = 0.1469 for ψ_{Pb_2}. Each $[Pb2O_3]$ unit shares a common corner with a $[Pb1O_3]$ group, forming a $[Pb_2O_5]$ dimer (Figure 117). Two of these $[Pb_2O_5]$ groups would, in theory, share an edge, however, because of the partial occupation of the Pb2 position (details in the following paragraphs), this contact most likely does not exist (Figure 118).

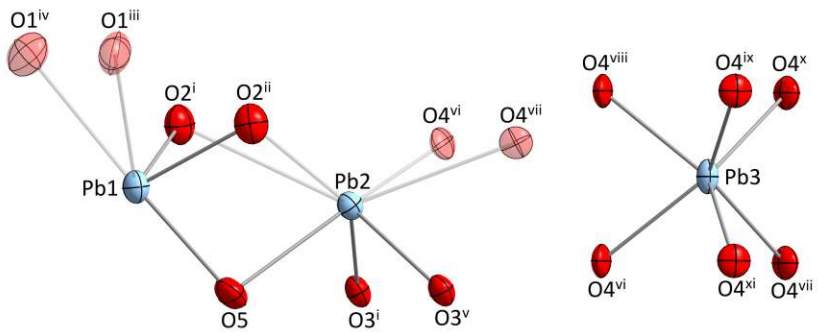

Figure 117. Atomic environments of the Pb atoms in the crystal structure of $K_{14}Pb^{IV}Pb^{II}_{9}Te_7O_{36}(OH)_6(H_2O)_6$. Symmetry codes refer to Table 46. Contacts of the second coordination sphere are drawn transparent.

Occupational disorder

In the $P\bar{6}2m$ model of $K_{14}Pb^{IV}Pb^{II}_9Te_7O_{36}(OH)_6(H_2O)_6$, several cases of disorder are present. No superstructure reflections hinting at an overlooked larger unit-cell or signs of diffuse scattering were discernable from the reconstructed reciprocal space images. Attempts to resolve this disorder by reducing the space group symmetry failed: None of the lower-symmetric approaches resulted in models with a higher degree of order, and, on ther contrary, resulted in refinements with worse reliability factors. Therefore, the $P\bar{6}2m$ model is the best that could be obtained and is presented here.

a) Lead-potassium

The most severe disorder concerns the Pb2 and K1 sites, which are at a very close distance of 0.496(6) Å from each other, both with an s.o.f. of 1/2. When the site occupation factors of the two atoms are refined relative to each other, a ratio of 0.507:0.493(3) (Pb2:K1) is obtained, which justifies fixing both values at 1/2. The K1 site is positioned farther away from the three close oxygen contacts of the Pb^{II} atom. S.o.f.s of exactly 1/2 for both atoms are also reasonable from a crystal-chemical point of view, and from charge-balance considerations. Two $[Pb2O_3]/[K1O_7]$ units share an edge of two O3 sites (Figure 118). If the BVS of this O3 position is calculated without the contributions from the Pb2/K1 sites, a value of 1.35 v.u. is obtained. A bond to a single Pb2 site contributes with a bond valence of 0.47 v.u., while a bond to a single K1 site only adds a bond valence of 0.22 v.u.. Hence, the most accurate BVS for the O3 position is obtained if it has one Pb2 and one K1 neighbor each (2.04 v.u.), whereas two Pb^{II} atoms or two K^+ cations would lead to significant over- (2.29 v.u.) or under-bonding (1.79 v.u.).

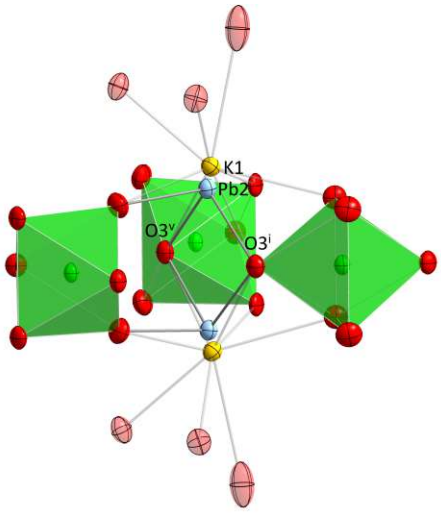

Figure 118. A pair of disordered (K/Pb) sites in the crystal structure of $K_{14}Pb^{IV}Pb^{II}_9Te_7O_{36}(OH)_6(H_2O)_6$.

b) Hydroxide-oxygen

While hydrogen atoms could not be localized, their adjacent oxygen atoms were identified as such based on their respective BVS values. The O6 position (0.40 v.u.) is occupied by a water molecule, while the O1 site (1.48 v.u.) can represent a hydroxide group. The O1 position has a close distance of 2.542(8) Å to one of its own symmetry equivalents (orange dashed lines in Figure 119), which is also the only reasonable acceptor for a potential hydrogen bond. Hence, it can be assumed that half of the O1 positions is occupied by the donor (OH) and the other half by the acceptor (O) atoms for strong hydrogen-bonding, resulting in an $[Te1O_{4.5}(OH)_{1.5}]$ coordination polyhedron and, in total, six OH groups p.f.u.. The exact location and distribution of the hydrogen atoms cannot be determined in space group $P\bar{6}2m$. Likewise, lower-symmetric approaches were not successful in this regard.

c) Potassium

The K^+ cations exhibit coordination numbers of [7+1], [6+3], [4+4], 10 and 6 for K1−K5, respectively. When freely refining the occupancies of the K sites, all values stay very close to the symmetrically allowed maximum, except for K1 (0.5, see a)) and K3, which adopts a s.o.f. very close to 2/3. Thus, K3 contributes only two instead of three atoms p.f.u. resulting in the gross formula of $K_{14}Pb^{IV}Pb^{II}_9Te_7O_{36}(OH)_6(H_2O)_6$. Further information on the actual distribution of the disordered K3 atoms could not be obtained from the recorded diffraction data.

Layered architecture

The crystal structure of $K_{14}Pb^{IV}Pb^{II}_9Te_7O_{36}(OH)_6(H_2O)_6$ (Figure 119) can be decomposed into three layer-types, which are denominated L^1, L^2 and L^3. L^1 ($z \approx 0$) consists of the Te2, Pb3, K2 and the disordered Pb2/K1 sites and their respective coordination polyhedra. Each L^1 layer contains two layers of disordered Pb2/K1 positions. The simplest ordering of these would be one layer of pure Pb and K occupancy each, resulting in the space group *P*31*m*. As already discussed, a refinement in the lower-symmetric space group (with m_z as the twin operation) was not successful in this regard.

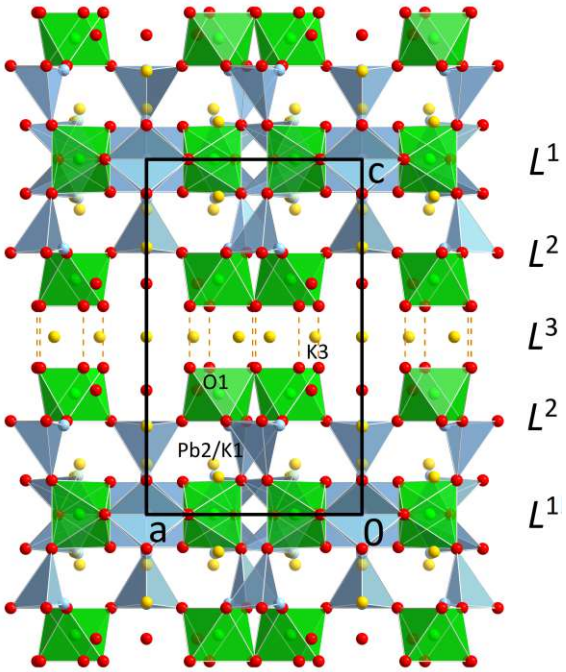

Figure 119. The crystal structure of $K_{14}Pb^{IV}Pb^{II}_9Te_7O_{36}(OH)_6(H_2O)_6$ viewed along [0$\bar{1}$0]. Donor- and acceptor O atoms of potential hydrogen bonds are connected by orange, dashed lines.

The L^1 layer is connected on both sides to an L^2 layer ($z \approx 0.25, 0.75$), consisting of $[Te1O_{4.5}(OH)_{1.5}]$ octahedra and trigonal $[Pb1O_3]$ pyramids, which are connected by corner-sharing, forming a loose honeycomb net with large hexagonal cavities (Figure 120, middle) . These cavities are inhabited by the K5 and crystal water O6 positions. The hydrogen atoms bound to half of the O1 positions of the $[Te1O_{4.5}(OH)_{1.5}]$ groups protrude into the adjacent L^3 layer ($z \approx 0.5$), which consists of the K4 and disordered K3 sites. Since the assumed hydrogen bonds of the O1 atoms are in the region of the L^3 layer as well, the O1 positions were included into the graphical representation of L^3 as well.

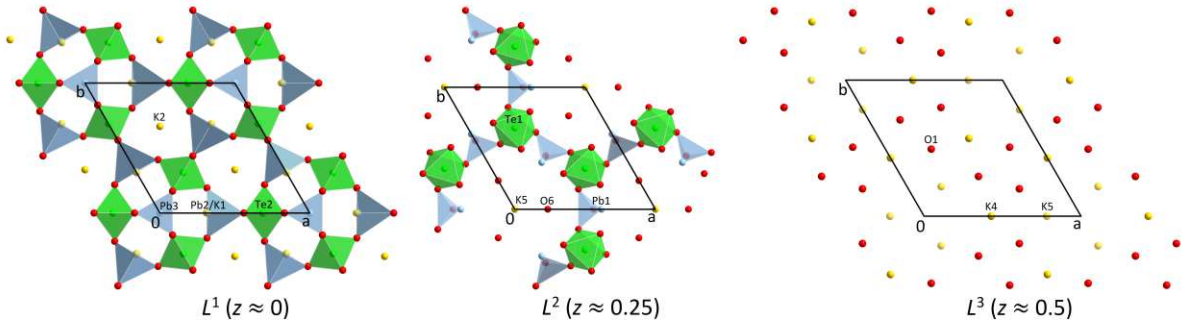

Figure 120. The three different layer types in the crystal structure of $K_{14}Pb^{IV}Pb^{II}_9Te_7O_{36}(OH)_6(H_2O)_6$ viewed along [00$\bar{1}$].

One possible reason why no superstructure reflections or diffuse scattering was observed and also no reasonable lower-symmetric models were obtained, lies in the multi-layered architecture of $K_{14}Pb^{IV}Pb^{II}_9Te_7O_{36}(OH)_6(H_2O)_6$. Due to the presence of several different layers extending parallel to (001), the disordered features within one layer assumably have little or no influence on the same features in the next layer of the same type. Thus, no longer-range order is established.

Table 46. Selected interatomic distances in the crystal structure of $K_{14}Pb^{IV}Pb^{II}_9Te_7O_{36}(OH)_6(H_2O)_6$.

	d / Å		*d* / Å
Pb1—O2^{i}	2.230(6)	K1—O4^{vi}	2.850(4)
Pb1—O2^{ii}	2.230(6)	K1—O4^{vii}	2.850(4)
Pb1—O5	2.335(8)	K1—O6	3.142(13)
Pb1—O1^{iii}	2.966(6)	K2—O3^{xiii}	2.746(6)
Pb1—O1^{iv}	2.966(6)	K2—O3	2.746(6)
Pb2—K1	0.496(5)	K2—O3^{xii}	2.746(6)
Pb2—O3^{i}	2.332(5)	K2—O2^{xii}	2.793(7)
Pb2—O3^{v}	2.332(5)	K2—O2^{xiii}	2.793(7)
Pb2—O5	2.465(7)	K2—O2	2.793(7)
Pb2— O2^{i}	2.848(5)	K2—O5^{xvi}	3.0199(15)
Pb2— O2^{ii}	2.848(5)	K2—O5^{xvii}	3.0199(15)
Pb2—O4^{vi}	3.106(5)	K2—O5^{vii}	3.0199(15)
Pb2—O4^{vii}	3.106(5)	K3—O1^{iv}	2.827(8)
Pb3—O4^{vii}	2.188(7)	K3—O1^{xviii}	2.827(8)
Pb3—O4^{viii}	2.188(7)	K3—O1^{xix}	2.827(8)
Pb3—O4^{ix}	2.188(7)	K3—O1^{iii}	2.827(8)
Pb3—O4^{x}	2.188(7)	K3—O6^{xix}	3.192(10)
Pb3—O4^{vi}	2.188(7)	K3—O6^{xx}	3.192(10)
Pb3—O4^{xi}	2.188(7)	K3—O6^{xxi}	3.192(10)
Te1—O2	1.927(6)	K3—O6^{iv}	3.192(10)
Te1—O2^{xii}	1.927(6)	K4—O1^{xviii}	2.854(7)
Te1—O2^{xiii}	1.927(6)	K4—O1^{iii}	2.854(7)
Te1—O1	1.933(6)	K4—O1^{iv}	2.854(7)
Te1—O1^{xii}	1.933(6)	K4—O1^{xix}	2.854(7)
Te1—O1^{xiii}	1.933(6)	K4—O6^{xxii}	2.957(11)
Te2—O5	1.916(8)	K4—O6	2.957(11)
Te2—O5^{xiv}	1.916(8)	K4—O1^{i}	3.001(7)
Te2—O3^{iv}	1.930(7)	K4—O1^{xxiii}	3.001(7)
Te2—O3^{xv}	1.930(7)	K4—O1^{xxiv}	3.001(7)
Te2—O4	1.990(7)	K4—O1^{ii}	3.001(7)
Te2—O4^{xiv}	1.990(7)	K5—O6	2.827(10)
K1—O5	2.641(8)	K5—O6^{xvi}	2.827(10)
K1—O3^{i}	2.686(7)	K5—O6^{i}	2.827(10)
K1—O3^{v}	2.686(7)	K5—O4^{vi}	2.861(8)
K1—O2^{ii}	2.721(7)	K5—O4^{xi}	2.861(8)
K1—O2^{i}	2.721(7)	K5—O4^{vii}	2.861(8)

Symmetry codes: (i) −*x*+*y*, −*x*, *z*; (ii) *y*, *x*, *z*; (iii) 1−*x*, −*x*+*y*, *z*; (iv) 1−*y*, *x*−*y*, *z*; (v) *y*, *x*, −*z*; (vi) −*y*, −1+*x*−*y*, *z*; (vii) 1−*x*+*y*, 1−*x*, *z*; (viii) −*y*, −1+*x*−*y*, −*z*; (ix) −1+*x*, *y*, −*z*; (x) 1−*x*+*y*, 1−*x*, −*z*; (xi) −1+*x*, *y*, *z*; (xii) −*x*+*y*, 1−*x*, *z*; (xiii) 1−*y*, 1+*x*−*y*, *z*; (xiv) *x*, *y*, −*z*; (xv) 1−*x*, −*x*+*y*, −*z*; (xvi) −*y*, *x*−*y*, *z*; (xvii) *x*, 1+*y*, *z*; (xviii) 1−*x*, −*x*+*y*, 1−*z*; (xix) 1−*y*, *x*−*y*, 1−*z*; (xx) 1−*x*+*y*, −*x*, *z*; (xxi) 1−*x*+*y*, −*x*, 1−*z*; (xxii) *x*, *y*, 1−*z*; (xxiii) *y*, *x*, 1−*z*; (xxiv) −*x*+*y*, −*x*, 1−*z*.

4.2.2.8 $K_6Bi_4Te_3O_{17}(CO_3)(H_2O)_3$

Single crystals of $K_6Bi_4Te_3O_{17}(CO_3)(H_2O)_3$ were obtained from a carbonate-based mild hydroflux experiment employing the starting materials Bi_2O_3, TeO_2, K_2CO_3 (molar ratios 2:3:10), and three droplets of water (H276). When observed under an optical microscope, the reaction product consisted for the most part of a grey powder (supposedly the main product Bi_2TeO_5; Mercurio et al., 1983) with two types of colorless crystals as minor constituents. Thin needles were identified as $KTeO_3(OH)$ (Lindqvist, 1972), while crystals of $K_6Bi_4Te_3O_{17}(CO_3)(H_2O)_3$ had the form of broader bars with angled corners. Both of these side products are oxidotellurates(VI), indicating a partial oxidation of the employed Te^{IV}.

Crystal structure

The unit-cell of $K_6Bi_4Te_3O_{17}(CO_3)(H_2O)_3$ has orthorhombic metrics (a = 17.5046(5) Å, b = 15.2624(3) Å, c = 8.7214(3) Å, β = 90.000(3)°, V = 2330.03(11) Å^3) and initial attempts to solve the crystal structure were done in space group *Cmmm*. While the framework constituting the heavy atoms of the structure followed this symmetry in a straightforward manner, some potassium cations and oxygen sites not directly bound to the Te^{VI} or Bi^{III} atoms exhibited disorder indicated by unrealistically close interatomic distances and lower site occupation factors. These issues could be resolved by an orthorhombic-to-monoclinic symmetry reduction to space group *C*2/*c*, a maximal, non-isomorphic subgroup of *Cmmm*. As crystal structures related to $K_6Bi_4Te_3O_{17}(CO_3)(H_2O)_3$ are not know so far, atom labels were assigned with the help of *STRUCTURE TIDY*.

The crystal structure of $K_6Bi_4Te_3O_{17}(CO_3)(H_2O)_3$ is built by a tri-periodic $[Bi_4Te_3O_{17}]$ framework, which is perforated by large channels oriented parallel to [001] (Figure 121). The K^+ and CO_3^{2-} ions, as well as the water molecules, inhabit these channels. The asymmetric unit comprises two Bi, two Te, four K, one C and 15 O sites; hydrogen atoms could not be located. Te2, K3, K4, O7, O8, O9, OW2, C1 and OC2 are located at sites with site symmetry *m* (Wyckoff position 4 *i*), O10 (4 *h*) and O11 (4 *g*) exhibit site symmetry 2 and the other atoms are located at general positions (8 *j*).

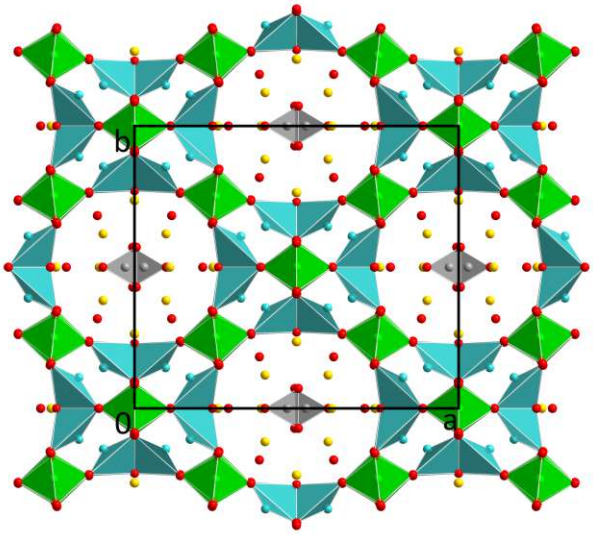

Figure 121. The crystal structure of $K_6Bi_4Te_3O_{17}(CO_3)(H_2O)_3$ viewed along [00$\bar{1}$]. Bi atoms are drawn in turquoise, C atoms in grey.

Six oxygen atoms within a slightly distorted octahedral shape coordinate both Te^{VI} atoms. The Te—O bond lengths vary in an interval of 1.884(8)–2.028(6) Å with always two of the oxygen atoms being at almost the same distance (Table 47). The octahedra are connected to one adjacent $[TeO_6]$ unit by edge-sharing, thus forming $[Te_2O_{10}]$ dimers (◯=◯). The BVS of the Te^{VI} atoms amount to values of 5.80 (Te1) and 5.73 (Te2) v.u..

The two Bi^{III} atoms are both coordinated by five oxygen atoms with distances in the range of 2.058(6)–2.512(8) Å. The $[BiO_5]$ units have a square-pyramidal shape with the non-bonding $6s^2$ electron pair sitting on the opposite side of the pyramid. The locations of the lone-pairs were calculated to x = 0.1415, y = 0.1394, z = 0.5057 for ψ_{Bi_1} and x = 0.3790, y = 0.4137, z = −0.0019 for ψ_{Bi_2}. Each $[BiO_5]$ pyramid is connected to a second unit by plane-sharing, forming $[Bi_2O_7]$ dimers (Figure 122). By corner-sharing with $[TeO_6]$ octahedra, the $[Bi_2O_7]$ groups form a tri-periodic framework (Figure 123) with large

channels extending parallel to [001]. Interestingly, the lone pairs of the Bi^{III} atoms are not directed into the large [001] channels.

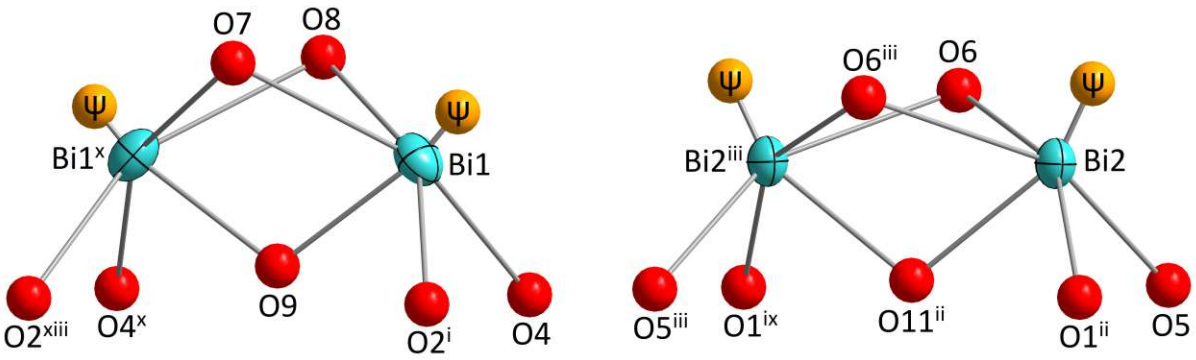

Figure 122. $[Bi_2O_8]$ dimers in the crystal structure of $K_6Bi_4Te_3O_{17}(CO_3)(H_2O)_3$. Symmetry codes refer to Table 47.

The O atoms of water molecules OW1 and OW2 were identified by their low BVS of 0.41 (OW1) and 0.31 (OW2) v.u. as hydrogen atoms were not located. The carbonate group situated in the center of the channels is formed by the C1, OC1 and OC2 positions. Their C—O bond lengths range from 1.22(3) to 1.24(2) Å. Both OC1 and OC2 are connected to four K^+ cations with distances of less than 3 Å. The potassium cations form also bonds to the oxygen atoms of the framework and crystal water molecules. Their coordination number is 7 or 8 for all four K sites.

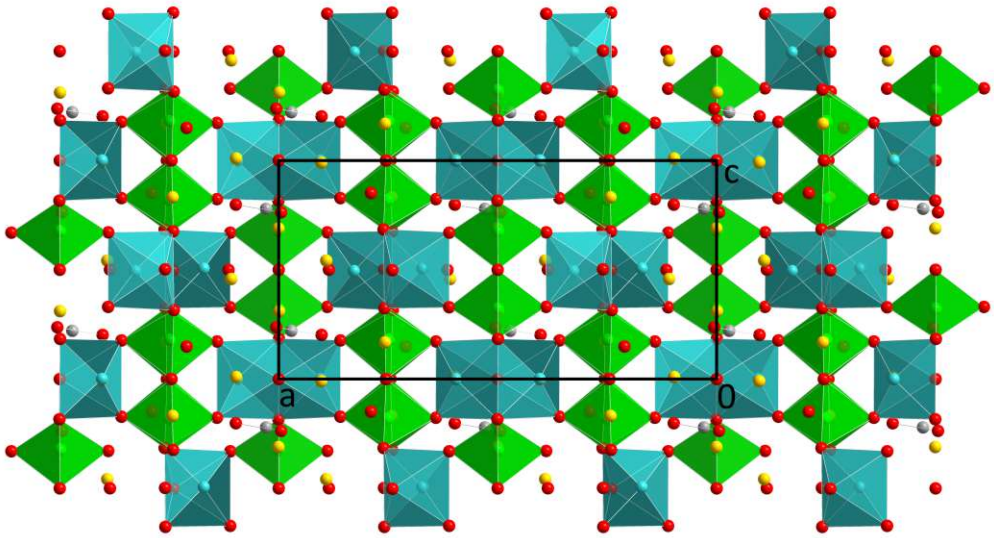

Figure 123. The crystal structure of $K_6Bi_4Te_3O_{17}(CO_3)(H_2O)_3$ viewed along $[0\bar{1}0]$.

Table 47. Selected interatomic distances in the crystal structure of $K_6Bi_4Te_3O_{17}(CO_3)(H_2O)_3$.

	d / Å		*d* / Å
Bi1—O9	2.058(6)	K1—OC1^{vii}	2.89(2)
Bi1—O2^{i}	2.298(8)	K1—OW2^{viii}	2.941(15)
Bi1—O4	2.323(8)	K2—OC1^{ix}	2.61(2)
Bi1—O7	2.446(7)	K2—OW1^{i}	2.716(11)
Bi1—O8	2.512(8)	K2—OW1^{ix}	2.731(11)
Bi2—O11^{ii}	2.122(6)	K2—O5	2.756(9)
Bi2—O5	2.213(8)	K2—O11^{ii}	2.760(3)
Bi2—O1^{ii}	2.224(8)	K2—O1^{ix}	2.787(8)
Bi2—O6	2.430(8)	K2—O6	2.809(9)
Bi2—O6^{iii}	2.450(8)	K2—O10^{i}	3.182(9)
Te1—O4	1.895(8)	K3—OC2	2.55(3)
Te1—O2	1.896(8)	K3—O4	2.773(8)
Te1—O1	1.914(8)	K3—O4^{x}	2.773(8)
Te1—O5	1.926(8)	K3—OW2^{xi}	2.824(17)
Te1—O3	2.000(7)	K3—O9	2.891(11)
Te1—O3^{ii}	2.021(7)	K3—O8	2.924(11)
Te2—O6^{iv}	1.884(8)	K3—O3^{xii}	2.954(8)
Te2—O6^{v}	1.884(8)	K3—O3^{ii}	2.954(8)
Te2—O8	1.936(11)	K4—O9	2.669(12)
Te2—O7^{vi}	1.938(11)	K4—OW1^{xiii}	2.812(11)
Te2—O10^{vi}	2.028(6)	K4—OW1^{i}	2.812(11)
Te2—O10	2.028(6)	K4—OC1^{i}	2.85(2)
K1—OC2^{ii}	2.576(19)	K4—OC1^{xiii}	2.85(2)
K1—OC1	2.65(2)	K4—OC2	2.97(3)
K1—O3	2.694(8)	K4—OW2^{xiv}	3.231(18)
K1—O1	2.722(9)	C1—OC2	1.22(3)
K1—O5^{ii}	2.879(9)	C1—OC1^{x}	1.24(2)
K1—O11	2.883(9)	C1—OC1^{xv}	1.24(2)

Symmetry codes: (i) 1/2−*x*, 1/2−*y*, 1−*z*; (ii) 1/2−*x*, 1/2−*y*, −*z*; (iii) 1−*x*, *y*, −*z*; (iv) −1/2+*x*, −1/2+*y*, *z*; (v) −1/2+*x*, 1/2−*y*, *z*; (vi) −*x*, −*y*, 1−*z*; (vii) −*x*, *y*, −*z*; (viii) −1/2+*x*, 1/2+*y*, *z*; (ix) 1/2+*x*, 1/2−*y*, *z*; (x) *x*, −*y*, *z*; (xi) 1−*x*, −*y*, −*z*; (xii) 1/2−*x*, −1/2+*y*, −*z*; (xiii) 1/2−*x*, −1/2+*y*, 1−*z*; (xiv) 1−*x*, −*y*, 1−*z*; (xv) 1/2+*x*, −1/2+*y*, *z*.

4.2.2.9 Other K–M^{III}–Te^{VI}–O-phases

The pyrochlore-type phase $K_{1.5}Cr_{0.5}Te_{1.5}O_6(H_2O)_{0.5}$ (or $K_3CrTe_3O_{12}(H_2O)$) has a face-centered cubic crystal structure with $a \approx 10.03$ Å (Isasi et al., 1995). The same size of unit-cell was reported for the defect pyrochlores $KM_{0.33}Te_{1.67}O_6$ ($K_3MTe_5O_{18}$; M = Al, Cr, Fe) reported by Guje et al. (2015). Given the different literature compositions ($K_{1.5}Cr_{0.5}Te_{1.5}O_6(H_2O)_{0.5}$ and $KCr_{0.33}Te_{1.67}O_6$) for isotypic phases with very similar lattice parameters, it can be assumed that a certain compositional variability for such ($K_{3n}M^{III}{}_nTe^{VI}{}_{2-n}O_6$) phases with pyrochlore structures exists.

A similar unit-cell than for these defect pyrochlore compounds was observed in several PXRD patterns of hydrothermal products, including NH_3 as a source but no source of potassium (H50–H55). In order to gain more insight into the crystal structure of this assumed "$(NH_4)Te_2O_{6.5}(H_2O)$" phase and also because the crystal structures of these K-based defect pyrochlore phases have only been investigated based on PXRD data, a series of solid-state reactionsewas conducted. Mixtures of M_2O_3 (M = Cr^{III}, Fe^{III}, Al^{III}, Ga^{III}), KNO_3 and H_6TeO_6 were heated in air at 425 °C – like in the synthesis of $K_3CrTe_3O_{12}(H_2O)$ (Isasi et al., 1995). Experiments S33–S36 accidentally used the wrong stoichiometric ratios of 3:2:2, they were corrected to 1:6:6 in S37–S40. Reactions S37–S40 were subsequently repeated at a higher reaction temperature of 550 °C (S41–S44). Details on the performed syntheses are compiled in Table 66.

Most syntheses resulted in phase-mixtures including numerous reflections that could not be assigned to literature phases. The most frequently observed known products in the leached samples were the educt oxides M_2O_3, the mixed-valent KTe_2O_6 (or more accurately $K_2Te^{IV}Te_3^{VI}O_{12}$; Daniel et al., 1978) and traces of KNO_3. A phase with an apparent face-centered cubic crystal structure with $a \approx 10$ Å was observed in all Cr^{III}- and Fe^{III}-based samples (S33, 34, 37, (38), 41 and 42). The relative intensities of the reflections of the $K_{3n}Cr_nTe_{2-n}O_6$ patterns vary between the samples and are more similar to those of $K_3CrTe_3O_{12}(H_2O)$ for S37, $K_3CrTe_5O_{18}$ for S41 and somewhere in-between for S33. The lattice parameter a was refined to 10.04396(11) Å for S33, 10.04392(4) Å for S37 and 10.03710(8) Å for S41, which was obtained at a higher reaction temperature. The $K_{3n}Cr_nTe_{2-n}O_6$ phase was the main product in all three samples, with Cr_2O_3 as a major by-product in S33.

Two sets of unassigned reflections corresponding to unknown phases (most probably as side-products) appeared in several samples. The first phase has its first four reflections at 2θ values of 12.58° (weak), 14.25° (strong), 17.93° (weak) and 18.39° (weak) and appeared in S36 (Ga^{III}), S38 (Fe^{III}), S39 (Al^{III}) and S40 (Ga^{III}). The second phase appeared in two samples heat-treated at 550 °C, S42 (Fe^{III}) and S44 (Ga^{III}), and has its first reflections at 2θ values of 11.61° (strong), 14.48° (weak), 15.95° (weak), 16.59° (weak) and 16.85° (medium). Single-crystalline material was not obtained for any of these samples to reveal the nature of these side-products.

4.2.3 Rubidium

Although it was not deliberately tried to synthesize Rb–*M*–Te^{VI}–O-phases, single crystals of $RbPb_3Te_2O_9(OH)$ were obtained from an experiment, where Te had been introduced as TeO_2.

4.2.3.1 $RbPb_3Te_2O_9(OH)$

Single crystals of $RbPb_3Te_2O_9(OH)$ have the shape of broad, elongated colorless bars and appear frequently but not exclusively as twinned crystals. The crystal structure of $RbPb_3Te_2O_9(OH)$ ($P\bar{1}$; a = 7.3829(2) Å, b = 7.4064(2) Å, c = 10.0999(3) Å, α = 103.588(2)°, β = 100.045(2)°, γ = 94.172(2)°, V = 524.84(3) Å^3) is defined by seventeen crystallographic sites in the asymmetric unit, three Pb, two Te, one Rb, ten O and one H. All atoms are located at sites corresponding to general 2 *i* Wyckoff positions.

The two Te^{VI} positions are coordinated by six oxygen atoms in a slightly distorted octahedral shape. The $[Te1O_6]$ and $[Te2O_5(OH)]$ units are connected to one symmetry-equivalent group by edge-sharing, forming $[Te1_2O_{10}]$ or $[Te2O_8(OH)_2]$ dimers. The oxygen atom of the hydroxide group is located at the O8 site, the adjacent hydrogen atom H1 could be located based on difference-Fourier maps. The O8—H1 bond length was not restrained and refined to a value of 1.02(7) Å. The O8—H1 hydroxide group forms a strong hydrogen bond towards the O9 position with an O8—H1···O9 distance of 2.595(5) Å. The BVS of the Te^{VI} atoms were calculated to 5.88 (Te1) and 5.86 (Te2) v.u..

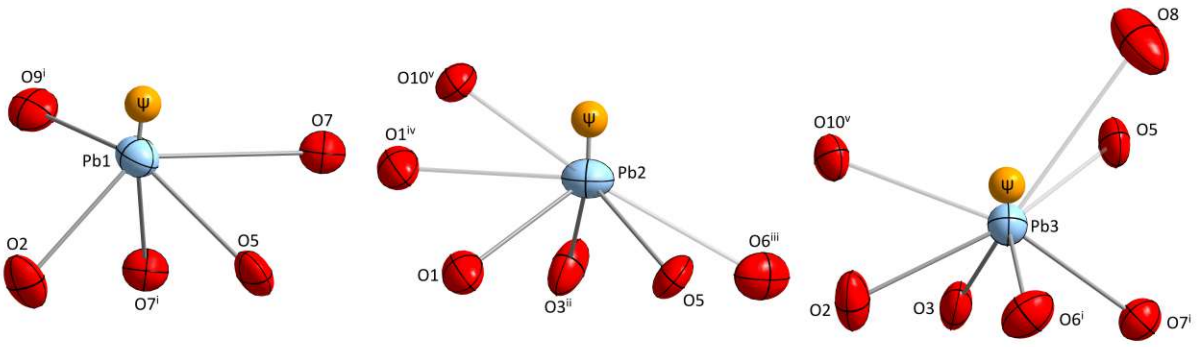

Figure 124. Atomic environments of the Pb^{II} atoms including the 6s^2 lone pair ψ in the crystal structure of $RbPb_3Te_2O_9(OH)$. Bonds of oxygen contacts outside the closest coordination sphere are drawn transparent. Symmetry codes refer to Table 48.

Each of the three Pb^{II} sites exhibits a different coordination environment. Pb1 is surrounded by three close (2.317(3)–2.378(3) Å) and two medium-ranged (2.600(3), 2.693(3) Å) oxygen atoms, Pb2 is coordinated by three close (2.268(3)–2.306(3) Å) and three remote oxygen atoms (2.831(3)–3.106(3) Å), while Pb3 has four close (2.309(3)–2.493(3) Å) and, again, three remote oxygen ligands (2.917(3)–3.171(3) Å). For the graphical representations (Figure 125), only the close and medium-ranged contacts were considered, resulting in CNs of 5, 3 and 4 for Pb1, Pb2 and Pb3, respectively. For the BVS calculation, it is necessary to take the more distant contacts into account as well. Based on the oxygen contacts given in Table 48, the BVS of the Pb^{II} atoms are 1.89 (Pb1), 1.93 (Pb2) and 2.05 (Pb3) v.u.. Irrespective of the chosen coordination sphere, the $[PbO_n]$ units have an asymmetric, one-sided shape (Figure 124) due to the steric influence of the non-boning 6s^2 pairs ψ. The coordinates of ψ were determined to x = 0.1698, y = 0.3722, z = 0.4820 for ψ_{Pb_1}, x = 0.3423, y = 0.1067, z = 0.0079 for ψ_{Pb_2} and x = 0.4478, y = 0.5580, z = 0.1650 for ψ_{Pb_3} and are included in Figure 125.

Based on the close and medium oxygen contacts, the $[PbO_{3-5}]$ units are connected to each other by edge and corner-sharing. Via edge-sharing, two $[Pb1O_5]$ and two $[Pb3O_4]$ groups form $[Pb_4O_{6/3}O_{4/2}O_{8/1}]$

units, which are connected by [Pb2O$_3$] pyramids by corner-sharing into $^1_\infty$[Pb$_6$O$_{6/3}$O$_{12/2}$O$_{6/1}$] chains, which propagate parallel to [010]. The $^1_\infty$[Pb$_6$O$_{14}$] chains are interconnected by the [Te$_2$O$_{10}$]/[Te$_2$O$_8$(OH)$_2$] dimers, forming layers extending parallel to (10$\bar{1}$). The space between these layers is occupied by the lone pairs of the Pb^{II} atoms, the Rb$^+$ cations and the hydrogen bonds formed by the hydroxide group at the O8 position towards an O9 position of an adjacent layer. The Rb1 position is coordinated by seven oxygen atoms with distances in the range of 2.868(2)−3.133(3) and has a BVS of 0.99 v.u..

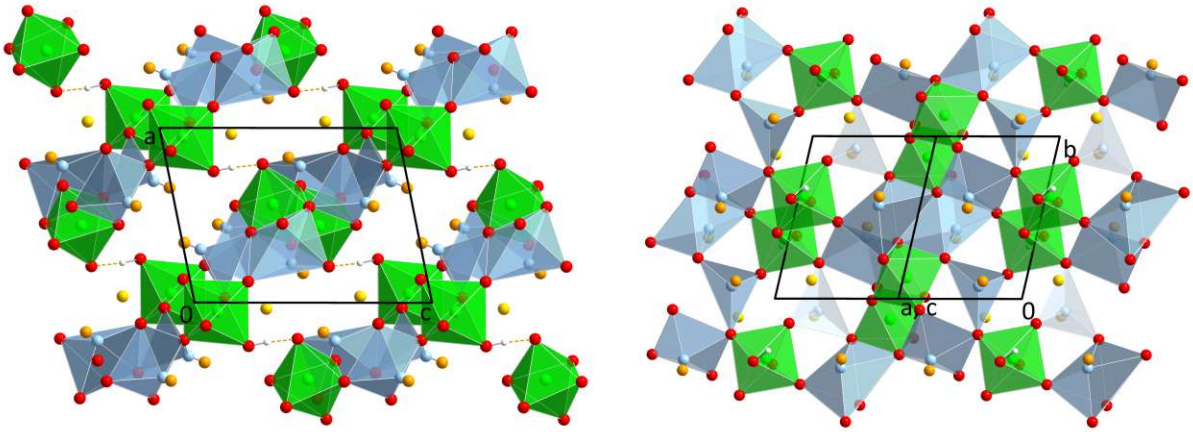

Figure 125. The crystal structure of RbPb$_3$Te$_2$O$_9$(OH) viewed along [0$\bar{1}$0] (left) and [10$\bar{1}$] (right), including non-bonding lone pairs ψ.

Table 48. Selected interatomic distances in the crystal structure of RbPb$_3$Te$_2$O$_9$(OH).

	d / Å		*d* / Å
Pb1—O2	2.317(3)	Te1—O6^{iii}	1.886(3)
Pb1—O7^{i}	2.329(3)	Te1—O5	1.914(3)
Pb1—O5	2.378(3)	Te1—O7	1.957(3)
Pb1—O9^{i}	2.600(3)	Te1—O4^{iii}	1.962(3)
Pb1—O7	2.693(3)	Te1—O4	2.012(3)
Pb2—O3^{ii}	2.268(3)	Te2—O1^{vi}	1.879(3)
Pb2—O1	2.287(3)	Te2—O2^{vi}	1.906(3)
Pb2—O5	2.306(3)	Te2—O8	1.907(3)
Pb2—O6^{iii}	2.831(3)	Te2—O3^{v}	1.922(3)
Pb2—O1^{iv}	3.023(3)	Te2—O10^{vii}	2.001(3)
Pb2—O10^{v}	3.106(3)	Te2—O10	2.005(3)
Pb3—O6^{i}	2.309(3)	Rb1—O4^{viii}	2.868(2)
Pb3—O7^{i}	2.362(3)	Rb1—O1^{viii}	2.928(3)
Pb3—O3	2.370(3)	Rb1—O2^{ix}	2.946(3)
Pb3—O2	2.493(3)	Rb1—O10^{i}	2.986(3)
Pb3—O10^{v}	2.917(3)	Rb1—O6	3.041(3)
Pb3—O8	3.055(4)	Rb1—O9^{iii}	3.056(3)
Pb3—O5	3.171(3)	Rb1—O3^{ix}	3.133(3)
Te1—O9	1.878(3)		
O8—H1	1.02(7)	O8—H1···O9	2.595(5)

Symmetry codes: (i) 1−*x*, 1−*y*, 1−*z*; (ii) *x*, −1+*y*, *z*; (iii) 1−*x*, −*y*, 1−*z*; (iv) −*x*, −*y*, −*z*; (v) 1−*x*, 1−*y*, −*z*; (vi) 1+*x*, *y*, *z*; (vii) 2−*x*, 1−*y*, −*z*; (viii) −*x*, −*y*, 1−*z*; (ix) −*x*, 1−*y*, 1−*z*.

5 Novel ternary transition metal oxidotellurates

5.1 Manganese(II) oxidotellurates(IV)

5.1.1 Hydrothermal experiments

Extensive investigations on the Mn^{II}–Te^{IV}–O-system (Eder & Weil, 2022b; Eder et al., 2022b), initiated in four hydrothermal experiments (H58–H61), which were based on mixtures of $MnCO_3$ and TeO_2 in a 1:1 ratio and different combinations of the bases NH_3, KOH and K_2CO_3. The NH_3-containing experiments H58 and H60 only yielded $Mn_2Te_3O_8$ (Cooper & Hawthorne, 1996) and educt $MnCO_3$. The PXRD patterns of H59 (KOH) and H61 (KOH, K_2CO_3) contained several unidentified phases, which were subsequently identified as *γ*-$MnTeO_3$ (5.1.5; H59), $Mn_6Te_5O_{16}$ (5.1.6; H61), and "$Mn_3(TeO_3)_2(OH)_2$" (3.7.2; both samples).

Attempts to synthesize phase-pure products of both *γ*-$MnTeO_3$ and $Mn_6Te_5O_{16}$ were likewise conducted (Table 67). Based on $MnCO_3$ and TeO_2 in a 1:1 ratio, six hydrothermal experiments employing different amounts of KOH and K_2CO_3 as the base were performed (H178–H183). Without any alkaline addition, a mixture of the starting materials $MnCO_3$ and *α*-TeO_2 and the literature phases $Mn_2Te_3O_8$ (Cooper & Hawthorne, 1996), *α*- and *β*-$MnTe_2O_5$ (Walitzi, 1965; Johnston & Harrison, 2002) was obtained (H178). Gradual increase of the alkalinity at first leads to $Mn_2Te_3O_8$ (H179, H182) as the only product, then to a mixture of $Mn_2Te_3O_8$, *γ*-$MnTeO_3$, $Mn_6Te_5O_{16}$ and "$Mn_3(TeO_3)_2(OH)_2$" (H180), the disappearance of $Mn_2Te_3O_8$ and *γ*-$MnTeO_3$ (H183), and at the highest base concentrations of the series, only "$Mn_3(TeO_3)_2(OH)_2$" was identified (H181). Repeating these six experiments in an open hydrothermal setup led to products with lower crystallinity and the formation of fewer of the desired phases. Next to the starting materials, the oxidation product Mn_3O_4 (Aminoff, 1926) could be identified.

Hydrothermal reactions between $MnCO_3$ and K_2TeO_3 without any additional base resulted in mixtures of $Mn_2Te_3O_8$ and $Mn_6Te_5O_{16}$, however, with the latter not in the desired phase-pure form (H245, H246). A single phase product (PXRD of batch H248) was eventually synthesized from a mixture of $MnCO_3$, TeO_2, KOH and K_2CO_3 in molar ratios of 3:2:4:4.

Several hydrothermal attempts were made employing the magnetically stirred Mars 6 Microwave reactor (Table 65). Experiments M18–29 were aimed at the synthesis of the first two manganese(II) oxidotellurates(IV) obtained by hydrothermal synthesis, *γ*-$MnTeO_3$ and $Mn_6Te_5O_{16}$. M18–23 and M24–29 only differ by a slightly different Mn:Te ratio (1:1 and 6:5) and led to similar results. A complete omission of the external base did not result in any reaction, and only the starting materials $MnCO_3$ and TeO_2 were found (M18, M24). An increase in alkalinity led to the formation of $Mn_2Te_3O_8$ (Cooper & Hawthorne, 1996) as the stable phase (M19, M25), followed by $Mn_6Te_5O_{16}$ as the main product (M20, M26) at even higher base concentrations. A further increase of the pH-value yielded Mn_3O_4 (Aminoff, 1926) as a reaction product. At the highly alkaline conditions, Mn^{II} is oxidized by remaining oxygen from the air to Mn_3O_4. The amount of oxygen in the air and the introduced water of the Teflon reaction chamber in theory suffices to oxidize all employed Mn^{II} (0.1–0.2 g $MnCO_3$) to Mn_3O_4.

5.1.2 Experiments in a large-scale autoclave

The Mn^{II}–Te^{IV}–O-system was chosen as the test system for first experiments in a Berghof BW-700 high-pressure reactor (2.1.2). The main goal was the synthesis of $Mn_6Te_5O_{16}$, and a Mn^{II}:Te^{IV} ratio of 6:5 was chosen for all but one of the batches, which are summarized in Table 49. The starting materials amounted to a total weight of 0.5–1 g with the exception of experiments A6 and A9 (> 3 g K_2CO_3). All reaction products were fine brown powders lacking any material suitable for single-crystal diffraction.

The prevalent issue with this experimental setup − small amounts of educts in a large reactor − turned out to be the potential oxidation of reactants by residual oxygen from the air or dissolved in the introduced water. Experiments A1 and A2 were conducted under ambient atmosphere. The resulting phases were Mn_3O_4 (Aminoff, 1926), a frequently observed oxidation product of Mn^{II} in hydrothermal setups, and an unidentified phase with probably hexagonal structure, given the symmetry of phases with similar PXRD patterns. Based on $MnGeTeO_6$ (Kim et al., 2017) and $LiMnFeF_6$ (Courbion et al., 1982) with related powder patterns, compositions of $Mn^{III}_2Te^{VI}O_6$ or $MnTe^{IV}Te^{VI}O_6$ are educated guesses. However, the observed PXRD pattern does not match those of the two known polymorphs of Mn_2TeO_6 (Matsubara et al., 2017).

Experiments A3 and A4 were conducted under an atmosphere consisting of 98% Ar with 2% H_2. "$Mn_3(TeO_3)_2(OH)_2$", or more accurately $Mn_3(TeO_3)_2(OH)_{2-2n}(CO_3)_n$ ($n \leq 0.25$), (3.7.2), was obtained besides Mn_3O_4. Experiment A4 was performed without magnetic stirring. This set-up led only to a significant presence of unreacted starting materials but not to the formation of larger crystals.

Subsequently, H_2-free argon gas was used as an alternative, applying an additional pressure of 11−12 bar in the reaction container. However, batches A5 and A6 did not lead to any "$Mn_3(TeO_3)_2(OH)_2$" phase, but yielded Mn_3O_4, $MnCO_3$ and, for A5, again the hexagonal phase observed in A1 and A2.

The pH-stability region of the apparent hexagonal phase seems to be limited, because the addition of K_2CO_3 to experiment A5 instead of KOH like in batch A7 led to the disappearance of this phase. Surprisingly, A8 is the only experiment without Mn_3O_4 as a side product.

Experiment A10 started with a completely different composition of starting materials and likewise also yielded a different phase besides Mn_3O_4. The diffraction pattern matches that of a tetragonal body-centered phase with $a \approx 10.25$ Å, $c \approx 3.01$ Å. This fits the broad spectrum of hollandite-type phases, named after the corresponding mineral $Ba_2Mn_8O_{16}$ (Miura, 1986). Reference patterns of phases with similar PXRD patterns like $K_2Fe_2Ti_6O_{16}$ (Knyazev et al., 2011) or $K_{1.4}Mn_{1.4}Ti_{6.6}O_{16}$ (Moetakef et al., 2014) make an assumed composition of $K_2Mn^{III}_2Mn^{IV}_6O_{16}$ the most promising candidate. Alternatively, a composition of MnO(OH), isotypic with *β*-FeO(OH) (MacKay, 1962) seems plausible, as revealed by the similar PXRD patterns. The presence of both presumed phases again is accompanied by a (partial) oxidation of the employed Mn^{II}. This signifies that this method is not well-suited to synthesize small amounts of phases in the Mn^{II}–Te^{IV}–O-system. The setup needs be improved by connecting a vacuum pump to the system in order to remove oxygen from the reactor and also from the introduced water more effectively.

Table 49. Results of experiments in the Berghof BTC-3000 autoclave.

Batch	Educts	Molar ratios	Atmosphere	p_{add} / bar	Stirring	T_{max} / °C	V_{H_2O} / ml	Identified phases
A1	$MnCO_3/K_2TeO_3$	6/5	air	–	on	210	350	Mn_3O_4, hex.
A2	$MnCO_3/K_2TeO_3$	6/5	air	–	off	210	350	Mn_3O_4, hex.
A3	$MnCO_3/K_2TeO_3$	6/5	Ar, 2% H_2	–	on	210	350	Mn_3O_4, "$Mn_3(TeO_3)_2(OH)_2$"
A4	$MnCO_3/K_2TeO_3$	6/5	Ar, 2% H_2	–	off	210	350	Mn_3O_4, $MnCO_3$, TeO_2, "$Mn_3(TeO_3)_2(OH)_2$"
A5	$MnCO_3/K_2TeO_3$	6/5	Ar	11	on	210	500	Mn_3O_4, $MnCO_3$, hex.
A6	$MnCO_3/K_2TeO_3/K_2CO_3$	6/5/excess	Ar	12	on	210	500	Mn_3O_4, $MnCO_3$
A7	$MnCO_3/TeO_2/KOH$	6/5/20	Ar	12	on	210	500	Mn_3O_4, $MnCO_3$, hex.
A8	$MnCO_3/TeO_2$	6/5	Ar	12	on	210	500	$Mn_2Te_3O_8$, TeO_2
A9	$MnCO_3/TeO_2/K_2CO_3$	6/5/excess	Ar	12	on	210	500	Mn_3O_4, $MnCO_3$
A10	$MnSO_4/TeO_2/K_2CO_3/KOH$	1/1/2/4	Ar	12	on	210	500	Mn_3O_4, tetr.

hex. = assumed hexagonal phase, $a \approx 5.00$ Å, $c \approx 4.68$ Å; tetr. = assumed tetragonal phase, $a \approx 10.23$ Å, $c \approx 3.01$ Å.

5.1.3 Solid-state reactions

The phases *γ*-$MnTeO_3$ and $Mn_6Te_5O_{16}$ were obtained by hydrothermal reactions. $Mn_6Te_5O_{16}$ has originally been reported with an incorrect composition of $Mn_4Te_3O_{10}$ (Trömel & Schmidt, 1972) and was synthesized by means of a solid-state reaction from MnO and TeO_2 (molar ratios 6:5) at 650 °C (Trömel & Scheller, 1976). However, no single-crystal structure determination has been performed at that time. In the first publication (Trömel & Schmidt, 1972), the synthesis of *α*-$MnTeO_3$ from MnO and TeO_2 (molar ratios 1:1) at 720 °C inside of gold foil was reported. Again, no structure determination based on single-crystal X-ray diffraction was performed at the time.

A series of solid-state reactions (S21−S32; Table 50) starting from MnO and TeO_2 was conducted with two main goals: First, the re-synthesis of $Mn_6Te_5O_{16}$ as obtained under hydrothermal conditions, and second, the determination of the crystal structure of *α*-$MnTeO_3$ by means of single-crystal diffraction.

Table 50. Reaction products of solid-state reactions in the MnO-TeO_2 system as determined from PXRD.

Batch	Atmosphere	T / °C	*α*-$MnTeO_3$	$Mn_2Te_3O_8$	$MnTe_2O_5$	$Mn_6Te_5O_{16}$	$MnTe_6O_{13}$	Mn_3TeO_6	Mn_2TeO_6	Mn_3O_4	Mn_2O_3
S21	argon	650	84%	7%				9%			
S22	argon	650	64%			20%		5%		12%	
S23	vacuum	720	100%								
S24	vacuum	650		56%						19%	
S25	air	720			55%			4%	33%	1%	7%
S26	air	650		40%	26%			26%		1%	7%
S27	vacuum	700	99%								1%
S28	vacuum	675	97%							3%	
S29	vacuum	650	89%	4%						7%	
S30	vacuum	750*		28%			16%	39%		17%	
S31	vacuum	650		92%						5%	
S32	vacuum	650	9%	88%						3%	

*Assumed leaks in the ampoule due to corrosion

Additional side products: S24: MnO, MnO_2; S31: MnO;

The presence of oxygen during the reactions (S25, S26) led to the oxidation of some of the introduced Te^{IV} and Mn^{II}, indicated by the products $Mn_3Te^{VI}O_6$ (Weil, 2006), $Mn_2^{III}Te^{VI}O_6$ (Matsubara et al., 2017) and $Mn_2^{III}O_3$ (Aminoff, 1931). Therefore, the other experiments were conducted either under inert gas (Ar) or in evacuated, sealed silica glass tubes. *α*-$MnTeO_3$ was obtained in several experiments at temperatures of 650−720 °C. In the temperature range of 675−720 °C, *α*-$MnTeO_3$ was obtained almost exclusively, judging from the PXRD patterns. However, the corresponding samples all contained small droplets of elemental Te. The latter and manganese(III) oxides are the products of an internal redox-reaction between Te^{IV} and Mn^{II}. The reaction temperature of 750 °C (S30) led to a severe attack of the ampoule material, possibly accompanied with the intrusion of air into the reaction.

In all but one experiments, it was not possible to obtain any PXRD-detectable amounts of $Mn_6Te_5O_{16}$. Trömel & Schmidt (1972) hinted that this compound might be metastable during solid-state synthesis, claiming that the yield of $Mn_6Te_5O_{16}$ decreased with elongated reaction time. They suggested therefore a reaction time of 10 h at 650 °C. Following these instructions, $Mn_6Te_5O_{16}$ was indeed obtained, but only as a by-product next to *α*-TeO_3, Mn_3TeO_6 and Mn_3O_4 under Ar-atmosphere, and not in form of larger crystals. Experiments S31 and S32 were quenched from 650 °C under running water after reaction times of 5 and 10 h, respectively. When the ampoules were taken out of the furnace, they were filled with an intense yellow vapor. No $Mn_6Te_5O_{16}$ could be detected after quenching.

5.1.4 α-$MnTeO_3$

The phase α-$MnTeO_3$ has first been reported by Trömel & Schmidt (1972). Re-synthesis from MnO and TeO_2 in a solid-state reaction at 720 °C in vacuum yielded the same product with the same PXRD pattern (Figure 127). Furthermore, single crystals for diffraction experiments were available now for the first time.

The crystal structure of α-$MnTeO_3$ is orthorhombic (*Pbca*, a = 10.0662(3) Å, b = 8.0958(2) Å, c = 14.1654(4) Å, V = 1154.39(6) Å^3). Its asymmetric unit contains two Te, two Mn and six O atoms. The Te^{IV} atoms are coordinated by three oxygen atoms in a trigonal-pyramidal shape, and the $[TeO_3]$ units are isolated from each other. The Mn^{II} positions exhibit CNs of 6 (Mn1) and [5+1] (Mn2) and the $[MnO_6]$ polyhedra are connected to two neighboring units by edge-sharing. The hereby formed $^1_\infty[Mn_2O_{8/2}O_{4/1}]$ zig-zag chains propagate parallel to [100] and are cross-linked to each other by corner-sharing. The so-formed layers extend parallel to (001) and are interconnected by the $[TeO_3]$ groups (Figure 126). α-$MnTeO_3$ is not isotypic to any other transition metal oxidotellurate(IV) with $MTeO_3$ composition. Its closest structural relatives are $NaGaTe_2O_6$ (Miletich & Pertlik, 1998) and $NaFeTe_2O_6$ (Weil & Stöger, 2008).

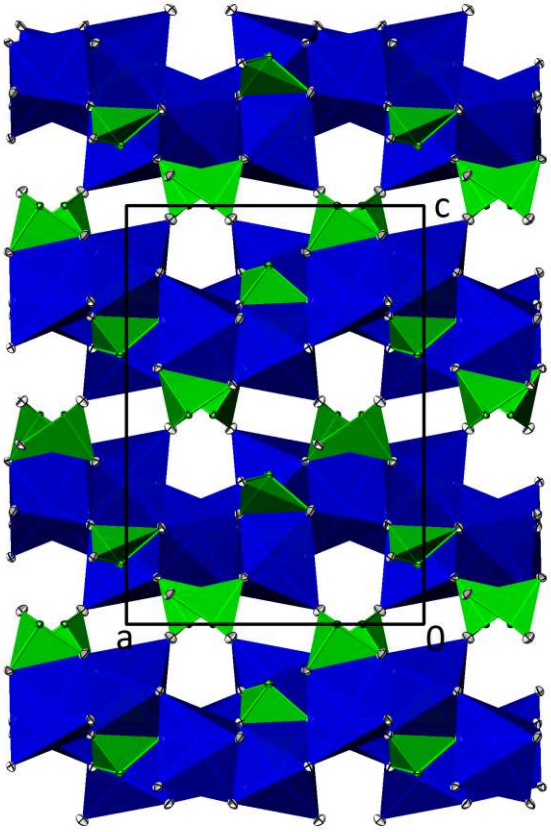

Figure 126. The crystal structure of α-$MnTeO_3$ viewed along [0$\bar{1}$0]. Structure representation was generated with ATOMS (Dowty, 2006).

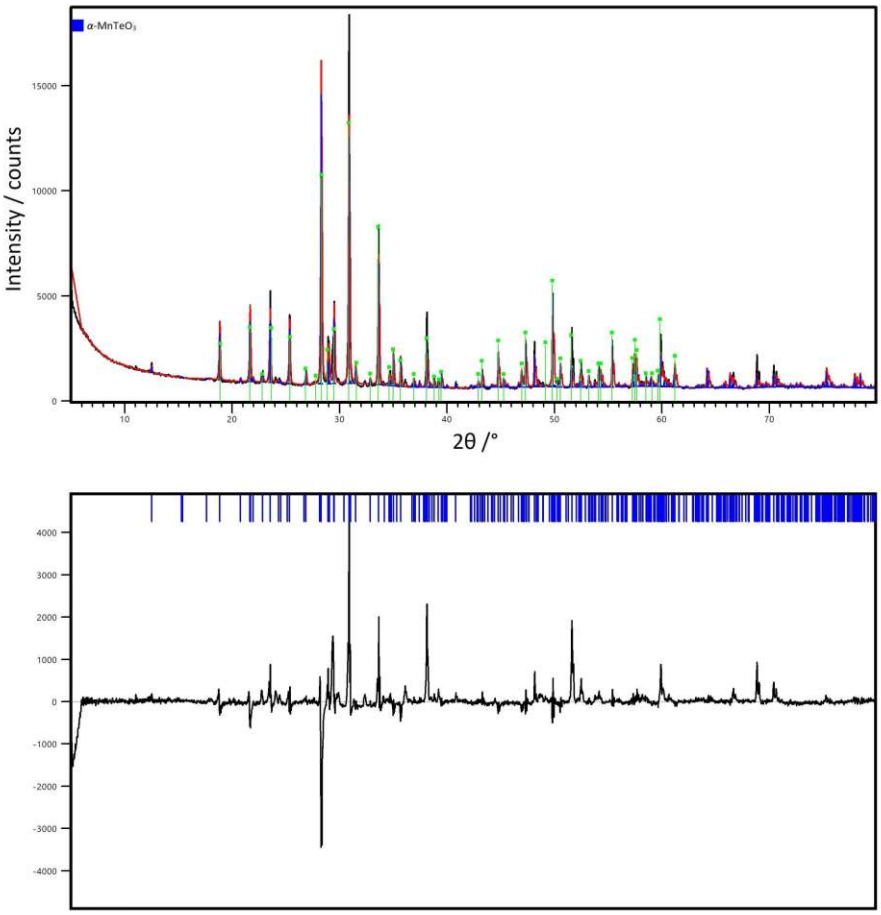

Figure 127. Rietveld refinement of α-$MnTeO_3$ based on the PXRD pattern of solid-state reaction S23. Reflections reported by Trömel & Schmidt (1972) are drawn in green (upper half).

5.1.5 γ-$MnTeO_3$

Single crystals of γ-$MnTeO_3$ have a plate-like form and a brown color. They were obtained as a side product in a hydrothermal reaction of $MnCO_3$, TeO_2 and KOH (molar ratios 1:1:2; batch H59). In none of the numerous follow-up experiments, it was possible to obtain γ-$MnTeO_3$ as the main phase.

The crystal structure of γ-$MnTeO_3$ (*Pbca*; a = 7.4535(12) Å, b = 6.4164(11) Å, c = 12.843(2) Å, V = 614.2(2) Å^3) is isotypic with $ZnTeO_3$ (Hanke, 1967). The asymmetric unit contains one Te, one Mn and three oxygen atoms. The Te^{IV} atoms form trigonal [TeO_3] pyramids, which are isolated from each other. The Mn^{II} atoms are coordinated by five oxygen atoms. Like in α-$MnTeO_3$, the coordination polyhedra of the Mn^{II} atoms are connected to each other by corner- and edge-sharing and form layers, which are cross-linked by the [TeO_3] groups (Figure 128). Different to the α-form, each [MnO_5] unit shares only one edge instead of two with a neighboring group, and the Mn−O-layers consist of [Mn_2O_8] dimers connected by corner-sharing instead of the $^1_\infty[Mn_2O_{8/2}O_{4/1}]$ chains in α-$MnTeO_3$. γ-$MnTeO_3$ is assumed to be metastable with respect to the α-form, based on its significantly larger relative cell volume and therefore lower density.

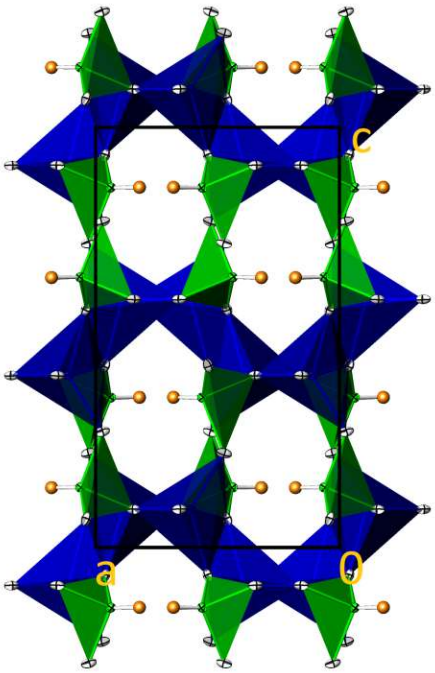

Figure 128. The crystal structure of γ-$MnTeO_3$ viewed along [0$\bar{1}$0]. Structure representation was generated with ATOMS (Dowty, 2006).

5.1.6 $Mn_6Te_5O_{16}$

$Mn_6Te_5O_{16}$ was obtained with the highest yield from a hydrothermal reaction of $MnCO_3$, TeO_2, KOH and K_2CO_3 in molar ratios of 3:2:4:4 (H248). A synthesis by solid-state reaction at 650 °C for 10 hours, as reported by Trömel & Schmid (1972), from MnO and TeO_2 (ratios 6:5) was successful under Ar atmosphere (S22) but did not yield $Mn_6Te_5O_{16}$ as the majority phase.

The crystal structure of $Mn_6Te_5O_{16}$ (*Pnma*; a = 11.3560(3) Å, b = 10.5282(2) Å, c = 10.1913(2) Å, V = 1577.28(6) Å^3) is isotypic with that of $Co_6Te_5O_{16}$ (Trömel & Scheller, 1976). Of the three Mn sites, one (Mn1) is coordinated by five, and the others (Mn2, Mn3) by six oxygen atoms in a trigonal-bipyramidal and an octahedral environment, respectively. By edge-sharing, they form [Mn_2O_8] dimers (Mn1) and [Mn_4O_{16}] oligomers (Mn2 and Mn3), which are linked to each other by corner-sharing to form a loose tri-periodic framework. The spaces in-between are occupied by [TeO_3] and [TeO_4] units, which are all isolated from each other (Figure 129).

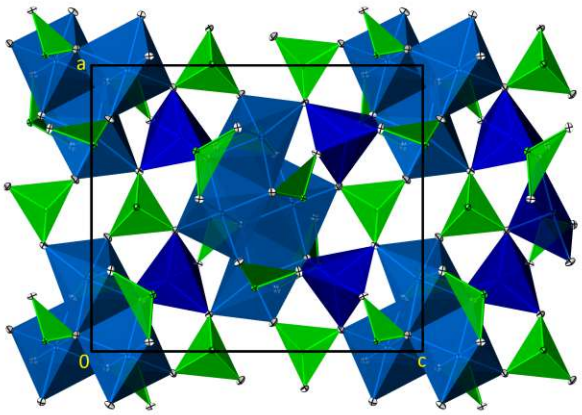

Figure 129. The crystal structure of $Mn_6Te_5O_{16}$ viewed along [0$\bar{1}$0]. Structure representation was generated with ATOMS (Dowty, 2006).

For more details on the preparation conditions and crystal structures of α-$MnTeO_3$, γ-$MnTeO_3$ and $Mn_6Te_5O_{16}$, see:

Eder, F. & Weil, M. (2022b). Phase formation studies and crystal structure refinements in the $Mn^{II}/Te^{IV}/O/(H)$ system. *Z. Anorg. Allg. Chem*. **648**, e202200205.

5.2 Cadmium(II) oxidotellurates(IV)

5.2.1 *β*-$CdTe_2O_5$

Crystals of *β*-$CdTe_2O_5$ are colorless and block-shaped and were synthesized in a hydrothermal reaction of $Cd(NO_3)_2(H_2O)_6$, TeO_2, H_6TeO_6 and $NH_{3\ aq.}$ in molar ratios of 2:1:1:6 (H112). Cd_3TeO_6 (Burckhardt et al., 1982) was obtained as a side product. The unit-cell of *β*-$CdTe_2O_5$ is monoclinic ($P2_1/c$, a = 9.4535(5) Å, b = 5.5806(3) Å, c = 10.8607(5) Å, V = 521.67(5) Å^3) and its asymmetric unit contains two Te, one Cd and five oxygen atoms, all located at general 4 *e* positions.

The Te^{IV} atoms are coordinated by four oxygen atoms in a bisphenoidal shape. Two [Te2O_4] units form [Te_2O_6] dimers by edge-sharing, which are further connected to four adjacent [Te1O_4] groups by corner-sharing (connectivities Q^{2200} for Te1 and Q^{0410} for Te2). This way, undulated $^2_\infty[Te_2O_{6/2}O_{2/1}]$ layers extending parallel to (100) are formed (Figure 130). They alternate with layers, which consist of [CdO_7] polyhedra, connected to each other by corner- and edge-sharing. The crystal structure of *β*-$CdTe_2O_5$ is isotypic with that of ε-$CaTe_2O_5$ (Weil & Stöger, 2008b).

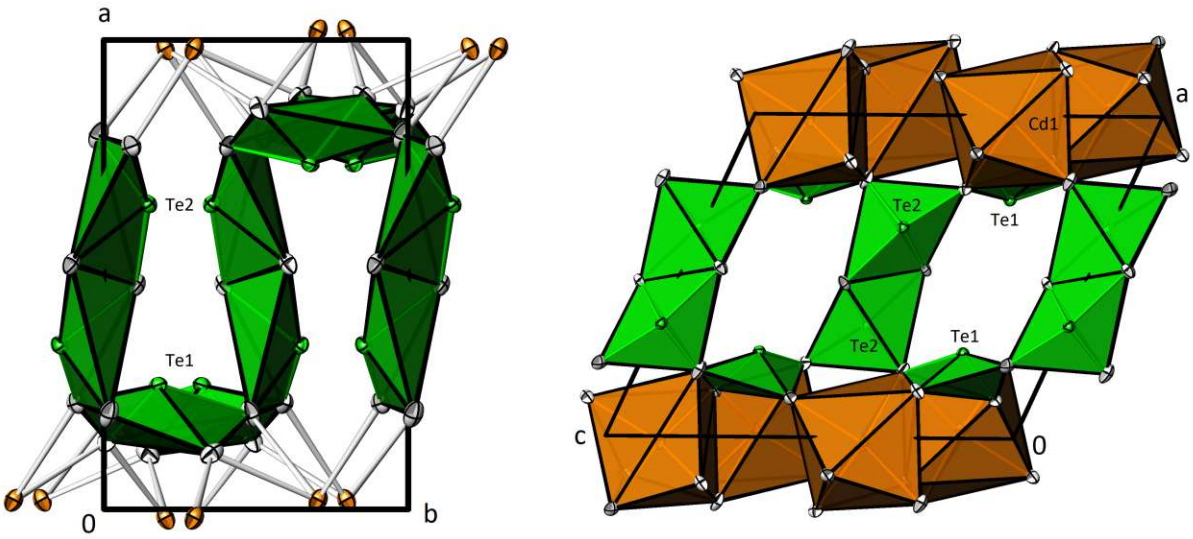

Figure 130. The crystal structure of *β*-$CdTe_2O_5$ viewed along [00$\bar{1}$] (left) and [0$\bar{1}$0]. Cd atoms are drawn orange. Structure representations were generated with ATOMS (Dowty, 2006).

For more details on the crystal structure of *β*-$CdTe_2O_5$, see:

Eder, F. & Weil, M. (2020b). The crystal structure of a new $CdTe_2O_5$ polymorph, isotypic with ε-$CaTe_2O_5$. *Acta Cryst.* E**76**, 831–834.

5.2.2 $Cd_4Te_5O_{14}$

Single crystals of $Cd_4Te_5O_{14}$ were obtained as minor by-products in several hydrothermal experiments targeted at cadmium oxidotellurate(IV) nitrate phases. Single crystals of $Cd_4Te_5O_{14}$ are colorless and have an elongated bar-like form. It appears that this phase has formed in only small amounts in each case, because the PXRD data of samples containing crystals of $Cd_4Te_5O_{14}$ revealed a negligible fraction of this phase relative to the obtained bulk products.

The unit-cell of $Cd_4Te_5O_{14}$ is monoclinic with a = 11.9074(3) Å, b = 14.3289(3) Å, c = 8.7169(2) Å, β = 113.6290(10)°, V = 1362.58(6) Å^3. Of the thirteen atoms in the asymmetric unit, three (Te3, Cd2, Cd3) are located at a position with site symmetry 2 (4 *e*), while the other ten (two Te, one Cd and seven O) all belong to general 8 *f* positions.

The Te^{IV} atoms are all coordinated by four oxygen atoms in a bisphenoidal shape. While for Te3 the four oxygen contacts have comparable distances, in Te1 and Te2, the coordination is better described as [3+1]. The [TeO_4] units are connected to each other forming $^1_\infty[Te_{10}O_{24/2}O_{16/1}]$ chains propagating in the [203] direction (Figure 131). The translational unit of the chain is ten Te^{IV} atoms long and corresponds to a translation of 2**a** + 3**c**. Using the nomenclature by Christy et al. (2016), the connectivities of the Te^{IV} atoms are denoted as Q^{1301} (Te1) and Q^{2200} (Te2 and Te3), and the chains are categorized as *zehner*-chains (Liebau, 1985) with a symbol of (…–◊–◊=◊–◊–◊–◊–◊=◊–◊–◊–…). The chains form loops leading to the shape of an "8" when viewed along the propagating direction. This structural element has not been described yet for oxidotellurates (Christy et al., 2016).

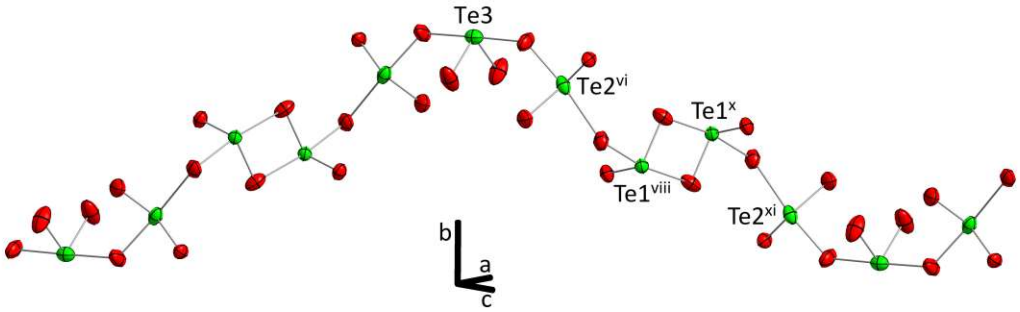

Figure 131. $^1_\infty[Te_{10}O_{28}]$ chain in the crystal structure of $Cd_4Te_5O_{14}$. Symmetry codes refer to Table 51; x) 1/2+*x*, 1/2+*y*, 1+*z*; xi) 1−*x*, *y*, 3/2−*z*.

It should be noted that the fourth oxygen contact of Te1 has a distance of 2.476(2) Å and thus is slightly above the bond-length threshold of 2.40−2.45 Å. The latter was suggested by Christy et al. (2016) to distinguish between "structural unit" and "interstitial complex" (Hawthorne, 2014). However, the BVS of Te1 is perfectly defined with the parameters of Brese and O'Keeffe (1991), resulting in a value of 4.00 v.u. compared to 3.74 v.u. without the fourth O atom. Hence, Te1 was considered as fourfold-coordinated as well.

If the slightly too long Te1—O2^{iii} contact is not taken into account, the chains are broken, resulting in [Te_5O_{14}] units (Δ–◊–◊–◊–Δ) with connectivities of Q^{2100} (Te1) and Q^{2200} (Te2 and Te3), which would be a novel structural element for oxidotellurates as well. If the most distant oxygen contact of Te2 (2.441(2) Å) is also not considered, the crystal structure is formed by isolated [$Te1O_3$] and [Te_3O_8] groups (Δ and Δ–◊–Δ) and the connectivities of the Te^{IV} atoms change to Q^{3000} (Te1), Q^{2100} (Te2) and Q^{2200} (Te3). The BVS of the three Te^{IV} atoms amount to 4.01 (Te1), 3.93 (Te2) and 4.00 (Te3) v.u. applying the revised parameters (Mills & Christy, 2013).

The three Cd^{II} atoms are coordinated by six oxygen atoms with distances between 2.235(2) and 2.539(2) Å. The [Cd1O_6] polyhedron has a distorted trigonal-prismatic shape, while the [Cd2/3O_6] units have rather irregular shapes, which in both cases are caused by the presence of two additional oxygen contacts at distances of 2.809(3) Å (Cd2) and 2.860(3) Å (Cd3). Hence, the CNs of the Cd^{II} atoms are best described as 6 for Cd1 and [6+2] for Cd2 and Cd3. The necessity to include the weakly bonded oxygen atoms as well is underlined by the BVS of the Cd^{II} atoms, which, based on sixfold coordination, amount to 2.00 (Cd1), 1.79 (Cd2) and 1.71 (Cd3) v.u.. The latter two values increase to 1.97 (Cd2) and 1.86 (Cd3) v.u. under consideration of the additional oxygen atoms. The three [CdO_x] coordination polyhedra form, together with the Te–O-chains, a rather dense tri-periodic framework (Figure 132).

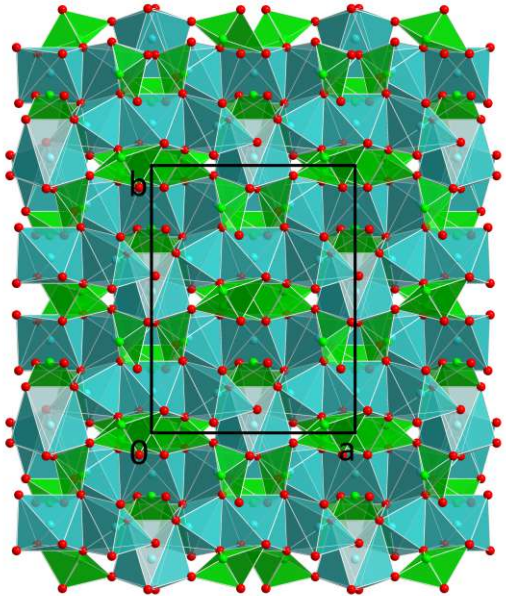

Figure 132. The crystal structure of $Cd_4Te_5O_{14}$ viewed along [00$\bar{1}$].

Other than *β*-$CdTe_2O_5$, which is isotypic with the corresponding Ca-compound, the crystal structure of $Cd_4Te_5O_{14}$ has no structural relationship to the two polymorphs of $Ca_4Te_5O_{14}$. In *α*-$Ca_4Te_5O_{14}$ (Weil, 2004), the Te^{IV} atoms form branched [Te_8O_{22}] *achter*-single chains (…–(◊–Δ)–◊–◊–(◊–Δ)–◊–◊–…) as well as isolated [TeO_3] (Δ) groups. The high-pressure *β*-polymorph (Weil et al., 2016) consists of isolated [Te_3O_8] (Δ–◊–Δ) and [TeO_3] (Δ) units. If a Te—O contact of 2.479(2) Å is considered as well, two [Te_3O_8] units are connected to form a [Te_6O_{16}] group (Δ–◊–◊–◊–◊–Δ).

Table 51. Selected interatomic distances in the crystal structure of $Cd_4Te_5O_{14}$.

	d / Å		*d* / Å
Te1—O2^{i}	1.873(2)	Cd1—O4	2.539(2)
Te1—O5	1.882(2)	Cd2—O4^{iii}	2.327(2)
Te1—O6^{ii}	1.936(2)	Cd2—O4	2.327(2)
Te1—O2^{iii}	2.476(2)	Cd2—O5^{iii}	2.339(2)
Te2—O1	1.859(2)	Cd2—O5	2.339(2)
Te2—O4	1.890(2)	Cd2—O2^{iii}	2.395(2)
Te2—O3	1.928(2)	Cd2—O2	2.395(2)
Te2—O6	2.441(2)	Cd2—O3	2.809(3)
Te3—O7^{iv}	1.876(2)	Cd2—O3^{iii}	2.809(3)
Te3—O7^{v}	1.876(2)	Cd3—O1^{iii}	2.318(2)
Te3—O3^{vi}	2.088(2)	Cd3—O1	2.318(2)
Te3—O3^{vii}	2.088(2)	Cd3—O6^{iii}	2.330(2)
Cd1—O7	2.235(2)	Cd3—O6	2.330(2)
Cd1—O4^{viii}	2.237(2)	Cd3—O7^{v}	2.478(3)
Cd1—O5	2.262(2)	Cd3—O7^{iv}	2.478(3)
Cd1—O1^{ix}	2.314(2)	Cd3—O1^{vi}	2.860(3)
Cd1—O6^{viii}	2.353(2)	Cd3—O1^{vii}	2.860(3)

Symmetry codes: (i) *x*, −*y*, −1/2+*z*; (ii) 1/2−*x*, −1/2+*y*, 1/2−*z*; (iii) −*x*, *y*, 1/2−*z*; (iv) −1/2+*x*, 1/2+*y*, *z*; (v) 1/2−*x*, 1/2+*y*, 1/2−*z*; (vi) *x*, 1−*y*, 1/2+*z*; (vii) −*x*, 1−*y*, −*z*; (viii) 1/2−*x*, 1/2−*y*, 1−*z*; (ix) 1/2+*x*, 1/2−*y*, 1/2+*z*.

6 Other phases

6.1 $K_2Te^{IV}_4O_9(H_2O)_3$

Single crystals of $K_2Te_4O_9(H_2O)_3$ were obtained serendipitously as a by-product in the mild hydroflux experiment H270, based on $Ba(OH)_2(H_2O)_8$, TeO_2 and K_2CO_3 in molar ratios of 2:3:10 with the addition of three droplets of water. Single crystals of $K_2Te_4O_9(H_2O)_3$ occur as colorless plates.

Crystal structure

Despite initial suggestions by the evaluation software to use the centrosymmetric space group $P\bar{3}1c$, the crystal structure of $K_2Te_4O_9(H_2O)_3$ was ultimately solved and refined in $P31c$ (a = 10.7416(12) Å, c = 13.358(2) Å, V = 1334.8(4) Å^3) under consideration of twinning. The twin law connecting the two domains (refined ratio 0.501:0.499(2)) is no symmetry operation of $P\bar{3}1c$, but one of the *.m.* planes, resulting in one possible transformation matrix of

$$\begin{pmatrix} \bar{1} & 0 & 0 \\ 1 & 1 & 0 \\ 0 & 0 & 1 \end{pmatrix}.$$

Of the fourteen atoms in the asymmetric unit, four Te, two K and eight O, three are located at special positions with site symmetry 3.. (Te3, Te4: 2 *b*; K2: 2 *a*), while the other eleven all occupy general 6 *c* sites. The origin of the unit-cell was chosen to coincide with the K2 position.

The Te^{IV} atoms exhibit CNs of 4 (Te1, Te2) and 3 (Te3, Te4). The $[TeO_{3/4}]$ units are connected to each other by corner-sharing (connectivities Q^{1300} for Te1 and Te2, and Q^{0300} for Te3 and Te4), leading to the formation of $^2_\infty[Te_8O_{24/2}O_{6/6}]$ layers oriented parallel to (001) (Figure 133). These layers are categorized as Te_8X_{18} single layers consisting of [−◊−◊−Δ−◊−◊−Δ−] and [−◊−◊−◊−◊−◊−◊−] 6-rings (Christy et al., 2016). This structural element has previously been described for triclinic $K_2Te_4O_9(H_2O)_{3.2}$ (Ok & Halasyamani, 2001).

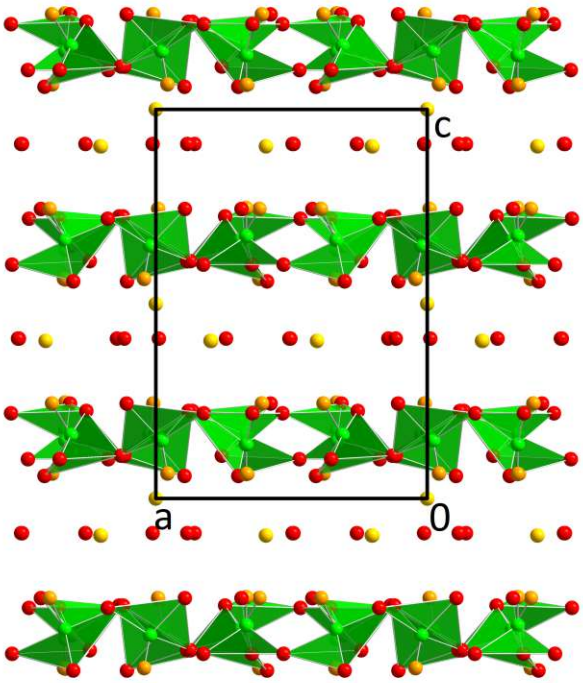

Figure 133. The crystal structure of $K_2Te_4O_9(H_2O)_3$ viewed along [0$\bar{1}$0], including Te^{IV} lone pairs ψ.

The Te^{IV} atoms of the layers are located roughly at $x \approx 0$, 1/3, 2/3 and $y \approx 0$, 1/3, 2/3, except for $x = y = 0$, where a void in the layer exists. The lone pairs ψ of the Te^{IV} atoms are directed away from the layers (coordinates x = 0.3813, y = 0.0431, z = 0.0642 for ψ_{Te_1}, x = 0.3821, y = 0.3911, z = 0.2444 for ψ_{Te_2}, x = 1/3, y = 2/3, z = 0.5630 for ψ_{Te_3} and x = 1/3, y = 2/3, z = 0.2467 for ψ_{Te_4}). The BVS of the Te^{IV} atoms show some variance with values of 3.88 (Te1), 3.90 (Te2), 3.84 (Te3) and 4.15 (Te4) v.u..

The space between the layers is occupied by the K^+ cations K1 and K2, and crystal water molecules OW1 and OW2. The K positions are coordinated by seven (K1) or six (K2) oxygen atoms. The crystal water molecules were identified as such by the lack of any contacts closer than 2.69 Å. No hydrogen atoms could be located from difference-Fourier maps, but assumptions concerning potential hydrogen

bonds can be made. The two closest oxygen contacts of the OW1 and OW2 sites are in both cases the O1 and O4 positions, which correspond to the only terminal oxygen atoms of the layers and exhibit substantial under-bonding with BVS of 1.47 (O1) and 1.67 (O4) v.u., respectively. The hydrogen bonds formed with O1 are stronger (O—H···O distances of 2.70(5) and 2.73(6) Å) than those with O4 (2.85(5) and 2.87(4) Å), which is in agreement with the more pronounced under-bonding for the O1 position.

Stacking disorder

Not uncommon for layered oxidotellurates(IV), the crystals of $K_2Te_4O_9(H_2O)_3$ exhibit stacking disorder, notable in both the diffraction pattern and in the refinement. In reconstructed reciprocal *nkl* or *hnl* ($n \in \mathbb{Z}$) lattice planes, weak diffuse scattering is discernable in the **c*** direction, which corresponds to the reciprocal stacking direction of the (001) planes (Figure 134). In the crystal structure refinement, this leads to the presence of weak "shadow atoms" corresponding to differently oriented layers. In the case of $K_2Te_4O_9(H_2O)_3$, only one significant peak of difference electron density was present, which corresponds to the void in the $^2_\infty[Te_8O_{18}]$ layers at $x = y = 0$. All other Te shadow atoms are located too close to the actual Te sites to be noticed as separate atoms, and the "shadows" of the lighter atoms do not result in high remaining electronic-density peaks.

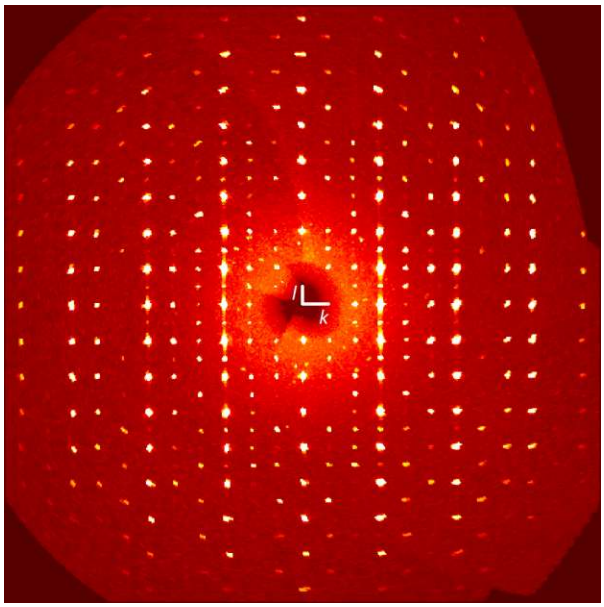

Figure 134. Reconstructed reciprocal 0*kl* plane of $K_2Te_4O_9(H_2O)_3$.

To account for the effects of the stacking disorder in the model, the Te5 atom was placed on the "shadow atom" position, which is located at $x = y = 0$, $z = 0.1675$ (site symmetry 3..; 2 *a*). In order to maintain the same stoichiometry, the occupancy of Te5 was linked to those of the other two Te sites with site symmetry 3.., Te3 and Te4, resulting in s.o.f.s of 0.969(3) for Te3 and Te4, and 0.062(6) for Te5. The observed stacking disorder and the twinned crystal are most likely the cause for the qualitatively poor dataset, as visible from the high uncertainties of the determined interatomic distances (Table 52).

Comparison with $K_2Te_4O_9(H_2O)_{3.2}$

In 2001, Ok & Halasyamani, reported the triclinic crystal structure of $K_2Te_4O_9(H_2O)_{3.2}$ with lattice parameters of $a = 7.5046(5)$ Å, $b = 10.7097(8)$ Å, $c = 10.7159$ (8) Å, $\alpha = 60.849(1)°$, $\beta = 69.918(1)°$, $\gamma = 85.968(1)°$, $V = 701.49(9)$ Å^3 in space group *P*1. Indicated by the similar length of **b** and **c**, enclosing an angle of *ca*. 60°, the crystal structure consists of layers that are built in the same way as in $K_2Te_4O_9(H_2O)_3$. However, while in $K_2Te_4O_9(H_2O)_3$, adjacent layers are not translationally equivalent (but connected by the ..*c* glide plane), this is the case in the 3.2-hydrate. Furthermore, when projecting along the normal of the layer plane, the void in the $^2_\infty[Te_8O_{18}]$ layers always stays at the same position in $K_2Te_4O_9(H_2O)_3$ but changes its place along the tilted stacking vector **a** in $K_2Te_4O_9(H_2O)_{3.2}$. A similar difference was observed for the different polytypes (I) and II)) of $K_4Sn_3Te_8O_{24}$ (4.1.3.6).

In the interspace, more crystal water sites, corresponding to four oxygen atoms p.f.u., are present in $K_2Te_4O_9(H_2O)_{3.2}$ (Figure 135). However, each of these was refined with an s.o.f. of only 0.8, resulting in

the reported crystal water content of 3.2, which was chosen in order to comply with thermogravimetric measurements.

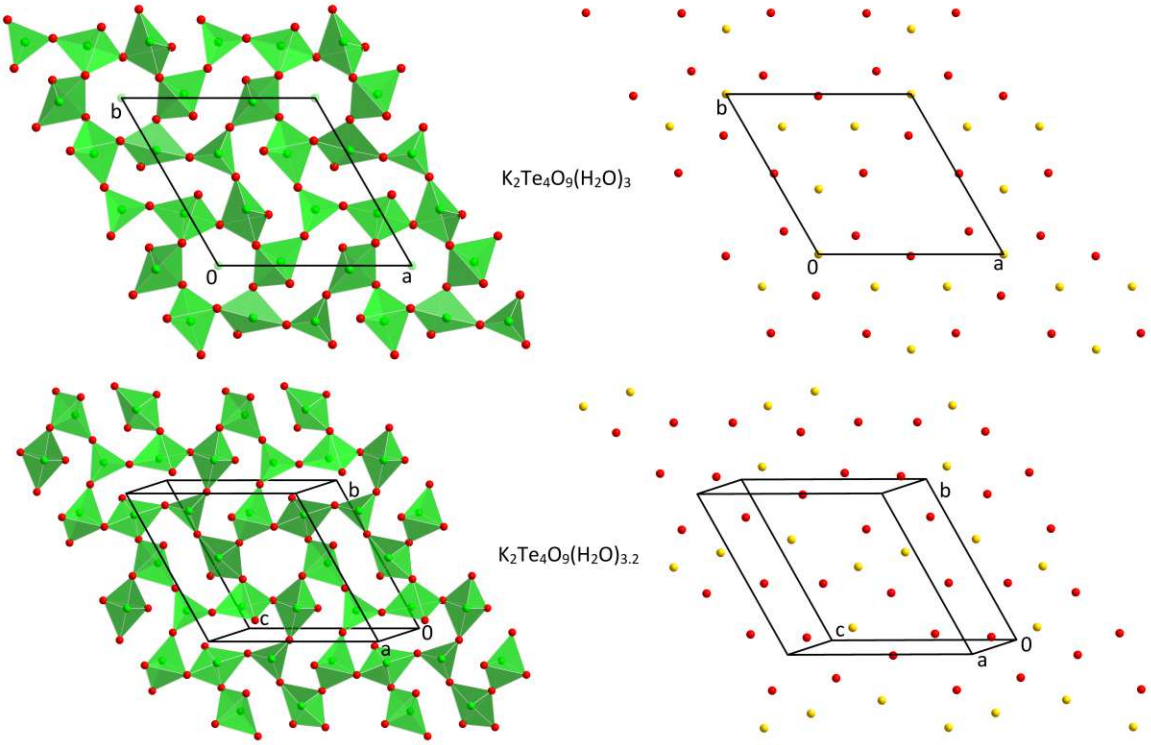

Figure 135. Comparison of the two layer types in the crystal structures of $K_2Te_4O_9(H_2O)_3$ and $K_2Te_4O_9(H_2O)_{3.2}$ (Ok & Halasyamani, 2001).

Table 52. Selected interatomic distances in the crystal structure of $K_2Te_4O_9(H_2O)_3$.

	d / Å		*d* / Å
Te1—O4^{i}	1.820(18)	K1—OW2	2.75(6)
Te1—O3	1.926(16)	K1—O3	2.784(16)
Te1—O2^{i}	2.134(15)	K1—OW2^{vii}	2.76(6)
Te1—O6	2.17(2)	K1—O6	2.91(2)
Te2—O2	1.861(16)	K1—O5^{iii}	3.02(3)
Te2—O1	1.88(2)	K1—O2^{iii}	3.126(17)
Te2—O5	2.08(3)	K1—OW1^{i}	3.17(3)
Te2—O3	2.219(15)	K2—OW1^{viii}	2.693(17)
Te3—O6^{ii}	1.91(2)	K2—OW1^{ix}	2.693(17)
Te3—O6^{iii}	1.91(2)	K2—OW1^{x}	2.693(17)
Te3—O6^{iv}	1.91(2)	K2—O2^{i}	2.696(16)
Te4—O5	1.87(3)	K2—O2^{xi}	2.696(16)
Te4—O5^{v}	1.87(3)	K2—O2	2.696(16)
Te4—O5^{vi}	1.87(3)		

Symmetry codes: (i) $-x+y, -x, z$; (ii) $x-y, 1-y, 1/2+z$; (iii) $y, x, 1/2+z$; (iv) $1-x, 1-x+y, 1/2+z$; (v) $-x+y, 1-x, z$; (vi) $1-y, 1+x-y, z$; (vii) $1-x+y, 1-x, z$; (viii) $y, x, -1/2+z$; (ix) $x-y, -y, -1/2+z$; (x) $-x, -x+y, -1/2+z$; (xi) $-y, x-y, z$.

6.2 $Na_2Te^{IV}_4O_9(H_2O)_{10}$

$Na_2Te_4O_9(H_2O)_{10}$ is the only phase in this work that was obtained by crystal growth from aqueous solution. In an attempt to grow crystals of the assumed phase $NaHTeO_3$, aqueous NaOH solution was added to TeO_2 (Na:Te ratio of 1:1) and after mixing, the remaining solid residue was filtered off. The filtrate was left in an open vessel for several days. Single crystals of $Na_2Te_4O_9(H_2O)_{10}$ were directly isolated from the mother liquor and have the form of thin, colorless plates. The crystals are prone to weathering, if exposed to atmospheric conditions for a longer amount of time. This is the reason why single crystals of $Na_2Te_4O_9(H_2O)_{10}$ could not be investigated at room temperature but were measured at −173 °C instead. The fast dehydration of $Na_2Te_4O_9(H_2O)_{10}$ can be monitored by PXRD measurements. A freshly prepared sample of $Na_2Te_4O_9(H_2O)_{10}$ was measured repeatedly with 10-minute measurements over the course of four hours and again after one week (Figure 136). The reflections of the dehydration product were clearly visible starting from the second measurement.

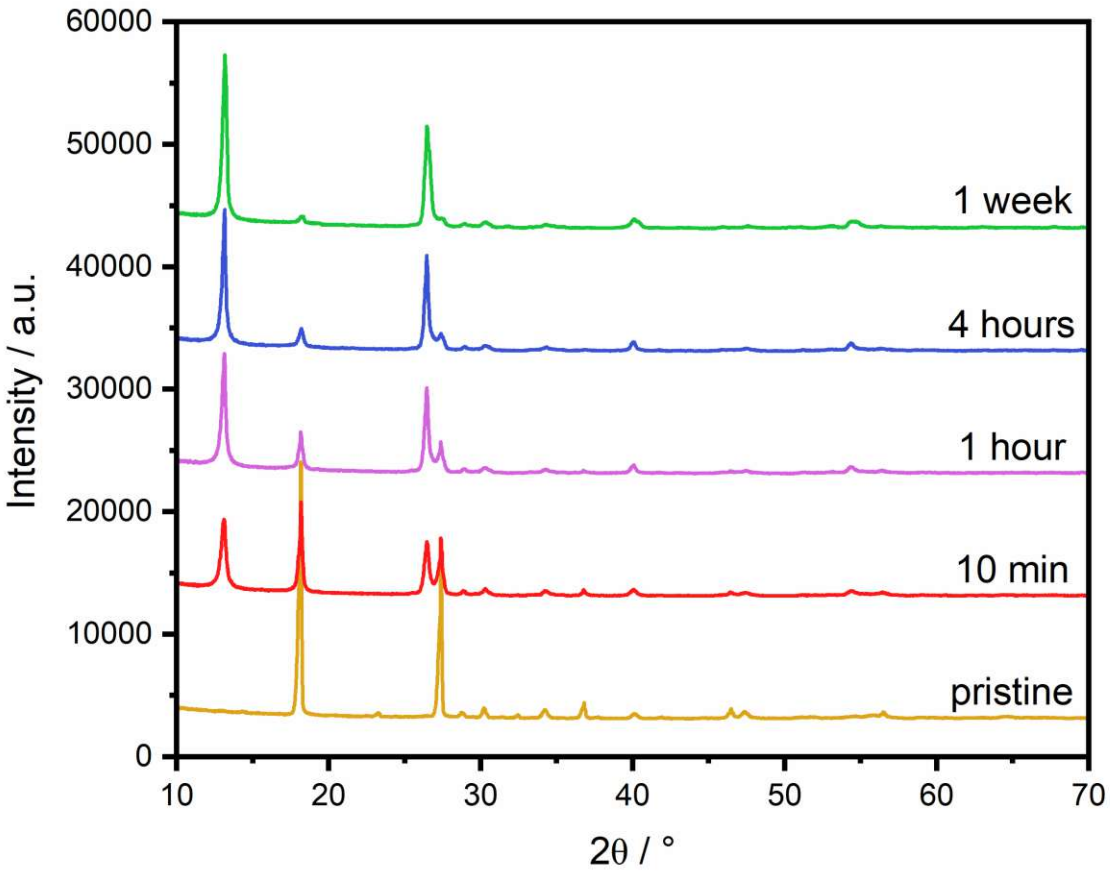

Figure 136. PXRD patterns of $Na_2Te_4O_9(H_2O)_{10}$ taken directly out of solution and after certain amounts of time.

Crystal structure

The crystal structure of $Na_2Te_4O_9(H_2O)_{10}$ has triclinic symmetry ($P\bar{1}$) with lattice parameters of a = 15.8811(8) Å, b = 16.1225(8) Å, c = 18.2439(9) Å, α = 110.9970(10)°, β = 103.5810(10)°, γ = 108.6920(10)°, V = 3794.4(3) Å^3. In order to better describe the layered features of the crystal structure, the setting of the unit-cell was changed by the transformation matrix

$$\begin{pmatrix} 1 & 0 & 0 \\ \bar{1} & \bar{1} & 0 \\ \bar{1} & 0 & \bar{1} \end{pmatrix}$$

to a = 15.8738(8) Å, b = 18.6481(9) Å, c = 21.1802(10) Å, α = 90.4760(10)°, β = 123.1820(10)°, γ = 125.0530(10)°, V = 3789.4(3) Å^3 (small changes in the unit-cell volume result from a repeated integration), which changes the orientation of the layers from ($\bar{1}$11) to a more convenient layer direction parallel to (100). Owing to the large unit-cell dimensions and the low symmetry, shadowing of the beam stop resulted in more damaged intensities of low-angle reflections than usual. In total, 20 reflections had to be manually omitted from the refinement.

The asymmetric unit contains a total of 100 atoms, thereof 16 Te, eight Na and 76 O, all located at general 2 *I* positions. The large and low-symmetric unit-cell caused the *STRUCTURE TIDY* program implemented in *PLATON* not to work. Atoms were finally labeled on basis of structural-chemical considerations.

The Te^{IV} atoms exhibit two different coordination numbers. Te1−Te12 are coordinated by four oxygen atoms in a bisphenoidal shape, while Te13−Te16 are bonded to three oxygen atoms, forming trigonal pyramids. The [TeO_4] and [TeO_3] groups are connected to each other by corner-sharing, forming $^2_\infty$[$Te_8O_{24/2}O_{6/1}$] layers at x ≈ 0.5 that are categorized as Te_8X_{18} single layers consisting of [−◊−◊−Δ−◊−◊−Δ−] and [−◊−◊−◊−◊−◊−◊−] 6-rings (Christy et al., 2016) (Figure 137). The buildup of the layers is the same as in $K_2Te_4O_9(H_2O)_3$ (6.1) and $K_2Te_4O_9(H_2O)_{3.2}$ (Ok & Halasyamani, 2001). Details regarding connectivity, BVS and coordinates for the lone pair for each Te^{IV} atom are collated in Table 53.

Table 53. Connectivity, BVS and ψ coordinates of the Te^{IV} atoms in $Na_2Te_4O_9(H_2O)_{10}$.

Atom label	Connectivity	BVS / v.u.	x (ψ)	y (ψ)	z (ψ)
Te1	Q^{1300}	4.00	0.3321	0.1543	−0.0037
Te2	Q^{1300}	4.04	0.3708	0.5263	0.4678
Te3	Q^{1300}	3.98	0.6411	0.1297	0.5092
Te4	Q^{1300}	4.01	0.6302	0.4806	1.0324
Te5	Q^{1300}	3.96	0.3284	0.3679	0.2273
Te6	Q^{1300}	4.00	0.6699	1.0050	0.3115
Te7	Q^{1300}	3.98	0.3586	−0.0198	0.2123
Te8	Q^{1300}	3.97	0.3681	0.6688	0.2571
Te9	Q^{1300}	4.01	0.3625	0.8666	−0.0012
Te10	Q^{1300}	3.97	0.5872	0.2952	0.2197
Te11	Q^{1300}	4.00	0.6553	0.8541	0.5167
Te12	Q^{1300}	3.98	0.6885	0.6351	0.2848
Te13	Q^{0300}	3.95	0.6869	1.0167	0.4480
Te14	Q^{0300}	3.93	0.3346	−0.0045	0.0600
Te15	Q^{0300}	3.93	0.3604	0.5178	0.3201
Te16	Q^{0300}	3.98	0.6240	0.4769	0.1735

All Na^+ cations are coordinated by oxygen atoms within the distance range of 2.30–2.60 Å, exhibiting different CNs of 5 (Na5), 6 (Na1, Na3, Na5, Na6, Na7) or 7 (Na2, Na4). Most Na^+ cations do not share any atom with the $^2_\infty[Te_8O_{18}]$ layers, but rather form a second layer at $x \approx 0$ (Figure 138), together with the water molecules of crystallization. The Na2 and Na4 sites make an exception of that, as they are closely connected to the $^2_\infty[Te_8O_{18}]$ layers and are positioned directly above or below the hexagonal voids of the layers. On the other hand, there are two crystal water molecules, O46 and O59, which are situated in the middle of the Na^+-layer at $x \approx 0$. The environment of four oxygen atoms with distances between 2.7 and 2.9 Å in a distorted tetrahedral shape confirms O46 and O59 as water molecules and not Na^+ cations (despite similar scattering factors for O and Na). The BVS of the Na^+ cations were determined to values of 1.14 (Na1), 1.25 (Na2), 1.13 (Na3), 1.32 (Na4), 1.02 (Na5), 1.18 (Na6), 1.25 (Na7) and 1.11 (Na8) v.u..

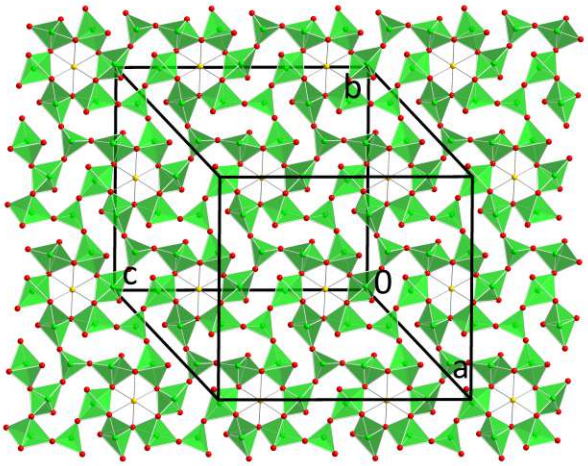

Figure 137. $^2_\infty[Te_8O_{18}]$ layer in the crystal structure of $Na_2Te_4O_9(H_2O)_{10}$ located at $x \approx 0.5$. Na2 and Na4 atoms are included into the representation.

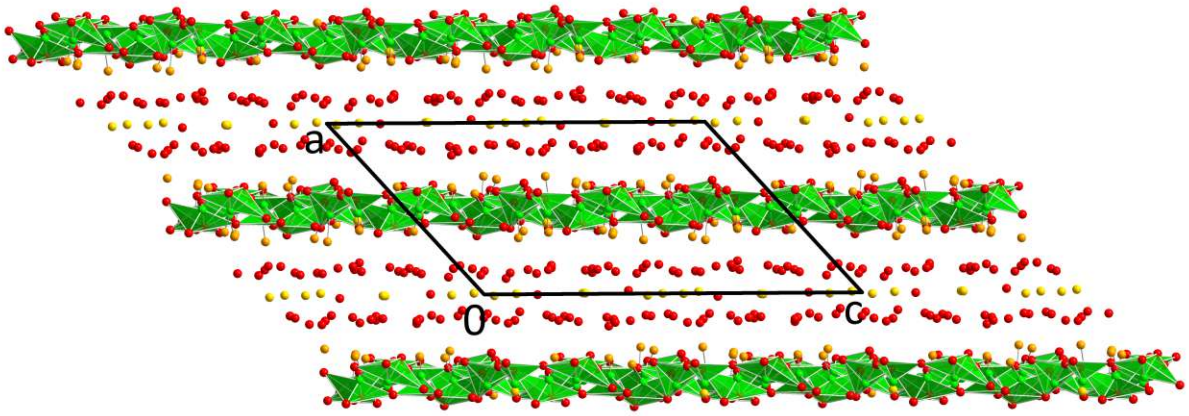

Figure 138. The crystal structure of $Na_2Te_4O_9(H_2O)_{10}$ viewed along $[0\bar{1}0]$ including Te^{IV} lone pairs ψ.

Hydrogen-bonding network

The oxygen atoms O1–O36 are part of the $^2_\infty[Te_8O_{18}]$ layers, while O37–O76 represent the water molecules. No hydrogen atoms could be located from difference-Fourier maps. Within the $^2_\infty[Te_8O_{18}]$ layer, the bridging oxygen atoms between two Te^{IV} atoms exhibit saturated bond valences, while the terminal oxygens show under-bonding with BVS in the range 1.4–1.5 v.u.. This under-saturation is compensated by the presence of one or two crystal water molecules with distances in the range of 2.7–2.9 Å for all of these sites. Most of the crystal water O atoms have four contacts, either Na or O sites, with distances < 3 Å, arranged in a distorted tetrahedral shape.

Based on the O—Na and O···O contacts, it was tried to fathom the hydrogen-bonding network in $Na_2Te_4O_9(H_2O)_{10}$ despite the absence of hydrogen atoms in the model. Each of the O37–O76 positions has two O-sided and two H-sided contacts. Under the conditions that all contacts to Na sites are O-sided and that all contacts to the O1–O36 atoms of the $^2_\infty[Te_8O_{18}]$ layers are H-sided, a model of the hydrogen-bonding network could be developed. The assignment of donor- and acceptor-O atoms

could not be conducted unambigously. However, after randomly assigning the O43 and O67 contacts of O37, the remaining network could be worked out unambigously. This model is presented in Table 54. The O71 site has no fourth contact in reasonable distance, and O49···O52 belongs to the four closest contacts of O49, but not of O52.

Table 54. One possible model for the hydrogen-bonding network in the crystal structure of $Na_2Te_4O_9(H_2O)_{10}$.

	O-sided				H-sided			
Site	contact	d / Å	contact	d / Å	contact	d / Å	contact	d / Å
O37	Na8	2.354(4)	O43	2.777(7)	O3	2.702(7)	O67	2.836(6)
O38	Na8	2.346(8)	O74	2.824(8)	O45	2.805(8)	O3	2.842(5)
O39	Na8	2.365(7)	O59	2.746(7)	O69	2.802(7)	O34	2.946(6)
O40	Na8	2.350(6)	O56	2.761(7)	O34	2.721(7)	O50	2.775(7)
O41	O42	2.742(7)	O46	2.761(10)	O43	2.828(5)	O7	2.906(8)
O42	Na8	2.389(5)	O47	2.840(7)	O41	2.742(7)	O33	2.856(7)
O43	O68	2.818(6)	O41	2.828(5)	O37	2.777(7)	O16	2.900(9)
O44	O75	2.642(8)	O46	2.688(8)	O16	2.714(6)	O73	2.816(8)
O45	Na1	2.430(4)	O38	2.805(8)	O17	2.672(8)	O46	2.798(7)
O46	O48	2.738(5)	O45	2.798(7)	O44	2.688(8)	O41	2.761(10)
O47	Na1	2.434(8)	O50	2.754(8)	O42	2.840(7)	O24	3.018(6)
O48	Na1	2.311(8)	Na1	2.451(5)	O25	2.728(8)	O46	2.738(5)
O49	Na7	2.398(6)	O52	3.001(6)	O29	3.027(8)	O21	3.171(11)
O50	Na1	2.366(5)	O40	2.775(7)	O47	2.754(8)	O18	2.836(8)
O51	Na7	2.363(4)	Na1	2.425(7)	O20	2.835(6)	O56	2.845(6)
O52	Na7	2.368(4)	O72	2.935(10)	O75	2.720(7)	O28	2.744(7)
O53	Na6	2.367(9)	Na7	2.424(5)	O30	2.852(6)	O11	3.063(7)
O54	O59	2.781(10)	O58	3.008(10)	O4	2.901(9)	O74	2.912(8)
O55	Na6	2.408(4)	Na7	2.450(8)	O72	2.846(7)	O10	3.014(6)
O56	Na6	2.352(4)	O51	2.845(6)	O9	2.757(8)	O40	2.761(7)
O57	Na6	2.390(4)	O75	2.707(5)	O31	2.700(6)	O62	2.815(7)
O58	Na6	2.544(4)	Na5	2.567(8)	O31	2.770(6)	O54	3.008(10)
O59	O63	2.751(7)	O61	2.768(12)	O39	2.746(7)	O54	2.781(10)
O60	Na5	2.394(4)	Na6	2.395(6)	O9	2.733(5)	O76	2.751(7)
O61	Na5	2.433(5)	Na3	2.456(4)	O35	2.760(6)	O59	2.768(12)
O62	Na5	2.485(6)	O57	2.815(7)	O32	2.826(5)	O65	2.862(10)
O63	Na3	2.408(9)	O67	2.837(9)	O59	2.751(7)	O23	3.080(7)
O64	Na5	2.430(4)	Na3	2.524(5)	O22	2.706(9)	O70	3.022(8)
O65	O76	2.739(6)	O62	2.862(10)	O66	2.846(6)	O32	2.888(8)
O66	Na5	2.463(8)	O65	2.846(6)	O68	2.800(7)	O27	3.038(9)
O67	Na3	2.403(5)	O37	2.836(6)	O63	2.837(9)	O36	2.855(8)
O68	Na3	2.374(8)	O66	2.800(7)	O26	2.761(6)	O43	2.818(6)
O69	Na3	2.383(4)	O39	2.802(7)	O6	2.767(7)	O70	2.847(8)
O70	O69	2.847(8)	O64	3.022(8)	O71	2.830(10)	O14	2.890(5)
O71	O70	2.830(10)			O1	3.146(9)	O15	3.163(6)
O72	O73	2.822(9)	O55	2.846(7)	O28	2.813(5)	O52	2.935(10)
O73	O44	2.816(8)	O76	2.835(6)	O13	2.683(8)	O72	2.822(9)
O74	Na1	2.404(4)	O54	2.912(8)	O38	2.824(8)	O12	2.835(6)
O75	Na4	2.344(5)	O52	2.720(7)	O44	2.642(8)	O57	2.707(5)
O76	Na2	2.393(6)	O60	2.751(7)	O65	2.739(6)	O73	2.835(6)

Table 55. Selected interatomic distances in the crystal structure of $Na_2Te_4O_9(H_2O)_{10}$.

	d / Å		*d* / Å
Te1—O3	1.843(3)	Te15—O21	1.900(3)
Te1—O2^{i}	1.890(3)	Te15—O20	1.910(3)
Te1—O1^{i}	2.096(3)	Te15—O10	1.915(3)
Te1—O4	2.145(3)	Te16—O27	1.895(3)
Te2—O9	1.847(3)	Te16—O26	1.905(3)
Te2—O8	1.878(3)	Te16—O15	1.913(3)
Te2—O10	2.089(3)	Na1—O50	2.365(4)
Te2—O18^{ii}	2.158(3)	Na1—O74^{vi}	2.404(4)
Te3—O13	1.850(3)	Na1—O51	2.425(4)
Te3—O14	1.891(3)	Na1—O45	2.430(4)
Te3—O7^{iii}	2.100(3)	Na1—O47^{vi}	2.435(4)
Te3—O33^{ii}	2.168(3)	Na1—O48^{vi}	2.450(4)
Te4—O16	1.844(3)	Na2—O8	2.378(3)
Te4—O1	1.889(3)	Na2—O76	2.393(4)
Te4—O15^{iv}	2.077(3)	Na2—O19^{ii}	2.395(3)
Te4—O36^{ii}	2.177(3)	Na2—O24^{ii}	2.425(4)
Te5—O17	1.847(3)	Na2—O14^{ii}	2.467(3)
Te5—O18	1.889(3)	Na2—O33	2.477(4)
Te5—O19	2.116(3)	Na2—O18^{ii}	2.583(3)
Te5—O20	2.156(3)	Na3—O68	2.375(4)
Te6—O22	1.836(3)	Na3—O69^{vi}	2.383(4)
Te6—O23	1.885(3)	Na3—O67^{i}	2.403(4)
Te6—O6	2.087(3)	Na3—O63^{vi}	2.408(4)
Te6—O30	2.167(3)	Na3—O61^{i}	2.455(4)
Te7—O25	1.832(3)	Na3—O64^{vi}	2.525(4)
Te7—O24	1.889(3)	Na4—O75	2.344(4)
Te7—O12	2.109(3)	Na4—O23	2.404(4)
Te7—O14	2.153(3)	Na4—O29	2.408(4)
Te8—O28	1.850(3)	Na4—O1^{ii}	2.416(3)
Te8—O29	1.895(3)	Na4—O2^{ii}	2.432(4)
Te8—O21	2.122(3)	Na4—O30	2.479(3)
Te8—O23	2.147(3)	Na4—O36	2.483(3)
Te9—O31	1.853(3)	Na5—O60	2.394(4)
Te9—O30	1.890(3)	Na5—O64^{vii}	2.429(4)
Te9—O11^{v}	2.111(3)	Na5—O61	2.433(4)
Te9—O2^{ii}	2.130(3)	Na5—O66	2.464(4)
Te10—O32	1.840(3)	Na5—O62^{vi}	2.486(4)
Te10—O19	1.894(3)	Na5—O58^{vi}	2.568(4)
Te10—O27	2.144(3)	Na6—O56	2.352(4)
Te10—O24	2.147(3)	Na6—O53^{vi}	2.366(4)
Te11—O34	1.847(3)	Na6—O57^{vi}	2.390(4)
Te11—O33	1.890(3)	Na6—O60	2.395(4)
Te11—O8	2.105(3)	Na6—O55	2.409(4)
Te11—O5	2.134(3)	Na6—O58^{vi}	2.545(4)
Te12—O35	1.848(3)	Na7—O48	2.311(4)
Te12—O36	1.892(3)	Na7—O51^{viii}	2.362(4)
Te12—O29	2.113(3)	Na7—O52	2.369(4)
Te12—O26	2.152(3)	Na7—O49^{viii}	2.398(6)
Te13—O5	1.884(3)	Na7—O53	2.424(5)
Te13—O7	1.902(3)	Na7—O55^{viii}	2.449(4)
Te13—O6	1.927(3)	Na8—O38^{viii}	2.347(4)
Te14—O4	1.893(3)	Na8—O40	2.349(4)
Te14—O11	1.894(3)	Na8—O37^{viii}	2.351(4)
Te14—O12	1.918(3)	Na8—O39	2.366(4)
		Na8—O42	2.389(4)

Symmetry codes: (i) *x*, *y*, −1+*z*; (ii) 1−*x*, 1−*y*, 1−*z*; (iii) *x*, −1+*y*, *z*; (iv) *x*, *y*, 1+*z*; (v) *x*, 1+*y*, *z*; (vi) 1+*x*, *y*, *z*; (vii) 1+*x*, *y*, 1+*z*; (viii) −1+*x*, *y*, *z*.

6.3 $RbTe^{VI}O_3(OH)$

Needle-shaped crystals of $RbTeO_3(OH)$ were obtained as the main product during the re-synthesis of $Rb_2Te^{IV}Te^{VI}O_4(OH)_4$ (Völkl et al., 2022) in experiments H368 and H369. The syntheses started from a 1:1:4 mixture of TeO_2, H_6TeO_6 and Rb_2CO_3 and were performed under normal hydrothermal conditions (H368) or with the addition of only three droplets of water (H369). The colorless thin bars of $RbTeO_3(OH)$ were easily distinguishable from the large hexagonal plates of the other product $Rb_2Te^{IV}Te^{VI}O_4(OH)_4$. $RbTeO_3(OH)$ exhibits a phase-transition, coupled with a doubling of the unit-cell volume (Table 56), when cooled down from room temperature (20 °C) to −173 °C.

6.3.1 Low-temperature phase

The asymmetric unit contains two Te, two Rb, eight O and two H sites, all located at general 2 *I* positions. Besides the H1 and H2 sites, the structure is (pseudo-)body-centered, which corresponds to the small, primitive triclinic cell of the high-temperature phase. The pseudo-*I*-centering connects the pairs of the Te1−Te2, Rb1−Rb2, O1−O8, O2−O7, O3−O6 and O4−O5 sites.

The Te^{VI} atoms are octahedrally coordinated by five oxygen atoms and a hydroxide group. Each $[TeO_5(OH)]$ group shares two edges with neighboring units, forming $^1_\infty[Te_2O_{8/2}O_{2/1}(OH)_{2/1}]$ zig-zag chains oriented parallel to [100]. These $^1_\infty[Te_2O_6(OH)_2]$ rods are connected to each other by hydrogen bonds between the terminally bound OH and O groups of the Te^{VI} atoms, and by the Rb^+ cations (Figure 139). The structural element of edge-sharing Te_2X_8 single chains has been observed already in the crystal structures of Na_2TeO_4 (Kratochvil & Jensovský, 1977), $CaTeO_4$ and $SrTeO_4$ (Hottentot & Loopstra, 1979), $Pb(W_{0.56}Te_{0.44})O_4$ (Andrade et al., 2014), $KTeO_3(OH)$ (Lindqvist, 1972) and $NH_4TeO_3(OH)$ (Benmiloud et al., 1980). The latter two phases share the same formula type with $RbTeO_3(OH)$. The unit-cell of $KTeO_3(OH)$ has metrics similar to the low-temperature modification of $RbTeO_3(OH)$, but monoclinic symmetry ($P2_1/a$, a = 6.4981(5) Å, b = 11.6960(10) Å, c = 5.1210(3) Å, β = 93.861(6)°). The crystal structure of $NH_4TeO_3(OH)$ is triclinic with a similar unit-cell volume as the high-temperature modification of $RbTeO_3(OH)$, but with a different setting of unit-cell vectors (a = 5.149(2) Å, b = 7.095(3) Å, c = 7.349(3) Å, α = 123.27(2)°, β = 111.79(2)°, γ = 70.85(2)°).

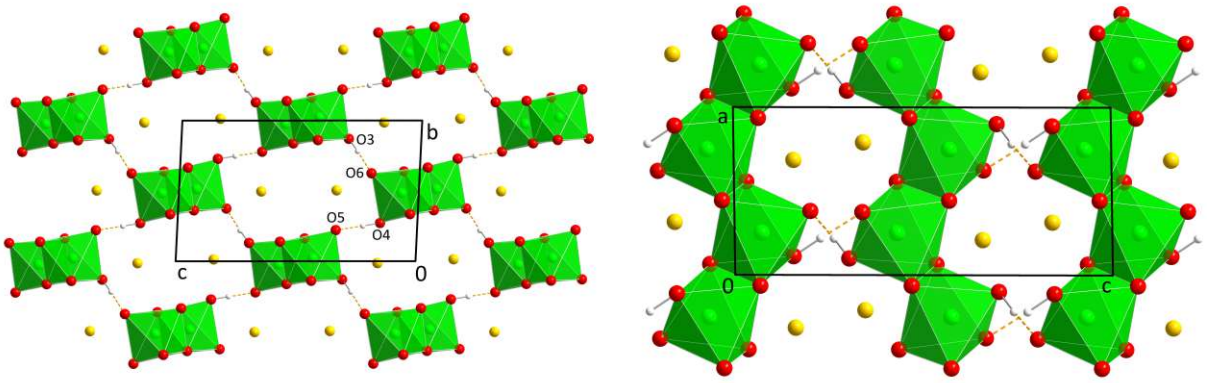

Figure 139. The crystal structure of the low-temperature modification of $RbTeO_3(OH)$ viewed along [$\bar{1}$00] (left) and [0$\bar{1}$0] (right).

Hydrogen-bonding

Based on the BVS of the O atoms, O3 and O4 were identified as OH groups, while O5 and O6, which are located at distances of 2.543(5) Å and 2.511(5) Å from O4 and O3, respectively, are the acceptors of the strong hydrogen bonds (Table 56). The hydrogen atoms could be located from difference-electron density maps, and no constraints on their coordinates or the O—H distance were necessary.

6.3.2 Phase transition and high-temperature phase

The measurement at 20 °C exhibited less reflections than at −173 °C (Figure 141), indicating a smaller unit-cell. The new, likewise triclinic cell is related to that of the low-temperature modification cell by

$$\begin{pmatrix} \bar{1} & 0 & 0 \\ 0 & \bar{1} & 0 \\ 1/2 & 1/2 & 1/2 \end{pmatrix}$$

Atom labels were assigned in correspondence with the low-temperature phase.

The reduced translational symmetry of the high-temperature phase is caused by the loss of the ordering of the hydrogen atoms. While at −173 °C, the H atoms could be located at one of the oxygen atoms of the O3···O6 and O4···O5 pairs, in the smaller unit-cell at 20 °C, these pairs are formed by two atoms corresponding to the same crystallographic site. The BVS of the resulting site amounts to the average value of the two sites in the low-temperature phase. In total, the asymmetric unit only contains one Te, one Rb and four O positions. The hydrogen atoms, which would correspond to two half-occupied H positions, could not be localized and are assumed to be disordered between the two oxygen atoms (Figure 140).

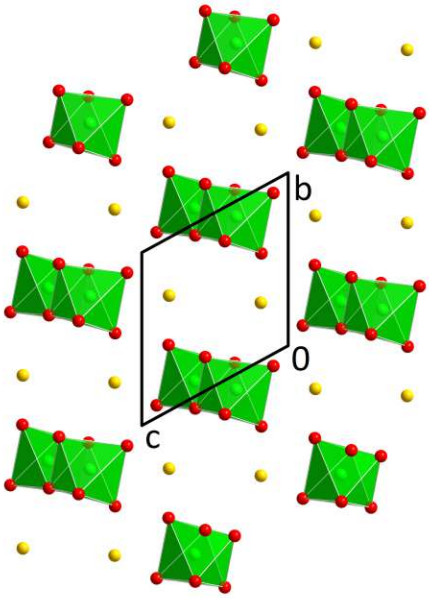

Figure 140. The crystal structure of the room temperature modification of $RbTeO_3OH$ viewed along $[\bar{1}00]$.

Table 56. Comparison of the two modifications of $RbTeO_3(OH)$.

	−173 °C	20 °C
a / Å	5.1302(16)	5.150(2)
b / Å	6.786(2)	6.826(3)
c / Å	11.564(4)	6.979(3)
α /°	92.763(9)	115.866(14)
β /°	90.818(9)	109.812(14)
γ /°	92.444(9)	92.375(14)
V / Å³	401.7(2)	202.43(16)
BVS Te1 / v.u.	5.84	5.90
BVS Te2 / v.u.	5.85	
BVS Rb1 / v.u.	1.11	1.11
BVS Rb2 / v.u.	1.16	
BVS O1 / v.u.*	2.10/1.95	-/1.94
BVS O8 / v.u.*	2.09/1.97	
BVS O2 / v.u.*	2.12/1.95	-/1.94
BVS O7 / v.u.*	2.10/1.95	
BVS O3 / v.u.*	2.16/1.42	-/1.51
BVS O6 / v.u.*	2.11/1.64	
BVS O4 / v.u.*	2.02/1.32	-/1.45
BVS O5 / v.u.*	1.99/1.57	

* Values given with and without hydrogen contacts

Phases with similar composition:

$CsTeO_3(OH)$, another novel phase, is isotypic with $RbTeO_3(OH)$ and exhibits the same kind of order-disorder phase transition (Völkl et al., 2022). The literature phases $KTeO_3(OH)$ (Lindqvist, 1972) and $NH_4TeO_3(OH)$ (Benmiloud et al., 1980) have the same structural set-up. In neither of these crystal structures the hydrogen atoms were localized, which is not surprising, given that they were both investigated at room temperature. Cooling $KTeO_3(OH)$ and $NH_4TeO_3(OH)$ down to −173 °C might indeed reveal ordering of their hydrogen bonds as well.

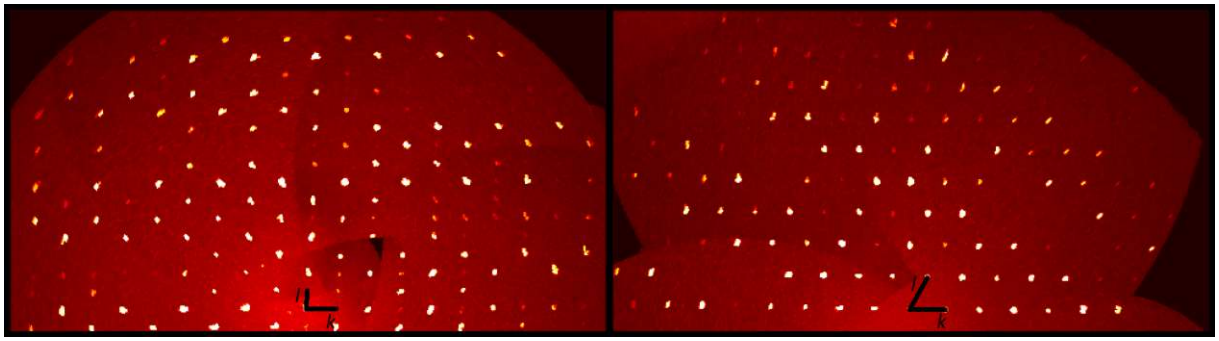

Figure 141. Reconstructed reciprocal 2*kl* plane of $RbTeO_3(OH)$ at −173 °C (left) and room temperature (right).

Table 57. Selected interatomic distances in the crystal structures of $RbTeO_3(OH)$.

100 K		293 K	
	d / Å		*d* / Å
Te1—O5	1.843(3)	Te1—O3	1.867(2)
Te1—O3^{i}	1.897(3)	Te1—O4^{i}	1.868(2)
Te1—O1^{ii}	1.947(3)	Te1—O1^{ii}	1.953(2)
Te1—O7^{iii}	1.953(3)	Te1—O2^{iii}	1.9567(19)
Te1—O7	1.991(3)	Te1—O2	1.986(2)
Te1—O1^{i}	2.002(3)	Te1—O1^{iv}	1.997(2)
Te2—O6	1.833(3)		
Te2—O4	1.906(3)		
Te2—O8	1.952(3)		
Te2—O2^{ii}	1.963(3)		
Te2—O2^{iv}	1.977(3)		
Te2—O8^{v}	1.993(3)		
Rb1—O5^{vi}	2.804(3)	Rb1—O3^{v}	2.849(2)
Rb1—O6^{vi}	2.823(4)	Rb1—O4	2.852(2)
Rb1—O7	2.898(3)	Rb1—O2	2.918(2)
Rb1—O1	2.901(3)	Rb1—O1	2.922(2)
Rb1—O3^{ii}	2.950(3)	Rb1—O3^{vi}	2.955(2)
Rb1—O4^{ii}	3.149(3)	Rb1—O4^{vii}	3.120(3)
Rb1—O1^{ii}	3.332(3)	Rb1—O1^{ii}	3.301(2)
Rb2—O3^{ii}	2.841(4)		
Rb2—O4^{vii}	2.860(3)		
Rb2—O2	2.905(3)		
Rb2—O6^{vi}	2.916(3)		
Rb2—O8^{iii}	2.926(3)		
Rb2—O5^{iii}	3.069(3)		
Rb2—O8^{viii}	3.221(3)		
Rb2—O7	3.376(4)		
O3—H1	0.98(6)		
O3—H1···O6	2.511(5)	O3···O3^{viii}	2.487(4)
O4—H2	1.00(6)		
O4—H2···O5	2.543(5)	O4···O4^{ix}	2.535(4)
Symmetry codes: (i) *x*, −1+*y*, *z*; (ii) −*x*, 1−*y*, 1−*z*; (iii) 1−*x*, −*y*, 1−*z*; (iv) *x*, *y*, −1+*z*; (v) 1−*x*, 1−*y*, −*z*; (vi) 1−*x*, 1−*y*, 1−*z*; (vii) −*x*, −*y*, 1−*z*; (viii) *x*, *y*, 1+*z*.		Symmetry codes: (i) 1−*x*, 1−*y*, 1−*z*; (ii) −*x*, 1−*y*, 1−*z*; (iii) 1−*x*, −*y*, 1−*z*; (iv) *x*, −1+*y*, *z*; (v) *x*, *y*, −1+*z*; (vi) −*x*, −*y*, 1−*z*; (vii) −*x*, 1−*y*, −*z*; (viii) 1−*x*, −*y*, 2−*z*; (ix) 1−*x*, 1−*y*, *z*.	

6.4 $KCoPtO_4$

This phase is the result of an accidental side-reaction with the crucible material during the search for novel K–Co–oxidotellurate(VI)-phases. $CoCO_3$, TeO_2, H_6TeO_6 (molar ratios 2:1:1) and an excess of KNO_3 were heated at a temperature of 900 °C for 12 hours in a platinum crucible in air. After washing with water, the resulting product was a black solid and the obtained dark crystals were opaque. When cut into very small pieces, the edges of the crystals had a dark orange/brown color.

The diffraction patterns of the investigated crystals exhibit intense reflections of a hexagonal unit-cell with $a \approx 3$ Å, $c \approx 6.85$ Å and weaker superstructure reflections at $l = n \pm 1/2$, indicating a doubling of **c** (Figure 145). The lattice parameters of the final model are $a = 2.9870(3)$ Å and $c = 13.7044(14)$ Å.

The crystal structure consists of MoS_2-type (Dickinson & Pauling, 1923; Bell & Hefert, 1957) MO_2 layers with K^+ cations situated between the layers (Figures 142, 144). Such structural features and similar unit-cell parameters and symmetries have been reported for $K_xCo_2O_4$ (Jansen & Hoppe, 1974a; Pollet et al., 2009) and for $Na_xCo_2O_4$ phases (Jansen & Hoppe, 1974b, Balsys & Davis, 1997; Ono et al., 2003). Compared to the literature phases (a = 2.845 Å, c = 12.35 Å for KCo_2O_4 and a = 2.843 Å, c = 10.811 Å for $NaCo_2O_4$; Jansen & Hoppe, 1974a, b), the larger size of the $KCoPtO_4$ unit-cell indicated the inclusion of different atoms into the layers. This is underlined by the longer M—O-distances of 1.979(6) Å compared to $K_xCo_2O_4$ (1.914 Å).

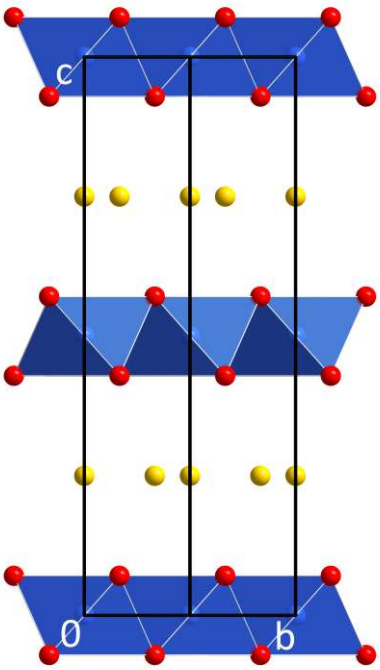

Figure 142. The crystal structure of $KCoPtO_4$ viewed along $[\bar{1}00]$. The mixed Co/Pt position is drawn blue.

While it was initially assumed that Te^{VI}, in accordance with the usual octahedral coordination, was part of the crystal structure, SEM-EDS measurements (Table 58) revealed the presence of crucible-material Pt instead. The measured data points show a rather great variance, which can be attributed to two factors. First, the EDS-measurement itself was not performed under ideal conditions, as plane surfaces of the sample were not found easily. Second, given the synthesis conditions of diffusion of crucible material into the reaction, various crystals could exhibit a wide compositional variability. The main conclusion drawn from this data is that K, Co and Pt are present at similar amounts with an oxygen content about four times larger than that of an individual metal species.

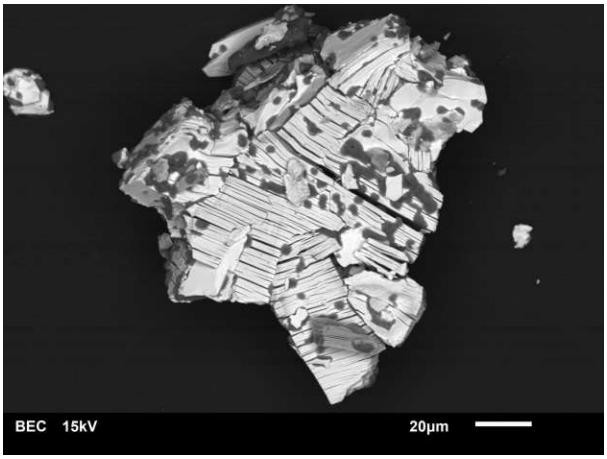

Figure 143. SEM-BE picture of a $KCoPtO_4$ crystal.

The $KCo^{III}Pt^{IV}O_4$ crystals, as revealed by SEM measurements, point to a layered structure, consisting of a multitude of single layers separated by small cracks (Figure 143). Such a conglomerate of different layers, in combination with the opacity of the crystals, was the reason, why isolation of single-crystalline material was a laborious task. The small globular impurities on top of the crystals (Figure 143) presumably consist of K_2CO_3 (only K and O detected), which apparently had not been washed away completely during the leaching process.

Table 58. SEM-EDS data of various $KCoPtO_4$ crystals.

Data point	K /%	Co /%	Pt /%	O /%
1	15.1	15.7	19.8	49
2	16.5	8.7	14	61
3	15.1	13.7	17.8	53
4	19.3	14.7	16.4	58
5	15.6	11.1	13	60
6	9.6	12.1	10.9	67
Average	15(3)	13(3)	15(3)	58(6)

Given the stoichiometric ratios determined by EDS, an overall composition of $KCo^{III}Pt^{IV}O_4$ seems reasonable. Co^{III} and Pt^{IV} fit together very well from a structural point of view, as their respective ionic radii (0.61 Å for high-spin Co^{III} and 0.625 Å for Pt^{IV}; Shannon, 1976) are very similar. The sum of the respective ionic radii and the ionic radius of three-coordinate oxygen (1.36 Å) is in very good agreement (1.97 and 1.985 Å) with the determined *M*—O bond length of 1.979(6) Å (Table 59).

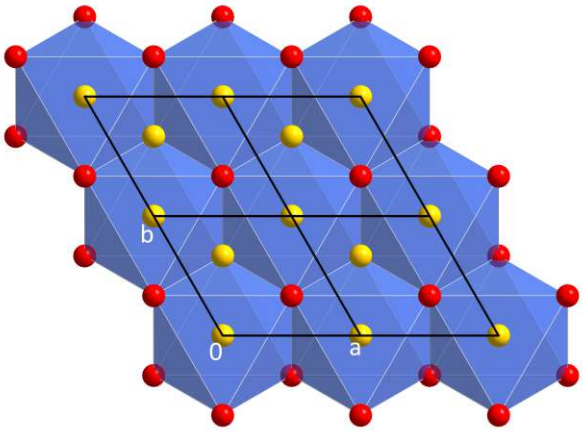

Figure 144. The crystal structure of $KCoPtO_4$ viewed along $[00\bar{1}]$.

In the refinement of $KCo^{III}Pt^{IV}O_4$, the Co^{III} and Pt^{IV} atoms were modelled with mixed occupancies at the common *M*1 site with site symmetry $\bar{3}m$. (2 *a*). The s.o.f.s of Co1 and Pt1 refined to a ratio of 0.51:0.49(4) and were subsequently fixed to 1/2 for both atoms. The potassium cations exhibit positional disorder and are split on the K1 and K2 positions (both with site symmetry $\bar{6}2m$; Wyckoff positions 2 *b* and 2 *d*, respectively), which have an identical coordination by six oxygen atoms in a trigonal-prismatic environment. The s.o.f.s of the two K sites were constrained so that they correspond to one K atom p.f.u. (refined values of 0.27(3) and 0.23(3)). Again, as an equal occupancy for both K sites was within standard uncertainty, the s.o.f.s for both sites were constrained to 1/4. The atoms on the two K sites exhibit significantly larger displacement parameters than the other atoms. When K1 and K2 are refined with ADPs, this results in elongated ellipsoids, which are much larger for U^{11} and U^{22} (parallel to the hexagonal plane) than for U^{33} (parallel to **c**).

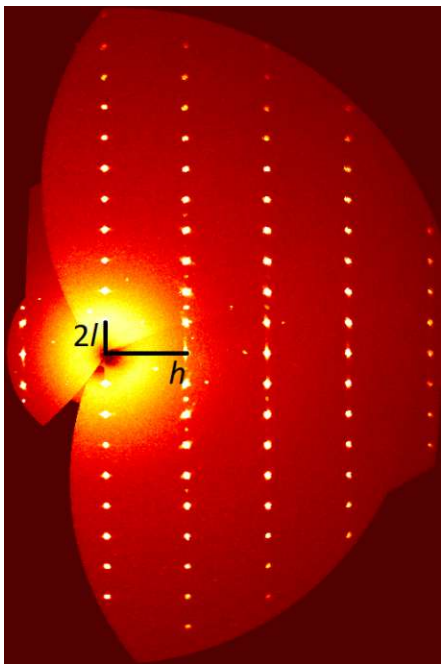

Figure 145. Reconstructed reciprocal *h*0*l* plane of $KCoPtO_4$.

The distribution of the disordered K^+ cations is most probably more complicated than the model with the two highly symmetric point symmetries for the two K^+ cations makes it appear. Depending on the location of other K^+ cations in their vicinity, they will probably show some displacement from the high-symmetric K1 and K2 positions, as indicated by their large ADPs. For some layered oxides, cation ordering has been observed by the presence of superstructure reflections indicating a symmetry reduction and a larger unit-cell (especially along **a** and **b**). As an example, for the phase $K_4Co_7O_{14}$ ($K_{0.57}CoO_2$) a hexagonal unit-cell with a = 7.517(1) Å, c = 12.37(1) Å was reported (Blangero et al., 2005). However, in

the case of $KPtCoO_4$, only reflections corresponding to the given unit-cell were observed (Figure 145). Furthermore, along **c***, signs of diffuse scattering can be observed, indicating some stacking disorder. It was attempted to resolve the Pt/Co and/or K disorder in models of lower-symmetric space groups and additional twinning. However, this approach was not successful, and the high-symmetric $P6_3/mmc$ model with disordered sites remained to be the most reasonable.

Table 59. Selected interatomic distances in the crystal structure of $KCoPtO_4$.

	d / Å
*M*1—O1 (6×)	1.979(6)
K1—O1 (6×)	3.000(10)
K2—O1 (6×)	3.000(10)

6.5 $(NH_4)Ni_3(HAsO_4)(AsO_4)(OH)_2$

Single crystals of $(NH_4)Ni_3(HAsO_4)(AsO_4)(OH)_2$ have the form of small light green blocks and were the main product of hydrothermal experiment H36 (NiO, TeO_2, As_2O_3, NH_3 in molar ratios of 2:1:1:7). The crystal used for the diffraction measurement was twinned into three domains by a 120° rotation along the **c*** axis. As one domain resulted in significantly higher intensities than the other two, integration was attempted both as a threefold twin and by considering only the predominant domain. The intensity data based of a single-domain integration resulted in significantly lower reliability factors (0.050 vs. 0.068) and was therefore chosen for the final model. This is surprising, given that the minor domains contributed significantly to the diffraction pattern and the ratios of the twin domains were refined to 0.653(4):0.264(4):0.093(2) based on *hkl*5-type intensity data of the three-domain integration.

Crystal structure

The asymmetric unit of the monoclinic unit-cell (*C*2/*m*; *a* = 10.1908(16) Å, *b* = 5.9113(8) Å, *c* = 7.7148(11) Å, *β* = 112.702(11)°, *V* = 428.74(11) Å^3) contains ten atoms: one As, two Ni, four O, one N and two H. The H atoms belonging to the ammonium group could not be localized. Most atoms are located at a 4 *i* position with site symmetry *m*, Ni1 (2 *a*) and N1 (2 *c*) exhibit site symmetry 2/*m*, Ni2 (4 *e*) site symmetry $\bar{1}$, and O3 is located at a general 8 *j* position.

The As^V atom is coordinated tetrahedrally (τ_4 = 0.962) by four oxygen contacts. The average As—O bond length is 1.696(6) Å for the resulting $[AsO_4(H)]$ unit, which is comparable to the mean As—O bond length of 1.687(26) Å determined by Gagné & Hawthorne (2018). The BVS of the As^V atoms is 4.79 v.u..

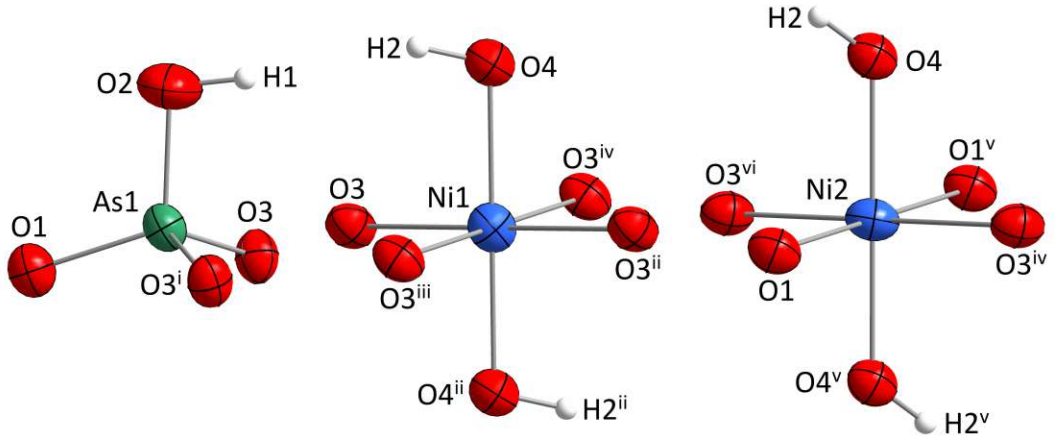

Figure 146. Atomic environments of the Ni^{II} and As^V atoms in the crystal structure of $(NH_4)Ni_3(HAsO_4)(AsO_4)(OH)_2$.

The Ni^{II} atoms are connected to six oxygen atoms, two of them being hydroxide groups. The $[NiO_4(OH)_2]$ units have a distorted octahedral shape with the hydroxide groups being in *trans*-position (Figure 146). The OH-contacts have the shortest Ni—O bond lengths in both coordination polyhedra. The BVS of the Ni^{II} atoms were calculated as 2.05 (Ni1) and 2.00 (Ni2) v.u.. The $[NiO_4(OH)_2]$ groups are connected to each other by sharing edges with four neighbors, forming $^2_\infty[Ni_3(OH)_{6/3}O_{12/2}]$ layers extending parallel to (001) (Figure 147). These layers contain voids, which, in principle, could accommodate a fourth Ni atom p.f.u. to form a pseudo-hexagonal grid. The three oxygen atoms around the void are shared with two $[AsO_4(H)]$ units above and below the layer, resulting in corrugated $^2_\infty[Ni_3As_2(OH)_{6/3}O_{18/3}O_{1/1}(OH)_{1/1}]$ layers oriented parallel to (001). The arsenate groups form a hydrogen bond between their terminal O/OH (O2) sites towards the adjacent layer. The hydroxide groups located

at the O4 position form hydrogen bonds to the O2 position as well. The remaining interspace is occupied by the $(NH_4)^+$ cation (Figure 147).

For the ammonium group associated with the N1 site, no hydrogen atoms could be located. The closest oxygen atoms for hydrogen-bonding are located at a distance of 2.928(3) Å (4×), which would correspond to hydrogen bonds of medium strength. The site symmetry (2/*m*) of the N1 atom makes it most likely that the tetrahedral $(NH_4)^+$ cation is disordered, which complicates the localization of the hydrogen atoms.

Symmetry reduction caused by hydrogen-bonding

As it was already indicated by the nature of the $[AsO_4(H)]$ coordination polyhedron, the O2 site is occupied by half an O atom and half an OH group; the adjacent H1 site exhibits an s.o.f. of 1/2. Two O2 sites have a distance of 2.584(8) Å from each other. The disorder of the H1 site can be resolved by a symmetry reduction to *Cm*. In this lower-symmetric space group, the As1 and O2 sites are split into two positions and the H1 site, in theory, is positioned next to only one of the two "O2-type" positions. In various refinement attempts in *Cm*, no clear indication on the placement of the H1 atom was given.

Furthermore, the only atom breaking the *C*2/*m* symmetry is a hydrogen atom, which in fact does not contribute remarkably to the scattered intensities. Overall, the models in *Cm* were of inferior quality. The s.u.s of all interatomic distances were about three times higher compared to the models in *C*2/*m*, the oxygen atoms exhibited negative ADPs and had to be refined isotropically, the ADPs of the (in *C*2/*m* symmetry-equivalent) As^V atoms had to be constrained with an EADP command, and the overall reliability factors were higher as well. Therefore, and in accordance with the model of the isotypic literature phase $KCu_3(HAsO_4)(AsO_4)(OH)_2$ (Effenberger, 1988), *C*2/*m* was chosen as the space group of the final model, assuming that O and OH are equally distributed over the O2 site.

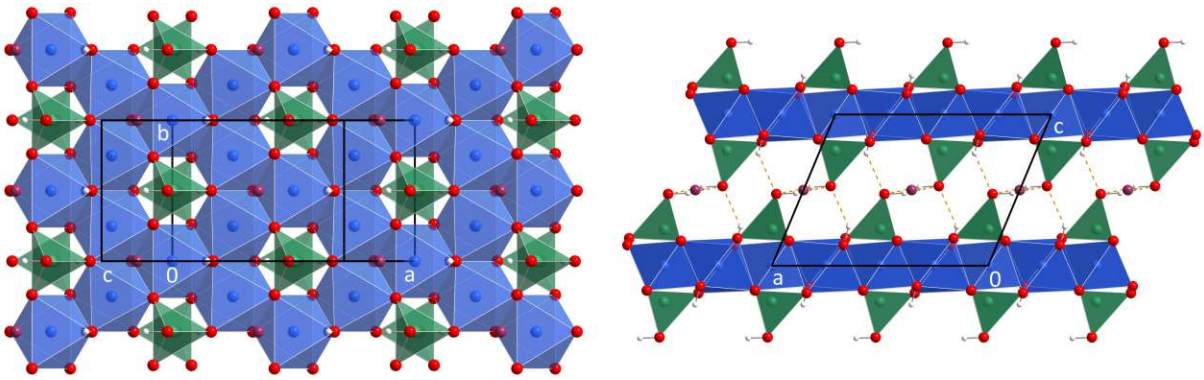

Figure 147. The crystal structure of $(NH_4)Ni_3(HAsO_4)(AsO_4)(OH)_2$ projected on (001) (left) and viewed along $[0\bar{1}0]$ (right).

The crystal structure of $(NH_4)Ni_3(HAsO_4)(AsO_4)(OH)_2$ was quantitatively compared with isotypic $KCu_3(HAsO_4)(AsO_4)(OH)_2$ (Effenberger, 1988) with *compstru*. The degree of lattice distortion *S* is 0.0246, the arithmetic mean of the distances between paired atoms $d_{av.}$ is 0.0927 Å and the measure of similarity Δ is 0.031. For the higher-symmetric *M*1, *M*2 and N/K sites, the distance between paired atoms is 0. For the other sites, values of 0.2973 Å (O1; the highest value), 0.1427 Å (O2), 0.0334 Å (O3), 0.1156 Å (O4) and 0.1189 Å (As1) were obtained. The main differences between the two structures originate in the higher distortion of the $[CuO_6]$-polyhedra in $KCu_3(HAsO_4)(AsO_4)(OH)_2$ compared to the $[NiO_6]$ units, which can be attributed to the strong influence of JT-effects for Cu^{II}. Especially the Cu2 site exhibits a massive axial distortion, resulting in increased Cu2—O1 distances of 2.428(3) Å compared to 1.934(2)–2.000(2) Å for the other contacts (Table 60). These differences can also be

noticed in the distance distortion ζ of the *M* atoms, which is 0.368 (Ni1) and 0.439 Å (Ni2) in $(NH_4)Ni_3(HAsO_4)(AsO_4)(OH)_2$ but is 0.765 (Cu1) and 1.229 Å (Cu2) in $KCu_3(HAsO_4)(AsO_4)(OH)_2$ (Effenberger, 1988). The strong distortion of the [Cu2O$_6$] polyhedron is even reflected in the title of its publication "An uncommon $Cu^{[2+4]}O_6$ coordination polyhedron in the crystal structure of $KCu_3(OH)_2[(AsO_4)]H(AsO_4)]$ (with a comparison to related structure types)".

Table 60. Comparison of structure data and interatomic distances in the crystal structures of $(NH_4)Ni_3(HAsO_4)(AsO_4)(OH)_2$ with isotypic $KCu_3(HAsO_4)(AsO_4)(OH)_2$ (Effenberger, 1988).

	$(NH_4)Ni_3(HAsO_4)(AsO_4)(OH)_2$	$KCu_3(HAsO_4)(AsO_4)(OH)_2$
a / Å	10.1908(16)	10.292(5)
b / Å	5.9113(8)	5.983(3)
c / Å	7.7148(11)	7.877(4)
β /°	112.702(11)	117.86(2)
V / Å^3	428.74(11)	428.82
Selected interatomic distances / Å		
As1—O2	1.691(4)	1.704(3)
As1—O1	1.699(4)	1.661(4)
As1—O3	1.705(2)	1.704(2)
As1—O3^{i}	1.705(2)	1.704(2)
*M*1—O4^{ii}	1.966(3)	1.899(2)
*M*1—O4	1.966(3)	1.899(2)
*M*1 —O3^{ii}	2.104(3)	2.186(2)
*M*1—O3^{iii}	2.104(3)	2.186(2)
*M*1—O3^{iv}	2.104(3)	2.186(2)
*M*1—O3	2.104(3)	2.186(2)
*M*2—O4	1.961(2)	1.934(2)
*M*2—O4^{v}	1.961(2)	1.934(2)
*M*2—O3^{vi}	2.091(3)	2.000(2)
*M*2—O3^{iv}	2.091(3)	2.000(2)
*M*2—O1	2.160(3)	2.428(3)
*M*2—O1^{v}	2.160(3)	2.428(3)
O2—H1	0.9(2)	
O2—H1···O2^{vii}	2.584(8)	2.491(5)
O4—H2	0.89(2)	
O4—H2···O2^{viii}	2.826(5)	2.692(3)
* Value constrained to 0.89 Å with DFIX command.		
Symmetry codes: (i) *x*, 1−*y*, *z*; (ii) −*x*, −*y*, −*z*; (iii) *x*, −*y*, *z*; (iv) −*x*, *y*, −*z*; (v) 1/2−*x*, 1/2−*y*, −*z*; (vi) 1/2+*x*, 1/2−*y*, *z*; (vii) −*x*, *y*, 1−*z*; (viii) 1/2−*x*, −1/2+*y*, 1−*z*.		

6.6 $Cd_2(PO_4)(OH)$ and $Cd_5(PO_4)_2(OH)_4$

Synthesis

$Cd_2(PO_4)(OH)$ was initially obtained from a hydrothermal reaction between $CdCO_3$, TeO_2 and H_3PO_4 in molar ratios of 1:1:1 (H83). Later, it was tried to resynthesize $Cd_2(PO_4)(OH)$ in order to obtain larger crystals and gather better diffraction data. Re-synthesis experiments were performed with and without TeO_2 (H163−H169). Surprisingly, only in reactions containing TeO_2 (H163, H168 and H169) the $Cd_2(PO_4)(OH)$ phase occured again. From the TeO_2-containing experiments, the three successful ones employed Cd^{II} and PO_4^{3-} in a 1:1 ratio, while the experiment using the reactants in the stoichiometric ratio corresponding to the molecular formula (Cd^{II}:PO_4^{3-} = 2:1, H166) resulted in a mixture of the educt $CdCO_3$ and $H_2Cd_5(PO_4)_4(H_2O)_4$ (Hideki et al., 1976). In a different re-synthesis attempt, starting from $Cd(NO_3)_2$, H_3PO_4 and KOH (molar ratios 2:1:12; H130), a different basic cadmium phosphate with a composition of $Cd_5(PO_4)_2(OH)_4$ was obtained. The unit-cell data of the two phases are collated in Table 61.

Table 61. Unit-cell data the two new basic cadmium phosphate phases.

	$Cd_2(PO_4)(OH)$	$Cd_5(PO_4)_2(OH)_4$
Space group, no.	*C*2/*c*, 15	$P2_12_12_1$, 19
a / Å	13.7519(13)	5.8901(4)
b / Å	6.6910(6)	9.3455(6)
c / Å	10.7087(10)	18.7423(13)
β /°	120.451(3)	
V / Å³	849.43(14)	1031.69(12)
Z	8	4

6.6.1 $Cd_2(PO_4)(OH)$

The asymmetric unit contains two Cd, one P and five O atoms, each located at general 8 *f* positions. Additionally, the O1 and O2 atoms are disordered over two sites, the s.o.f.s of the two possibilities were refined to 0.646:0.354(16). The two Cd^{II} positions are coordinated by six oxygen atoms forming distorted octahedra. The [CdO_6] units are connected to each other by edge-sharing to form a tri-periodic framework. The remaining interspace is occupied by the PO_4^{3-} anions (Figure 148). One of the four corners of the $[PO_4]^{3-}$ tetrahedra belongs to the disordered O2 position. The hydrogen atom of the hydroxide group could not be localized in the refinement procedure but is assumed to correspond with the OF position due to its significantly lower BVS of 1.67 v.u..

$Cd_2(PO_4)(OH)$ crystallizes isotypically with the mineral triplite $(Fe,Mn)_2(PO_4)F$ (Waldrop, 1968a) and is even closer related to Cd_2PO_4F (Rea & Kostiner, 1974). The O atom of the $Cd_2(PO_4)(OH)$ hydroxide anion is located at the same site as the fluoride anion in the reference phases and was therefore named in a similar way (OF; Table 62). $Cd_2(PO_4)(OH)$ is the first hydroxidic $M_2PO_4(OH)$ phase crystallizing in the triplite structure type, as usually the triploidite structure type is preferred by such phases like $Mn_2(PO_4)(OH)$ (Waldrop, 1968b) or $Fe_2(PO_4)(OH)$ (Hatert, 2007).

No disorder of any oxygen sites was observed for the triplite structures with the fluoride ion instead of the hydroxide anion. It is possible that the hydrogen bonds formed by the hydroxide group are correlated with the disorder of the O1 and O2 positions, as some of the split oxygen positions are positioned like potential acceptors of hydrogen bonds.

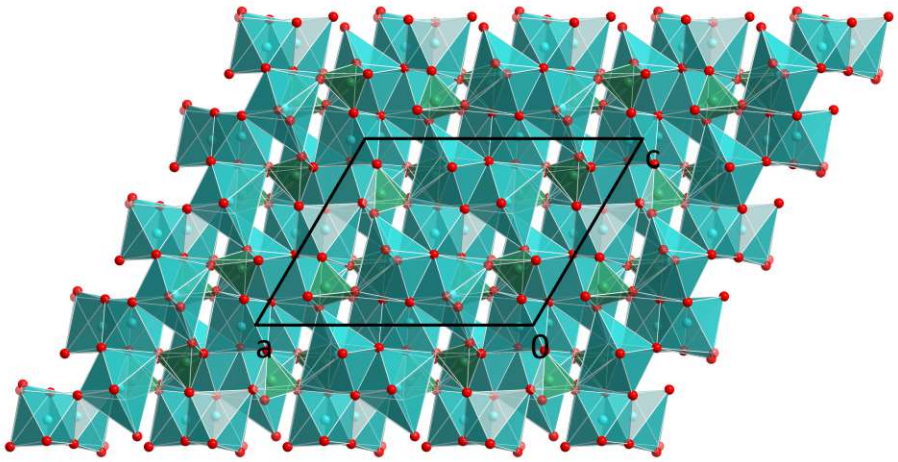

Figure 148. The crystal structure of $Cd_2(PO_4)(OH)$ viewed along $[0\bar{1}0]$. Cd^{II} atoms are drawn turquoise, P atoms are drawn green.

Table 62. Selected interatomic distances in the crystal structure of $Cd_2(PO_4)(OH)$.

	d / Å		*d* / Å
Cd1—O1B	2.05(2)	Cd2—O3	2.275(6)
Cd1—OF	2.101(6)	Cd2—O2B^{vi}	2.32(3)
Cd1—OF^{i}	2.173(7)	Cd2—O4^{vii}	2.350(6)
Cd1—O1A	2.242(12)	Cd2—OF^{viii}	2.484(7)
Cd1—O3^{ii}	2.251(6)	P1—O2B	1.41(3)
Cd1—O2A	2.350(13)	P1—O4	1.519(7)
Cd1—O1A^{iii}	2.556(14)	P1—O1A^{ii}	1.529(11)
Cd1—O2B	2.61(3)	P1—O2A	1.537(14)
Cd2—O4^{iv}	2.224(7)	P1—O3	1.543(6)
Cd2—OF^{v}	2.257(6)	P1—O1B^{ii}	1.59(2)
Cd2—O2A^{vi}	2.270(14)		

Symmetry codes: (i) −*x*, *y*, 1/2−*z*; (ii) 1/2−*x*, −1/2+*y*, 1/2−*z*; (iii) 1/2−*x*, 1/2−*y*, 1−*z*; (iv) 1−*x*, *y*, 1/2−*z*; (v) 1/2+*x*, 1/2−*y*, −1/2+*z*; (vi) 1/2−*x*, 1/2−*y*, −*z*; (vii) *x*, −*y*, −1/2+*z*; (viii) 1/2−*x*, 1/2+*y*, 1/2−*z*.

6.6.2 $Cd_5(PO_4)_2(OH)_4$

The asymmetric unit of $Cd_5(PO_4)_2(OH)_4$ comprises five Cd, two P, twelve O and four H atoms, all located at general 4 *a* positions. All five Cd^{II} atoms are coordinated by six oxygen atoms in form of distorted octahedra. The Cd—O bond lengths are in a range of 2.18−2.60 Å (Table 63), with average values of 2.340 Å (Cd1), 2.283 Å (Cd2), 2.222 Å (Cd3), 2.331 Å (Cd4) and 2.336 Å (Cd5). These values are in accordance with the ionic radii (Shannon, 1976) of Cd^{II} (CN6: 0.95 Å) and O (CN3: 1.36 Å) which would result in an average bond length of 2.31 Å. The BVS of the Cd^{II} atoms are 1.91 (Cd1), 2.16 (Cd2), 1.98 (Cd3), 2.00 (Cd4) and 1.90 (Cd5) v.u.. The [CdO_6] octahedra include one to four hydroxide groups (represented by O7, O8, O9, O11) in their

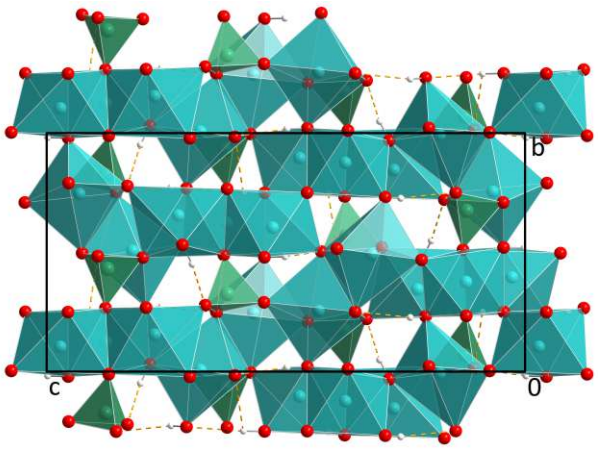

Figure 149. The crystal structure of $Cd_5(PO_4)_2(OH)_4$ in a view along $[\bar{1}00]$. Color codes refer to Figure 148. Hydrogen bonds are drawn as orange dashed lines.

coordination spheres, and share corners and edges with each other, leading to the formation of a tri-periodic Cd−O-framework (Figure 149).

The two P sites are coordinated by four oxygen atoms at distances of 1.522(6)−1.563(6) Å. The τ_4 values of 0.955 (P1) and 0.970 (P2) confirm a rather regular shape of the $[PO_4]^{3-}$ anions. Of the twelve O sites, eight are part of the phosphate anions and the other four, which belong only to the Cd−O-framework, correspond to the hydroxide groups. The hydrogen atoms were located from difference-Fourier maps, and the O—H distances were constrained in the refinement. The hydroxide groups are all connected to three Cd^{II} atoms and form weak hydrogen bonds with O···O distances of 2.900(8)−3.070(8) Å to other oxygen atoms.

$Cd_5(PO_4)_2(OH)_4$ crystallizes isotypically with the mineral arsenoclasite $Mn_5(AsO_4)_2(OH)_4$ (Moore & Molin-Case, 1971) and the phosphate/arsenate compounds $Mn_5(PO_4)_2(OH)_4$ and $Co_5(AsO_4)_2(OH)_4$ (Ruszala et al., 1977).

Table 63. Selected interatomic distances in the crystal structure of $Cd_5(PO_4)_2(OH)_4$.

	d / Å		*d* / Å
Cd1—O9	2.241(7)	Cd4—O10	2.247(6)
Cd1—O9^{i}	2.266(6)	Cd4—O12^{vi}	2.332(6)
Cd1—O8^{ii}	2.269(6)	Cd4—O2^{vii}	2.364(6)
Cd1—O12^{i}	2.314(6)	Cd4—O10^{v}	2.407(6)
Cd1—O6	2.410(6)	Cd4—O1	2.429(6)
Cd1—O4^{iii}	2.542(6)	Cd5—O9	2.239(6)
Cd2—O7	2.197(6)	Cd5—O8^{vi}	2.243(6)
Cd2—O3^{iv}	2.226(6)	Cd5—O7^{vii}	2.257(6)
Cd2—O11^{iv}	2.300(6)	Cd5—O11	2.301(7)
Cd2—O5^{v}	2.323(6)	Cd5—O6	2.321(6)
Cd2—O2	2.349(6)	Cd5—O4^{viii}	2.336(6)
Cd2—O12^{iv}	2.597(6)	P1—O3^{ii}	1.522(6)
Cd3—O7^{v}	2.182(6)	P1—O5	1.540(6)
Cd3—O11	2.193(6)	P1—O4	1.541(7)
Cd3—O5	2.304(6)	P1—O12^{vi}	1.563(6)
Cd3—O1	2.316(6)	P2—O10^{ix}	1.524(6)
Cd3—O4^{iii}	2.434(6)	P2—O6	1.544(7)
Cd3—O6	2.554(6)	P2—O1^{ii}	1.545(6)
Cd4—O8	2.235(7)	P2—O2^{ix}	1.555(6)
O7—H1*	0.88(3)	O7—H1···O1^{iv}	2.900(8)
O9—H2*	0.87(3)	O9—H2···O11	3.070(8)
O8—H3*	0.87(3)	O8—H3···O3^{iv}	2.932(8)
O11—H4*	0.86(3)	O11—H4···O2^{vii}	3.006(8)

* Value constrained to 0.89 Å with DFIX command.

Symmetry codes: (i) −1/2+*x*, 1/2−*y*, −*z*; (ii) −*x*, 1/2+*y*, 1/2−*z*; (iii) −*x*, −1/2+*y*, 1/2−*z*; (iv) 1/2−*x*, −*y*, 1/2+*z*; (v) −1/2+*x*, 1/2−*y*, 1−*z*; (vi) 1−*x*, 1/2+*y*, 1/2−*z*; (vii) 1/2+*x*, 1/2−*y*, 1−*z*; (viii) 1−*x*, −1/2+*y*, 1/2−*z*; (ix) 1/2−*x*, 1−*y*, −1/2+*z*.

6.7 $K_6[Zn(CO_3)_4]$

$K_6[Zn(CO_3)_4]$ was initially obtained from a mild hydroflux reaction between ZnO, H_6TeO_6 and K_2CO_3 (molar ratios 2:3:10; H224). Attempts were made for re-synthesis of $K_6[Zn(CO_3)_4]$ in mild hydroflux reactions (H298, H299), and two "open" hydrothermal experiments (H300, H301). For three of the four batches, only ZnO and various known potassium carbonate phases were obtained. In the PXRD pattern of H301, reflections of $K_6[Zn(CO_3)_4]$ could be identified besides ZnO, $K_2CO_3(H_2O)_{1.5}$ and another unknown phase with a rather large unit-cell (the first reflections appear at 6.78° 2θ (13.02 Å) and 8.56° 2θ (10.32 Å)).

The crystal structure of $K_6[Zn(CO_3)_4]$ is monoclinic (*C*2/*c*, a = 7.1850(6) Å, b = 18.1117(14) Å, c = 10.5206(8) Å, β = 93.579(2)°, V = 1366.4(2) Å^3. The asymmetric unit contains one Zn, four K, six O and two C sites, of which the Zn1, K3 and K4 positions have a site symmetry of 2 (4 *e*), while the remaining sites correspond to general 8 *f* positions. The Zn^{II} atoms are coordinated tetrahedrally (τ_4 = 0.918) by four oxygen atoms belonging to four different carbonate anions. The C—O bond lengths in the CO_3^{2-} anions vary in a narrow range of 1.268(3)–1.319(3) Å with average values of 1.290(25) and 1.285(25) Å for C1 and C2, respectively (Table 64). These values correspond very well to the average C—O bond length of 1.284(20) Å determined by Gagné & Hawthorne (2018b) for carbonate groups.

The $[Zn(CO_3)_4]^{6-}$ anions are embedded in a matrix of K^+ cations (Figure 150). The presence of $[Zn(CO_3)_4]^{6-}$ units, which are completely isolated from each other, has not been observed in other mixed alkali metal-transition metal carbonate phases yet. The lack of condensation into larger units is caused by the massive excess of K^+ cations during the synthesis and consequently in the crystal structure. None of the other known mixed alkali metal-transition metal carbonates has such a large alkali-metal excess as $K_6[Zn(CO_3)_4]$.

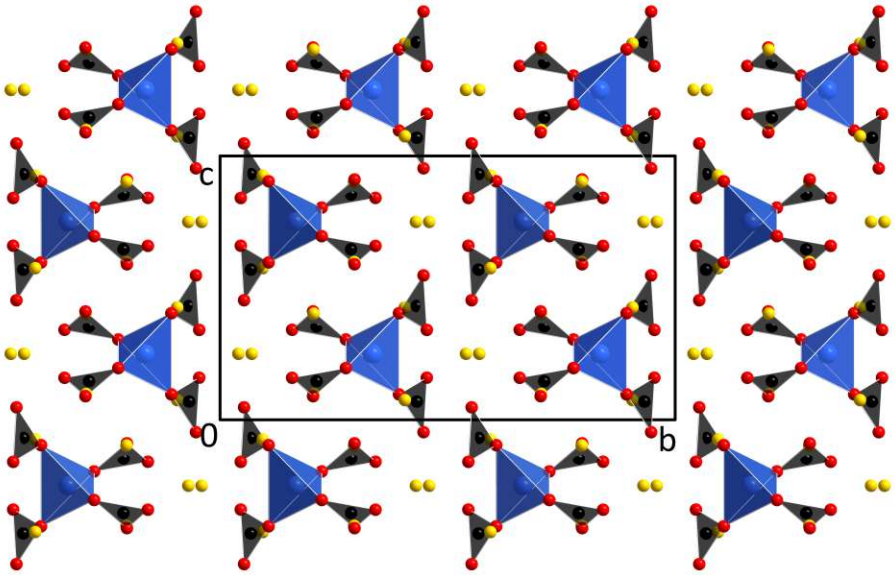

Figure 150. The crystal structure of $K_6[Zn(CO_3)_4]$ viewed along [$\bar{1}$00]. Carbon atoms are drawn black.

Table 64. Selected interatomic distances in the crystal structure of $K_6[Zn(CO_3)_4]$.

	d / Å		*d* / Å
Zn1—O4	1.9554(18)	K3—O5	2.7344(19)
Zn1—O4^{i}	1.9554(18)	K3—O6^{vii}	2.738(2)
Zn1—O1^{i}	1.9838(18)	K3—O6^{viii}	2.738(2)
Zn1—O1	1.9839(18)	K3—O3	2.7910(18)
K1—O5^{ii}	2.756(2)	K3—O3^{i}	2.7910(18)
K1—O6^{iii}	2.804(2)	K3—O2^{i}	2.972(2)
K1—O3^{iv}	2.8113(18)	K3—O2	2.972(2)
K1—O1	2.8448(19)	K4—O6^{i}	2.782(2)
K1—O4^{i}	2.879(2)	K4—O6	2.783(2)
K1—O2^{iv}	2.901(2)	K4—O3^{ii}	2.7908(18)
K1—O6	2.965(2)	K4—O3^{ix}	2.7908(18)
K2—O2^{v}	2.6590(19)	K4—O5^{ix}	2.868(2)
K2—O3^{iii}	2.6697(19)	K4—O5^{ii}	2.868(2)
K2—O4^{vi}	2.726(2)	C1—O1	1.319(3)
K2—O1	2.7426(19)	C1—O2	1.273(3)
K2—O3	2.7561(18)	C1—O3	1.278(3)
K2—O2^{i}	2.810(2)	C2—O4	1.313(3)
K2—O5	2.980(2)	C2—O5^{vi}	1.268(3)
K3—O5^{i}	2.7344(19)	C2—O6	1.273(3)

Symmetry codes: (i) −*x*, *y*, 1/2−*z*; (ii) 1/2−*x*, 1/2+*y*, 1/2−*z*; (iii) 1−*x*, *y*, 1/2−*z*; (iv) 1/2−*x*, 1/2−*y*, −*z*; (v) 1/2+*x*, 1/2−*y*, 1/2+*z*; (vi) 1/2−*x*, 1/2−*y*, 1−*z*; (vii) −1/2+*x*, −1/2+*y*, *z*; (viii) 1/2−*x*, −1/2+*y*, 1/2−*z*; (ix) −1/2+*x*, 1/2+*y*, *z*.

7 References

Addison, A. W., Rao, N. T., Reedijk, J. van Rijn, J. & Verschoor, G. C. (1984). Synthesis, structure, and spectroscopic properties of copper(II) compounds containing nitrogen–sulphur donor ligands; the crystal and molecular structure of aqua[1,7-bis(*N*-methylbenzimidazol-2'-yl)-2,6-dithiaheptane]copper(II) perchlorate. *J. Chem. Soc. Dalton Trans.* 1349–1356.

Al Ansari, S. V., Al Ansari, Y. F., Chumakov, V. M., Albov, D. V., Savinkina, E. V., Davydova, M. N. & Tsivadze, A. Y. (2007). Synthesis and structure of the stoichiometric sodium bis(dihydrotellurato)cuprate(III) $Na_5[Cu(H_2TeO_6)_2]\cdot 16H_2O$. *Crystallogr. Rep*. **52**, 235−238.

Albrecht, R., Hoelzel, M., Beccard, H., Rüsing, M., Eng, L., Doert, T. & Ruck, M. (2021). Potassium Ion Conductivity in the Cubic Labyrinth of a Piezoelectric, Antiferromagnetic Oxoferrate(III) Tellurate(VI). *Chem. Eur. J.* **27**, 14299–14306.

Aminoff, G. (1926). Ueber die Kristallstruktur von Hausmannit ($MnMn_2O_4$). *Z. Kristallogr*. **64**, 475–490.

Aminoff, G. (1931). Lattice dimensions and space group of braunite. *K. vet. akad. handl*. **9**, 14−22.

Andrade, M. B., Yang, H., Downs, R. T., Jenkins, R. A. & Fay, I. (2014). Te-rich raspite, $Pb(W_{0.56}Te_{0.44})O_4$, from Tombstone, Arizona, U.S.A.: The first natural example of Te^{6+} substitution for W^{6+}. *Am. Min.* **99**(7), 1507−1510.

Antonenko, A., M., Domoratsly, K. V., Kuzdin, A. Y. & Sadovskaya, L. Y. (2001). Electromechanical nonlinearity of Bi_2TeO_5. *Phys. Solid State* **43**, 914−915.

Artner, C. (2010). New lead-tellurium oxo compounds : structure determination and thermal behaviour. Diploma thesis. Technical University of Vienna.

Balraj, V. & Vidyasagar, K. (1998). Low-Temperature Syntheses and Characterization of Novel Layered Tellurites, $A_2Mo_3TeO_{12}$ (A = NH_4, Cs), and "Zero-Dimensional" Tellurites, $A_4Mo_6Te_2O_{24}\cdot 6H_2O$ (A = Rb, K). *Inorg. Chem.* **37**(19), 4764–4774.

Balsys, R. J. & Davis, R. L. (1997). Refinement of the structure of $Na_{0.74}CoO_2$ using neutron powder diffraction. *Solid State Ion*. **93**(3−4), 279−282.

Becker, R., Johnsson, M. & Berger, H. (2006). A new synthetic cobalt tellurate: Co_3TeO_6. *Acta Cryst*. C**62**(8), i67−i69.

Becker, C. R., Tagg, S. L., Huffman, J. C. & Zwanziger, J. W. (1997). Crystal structures of potassium tetratellurite, $K_2Te_4O_9$, and potassium ditellurite, $K_2Te_2O_5$, and structural trends in solid alkali tellurites. *Inorg. Chem*. **36**, 5559–5564.

Bell, R. E. & Herfert, R. E. (1957). Preparation and characterization of a new crystalline form of molybdenum bisulfide. *J. Am. Chem. Soc.* **79**, 3351−3354.

Bell, A. M. T., Redfern, S. A. T., Henderson, C. M. B. & Kohn, S. C. (1994). Structural relations and tetrahedral ordering pattern of synthetic orthorhombic $Cs_2CdSi_5O_{12}$ leucite: a combined synchrotron X-ray powder diffraction and multinuclear MAS NMR study. *Acta Cryst.* B**50**, 560−566.

Bell, A. M. T. & Stone, A. H. (2021). Crystal structures and X-ray powder diffraction data for $Cs_2NiSi_5O_{12}$, $RbGaSi_2O_6$, and $CsGaSi_2O_6$ synthetic leucite analogues. *Powder Diffr.* **36**(4), 273−281.

Bera, A. K., Yusuf, S. M., Kumar, A. & Ritter, C. (2017). Zigzag antiferromagnetic ground state with anisotropic correlation lengths in the quasi-two-dimensional honeycomb lattice compound $Na_2Co_2TeO_6$. *Phys. Rev*. B **95**, 094424.

Belokoneva, E. L., Ruchkina, E. A., Dimitrova, O. V. & Stefanovich, S. Y. (2002). Synthesis and crystal structure of a new trigonal modification of $Na_3Fe_2(PO_4)_3$ (transl.). *Zh. Neorg. Khim*. **47**(9), 1423−1426.

Benmiloud, L., Moret, J., Maurin, M. & Philippot, E. (1980). Structure d'un tellurate d'ammonium: $NH_4TeO_3(OH)$. *Acta Cryst*. **B**36, 139−141.

Berchenko, M. A. & Belayaev, A. L. (1967). Preparation of lead, barium, and copper tellurites by precipitation from solution (transl.). Zh. *Neorg. Khim*. **12**, 933.

Bergerhoff, G., Berndt, M., Brandenburg, K. & Degen, T. (1999). Concerning inorganic crystal structure types. *Acta Cryst.* B**55**, 147–156.

Beyer, H. (1967). Verfeinerung der Kristallstruktur von Tellurit, dem rhombischen TeO_2. *Z. Kristallogr. – Cryst. Mater.* **124**, 228–237.

Brandenburg, K. (2016). DIAMOND (Version 4.0). Crystal and Molecular Structure Visualization, Crystal Impact, Bonn, Germany.

Brese, N. E. & O'Keeffe, M. (1991). Bond-valence parameters for solids. *Acta Cryst.* B**47**, 192–197.

Brooker, M. H., Sunder, S., Taylor, P. & Lopata, V. J. (1983). Infrared and Raman spectra and X-ray diffraction studies of solid lead(II) carbonates. *Can. J. Chem*. **61**(3), 494−502.

Brown, I. D. (2002). The Chemical Bond in Inorganic Chemistry: The Bond Valence Model. Oxford University Press, Oxford.

Bruker (2021a). APEX-4. Bruker AXS Inc, Madison, Wisconsin, USA.

Bruker (2021b). SAINT. Bruker AXS Inc, Madison, Wisconsin, USA.

Bugaris, D. E., Smith, M. D. & zur Loye, H.-C. (2013). Hydroflux Crystal Growth of Platinum Group Metal Hydroxides: $Sr_6NaPd_2(OH)_{17}$, $Li_2Pt(OH)_6$, $Na_2Pt(OH)_6$, $Sr_2Pt(OH)_8$, and $Ba_2Pt(OH)_8$. *Inorg. Chem.* **52**(7), 3836–3844.

Burckhardt, H.-G., Platte & C., Trömel, M. (1982). Cadmiumorthotellurat(VI) Cd_3TeO_6: ein pseudoorthorhombischer Kryolith im Vergleich mit Ca_3TeO_6. *Acta Cryst*. B**38**, 2450–2452.

Bystroem, A. & Westgren, A. (1943). The crystal structure of Pb_3O_4 and $SnPb_2O_4$. *Ark. Kem. Mineral. Geol.* **16**(1), 1−7.

Cachau-Herreillat, D., Norbert, A., Maurin, M. & Philippot, E. (1981). Etude cristallochimique comparé e et conductivité ionique des deux variétés $Li_2Te_2O_5$ α et *β*. *J. Solid State Chem.* **37**(3), 352−361.

Cametti, G., Churakov, S. & Armbruster, T. (2017). Reinvestigation of the zemannite structure and its dehydration behavior: a single-crystal X-ray and atomistic simulation study. *Eur. J. Mineral.* **29**, 53–61.

Champarnaud-Mesjard, J. C., Blanchandin, S., Thomas, P., Mirgorodsky, A., Merle-Méjean, T. & Frit, B. (2000). Crystal structure, Raman spectrum and lattice dynamics of a new metastable form of tellurium dioxide: *γ*-TeO_2. *J. Phys. Chem. Solids* **61**, 1499–1507.

Chance, W. M., Bugaris, D. E., Sefat, A. S. & zur Loye, H.-C. (2013). Crystal Growth of New Hexahydroxometallates Using a Hydroflux. *Inorg. Chem.* **52**(20), 11723–11733.

Chen, Y.-G., Yang, N., Yao, X.-N., Li, C.-B., Guo, Y. & Zhang, X.-M. (2018). Synergetic Influence of Alkali-Metal and Lone-Pair Cations on Frameworks of Tellurites. *Inorg. Chem.* **57**(9), 5406–5412.

Chen, K., Lin, C., Peng, G., Chen, Y., Huang, H., Chen, E., Min, Y., Yan, T., Luo, M. & Ye, Y. (2021). $LiNbTeO_5$: A High-Performance Multifunctional Crystal Material with a Very Large Second-Harmonic Generation Response and Piezoelectric Coefficient. *Chem. Mater.* **34**(1), 399–404.

Chi, E. O., Ok, K. M., Porter, Y. & Halasyamani, P. S. (2006). $Na_2Te_3Mo_3O_{16}$: A New Molybdenum Tellurite with Second-Harmonic Generating and Pyroelectric Properties. *Chem. Mater.* **18**(8), 2070–2074.

Chigagov, A. V., Ilyukhin, V. V. & Belov, N. V. (1966). Crystal structure of cadmium wolframate (transl.). *Dokl. Akad. Nauk SSSR* **166**, 87−89.

Christy, A. G., Mills, S. J. & Kampf, A. R. (2016). A review of the structural architecture of tellurium oxycompounds *Miner. Mag.* **80**, 415–545.

Cirpus, V., Wittrock, J. & Adam, A. (2001). Carbonat-Hydrate der schweren Alkalimetalle: Darstellung und Struktur von $Rb_2CO_3 \cdot 1.5\ H_2O$ und $Cs_2CO_3 \cdot 3\ H_2O$. *Z. Anorg. Allg. Chem*. **627**, 533–538.

Cirpus, V. & Adam, A. (1995). Die ersten Hydrogencarbonate mit einer trimeren $[H_2(CO_3)_3]^{4-}$-Baugruppe: Zur Darstellung und Kristallstruktur von $Rb_4H_2(CO_3)_3 \cdot H_2O$ und $K_4H_2(CO_3)_3 \cdot 1{,}5\ H_2O$. *Z. Anorg. Allg. Chem.* **621**, 1197–1204.

Cooper, M. A. & Hawthorne, F. C. (1996). The crystal structure of spiroffite. *Can. Mineral*. **34**, 821–826.

Courbion, G., Jacoboni, C. & De Pape, R. (1982). The dimorphism of $LiMnFeF_6$: A new kind of cationic order in the structural type Na_2SiF_6. *J. Solid State Chem.* **45**(1), 127−134.

Daniel, F., Moret, J., Philippot, E. & Maurin, M. (1977). Etude structurale de Li_2TeO_4. Coordination du tellure VI et du lithium par les atomes d'oxygéne. *J. Solid State Chem.* **22**(2), 113−119.

Daniel, F., Moret, J., Maurin, M. & Philippot, E. (1978). Structure cristalline d'un oxotellurate mixte, Te^{IV} et Te^{VI}: $K_2Te^{IV}Te^{VI}{}_3O_{12}$. Pentacoordination du tellure(IV) par les atomes d'oxygène. *Acta Cryst.* B**34**, 1782−1786.

Day, P. (1981). Mixed valent chemistry: a survey of 10 Years progress. *Int. Rev. Phys. Chem*. **1**, 149–193.

Degen, T., Sadki, M., Bron, E., König, U. & Nénert, G. (2014). The highscore suite. *Powder Diffr*. **29**, S2, 13–18.

Dho, J., Ki, S., Gubkin, A. F., Park, J. M. S. & Sherstobitova, E. A. (2010). A neutron diffraction study of half-metallic ferromagnet CrO_2 nanorods. *Solid State Commun.* **150**(1−2), 86−90.

Dickinson, R. G., Pauling, L. (1923). The crystal structure of molybdenite. *J. Am. Chem. Soc.* **45**, 1466−1471.

Dill, S., Kawamoto, Y., Grigoraviciute, I., Kareiva, A. & Meyer, H.-J. (2006). Synthese und Charakterisierung der Lanthanoidbleioxidnitrate *Ln*PbO_2NO_3 mit *Ln* = La, Pr, Nd und Sm. *Z. Naturforsch.* **61b**, 503−508.

Dornberger-Schiff, K. & Grell-Niemann, H. (1961). On the theory of order–disorder (OD) structures. *Acta Cryst.* **14**, 167–177.

Dornberger-Schiff, K. (1982). Geometrical properties of MDO polytypes and procedures for their derivation. I. General concept and applications to polytype families consisting of OD layers all of the same kind. *Acta Cryst*. A**38**, 483–491.

Dornberger-Schiff, K. & Grell, H. (1982a). Symbols for OD groupoid families referring to OD structures (polytypes) consisting of more than one kind of layer. *Acta Cryst.* A**38**, 49–54.

Dornberger-Schiff, K. & Grell, H. (1982b). Geometrical properties of MDO polytypes and procedures for their derivation. II. OD families containing OD layers of M > 1 kinds and their MDO polytypes. *Acta Cryst*. A**38**, 491–498.

Dowty, E. (2006). ATOMS for Windows. Shape Software, Kingsport, Tennessee, USA.

Ďurovič S. (1979). Desymmetrization of OD structures. *Krist. Tech.* **14**, 1047–1053.

Eder, F. & Weil, M. (2020a). $Ni_3Te_2O_2(PO_4)_2(OH)_4$, an open-framework structure isotypic with $Co_3Te_2O_2(PO_4)_2(OH)_4$. *Acta Cryst*. E**76**, 625–628.

Eder, F. & Weil, M. (2020b). The crystal structure of a new $CdTe_2O_5$ polymorph, isotypic with ε-$CaTe_2O_5$. *Acta Cryst.* E**76**, 831–834.

Eder, F. & Weil, M. (2021). Crystal structure of $Zn_2(HTeO_3)(AsO_4)$. *Acta Cryst*. E**77**, 555–558.

Eder, F. & Weil, M. (2022a). The alkali metal copper(II) oxidotellurates(IV) $Li_2Cu_2Te_3O_9$, $Li_2Cu_3Te_4O_{12}$, $Rb_2Cu_3Te_6O_{16}$ and $Cs_2Cu_3Te_6O_{16}$ – four new structure types. *Z. Anorg. Allg. Chem*. **648**, 23: e202200089.

Eder, F. & Weil, M. (2022b). Phase formation studies and crystal structure refinements in the $Mn^{II}/Te^{IV}/O/(H)$ system. *Z. Anorg. Allg. Chem*. **648**, 24.

Eder, F. & Weil, M. (2023). Garnet-type $Na_3Te_2(FeO_4)_3$. *Acta Cryst*. E**79**, 328–330.

Eder, F., Stöger, B. & Weil, M. (2022a). Order-disorder (OD) structures of $Rb_2Zn(TeO_3)(CO_3)\cdot H_2O$ and $Na_2Zn_2Te_4O_{11}$. *Z. Kristallogr. – Cryst. Mater.* **237**, 8–9, 329–341.

Eder, F., Weil, M., Missen, O. P., Kolitsch, U. & Libowitzky, E. (2022b). The Family of $M^{II}_3(Te^{IV}O_3)_2(OH)_2$ (*M* = Mg, Mn, Co, Ni) Compounds—Prone to Inclusion of Foreign Components into Large Hexagonal Channels. *Crystals* **12**, 1380.

Eder, F., Weil, M., Pramanik, P. & Mathieu, R. (2023a). The Cobalt(II) Oxidotellurate(IV) Hydroxides $Co_2(TeO_3)(OH)_2$ and $Co_{15}(TeO_3)_{14}(OH)_2$. *Crystals* **13**, 176.

Eder, F., Marsollier, A. & Weil, M. (2023b). Structural studies on synthetic $A_{2-x}[M_2(TeO_3)_3]\cdot nH_2O$ phases (*A* = Na, K, Rb, Cs; *M* = Mn, Co, Ni, Cu, Zn) with zemannite-type structures. *Mineral. Petrol.* https://doi.org/10.1007/s00710-023-00814-5.

Eder, F., Miletich, R. & Weil, M. (2023c). $K[(Cu^{II},Mn^{II},Mn^{III})_2(TeO_3)_3]\cdot 2\ H_2O$, the first zemannite-type structure based on a Jahn-Teller-distorted framework. *Mineral. Petrol*. https://doi.org/10.1007/s00710-022-00808-9.

Effenberger, H. S. (1989). An uncommon $Cu^{[2+4]}O_6$ coordination polyhedron in the crystal structure of $KCu_3(OH)_2[(AsO_4)]H(AsO_4)]$ (with a comparison to related structure types). *Z. Kristallogr. – Cryst. Mater.* **188**, 43–56.

Effenberger, H. S. & Tillmanns, E. (1993). The crystal structure of $K_2\{Cu[TeO_4(OH)_2]\}\cdot H_2O$. *Z. Kristallogr. – Cryst. Mater.* **205**(1–2), 41–53.

Effenberger, H. S., Ende, M. & Miletich, R. (2023). New insights into the crystal chemistry of zemannite: Trigonal rather than hexagonal symmetry due to ordering within the host-guest structure. *Mineral. Petrol.* https://doi.org/10.1007/s00710-023-00820-7.

Feger, C. R., Schimek, G. L. & Kolis, J. W. (1999). Hydrothermal Synthesis and Characterization of $M_2Te_3O_8$(*M*=Mn, Co, Ni, Cu, Zn): A Series of Compounds with the Spiroffite Structure. *J. Solid State Chem.* **143**(2), 246–253.

Feng, Y., Fan, H., Zhong, Z., Wang, H. & Qiu, D. (2016). $Cd_3(MoO_4)(TeO_3)_2$: A Polar 3D Compound Containing d^{10}–d^0 SCALP-Effect Cations. *Inorg. Chem.* **55**(22), 11987–11992.

Filipenko, O. S., Pobedimskaya, E. A. & Belov, N. V. (1968). Crystal structure of $ZnWO_4$. Kristallografiya **13**, 163–165.

Flor, G. de la, Orobengoa, D., Tasci, E., Perez-Mato, J. M. & Aroyo, M. I. (2016). Comparison of structures applying the tools available at the Bilbao Crystallographic Server. *J. Appl. Cryst*. **49**, 653–664.

Frau, A. F., Kim, J. H. & Halasyamani, P. S. (2008). $Na_3Ga_3Te_2O_{12}$: Synthesis, single crystal structure and characterization. *Solid State Sci*. **10**, 1263–1268.

Gagné, O. C. & Hawthorne, F. C. (2018a). Bond-length distributions for ions bonded to oxygen: metalloids and post-transition metals. *Acta Cryst.* B**74**, 63–78.

Gagné, O. C. & Hawthorne, F. C. (2018b). Bond-length distributions for ions bonded to oxygen: results for the non-metals and discussion of lone-pair stereoactivity and the polymerization of PO_4. *Acta Cryst.* B**74**, 79–96.

Galy, J., Meunier, G., Andersson, S. & Åström, A. (1975). Stéréochimie des eléments comportant des paires non liées: Ge (II), As (III), Se (IV), Br (V), Sn (II), Sb (III), Te (IV), I (V), Xe (VI), Tl (I), Pb (II), et Bi (III) (oxydes, fluorures et oxyfluorures). *J. Solid State Chem.* **13**, 142–159.

García-Martín, S., Veiga, M. L., Iborra, E., Jerez, A. & Pico, C. (1988). Synthesis and ionic conductivity of mixed oxides $(H_2ONH_4)MTeO_{6.5}$ (M = Cr, W). *Mater. Res. Bull*. **23**(8), 1107–1117.

Gelato, L. M. & Parthé, E. (1987). *STRUCTURE TIDY* - a computer program to standardize crystal structure data. *J. Appl. Cryst.* **20**, 139–143.

Goodey, J., Broussard, J., & Halasyamani, P. S. (2002). Synthesis, Structure, and Characterization of a New Second-Harmonic-Generating Tellurite: $Na_2TeW_2O_9$. *Chem. Mater.* **14**(7), 3174–3180.

Goodey, J., Ok, K. M., Broussard, J., Hofmann, C., Escobedo, F. V. & Halasyamani, P. S. (2003). Syntheses, structures, and second-harmonic generating properties in new quaternary tellurites: $A_2TeW_3O_{12}$ (*A*=K, Rb, or Cs). *J. Solid State Chem.* **175**(1), 3–12.

Grundish, N. S., Seymour, I. D., Henkelman, G. & Goodenough, J. B. (2019). Electrochemical Properties of Three $Li_2Ni_2TeO_6$ Structural Polymorphs. *Chem. Mater.* **31**(22), 9379–9388.

Guje, R., Ravi, G., Palla, S., Ngeshwar Rao, K. & Vithal, M. (2015). Synthesis, characterization, photocatalytic and conductivity studies of defect pyrochlore $KM_{0.33}Te_{1.67}O_6$ (M=Al, Cr and Fe). *Mater. Sci. Eng*. B **198**, 1–9.

Guo, X., Gao, Z. & Tao, X. (2022). Recent advances in tellurite molybdate/tungstate crystals. *CrystEngComm*, **24**, 7516−7529.

Hahn, T. & Aroyo, M. I. (2016). Symbols of symmetry elements. In Space group Symmetry, Volume A of International Tables for Crystallography; IUCr: Chester, 144–148, chapter 2.1.2.

Hamani, D. & Masson, O. (2019). *LPLoc*. IRCER – UMR CNRS 7315, Université de Limoges, France.

Hamani, D., Masson, O. & Thomas, P. (2020). Localization and steric effect of the lone electron pair of the tellurium Te^{4+} cation and other cations of the *p*-block elements. A systematic study. *J. Appl. Cryst.* **53**, 1243−1251.

Harrison, W. T. A., Dussack, L. L. & Jacobson, A. J. (1994). Syntheses, Crystal Structures, and Properties of New Layered Molybdenum(VI) Selenites: $(NH_4)_2(MoO_3)_3SeO_3$ and $Cs_2(MoO_3)_3SeO_3$. *Inorg. Chem*. **33**(26), 6043–6049.

Han, M., Wang, C., Niu, K., Yang, Q., Wang, C., Zhang, X., Dai, J., Wang, Y., Ma, X., Wang, J., Kang, L., Ji, W. & Lin, J. (2022). Continuously tunable ferroelectric domain width down to the single-atomic limit in bismuth tellurite. *Nat. Commun.* **13**, 5903.

Hanke, K. (1966). Die Kristallstruktur von $Zn_2Te_3O_8$. *Sci. Nat*. **55**, 273.

Hanke, K. (1967). Zinktellurit: Kristallstruktur und Beziehungen zu einigen Seleniten. *Sci. Nat*. **54**, 199.

Hanke, K., Kupcik, V. & Lindqvist, O. (1973). The crystal structure of $CuTe_2O_5$. *Acta Cryst.* B**29**, 963−970.

Hatert, F. (2007). $Fe^{II}_2(PO_4)(OH)$, a synthetic analogue of wolfeite. *Acta Cryst*. C**63**, 119−121.

Hawthorne, F. C. (2014). The structure hierarchy hypothesis. *Mineral. Mag.* **78**, 957–1027.

He, Z., Cui, M. & Qiu, C. (2018). Synthesis, structure and magnetic behaviors of a new spin-1/2 chain compound Na_4CuTeO_6. *J. Alloys Compd*. 794−797.

Hostachy, A. & Coing-Boyat, J. (1968). Structure cristalline de Cu_3TeO_6. *C. r. hebd. séances Acad. sci., Sér. B, Sci. phys*. **267**, 1435−1438.

Hottentot, D. & Loopstra, B. O. (1979). Structures of calcium tellurate, $CaTeO_4$, and strontium tellurate, $SrTeO_4$. *Acta Cryst.* B**35**, 728−729.

Isasi, J. (2001). New MM'O4 oxides derived from the rutile type: synthesis, structure and study of magnetic and electronic properties. *J. Alloys Compd.* **322**(1−2), 89−96.

Isasi, J., López, M. L., Veige, M. L., Ruiz-Hitzky & E., Pico, C. (1995). Structural Characterization and Electrical Properties of a Novel Defect Pyrochlore. *J. Solid State Chem*. **116**(2), 290−295.

Jansen, M. & Hoppe, R. (1974a). Zur Kenntnis der Oxocobaltate $A_xCo_2O_4$ mit A = Cs, Rb, K. *Z. Anorg. Allg. Chem.* **408**(2), 97−103.

Jansen, M. & Hoppe, R. (1974b). Notiz zur Kenntnis der Oxocobaltate des Natriums. *Z. Anorg. Allg. Chem.* **408**(2), 104−106.

Johnston, M. G. & Harrison, W. T. A. (2002). Manganese tellurite, *β*-$MnTe_2O_5$. *Acta Cryst.* E**58**, i59−i61.

Johnston, M. G. & Harrison, W. T. A. (2011). New BaM_2(SeO$_3$)$_3$·nH$_2$O (M = Co, Ni, Mn, Mg; n ≈ 3) zemannite-type frameworks: single-crystal structures of BaCo$_2$(SeO$_3$)$_3$·3H$_2$O, BaMn$_2$(SeO$_3$)$_3$·3H$_2$O and BaMg$_2$(SeO$_3$)$_3$·3H$_2$O. *Eur. J. Inorg. Chem.* 2967–2974.

Keeling, R. O. (1957). The structure of NiWO$_4$. *Acta Cryst.* **10**, 209−213.

Ketkaew, R., Tantirungrotechai. Y., Harding, P., Chastanet, G., Guionneau, P., Marchivie, M. & Harding, D. J. (2021). OctaDist: A Tool for Calculating Distortion Parameters in Spin Crossover and Coordination Complexes. *Dalton Trans.* **50**, 1086–1096.

Kim, S. W., Deng, Z., Yu, S., Padmanabhan, H., Zhang, W., Gopalan, V., Jin, C. & Greenblatt, M. (2017). A(II)GeTeO$_6$ (A = Mn, Cd, Pb): Non-Centrosymmetric Layered Tellurates with PbSb$_2$O$_6$-Related Structure. *Inorg. Chem.* **56**(15), 9019–9024.

Kim, J. H., Baek, J. & Halasyamani, P. S. (2007). (NH$_4$)$_2$Te$_2$WO$_8$: A New Polar Oxide with Second-Harmonic Generating, Ferroelectric, and Pyroelectric Properties. *Chem. Mater.* **19**(23), 5637–5641.

Kim, Y. H., Lee, D. W. & Ok, K. M. (2014). Strong Second Harmonic Generation (SHG) Originating from Combined Second-Order Jahn–Teller (SOJT) Distortive Cations in a New Noncentrosymmetric Tellurite, InNb(TeO$_4$)$_2$. *Inorg. Chem.* **53**(10), 5240–5245.

Knyazew, A. V., Chernorukov, N. G., Ladenkov, I. V. & Belopolskaya, S. S. (2011). Synthesis, structure, and thermal expansion of M$_2$Fe$_2$Ti$_6$O$_{16}$ and MFeTiO$_4$ compounds. *Inorg. Mater*. **47**, 999−1005.

Kong, F., Xu, X. & Mao, J. G. (2010). A Series of New Ternary and Quaternary Compounds in the Li^{I}–Ga^{III}–Te^{IV}–O System. *Inorg. Chem.* **49**(24), 11573−11580.

Kong, F. & Mao, J. G. (2020). Recent progress in selenite and tellurite based SHG materials. *Dalton Trans.* **49**, 8433−8437.

Koziskova, J., Hahn, F., Richter, J. & Kozisek, J. (2016). Comparison of different absorption corrections on the model structure of tetrakis(μ2-acetato)-diaqua-di-copper(II). *Acta Chim. Slov.* **9**, 136−140.

Kozłowski, R. & Słkoczyński, J. (1976). CoTeMoO$_6$, Co$_4$TeMo$_3$O$_{16}$: Two new cobalt molybdotellurates. *J. Solid State Chem*. **18**, 51−55.

Kratochwil, B. & Jensovský, L. (1977). The crystal structure of sodium metatellurate. *Acta Cryst*. B**33**, 2596−2598.

Krause, L., Herbst-Irmer, R., Sheldrick, G. M. & Stalke, D. (2015). Comparison of silver and molybdenum microfocus X-ray sources for single-crystal structure determination. *J. Appl. Cryst.* **48**, 3–10.

Kumar, V., Gupta, A. & Uma, S. (2013). Formation of honeycomb ordered monoclinic Li$_2$M$_2$TeO$_6$ (M = Cu, Ni) and disordered orthorhombic Li$_2$Ni$_2$TeO$_6$ oxides. *Dalton Trans.* **42**, 14992−14998.

Kunnmann, W., La Placa, S., Corliss, L. M., Hastings, J. M. & Banks, E. (1968). Magnetic structures of the ordered trirutiles Cr$_2$WO$_6$, Cr$_2$TeO$_6$ and Fe$_2$TeO$_6$. *J. Phys. Chem. Solids* **29**(8), 1359−1364.

Kurbakov, A. I., Korshunov, A. N., Podchezertsev, S. Y., Stratan, M. I., Raganyan, G. V. & Zvereva, E. A. (2020). Long-range and short-range ordering in 2D honeycomb-lattice magnet Na$_2$Ni$_2$TeO$_6$. *J. Alloys Compd*. **820**, 153354.

Levason, W., Spicer, M. D. & Webster, M. (1988). Co-ordination chemistry of higher oxidation states. Part 26. Spectroscopic studies of tellurate complexes of the trivalent group 1b metals. *X*-ray structure of $Na_5[Cu\{TeO_4(OH)_2\}_2]\cdot 16H_2O$. *J. Chem. Soc., Dalton Trans.* 1377−1381.

Libowitzky, E. (1999). Correlation of O-H stretching frequencies and O-H . . . O hydrogen bond lengths in minerals. *Monatsh. Chem*. **130**, 1047–1059.

Liebau, F. (1985). Structural Chemistry of Silicates. Structure, Bonding and Classification. Springer-Verlag, Berlin – Heidelberg. 347 pp.

Linda, D., Dutreilh-Colas, M., Loukil, M., Mirgorodsky, A., Masson, O., Duclère, J. R., Thomas, P. & Kabadou, A. (2010). Crystal structure and dynamical properties of a new tellurite: $AgTlTeO_3$. *Mater. Res. Bull.* **45**(12), 1883−1888.

Lindqvist, O. (1972). A redetermination of the crystal structure of $KTeO_3(OH)$. *Acta Chem. Scand*. **26**, 4109−4120.

Lindqvist, O. & Moret, J. (1973). The crystal structure of a tellurium(IV,VI) oxyhydroxide, $H_2Te_2O_6$. *Acta Cryst.* B**29**, 956−963.

Loeksmanto, W., Moret, J., Maurin, M. & Phillipot, E. (1980). Etude cristallochimique comparée et conductivité électrique de deux tellurates mixtes: $Ag_xNa_{2-x}Te_2^{IV}Te_3^{VI}O_{14}$ (x = 0,4) et $K_2Te^{IV}Te_3^{VI}O_{12}$. *J. Solid State Chem*. **33**, 209−217.

Loopstra, B. O. & Goubitz, K. (1986). The structures of four cesium tellurates. *Acta Cryst.* C**42**, 520−523.

Lü, M., Jo, H., Oh, S.-J., Lee, S., Choi, K.-Y., Yu, Y. & Ok, K. M. (2017). Syntheses, Structures, and Characterization of Quaternary Tellurites, $Li_3MTe_4O_{11}$ (M = Al, Ga, and Fe). *Inorg. Chem.* **56**(10), 5873–5879.

Lü, M., Jiang, J., Zhu, B., Zhao, Y., Zhu, T., Yang, H., Jin, Y., Kabbour, H., Choi, K. Y. & Harrison, W. T. A. (2020). Lone-pair self-containment in pyritohedron-shaped closed cavities: optimized hydrothermal synthesis, structure, magnetism and lattice thermal conductivity of $Co_{15}F_2(TeO_3)_{14}$. *Dalton Trans*. **49**, 2234–2243.

Lufaso, M. W. & Woodward, P. M. (2004). Jahn-Teller distortions, cation ordering and octahedral tilting in perovskites. *Acta Cryst.* B**60**, 10–20.

Mackay, A. L. (1962). *β*-Ferric oxyhydroxide—akaganéite. *Mineral. Mag*. **33**(259), 270−280.

Mariolacos, K. (1969). Die Kristallstruktur von $PbTeO_3$. *Anz. Österr. Akad*. **106**, 129−131.

Matsubara, N., Damay, F., Vertruyen, B., Barrier, N., Lebedev, O. I., Boullay, P., Elkaim, E., Manuel, P., Khalyavin, D. & Martin, C. (2017). Mn_2TeO_6: a Distorted Inverse Trirutile Structure. *Inorg. Chem.* **56**(16), 9742−9753.

Matzat, E. (1967). Die Kristallstruktur eines unbenannten zeolithartigen Telluritminerals, $\{(Zn, Fe)_2[TeO_3]_3\}Na_xH_{2-x}\cdot yH_2O$. *Tschermaks min. u. petr. Mitt.* **12**, 108–117.

Mercurio, D., El Farissi, M., Frit, B. & Goursat, P. (1983). Etude structurale et densification d'un nouveau materiau piezoelectrique: Bi_2TeO_5. *Mater. Chem. Phys*. **9**(5), 467−476.

Meunier, G & Galy, J. (1971). Sur une déformation inédite du reseau de type fluorine. Structure cristalline des phases MTe_3O_8 (M = Ti, Sn, Hf, Zr). *Acta. Cryst.* B**27**, 602−608.

Miletich, R. (1993a). Kristallchemische Untersuchungen an natürlichen und synthetischen Telluriten mit zeolithartigen Kristallstrukturen. Dissertation, University of Vienna.

Miletich, R. (1995a). Crystal chemistry of the microporous tellurite minerals zemannite and kinichilite, $Mg_{0.5}(Me^{2+}Fe^{3+}(TeO_3)_3)\cdot 4.5H_2O$, ($Me^{2+}$=Zn; Mn). *Eur. J. Mineral.* **7**, 509–523.

Miletich R. (1995b). The synthetic microporous tellurites $Na_2[Me_2(TeO_3)_3]\cdot 3H_2O$ (Me=Zn, Co): Crystal structure, De- and rehydration, and ion exchange properties. *Monatsh. Chem.* **126**, 417–430.

Miletich, R. & Pertlik, F. (1998). Crystal structure of $NaGaTe_2O_6$: Aspects of Te_nO_m polyhedral polymerization in a layer tellurite. *J. Alloys Compd*. **268**, 107–111.

Mills, S. J. & Christy, A. G. (2013). Revised values of the bond-valence parameters for Te^{IV}–O, Te^{VI}–O and Te^{IV}–Cl. *Acta Cryst.* B**69**, 145–149.

Missen, O. P., Mills, S. J., Spratt, J., Birch, W. D. & Brugger. J. (2019). Crystal chemistry of zemannite-type structures: I. A re-examination of zemannite from Moctezuma, Mexico. *Eur. J. Mineral.* **31**, 519–527.

Missen, O. P., Ram, R., Mills, S. J., Etschmann, B., Reith, F., Shuster, J., Smith, D., J. & Brugger, J. (2020). Love is in the Earth: A review of tellurium (bio)geochemistry in surface environments. *Earth-Science Reviews* **204**.

Miura, H. (1986). The crystal structure of hollandite. *Mineral. J.*, **13**, 119−129.

Moetakef, P., Larson, A. M., Hodges, B. C., Zavalii, P. Y., Gaskell, K. J., Piccoli, P. M. B. & Rodriguez, E. E. (2014). Synthesis and crystal chemistry of microporous titanates $K_x(Ti,M)_8O_{16}$ where *M*=Sc−Ni". *J. Solid State Chem*. **220**, 45−53.

Moore, P. B. & Molin-Case, J. (1971). Crystal Chemistry of the Basic Manganese Arsenates: V. Mixed Manganese Coordination in the Atomic Arrangement of Arsenoclasite. *Am. Min*. **56**, 1539−1552.

Murase, R., Leong, C. F. & D'Allesandro, D. M. (2017). Mixed valency as a strategy for achieving charge delocalization in semiconducting and conducting framework materials. *Inorg. Chem*. **56**, 14373–14382.

Nalbandyan, V. & Evstigneeva, M. (2007). Southern Federal Univ., Rostov-na-Donu, Russian Federation. ICDD Grant-in-Aid. (Entry from PDF-4+ database).

Natta, G. & Reina, A. (1926). Cobalt oxides and oxide hydrates, crystal structures. *Rend. Lincei-Mat. Appl.* Serie 7, **4**(7), 48−52.

Newnham, R. E. & Meagher, E. P. (1967). Crystal structure of Ni_3TeO_6. *Mater. Res. Bull*. **2**, 549−554.

Ok, K. M., Chi, E. O. & Halasyamani, P. S. (2006). Bulk characterization methods for non-centrosymmetric materials: second-harmonic generation, piezoelectricity, pyroelectricity, and ferroelectricity. *Chem. Soc. Rev*., **35**, 710−717.

Ok, K. M. & Halasyamani, P. S. (2001). New Tellurites: Syntheses, Structures, and Characterization of $K_2Te_4O_9\cdot 3.2H_2O$, $KGaTe_6O_{14}$, and $KGaTe_2O_6\cdot 1.8H_2O$. *Chem. Mater.* **13**(11), 4278–4284.

Ono, Y., Kato, N., Ishii, Y., Miyazaki, Y. & Kajitani, T. (2003). Crystal Structure and Transport Properties of *γ*-Na_xCoO_2 (x=0.67 ~ 0.75). *Funtai Oyobi Fummatsu Yakin* **50**(6), 469−474.

Perez, G., Lasserre, F., Moret, J. & Maurin, M. (1976). Structure cristalline des hydroxytellurites de nickel et de cobalt. *J. Solid State Chem.* **17**, 143–149.

Petříček, V., Dušek, M. & Palatinus, L. (2014). Crystallographic computing system JANA2006: general features. *Z. Kristallogr. – Cryst. Mater.* **229**, 345–352.

Philippot, E., Benmiloud, L., Maurin, M. & Moret, J. (1979). Pentacoordination de l'atome de tellure(IV) par les atomes d'oxygène. Etude cristallochimique d'un oxotellurate mixte: $NH_4[Te^{IV}Te^{VI}O_5(OH)]$. *Acta Cryst.* B**35**, 1986−1989.

Plakhtii, V. P., Golosovskii, I. V., Bedrisova, M. N., Smirnov, O. P., Sokolov, V. I., Mill, B. V. & Parfenova, N. N. (1977). Magnetic ordering and bond geometry in garnets with Fe^{3+} ions in the tetrahedral sublattice. *Phys. Status Solidi* A, **39**, 683–695.

Pollet, M., Blangero, M., Doumerc, J.-P., Decourt, R., Carlier, D., Denage, C. & Delmas, C. (2009). Structure and Properties of Alkali Cobalt Double Oxides $A_{0.6}CoO_2$ (A = Li, Na, and K). *Inorg. Chem.* **48**(20), 9671–9683.

Poupon, M., Barrier, N., Pautrat, A., Petit, S., Perez, O. & Bazin, P. (2019). Investigation of $Co_6(OH)_3(TeO_3)_4(OH)_{\sim 0.9}(H_2O)$: Synthesis, crystal and magnetic structures, magnetic and dielectric properties. *J. Solid State Chem*. **270**, 147–155.

Proffen, T. & Neder, R. B. (1997). DISCUS: a program for diffuse scattering and defect-structure simulation *J. Appl. Cryst.* **30**, 171–175.

Rai, R., Sharma, S. & Choudhary, R. N. P. (2002). Ferroelectric phase transition in calcium tellurite ceramics. *J. Mater. Sci.* **21**, 297−299.

Rea, J. R. & Kostiner, E. (1974). Cadmium fluorophosphate, $Cd_2(PO_4)F$. *Acta Cryst*. B**30**, 2901−2903.

Robin, M. B., Day, P. (1968). Mixed Valence Chemistry-A Survey and Classification. *Adv. Inorg. Chem.* **10**, 247−422.

Ruszala, F. A., Anderson, J. B. & Kostiner, E. (1977). Crystal structures of two isomorphs of arsenoclasite: $Co_5(PO_4)_2(OH)_4$ and $Mn_5(PO_4)_2(OH)_4$. *Inorg. Chem.* **16**(9), 2417–2422.

Shannon, R. D. (1976). Revised effective ionic radii and systematic studies of interatomic distances in halides and chalcogenides. *Acta Cryst*. A**32**, 751–767.

Sheldrick, G. M. (2015a). SHELXT - Integrated space group and crystal-structure determination. *Acta Cryst.* A**71**, 3–8.

Sheldrick, G. M. (2015b). Crystal structure refinement with SHELXL. *Acta Cryst.* C**71**, 3–8.

Sicher, P. (2020). Hydrothermalsynthese von Mangantelluriten mit Methodenvergleich sowie Synthese und Strukturaufklärung von Kaliumkupfertelluraten. Bachelor Thesis, Technical University of Vienna. Supervised by Felix Eder and Matthias Weil.

Spek, A. L. (2003). Single-crystal structure validation with the program PLATON. *J. Appl. Cryst.* **36**, 7−13.

Słkoczyński, J. & Śliwa, B. (1978). Telluromolybdates of Transition Metals. *Z. Anorg. Allg. Chem.* **438**(1), 295−304.

Stehlik, B. & Balak, L. (1948). Krystalovâ structura kysliénika telûricitého. *Chem. Zvesti*. **2**, 6–12.

Stoe & Cie GmbH (2021). X-Area, version 2.0 Darmstadt, Germany.

Stöger, B. (2010). Synthesis, characterization and crystal structures of novel alkaline earth oxotellurates. Dissertation, Technical University of Vienna.

Stöger, B. & Weil, M. (2013). The calcium oxotellurate(IV) nitrates $Ca_5Te_4O_{12}(NO_3)_2(H_2O)_2$ and $Ca_6Te_5O_{15}(NO_3)_2$ - Non-classic order/disorder polytypism and a rigid framework structure. *Mineral. Petrol.* **107**, 253–263.

Tananaev & Novoselova, (1967). *Inorg. Mater. (Engl. Transl.)*, **3**, 92. (Entry from PDF-4+ database)

Treacy, M. M. J., Newsam, J. M. & Deem, M. W. (1991). A General Recursion Method for Calculating Diffracted Intensities From Crystals Containing Planar Faults. *Proc. Roy. Soc. Lond.* **A433**, 499–520.

Trömel, M. & Schmid, D. (1972). Tellurite des zweiwertigen Mangans, Kobalts und Nickels. *Z. Anorg. Allg. Chem*. 387, 230–240.

Trömel, M. & Scheller, T. (1976). Die Kristallstruktur von $Co_6Te_5O_{16}$. Z. *Anorg. Allg. Chem*. **427**, 229–234.

Untenecker, H. & Hoppe, R. (1986). Die Koordinationszahl 5 bei Telluraten: $Cs_2K_2[TeO_5]$. *J. less-common met.* **124**, 29–40.

Vannier, R. N., Pernot, E., Anne, M., Isnard, O., Nowogrocki, G. & Mairesse, G. (2003). $Bi_4V_2O_{11}$ polymorph crystal structures related to their electrical properties. *Solid State Ion.* **157**(1−4), 147−153.

Völkl, H., Eder, F., Stöger, B. & Weil, M. (2022). Mixed-valent 1:1 oxidotellurates(IV/VI) of Na, K and Rb: superstructure and three-dimensional disorder. *Z. Kristallogr. – Cryst. Mater.* **238**(1−2), 7−15.

Waldrop, L. (1968a). Crystal structure of triplite. *Sci. Nat*. **55**, 178.

Waldrop, L. (1968b). Crystal structure of triploidite. *Sci. Nat*. **55**, 296−297.

Walitzi, E. M. (1965). Die Kristallstruktur von Denningit, $(Mn,Ca,Zn)Te_2O_5$. Ein Beispiel für die Koordination um vierwertiges Tellur. *Tschermaks min. u. petr. Mitt.* **10**, 241−255.

Weast, R. C. & Astle, M. J. (1982). *CRC Handbook of Chemistry and Physics*, 63rd Edition, D-173. Boca Raton: CRC Press.

Wedel, B. & Sugiyama, K. (1999). Crystal structure of sodium iron aluminium tellurate, a new tellurium compound with garnet structure, $Na_3(Fe,Al)_3Te_2O_{12}$. *Z. Kristallogr. New Cryst. Struct*. **214**, 151–152.

Weidlein, J., Müller, U. & Dehnicke, K. (1981). Schwingungsfrequenzen I (Hauptgruppenelemente); Georg Thieme Verlag: Stuttgart, Germany.

Weil, M. (2004). New phases in the systems Ca–Te–O and Cd–Te–O: the calcium tellurite(IV) $Ca_4Te_5O_{14}$, and the cadmium compounds $Cd_2Te_3O_9$ and $Cd_2Te_2O_7$ with mixed-valent oxotellurium(IV/VI) anions. *Solid State Sci*. **6**, 29−37.

Weil, M. (2006). Mn_3TeO_6. *Acta Cryst.* E**62**, i244−i245.

Weil, M. (2007). New Silver Tellurates – The Crystal Structures of a Third Modification of $Ag_2Te_2O_6$ and of Ag_4TeO_5. *Z. Anorg. Allg. Chem.* **633**(8), 1217−1222.

Weil, M. (2013). Two Modifications of $(TeO)(HAsO_4)$ and its Dehydration Product $(Te_3O_3)(AsO_4)_2$ – Three more Examples of Tellurium(IV) with a Fivefold Oxygen Coordination. *Z. Anorg. Allg. Chem.* **640**(1), 128−135.

Weil, M., Heymann, G. & Huppertz, H. (2016). The High-Pressure Polymorph of $Ca_4Te_5O_{14}$ and the Mixed-Valent Compound $Ca_{13}Te^{VI}_{2/3}Te^{IV}_{3.75}O_{15}(BO_3)_4(OH)_3$. *Eur. J. Inorg. Chem*. 3574–3579.

Weil, M. (2017). Crystal structure of dilead(II) oxochromate(VI) oxotellurate(IV). *Acta Cryst.* E**73**, 853–855.

Weil, M. & Shirkhanlou, M. (2017a). Incorporation of Sulfate or Selenate Groups into Oxotellurates(IV): I. Calcium, Cadmium, and Strontium Compounds. *Z. Anorg. Allg. Chem.* **643**(4), 330–339.

Weil, M. & Shirkhanlou, M. (2017b). Incorporation of Sulfate or Selenate Groups into Oxotellurates(IV): II. Compounds with Divalent Lead. *Z. Anorg. Allg. Chem.* **643**(12), 757–765.

Weil, M. & Shirkhanlou, M. (2017c). Incorporation of Sulfate or Selenate Groups into Oxotellurates(IV): III. Compounds with Magnesium or Zinc. *Z. Anorg. Allg. Chem.* **643**(12), 749–756.

Weil, M., Shirkhanlou, M., Füglein, E. & Libowitzky, E. (2018). Determination of the Correct Composition of "Hydrous Lead(II) Oxotellurate(IV)" as $PbTeO_3$, Crystallizing as a New Polymorph. *Crystals* **8**(1), 51.

Weil, M., Shirkhanlou, M. & Stürzer, T. (2019). Phase Formation Studies of Lead(II) Copper(II) Oxotellurates: The Crystal Structures of Dimorphic $PbCuTeO_5$, $PbCuTe_2O_6$, and $[Pb_2Cu_2(Te_4O_{11})](NO_3)_2$. *Z. Anorg. Allg. Chem.* **645**(3), 347–353.

Weil, M. & Stöger, B. (2008a). $NaFe(TeO_3)_2$. *Acta Cryst*. E**64**, i3.

Weil, M. & Stöger, B. (2008b). A non-twinned polymorph of $CaTe_2O_5$ from a hydro-thermally grown crystal. *Acta Cryst*. C**64**, 79–81.

Weitzel, H. (1976). Kristallstrukturverfeinerung von Wolframiten und Columbiten. *Z. Kristallogr. – Cryst. Mater.* **144**, 238–258.

Weller, M. T., Pack, M. J., Binsted, N. & Dann, S. E. (1999). The structure of cesium tellurate (VI) by combined EXAFS and powder X-ray diffraction. J. Alloys Compd. **282**(1–2), 76–78.

Wisser, T. & Hoppe, R. (1990a). Ein Oxotellurat (VI) neuen Typs: $Rb_6[TeO_5][TeO_4]$. *Z. Anorg. Allg. Chem.* **584**, 105–113.

Wojdyr, M. (2010). Fityk: A general-purpose peak fitting program. *J. Appl. Crystallogr*. **43**, 1126–1128.

Wontcheu, J. & Schleid, T. (2003). $Sc_2Se_3O_9$: Scandium(III) Oxoselenate(IV) According to $Sc_2[SeO_3]_3$ with a Hexagonal "Lone-Pair" Channel Structure. *Z. Anorg. Allg. Chem.* **629**(9), 1463–1465.

Woodward, P. M., Sleight, A. W., Du, L.-S. & Grey, C. P. (1999). Structural Studies and Order–Disorder Phenomenon in a Series of New Quaternary Tellurates of the Type $A^{2+}M^{4+}Te^{6+}O_6$ and $A^{1+}{}_2M^{4+}Te^{6+}O_6$. *J. Solid State Chem*. **147**(1), 99–116.

Wu, M., Su, Q., Hu, N. & Ren, Y. (1992). Synthesis, crystal structure and UV absorption spectrum of bis(dihydrogen tellurato)cuprate (III). *Chin. J. Chem*. **9**(5), 65–69.

Xu, J., Assoud, A., Soheilnia, N., Derakhshan, S., Cuthbert, H. L., Greedan, J. E., Whangbo, M. H. & Kleinke, H. (2005). Synthesis, Structure, and Magnetic Properties of the Layered Copper(II) Oxide $Na_2Cu_2TeO_6$. *Inorg. Chem.* **44**(14), 5042–5046.

Yamada, T. & Iwasaki, H. (1973). Ferroelectric, piezoelectric, and optical properties of $SrTeO_3$ single crystals and phase-transition points in the solid-solution systems. *J. Appl. Phys.* **44**, 3934.

Yamaura, J.-I., Yonezawa, S., Muraoka, Y. & Hiroi, Z. (2006). Crystal structure of the pyrochlore oxide superconductor KOs_2O_6. *J. Solid State Chem*. **179**(1), 336−340.

Yang, L., Powell, D. R. & Houser, R. P. (2007). Structural variation in copper(i) complexes with pyridylmethylamide ligands: structural analysis with a new four-coordinate geometry index, τ_4. *Dalton Trans.* 955−964.

Yu, R., Ok, K. M. & Halasyamani, P. S. (2004). Synthesis and characterization of two novel mixed metal tellurates: $KGaTeO_5{\cdot}H_2O$ and $K_3GaTe_2O_8(OH)_2{\cdot}H_2O$. *Dalton Trans.* 392−396.

Zagorac, D., Müller, H., Ruehl, S., Zagorac, J. & Rehme, S. (2019). Recent developments in the Inorganic Crystal Structure Database: theoretical crystal structure data and related features. *J. Appl. Cryst.* **52**, 918–925.

Zemann, J. (1948). Formel und Strukturtyp des Pharmakosiderits. *Tschermaks min. u. petr. Mitt.* **1**, 1−13.

Zhang, J., Tao, X., Sun, Y., Zhang, Z., Zhang, C., Gao, Z., Xia, H. & Xia, S. (2011). Top-Seeded Solution Growth, Morphology, and Properties of a Polar Crystal $Cs_2TeMo_3O_{12}$. *Cryst. Growth Des.* **11**(5) 1863–1868.

Zhang, J., Zhang, Z.., Sun, Y., Zhang, C., Zhang, S., Liu, Y. & Tao, X. (2012). $MgTeMoO_6$: A neutral layered material showing strong second-harmonic generation. *J. Mater. Chem*. **22**, 9921−9927.

Zhang, Z., Tao, X., Zhang, J., Sun, Y., Zhang, C. & Li, B. (2013). Synthesis, crystal growth, and characterization of the orthorhombic $BaTeW_2O_9$: a new polymorph of $BaTeW_2O_9$. *CrystEngComm.* **15**, 10197−10204.

Zhao, S., Jiang, X., He, R., Zhang, S. Q., Sun, Z., Juo, J., Lin, Z. & Hong, M. (2013). A combination of multiple chromophores enhances second-harmonic generation in a nonpolar noncentrosymmetric oxide: $CdTeMoO_6$. *J. Mater. Chem. C* **1**, 2906−2912.

Zhao, P., Cong, H., Tian, X., Sun, Y., Zhang, Z., Xia, S., Gao, Z. & Tao, X. (2015). Top-Seeded Solution Growth, Structure, Morphology, and Functional Properties of a New Polar Crystal — $Cs_2TeW_3O_{12}$. *Cryst. Growth Des.* **15**(9), 4484–4489.

Ziegler, P., Grigoraviciute, I., Gibson, K., Glaser, J., Kareiva, A. & Meyer, H.-J. (2004). On the characterization of $BiMO_2NO_3$ (*M*=Pb, Ca, Sr, Ba) materials related with the Sillén X1 structure. *J. Solid State Chem*. **177**(10), 3610−3615.

Zimmermann, I., Kremer, R. K. & Johnsson, M. (2011). Synthesis, crystal structure and magnetic properties of the open framework compound $Co_3Te_2O_2(PO_4)_2(OH)_4$. *J. Solid State Chem*. **184**, 3080–3084.

8 Supplementary information

8.1 Details on performed experiments

Information of the synthesis and the obtained phases form experiments performed in this work is collated in Tables 65−67. New phases are presented underlined. If the reaction products were washed with water prior to the analysis, this is signaled by "w:". Dominant unidentified phases are marked with "?". Phases in quotation marks " " are assumed compositions based on similar literature phases.

Table 65. Results of the hydrothermal experiments in the CEM Mars6 240/50 microwave-heated furnace.

Batch	Starting materials	Molar ratios	Color	Identified phases
M1	$Cu(NO_3)_2(H_2O)_{2.5}$, TeO_2, H_6TeO_6	1:1:1	light green	α-TeO_2, γ-TeO_2
M2	$Cu(NO_3)_2(H_2O)_{2.5}$, TeO_2, H_6TeO_6, NH_3	1:1:1:4	green	α-TeO_2, γ-TeO_2, amorphous
M3	$Cu(NO_3)_2(H_2O)_{2.5}$, TeO_2, H_6TeO_6, NH_3	1:1:1:8	green	α-TeO_2, γ-TeO_2, amorphous
M4	$Cu(NO_3)_2(H_2O)_{2.5}$, TeO_2, H_6TeO_6, NH_3	1:1:1:12	light green	α-TeO_2, ?
M5	$Cu(NO_3)_2(H_2O)_{2.5}$, TeO_2, H_6TeO_6, KOH	1:1:1:4	brown	α-TeO_2, CuO, ?
M6	$Cu(NO_3)_2(H_2O)_{2.5}$, TeO_2, H_6TeO_6, KOH	1:1:1:8	greenish brown	Cu_3TeO_6, $Cu_3TeO_6(H_2O)$
M7	$Pb(NO_3)_2$, TeO_2, KOH	2:1:2	white, brownish tinge	α-TeO_2, γ-TeO_2, PbO
M8	$Pb(NO_3)_2$, TeO_2	3:2	white, brownish tinge	α-TeO_2, γ-TeO_2, $Pb_2Te_3O_8$
M9	$Pb(NO_3)_2$, TeO_2, KOH	3:2:4	white, brownish tinge	$PbTeO_3$, PbO, ?
M10	$Pb(NO_3)_2$, TeO_2, KOH	3:2:8	white, brownish tinge	$PbTeO_3$, PbO, ?
M11	$Pb(NO_3)_2$, TeO_2, KOH	1:1:2	white, brownish tinge	$PbTeO_3$, $KPbO_2$
M12	$Pb(NO_3)_2$, TeO_2, KOH	1:1:4	white, brownish tinge	$PbTeO_3$, $KPbO_2$
M13	$Cu(NO_3)_2(H_2O)_{2.5}$, H_6TeO_6, KOH	2:1:2	light green	Cu_3TeO_6, $Cu_3TeO_6(H_2O)$
M14	$Cu(NO_3)_2(H_2O)_{2.5}$, H_6TeO_6, KOH	2:1:6	light green	Cu_3TeO_6, $Cu_3TeO_6(H_2O)$
M15	$Cu(NO_3)_2(H_2O)_{2.5}$, H_6TeO_6, KOH	2:1:10	light green	Cu_3TeO_6, $Cu_3TeO_6(H_2O)$
M16	$Cu(NO_3)_2(H_2O)_{2.5}$, H_6TeO_6, KOH	2:1:16	green	CuO, $K_6Cu_9Te_4O_{24}(H_2O)_2$
M17	CuO, H_6TeO_6, KOH	2:1:2	black	CuO
M18	$MnCO_3$, TeO_2	1:1	light brown	α-TeO_2, γ-TeO_2, $MnCO_3$
M19	$MnCO_3$, TeO_2, KOH	1:1:1	brown	$Mn_2Te_3O_8$
M20	$MnCO_3$, TeO_2, KOH	1:1:2	dark brown	$Mn_6Te_5O_{16}$
M21	$MnCO_3$, TeO_2, KOH	1:1:4	brown	Mn_3O_4
M22	$MnCO_3$, TeO_2, K_2CO_3	1:1:2	brown	Mn_3O_4
M23	$MnCO_3$, TeO_2, KOH, K_2CO_3	1:1:2:2	brown	Mn_3O_4
M24	$MnCO_3$, TeO_2	6:5	light brown	α-TeO_2, γ-TeO_2, $MnCO_3$
M25	$MnCO_3$, TeO_2, KOH	6:5:5	brown	$Mn_2Te_3O_8$
M26	$MnCO_3$, TeO_2, KOH	6:5:10	dark brown	$Mn_6Te_5O_{16}$, $MnCO_3$, $K_6Mn_2O_6$
M27	$MnCO_3$, TeO_2, KOH	6:5:20	brown	Mn_3O_4
M28	$MnCO_3$, TeO_2, K_2CO_3	6:5:10	brown	Mn_3O_4
M29	$MnCO_3$, TeO_2, KOH, K_2CO_3	6:5:10:10	brown	Mn_3O_4

Table 66. Results of performed solid-state reactions.

Batch	Starting materials	Molar ratios	Crucible	T / °C	Atm.	Color	Identified phases
S1	$[Ni(OH)_2]_2(NiCO_3)(H_2O)_4$, TeO_2, WO_3	1:3:3	Pt	760	air	dark yellow	$NiWO_4$, α-TeO_2
S2	$CoC_2O_4(H_2O)_2$, TeO_2, WO_3	1:1:1	Pt	760	air	dark blue	$CoWO_4$, α-TeO_2
S3	$[Ni(OH)_2]_2(NiCO_3)(H_2O)_4$, TeO_2, WO_3	4:3:3	Pt	760	air	dark yellow	$NiWO_4$, NiO, Ni_3TeO_6
S4	"$NiTeO_3$", WO_3	2:1	Pt	760	air	dark yellow, green	Ni_3TeO_6, $NiWO_4$
S5	$[Ni(OH)_2]_2(NiCO_3)(H_2O)_4$, TeO_2, WO_3	1:3:3	Pt	600	air	yellow	α-TeO_2, $NiWO_4$
S6	$[Ni(OH)_2]_2(NiCO_3)(H_2O)_4$, TeO_2, WO_3	1:3:6	Pt	600	air	dark yellow	$NiWO_4$, α-TeO_2, WO_3
S7	"$NiTeO_3$", WO_3	2:1	Pt	600	air	dark yellow	TeO_2, $NiTe_2O_5$ $NiWO_4$
S8	"$CoTeO_3$", WO_3	2:1	Pt	600	air	dark purple, brown	TeO_2, $CoWO_4$
S9	$Fe(NO_3)_3(H_2O)_9$, K_2TeO_3, KNO_3	1:1:>25	Pt	360	air	brown	w: Fe_2TeO_6
S10	$Ni(NO_3)_2(H_2O)_6$, K_2TeO_3, KNO_3	1:1:>30	Pt	360	air	brown grey	w: NiO, $NiTeO_4$, , "$KTe_2O_{6.5}(H_2O)$"
S11	$ZrO(NO_3)_2(H_2O)_6$, TeO_2, WO_3	1:3:3	Pt	750	air	bright yellow	$ZrTe_3O_8$, WO_3
S12	$Ni(NO_3)_2(H_2O)_6$, TeO_2, As_2O_3	2:1:3	Pt	400	air	light green	α-TeO_2, NiO
S13	$Cu(NO_3)_2(H_2O)_{2.5}$, H_6TeO_6, KOH	2:1:8	Pt	500	air	black, green	w: $K_2Cu_2TeO_6$, CuO,
S14	$Fe(NO_3)_3(H_2O)_9$, H_6TeO_6, KOH	3:2:15	Pt	500	air	light brown, dark brown, red brown	w: $K_{12}Fe_6Te_4O_{27}(H_2O)_3$
S15	Fe_2O_3, H_6TeO_6, KOH	3:2:6	Pt	600	air	red brown, yellow	w: Fe_2O_3, ?
S16	$CoCO_3$, TeO_2, H_6TeO_6, KNO_3	2:1:1:exc.	Pt	900	air	black	w: KCo_2O_4, $KCoPtO_4$
S17	$CoCO_3$, TeO_2, H_6TeO_6, KCl	2:1:1:exc.	Pt	900	air	black	w: Co_3TeO_6
S18	Fe_2O_3, H_3BO_3, H_6TeO_6	1:1:1	Pt	800	air	brown, orange tinge	Fe_2TeO_6
S19	$CuCO_3Cu(OH)_2$, H_6TeO_6, KNO_3, K_2CO_3	1:2:0.8:0.8	Pt	800	air	green	w: CuO, $K_2Cu_2TeO_6$, ?
S20	$[Ni(OH)_2]_2(NiCO_3)(H_2O)_4$, TeO_2, KNO_3, K_2CO_3	1:3:1.2:1.2	Pt	800	air	olive green	w: ?
S21	MnO, TeO_2	5:3	Pt	650	Ar	brown	α-$MnTeO_3$, $Mn_2Te_3O_8$, Mn_3TeO_6
S22	MnO, TeO_2	2:1	Pt	650	Ar	brown	α-$MnTeO_3$, $Mn_6Te_5O_{16}$, Mn_3TeO_6, Mn_3O_4
S23	MnO, TeO_2	1:1	silica glass	720	vacuum	brown	α-$MnTeO_3$
S24	MnO, TeO_2	6:5	silica glass	650	vacuum	brown	$Mn_2Te_3O_8$, Mn_3O_4, MnO, MnO_2
S25	MnO, TeO_2	1:1	silica glass	720	air	brown	Mn_2TeO_6, $MnTe_2O_5$, Mn_3TeO_6, Mn_2O_3, Mn_3O_4
S26	MnO, TeO_2	6:5	silica glass	650	air	brown	$Mn_2Te_3O_8$, Mn_3TeO_6, $MnTe_2O_5$, Mn_2O_3, Mn_3O_4
S27	MnO, TeO_2	1:1	silica glass	700	vacuum	brown	α-$MnTeO_3$, Mn_2O_3
S28	MnO, TeO_2	1:1	silica glass	675	vacuum	brown	α-$MnTeO_3$, Mn_3O_4
S29	MnO, TeO_2	1:1	silica glass	650	vacuum	brown	α-$MnTeO_3$, $Mn_2Te_3O_8$, Mn_3O_4
S30	MnO, TeO_2	1:1	silica glass	750	vacuum	brown	$Mn_2Te_3O_8$, Mn_3TeO_6, Mn_3O_4, $MnTe_6O_{13}$
S31	MnO, TeO_2	1:1	silica glass	650	vacuum	brown	$Mn_2Te_3O_8$, Mn_3O_4, MnO
S32	MnO, TeO_2	1:1	silica glass	650	vacuum	brown	$Mn_2Te_3O_8$, Mn_3O_4, α-$MnTeO_3$
S33	Cr_2O_3, KNO_3, H_6TeO_6	3:2:2	glass	425	air	green	Cr_2O_3, $K_3CrTe_3O_{12}(H_2O)$
S34	Fe_2O_3, KNO_3, H_6TeO_6	3:2:2	glass	425	air	dark red	Fe_2O_3, SiO_2, KTe_2O_6, $K_3FeTe_5O_{18}$
S35	Al_2O_3, KNO_3, H_6TeO_6	3:2:2	glass	425	air	white	KTe_2O_6, α-TeO_2, γ-Al_2O_3
S36	Ga_2O_3, KNO_3, H_6TeO_6	3:2:2	glass	425	air	light yellow	Ga_2O_3, KTe_2O_6, ?
S37	Cr_2O_3, KNO_3, H_6TeO_6	1:6:6	glass	425	air	green	$K_3CrTe_3O_{13}(H_2O)$
S38	Fe_2O_3, KNO_3, H_6TeO_6	1:6:6	glass	425	air	dark red	Fe_2O_3, KTe_2O_6, Te, $K_3FeTe_5O_{18}$, ?
S39	Al_2O_3, KNO_3, H_6TeO_6	1:6:6	glass	425	air	white	KTe_2O_6, KNO_3, ?
S40	Ga_2O_3, KNO_3, H_6TeO_6	1:6:6	glass	425	air	light yellow	KTe_2O_6, Ga_2O_3, $K_3GaTe_3O_{12}$, ?
S41	Cr_2O_3, KNO_3, H_6TeO_6	1:6:6	glass	550	air	green	$K_3CrTe_5O_{18}$
S42	Fe_2O_3, KNO_3, H_6TeO_6	1:6:6	glass	550	air	dark red	$FeCO_3$, Fe_2O_3, ?
S43	Al_2O_3, KNO_3, H_6TeO_6	1:6:6	glass	550	air	white	KTe_2O_6, ?

S44	Ga_2O_3, KNO_3, H_6TeO_6	1:6:6	glass	550	air	light yellow	Ga_2O_3, KTe_2O_6, $K_3GaTe_3O_{12}$, ?
S45	PbO, TeO_2, Cr_2O_3	2:1:1	Al	600	air	dark green, orange	?
S46	CuO, TeO_2, Cr_2O_3	2:1:1	Al	600	air	dark	Cu_3TeO_6, Cr_2TeO_6, CuO, α-TeO_2
S47	CdO, TeO_2, Cr_2O_3	2:1:1	Al	600	air	green, bright yellow	$CdCr_2O_4$, Cd_3TeO_6, α-$CdTe_2O_5$, $Cd_2Te_2O_7$
S48	MnO, TeO_2, WO_3	2:1:1	Al	600	air	green brown	α-TeO_2, WO_3, $MnWO_4$, Mn_3O_4
S49	CdO, TeO_2, WO_3	2:1:1	Al	600	air	bright yellow	$CdWO_4$, γ-TeO_2
S50	CoO, TeO_2, TeO_3	2:1:1	Al	600	air	red brown	Co_3O_4, α-TeO_2, $CoTeO_4$, Co_2TeO_4
S51	CuO, TeO_2, TeO_3	2:1:1	Al	600	air	black	Cu_3TeO_6, ?
S52	Fe_2O_3, TeO_2, TeO_3	3:2:2	Al	600	air	red brown	α-TeO_2, Fe_2TeO_6
S53	ZnO, TeO_2, TeO_3	2:1:1	Al	600	air	pale yellow	$Zn_2Te_3O_8$, Zn_3TeO_6
S54	Cr_2O_3, TeO_2, TeO_3	3:2:2	Al	600	air	green	Cr_2O_3, Cr_2TeO_6, α-TeO_2
S55	NiO, TeO_2, TeO_3	2:1:1	Al	600	air	yellow green	NiO, $NiTe_2O_5$
S56	CdO, TeO_2, TeO_3	2:1:1	Al	600	air	bright yellow	$Cd_2Te_2O_7$, α-$CdTe_2O_5$, Cd_3TeO_6
S57	MnO, TeO_2, TeO_3	2:1:1	Al	600	air	black	$MnTe_2O_5$, Mn_2TeO_6, $MnTe_6O_{13}$, Mn_3O_4
S58	MnO, TeO_2, B_2O_3	2:1:6	Al	600	air	dark grey	MnO, $MnTe_6O_{13}$
S59	CuO, TeO_2, B_2O_3	2:1:6	Al	600	air	blue	CuB_2O_4, α-TeO_2
S60	Fe_2O_3, TeO_2, B_2O_3	1:1:6	Al	600	air	red brown	Fe_2O_3, Fe_2TeO_6, ?
S61	ZnO, TeO_2, B_2O_3	2:1:6	Al	600	air	bright yellow	$Zn_2Te_3O_8$, ZnB_4O_7
S62	Cr_2O_3, TeO_2, B_2O_3	1:1:6	Al	600	air	green	Cr_2O_3, α-TeO_2, B_2O_3
S63	NiO, TeO_2, B_2O_3	2:1:6	Al	600	air	bright green	NiO, α-TeO_2, ?
S64	CdO, TeO_2, B_2O_3	2:1:6	Al	600	air	pale yellow	CdB_4O_7, α-$CdTe_2O_5$
S65	PbO, TeO_2, B_2O_3	2:1:6	Al	600	air	pale brown	PbB_4O_7, $Pb_2Te_3O_8$
S66	MnO, TeO_3, B_2O_3	2:1:6	Al	600	air	black, white	MnO, α-TeO_2, $MnTe_6O_{13}$, MnB_4O_7, B_2O_3, $Mn_2Te_3O_8$
S67	CuO, TeO_3, B_2O_3	2:1:6	Al	600	air	blue	CuB_2O_4, α-TeO_2
S68	Fe_2O_3, TeO_3, B_2O_3	1:1:6	Al	600	air	dark red brown	Fe_3BO_6, B_2O_3
S69	ZnO, TeO_3, B_2O_3	2:1:6	Al	600	air	white	$Zn_2Te_3O_8$, ZnB_4O_7, α-TeO_2
S70	Cr_2O_3, TeO_3, B_2O_3	1:1:6	Al	600	air	green	Cr_2O_3, α-TeO_2, B_2O_3
S71	NiO, TeO_3, B_2O_3	2:1:6	Al	600	air	bright green	NiO, α-TeO_2, $NiTe_2O_5$, H_3BO_3
S72	CdO, TeO_3, B_2O_3	2:1:6	Al	600	air	pale yellow	CdB_4O_7, α-$CdTe_2O_5$
S73	PbO, TeO_3, B_2O_3	2:1:6	Al	600	air	pale brown	PbB_4O_7, α-$PbTeO_3$
S74	CuO, H_6TeO_6, KOH	1:1:8	Pt	400	air	black, brown	$K_{10}Cu_2Te_3O_{16}$, $K_2CO_3(H_2O)_{1.5}$
S75	CuO, H_6TeO_6, KOH	2:3:10	Pt	400	air	olive green	CuO, $KHCO_3$, $K_5CuTe_2O_8(OH)_4(H_2O)_8$*

* For details on the formation conditions of $K_5CuTe_2O_8(OH)_4(H_2O)_8$, see 4.2.2.6.2.

Table 67. Details on experiments performed under hydrothermal conditions.

Batch	Starting Materials	Molar ratios	Water	Color	Identified phases
H1	$Co(NO_3)_2(H_2O)_6$, TeO_2, KOH	2:1:2	yes	black, brown	$CoTeO_4$, Co_3O_4
H2	$Cu(NO_3)_2(H_2O)_{2.5}$, TeO_2, KOH	2:1:2	yes	bright green	Cu_3TeO_6, $CuTe_2O_5$, KNO_3
H3	$Fe(NO_3)_3(H_2O)_9$, TeO_2, KOH	2:1:2	yes	light brown	Fe_2TeO_6, Fe_2O_3
H4	$Zn(NO_3)_2(H_2O)_6$, TeO_2, KOH	2:1:2	yes	white	$ZnTeO_3$, $Zn_2Te_3O_8$
H5	$Cr(NO_3)_3(H_2O)_9$, TeO_2, KOH	2:1:2	yes	brown	Cr_2TeO_6
H6	$Ni(NO_3)_2(H_2O)_2$, TeO_2, KOH	2:1:2	yes	bright green, red	"$Ni_3(TeO_3)_2(OH)_2$", $Ni_2Te_3O_8$
H7	$Cd(NO_3)_2(H_2O)_6$, TeO_2, KOH	2:1:2	yes	very light brown	$\underline{Cd_5(TeO_3)_4(NO_3)_2}$
H8	$Pb(NO_3)_2$, TeO_2, KOH	2:1:2	yes	white, bright yellow	$Pb(NO_3)_2$, $\underline{Pb_3Te_2O_6(NO_3)_2}$
H9	$Co(NO_3)_2(H_2O)_6$, TeO_2, HNO_3	1:1:5	yes	yellow	α-TeO_2
H10	$Cu(NO_3)_2(H_2O)_{2.5}$, TeO_2, HNO_3	1:1:5	yes	yellow	α-TeO_2
H11	$Fe(NO_3)_3(H_2O)_9$, TeO_2, HNO_3	1:1:5	yes	brown	Fe_2TeO_6
H12	$Zn(NO_3)_2(H_2O)_6$, TeO_2, HNO_3	1:1:5	yes	yellow	α-TeO_2
H13	$Cr(NO_3)_3(H_2O)_9$, TeO_2, HNO_3	1:1:5	yes	dark brown	"$Cr_{1-x}Te_xO_2$"
H14	$Ni(NO_3)_2(H_2O)_2$, TeO_2, HNO_3	1:1:5	yes	yellow	α-TeO_2
H15	$Cd(NO_3)_2(H_2O)_6$, TeO_2, HNO_3	1:1:5	yes	yellow	α-TeO_2
H16	$Pb(NO_3)_2$, TeO_2, HNO_3	1:1:5	yes	yellow	α-TeO_2
H17	$Co(NO_3)_2(H_2O)_6$, TeO_2, NH_3	2:1:10	yes	black	$Co_{\sim 2.7}O_4$, TeO_2, "$Co_3(TeO_3)_2(OH)_2$", $Co_2Te_3O_8$
H18	$Cu(NO_3)_2(H_2O)_{2.5}$, TeO_2, NH_3	2:1:10	yes	yellow green, green	$CuTeO_3$, Cu_3TeO_6
H19	$Fe(NO_3)_3(H_2O)_9$, TeO_2, NH_3	2:1:10	yes	orange brown	Fe_2O_3, α-TeO_2
H20	$Zn(NO_3)_2(H_2O)_6$, TeO_2, NH_3	2:1:10	yes	white	$ZnTeO_3$
H21	$Cr(NO_3)_3(H_2O)_9$, TeO_2, NH_3	2:1:10	yes	green	CrO(OH) (amorphous)
H22	$Ni(NO_3)_2(H_2O)_2$, TeO_2, NH_3	2:1:10	yes	bright green	$NiTe_2O_5$, $Ni_2Te_3O_8$, "$Ni_3(TeO_3)_2(OH)_2$", $Ni(NO_3)(OH)(H_2O)_{0.5}$
H23	$Cd(NO_3)_2(H_2O)_6$, TeO_2, NH_3	2:1:10	yes	white	$CdTeO_3$, α-TeO_2
H24	$Pb(NO_3)_2$, TeO_2, NH_3	2:1:10	yes	bright brown	PbO, α-TeO_2, "$MPbO_2(NO_3)$"
H25	CuO, TeO_2, WO_3	4:2:3	yes	yellow, grey	CuO, α-TeO_2, γ-TeO_2, WO_3
H26	Fe_2O_3, TeO_2, WO_3	2:2:3	yes	yellow, red	Fe_2O_3, α-TeO_2, γ-TeO_2, WO_3
H27	ZnO, TeO_2, WO_3	4:2:3	yes	white	$ZnWO_4$, $ZnTeO_3$, ?
H28	Cr_2O_3, TeO_2, WO_3	2:2:3	yes	yellow, green	Cr_2O_3, α-TeO_2, γ-TeO_2, WO_3
H29	NiO, TeO_2, WO_3	4:2:3	yes	yellow, green	NiO, TeO_2, WO_3
H30	CdO, TeO_2, WO_3	4:2:3	yes	light brown	$CdWO_4$, WO_3
H31	PbO, TeO_2, WO_3	4:2:3	yes	light green	PbO, TeO_2, $PbWO_4$
H32	MnO, TeO_2, WO_3	4:2:3	yes	yellow, dark green, brown	$MnWO_4$, MnO, WO_3, ?
H33	NiO, TeO_2, WO_3, KOH	4:2:3:12	yes	green	NiO
H34	NiO, TeO_2, WO_3, NH_3	4:2:3:16	yes	yellow, green	NiO, TeO_2, "$(NH_4)_2W_3O_9(TeO_3)$", ?
H35	NiO, TeO_2, As_2O_3	2:1:1	yes	green	As_2O_3, NiO, TeO_2, Te, $H_{1.84}Ni_{6.58}(AsO_4)_4(OH)_3$
H36	NiO, TeO_2, As_2O_3, NH_3	2:1:1:7	yes	dark green	$(NH_4)H_2AsO_4$, Te, $\underline{(NH_4)Ni_3(HAsO_4)(AsO_4)(OH)_2}$
H37	NiO, TeO_2, As_2O_3, KOH	2:1:1:6	yes	light green	NiO, Te
H38	NiO, TeO_2, As_2O_3	2:2:1	yes	green	NiO, TeO_2, As_2O_3, $H_{1.84}Ni_{6.58}(AsO_4)_4(OH)_3$
H39	CuO, TeO_2, WO_3, NH_3	4:2:3:12	yes	bright green, black	CuO, $Cu_2WO_4(OH)_2$, α-TeO_2
H40	Fe_2O_3, TeO_2, WO_3, NH_3	2:2:3:12	yes	red, light brown	Fe_2O_3, α-TeO_2, γ-TeO_2, "$(NH_4)_2W_3O_9(TeO_3)$"
H41	ZnO, TeO_2, WO_3, NH_3	4:2:3:12	yes	white, light yellow	$ZnWO_4$, $ZnTeO_3$
H42	Cr_2O_3, TeO_2, WO_3, NH_3	2:2:3:12	yes	green, light yellow	Cr_2O_3, TeO_2, WO_3, "$(NH_4)_2W_3O_9(TeO_3)$"
H43	NiO, TeO_2, WO_3, NH_3	4:2:3:12	yes	light green, light yellow	NiO, α-TeO_2, "$(NH_4)_2W_3O_9(TeO_3)$"
H44	CdO, TeO_2, WO_3, NH_3	4:2:3:12	yes	white	$CdWO_4$, "$Cd_3WO_4(TeO_3)_2$"
H45	PbO, TeO_2, WO_3, NH_3	4:2:3:12	yes	light yellow, orange	$PbWO_4$, PbO, "$(NH_4)_2W_3O_9(TeO_3)$"
H46	MnO, TeO_2, WO_3, NH_3	4:2:3:12	yes	light brown	$MnWO_4$, $MnTe_2O_5$, "$(NH_4)_2W_3O_9(TeO_3)$"
H47	NiO, TeO_2, H_6TeO_6, KOH	4:1:1:2	yes	green, light brown	NiO, $KTeO_3(OH)$, ?
H48	NiO, TeO_2, H_6TeO_6, NH_3	4:1:1:2	yes	green	NiO, α-TeO_2, ?
H49	NiO, TeO_2, H_6TeO_6	4:1:1	yes	brown yellow	α-TeO_2, $NiTeO_4$
H50	MnO, TeO_2, H_6TeO_6, NH_3	2:1:2:12	yes	black, light brown	MnO, $(NH_4)Te_2O_5(OH)$, "$(NH_4)Te_2O_{6.5}(H_2O)$"
H51	CuO, TeO_2, H_6TeO_6, NH_3	2:1:2:12	yes	light green, dark green, red brown	Cu_3TeO_6, "$(NH_4)Te_2O_{6.5}(H_2O)$", $(NH_4)Te_2O_5(OH)$, $\underline{Cu_2Te_4O_{12}(H_2O)_2(NH_3)}$
H52	Fe_2O_3, TeO_2, H_6TeO_6, NH_3	2:1:2:12	yes	red, light brown	Fe_2O_3, $(NH_4)Te_2O_5(OH)$, "$(NH_4)Te_2O_{6.5}(H_2O)$"
H53	ZnO, TeO_2, H_6TeO_6, NH_3	2:1:2:12	yes	light yellow, dark yellow	$(NH_4)Te_2O_5(OH)$, "$(NH_4)Te_2O_{6.5}(H_2O)$", Zn_3TeO_6
H54	Cr_2O_3, TeO_2, H_6TeO_6, NH_3	2:1:2:12	yes	green, light yellow	Cr_2O_3, $(NH_4)Te_2O_5(OH)$, "$(NH_4)Te_2O_{6.5}(H_2O)$"
H55	NiO, TeO_2, H_6TeO_6, NH_3	2:1:2:12	yes	light green, brown	NiO, $(NH_4)Te_2O_5(OH)$, "$(NH_4)Te_2O_{6.5}(H_2O)$"
H56	CdO, TeO_2, H_6TeO_6, NH_3	2:1:2:12	yes	light yellow, dark yellow	α-TeO_2, ?
H57	PbO, TeO_2, H_6TeO_6, NH_3	2:1:2:12	yes	white, brown	PbO, Pb_2OCO_3, $(NH_4)Te_2O_5(OH)$
H58	$MnCO_3$, TeO_2, NH_3	1:1:2	yes	dark brown, flesh-colored	$Mn_2Te_3O_8$, $MnCO_3$

H59	$MnCO_3$, TeO_2, KOH	1:1:2	yes	dark brown, light brown	$Mn_2Te_3O_8$, $\underline{\gamma\text{-}MnTeO_3}$, "$\underline{Mn_3(TeO_3)_2(OH)_2}$"
H60	$MnCO_3$, TeO_2, NH_3, K_2CO_3	1:1:2:2	yes	dark brown, light brown	$Mn_2Te_3O_8$, $MnCO_3$
H61	$MnCO_3$, TeO_2, KOH, K_2CO_3	1:1:2:2	yes	brown, white	$\underline{Mn_6Te_5O_{16}}$, "$\underline{Mn_3(TeO_3)_2(OH)_2}$"
H62	$NiCO_3(Ni(OH)_2)_2(H_2O)_4$, TeO_2, H_3PO_4	1:3:3	yes	light green, light yellow	α-TeO_2, $\underline{Ni_3Te_2O_2(PO_4)_2(OH)_4}$
H63	$NiCO_3(Ni(OH)_2)_2(H_2O)_4$, TeO_2, H_3PO_4, KOH	1:3:3:9	yes	turquoise	$Ni(OH)_2$, ?
H64	$NiCO_3(Ni(OH)_2)_2(H_2O)_4$, TeO_2, H_3PO_4, NH_3	1:3:3:12	yes	light green, red brown	$Ni_2Te_3O_8$, $Ni(NH_4)PO_4(H_2O)$
H65	MnO, TeO_2, H_6TeO_6, KOH	2:1:2:15	yes	dark brown	MnO, $KMn_4O_8(H_2O)_3$
H66	CuO, TeO_2, H_6TeO_6, KOH	2:1:2:15	yes	green	CuO, ?
H67	Fe_2O_3, TeO_2, H_6TeO_6, KOH	1:1:2:15	yes	red	Fe_2O_3
H68	ZnO, TeO_2, H_6TeO_6, KOH	2:1:2:15	yes	white	Zn_3TeO_6
H69	Cr_2O_3, TeO_2, H_6TeO_6, KOH	1:1:2:15	yes	green	Cr_2O_3
H70	NiO, TeO_2, H_6TeO_6, KOH	2:1:2:15	yes	bright green, light brown	NiO
H71	CdO, TeO_2, H_6TeO_6, KOH	2:1:2:15	yes	bright yellow	β-Cd_3TeO_6
H72	PbO, TeO_2, H_6TeO_6, KOH	2:1:2:15	yes	bright yellow	Pb_2TeO_5
H73	$Ni(NO_3)_2(H_2O)_6$, TeO_2, H_6TeO_6	2:1:2	yes	brown	$NiTeO_4$, TeO_2
H74	$Ni(NO_3)_2(H_2O)_6$, TeO_2, H_6TeO_6, KOH	2:1:2:15	yes	light green	KNO_3, ?
H75	$Ni(NO_3)_2(H_2O)_6$, TeO_2, H_6TeO_6, NH_3	2:1:2:12	yes	turquoise, green, brown	TeO_2, "$(NH_4)Te_2O_{6.5}(H_2O)$", ?
H76	$Ni(NO_3)_2(H_2O)_6$, TeO_2, H_6TeO_6, KOH	2:1:2:8	yes	light green,	$KTeO_3(OH)$
H77	$MnCO_3$, TeO_2, H_3PO_4	1:1:1	yes	brown, light brown	α-TeO_2, γ-TeO_2, $Mn_{2.5}(HPO_4)(PO_4)(H_2O)_2$
H78	$CuCO_3(Cu(OH)_2)_2$, TeO_2, H_3PO_4	1:3:3	yes	dark green, white	α-TeO_2, γ-TeO_2, $Cu_2PO_4(OH)$
H79	$Fe(NO_3)_3(H_2O)_9$, TeO_2, H_3PO_4, NH_3	1:1:1:2	yes	dark yellow	$Fe_{1.19}(PO_4)O_{0.57}(H_2O)_{0.43}$, α-TeO_2, H_6TeO_6
H80	$Zn(NO_3)_2(H_2O)_6$, TeO_2, H_3PO_4, NH_3	1:1:1:2	yes	dark yellow, light yellow	α-TeO_2, γ-TeO_2, $Zn_3(PO_4)_2(H_2O)$
H81	$Cr(NO_3)_3(H_2O)_9$, TeO_2, H_3PO_4, NH_3	1:1:1:2	yes	light brown, dark brown	$CrPO_4(H_2O)_6$, "$Cr_{1-x}Te_xO_2$", H_6TeO_6
H82	$NiCO_3(Ni(OH)_2)_2$, TeO_2, H_3PO_4	2:4:5	yes	light green, white	$\underline{Ni_3Te_2O_2(PO_4)_2(OH)_4}$, α-TeO_2
H83	$CdCO_3$, TeO_2, H_3PO_4	1:1:1	yes	white, light yellow	α-TeO_2, $\underline{Cd_2(PO_4)(OH)}$
H84	$Pb(OH)_2(PbCO_3)_2$, TeO_2, H_3PO_4	1:3:3	yes	white	α-TeO_2, $HPbPO_4$
H85	$Ni(NO_3)_2(H_2O)_6$, TeO_2, H_6TeO_6, KOH	4:1:1:4	yes	yellow brown	$NiTeO_4$
H86	$Ni(NO_3)_2(H_2O)_6$, TeO_2, H_6TeO_6, KOH	4:1:1:8	yes	green	"$Ni_3(TeO_3)_2(OH)_2$", KNO_3
H87	$Ni(NO_3)_2(H_2O)_6$, TeO_2, H_6TeO_6, NH_3	4:1:1:4	yes	yellow brown	$NiTeO_4$
H88	$Ni(NO_3)_2(H_2O)_6$, TeO_2, H_6TeO_6, NH_3	4:1:1:10	yes	pale green	?
H89	NiO, $As_2O_5(H_2O)_{2.5}$, NH_3	2:1:20	yes	green	NiO, ?
H90	TeO_2, WO_3, NH_3	1:3:12	yes	white	"$(NH_4)_2W_3O_9(TeO_3)$"
H91	$Ni(NO_3)_2(H_2O)_6$, $As_2O_5(H_2O)_{2.5}$, NH_3	5:1:50	yes	green	$\underline{(NH_4)Ni_3(HAsO_4)(AsO_4)(OH)_2}$, ?
H92	$MnCO_3$, TeO_2, H_3PO_4, NH_3	1:1:1:6	yes	light brown	$MnTe_2O_5$, $Mn(NH_4)PO_4(H_2O)$
H93	$CuCO_3(Cu(OH)_2)_2$, TeO_2, H_3PO_4, NH_3	1:1:1:6	yes	green	$CuTe_2O_5$
H94	$Fe(NO_3)_3(H_2O)_9$, TeO_2, H_3PO_4, NH_3	1:1:1:6	yes	light brown	α-TeO_2, γ-TeO_2, $NH_4Fe_2(PO_4)(OH)(H_2O)_2$
H95	$Zn(NO_3)_2(H_2O)_6$, TeO_2, H_3PO_4, NH_3	1:1:1:6	yes	light grey, light yellow	α-TeO_2, $Zn(NH_4)PO_4$, $Zn_3(PO_4)_2(H_2O)$
H96	$Cr(NO_3)_3(H_2O)_9$, TeO_2, H_3PO_4, NH_3	1:1:1:6	yes	grey green	α-TeO_2, γ-TeO_2, amorphous
H97	$NiCO_3(Ni(OH)_2)_2$, TeO_2, H_3PO_4, NH_3	1:1:1:6	yes	light green, brown	$Ni(NH_4)PO_4(H_2O)$, $Ni_2Te_3O_8$
H98	$CdCO_3$, TeO_2, H_3PO_4, NH_3	1:1:1:6	yes	white, light brown	α-$CdTe_2O_5$, $Cd_5(PO_4)_4(OH)_2$
H99	$Pb(OH)_2(PbCO_3)_2$, TeO_2, H_3PO_4, NH_3	1:1:1:6	yes	white, light yellow	$Pb_3(PO_4)_2$, $Pb_5(PO_4)_3(OH)$, α-TeO_2, $Pb_2Te_3O_8$
H100	CuO, TeO_2, H_6TeO_6, KOH	2:1:2:15	? (no)	green, blue, white	CuO, $K_2CO_3(H_2O)_{1.5}$, $\underline{K_2Cu_2TeO_6}$, $\underline{K_3CuTeO_5(OH)(H_2O)}$
H101	Fe_2O_3, TeO_2, H_6TeO_6, KOH	1:1:2:15	? (no)	red brown, white	w: $\underline{K_{12}Fe_6Te_4O_{27}(H_2O)_3}$, Fe_2O_3
H102	ZnO, TeO_2, H_6TeO_6, KOH	2:1:2:15	? (no)	white	$K_2CO_3(H_2O)_{1.5}$, ZnO
H103	Cr_2O_3, TeO_2, H_6TeO_6, KOH	1:1:2:15	? (no)	green, white	Cr_2O_3, $K_2CO_3(H_2O)_{1.5}$
H104	CuO, H_6TeO_6, KOH	2:1:5	no	green	$K_2CuTeO_4(OH)_2(H_2O)$, $K_2CO_3(H_2O)_{1.5}$, CuO, $\underline{K_2Cu_2TeO_6(H_2O)}$ w: $\underline{K_2Cu_2TeO_6}$, CuO

H105	CuO, H_6TeO_6, KOH	2:1:5	open	turquoise, grey, light yellow	w: ?
H106	$Co(NO_3)_2(H_2O)_6$, TeO_2, H_6TeO_6, NH_3	2:1:1:6	yes	brown	$CoTeO_4$, $Co_2Te_3O_8$
H107	$Cu(NO_3)_2(H_2O)_{2.5}$, TeO_2, H_6TeO_6, NH_3	2:1:1:6	yes	bright green	Cu_3TeO_6, α-TeO_2, CuO, ?
H108	$Fe(NO_3)_3(H_2O)_9$, TeO_2, H_6TeO_6, NH_3	2:1:1:6	yes	dark yellow, brown	Fe_2TeO_6
H109	$Zn(NO_3)_2(H_2O)_6$, TeO_2, H_6TeO_6, NH_3	2:1:1:6	yes	white, light brown	α-TeO_2, $ZnTeO_3$, "$(NH_4)Te_2O_{6.5}(H_2O)$"
H110	$Cr(NO_3)_3(H_2O)_9$, TeO_2, H_6TeO_6, NH_3	2:1:1:6	yes	dark brown	amorphous
H111	$Ni(NO_3)_2(H_2O)_2$, TeO_2, H_6TeO_6, NH_3	2:1:1:6	yes	turquoise, red brown	TeO_2, $NiTeO_4$, "$(NH_4)Te_2O_{6.5}(H_2O)$", ?
H112	$Cd(NO_3)_2(H_2O)_6$, TeO_2, H_6TeO_6, NH_3	2:1:1:6	yes	bright yellow	β-$CdTe_2O_5$, Cd_3TeO_6
H113	$Pb(NO_3)_2$, TeO_2, H_6TeO_6, NH_3	2:1:1:6	yes	bright yellow	$Pb_2Te_3O_8$, $PbTeO_3$
H114	NiO, TeO_2, H_6TeO_6, KOH	3:2:2:15	no	white, pale green	NiO, $K_2CO_3(H_2O)_{1.5}$
H115	NiO, TeO_2, H_6TeO_6	3:2:2	no	yellow, light brown	$Te_2O_4(OH)_2$, TeO_2, NiO, $NiTeO_4$
H116	$Ni(NO_3)_2(H_2O)_6$, TeO_2, H_6TeO_6, KOH	3:2:2:15	no	light green, green	$Ni(NO_3)_2(H_2O)_{2?}$, $Ni_3(NO_3)_2(OH)_4$, KNO_3, $Ni_2Te_3O_8$
H117	$Ni(NO_3)_2(H_2O)_6$, TeO_2, H_6TeO_6	3:2:2	no	light yellow, brown	$NiTeO_4$, $Te_2O_4(OH)_2$
H118	$Ni(NO_3)_2(H_2O)_6$, TeO_2, KOH	3:2:15	no	light green	KNO_3, $K_2TeO_3(H_2O)_3$, $Ni(OH)_2$, $K_2CO_3(H_2O)_{1.5}$
H119	$Ni(NO_3)_2(H_2O)_6$, TeO_2	3:2	no	light green, green	$Ni(NO_3)_2(H_2O)_6$, α-TeO_2, γ-TeO_2
H120	$Ni(NO_3)_2(H_2O)_6$, TeO_2, H_6TeO_6, KOH	3:2:2:15	no	light green, dark green, brown	$NiTeO_3$, "$Ni_3(TeO_3)_2(OH)_2$"
H121	$Co(NO_3)_2(H_2O)_6$, TeO_2, H_3AsO_4, KOH	2:1:1:6	yes	purple	"$Co_3(TeO_3)_2(OH)_2$", $Co(NO_3)_2(H_2O)_6$
H122	$Cu(NO_3)_2(H_2O)_{2.5}$, TeO_2, H_3AsO_4, KOH	2:1:1:6	yes	brown, light green	$Cu_2AsO_4(OH)$, CuO, KNO_3
H123	$Fe(NO_3)_3(H_2O)_9$, TeO_2, H_3AsO_4, KOH	2:1:1:6	yes	orange brown	Fe_2TeO_6, KNO_3
H124	$Zn(NO_3)_2(H_2O)_6$, TeO_2, H_3AsO_4, KOH	2:1:1:6	yes	white	$ZnTeO_3$, $Zn_2Te_3O_8$, $KZnAsO_4$, NH_4HAsO_4
H125	$Cr(NO_3)_3(H_2O)_9$, TeO_2, H_3AsO_4, KOH	2:1:1:6	yes	green	KNO_3, amorphous
H126	$Ni(NO_3)_2(H_2O)_2$, TeO_2, H_3AsO_4, KOH	2:1:1:6	yes	light green, light yellow	KNO_3, ?
H127	$Cd(NO_3)_2(H_2O)_6$, TeO_2, H_3AsO_4, KOH	2:1:1:6	yes	white, yellow	$Cd_5(TeO_3)_4(NO_3)_2$, ?
H128	$Pb(NO_3)_2$, TeO_2, H_3AsO_4, KOH	2:1:1:6	yes	white, yellow	$PbTeO_3$, $PbTe_3O_7$, $Pb_5(AsO_4)_3(OH)$, PbO
H129	$Cu(NO_3)_2(H_2O)_{2.5}$, H_6TeO_6, KOH	2:1:16	yes	green	$K_6Cu_9Te_4O_{24}(H_2O)_2$
H130	$Cd(NO_3)_2(H_2O)_6$, H_3PO_4, KOH	2:1:12	yes	white	$Cd_5(PO_4)_2(OH)_4$, $Cd(OH)_2$
H131	$Co(NO_3)_2(H_2O)_6$, TeO_2, H_3AsO_4, NH_3	2:1:3:10	yes	purple	$Co_2Te_3O_8$, $Co_3(AsO_4)_2$, CoO
H132	$Cu(NO_3)_2(H_2O)_{2.5}$, TeO_2, H_3AsO_4, NH_3	4:2:3:20	yes	pale green, green	$CuTe_2O_5$, $Cu_2AsO_4(OH)$
H133	$Fe(NO_3)_3(H_2O)_9$, TeO_2, H_3AsO_4, NH_3	4:2:5:20	yes	yellow green	? (NH_4–Fe–As–O)-phase
H134	$Zn(NO_3)_2(H_2O)_6$, TeO_2, H_3AsO_4, NH_3	2:1:2:10	yes	white	$(NH_4)ZnAsO_4$, α-TeO_2, $Zn_2(HTeO_3)(AsO_4)$
H135	$Cr(NO_3)_3(H_2O)_9$, TeO_2, H_3AsO_4, NH_3	2:1:1:10	yes	grey green	amorphous
H136	$Ni(NO_3)_2(H_2O)_2$, TeO_2, H_3AsO_4, NH_3	2:1:1:10	yes	yellow green, light turquoise	$Ni_3(AsO_4)_2(H_2O)$, $(NH_4)H_2AsO_4$, ?
H137	$Cd(NO_3)_2(H_2O)_6$, TeO_2, H_3AsO_4, NH_3	2:1:1:10	yes	white, light yellow	$Cd_2AsO_4(OH)$
H138	$Pb(NO_3)_2$, TeO_2, H_3AsO_4, NH_3	2:1:1:10	yes	white	$Pb_5(AsO_4)_3(OH)$, $Pb_3As_2O_8$, $Pb_2Te_3O_8$
H139	MnO, TeO_2, H_6TeO_6, KOH	2:1:2:15	no	orange, dark	$K_2CO_3(H_2O)_{1.5}$
H140	CuO, TeO_2, H_6TeO_6, KOH	2:1:2:15	no	green	w: $K_2Cu_2TeO_6$
H141	Fe_2O_3, TeO_2, H_6TeO_6, KOH	1:1:2:15	no	red brown	w: $K_{12}Fe_6Te_4O_{27}(H_2O)_3$, Fe_2O_3
H142	ZnO, TeO_2, H_6TeO_6, KOH	2:1:2:15	no	white	w: ZnO, ?
H143	Cr_2O_3, TeO_2, H_6TeO_6, KOH	1:1:2:15	no	green	Cr_2O_3, $K_2CO_3(H_2O)_{1.5}$, $K_3TeO_3(OH)(H_2O)_7$
H144	NiO, TeO_2, H_6TeO_6, KOH	2:1:2:15	no	pale green	NiO, $K_2CO_3(H_2O)_{1.5}$
H145	CdO, TeO_2, H_6TeO_6, KOH	2:1:2:15	no	white	w: ?
H146	PbO, TeO_2, H_6TeO_6, KOH	2:1:2:15	no	white	w: $KPb_2TeO_5(OH)$
H147	CuO, TeO_2, H_3BO_3	2:1:1	yes	grey, black	α-TeO_2, CuO, $CuTe_2O_5$
H148	$Cu(NO_3)_2(H_2O)_{2.5}$, TeO_2, H_3BO_3	2:1:1	yes	bright green	α-TeO_2, γ-TeO_2
H149	CuO, TeO_2, H_3BO_3, KOH	2:1:1:6	yes	black	CuO
H150	$Cu(NO_3)_2(H_2O)_{2.5}$, TeO_2, H_3BO_3, KOH	2:1:1:6	yes	dark brown, green	CuO, $CuTeO_3$, KNO_3

H151	CuO, H_6TeO_6, H_3BO_3	2:1:1	yes	dark yellow, light green, dark green	CuO, CuB_2O_4, $CuTeO_4$
H152	$Cu(NO_3)_2(H_2O)_{2.5}$, H_6TeO_6, H_3BO_3	2:1:1	yes	green	$CuTeO_4$
H153	CuO, H_6TeO_6, H_3BO_3, KOH	2:1:1:6	yes	black, green, white	CuO, ?
H154	$Cu(NO_3)_2(H_2O)_{2.5}$, H_6TeO_6, H_3BO_3, KOH	2:1:1:6	yes	green, yellow green, turquoise	Cu_3TeO_6, $KTeO_3(OH)$
H155	MnO, TeO_2, H_6TeO_6, NaOH	2:1:1:15	no	dark pink, brown	Na_2CO_3, $NaMnO_2$, Na_2TeO_3; w: -
H156	CuO, TeO_2, H_6TeO_6, NaOH	2:1:1:15	no	blue	w: Na_4CuTeO_6, CuO, $Na_2Te_4O_9(H_2O)_{4.5}$
H157	Fe_2O_3, TeO_2, H_6TeO_6, NaOH	1:1:1:15	no	red brown, light green	Fe_2O_3
H157b	$Fe(NO_3)_3(H_2O)_9$, TeO_2, H_6TeO_6, NaOH	2:1:1:15	yes	light brown, yellow	w: $Na_3Fe_3Te_2O_{12}$, $Na_3FeTe_2O_9$, Fe_3O_4
H158	ZnO, TeO_2, H_6TeO_6, NaOH	2:1:1:15	no	white	Na_4ZnTeO_6, Na_2CO_3, Na_2TeO_3, ZnO
H159	Cr_2O_3, TeO_2, H_6TeO_6, NaOH	1:1:1:15	no	green	w: Cr_2O_3, ?
H160	NiO, TeO_2, H_6TeO_6, NaOH	2:1:1:15	no	light green	w: NiO, $Na_2H_4TeO_6$
H161	CdO, TeO_2, H_6TeO_6, NaOH	2:1:1:15	no	white	w: CdO, $Na_2H_4TeO_6$
H162	PbO, TeO_2, H_6TeO_6, NaOH	2:1:1:15	no	orange, dark purple	w: PbO
H163	$CdCO_3$, TeO_2, H_3PO_4	1:1:1	yes	bright yellow	TeO_2, $Cd_2(PO_4)(OH)$
H164	$CdCO_3$, H_3PO_4	2:1	yes	white	$CdCO_3$, $Cd_5(PO_4)_3(OH)$
H165	$CdCO_3$, H_3PO_4, KOH	2:1:2	yes	white	$CdCO_3$, $Cd_5(PO_4)_3(OH)$
H166	$CdCO_3$, TeO_2, H_3PO_4	2:1:1	yes	white	$CdCO_3$, $H_2Cd_5(PO_4)_4(H_2O)_4$
H167	$CdCO_3$, H_3PO_4	1:1	yes	white	$Cd_5(PO_4)_3(OH)$
H168	$CdCO_3$, TeO_2, H_3PO_4	2:1:2	yes	light yellow	$Cd_2(PO_4)(OH)$
H169	$CdCO_3$, TeO_2, H_3PO_4	4:1:4	yes	white, light yellow	$Cd_2(PO_4)(OH)$, $H_2Cd_5(PO_4)_4(H_2O)_4$
H170	Fe_2O_3, H_6TeO_6, KOH	3:4:15	no	red brown, white	w: $K_{12}Fe_6Te_4O_{27}(H_2O)_3$, Fe_2O_3
H171	Fe_2O_3, H_6TeO_6, KOH	3:4:30	no	red brown, white	w: $K_{12}Fe_6Te_4O_{27}(H_2O)_3$, Fe_2O_3
H172	Fe_2O_3, H_6TeO_6, KOH	3:4:15	open	red brown	w: $K_{12}Fe_6Te_4O_{27}(H_2O)_3$, Fe_2O_3
H173	Fe_2O_3, H_6TeO_6, KOH	3:4:30	open	red brown, white, yellow	w: $K_{12}Fe_6Te_4O_{27}(H_2O)_3$, Fe_2O_3
H174	CuO, H_6TeO_6, KOH	1:1:6	no	light green	$K_2Cu_2TeO_6$, $K_2CuTeO_4(OH)_2$
H175	CuO, H_6TeO_6, KOH	1:1:6	yes	light green	$K_6Cu_9Te_4O_{24}(H_2O)_2$
H176	CuO, H_6TeO_6, KOH	1:1:8	no	blue, green	$K_2Cu_2TeO_6(H_2O)_4$, $K_2Cu_2TeO_6$, ?
H177	CuO, H_6TeO_6, KOH	1:1:8	yes	green	$K_6Cu_9Te_4O_{24}(H_2O)_2$
H178	$MnCO_3$, TeO_2	1:1	yes	light brown, dark brown	$MnCO_3$, α-TeO_2, $MnTe_2O_5$, $Mn_2Te_3O_8$
H179	$MnCO_3$, TeO_2, KOH	1:1:1	yes	light brown, dark brown	$Mn_2Te_3O_8$
H180	$MnCO_3$, TeO_2, KOH	1:1:2	yes	brown	"$Mn_3(TeO_3)_2(OH)_2$", γ-$MnTeO_3$, $Mn_6Te_5O_{16}$, $Mn_2Te_3O_8$
H181	$MnCO_3$, TeO_2, KOH	1:1:4	yes	red brown	"$Mn_3(TeO_3)_2(OH)_2$"
H182	$MnCO_3$, TeO_2, K_2CO_3	1:1:2	yes	dark brown	$Mn_2Te_3O_8$
H183	$MnCO_3$, TeO_2, KOH, K_2CO_3	1:1:2:2	yes	dark brown, light brown	$Mn_6Te_5O_{16}$, "$Mn_3(TeO_3)_2(OH)_2$"
H184	$MnCO_3$, TeO_2	1:1	open	pale brown, light brown	$MnCO_3$, α-TeO_2, γ-TeO_2
H185	$MnCO_3$, TeO_2, KOH	1:1:1	open	dark brown	$MnCO_3$, α-TeO_2, ?
H186	$MnCO_3$, TeO_2, KOH	1:1:2	open	dark brown	$MnCO_3$, α-TeO_2, ?
H187	$MnCO_3$, TeO_2, KOH	1:1:4	open	dark brown	Mn_3O_4, ?
H188	$MnCO_3$, TeO_2, K_2CO_3	1:1:2	open	dark brown	$MnCO_3$, Mn_3O_4, ?
H189	$MnCO_3$, TeO_2, KOH, K_2CO_3	1:1:2:2	open	dark brown	$K_2CO_3(H_2O)_{1.5}$, K_2TeO_3
H190	PbO, TeO_2, H_6TeO_6, KOH	2:1:2:15	no	white, light yellow	w: $KPb_2TeO_5(OH)$
H191	PbO, TeO_2, H_6TeO_6, KOH*	2:1:2:15	no	white, light yellow	w: $KPb_2(CO_3)_2(OH)$, $K_2Pb_3TeO_7$, amorphous
H192	PbO, H_6TeO_6, KOH	1:1:8	no	white, orange	w: $K_2Pb_3TeO_7$
H193	PbO, H_6TeO_6, KOH	1:1:4	no	light green, white, light yellow	w: $K_{14}Pb_{10}Te_7O_{36}(OH)_6(H_2O)_7$
H194	PbO, H_6TeO_6, KOH	1:1:12	no	white	w: $K_2Pb_3TeO_7$, $KPb_2(CO_3)_2(OH)$
H195	PbO, H_6TeO_6, KOH	2:1:10	no	dark pink, brown, white	w: $K_2Pb_3TeO_7$, $KPb_2(CO_3)_2(OH)$, Pb_3O_4
H196	PbO, H_6TeO_6, KOH	2:1:6	no	dark pink	w: PbO, Pb_3O_4, α-TeO_2
H197	PbO, H_6TeO_6, KOH	2:1:15	no	orange	w: $K_2Pb_3TeO_7$, $KPb_2(CO_3)_2(OH)$, Pb_3O_4
H198	PbO, H_6TeO_6, KOH	3:1:12	no	brown	w: $K_2Pb_3TeO_7$, $KPb_2(CO_3)_2(OH)$
H199	PbO, H_6TeO_6, KOH	3:1:6	no	dark pink, white	w: Pb_5TeO_8, PbO, Pb_3O_4
H200	PbO, H_6TeO_6, KOH	3:1:18	no	orange, white	w: $K_2Pb_3TeO_7$, $KPb_2(CO_3)_2(OH)$, PbO
H201	PbO, H_6TeO_6, K_2CO_3	1:1:2	no		Pb_2TeO_5, $KHCO_3$, $KTeO_3(OH)$
H202	PbO, H_6TeO_6, KOH	1:1:4	yes		Pb_2TeO_5
H203	CuO, H_6TeO_6, KOH	2:3:10	no	light green	$K_3Cu_2TeO_5(OH)(CO_3)(H_2O)$, β-$KCuTeO_4(OH)$
H204	CuO, H_6TeO_6, KOH	2:3:10	yes	olive green	$Cu_3TeO_6(H_2O)$, α-$KCuTeO_4(OH)$
H205	CuO, H_6TeO_6, KOH	2:3:20	no	blue	CuO, $K_2Cu_2TeO_6$, like H176(w)
H206	CuO, H_6TeO_6, KOH	2:3:20	yes	olive green	$K_2CuTeO_4(OH)_2$, $K_2Cu_2TeO_6(H_2O)_x$
H207	CuO, H_6TeO_6, K_2CO_3	1:1:4	no	light green	$KTeO_3(OH)$, $K_3Cu_2TeO_5(OH)(CO_3)(H_2O)$, $K_2CO_3(H_2O)_{1.5}$

H208	CuO, H_6TeO_6, K_2CO_3	1:1:4	yes	light green	α-$KCuTeO_4(OH)$, Cu_3TeO_6
H209	CuO, H_6TeO_6, K_2CO_3	2:1:4	no	green, blue, white	$K_3Cu_2TeO_5(OH)(CO_3)(H_2O)$, β-$KCuTeO_4(OH)$
H210	CuO, H_6TeO_6, K_2CO_3	2:1:4	yes	olive green	α-$KCuTeO_4(OH)$, Cu_3TeO_6
H211	CuO, H_6TeO_6, K_2CO_3	2:3:10	yes	dark green, white	Cu_3TeO_6, $KTeO_3(OH)$, α-$KCuTeO_4(OH)$
H212	CuO, H_6TeO_6, K_2CO_3	1:4:15	yes	dark green, white	Cu_3TeO_6, $KTeO_3(OH)$, α-$KCuTeO_4(OH)$
H213	CuO, H_6TeO_6, KOH, $KHCO_3$	2:3:10:10	yes	green, white	$K_3Cu_2TeO_5(OH)(CO_3)(H_2O)$, $K_4CuTe_4O_{14}(OH)_2$
H214	$MnCO_3$, TeO_2, KOH, K_2CO_3	3:2:4:4	yes	brown	"$Mn_3(TeO_3)_2(OH)_2$", Mn_3O_4, Te
H215	$MnSO_4(H_2O)$, TeO_2, KOH, K_2CO_3	1:1:4:2	yes	brown	"$Mn_3(TeO_3)_2(OH)_2$", Mn_3O_4
H216	$Mn(CH_3COO)_2(H_2O)_4$, TeO_2, KOH, K_2CO_3	1:1:4:2	yes	brown	"$Mn_3(TeO_3)_2(OH)_2$", Mn_3O_4, Te
H217	$MnCO_3$, TeO_2, KOH	1:1:4	yes	brown	Mn_3O_4, Te
H218	$MnSO_4(H_2O)$, TeO_2, KOH	1:1:4	yes	brown	"$Mn_3(TeO_3)_2(OH)_2$", Mn_3O_4, Te
H219	$Mn(CH_3COO)_2(H_2O)_4$, TeO_2, KOH	1:1:4	yes	brown	$Mn_6Te_5O_{16}$, Mn_3TeO_6, "$Mn_3(TeO_3)_2(OH)_2$"
H220	$MnCO_3$, K_2TeO_3	6:5	yes	brown	$Mn_6Te_5O_{16}$, K_2CO_3
H221	MnO, H_6TeO_6, K_2CO_3	2:3:10	no	pale pink	w: $KTeO_3(OH)$, MnO, $K_4Mn_2Te_3O_{12}(OH)_4$
H222	CuO, H_6TeO_6, K_2CO_3	2:3:10	no	green	w: $KTeO_3(OH)$, $K_3Cu_2TeO_5(OH)(CO_3)(H_2O)$
H223	Fe_2O_3, H_6TeO_6, K_2CO_3	1:3:10	no	red brown	w: $KTeO_3(OH)$, Fe_2O_3
H224	ZnO, H_6TeO_6, K_2CO_3	2:3:10	no	white	w: $KTeO_3(OH)$, ZnO, $K_6[Zn(CO_3)_4]$
H225	Cr_2O_3, H_6TeO_6, K_2CO_3	1:3:10	no	green	w: $KTeO_3(OH)$, Cr_2O_3
H226	NiO, H_6TeO_6, K_2CO_3	2:3:10	no	light green	w: $KTeO_3(OH)$, NiO
H227	CdO, H_6TeO_6, K_2CO_3	2:3:10	no	light yellow	w: $KTeO_3(OH)$, β-Cd_3TeO_6
H228	PbO, H_6TeO_6, K_2CO_3	2:3:10	no	light yellow	w: $KTeO_3(OH)$, Pb_2TeO_5, $PbTeO_3$, PbH_4TeO_6
H229	MnO, TeO_2, K_2CO_3	2:3:10	3 dr.	pale pink, light brown	w: $K_2Mn_2Te_3O_9(H_2O)$
H230	CuO, TeO_2, K_2CO_3	2:3:10	3 dr.	green, blue, black	w: CuO, $K_2Cu_3Te_4O_{12}$, $K_2Te_4O_9(H_2O)_x$
H231	Fe_2O_3, TeO_2, K_2CO_3	1:3:10	3 dr.	red brown	w: Fe_2O_3, $K_3FeTe_2O_8(OH)_2(H_2O)$
H232	ZnO, TeO_2, K_2CO_3	2:3:10	3 dr.	white	w: ZnO, ?
H233	Cr_2O_3, TeO_2, K_2CO_3	1:3:10	3 dr.	green	w: Cr_2O_3
H234	NiO, TeO_2, K_2CO_3	2:3:10	3 dr.	pale green	w: NiO, ?
H235	CdO, TeO_2, K_2CO_3	2:3:10	3 dr.	yellow	w: $K_2Cd_2Te_3O_9(H_2O)$
H236	PbO, TeO_2, K_2CO_3	2:3:10	3 dr.	pale yellow	w: $PbTeO_3$, PbO_2, $PbTeO_3(H_2O)_{2/3}$
H237	$Cd(NO_3)_2(H_2O)_4$, TeO_2, KOH	2:1:2	yes	light yellow	$Cd_5(TeO_3)_4(NO_3)_2$, $Cd_2Te_3O_9$
H238	$Cd(NO_3)_2(H_2O)_4$, K_2TeO_3	2:1	yes	yellow	$Cd_5(TeO_3)_4(NO_3)_2$, $Cd_4Te_5O_{14}$, $Cd_4Te_4O_{11}(NO_3)_2$, α-TeO_2, β-Cd_3TeO_6
H239	$Cd(NO_3)_2(H_2O)_4$, TeO_2, KOH	2:1:2	no	white, yellow	$Cd_5(TeO_3)_4(NO_3)_2$, $CdNO_3(OH)(H_2O)$, KNO_3
H240	$Cd(NO_3)_2(H_2O)_4$, K_2TeO_3	2:1	no	pale brown	KNO_3, H242
H241	$Cd(NO_3)_2(H_2O)_4$, TeO_2, KOH	5:4:8	yes	white	$Cd_3(NO_3)(OH)_5$, α-TeO_2, γ-TeO_2, KNO_3
H242	$Cd(NO_3)_2(H_2O)_4$, K_2TeO_3	5:4	yes	light brown	?, $Cd_4Te_5O_{14}$
H243	$Cd(NO_3)_2(H_2O)_4$, TeO_2, KOH	5:4:8	no	light yellow, yellow	$Cd_5(TeO_3)_4(NO_3)_2$, KNO_3, $Cd_4Te_4O_{11}(NO_3)_2$
H244	$Cd(NO_3)_2(H_2O)_4$, K_2TeO_3	5:4	no	pale brown	KNO_3, H242
H245	$MnCO_3$, K_2TeO_3	1:1	yes	light brown	$Mn_6Te_5O_{16}$, $Mn_2Te_3O_8$
H246	$MnCO_3$, K_2TeO_3	6:5	yes	brown	$Mn_2Te_3O_8$, $Mn_6Te_5O_{16}$
H247	$MnCO_3$, TeO_2, KOH, K_2CO_3	3:2:8:8	yes	dark brown	"$Mn_3(TeO_3)_2(OH)_2$", Mn_3O_4, $Mn_6Te_5O_{16}$
H248	$MnCO_3$, TeO_2, KOH, K_2CO_3	3:2:4:4	yes	brown	$Mn_6Te_5O_{16}$
H249	$Cd(NO_3)_2(H_2O)_4$, K_2TeO_3	2:1	yes	light yellow	$Cd_5(TeO_3)_4(NO_3)_2$, $Cd_4Te_4O_{11}(NO_3)_2$
H250	$Cd(NO_3)_2(H_2O)_4$, K_2TeO_3	1:1	yes	light yellow	$CdTeO_3$, ?
H251	$Cd(NO_3)_2(H_2O)_4$, TeO_2, KOH	1:1:2	little	white, yellow	$Cd_5(TeO_3)_4(NO_3)_2$, KNO_3, α-TeO_2
H252	$Cd(NO_3)_2(H_2O)_4$, TeO_2, KOH	1:1:2	no	white, yellow	$Cd_5(TeO_3)_4(NO_3)_2$, $CdTeO_3$, KNO_3
H253	MnO, TeO_2, K_2CO_3	2:3:10	yes	dark brown	$Mn_{15}(TeO_3)_{14}(OH)_2$, MnO, "$Mn_3(TeO_3)_2(OH)_2$", $Mn_6Te_5O_{16}$
H254	CuO, TeO_2, K_2CO_3	2:3:10	yes	black	CuO, $K_2[Cu_2(TeO_3)_3](H_2O)_2$, $K_2Te_4O_9(H_2O)_{3.2}$
H255	Fe_2O_3, TeO_2, K_2CO_3	1:3:10	yes	red	$K_2Te_4O_9(H_2O)_3$, Fe_2O_3
H256	ZnO, TeO_2, K_2CO_3	2:3:10	yes	white	$ZnTeO_3$,
H257	Cr_2O_3, TeO_2, K_2CO_3	1:3:10	yes	green	w: Cr_2O_3, $K_2Te_4O_9(H_2O)_{3.2}$
H258	NiO, TeO_2, K_2CO_3	2:3:10	yes	light green	NiO, $K_2Te_4O_9(H_2O)_4$
H259	CdO, TeO_2, K_2CO_3	2:3:10	yes	light yellow	α-$CdTeO_3$, β-$CdTeO_3$
H260	PbO, TeO_2, K_2CO_3	2:3:10	yes	yellow	$PbTeO_3$
H261	MnO, TeO_2, Na_2CO_3	2:3:10	3 dr.	pale yellow, grey	$Mn_2Te_3O_8$, $Na_2Te_4O_9(H_2O)_{4.5}$, MnO, Na_2CO_3
H262	CuO, TeO_2, Na_2CO_3	2:3:10	3 dr.	black, green	w: $Na_2Cu_3Te_4O_{12}$, CuO
H263	Fe_2O_3, TeO_2, Na_2CO_3	1:3:10	3 dr.	yellow green, red brown	w: $NaFe(TeO_3)_2$
H264	ZnO, TeO_2, Na_2CO_3	2:3:10	3 dr.	white	w: $ZnTeO_3$, $Zn_2Te_3O_8$, $Na_2Zn_2Te_4O_{11}$
H265	Cr_2O_3, TeO_2, Na_2CO_3	1:3:10	3 dr.	green	Cr_2O_3, $Na_2Te_4O_9(H_2O)_{4.5}$, $Na_2Te_4O_9$, Na_2CO_3,
H266	NiO, TeO_2, Na_2CO_3	2:3:10	3 dr.	light green	w: NiO, $Na_2Te_4O_9$, $Na_2[Ni_2Te_3O_9](H_2O)$
H267	CdO, TeO_2, Na_2CO_3	2:3:10	3 dr.	white	w: $CdTeO_3$, $CdCO_3$, ?
H268	PbO, TeO_2, Na_2CO_3	2:3:10	3 dr.	white	$PbTeO_3$, $Pb_2Te_3O_8$, $NaPb_2(CO_3)_2(OH)$, Na_2CO_3
H269	Ag_2O, TeO_2, K_2CO_3	1:3:10	3 dr.	brown green, pink	$KTeO_3(OH)$, Ag, $K_2Te_4O_9(H_2O)_{3.2}$
H270	$Ba(OH)_2(H_2O)_8$, TeO_2, K_2CO_3	2:3:10	3 dr.	green, light green	$BaCO_3$, $K_2Te_4O_9(H_2O)_3$
H271	CaO, TeO_2, K_2CO_3	2:3:10	3 dr.	white	$K_2Ca(CO_3)_2$, $K_2Te_4O_9(H_2O)_4$
H272	MgO, TeO_2, K_2CO_3	2:3:10	3 dr.	light brown	$MgCO_3$, MgO, K–Mg-zemannite
H273	SnO, TeO_2, K_2CO_3	2:3:10	3 dr.	white, black	SnO, $K_4Sn_3Te_8O_{24}$, $K_2Te_4O_9(H_2O)_{3.2}$

H274	SrO, TeO_2, K_2CO_3	2:3:10	3 dr.	white	$KTeO_3(OH)$, $SrCO_3$, $K_2Te_4O_9(H_2O)_{3.2}$
H275	HgO, TeO_2, K_2CO_3	2:3:10	3 dr.	white, grey	w: $KTeO_3(OH)$
H276	Bi_2O_3, TeO_2, K_2CO_3	1:3:10	3 dr.	grey, light yellow	w: Bi_2TeO_5, $K_6Bi_4Te_3O_{17}(OH)_2(H_2O)_3$, $KTeO_3(OH)$, ?
H277	MnO, TeO_2, K_2CO_3	2:3:10	yes	brown, grey	$Mn_2Te_3O_8$, MnO, $Mn_{15}(TeO_3)_{14}(OH)_2$
H278	MnO, TeO_2, K_2CO_3	2:3:5	yes	brown, grey	$Mn_2Te_3O_8$, MnO, ?
H279	MnO, TeO_2, K_2CO_3	15:14:40	yes	red brown	$Mn_{15}(TeO_3)_{14}(OH)_2$, $MnTe_2O_5$
H280	MnO, TeO_2, Na_2CO_3	2:3:10	yes	brown	w: $Mn_{15}(TeO_3)_{14}(OH)_2$, $Mn_2Te_3O_8$
H281	CuO, TeO_2, Na_2CO_3	2:3:10	yes	dark green	w: CuO, $Na_2Cu_3Te_4O_{12}$, $Na_2[Cu_2(TeO_3)_3](H_2O)_{1.5}$
H282	Fe_2O_3, TeO_2, Na_2CO_3	1:3:10	yes	red	w: Fe_2O_3, $NaFeTe_2O_6$, $Na_2Te_4O_9(H_2O)_x$
H283	ZnO, TeO_2, Na_2CO_3	2:3:10	yes	white	w: $ZnTeO_3$
H284	Cr_2O_3, TeO_2, Na_2CO_3	1:3:10	yes	green	w: Cr_2O_3, $Na_2Te_4O_9(H_2O)_{4.5}$, $Na_2Te_2O_7$
H285	NiO, TeO_2, Na_2CO_3	2:3:10	yes	light green	w: NiO, $Na_2Te_4O_9(H_2O)_{4.5}$
H286	CdO, TeO_2, Na_2CO_3	2:3:10	yes	white, pale brown	w: $CdTeO_3$
H287	PbO, TeO_2, Na_2CO_3	2:3:10	yes	light yellow	w: PbO, $PbTeO_3$, $NaPb_2(CO_3)_2(OH)$
H288	MnO, TeO_2, K_3PO_4	1:1:3	yes		$KMnPO_4(H_2O)$, MnO, MnO_2, Te
H289	CuO, TeO_2, K_3PO_4	1:1:3	yes		w: CuO
H290	ZnO, TeO_2 K_3PO_4	1:1:3	yes		w: $KZnPO_4$
H291	NiO, TeO_2, K_3PO_4	1:1:3	yes		w: NiO, ?
H292	CdO, TeO_2, K_3PO_4	1:1:3	yes		β-$CdTeO_3$
H293	PbO, TeO_2, K_3PO_4	1:1:3	yes		$KPb_4(PO_4)_3$, PbO
H294	$MnCO_3$, K_2TeO_3	6:5	yes	brown	$Mn_{15}(TeO_3)_{14}(OH)_2$
H295	$MnCO_3$, Na_2TeO_3	6:5	yes	dark brown	$Mn_{15}(TeO_3)_{14}(OH)_2$, $Mn_6Te_5O_{16}$
H296	CuO, H_6TeO_6, K_2CO_3	2:1:8	3 dr.	green	CuO, $K_2Cu_2TeO_6$
H297	Fe_2O_3, H_6TeO_6, KOH	3:4:15	3 dr.	dark red	Fe_2O_3
H298	ZnO, K_2CO_3	1:4	3 dr.	white	ZnO, $K_4(CO_3)_2(H_2O)_3$
H299	$Zn(NO_3)_2(H_2O)_6$, K_2CO_3	1:4	3 dr.	light yellow	ZnO, KNO_3, $KHCO_3$, $K_2CO_3(H_2O)_{1.5}$
H300	ZnO, K_2CO_3	1:5	open	white	ZnO, K_2CO_3, $K_2CO_3(H_2O)_{1.5}$
H301	$Zn(NO_3)_2(H_2O)_6$, K_2CO_3	1:5	open	white	ZnO, $K_2CO_3(H_2O)_{1.5}$, $K_6[Zn(CO_3)_4]$, ?
H302	MnO, TeO_2, Li_2CO_3	2:3:10	3 dr.	dark green, light yellow	w: β-$Li_2Te_2O_5$, MnO, Li_2CO_3, $Mn_2Te_3O_8$, α-TeO_2,
H303	CuO, TeO_2, Li_2CO_3	2:3:10	3 dr.	green, black	w: Li_2CO_3, α-TeO_2, CuO, $CuTe_2O_5$, ?
H304	Fe_2O_3, TeO_2, Li_2CO_3	1:3:10	3 dr.	brown	w: Li_2CO_3, Fe_2O_3, $Li_3FeTe_4O_{11}$, β-$Li_2Te_2O_5$
H305	ZnO, TeO_2, Li_2CO_3	2:3:10	3 dr.	white, light yellow	w: Li_2CO_3, $Zn_2Te_3O_8$, α-TeO_2, $ZnTeO_3$
H306	Cr_2O_3, TeO_2, Li_2CO_3	1:3:10	3 dr.	green	w: β-$Li_2Te_2O_5$, Cr_2O_3, α-TeO_2, Li_2CO_3
H307	NiO, TeO_2, Li_2CO_3	2:3:10	3 dr.	light green	w: Li_2CO_3, α-TeO_2, NiO, β-$Li_2Te_2O_5$
H308	CdO, TeO_2, Li_2CO_3	2:3:10	3 dr.	white, brown	w: β-$Li_2Te_2O_5$, CdO, $CdTe_2O_5$, α-$CdTeO_3$
H309	PbO, TeO_2, Li_2CO_3	2:3:10	3 dr.	pale brown	w: Li_2CO_3, PbO, $PbTeO_3$, $Pb_2Te_3O_8$ Pb_2OCO_3
H310	MnO, TeO_2, Rb_2CO_3	2:3:6	3 dr.	light brown	$Mn_2Te_3O_8$, $MnCO_3$, $Rb_{1.5}[Mn_2(TeO_3)_3](H_2O)_{1.25}$, $Mn_{15}(TeO_3)_{14}(OH)_2$
H311	CuO, TeO_2, Rb_2CO_3	2:3:6	3 dr.	light blue -> green	CuO, $Rb_2Cu_3Te_6O_{16}$
H312	Fe_2O_3, TeO_2, Rb_2CO_3	1:3:6	3 dr.	red brown	Fe_2O_3, $Fe(OH)_3$, $Fe(OH)_{2.25}(H_2O)_{0.5}$, ?
H313	ZnO, TeO_2, Rb_2CO_3	2:3:6	3 dr.	white	$Rb_2Zn(TeO_3)(CO_3)(H_2O)$, $Rb_4(HCO_3)_2(CO_3)(H_2O)$
H314	Cr_2O_3, TeO_2, Rb_2CO_3	1:3:6	3 dr.	green	w: Cr_2O_3, α-TeO_2
H315	NiO, TeO_2, Rb_2CO_3	2:3:6	3 dr.	light green	w: NiO, α-TeO_2 ?
H316	CdO, TeO_2, Rb_2CO_3	2:3:6	3 dr.	light brown	w: β-$CdTeO_3$
H317	PbO, TeO_2, Rb_2CO_3	2:3:6	3 dr.	pale brown	w: $PbTeO_3$, $Pb_2Te_3O_8$, $RbPb_3Te_2O_9(OH)$
H318	MnO, TeO_2, Rb_2CO_3	2:3:6	yes	brown	$Mn_2Te_3O_8$, MnO, $Mn_{15}(TeO_3)_{14}(OH)_2$
H319	CuO, TeO_2, Rb_2CO_3	2:3:6	yes	dark green, black, turquoise	CuO, $Rb_2Cu_3Te_6O_{16}$
H320	Fe_2O_3, TeO_2, Rb_2CO_3	1:3:6	yes	red brown, white	Fe_2O_3, $Rb_2Te_4O_9$, $Rb_6Te_2O_9$
H321	ZnO, TeO_2, Rb_2CO_3	2:3:6	yes	white	$ZnTeO_3$
H322	Cr_2O_3, TeO_2, Rb_2CO_3	1:3:6	yes	white, green	Cr_2O_3, $Rb_2Te_4O_9(H_2O)_2$
H323	NiO, TeO_2, Rb_2CO_3	2:3:6	yes	white, light green	NiO, $Rb_2Te_4O_9(H_2O)_2$
H324	CdO, TeO_2, Rb_2CO_3	2:3:6	yes	light yellow	β-$CdTeO_3$
H325	PbO, TeO_2, Rb_2CO_3	2:3:6	yes	white, light pink, orange	PbO, $PbTeO_3((H_2O)_{1/3})$, $Pb_5(CO_3)_3O(OH)_2$, $PbTeO_3$
H326	MnO, TeO_2, Li_2CO_3	2:3:10	yes	brown	MnO, $Li_2Te_2O_5$, $Mn_2Te_3O_8$
H327	CuO, TeO_2, Li_2CO_3	2:3:10	yes	dark green	$CuTe_2O_5$, CuO, Li_2CO_3, $Li_2Cu_2Te_3O_9$, $Li_2Cu_3Te_4O_{12}$
H328	Fe_2O_3, TeO_2, Li_2CO_3	1:3:10	yes	light brown	$Li_3FeTe_4O_{11}$, Fe_2O_3
H329	ZnO, TeO_2, Li_2CO_3	2:3:10	yes	white	$ZnTeO_3$, $Zn_2Te_3O_8$, Li_2CO_3
H330	Cr_2O_3, TeO_2, Li_2CO_3	1:3:10	yes	green	Cr_2O_3, Li_2CO_3, α-TeO_2
H331	NiO, TeO_2, Li_2CO_3	2:3:10	yes	light green	NiO, Li_2CO_3, ?
H332	CdO, TeO_2, Li_2CO_3	2:3:10	yes	light brown	α-$CdTeO_3$, ?
H333	PbO, TeO_2, Li_2CO_3	2:3:10	yes	light pink, orange	PbO, $Pb_2Te_3O_8$, Li_2CO_3
H334	MnO, TeO_2, Cs_2CO_3	2:3:6	3 dr.	brown	w: MnO, $Mn_2Te_3O_8$, $Cs[Mn_2(TeO_3)_3](H_2O)$
H335	CuO, TeO_2, Cs_2CO_3	2:3:6	3 dr.	green	w: $Cs_2Cu_3Te_6O_{16}$
H336	Fe_2O_3, TeO_2, Cs_2CO_3	1:3:6	3 dr.	brown, yellow	w: Fe_2O_3, ~$CsTe_2O_6$
H337	ZnO, TeO_2, Cs_2CO_3	2:3:6	3 dr.	white	w: amorphous
H338	Cr_2O_3, TeO_2, Cs_2CO_3	1:3:6	3 dr.	green, white	w: Cr_2O_9, $Cs_2Te_4O_9$
H339	NiO, TeO_2, Cs_2CO_3	2:3:6	3 dr.	light green, white	w: NiO, $Cs_2Te_4O_9$, ?
H340	CdO, TeO_2, Cs_2CO_3	2:3:6	3 dr.	white	w: β-$CdTeO_3$

H341	PbO, TeO_2, Cs_2CO_3	2:3:6	3 dr.	white	w: $PbTeO_3$, amorphous
H342	MnO, TeO_2, Cs_2CO_3	2:3:6	yes	brown	$Mn_2Te_3O_8$, MnO
H343	CuO, TeO_2, Cs_2CO_3	2:3:6	yes	green	CuO, Cu_3TeO_6, $CuTeO_3$
H344	Fe_2O_3, TeO_2, Cs_2CO_3	1:3:6	yes		Fe_2O_3, ?
H345	ZnO, TeO_2, Cs_2CO_3	2:3:6	yes	white	$ZnTeO_3$
H346	Cr_2O_3, TeO_2, Cs_2CO_3	1:3:6	yes	green	Cr_2O_3
H347	NiO, TeO_2, Cs_2CO_3	2:3:6	yes	light green	NiO, ?(layers)
H348	CdO, TeO_2, Cs_2CO_3	2:3:6	yes	light yellow	α-$CdTeO_3$, β-$CdTeO_3$
H349	PbO, TeO_2, Cs_2CO_3	2:3:6	yes	light yellow	$PbTeO_3$, $PbTe_2O_5$
H350	$MnCO_3$, TeO_2, Cs_2CO_3	2:3:6	yes	brown	$Mn_2Te_3O_8$, $HCsCO_3$
H351	$CuCO_3Cu(OH)_2$, TeO_2, Cs_2CO_3	1:3:6	yes	green	$Cs_2Cu_3Te_6O_{16}$, α-TeO_2
H352	$CoCO_3$, TeO_2, Cs_2CO_3	2:3:6	yes	purple	$HCsCO_3$, α-TeO_2
H353	$NiCO_3(Ni(OH)_2)_2$, TeO_2, Cs_2CO_3	2:9:18	yes	light green	$HCsCO_3$
H354	$CdCO_3$, TeO_2, Cs_2CO_3	2:3:6	yes	white	$HCsCO_3$
H355	$CoSO_4(H_2O)_7$, TeO_2, KOH	3:2:9	yes	purple	"$Co_3(TeO_3)_2(OH)_2$", $Co(OH)_2$
H356	$Co(NO_3)_2(H_2O)_6$, TeO_2, KOH	3:2:9	yes	purple	"$Co_3(TeO_3)_2(OH)_2$", $Co(OH)_2$, Co_3O_4
H357	$NiSO_4(H_2O)_6$, TeO_2, KOH	3:2:9	yes	light green	"$Ni_3(TeO_3)_2(OH)_2$", $Ni(OH)_2$, $K_2[Ni_2(TeO_3)_3](H_2O)$
H358	$Ni(NO_3)_2(H_2O)_6$, TeO_2, KOH	3:2:9	yes	light green	"$Ni_3(TeO_3)_2(OH)_2$", $Ni(OH)_2$, $K_2[Ni_2(TeO_3)_3](H_2O)$
H359	$MgSO_4$, TeO_2, KOH	3:2:9	yes	white, grey	$Mg(OH)_2$, Te, "$Mg_3(TeO_3)_2(OH)_2$"
H360	$Mg(NO_3)_2$, TeO_2, KOH	3:2:9	yes	white, grey	$Mg(OH)_2$, Te (dirty autoclave)
H361	$MnSO_4(H_2O)$, TeO_2, KOH, K_2CO_3	1:1:4:2	yes	brown	"$Mn_3(TeO_3)_2(OH)_2$", $Mn_{15}(TeO_3)_{14}(OH)_2$, Mn_3O_4
H362	$MnCl_2(H_2O)_4$, TeO_2, KOH, K_2CO_3	1:1:4:2	yes	brown	"$Mn_3(TeO_3)_2(OH)_2$", $Mn_{15}(TeO_3)_{14}(OH)_2$, Mn_3O_4
H363	$CoCO_3$, TeO_2, KOH	3:2:9	yes	purple, brown	$Co_2(TeO_3)(OH)_2$
H364	$NiCO_3(Ni(OH)_2)_2$, TeO_2, KOH	3:2:9	yes	light green	$Ni(OH)_2$
H365	$MgSO_4$, TeO_2, KOH	3:2:9	yes	white	$Mg(OH)_2$, $Mg_3(TeO_3)_2(OH)_2$
H366	$CoC_2O_4(H_2O)_2$, TeO_2, KOH	3:2:9	yes	purple	$Co_2(TeO_3)(OH)_2$, $Co(OH)_2$, $Co_{15}(TeO_3)_{14}(OH)_2$
H367	$Ni(CH_3COO)_2(H_2O)_6$, TeO_2, KOH	3:2:9	yes	light green	"$Ni_3(TeO_3)_2(OH)_2$", $Ni(OH)_2$, $K_2[Ni_2(TeO_3)_3](H_2O)$
H368	$Mg(NO_3)_2(H_2O)$, TeO_2, KOH	3:2:9	yes	white	$Mg(OH)_2$
H369	$MnSO_4(H_2O)$, TeO_2, KOH	3:2:9	open	dark brown	Mn_3O_4, K_2SO_4, ?
H370	$MnCl_2(H_2O)_4$, TeO_2, KOH	3:2:9	yes	brown	Mn_3O_4, $Mn_6Te_5O_{16}$, $Mn_{15}(TeO_3)_{14}(OH)_2$
H371	$CoCO_3$, TeO_2, KOH	3:2:4	yes	purple	$Co_{15}(TeO_3)_{14}(OH)_2$, $Co_2(TeO_3)(OH)_2$, "$Co_3(TeO_3)_2(OH)_2$"
H372	$CoC_2O_4(H_2O)_2$, TeO_2, KOH	3:2:4	yes	purple	$Co_{15}(TeO_3)_{14}(OH)_2$, $Co_2(TeO_3)(OH)_2$, $CoCO_3$
H373	$NiSO_4(H_2O)_6$, TeO_2, K_2CO_3	3:2:4	yes	light green	"$Ni_3(TeO_3)_2(OH)_2$"
H374	$Ni(NO_3)_2(H_2O)_6$, TeO_2, K_2CO_3	3:2:4	yes	light green	"$Ni_3(TeO_3)_2(OH)_2$"
H375	$MgSO_4$, TeO_2, K_2CO_3	3:2:4	yes	white	$Mg_2Te_3O_8$
H376	$Mg(NO_3)_2$, TeO_2, K_2CO_3	3:2:4	yes	white	$Mg_2Te_3O_8$, "$Mg_3(TeO_3)_2(OH)_2$"
H377	$MnCO_3$, TeO_2, KOH	3:2:9	yes	brown	Mn_3O_4, $Mn_{15}(TeO_3)_{14}(OH)_2$, "$Mn_3(TeO_3)_2(OH)_2$"
H378	$Mn(CH_3COO)_2(H_2O)_4$, TeO_2, $NaOH$	1:1:4	yes	brown	"$Mn_3(TeO_3)_2(OH)_2$", Mn_3O_4, Te
H379	$MnSO_4(H_2O)$, TeO_2, $NaOH$	1:1:4	yes	brown	"$Mn_3(TeO_3)_2(OH)_2$", Mn_3O_4, Te
H380	$MnCl_2(H_2O)_4$, TeO_2, $NaOH$	1:1:4	yes	brown	"$Mn_3(TeO_3)_2(OH)_2$", Mn_3O_4, Te
H381	$MnBr_2(H_2O)_4$, TeO_2, $NaOH$	1:1:4	yes	brown	"$Mn_3(TeO_3)_2(OH)_2$", Mn_3O_4, Te
H382	MnO, TeO_2, $NaOH$	1:1:4	yes	brown	Mn_3O_4, Te
H383	$MnCO_3$, TeO_2, $NaOH$	1:1:4	yes	brown	"$Mn_3(TeO_3)_2(OH)_2$", Mn_3O_4, Te
H384	TeO_2, H_6TeO_6, Cs_2CO_3	1:1:4	yes	-	-
H385	TeO_2, H_6TeO_6, Cs_2CO_3	1:1:4	3 dr.	white	$Cs_2Te_4O_{12}$, $Cs_2CO_3(H_2O)_x$
H386	TeO_2, H_6TeO_6, Rb_2CO_3	1:1:4	yes	white	$RbTeO_3(OH)$, $Rb_2Te_2O_4(OH)_4$
H387	TeO_2, H_6TeO_6, Rb_2CO_3	1:1:4	3 dr.	white	w: $RbTeO_3(OH)$
H388	TeO_2, H_6TeO_6, K_2CO_3	1:1:4	yes	white	$KTeO_3(OH)$
H389	TeO_2, H_6TeO_6, K_2CO_3	1:1:4	3 dr.	white	w: $KTeO_3(OH)$
H390	TeO_2, H_6TeO_6, K_2CO_3	1:1:2	yes	white	$KTeO_3(OH)$
H391	TeO_2, H_6TeO_6, Rb_2CO_3	1:1:4	open	white	$Rb_2Te_2O_4(OH)_4$, $Rb_2CO_3(H_2O)_{1.5}$, ?
H392	TeO_2, H_6TeO_6, K_2CO_3	1:1:4	open	white	K_2CO_3, ($K_2Te_2O_4(OH)_4$), ?
H393	TeO_2, SnO, KOH, K_2CO_3	1:1:2:2	yes	brown	SnO, SnO_2, Te
H394	TeO_2, SnO_2, KOH, K_2CO_3	1:1:2:2	yes	white	SnO_2
H395	TeO_2, H_6TeO_6, K_2CO_3	1:1:4	yes	white	$KTeO_3(OH)$, $K_2Te_2O_4(OH)_4$
H396	TeO_2, H_6TeO_6, K_2CO_3	2:1:4	yes	white	$KTeO_3(OH)$
H397	TeO_2, H_6TeO_6, KOH	1:1:10	yes	-	-
H398	TeO_2, H_6TeO_6, KOH	1:1:6	yes	-	-
H399	TeO_2, H_6TeO_6, KOH	1:1:4	yes	-	-
H400	K_2TeO_3, H_6TeO_6	1:1	yes	pale white	$KTeO_3(OH)$, ?
H401	CuO, TeO_2, Li_2CO_3	2:3:1	yes	dark green	CuO, α-TeO_2, $CuTe_2O_5$
H402	CuO, TeO_2, Li_2CO_3	3:4:12	yes	pale turquoise	CuO, Li_2CO_3, $CuTe_2O_5$
H403	CuO, TeO_2, Li_2CO_3	3:4:2	yes	pale green	$CuTe_2O_5$, α-TeO_2, Li_2CO_3, CuO
H404	CuO, TeO_2, Rb_2CO_3	1:2:4	3 dr.	turquoise	w: $Rb_2Cu_3Te_6O_{16}$, CuO
H405	CuO, TeO_2, Rb_2CO_3	3:6:1	3 dr.	black, white, green	w: $Rb_2Cu_3Te_6O_{16}$
H406	CuO, TeO_2, Cs_2CO_3	1:2:4	yes	dark green	Cu_3TeO_6, CuO
H407	CuO, TeO_2, Cs_2CO_3	3:6:1	yes	pale green	CuO, α-TeO_2, $CuTe_2O_5$
H408	$MnCl_2(H_2O)_4$, $CuCl_2(H_2O)_2$, TeO_2, KOH	1:2:6:exc.	yes	brown	$CuTeO_3$, $K_x[(Cu,Mn)_2(TeO_3)_3](H_2O)_y$

H409	$MnCl_2(H_2O)_4$, $CuCl_2(H_2O)_2$, TeO_2, KOH	1:2:6:exc.	open	brown	$MnTe_2O_5$, KCl, $K_x[(Cu,Mn)_2(TeO_3)_3](H_2O)_y$
H410	$MnCl_2(H_2O)_4$, $CuCl_2(H_2O)_2$, TeO_2, K_2CO_3	1:1:4:8	3 dr.	brown	$Mn_2Te_3O_8$, $K_x[(Cu,Mn)_2(TeO_3)_3](H_2O)_y$
H411	$MnCl_2(H_2O)_4$, $CuCl_2(H_2O)_2$, TeO_2, K_2CO_3	1:1:4:8	yes	brown	$CuMnTe_4O_{10}$, $K_x[(Cu,Mn)_2(TeO_3)_3](H_2O)_y$, ?
H412	$MnCl_2(H_2O)_4$, MnO_2, $CuCl_2(H_2O)_2$, TeO_2, K_2CO_3	1:1:2:7:16	3 dr.	brown	$K_x[(Cu,Mn)_2(TeO_3)_3](H_2O)_y$, Mn_3O_4, $Cu_2(CO_3)(OH)_2$
H413	$MnCl_2(H_2O)_4$, MnO_2, $CuCl_2(H_2O)_2$, TeO_2, K_2CO_3	1:1:2:7:16	yes	brown	$K_x[(Cu,Mn)_2(TeO_3)_3](H_2O)_y$, $K_2Cu_2Te_4O_{11}(H_2O)_2$, $K_2Cu_3Te_6O_{16}$
H414	CuO, TeO_2, H_6TeO_6, KOH	2:1:2:15		green	$K_2Cu_2TeO_6$
H415	CuO, TeO_2, H_6TeO_6, KOH	2:1:1:10		green	$K_2Cu_2TeO_6$
H416	CuO, H_6TeO_6, KOH	2:1:10		green	$K_2Cu_2TeO_6$
H417	$CoCO_3$, TeO_2	3:2	yes		α-TeO_2, $CoCO_3$, $Co_2Te_3O_8$
H418	$CoCO_3$, TeO_2, KOH	3:2:2	yes		$CoCO_3$, $Co_2Te_3O_8$, "$Co_3(TeO_3)_2(OH)_2$", $Co_{15}(TeO_3)_{14}(OH)_2$
H419	$CoCO_3$, TeO_2, KOH	3:2:4	yes		"$Co_3(TeO_3)_2(OH)_2$", $Co_{15}(TeO_3)_{14}(OH)_2$
H420	$CoCO_3$, TeO_2, KOH	3:2:6	yes		$Co_2(TeO_3)(OH)_2$, $Co_{15}(TeO_3)_{14}(OH)_2$
H421	$CoCO_3$, TeO_2, KOH	3:2:9	yes		$Co_2(TeO_3)(OH)_2$, $Co(OH)_2$
H422	$CoCO_3$, TeO_2, KOH	3:2:12	yes		$Co(OH)_2$, $Co_2(TeO_3)(OH)_2$
H423	$Fe(NO_3)_3(H_2O)_9$, TeO_2, H_3AsO_4, NH_3	2:1:1:30+ extra H_2O	yes	brown	$Fe_2(TeO_3)_3$, H133
H424	$Fe(NO_3)_3(H_2O)_9$, TeO_2, H_3AsO_4, NH_3	2:1:1:30	yes	brown	$Fe_2(TeO_3)_3$, FeO(OH), H133
H425	$FeCl_2(H_2O)_4$, TeO_2, NH_3	2:1:exc.	yes	brown	$Fe_2(TeO_3)_3$, Fe_2O_3
H426	$FeCl_2(H_2O)_4$, TeO_2, NH_3	3:2:exc.	yes	brown	$Fe_2(TeO_3)_3$, Fe_2O_3
H427	$FeCl_2(H_2O)_4$, TeO_2, NH_3	1:1:exc.	yes	brown	$Fe_2(TeO_3)_3$, Fe_2O_3
H428	NiO, TeO_2, Na_2CO_3	2:3:10	yes	light green	NiO, $Na_2[Ni_2(TeO_3)_3](H_2O)$, $Na_2Te_4O_9(H_2O)_x$
H429	CuO, TeO_2, Na_2CO_3	2:3:10	yes	green	CuO, $Na_2[Cu_2(TeO_3)_3](H_2O)_{1.5}$, $Na_2Te_4O_9(H_2O)_x$
H430	CoO, TeO_2, Na_2CO_3	2:3:10	yes	purple	$Na_2[Co_2(TeO_3)_3](H_2O)_3$, "$Co_3(TeO_3)_2(OH)_2$", $Co_{15}(TeO_3)_{14}(OH)_2$
H431	MnO, TeO_2, Na_2CO_3	2:3:10	yes	brown	$Mn_2Te_3O_8$
H432	ZnO, TeO_2, Na_2CO_3	2:3:10	yes	white	$ZnTeO_3$
H433	CdO, TeO_2, Na_2CO_3	2:3:10	yes	white	β-$CdTeO_3$
H434	NiO, TeO_2, K_2CO_3	2:3:10	yes	light green	NiO
H435	CuO, TeO_2, K_2CO_3	2:3:10	yes	green	CuO, Cu_3TeO_6
H436	CoO, TeO_2, K_2CO_3	2:3:10	yes	purple	$Co_2(TeO_3)(OH)_2$, $Co_{15}(TeO_3)_{14}(OH)_2$
H437	MnO, TeO_2, K_2CO_3	2:3:10	yes	brown	$Mn_2Te_3O_8$
H438	ZnO, TeO_2, K_2CO_3	2:3:10	yes	white	ZnO, ??
H439	CdO, TeO_2, K_2CO_3	2:3:10	yes	white	β-$CdTeO_3$
H440	NiO, TeO_2, Rb_2CO_3	2:3:6	yes	light green	NiO
H441	CuO, TeO_2, Rb_2CO_3	2:3:6	yes	green	CuO, $CuTeO_3$
H442	CoO, TeO_2, Rb_2CO_3	2:3:6	yes	purple	$Co_{15}(TeO_3)_{14}(OH)_2$
H443	MnO, TeO_2, Rb_2CO_3	2:3:6	yes	brown	$Mn_2Te_3O_8$
H444	ZnO, TeO_2, Rb_2CO_3	2:3:6	yes	white	$ZnTeO_3$
H445	CdO, TeO_2, Rb_2CO_3	2:3:6	yes	white	β-$CdTeO_3$
H446	NiO, TeO_2, K_2CO_3	2:3:10	3 dr.	light green	NiO, $K_2Te_4O_9(H_2O)_x$, $K_2[Ni_2(TeO_3)_3](H_2O)$
H447	CuO, TeO_2, K_2CO_3	2:3:10	3 dr.	green	$K_2[Cu_2(TeO_3)_3](H_2O)_2$, $K_2Cu_3Te_4O_{12}$
H448	CoO, TeO_2, K_2CO_3	2:3:10	3 dr.	purple	$K_2[Co_2(TeO_3)_3](H_2O)_2$
H449	MnO, TeO_2, K_2CO_3	2:3:10	3 dr.	brown	MnO, $K_2Mn_2Te_3O_9(H_2O)$
H450	ZnO, TeO_2, K_2CO_3	2:3:10	3 dr.	white	ZnO, $K_2[Zn_2(TeO_3)_3](H_2O)_2$, ?
H451	CdO, TeO_2, K_2CO_3	2:3:10	3 dr.	white	β-$CdTeO_3$
H452	NiO, TeO_2, Rb_2CO_3	2:3:6	3 dr.	light green	NiO, "$Rb_2Te_4O_9(H_2O)_x$"
H453	CuO, TeO_2, Rb_2CO_3	2:3:6	3 dr.	green	$Rb_2Cu_3Te_6O_{16}$, CuO, "$Rb_2Te_4O_9(H_2O)_x$"
H454	CoO, TeO_2, Rb_2CO_3	2:3:6	3 dr.	purple	$Co_{15}(TeO_3)_{14}(OH)_2$, "$Rb_2Te_4O_9(H_2O)_x$",
H455	MnO, TeO_2, Rb_2CO_3	2:3:6	3 dr.	brown	$Rb_{1.24}[Mn_2(TeO_3)_3](H_2O)_2$, $Mn_2Te_3O_8$, MnO
H456	ZnO, TeO_2, Rb_2CO_3	2:3:6	3 dr.	white	$ZnTeO_3$, "$Rb_2Te_4O_9(H_2O)_x$"
H457	CdO, TeO_2, Rb_2CO_3	2:3:6	3 dr.	white	β-$CdTeO_3$
H458	NiO, TeO_2, Cs_2CO_3	2:3:6	3 dr.	light green	NiO, ?
H459	CuO, TeO_2, Cs_2CO_3	2:3:6	3 dr.	green	CuO, ?
H460	CoO, TeO_2, Cs_2CO_3	2:3:6	3 dr.	purple	$Co_{15}(TeO_3)_{14}(OH)_2$, ?
H461	MnO, TeO_2, Cs_2CO_3	2:3:6	3 dr.	brown	$Mn_2Te_3O_8$, $Cs[Mn_2(TeO_3)_3](H_2O)$
H462	ZnO, TeO_2, Cs_2CO_3	2:3:6	3 dr.	white	$ZnTeO_3$, amorphous
H463	CdO, TeO_2, Cs_2CO_3	2:3:6	3 dr.	white	β-$CdTeO_3$
H464	MgO, TeO_2, Na_2CO_3	2:3:10	3 dr.	white	$Na_{2-2x}Mg_x[Mg_2(TeO_3)_3](H_2O)_x$, ?

dr. = droplets; exc. = excess

8.2 Crystallographic data of single-crystal X-ray diffraction experiments

Table 68. Details on data collection and refinement of the crystal structures of $Cd_5(TeO_3)_4(NO_3)_2$, $Cd_4Te_4O_{11}(NO_3)_2$ and $Pb_3(TeO_3)_2(NO_3)_2$.

Empirical formula	$Cd_5N_2O_{18}Te_4$	$Cd_4N_2O_{17}Te_4$	$N_2O_{12}Pb_3Te_2$
Structural formula	$Cd_5(TeO_3)_4(NO_3)_2$	$Cd_4Te_4O_{11}(NO_3)_2$	$Pb_3(TeO_3)_2(NO_3)_2$
M / g·mol^{-1}	1388.42	1260.02	1096.79
Measurement temperature / °C	27	−173	20
Space group, No.	$P2_1/c$, 14	$P1$, 1	Cm, 8
a / Å	9.9442(4)	9.4304(15)	18.683(5)
b / Å	5.6173(2)	9.4301(15)	5.6720(16)
c / Å	16.6136(7)	9.6096(16)	11.907(4)
α /°		92.142(6)	
β /°	102.737(1)	108.293(6)	111.712(5)
γ /°		109.514(5)	
V / Å^3	905.19(6)	755.1(2)	1172.3(6)
Z	2	2	4
Crystal size / mm^{-3}	0.08 × 0.03 × 0.02	0.12 × 0.04 × 0.02	0.13 × 0.03 × 0.02
Crystal shape, color	bar, colorless	plank, colorless	bar, colorless
μ / mm^{-1}	12.19	13.23	47.92
Diffractometer	Bruker *APEX*-II	Bruker *APEX*-II	Bruker *APEX*-II
Radiation type	Mo-K_α	Mo-K_α	Mo-K_α
Reflections used	17368	4775	3471
ϑ_{min} – ϑ_{max} /°	2.514 – 36.204	5.3805 – 30.5235	2.339 – 24.133
h	−16 – 16	−13 – 13	−23 – 3
k	−9 – 9	−13 – 13	−7 – 7
l	−27 – 27	0 – 13	−14 – 14
Independent reflections	4388	4775	2278
Observed reflections ($I > 2s(I)$)	3381	3894	1660
R_{int}	0.050	0.058	0.054
Absorption correction	multiscan, SADABS	multiscan, SADABS	multiscan, SADABS
T_{min}, T_{max}	0.517, 0.747	0.572, 0.746	0.357, 0.562
No. of parameters	133	218	115
R1 ($F^2>2\sigma(F^2)$)	0.030	0.075	0.066
wR2(F^2 all)	0.061	0.182	0.149
GOF	0.99	1.06	1.03
Twin handling	–	two-domain integration	transformation matrix: $\bar{1}$ 0 0, 0 1 0, 0 0 $\bar{1}$
Twin fractions		0.551:0.449(2)	0.50:0.50(6)
$\Delta\rho_{max}$, $\Delta\rho_{min}$ / e·Å^{-3}	1.56, −2.37	8.68, −5.43	6.78, −4.28

Table 69. Details on data collection and refinement of the crystal structures of $Cu_2Te_4O_{12}(NH_3)(H_2O)_2$, $K_2Mn_2(TeO_3)_3$ and $K_2Cd_2(TeO_3)_3$.

Empirical formula	$Cu_2H_7NO_{14}Te_4$	$K_2Mn_2O_9Te_3$	$K_2Cd_2O_9Te_3$
Structural formula	$Cu_2Te_4O_{12}(NH_3)(H_2O)_2$	$K_2Mn_2(TeO_3)_3$	$K_2Cd_2(TeO_3)_3$
M / g·mol^{-1}	882.55	714.88	829.80
Measurement temperature / °C	27	−173	23
Space group, No.	$P1$, 1	$P2_1/c$, 14	$P2_1/c$, 14
a / Å	6.7775(2)	7.2599(11)	7.3433(13)
b / Å	6.9042(2)	11.1968(16)	11.380(2)
c / Å	7.1158(2)	15.762(2)	16.041(3)
α /°	78.0813(8)		
β /°	75.7477(9)	122.989(2)	123.062(4)
γ /°	78.5470(8)		
V / Å^3	311.91(2)	1074.7(3)	1123.4(4)
Z	1	4	4
Crystal size / mm^{-3}	0.12 × 0.04 × 0.02	0.09 × 0.04 × 0.01	0.12 × 0.05 × 0.02
Crystal shape, color	needle, light green	plate, colorless	plate, colorless
μ / mm^{-1}	12.66	11.13	12.19
Diffractometer	Bruker *APEX*-II	Bruker *APEX*-II	Bruker *APEX*-II
Radiation type	Mo-K_α	Mo-K_α	Mo-K_α
Reflections used	3173	3959	3437
ϑ_{min} – ϑ_{max} /°	3.8475 – 32.923	3.0925 – 30.6845	3.0305 – 29.116
h	−10 – 11*	−11 – 9*	−11 – 8*
k	−11 – 11*	0 – 27*	0 – 16*
l	0 – 12*	0 – 23*	0 – 22*
Independent reflections	3173	3959	3437
Observed reflections ($I > 2s(I)$)	2712	2859	2077
R_{int}	0.0376	0.0624	0.0666
Absorption correction	multiscan, SADABS	multiscan, SADABS	multiscan, SADABS
T_{min}, T_{max}	0.624, 0.747	0.622, 0.746	0.342, 0.746
No. of parameters	138	147	108
R1 ($F^2>2\sigma(F^2)$)	0.033	0.053	0.069
wR2(F^2 all)	0.087	0.122	0.155
GOF	1.03	1.18	1.04
Twin handling	two-domain-integration	two-domain integration	two-domain integration
Twin fractions	0.983:0.017(4)	0.513:0.487(7)	0.728:0.272(11)
$\Delta\rho_{max}$, $\Delta\rho_{min}$ / e·Å^{-3}	3.11, −2.47	4.22, −3.42	5.76, −4.80

* A smaller interval than measured is given for at least one reciprocal coordinate because merging of reflections was performed during absorption correction after a multi-domain integration.

Table 70. Details on data collection and refinement of the crystal structures of $K_2Cu_3Te_4O_{12}$, $Na_2Cu_3Te_4O_{12}$ (average structure each) and $K_2Cu_3Te_6O_{16}$.

Empirical formula	$Cu_3K_2O_{12}Te_4$	$Cu_3Na_2O_{12}Te_4$	$Cu_3K_2O_{16}Te_6$
Structural formula	$K_2Cu_3Te_4O_{12}$	$Na_2Cu_3Te_4O_{12}$	$K_2Cu_3Te_6O_{16}$
M / g·mol^{-1}	971.24	939.00	1290.42
Measurement temperature / °C	−173	23	−173
Space group, No.	*P*4/*ncc*, 130	*P*4/*ncc*, 130	$P2_1/c$, 14
a / Å	8.426(9)	8.2980(17)	11.9120(14)
b / Å			7.9433(10)
c / Å	6.403(6)	6.1633(12)	9.2787(11)
β /°			98.456(3)
V / Å^3	454.5(10)	424.39(19)	868.41(18)
Z	4/3	4/3	2
Crystal size / mm^{-3}	0.14 × 0.03 × 0.03	0.12 × 0.03 × 0.03	0.12 × 0.08 × 0.04
Crystal shape, color	bar, dark green	bar, dark green	block, green
μ / mm^{-1}	13.69	14.08	14.08
Diffractometer	Bruker *APEX*-II	Bruker *APEX*-II	Bruker *APEX*-II
Radiation type	Mo-K_α	Mo-K_α	Mo-K_α
Reflections used	5491	6357	19168
ϑ_{min} – ϑ_{max} /°	3.415 – 29.421	3.489 – 31.427	3.099 – 33.050
h	−12 – 12	−12 – 12	−18 – 18
k	−12 – 12	−12 – 12	−12 – 12
l	−9 – 9	−9 – 8	−14 – 14
Independent reflections	352	354	3318
Observed reflections (I > 2s(I))	328	313	2779
R_{int}	0.040	0.038	0.051
Absorption correction	multiscan, SADABS	multiscan, SADABS	multiscan, SADABS
T_{min}, T_{max}	0.606, 0.746	0.497, 0.746	0.340, 0.495
No. of parameters	36	30	124
R1 (F^2>2σ(F^2))	0.024	0.020	0.024
wR2(F^2 all)	0.048	0.038	0.049
GOF	1.31	1.13	1.03
$\Delta\rho_{max}$, $\Delta\rho_{min}$ / e·Å^{-3}	0.42, −0.84	0.76, −0.50	1.04, −1.19

Table 71. Details on data collection and refinement of the crystal structures of $K_2Cu_2Te_4O_{11}(H_2O)_2$, and two polytypes of $K_4Sn_3Te_8O_{24}$.

Empirical formula	$Cu_2K_2H_4O_{13}Te_4$	$K_4O_{24}Sn_3Te_4$	$K_4O_{24}Sn_3Te_4$
Structural formula	$K_2Cu_2Te_4O_{11}(H_2O)_2$	$K_4Sn_3Te_8O_{24}$	$K_4Sn_3Te_8O_{24}$
M / g·mol^{-1}	975.28	1917.27	1917.27
Measurement temperature / °C	−173	23	23
Space group, No.	$P2_1/c$, 14	$P3_2$, 145	$C2/c$, 15
a / Å	7.3688(14)	11.2563(16)	19.536(12)
b / Å	9.8118(19)		11.278(7)
c / Å	19.675(4)	17.816(3)	12.477(7)
β /°	96.821(6)		107.002(8)
V / Å^3	1412.5(5)	1954.9(6)	2629(3)
Z	4	3	2
Crystal size / mm^{-3}	0.11 × 0.08 × 0.01	0.18 × 0.18 × 0.01	0.19 × 0.19 × 0.02
Crystal shape, color	plate, light green	hexagonal plate, colorless	hexagonal plate, colorless
μ / mm^{-1}	11.76	12.37	12.27
Diffractometer	Bruker *APEX*-II	Bruker *APEX*-II	Bruker *APEX*-II
Radiation type	Mo-K_α	Mo-K_α	Mo-K_α
Reflections used	27724	40222	12584
ϑ_{min} – ϑ_{max} /°	2.941 – 30.354	5.538 – 27.439	3.424 – 27.568
h	−10 – 8	−17 – 17	−26 – 23
k	−14 – 14	−17 – 17	−15 – 15
l	−28 – 28	−27 – 27	−16 – 16
Independent reflections	4321	9683	3332
Observed reflections ($I > 2s(I)$)	3392	6582	2490
R_{int}	0.083	0.095	0.078
Absorption correction	multiscan, SADABS	multiscan, SADABS	multiscan, SADABS
T_{min}, T_{max}	0.554, 0.746	0.441, 0.746	0.362, 0.746
No. of parameters	190	160	108
R1 ($F^2>2\sigma(F^2)$)	0.046	0.112	0.156
wR2(F^2 all)	0.095	0.315	0.410
GOF	1.16	1.12	1.08
Twin handling	–	transformation matrix $\bar{1}$ 0 0, 1 1 0, 0 0 1 (−4)	–
Twin fractions	–	0.28(16):0.21(2): 0.22(16):0.29(2)	–
$\Delta\rho_{max}$, $\Delta\rho_{min}$ / e·Å^{-3}	2.81, −1.93	26.52, −8.03	25.02, −7.66

Table 72. Details on data collection and refinement of the crystal structures of $Na_{1.79}Mg_{0.11}[Mg_2(TeO_3)_3](H_2O)_{3.86}$, $Fe_2(TeO_3)_3$ and the improved dataset of $Rb_2Cu_3Te_6O_{16}$.

Empirical formula	$H_{7.72}Mg_{2.11}Na_{1.79}O_{12.86}Te_3$	$Fe_2O_9Te_3$	$Cu_3O_{16}Rb_2Te_6$
Structural formula	$(Na_{1.79}Mg_{0.11})[Mg_2(TeO_3)_3]$-$(H_2O)_{3.86}$	$Fe_2(TeO_3)_3$	$Rb_2Cu_3Te_6O_{16}$
M / g·mol^{-1}	688.56	638.50	1383.16
Measurement temperature / °C	−173	23	20
Space group, No.	$P6_3/m$, 176	$P6_3/m$, 176	$P2_1/c$, 14
a / Å	9.3146(3)	9.24060(10)	12.1357(4)
b / Å			7.9699(3)
c / Å	7.7232(2)	7.5924(2)	9.3323(3)
β /°			98.7680(10)(8)
V / Å^3	580.30(4)	561.45(2)	892.07(5)
Z	2	2	2
Crystal size / mm^{-3}	0.07 × 0.02 × 0.02	0.14 × 0.02 × 0.02	0.09 × 0.07 × 0.04
Crystal shape, color	bar, colorless	needle, yellow	block, green
μ / mm^{-1}	7.74	10.24	18.66
Diffractometer	STOE STADIVARI	Bruker *APEX*-II	Bruker *APEX*-II
Radiation type	Mo-K_α	Mo-K_α	Mo-K_α
Reflections used	12646	7060	17462
ϑ_{min} – ϑ_{max} /°	2.52 – 36.33	4.411 – 34.171	3.069 – 35.937
h	−15 – 6	−17 – 17	−19 – 20
k	−8 – 15	−17 – 17	−13 – 13
l	−12 – 12	−27 – 27	−15 – 15
Independent reflections	904	962	4319
Observed reflections (I > 2s(I))	756	7822	3423
R_{int}	0.045	0.057	0.042
Absorption correction	multiscan, LANA	multiscan, SADABS	multiscan, SADABS
T_{min}, T_{max}	0.413, 0.521	0.505, 0.746	0.438, 0.645
No. of parameters	53	28	125
R1 (F^2>2σ(F^2))	0.023	0.038	0.026
wR2(F^2 all)	0.055	0.085	0.049
GOF	1.03	1.11	1.01
$\Delta\rho_{max}$, $\Delta\rho_{min}$ / e·Å^{-3}	1.06, −2.32	3.13, −2.15	1.49, −1.45

Table 73. Details on data collection and refinement of the crystal structures of $Na_3FeTe_2O_9$, $K_4Mn_2Te_3O_{12}(OH)_4$ and $K_{12}Fe_6Te_4O_{27}(H_2O)_3$.

Empirical formula	$FeNa_3O_9Te_2$	$H_4K_4Mn_2O_{16}Te_3$	$Fe_6H_6K_{12}O_{30}Te_4$
Structural formula	$Na_3FeTe_2O_9$	$K_4Mn_2Te_3O_{12}(OH)_4$	$K_{12}Fe_6Te_4O_{27}(H_2O)_3$
M / g·mol^{-1}	524.02	909.11	1800.76
Measurement temperature / °C	27	0	26
Space group, No.	$R\bar{3}$, 148	$P2_1/c$, 14	$I\bar{4}3d$, 220
a / Å	5.2598(8)	8.7372(10)	14.07307(12)
b / Å		7.6256(9)	
c / Å	15.778(3)	11.2504(13)	
β /°		95.164(3)	
V / Å^3	378.02(14)	764.53(15)	3196.5(8)
Z	2	2	4
Crystal size / mm^{-3}	0.05 × 0.04 × 0.01	0.07 × 0.02 × 0.02	0.08 × 0.08 × 0.08
Crystal shape, color	plate, colorless	block, brown	cube, amber
μ / mm^{-1}	9.76	8.64	7.90
Diffractometer	STOE STADIVARI	Bruker *APEX*-II	Bruker *APEX*-II
Radiation type	Mo-K_α	Mo-K_α	Mo-K_α
Reflections used	3266	13665	10923
ϑ_{min} – ϑ_{max} /°	3.87 – 31.29	2.341 – 24.959	3.388 – 40.072
h	−4 – 7	−12 – 13	−2 – 26
k	−7 – 5	−11 – 11	−21 – 17
l	−22 – 23	−16 – 16	−12 – 25
Independent reflections	454	2583	1685
Observed reflections (I > 2s(I))	383	1819	1490
R_{int}	0.043	0.114	0.039
Absorption correction	multiscan, LANA	multiscan, SADABS	multiscan, SADABS
T_{min}, T_{max}	0.519, 0.596	0.571, 0.746	0.439, 0.570
No. of parameters	17	123	48
R1 (F^2>2σ(F^2))	0.027	0.040	0.021
wR2(F^2 all)	0.066	0.070	0.043
GOF	1.03	0.99	1.05
Twin handling	transformation matrix: 1 0 0, $\bar{1}$ $\bar{1}$ 0, 0 0 1	–	–
Twin fractions	0.540:0.460(3)	–	–
$\Delta\rho_{max}$, $\Delta\rho_{min}$ / e·Å^{-3}	1.64, −1.30	1.45, −1.49	0.67, −0.82

Table 74. Details on data collection and refinement of the crystal structures of $K_3FeTe_2O_8(OH)_2(H_2O)$, $K_{10}Cu_2Te_3O_{16}$ and $K_5CuTe_2O_8(OH)_4(H_2O)_8$.

Empirical formula	$H_4FeK_3O_{11}Te_2$	$Cu_2K_{10}O_{16}Te_3$	$CuH_{20}K_5O_{20}Te_2$
Structural formula	$K_3FeTe_2O_8(OH)_2(H_2O)$	$K_{10}Cu_2Te_3O_{16}$	$K_5CuTe_2O_8(OH)_4(H_2O)_8$
M / g·mol^{-1}	608.39	1156.88	854.44
Measurement temperature / °C	23	0	−173
Space group, No.	$P\bar{1}$, 2	$C2/c$, 15	$Pna2_1$, 33
a / Å	7.435(6)	6.2482(10)	11.2034(17)
b / Å	7.496(6)	11.4304(18)	8.3541(14)
c / Å	11.533(9)	30.127(5)	21.302(4)
α /°	83.980(10)		
β /°	74.582(9)	90.992(3)	
γ /°	62.229(9)		
V / Å^3	548.2(7)	2151.3(6)	2036.7(6)
Z	2	4	4
Crystal size / mm^{-3}	0.07 × 0.06 × 0.02	0.11 × 0.10 × 0.08	0.18 × 0.02 × 0.02
Crystal shape, color	plate, colorless	block, blue	needle, orange
μ / mm^{-1}	7.78	7.97	4.99
Diffractometer	Bruker *APEX*-II	Bruker *APEX*-II	Bruker *APEX*-II
Radiation type	Mo-K_α	Mo-K_α	Mo-K_α
Reflections used	3336*	41494	19618
ϑ_{min} – ϑ_{max} /°	3.187 – 26.007	2.707 – 40.232	3.640 – 19.598
h	−10 – 10*	−11 – 11	−12 – 14
k	−10 – 10*	−20 – 20	−10 – 10
l	−0 – 16*	−54 – 54	−26 – 26
Independent reflections	3336	6747	4117
Observed reflections ($I > 2s(I)$)	2464	5998	2618
R_{int}	0.057	0.030	0.178
Absorption correction	multiscan, SADABS	multiscan, SADABS	multiscan, SADABS
T_{min}, T_{max}	0.489, 0.746	0.634, 0.748	0.523, 0.745
No. of parameters	155	142	253
R1 ($F^2>2\sigma(F^2)$)	0.076	0.020	0.067
wR2(F^2 all)	0.168	0.037	0.159
GOF	1.11	1.04	1.01
Twin handling	two-domain integration	–	–
Twin fractions	0.791:0.209(2)	–	–
$\Delta\rho_{max}$, $\Delta\rho_{min}$ / e·Å^{-3}	3.28, −2.28	1.43, −1.22	1.28, −1.19

* A smaller interval than measured is given for at least one reciprocal coordinate because merging of reflections was performed during absorption correction after a multi-domain integration.

Table 75. Details on data collection and refinement of the crystal structures of $K_3CuTeO_5(OH)(H_2O)$, $K_2Cu_2TeO_6$ and $K_2Cu_2TeO_6(H_2O)$.

Empirical formula	$CuH_3K_3O_7Te$	$Cu_2K_2O_6Te$	$Cu_2H_2K_2O_7Te$
Structural formula	$K_3CuTeO_5(OH)(H_2O)$	$K_2Cu_2TeO_6$	$K_2Cu_2TeO_6(H_2O)$
M / g·mol^{-1}	423.46	428.88	446.90
Measurement temperature / °C	−173	26	20
Space group, No.	$P2_1/c$, 14	$P2_1/c$, 14	$Cmcm$, 63
a / Å	6.4669(7)	6.4096(3)	8.7405(4)
b / Å	12.2103(13)	9.2386(4)	5.8193(3)
c / Å	10.1932(11)	5.2840(2)	12.7618(6)
β /°	101.481(3)	104.7060(10)	
V / Å^3	788.78(15)	302.65(2)	649.11(5)
Z	4	2	4
Crystal size / mm^{-3}	0.12 × 0.08 × 0.07	0.09 × 0.06 × 0.02	0.14 × 0.08 × 0.03
Crystal shape, color	block, blue	plate, green	plate, green
μ / mm^{-1}	7.97	13.10	12.23
Diffractometer	Bruker *APEX*-II	Bruker *APEX*-II	Bruker *APEX*-II
Radiation type	Mo-K_α	Mo-K_α	Mo-K_α
Reflections used	60672	9420	5690
ϑ_{min} – ϑ_{max} /°	3.215 – 45.062	3.288 – 36.279	3.193 – 39.919
h	−12 – 12	−10 – 10	−10 – 15
k	−24 – 24	−15 – 15	−10 – 10
l	−20 – 20	−8 – 8	−23 – 11
Independent reflections	6604	1470	1110
Observed reflections ($I > 2s(I)$)	5802	1252	976
R_{int}	0.049	0.046	0.033
Absorption correction	multiscan, SADABS	multiscan, SADABS	multiscan, SADABS
T_{min}, T_{max}	0.441, 0.573	0.436, 0.5676	0.372, 0.651
No. of parameters	121	52	38
R1 ($F^2>2\sigma(F^2)$)	0.016	0.027	0.024
wR2(F^2 all)	0.031	0.058	0.062
GOF	1.05	1.04	1.07
$\Delta\rho_{max}$, $\Delta\rho_{min}$ / e·Å^{-3}	0.63, −1.38	1.94, −1.39	2.06, −2.45

Table 76. Details on data collection and refinement of the crystal structures of $K_2Cu_2TeO_6(H_2O)_4$, *α*-$KCuTeO_4(OH)$ and *β*-$KCuTeO_4(OH)$.

Empirical formula	$Cu_2H_8K_2O_{10}Te$	$CuKHO_5Te$	$CuKHO_5Te$
Structural formula	$K_2Cu_2TeO_6(H_2O)_4$	$KCuTeO_4(OH)$	$KCuTeO_4(OH)$
M / g·mol^{-1}	500.96	311.25	311.25
Measurement temperature / °C	23	20	23
Space group, No.	$P2_1/c$, 14	$P\bar{1}$, 2	$P2_1/c$, 14
a / Å	9.810(11)	8.7693(7)	7.3945(3)
b / Å	9.400(10)	11.4715(9)	11.6097(5)
c / Å	10.654(12)	5.4687(4)	5.4024(3)
α /°		90.494(2)	
β /°	106.949(19)	80.9620(10)	105.2580(10)
γ /°		124.3240(10)	
V / Å^3	939.7(18)	446.53(6)	447.44(4)
Z	4	4	4
Crystal size / mm^{-3}	0.11 × 0.06 × 0.02	0.12 × 0.09 × 0.03	0.12 × 0.08 × 0.04
Crystal shape, color	plate, green	plate, blue green	plate, blue green
μ / mm^{-1}	8.49	12.14	12.12
Diffractometer	Bruker *APEX*-II	Bruker *APEX*-II	Bruker *APEX*-II
Radiation type	Mo-K_α	Mo-K_α	Mo-K_α
Reflections used	2695*	11548	19371
ϑ_{min} – ϑ_{max} /°	3.095 – 30.558	2.862 – 37.754	2.856 – 40.200
h	−13 – 13*	−14 – 15	−13 – 13
k	0 – 13*	−19 – 19	−21 – 21
l	0 – 15*	−9 – 9	−9 – 9
Independent reflections	2695	4786	2816
Observed reflections (I > 2s(I))	2200	3713	2533
R_{int}	0.053	0.037	0.035
Absorption correction	multiscan, SADABS	multiscan, SADABS	multiscan, SADABS
T_{min}, T_{max}	0.429, 0.648	0.491, 0.650	0.433, 0.570
No. of parameters	87	151	78
R1 (F^2>2σ(F^2))	0.073	0.034	0.017
wR2(F^2 all)	0.209	0.070	0.035
GOF	1.06	1.00	1.06
Twin handling	two-domain integration	–	–
Twin fractions	0.543:0.457(4)	–	–
$\Delta\rho_{max}$, $\Delta\rho_{min}$ / e·Å^{-3}	5.21, −4.86	4.00, −1.67	1.28, −1.22

* A smaller interval than measured is given for at least one reciprocal coordinate because merging of reflections was performed during absorption correction after a multi-domain integration.

Table 77. Details on data collection and refinement of the crystal structures of $K_3Cu_2TeO_5(OH)(CO_3)(H_2O)$, $K_4CuTe_4O_{14}(OH)_2$ and $K_6Cu_9Te_4O_{24}(H_2O)_2$.

Empirical formula	$CCu_2H_3K_3O_{10}Te$	$CuH_2K_4O_{16}Te_4$	$Cu_9H_4K_6O_{26}Te_4$
Structural formula	$K_3Cu_2TeO_5(OH)(CO_3)(H_2O)$	$K_4CuTe_4O_{14}(OH)_2$	$K_6Cu_9Te_4O_{24}(H_2O)_2$
M / g·mol^{-1}	547.01	988.36	1736.89
Measurement temperature / °C	−173	23	23
Space group, No.	$P2_1/c$, 14	$C2/m$, 12	$Pmn2_1$, 31
a / Å	10.3104(17)	13.4741(11)	12.6695(13)
b / Å	9.2675(16)	7.2275(6)	10.5976(11)
c / Å	10.5652(18)	7.6060(6)	9.2512(11)
β /°	93.024(6)	101.837(3)	
V / Å^3	1008.1(3)	724.95(10)	1242.1(2)
Z	4	2	2
Crystal size / mm^{-3}	0.11 × 0.08 × 0.02	0.08 × 0.03 × 0.02	0.13 × 0.11 × 0.02
Crystal shape, color	plate, green	plate, green	plate, green
μ / mm^{-1}	8.34	10.63	13.27
Diffractometer	Bruker *APEX*-II	Bruker *APEX*-II	Bruker *APEX*-II
Radiation type	Mo-K_α	Mo-K_α	Mo-K_α
Reflections used	14211	4650	2544*
ϑ_{min} – ϑ_{max} /°	3.958 – 29.002	2.738 – 28.227	2.726 – 29.003
h	−13 – 14	−17 – 17	0 – 18*
k	−13 – 13	−9 – 9	0 – 15*
l	−15 – 15	−9 – 10	0 – 13*
Independent reflections	3090	968	2544
Observed reflections ($I > 2s(I)$)	1948	728	1950
R_{int}	0.097	0.050	0.057
Absorption correction	multiscan, SADABS	multiscan, SADABS	multiscan, SADABS
T_{min}, T_{max}	0.627, 0.746	0.620, 0.746	0.510, 0.746
No. of parameters	154	68	156
R1 ($F^2>2\sigma(F^2)$)	0.056	0.028	0.044
wR2(F^2 all)	0.129	0.057	0.094
GOF	1.01	1.00	1.01
Twin handling	–	–	two-domain integration
Twin fractions	–	–	0.731:0.269(4)
$\Delta\rho_{max}$, $\Delta\rho_{min}$ / e·Å^{-3}	2.66, −1.29	0.89, −1.24	1.28, −1.22

* A smaller interval than measured is given for at least one reciprocal coordinate because merging of reflections was performed during absorption correction after a multi-domain integration.

Table 78. Details on data collection and refinement of the crystal structures of $KPb_2TeO_5(OH)$, $K_2Pb_3TeO_7$ and $K_{14}Pb_{10}Te_7O_{36}(OH)_6(H_2O)_6$.

Empirical formula	HKO_6Pb_2Te	$K_2O_7Pb_3Te$	$H_{18}K_{14}O_{48}Pb_{10}Te_7$
Structural formula	$KPb_2TeO_5(OH)$	$K_2Pb_3TeO_7$	$K_{14}Pb_{10}Te_7O_{36}(OH)_6(H_2O)_6$
M / g·mol^{-1}	678.09	939.37	1755.07
Measurement temperature / °C	−173	20	20
Space group, No.	*Cc*, 9	$P6_3/m$, 176	$P\bar{6}2m$, 189
a / Å	11.7017(4)	6.85330(10)	10.2304(2)
b / Å	19.6111 (6)		
c / Å	11.4303(3)	11.04340(10)	14.6263(3)
β /°	90.960(2)		
V / Å^3	2622.69(14)	449.190(10)	1325.71(6)
Z	16	2	1
Crystal size / mm^{-3}	0.04 × 0.03 × 0.01	0.11 × 0.07 × 0.03	0.09 × 0.06 × 0.02
Crystal shape, color	trigonal plate, colorless	block, colorless	plate, colorless
μ / mm^{-1}	56.25	60.19	36.68
Diffractometer	STOE STADIVARI	Bruker *APEX*-II	STOE STADIVARI
Radiation type	Mo-K_α	Mo-K_α	Mo-K_α
Reflections used	67358	14923	35605
ϑ_{min} – ϑ_{max} /°	3.57 – 36.83	3.433 – 44.981	2.69 – 38.90
h	−19 – 17	−12 – 13	−17 – 9
k	−32 – 32	−13 – 13	−10 – 17
l	−16 – 19	−21 – 22	−25 – 25
Independent reflections	10534	1308	2746
Observed reflections (I > 2s(I))	4868	1115	2671
R_{int}	0.056	0.049	0.060
Absorption correction	multiscan, LANA	multiscan, SADABS	multiscan, LANA
T_{min}, T_{max}	0.186, 0.266	0.444, 0.749	0.010, 0.020
No. of parameters	243	24	84
R1 (F^2>2σ(F^2))	0.025	0.019	0.030
wR2(F^2 all)	0.041	0.036	0.090
GOF	0.76	1.09	1.07
Twin handling	inversion twin	–	–
Twin fractions	0.536:0.464(8)	–	–
$\Delta\rho_{max}$, $\Delta\rho_{min}$ / e·Å^{-3}	1.96, −1.73	2.12, −2.95	7.66, −4.92

Table 79. Details on data collection and refinement of the crystal structures of $K_6Bi_4Te_3O_{17}(CO_3)(H_2O)_3$, $RbPb_3Te_2O_9(OH)$ and $Cd_4Te_5O_{14}$.

Empirical formula	$Bi_4CH_6K_6O_{23}Te_3$	$HO_{10}Pb_3RbTe_2$	$Cd_4O_{14}Te_5$
Structural formula	$K_6Bi_4Te_3O_{17}(CO_3)(H_2O)_3$	$RbPb_3Te_2O_9(OH)$	$Cd_4Te_5O_{14}$
M / g·mol^{-1}	1839.39	1123.25	1311.60
Measurement temperature / °C	20	−3	23
Space group, No.	$C2/m$, 12	$P\bar{1}$, 2	$C2/c$, 15
a / Å	17.5046(5)	7.3829(2)	11.9074(3)
b / Å	15.2624(3)	7.4064(2)	14.3289(3)
c / Å	8.7214(3)	10.0999(3)	8.7169(2)
α /°		103.588(2)	
β /°	90.000(3)	100.045(2)	113.6290(10)
γ /°		94.172(2)	
V / Å^3	2330.03(11)	524.84(3)	1362.58(6)
Z	12	2	4
Crystal size / mm^{-3}	0.10 × 0.05 × 0.02	0.09 × 0.05 × 0.02	0.09 × 0.07 × 0.06
Crystal shape, color	elongated hexagon, colorless	plate, colorless	shard, colorless
μ / mm^{-1}	34.93	58.09	16.73
Diffractometer	STOE STADIVARI	STOE STADIVARI	Bruker *APEX*-II
Radiation type	Mo-K_α	Mo-K_α	Mo-K_α
Reflections used	16328	25030	18799
ϑ_{min} – ϑ_{max} /°	2.67 – 36.75	2.82 – 36.63	2.347 – 36.599
h	−26 – 25	−12 – 12	−19 – 19
k	−12 – 23	−7 – 12	−23 – 23
l	−13 – 11	−16 – 16	−14 – 14
Independent reflections	4301	4998	3373
Observed reflections ($I > 2s(I)$)	3738	4352	3084
R_{int}	0.049	0.034	0.027
Absorption correction	multiscan, LANA	multiscan, LANA	multiscan, SADABS
T_{min}, T_{max}	0.028, 0.054	0.040, 0.077	0.595, 0.747
No. of parameters	118	149	106
R1 ($F^2>2\sigma(F^2)$)	0.048	0.021	0.022
wR2(F^2 all)	0.135	0.048	0.040
GOF	1.11	0.99	1.21
$\Delta\rho_{max}$, $\Delta\rho_{min}$ / e·Å^{-3}	5.77, −5.64	2.57, −1.84	1.10, −1.52

Table 80. Details on data collection and refinement of the crystal structures of $K_2Te_4O_9(H_2O)_3$, $Na_2Te_4O_9(H_2O)_{10}$ and $KCoPtO_4$.

Empirical formula	$H_6K_2O_{12}Te_4$	$H_{20}Na_2O_{19}Te_4$	$CoKO_4Pt$
Structural formula	$K_2Te_4O_9(H_2O)_3$	$Na_2Te_4O_9(H_2O)_{10}$	$KCoPtO_4$
M / g·mol^{-1}	786.66	880.58	357.12
Measurement temperature / °C	23	−173	23
Space group, No.	*P*31*c*, 159	$P\bar{1}$, 2	$P6_3/mmc$, 194
a / Å	10.7416(12)	15.8738(8)	2.9870(3)
b / Å		18.6481(9)	
c / Å	13.358(2)	21.1802(10)	13.7044(14)
α /°		90.4760(10)	
β /°		123.1820(10)	
γ /°		125.0530(10)	
V / Å^3	1334.8(4)	3789.4(3)	105.89(2)
Z	4	8	1
Crystal size / mm^{-3}	0.11 × 0.07 × 0.02	0.15 × 0.11 × 0.02	0.07 × 0.07 × 0.02
Crystal shape, color	plate, colorless	plate, colorless	block, black
μ / mm^{-1}	9.33	6.23	37.77
Diffractometer	Bruker *APEX*-II	Bruker *APEX*-II	Bruker *APEX*-II
Radiation type	Mo-K_α	Mo-K_α	Mo-K_α
Reflections used	21033	100860	1032
ϑ_{min} – ϑ_{max} /°	3.756 – 26.598	3.3525 – 35.407	2.972 – 31.595
h	−14 – 15	−26 – 25	−4 – 3
k	−15 – 15	−29 – 30	−1 – 4
l	−19 – 19	−32 – 34	−20 – 19
Independent reflections	2734	33111	101
Observed reflections (I > 2s(I))	2040	18850	83
R_{int}	0.061	0.036	0.031
Absorption correction	multiscan, SADABS	multiscan, SADABS	multiscan, SADABS
T_{min}, T_{max}	0.615, 0.746	0.494, 0.747	0.426, 0.746
No. of parameters	73	901	10
R1 (F^2>2σ(F^2))	0.038	0.037	0.036
wR2(F^2 all)	0.096	0.111	0.087
GOF	1.00	1.01	1.36
Twin handling	transformation matrix $\bar{1}$ 0 0, 1 1 0, 0 0 1	–	–
Twin fractions	0.501:0.499(2)	–	–
$\Delta\rho_{max}$, $\Delta\rho_{min}$ / e·Å^{-3}	2.58, −0.92	4.73, −2.93	1.86, −1.88

Table 81. Details on data collection and refinement of the crystal structures of high- and low-temperature $RbTeO_3(OH)$, and $(NH_4)Ni_3(HAsO_4)(AsO_4)(OH)_2$.

Empirical formula	HO_4RbTe	HO_4RbTe	$As_2H_7NNi_3O_{10}$
Structural formula	$RbTeO_3(OH)$	$RbTeO_3(OH)$	$(NH_4)Ni_3(HAsO_4)$-$(AsO_4)(OH)_2$
M / g·mol^{-1}	278.08	278.08	507.04
Measurement temperature / °C	20	−173	23
Space group, No.	$P\bar{1}$, 2	$P\bar{1}$, 2	$C2/m$, 12
a / Å	5.150(2)	5.1302(16)	10.1908(16)
b / Å	6.826(3)	6.786(2)	5.9113(8)
c / Å	6.979(3)	11.564(4)	7.7148(11)
α /°	115.866(14)	92.763(9)	
β /°	109.812(14)	90.818(9)	112.702(11)
γ /°	92.375(14)	92.444(9)	
V / Å^3	202.45(16)	401.7(2)	428.74(11)
Z	2	4	2
Crystal size / mm^{-3}	0.12 × 0.02 × 0.01	0.12 × 0.02 × 0.01	0.05 × 0.04 × 0.03
Crystal shape, color	needle, colorless	needle, colorless	block, green
μ / mm^{-1}	19.16	19.31	14.23
Diffractometer	Bruker *APEX*-II	Bruker *APEX*-II	STOE STADIVARI
Radiation type	Mo-K_α	Mo-K_α	Mo-K_α
Reflections used	8847	19448	6342
ϑ_{min} – ϑ_{max} /°	3.403 – 35.402	3.4125 – 38.279	2.86 – 35.97
h	−8 – 8	−8 – 8	−14 – 16
k	−11 – 11	−11 – 11	−9 – 9
l	−11 – 11	−20 – 20	−12 – 4
Independent reflections	1966	4407	1002
Observed reflections ($I > 2s(I)$)	1739	2807	897
R_{int}	0.040	0.070	0.053
Absorption correction	multiscan, SADABS	multiscan, SADABS	multiscan, LANA
T_{min}, T_{max}	0.464, 0.747	0.440, 0.748	0.491, 0.653
No. of parameters	55	115	52
R1 ($F^2>2\sigma(F^2)$)	0.023	0.039	0.050
wR2(F^2 all)	0.051	0.097	0.132
GOF	1.06	0.99	1.19
$\Delta\rho_{max}$, $\Delta\rho_{min}$ / e·Å^{-3}	0.92, −1.64	1.70, −3.37	3.47, −1.57

Table 82. Details on data collection and refinement of the crystal structures of $Cd_2(PO_4)(OH)$, $Cd_5(PO_4)_2(OH)_2$ and $K_6[Zn(CO_3)_4]$.

Empirical formula	Cd_2HO_5P	$Cd_5H_2O_{10}P_2$	$C_4K_6O_{12}Zn$
Structural formula	$Cd_2(PO_4)(OH)$	$Cd_5(PO_4)_2(OH)_2$	$K_6[Zn(CO_3)_4]$
M / g·mol^{-1}	336.78	819.97	540.01
Measurement temperature / °C	23	−173	23
Space group, No.	*C*2/*c*, 15	$P2_12_12_1$, 19	*C*2/*c*, 15
a / Å	13.7519(13)	5.8901(4)	7.1850(6)
b / Å	6.6910(6)	9.3455(6)	18.1117(14)
c / Å	10.7087(10)	18.7423(13)	10.5206(8)
β /°	120.451(3)		93.579(2)
V / Å^3	849.43(14)	1031.69(12)	1366.40(19)
Z	8	4	4
Crystal size / mm^{-3}	0.10 × 0.08 × 0.05	0.11 × 0.07 × 0.04	0.08 × 0.04 × 0.02
Crystal shape, color	block, colorless	block, colorless	block, colorless
μ / mm^{-1}	10.30	10.51	3.69
Diffractometer	Bruker *APEX*-II	Bruker *APEX*-II	Bruker *APEX*-II
Radiation type	Mo-K_α	Mo-K_α	Mo-K_α
Reflections used	7833	10057	8980
ϑ_{min} – ϑ_{max} /°	3.437 – 25.790	3.927 – 33.559	4.528 – 29.347
h	−20 – 20	−9 – 9	−11 – 11
k	−9 – 9	−11 – 14	−26 – 27
l	−15 – 15	−30 – 28	−15 – 16
Independent reflections	1477	4493	2592
Observed reflections (I > 2s(I))	1026	3588	1712
R_{int}	0.065	0.051	0.056
Absorption correction	multiscan, SADABS	multiscan, SADABS	multiscan, SADABS
T_{min}, T_{max}	0.600, 0.746	0.517, 0.747	0.665, 0.747
No. of parameters	80	184	106
R1 (F^2>2σ(F^2))	0.046	0.038	0.040
wR2(F^2 all)	0.099	0.057	0.072
GOF	1.04	0.96	0.98
$\Delta\rho_{max}$, $\Delta\rho_{min}$ / e·Å^{-3}	2.78, −3.64	1.53, −1.78	1.02, −0.63